INTERFACIAL STRESS ANALYSIS AND STRENGTH PREDICTION OF PLATED RC BEAMS

by Jian Yang

Submitted in accordance with the requirements for the degree of PhD

The University of Leeds, The School of Civil Engineering

May 2005

The candidate confirms that the work submitted is his own and that appropriate credit has been given where reference has been made to the work of others.

ACKNOWLEDGEMENTS

The author wishes to express his sincerest gratitude to all those who have assisted both directly, and indirectly during the course of this research, by the sharing of their knowledge, opinions and experiences and for their patience and encouragement.

Special thanks go to Dr. J. Ye of the University of Leeds and Professor R.N. Swamy of the University of Sheffield for their supervisions and constant enthusiasms. To Professor J. G. Teng of The Hong Kong Polytechnic University, Dr. J. F. Chen of the University of Edinburgh for their invaluable help in my research work.

Thanks go to ORS, the University of Leeds, the School of Civil Engineering for funding my Ph.D study. I am also grateful to Ms. D. Carr, the Postgraduate Research Secretary of the School of Civil Engineering for all the help.

Last but not least, sincerest thanks go to my wife Yi and my parents, without whose continued support and encouragement, this work would never have been completed.

ABSTRACT

Strengthening of reinforced concrete (RC) beams by external plate bonding (EPB) technique has become very popular for the last two decades, especially in the past few years with the increasing applications of the advanced composites. Unlike the unstrengthened beams, the composite structure shows an undesirable failure of plate debonding. It has been well recognized that central to this failure mode is the stress concentration at the plate end. It is prerequisite to well understand the stress characteristics at this zone. This thesis reports a systematic investigation on the stress distribution at the interface between the concrete and the bonded plate and the prediction of the failure loads using the obtained stresses.

A Finite Element Analysis (FEA) based on elastic fracture mechanics is carried out first to provide a detailed study on the stress fields near the plate ends. This becomes the benchmark for the analytic solutions presented in the following chapters. A completed analytical solution is developed by the principle of complementary energy and provides consistent results with the FEA with less computational efforts. A closed-form rigorous solution is proposed such that a spreadsheet package is sufficient to obtain the numerical results. This rigorous solution provides the basis to further develop a simplified solution of the interfacial stresses that are subsequently used to develop the strength models.

To consider the nonlinear properties of concrete a detailed nonlinear FEA simulation is conducted in the thesis and extensive results are computed at various load levels, from the elastic state to the ultimate state. In addition, a Nonlinear Fracture Mechanics (NLFM) method is developed taking into account the pre- and post-cracking behaviors and the interactions between the shear and transverse normal stresses. This solution is able to predict the load level at the onset of plate end cracking (serviceability load) and that at the ultimate failure state (ultimate load).

Finally some of the proposed solutions are applied to selected beams whose test results are available for comparison. In combination with existing material failure criteria, the elastic simplified solutions are also used to predict serviceability loads. Two

groups of serviceability loads predicted from the elastic solution and NLFM solution, respectively, and one group of ultimate load predicted from NLFM solution are all compared with the experimental data. Encouraging correlations are achieved. Other useful results, such as development length, the size of Fracture Process Zone (FPZ) are also calculated.

Before concluding the work, a series of parametric analyses are carried out to assess the impact of various parameters on the interfacial stress fields, which provides some fundamental information related to design of the strengthening scheme.

TABLE OF CONTENTS

INDEX OF FIGURES

INDEX OF TABLES

CHAPTER 1.

INTRODUCTION AND LITERATURE REVIEW

1.1 Introduction

As a nation's infrastructure ages, one of the major challenges to face the construction industry is that the number of deficient structures continues to grow. The deficiency is usually the result of insufficient reinforcement, structural damage (such as vehicular impact or fire damage), reinforcement corrosion, freeze-thaw action, poor concrete quality or insufficient capacity as a result of change of use. This can manifest itself by poor performances under service loading, in the form of excessive deflection and cracking, or inadequate ultimate strength. Also, revisions in structural design and loading codes may render many structures, previously thought to be satisfactory, non-compliant with current provisions. Under such circumstances, there are two possible solutions, i.e. demolish and rebuild or carry out a program of strengthening. The choice between these alternatives depends on many important factors, such as basic material and labour costs, time during which the structures are out of commission, and disruption of other facilities. In the present economic climate, rehabilitation of deficient or damaged concrete structures to meet the more stringent limits of serviceability and ultimate strength in current codes, and strengthening of existing concrete structures to carry higher permissible loads, seem to be a more attractive alternative to demolishing and rebuilding. The term 'rehabilitation', which implies the addition of structural components after initial construction, captures three operations, i.e. repairing, strengthening and retrofitting (Seible 2001). "Strengthening" is used in this thesis as a generic term to describe all operations.

1.1.1 What is External Plate Bonding (EPB)

Different techniques have been developed to strengthen a variety of structural deficiencies. Among them, some common ones are: introducing extra supports, adding extra reinforcement by subsequently removing and casting concrete, applying additional internal or external pre-stressing, replacing non-structural toppings by structural toppings and externally bonding steel or fiber-reinforced plastic (FRP) plates/sheets.

Application of the techniques of external plate bonding (EPB) using steel plates or FRP laminates to many real structures has shown that it is structurally sound and economically efficient and it offers a technically smart solution to the pressing problem.

External steel plate bonding is featured in being quick, causing minimal site disruption and producing only minimal change in section size. However, several problems have been encountered with the steel material, including the difficulty in handling heavy steel plates, corrosion of the steel, the need for massive and expensive false work to hold plates in position during adhesive curing, the need to prepare the steel surface for bonding and the need for butt joint systems as a result of limited workable lengths.

Non-metallic FRP materials in form of thin laminates or fabrics would appear to offer an ideal alternative to steel plates. Their beneficial characteristics include high strength-to-weight and stiffness-to-weight ratios, high corrosion resistance, electromagnetic neutrality, inherent tailorability, ease of application and the lower whole-life cost. FRP materials have mechanical and physical properties superior to those of steel, particularly with respect to their tensile and fatigue strengths and these qualities are observed under a wide range of temperatures. The main material types, which find uses as reinforcing fibers in FRP, are glass, carbon and aramid (Roastasy et al 1992). GFRP is known to have a lower elastic modulus than steel but is economically very attractive. CFRP is costly but can have an elastic modulus comparable with that of steel, and an ultimate strength, which can be as much as five times that of steel. In general, FRP is linearly elastic up to failure, and the ultimate failure strain is much higher than the yield strain of steel -- these two very important material characteristics, which have serious implications in the overall load response of the strengthened composite structure and the optimum use of the plate material. The main disadvantages in using these materials are high material cost (on a weight basis and compared with steel) and possible brittle failure modes. Moreover, some FRP materials, e.g. carbon and aramid, have incompatible thermal expansion coefficients with concrete. Finally, their exposure to high temperatures (e.g. in case of fire) may cause premature degradation and collapse -- some epoxy resins start softening at about 45-70°C (fib TG 9.3 'EBR' 2001).

1.1.2 The Features of EPB

Quite a few works on the application of EPB to reinforced concrete (RC) beams has highlighted a number of features of the technique, among which are:

1. Full composite action and structural integrity can be achieved between a concrete member and a bonded steel/FRP plate by the use of suitable epoxy glue (Swamy et al. 1987, Teng et al. 2001).
2. The range of elastic behaviour has been increased due to the reduced tensile strains (Ritchie et al. 1991).
3. A corresponding increase in serviceability load is obtained as the result of the delay of the appearance of the first visual cracks (Saadatmanesh and Ehsani 1991).
4. Plating has a considerable reducing effect on both flexural crack widths and deflections. The reductions are greater than that would be achieved by introducing additional internal reinforcement equivalent to that of the external plate (Jones et al. 1986, Meier and Kaiser 1991).
5. If some procedures are taken to maintain the composite action between the concrete beam and external plate for loads up to failure, the ultimate strength can be enhanced and be accurately predicted by using conventional RC beam theory (Quantrill et al. 1996a).
6. Suitable anchorage can be used to ensure ductility of the bonded structure at least as good as the un-plated one (Jones et al. 1988).
7. The method is equally effective in strengthening both precracked and uncracked beams (Swamy et al 1989).

However, the ultimate failure in many cases is catastrophic with little or no ductility, which is caused by the debonding of the FRP plate and leaves a considerable amount of the load-bearing capacity of the FRP plate unutilized.

1.1.3 The Evolution of EPB

1.1.3.1 *Bonded with Steel Plate*

Investigations into the performance of members strengthened by bonding with steel plates can be traced back into the late 1960's (L'hermite et al. 1967, Lerchental 1967 and Kajfasz, 1967) and it was investigated extensively from the early 1980's. Mac-

Donald and Calder (1982) studied the structure behaviour of concrete beams externally bonded with steel plates and the results showed that full composite action was provided by the adhesive and that significant improvements in performance could be achieved in terms of ultimate load, crack control and stiffness. Swamy et al. (1987) investigated the effect of glued steel plates on the first cracking load, cracking behavior, deformation, serviceability and ultimate strength of reinforced concrete beams. The results suggested that the addition of glued steel plates to a reinforced concrete beam could substantially increase the flexural stiffness, reduce cracking and structural deformations at all load levels and contribute to the ultimate flexural capacity. The net effect of the reduced structural deformations was that the serviceability loads were substantially increased by the stiffening action of the glued plates. Lapped plates, precracking prior to plating, variable glue thickness, and the presence of stress concentrations in the adhesive had no adverse effect on the structural behavior of the plated beams. Swamy et al. (1989) conducted a testing program to investigate the applicability of the steel plate bonding technique to strengthen structurally damaged RC beams. Three groups of strengthened beams, which were subjected to preloading conditions of 70, 50 and 30 percent of their flexural strength, were tested respectively. It was shown that strengthening significantly cracked beams by steel-plate bonding was structurally efficient and that the plated beams were restored to flexural stiffness and strength superior to that of the original unplated beams.

1.1.3.2 *Bonded with FRP Plate/Sheet (CFRP, GFRP and AFRP)*

The use of FRP plates, mainly carbon (CFRP), glass (GFRP) and aramid (AFRP), to replace steel in the strengthening applications was pioneered at the Swiss Federal Laboratory for Materials Testing and Research (EMPA) in Dubendorf (see Meier 1987, Kaiser 1989, Meier and Kaiser 1991, Meier et al 1992 and Meier 1995). Extensive research in this area has been carrying out all over the world since then. We can hardly keep pace with the exponential growth of all the related papers appearing in both journals and conference proceedings. Early review papers on this topic include Faza and GangaRao (1994), Swamy and Mukhopadhyaya (1995) and Garden (1997). Many research projects, e.g. ROBUST in the UK (Hollaway and Leeming 1999), have been conducted and several FRP systems for strengthening (e.g. Sika) have become commercially available. Recently Teng et al. (2001a) systematically provide a state-

of-the-art summary of the existing research on FRP strengthening of RC structures, with the emphasis on structural behavior and strength models. A number of comments and findings have been demonstrated from the literatures, not only in terms of the improvement in structural strength and stiffness with the flexural failure modes similar to the conventional RC beams, but also in terms of the undesirable premature failure modes, i.e. debonding failure modes, which occurs far before the strengthened RC beam develops its full strength. The latter failure mode is more critical and thus forms the focus of this thesis. Extensive literature reviews on this topic will be presented in more details in the following section. Recently, some guidelines with regard to FRP strengthening have been drafted or are being developed in various areas, e.g. U.S.A. (2001), Europe (2001), Japan (1999, 2001), U.K (2000), Sweden (1999), France (2001).

1.1.3.3 *Field Applications*

The applications of the EPB technique to buildings and bridges started with the steel plate bonding, like the corresponding researches. The first recorded case was in Durban, South Africa, in 1964, where epoxy-bonded steel plates were used to strengthen concrete beams in an apartment complex (see Dussek 1980), where part of the reinforcing steel in the building had been accidentally omitted during construction. Dussek (1980) also reported that four bridges at Swanley and Kent in England were strengthened by plating in 1975 and 1977, respectively, where inadequate tension reinforcement had originally been provided. Among them, other application cases include the application in Belgium (see Van Germent 1981), France (see Bresson 1971, 1972), Japan (see Iino and Otokawa 1981), Poland (see Ryback 1981), Switzerland (see Hugenschmidt 1976 and Ladner et al. 1981) and UK (see Barrett 1985, Mander 1974, Davis et al. 1984, Raithby 1980 and Leadbeater et al. 1988).

Of the applications of FRP strengthening reported in the existing literature, the majority arises in Switzerland where the technique was first proposed and developed (see Meier 1995). More than one thousand applications have been seen in Switzerland alone by 2001 (see Triantafillou and Matthys 2001). Some early applications of strengthening by FRP were reviewed by Garden (1997) and Buyukozturk and Hearing (1998). Recently, detailed surveys of field applications have been undertaken, respec-

tively, by Shaw and Drewett (1999), Bonacci and Maalej (2000) and Hamilton and Dolan (2000), while general overviews on FRPs for strengthening applications have been presented by Karbhari and Seible (2000) and Neale (2000).

1.1.4 Failure Modes of the Strengthened Structures

The observed nature of the primary failure modes of externally bonded RC beams (particularly for FRP bonding) was diverse in numerous experimental studies to date (e.g. Ratchie et al. 1991, Saadamanesh and Ehsani 1991, Triantafillou and Plevris 1992, Chajes et al. 1994, Sharif et al. 1994, Heffernan and Erki 1996, Shahawy et al. 1996, Takeda et al. 1996, Arduini and Nanni 1997, Buyukozturk and Hearing 1998, Garden et al. 1997, 1998, Grace et al. 1998, Ross et al. 1999, Swamy and Mukhopadhyaya 1999, Bonacci and Makeej 2000, Ashour 2001, Nguyen et al. 2001 and Rahimi and Hutchinson 2001, Smith and Teng 2002). A schematic representation of typical failure modes observed in tests is shown in Figure 1.1 and categorized as (a) steel yield and laminate tensile rupture; (b) crushing of compression concrete; (c) shear failure; (d) plate debonding at the cut-off point near the end support and along reinforcement; (e) delamination of FRP plate from the cut-off end along the bond line; (f) delamination of FRP plate from the bottom of a flexural crack and (g) laminate peeling from the point of the base of the diagonal shear/flexural shear crack. According to Malek (1998), these modes can be divided into two general categories of "flexural" and "local" failure. "Flexural failure" is defined as concrete crushing in compression or plate rupturing in tension (Modes a and b). "Local failure" is defined as the delaminataion or peeling of the FRP plate at the location of high interfacial stresses and debonding failure at the concrete cover between the plate and the longitudinal reinforcement (Modes d, e, f and g). It is noted that "shear failure" (Mode c), does not belong to either of the categories and the failure loads for this mode can be predicted using the similar method for conventional RC beams. All of the failure modes are determined by various factors such as the amount of internal flexural and shear reinforcement and geometric and material properties of the bonded plate, the adhesive layer and RC beam. In some case, the failure modes are not easy to distinguish from each other.

Failure modes (a) and (b) are characterized by large final deflection of the member and present a more desirable structural performance, particularly in relation to ductil-

ity. They could be anticipated with a basic knowledge of the behavior of a RC section under transverse loading. Mode (c) is controlled by the shear strength of the bonded beam, which is significantly affected by the bonded plate in terms of the position and the degree of inclination of the critical shear cracks (Buyukozturk and Hearing 1998). Failure mode (d), which can be commonly observed with both steel plates and FRP sheets, exhibits a brittle and premature failure behaviour and would occur before the full flexural capacity is attained (Ratchie ea al 1991, Sharif et al 1994, Garden et al. 1991, 1998, Tumialan et al 1999a, Nguyen et al. 2001 and Teng et al 2001). The same mode has been termed elsewhere as 'end-of-plate failure through concrete' (Ritchie et al. 1991), 'concrete rip-off failures' (Sharif et al 1994, Nguyen et al 2001), 'debond at rebar layer' (Buyukoztuk and Hearing 1998), 'local shear failure' (Saadatmanesh and Malek 1998), 'concrete cover delamination' (Tumialan et al. 1999a) and 'concrete cover separation' (Garden and Hollaway 1998a, Teng et al 2001). A generic term, "plate end debonding" is used in this thesis to cater for this failure mode. The fact that this type of failure occurs with both steel and FRP plates confirms the existence of complex normal and interface shear stresses at the plate end, which is far more critical to the overall stability and integrity of the strengthened structural member than any other mode of failure. Thus end anchorage become essential to resist and delay this type of failure and consequently to increase the failure load, utilizing more of the strengthening capacity of the bonded materials. Mode (e) occurs when thin (<1.0mm) laminate sheets are bonded on the uneven concrete surface. This mode, following Teng et al. (2001), is herein refereed to as "plate end interfacial debonding" and is less commonly observed (Saadatmanesh and Ehsani 1991, Quantrill et al 1996, Taljsten 1999), while, somehow, in real beams, mode (d) and mode (e) may be mixed together as seen in the beam tested by Hau (1999). The flexural cracks in the high bending moment range in the RC beam tend to open and may induce high interfacial shear stress, and hence mode (f) occurs. This was also supported by experimental studies by Wu et al. (1997), Tumialan et al. (1999a) and Bonacci and Maleej (2000). For mode (g), the FRP laminate debonded from the base point of the inclined shear crack and/or shear flexural crack, far away from the plate cut-off end and then propagated further, leading to a complete debonding of the plate up to the plate end (Triantafillou and Plevris 1992, Garden 1997, Rahimi and Hutchinson 2001). The plate debonding was triggered by the development of the shear/flexural cracks. If proper procedure was taken to prevent such cracks from occurrence in the shear span, this type of failure

modes may be avoided. From this observation it seems that the bond integrity of the CFRP bonded sheet is particularly sensitive to any crack in the shear span, which could cause vertical and/or horizontal displacements of the bonded elements at that particular section.

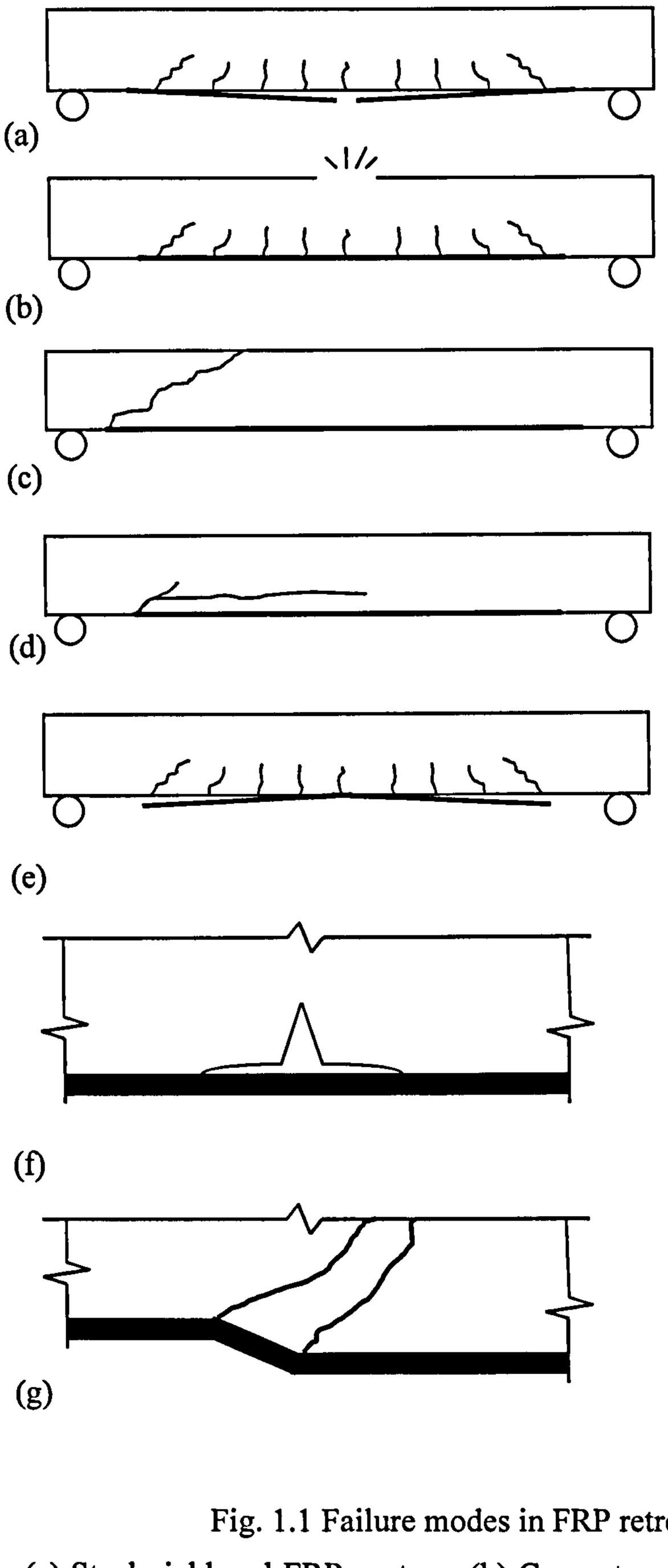

Fig. 1.1 Failure modes in FRP retrofitted concrete beams

(a) Steel yield and FRP rupture; (b) Concrete compression failure; (c) Shear failure; (d) Debonding of cover layer along reinforcement; (e) Delamination of FRP plate from the cut-off end; (f) Delamination of FRP plate from the base of a flexural crack and (g) Laminate peeling from the point of the base of the diagonal shear/flexural shear crack (Teng et al. 2001).

1.2 Literature Review

1.2.1 Stress Transfer Problem

If the technique of strengthening RC beams with epoxy-bonded steel or FRP plates is to be used in an effective manner it requires a sound understanding of stress transfer from concrete to the external reinforcement (steel plate or FRP plate) and the structural behavior in both the ultimate limit state and serviceability limit state. The problem of stress transfer also exists for the lap joints and cross-ply laminates with transverse matrix cracks, both of which were investigated relatively more extensively over last few decades. Many of the approaches can be directly applied here to model the stress transfer in strengthening RC beams. Some of the works are briefly reviewed as follows.

1.2.1.1 *Stress Transfer for Lap Joints*

For an adhesive-bonded lap joint, there exists stress concentration at the ends of adherends due to differential straining in the adherends (the shear-lag effect), bending induced by the non-axial loading and the end effects caused by the free edges. Renton and Vinson (1977) used the shear lag concept to develop an analytical model to determine the structural responses of single-lap and symmetric-lap joints composed of generally orthotropic material systems. The shear and normal stresses in the adhesive were assumed to be constant in the transverse direction. Delale et al (1981) used a similar assumption to obtain a closed-form solution for the stresses in adhesively bonded joints. A two-dimensional finite element method (FEM) was used to analyze the stresses in a metal-to-metal adhesive-bonded lap joint by Adams and Peppiatt (1974). Adams (1988) extended this finite element technique to include geometric and material nonlinearity in the lap joints. Adams and Mallick (1999) again extended the analysis to the general lap joint configuration and to incorporate the influence of adhesive plasticity and hydrothermal deformation and adherend anisotropy. Cheng et al (1990) determined the stress distribution in adhesive-bonded single-lap joints using two-dimensional elasticity theory, in conjunction with the variational principle of complemental energy. Tsai (1995) presented experimental and numerical analyses of a single-lap bonded joint with laminated polymeric composite adherend and with a spew fillet to address the mechanics and deformation of such material and bonding configuration. Yang and Pang (1996) proposed an analytical model to determine the

stress and strain distributions of adhesive-bonded composite single-lap joints based on the laminated anisotropic plate theory. The solution was given in the form of Fourier series. Wu et al (1997) extended Goland and Reissner (1944) classic lap joint theory to improve the inconsistent plane stress and plane strain relations existing in their original theory. Liu and Sawa (1999) developed a two-dimensional elastic solution of stress evaluation in single-lap band adhesive joints.

1.2.1.2 *Stress Transfer in Cross-ply Laminates with Transverse Matrix Cracks*

Stress transfer in cross-ply laminates with transverse cracks is an important subject in the mechanics of composites. Investigations have been carried out in recent years to study the stress field in the vicinity of transverse cracks occurring in matrix. Relatively accurate predictions have been obtained in many of the researches (Guild et al. 1993, Hashin 1997, MaCartney 1995) and due to the similarities in the nature of stress transfer to the strengthened beams, the stress transfer problems for cross-ply laminates with transverse matrix cracks is also reviewed herein.

Numerous investigators applied the shear-lag based analyses, which consist of varying degrees of sophistication, to model stress redistribution due to regularly spaced transverse ply cracks, that span the width and thickness of the ply (see, for example, Garrett and Bailey 1977; Highsmith and Reifsnider 1982; Flaggs 1985; Smith and Ogin 1999 and Smith and Ogin 2000). Laws & Dorak (1988) provided a comprehensive review on the works done before 1987. Berthelot et al. (1996) implemented a finite element analysis (FEA) to investigate the transverse cracking of cross-ply laminates subjected to uniaxial tensile loading. The multiple matrix crack propagation in a quasi-isotropic laminate has been simulated by using generalized plane-strain FEMs (Tong et al 1997), where the information concerning stress distribution in the vicinity of existing cracks was provided. Other numerical methods such as finite difference analysis can be found in the studies of Altus et al. (1981), Caslini et al. (1987) and Guild et al. (1993). Li et al. (1994) presented a finite strip analysis of cracked laminates based on a generalized plane strain assumption and the minimization of strain energy. Hashin (1985, 1987 and 1988) developed a variational method on the basis of the principle of minimum complementary energy. Both cracks occurred in uni-axial and bi-axial directions were considered to calculate stiffness reduction and stresses in cross-ply laminates. Nairn (1989) used this method to determine the two-dimensional

thermo-elastic stresses in cross-ply laminates. The approach was then used to calculate the energy release rate due to the formation of a new microcrack. On the basis of the principles of the minimum complementary energy and minimum strain energy, Narin (1995) obtained, respectively, the lower bound and upper bound on the effective modulus of a cross-ply laminate containing microcracks in the 90° plies. Schoeppner and Pagano (1998) developed a variational method to model the thermoelastic response of flat laminated composites using a large radius axisymmetric hollow layered cylinder model. The model can be used to examine the initiation/ propagation and interaction of damage for thermo-elastic problems in the laminate. McCartney (1992, 1995), developed a semi-analytical model based on a rigorous elasticity for generalized plane strain deformation of planar multilayered systems. McCartney and Pierse (1997a, 1997b) extended this model to the plane strain/bending deformation. Although these formulations do not include the crack tip singularities, the models can approximate the singular behavior of the stresses in the vicinity of the crack tip through layer element refinement. On the basis of the same plane strain assumption, Yang (2001) provided an alternative solution to the stress transfer problem by using Fourier series expansions in his transfer report.

From the stress distribution that had been calculated as a function of crack spacing, two techniques were used to predict crack formation, i.e. the strength based (Garrett and Bailey 1977, Manders 1983, Fukunaga 1984, Peter 1984) and the facture mechanics based (Wang and Crossman 1980, Poursartip 1983, Ogin 1985, Caslini 1987, Han 1988, Nairn 1989, Guild et al. 1993, Shahid and Chang 1995 and Boniface et al. 1997) techniques. In the strength based approaches, progressive cracking is assumed to be controlled by the transverse ply stress distribution. In the simplest way, progressive cracking is assumed to occur when the maximum transverse ply stress (which normally occurs midway between existing two neighboring cracks) is equal to the (constant) transverse ply failure strength, while for more sophisticated models, the transverse ply is assumed to have a statistical distribution of strengths along its length [often described using a Weibull distribution (Gurvich et al. 1997)] as a result of pre-existent flaws or a local fiber geometry which is prone to debonding. In the fracture mechanics based models the energy changes associated with crack formation at a particular location may be calculated and be compared with a critical strain energy release rate for crack formation.

1.2.1.3 *Stress Transfer in Strengthened RC Beams*

Central to the reinforcement effect of externally bonded concrete structures is the transferring of stresses from concrete to the external reinforcement, which is susceptible to cause the undesirable premature and brittle failure modes, such as the delamination initiated from the end of a flexural crack of concrete, the peeling initiated from the shear crack of concrete and the plate end debonding (PED).

The determination of interfacial stresses has been studied in the last decade for beams bonded with both steel and FRP plates. These extensive investigations can be categorized as follows.

(1) Stress Transfer at the Plate Ends of Strengthened RC Beams

(a) Experimental Studies

MacDonald and Calder (1982) tested beams with a range of plate aspect ratios, and nominal values of the shear stress in the adhesive at the end of the plate were estimated from strain gauge readings at the load level corresponding to the greatest strain gradient, values of between 0.13 MPa and 0.8 MPa were calculated, far below the concrete shear strength of 5 MPa. The large discrepancy was thought to have been due to the initiation of plate separation by high strain gradients (i.e. shear stresses) local to the tip of the plate; these highly localized gradients cannot be detected by a limited number of strain gauges (MacDonald and Calder 1982).

Jones et al. (1988) carried out tests to investigate the effectiveness of different anchorage arrangements against plate separation and concluded that the concentrating interfacial stresses at plate ends have limiting peak values in the region of $\sqrt{2}\times$ tensile splitting strength of the concrete. In their study, a classical theoretical elastic stress analysis was also conducted. However, the analysis showed no consistent relationship to the measured peak values. A factor was then introduced and that the modified stress could give a reasonable estimate of the peak values.

Oehlers and Moran (1990) identified two main types of plate end peeling failure for steel plated beams, namely shear peeling and flexural peeling, by studying the failure modes observed when the plate end was terminated in regions of varying proportions

of shear and flexural loading in previous tests. The tests cited by these authors were those of Ong et al. (1982) who tested specimens in which the plates terminated in regions bearing stresses by continuing the plates under the beam supports, Van Gemert (1981) in regions of pure shear, Jones et al. (1988) in regions of shear and flexural, and Johnson and Tait (1981) in regions of shear, flexural and axial loads. Two empirical constants k_c and k_a, which were included in a simple theoretical analysis of peeling stress in the bonded beams, were calibrated from the collected test data. Shear peeling is induced by shear cracks through the depth of the concrete at the end of the plate; this is a common failure mode when the plate end lies in a region of shear dominated loading. Flexural peeling is induced by an increasing curvature of the beam under flexural dominated loading and is associated with a more gradual separation of the plate than in shear peeling. Therefore, it is the predominance of shear or flexural cracks at the end of the plate that determines which type of peeling will occur.

Garden et al (1998) recorded the strain of a bonded CFRP plate along the bond-line in their tests. The results obtained from these tests showed that the peak shear stresses decreased as the shear span/depth ratio increased and the position of the peak moved away from the end of the plate.

Etman and Beeby (2000) carried out an experimental investigation on the bond stress along concrete-epoxy-plate (CFRP) interfaces. Various plate geometry and corrosion ratios were considered. It was found that the width to thickness ratio of the plate had significant effect on the bond stress concentration at its ends.

Ahmed et al (2001) tested a series of RC beams strengthened with CFRP laminates. The effect of the unplated lengths as well as the amounts of externally bonded CFRP laminates upon the interfacial shear stress was studied.

Maalej and Bian (2001) tested five identical RC beams strengthened by CFRP plate with different thickness and measured the interfacial shear stresses concentration at the plate curtailments. The effect of CFRP thickness on the shear stress concentration, failure modes and strengthening efficiency ratio was studied. The analytical results using Roberts' (1989) and Malek's (1998) formulas were also presented in order to

make the comparison with the experimental results. Bonacci and Maalej (2001) compiled an experimental database from the existing database, which includes a total of 127 specimens from 23 separate studies. Maalej et al (2001) used Roberts' (1989) formulas to predict the interfacial shear stresses and analyzed the debonding failure using Chaalal et al (1998)'s shear strength expression. Theoretical prediction was in close agreement with actual trend set by the experimental data from Bonacci and Maalej (2001)'s database. The effect on the interfacial stresses and shear strength of the most critical parameter, i.e. FRP relative axial rigidity, was examined.

Most of the experimental studies reviewed above provide relevant information on the parameters influencing the strengthening of RC beams by bonding steel or FRP plates. These parameters include the geometrical and material properties of RC beams and bonded plates, the loading arrangements and anchorage systems. This information leads to a better understanding of the application of EPB in engineering practice and on further investigation using both experimental and theoretical methods. However, more general and complete information cannot be extracted from a limited number of experimental investigations. As the experimental studies can be costly and time consuming, alternative methods such as numerical and analytical methods may provide a better option.

(a) Numerical Studies

The Linear Finite Element Method

Using a linear finite element model, Mays and Turnbull (1992) concluded that the peak shear stress at the plate ends was approximately 4τ, where τ is the classical elastic shear stress, and the peak normal stress was around 3.5 τ. Hutchinson and Rahimi (1995) performed finite element analyses and concluded that the stresses at the FRP plate ends were lower than those for the beams if they had been strengthened with thick steel plates. The effect of various plate-end geometric conditions of external plates was also studied. Besides, Taljsten 1997, Malek et al. 1998 and Rabinovich and Frostig 2000 also presented limited finite element results for interfacial stresses. Teng et al (2001b) recently conducted a FE study of interfacial stresses in plated RC beams to (a) investigate the complex stress distributions in the adhesive layer near the end of the plate; and (b) assess the accuracy of the simple approximate analytical solutions.

The Nonlinear Finite Element Method

Ziraba and Baluch (1995) developed a nonlinear finite element model for the flexure-shear response of RC beams strengthened externally by epoxy bonded steel plate

The model involved the introduction of a six-noded element to capture the characteristics of the interface between concrete and external steel plate as well as the bond between the internal reinforcement and concrete. A nine-noded Lagrangian element for simulating behavior of concrete and external steel plate and a three-noded element for internal main and shear reinforcement were also proposed. The metamorphosis of failure modes from plate yielding to separation was allowed for. Ascione and Feo (2000) used a finite element model to predict shear and normal stresses in the adhesive layer of RC beams plated with composite laminate. In their model, the adhesive layer was analogized as a continuous distribution of bilateral elastic springs and the kinematical model was driven from a suitable power expansion of the displacement field components with respect to the cross-section coordinates. The concrete and composite materials were assumed to be linearly elastic and orthotropic with a possible different behavior in tension and in compression (bimodular behavior). The Langrangian isoparametric elements were used and Newton-Raphson method was applied to solve the non-linear problem. Rahimi and Hutchinson (2001) conducted both experimental work and theoretical analyses for RC beams strengthened with FRP plates. The theoretical analyses included 2D nonlinear finite-element modeling using LUSAS program in which an isotropic damage model was incorporated to simulate the nonlinear behavior of concrete by means of a scalar variable called the damage or degradation parameter. Aprile et al (2001) used the displacement-based RC frame element considering the bond-slip relations. The element has two components, i.e. a two-node concrete beam and a strengthening plate. The nodal degrees of freedoms of the concrete beam and of the plate are different to permit slip. Beam and bond compatibility are both enforced in the strong form and element equilibrium was enforced in the weak form, when the stiffness matrix was derived. Using this model, the stiffness, load capacity, interfacial shear stress and the failure modes or RC beams strengthened with bonded steel or CFRP were predicted.

Discrete Section Analysis

Arduini et al. (1997a) developed a discrete section model to predict the load-deflection behavior of RC beams strengthened with externally bonded FRP plates or sheets as well as the distributions of interfacial stresses. The model takes into account the nonlinear properties of concrete in compression, the tensile strength of concrete and the adhesive interface properties. Also the model can predict different failure

mechanism, e.g. FRP rupture, shear failure in concrete, tensile fracture and local adhesive failure. Arduini and Nanni (1997a) used this model to conduct a parametric analysis of the effect of FRP reinforcements on serviceability, strength and failure mechanisms of repaired RC beams. FRP reinforcement parameters considered in the analysis included stiffness, bonded length, thickness and adhesive stiffness. Arduini and Nanni (1997b) used the discrete section analysis to simulate the process of RC beam strengthening, where the effects of precracking, unloading, repairing and the final loading cycle were included. Wang and Restrepo (2001) extended the work into considering the effects of diagonal tension cracking in the shear span of a beam. The modified compression field theory (MCFT) was incorporated into their approach. Better agreement with the experimental results was obtained compared with the predictions using Arduini and Nanni (1997)'s approach.

(c) Analytical Studies

Approximate Closed-form Solution

Several relatively simple approximate closed-form solutions for interfacial stresses have been developed based on a simple assumption for the adhesive layer. Among those studies, a common assumption was made, i.e. the adhesive layer was subject to shear and normal stresses that are constant across the thickness of the adhesive layer. Either a staged analysis approach (Roberts 1989, Roberts and Haji-Kazemi 1989) or deformation compatibility-based approach (Vilnay 1988, Liu and Zhu 1994, Taljsten 1997, Malek et al. 1998, Smith and Teng 2001) was employed using this assumption. A summary of the main differences between the analytical solutions is given in Table 1.1, in which some of them were reviewed by Smith and Teng (2001).

Besides these, Trantafillou and Deskovic (1991) used the shear-lag theory to obtain the shear stress between the RC beam and FRP sheet due to the release of prestresses. A nonlinear shear stress- strain relationship for epoxy adhesives was considered for RC beams with high shear strength, while for those with low shear strength, a nonlinear shear stress-slip relationship was considered. Ye (2001) proposed an analytical solution of interfacial shear stresses between RC beams and FRP plates, using a state space and iterative approach. The nonlinear constitutive relation of concrete was considered. Leung et al. (2001) predicted the shear stress in composite strengthened beams considering the concrete cracking and consequently reduced stiffness of the

concrete beam. A simple analytical approach was developed to obtain the equivalent stiffness of a cracked section as a function of moment acting on the section. Then the governing differential equation due to the shear-lag theory was solved by finite difference method. Generally, Leung et al. (2001)'s approach is similar to Ye (2001)'s except that the latter calculated the longitudinal strain in the discrete points of the extreme fiber of the RC beam rather than using the equivalent stiffness of the RC beam.

Mukhopadhyaya and Swamy (1999) presented a critical evaluation of the plate end stress on the basis of existing experimental data available in the literature. The analytical technique by Roberts (1989) was used. They found a wide variation of the results for different sources of experimental data. The inconsistence indicated that there must remain some unknown parameters, which influence peak normal and shear stress values at the instance of plate debonding, but they are not accounted for in Roberts's approximate elastic analysis. Mukhopadhyaya and Swamy (2001) carried out a similar critical review and developed a simple analytical approach for the interfacial shear stress.

All these approximate closed-form solutions exhibited two inherent inadequacies. Firstly, there is lack of fulfillment of point equilibrium within the thickness of the adhesive layer, because the interaction between the distributed shear and vertical springs were not considered. Secondly there exists the inability to control the fulfillment of boundary and continuity conditions of the shear stress within the adhesive layer and at its edges. These two inadequacies, accompanied with the presumed linear deformation pattern through the thickness of the adhesive layer and the uniform shear and peeling stresses distribution through this thickness, yield solutions that roughly approximate the edge stresses and in many cases are too conservative.

The Closed-Form High-Order (CFHO) Analysis

Rabinovich and Frostig (2000) presented a closed-form high-order analytical solution for the analysis of concrete beams strengthened with externally bonded FRP strips. The model is based on equilibrium and deformation compatibility requirements in and between all components of a strengthened beam, i.e. the concrete beam, the FRP strip and the adhesive layer. The governing equations representing the behavior of the strengthened beam, along with the appropriate boundary and continuity conditions,

are derived and solved. This approach fulfills all equilibrium requirements in the global and the point-to-point sense, as well as boundary and continuity conditions, including traction free at the free edge of the adhesive layer. However, the solution does not provide explicit expressions for the interfacial stresses, such that numerical results are not easily obtainable. This makes it difficult for the further exploitation in developing a design equation. Rabinovich and Frostig (2001a) used CFHO model to investigate the effect of adhesive layer profile on the interfacial stresses at the edges of the curved FRP strips. Numerical method was used to solve the linear governing equations with variable coefficients. The effect of the nonlinear constitutive relations of various materials was investigated in Rabinovich and Frostig (2001b). The overall nonlinear load-deflection response and the local stress concentration at the edges of the FRP strip were determined by introducing relevant nonlinear constitutive relations into the CFHO models.

The Closed-form Solution using Complementary Energy Method (CEM)

Shen et al. (2001) developed an explicit solution of interfacial shear and norm (peeling) stresses for a bonded beam under uniform distributed load using the complementary energy method. The salient features of this analysis include the consideration of non-uniform stress distribution and the satisfaction of the stress boundary conditions at the ends of the adhesive layer and plates. Yang et al. (2004) extended the investigation into the interfacial stresses analysis for a strengthened beam subjected to both symmetrically and non-symmetrically applied load. The close-form solutions for various types of load cases were presented.

(2) Stress Transfer in the Vicinity of Intermediate Cracks of Strengthen RC Beams

Malek et al. (1998) calculated the shear stress in the vicinity of large flexural cracks along the beam. The interfacial shear stresses were analyzed for an element between two consecutive cracks using the axial stresses in the plate at the crack locations as the boundary conditions. However, the transverse normal stress in the close vicinity of the flexural cracks was ignored. Yang and Ye (2001) used CEM to calculate the interfacial stresses for a cracked RC beams bonded with steel/FRP plates and subject to symmetrical tensile force and/or end bending moment. A representative element between two contiguous cracks is considered under the assumption of plane stresses. By means of the principle of minimum complementary energy, the analysis provides a

closed-form solution that can be used easily to predict the stress distributions near the cracks in the beam. A fracture mechanics based analysis was carried out by Leung (2001) to obtain the crack mouth opening displacement (CMOD) and the maximum shear stress for a strengthened beam subject to a moment. In his analysis the bridging forces from, respectively, the softening concrete, the reinforcing steel and the bonded plate were considered. Although, the nonlinear concrete softening was considered, the maximum interfacial shear stress was assumed to increase linearly with crack mouth opening. It was suggested that the maximum shear stress had to be taken as a parameter reflecting the intensity of the shear stress concentration near the crack. In that model, failure occurs when the maximum shear stress reaches a critical value, at which unstable delamination propagation starts. The failure process is similar to the unstable propagation of a crack as the stress intensity factor K reaches the fracture toughness K_c. Hence, the critical value of maximum shear stress is not necessarily related to the concrete strength measured under a uniform stress field, as there is no implicit relation between fracture toughness K_c and the strength of a material. Since at the stage when maximum shear stress occurs, the interfacial normal stress is compressive, which is beneficial to the bonding, the transverse normal stress was ignored in the analysis.

(3) Brief analysis of the above review for the strengthened RC beams

The preceding discussions of interfacial stresses at the ends of plate or in the vicinity of the intermediate cracks in RC beams strengthened with a soffit plate allow some useful comments to be made.

One of the important features with regard to the interfacial stress fields is that there exists strong singularity due to the geometric discontinuity or/and different material phases. Both the interfacial shear stress and transverse normal stress should approach to infinity in an elastic analysis. Alternatively, the linear elastic fracture mechanics method emerges to be an ideal approach to cater for this nature. However, in practical situation, these extremely high stresses will lead to nonlinear deformations for non-brittle materials in the local region. The peak stresses will then shift away slightly from the ends of plate. A nonlinear analysis is prerequisite to reflect this accordingly.

The most common method of estimating interface shear stress experimentally is based on the measured strain gradients along the reinforcement plates. The localized peak gradients cannot be detected by a limited number of strain gauges. In other words, all the stresses obtained from the experiments are the average values within the two adjacent strain gauges. It is the major reason why the big discrepancy between experimental and analytical results has always been observed. It is also worth noting that there has been no proper technique and method to measure the interfacial normal stresses so far.

The distribution of the interfacial stresses is very complex near the end of the plate, as revealed by the FEM study of Teng et al. (2001b). In particular, the FE results show that high peeling stress exists at the adhesive-concrete (AC) interface, and whereas the plate-adhesive (PA) interface may experience compression. This high peeling stress makes the AC interface the critical interface for debonding failures. This explains why PA interfacial debonding has been rarely reported in tests. Due to the singularity, the peak values of stresses depend on mesh refinement (Teng et al. 2001b) when linear FEM analysis is carried out and it is extremely difficult to converge in the vicinity of the singularity points.

Nevertheless, the linear elastic FE analysis cannot well simulate the plated RC structures, as the nonlinear behavior of concrete is frequently dominated by progressive cracking. As far as the nonlinear FEM is concerned, either the discrete crack approach or smear crack formulation are used. Material non-linearity of concrete is incorporated in the NLFEM analysis, and various bond-slip relationships are used to simulate the nonlinear behavior in terms of the slip in the steel rebars and/or the bonded plate. The dissimilar characteristics in both compression and tension of the concrete material make the NLFEM analysis even more difficult to implement.

However, few studies have discussed the effect of interfacial normal stress on the interfacial slip or debonding strength. As far as the author's view is concerned, when this normal stress reaches a comparative large value, e.g. at the end of the bonded plate, its effect might be quite significant. A further study accounting for this issue is necessary.

Furthermore, it is a fact that the use of the finite element method is tedious, computational expensive and sometime less reliable when material discontinuities are present. To model the singularity at the plate end, very fine finite element meshes have to be used to obtain a reasonably good solution. For nonlinear problems where iterations are required, this solution becomes even more computational expensive. Simple and explicit solutions, which present reasonable accuracy, are imperative.

Simple closed-form solutions assuming uniform stresses across the adhesive layer thickness are only capable of finding reasonable predictions of the stresses along the middle adhesive (MA) section, as these solutions do not distinguish the two interfaces. Most of the available solutions violate the zero shear stress condition. Although this violation may not be important for practical applications, as it affects only stress predictions in a tiny zone near the plate end, the inability of such solutions in predicting the high peeling stresses at the AC interface is of more concern. Nevertheless, they provide a useful and simple tool for understanding the interfacial stress behaviour and for use in developing a design rule. In the next section, several debonding strength models will be discussed on the basis of the interfacial stresses predicted from such a closed-form solution. In these models, debonding failure is deemed to occur when these stresses meet certain failure criteria. The correlation to the experimental data is not very encouraging. It naturally brings up the essentiality to seek some better alternative for the stress solutions.

Higher order solutions, such as that of Shen et al (2001) and Yang et al (2004), are capable of satisfying the zero shear stress condition and predicting the high peeling stresses. They are therefore a definite improvement over the simple approximate solutions in depicting a more accurate picture of interfacial behavior. However, some inherent assumptions, such as the predefined relationship between the shear and normal stresses, have limited the accuracy, especially to the interfacial normal stress. Additionally, their complexity prevented the wide application of these solutions. Reliable and simple stress solutions are sought before a more robust strength model is developed.

Only a few people conducted their analytical nonlinear analysis, e.g. Leng et al (2001), Rabinovich and Frostig (2001b) and Ye (2001). To the best of the author's

knowledge, they are the only few available in the literature. Owing to the complexity of the nature of the nonlinear analysis, all of them have to resort to numerical methods, e.g. iterative approach, finite difference method etc., to obtain the results. Also, it can be found that all of the work concerned only the nonlinear stress-strain relationship of concrete and the consequent flexural crack progress in the high bending moment area. No one concerned the nonlinear cracking behaviour near the end of the plate. However, it was reported that plate end debonding could be largely influenced by the softening characteristics of the concrete in the high local stress zone (see Meier and Kaiser 1991). From numerical analysis, it was found that the nonlinear compressive behavior and flexural cracking propagation due to the high bending moment did not affect the region in the concrete beam near the cut-off ends of the plate (see Rahimi and Hutchinson 2001 and Aprile et al 2001), while according to the elastic analysis of Yang et al (2004), the peak shear stress at the end of the plate is only determined by the bending moment and shear force applying at the section where the plate end locates. From these two arguments, the nonlinear behavior and cracking occurring in the high bending moment region of the RC beam can not explain the disproportional increase of the composite strain near the plate end with the applied load. A nonlinear fracture mechanics method (NLFM) is needed to investigate both the pre- and post-cracking behavior near the plate end, which is trusted to be more meaningful to elucidate the mechanism of the local failure.

1.2.2 Strength Models for Various Failure Modes

1.2.2.1 *Flexural Failure and Flexural Strength Predictions*

If the ends of the plate are properly anchored, the ultimate flexural capacity of the beam is reached when either the FRP fails by tensile rupture (mode a) or the compressive concrete is crushed (mode b). Apart from the improved ultimate strength, less ductility and less deformability, due to the high strength and brittleness of the bonded FRP plate, this failure mode is very similar to the customary flexural failure of RC beams,

Saadatmanesh and Ehsani (1991) carried out an experimental investigation on strengthening undamaged beams with FRP plates. Five rectangular beams and one T-beam were tested. Three different reinforcement ratios were used for the tension steel.

One beam was under-designed for shear while the remaining beams were slightly over-designed for shear according to ACI. One beam was cambered before the FRP plate was bonded to its tension flange, to observe the effects of external prestressing. All beams were strengthened with FRP plates bonded to their tension flanges. The results showed a significant increase in flexural strength, in particular for those with a lower steel reinforcement ratio. In addition, plating reduced crack size in the beams but somewhat reduced their ductility.

Philip et al. (1991) conducted another testing program on strengthening undamaged beams with FRP plates. The type of FRP plate, plate dimensions and anchoring schemes were investigated. The results demonstrated that bonded FRP plates improved the strength and stiffness of the reinforced concrete beams.

Quantrill et al (1996a) tested RC beams epoxy-bonded by FRP plates (GFRP and CFRP) and the results showed that plating increased the serviceability, yield and ultimate loads and increased the strengthened member stiffness after both cracking and yielding, while reduced the ductility. Investigation was also conducted to show the effects of different test parameters on overall flexural behavior.

El-Mihilmy and Tedesco (2000) listed some experimental data on the RC beams strengthened with externally bonded FRP laminates. All of the listed beams failed either by concrete crushing and FRP rupture.

Existing research suggests that the ultimate flexural strength of FRP-strengthened RC beams can be predicted using existing RC beam design approaches with appropriate modifications to account for the brittle nature of FRPs. Consequently, design equations for evaluating the flexural strength of RC beams flexurally strengthened with FRPs have been presented following the approaches of ACI code (ACI 318-95, 1999) by An et al (1991), Chajes et al (1994), Nanni et al. (1998), Saadatmanesh and Malek (1998), El-Mihilmy and Tedesco (2000) and Lam and Teng (2001); the Canadian code (CSA, 1994) by Chaallal et al. (1998) and British code (BS 8110, 1997) by Teng et al. (2000).

These design equations consider only flexural failure of the plated beam by either FRP rupture (mode a) or concrete crushing (mode b) without premature debonding failure. The preferred modes of failure to be designed for are concrete crushing following yielding of steel reinforcement or FRP rupture following yielding of steel reinforcement, with the former being the most favorable (El-Mihilmy and Tedesco 2000). In both modes, yielding of the steel reinforcement precedes failure by either concrete crushing or rupture of the FRP, which ensures that failure will occur after the formation of large flexural cracks. Such flexural cracks will give some warning of failure despite the fact that these failure modes generally show limited ductility. Failure by FRP rupture without yielding of steel reinforcement is expected to display roughly the same degree of ductility as that of FRP rupture following yielding of steel reinforcement, but this is unlikely to occur unless the steel reinforcement is located near the neutral axis of the beam. Failure by concrete crushing without yielding of steel reinforcement should be avoided as far as possible. A key assumption in developing flexural strength design equations is that a plane section remains plane. The design equations can be found in the guidelines documents referred above. Due to the limitation of space, they are not presented in this thesis.

1.2.2.2 *Shear Failure and the Strength Models*

Jansze (1997) pointed out that there are two types of shear failure, i.e. flexural shear failure (see Figure 1.2a) as reported in I'Hermite and Bresson (1967) and Taljsten (1994) and plate end shear (see Figure 1.2b) as observed by Sharif et al. (1994) and Hussain et al. (1995).

(1) Modified ACI Shear Strength

Baluch et al (1994) developed a modified shear strength model for externally bonded RC beam. A parameter k indicating the efficiency of the stirrups associated with the crack resulting from concrete rip-off failure at or below the level of reinforcement prior to a steep access to the point of loading was suggested. Then the modified ACI shear strength can be used to predict the shear capacity of the RC beam strengthened by steel plate and subjected to three point loading, that is

$$V_u = P_u/2 = V_c + kV_s \tag{1.1}$$

where V_u is the ultimate shear capacity of section; P_u is the ultimate load; V_c and V_s are, respectively, the shear capacities of the plain concrete and stirrups and

$$V_c = \frac{1}{6}\left(\sqrt{f_c'} + 100\rho_s\right) b_c d \tag{1.2}$$

$$V_s = A_{st} f_{yst} d / s \tag{1.3}$$

$$k = 2.4\exp\left(-0.08 C_{R1} C_{R2} \times 10^6\right) \tag{1.4}$$

$$C_{R1} = \left[1 + \left(\frac{K_s}{E_p b_p t_p}\right)^{0.5} a\right] \frac{b_p t_p}{I_{trc,p} b_a} \left(h_{trc,p} - h_p\right) \tag{1.5}$$

$$C_{R2} = t_p \left(\frac{K_n}{4 E_p I_p}\right)^{0.5} \tag{1.6}$$

where f_c' is the concrete cylinder compressive strength; $\rho_s = A_s / b_c d$ is the ratio of steel tension reinforcement, A_s is the area of steel tension reinforcement, b_c is the section width and d is the effective depth of the section ; A_{st} is the area of the stirrups; f_{yst} is the yield strength of the stirrups; s is the stirrup spacing; $K_s = G_a\left(b_a / t_a\right)$ is the shear stiffness of the adhesive layer; $K_n = E_a b_a / t_a$ is the normal stiffness of the adhesive layer; G_a, b_a and t_a are the shear modulus, width and thickness of the adhesive layer, respectively; $a = M_0 / V_0$ is the distance from the support to the nearer end of the bonded plate; M_0 and V_0 are the bending moment and shear force at the cut-off ends of the plate; E_p, b_p and t_p are the elastics modulus, width and thickness of the bonded plate; $I_{trc,p}$ is the second moment of area of the cracked plated section transformed into bonded plate; $h_{trc,p}$ is the neutral axis depth of this transformed cracked section (distance from the compression face to the neutral axis); I_p the second moment of area of the bonded plate alone; and h_p is the distance from the compression face of the RC beam to the centroid of the bonded plate,

(2) Modified Kim and White Shear Strength Model

Jansze (1997) proposed a plate-end shear model for the steel plate bonded RC beam, based on the critical crack section analyses of Kim and White (1991). By means of analogy between the distance from the support point to the critical crack section of conventionally reinforced beams and the unplated length for plated beams, a fictitious shear span was introduced. By using the fictitious shear span in combination with the CEB-FIP MC90 expression for flexural shear, the plate-end shear load was predicted.

This model didn't consider the contribution of shear reinforcement. The critical shear force in the RC beam at the plate end to cause debonding V_u is given as follows

$$V_u = \tau_{PES} b_c d \tag{1.7}$$

where

$$\tau_{PES} = 0.18 \sqrt[3]{3\frac{d}{B_{\text{mod}}}}\left(1+\sqrt{\frac{200}{d}}\right)\sqrt[3]{100\rho_s f_c'} \tag{1.8}$$

$$B_{\text{mod}} = \sqrt[4]{\frac{\left(1-\sqrt{\rho_s}\right)^2}{\rho_s} da^3} \tag{1.9}$$

Where B_{mod} is a modified shear span as given by Equation 1.9. If B_{mod} is greater than the actual shear span B of the beam then the modified shear span should be given by $(B_{\text{mod}}+B)/2$. Jansze's model appears to be invalid for soffit plates terminated at the support as B_{mod} becomes zero and Equation 1.8 predicts that shear failure is never possible.

Ahmed et al (2001) extended Jansze's (1997) plate-end shear model to the FRP plate bonded RC beam. An extra term was introduced, which reflected the difference of the shear stresses if the bonded CFRP laminates were replaced by the steel plate of 550 N/mm^2 yield strength. Moreover, the increase in shear strength offered by the stirrup was also included as seen in Equation 1.11 (see Ahemed and Van Gemert, 1999). Their model is given as follows

$$V_u = \left(\tau_{PES} + \Delta\tau_{\text{mod}}\right) b_c d \tag{1.10}$$

where

$$\Delta\tau_{MOD} = \tau_{PES} b_c d\left(\frac{S_s}{I_s b_p} - \frac{S_{frp}}{I_{frp} b_a}\right) + 6188.5\left(\frac{\tau - 4.121}{b_c d}\right) \tag{1.11}$$

$$\tau = \left(0.15776\sqrt{f_c'} + \frac{17.2366\rho_s d}{B}\right) + 0.9\frac{A_{sty} f_{yst}}{s b_c} \tag{1.12}$$

Where τ_{PES} is given by Equation 1.8, S_{frp} and S_s are, respectively, the first moment of area of the FRP plate and the equivalent steel plate, about the neutral axis of a cracked section transformed to concrete. The equivalent steel plate has the same tensile capacity and width as those of the CFRP plate, but has an equivalent thickness determined by assuming that the yield stress of steel is 550 MPa. I_{frp} and I_s are the second moments of area of a cracked plated section transformed to concrete with an FRP plate and an equivalent steel plate respectively, and b_p and b_a are the widths of the FRP and

adhesive respectively. The stirrup spacing is denoted by s, while A_{stv} and f_{yst} are the cross sectional area and the yield stress of the steel stirrups respectively. For all practical purposes b_a is equal to b_p.

(3) The Truss Analogy Model

Colotti and Spadea (2001) extended the truss analogy model for the conventional RC beams to the strengthened RC beams to predict the ultimate shear failure loads due to the occurrence of shear cracks. A plastic limit analysis approach was used. A perfectly plastic behavior of the materials (concrete and steel) is assumed and the constant bond strength model with a zero tension cutoff is adopted. The failure mechanism is characterized by slipping of the plate located in the shear span zone together with a diagonal crack along compression trajectory. The ultimate limit state was described as the bond stress value along the bondline reaches the ultimate bond strength and the stirrups across the compression trajectory reach their yield strength. Additionally, the contributions of the concrete in compression and the internal and external reinforcements were also incorporated. The FRP plate does not show plastic characteristics, so this model applies more suitably to the steel plate strengthening. Owing to the characteristics of the plastic limit analysis, the model predicts the upper bound of the ultimate loads and that is

$$\frac{\tau}{f_c} = \psi\left[\alpha + \phi - \sqrt{(\alpha+\phi)^2 - 2\phi\beta}\right],\ \psi > 0 \tag{1.13}$$

$$\frac{\tau}{f_c}\alpha = \eta \tag{1.14}$$

$$\left|\frac{\sigma_c}{f_c}\right| = \frac{U_y}{b_c f_c}\frac{\cot^2\theta + 1}{\cot\theta} \le 1 \tag{1.15}$$

where

$$\tau = \frac{V_u}{b_c d};\ \psi = \frac{p_y}{b_c f_c};\ \eta = \frac{T_y}{b_c d f_c} \tag{1.16a-c}$$

where $P_y = A_{st} f_{yst}/s$ is the stirrup strength; $f_c = \nu_c f_c^{'}$ is the effective compressive strength of concrete; ν_c is effectiveness factor for concrete; $T_y = A_s f_y + A_p f_{yp}$ is the yield strength of longitudinal reinforcement (bars and plate); $\alpha = B/d$ is the ratio of shear span to beam depth; $\beta = l_p/d$ is the ratio of plate length to beam depth; l_p is

plate length; $\phi = U_y / P_y$ is the ratio of bond strength to stirrup strength; U_y is the bond strenth; $\eta = T_y / b_c df_c$ is the degree of longitudinal reinforcement; θ is the angle between diagonal compression stress and beam axis as follows

$$\cot\theta = \frac{V_u}{P_y d} = \frac{\tau}{\psi f_c} \tag{1.17}$$

Colotti et al (2001) extended this model to the RC beams strengthened in flexure and/or shear with externally bonded FRP reinforcement.

(4) Critical Diagonal Crack Debonding Model

Ali et al. (2001) studied the critical diagonal crack (CDC) debonding modes and developed an ultimate strength model. In their model, the effect of the stirrups was not taken into account according to their preceding experimental finding (see Oehlers 1992). They adapted Zhang's (1997) shear strength model by considering the effects of the bonded plate and equated the shear load to cause diagonal cracking (V_{cr}) and the shear load to cause failure along cracked section (V_f) to predict the position and strength of the critical diagonal crack. That is

$$V_{cr} = \left(\frac{x^2 + d^2}{B}\right)\left[\frac{f_{tef} b_c}{2} + \frac{m f_t b_p t_p (d + 0.5 t_p)}{d^2}\right] \tag{1.18}$$

where f_{tef} is the effective tensile strength of the concrete, i.e.

$$f_{tef} = 0.156 f_c'^{2/3} \left(\frac{h}{100}\right)^{-0.3} \tag{1.19}$$

and x is the horizontal projection of diagonal crack; h is the overall height of the RC beam; $m = E_p / E_c$ modular ration; f_t is the direct tensile strength of the concrete and can be assumed to be $0.8 f_b$; f_b is the Brazilian tensile strength of the concrete.

$$V_f = 0.25\lambda \left(\frac{3.5}{\sqrt{f_c'}}\right)\left(0.27 + \frac{8.54}{\sqrt{d}}\right) f_3(\rho) f_c' \left(\sqrt{1 + \left(\frac{x}{d}\right)^2} - \frac{x}{d}\right) b_c d \tag{1.20}$$

where λ is an experimental constant that depends on load type and equals 1.6 for point loads; $f_3(\rho)$ is the parameter, which was firstly given by Zhang(1997) accounting for the restrain provided by the longitudinal reinforcement to the sliding failure along the cracked section and then modified by Ali et al (2001) additionally account-

ing for the restrain provided by the externally bonded steel plate to the sliding failure along the cracked section as

$$f_3(\rho)=\frac{15}{b_c h}\left(A_s+\frac{P_p}{f_{yp}}\right)+0.58\le 1.26 \tag{1.21}$$

where P_p is the longitudinal restraining force imposed by the bonded plate as follows

$$P_p = 71 f_t t_p b_p \text{ when } L_b > 65 t_p \text{; otherwise } P_p = 1.09 L_b f_t b_p \text{ and } P_p \le f_{yp} t_p b_p \quad \text{(1.22a-c)}$$

where L_b is the bonded length of the plate. Be equalizing Equation 1. 18 to Equation 1.20, the ultimate strength V_u and the location of the critical diagonal crack are obtained.

This strength model also applied to the plate end debonding failure modes when the bonded plate extends to the vicinity of the supports where the critical diagonal crack occurs near the plate end. Thus the shear peeling strength is given as follows

$$V_u=\left(\frac{x^2+d^2}{B}\right)\left[\frac{f_{tef} b_c}{2}+\frac{m f_t b_p t_p\left(d+0.5 t_p\right)}{d^2}\right] \tag{1.23}$$

1.2.2.3 *Local Failure and the Strength Models*

Although the plate-bonding technique has many practical advantages, ultimate failure of a reinforced concrete (RC) beam strengthened for flexure occurs in a brittle manner due to sudden debonding of the plate from the concrete. Such a mode of failure not only diminishes the strengthening potential of externally bonded plates but also is unacceptable from the point of view of structural safety. Various strength models dealing with such sort of failure modes have been developed in the existing literature and they are reviewed as follows. Some of them have been reviewed by Smith and Teng (2002), but for the sake of the completeness, they are also listed here.

(1) Empirical Models

Various empirical models were set up to establish a relationship between plates debonding and various geometrical or load parameters. Normally the plate width (b_p) to thickness (d_p) ratio was controlled to prevent plate debonding. MacDonald (1982) restricted it to a value of not less than 60, whereas Swamy et al. (1987) recommended a value of 50. Both of these recommendations were only for using steel plates, and there are no similar observations for FRP plates and laminates, probably because of

their wide range of material properties. However, even with steel plates, exceptions to this rule of thumb have been observed, as for example, in the beams FRB3 and FRB4 tested by Hussain et al. (1995) (see Mukhopadhyaya and Swamy 2001). Swamy and Mukhopadhyaya (1995) attributed the exception to the size effects.

Even if this plate aspect ratio requirement is met, it is still necessary to ensure that the plated section is under-reinforced to avoid the premature failures associated with over-reinforced sections. The neutral axis depth is the parameter that determines the under- or over-reinforcement condition; based on the ratios of neutral axis depth to effective depth for flexural and premature failures in the studies by Swamy et al. (1987) and Jones et al. (1982), a ratio of 0.40 or less was recommended to ensure flexural failures.

Swamy et al. (1989) listed the steps involved in an approximate assessment of the adequacy of the plate end region of a steel plated beam. The ultimate elastic horizontal shear stress is found for the transformed section using the long-term modulus of elasticity of the concrete, although the short-term value gives a similar stress magnitude. The peak shear stress will be approximately twice the elastic value (Swamy et al. 1989). This peak stress is compared with the ultimate shear strength of the plate/concrete interface; this strength equal to approximately $\sqrt{2}$ times the tensile strength of the concrete, as seen from the experimentally estimated stresses in the tests by Jones et al. (1988). The assessment concludes by finding the factor of safety against plate separation, given by the ultimate shear strength divided by the peak shear stress.

(2) Interfacial Stress-based Models

A popular and logical assumption is that plate end debonding (mode c) or plate end interfacial debonding is due to high interfacial stresses at the end of the soffit plate. The concrete in the vicinity of plate ends experiences complex stress state, which includes longitudinal stress, transverse stress and shear stress (see Figure 1.3). Interfacial stress-based models generally make use of interfacial stresses analysis, which are listed in detail in the preceding section, and a concrete failure criterion, e.g. Mohr-Coulomb failure criterion.

(a) Oehlers and Moran's Model (1990)

Oehlers and Moran (1990) proposed, respectively, the serviceability peeling strength and ultimate peeling strength for a simply supported RC beam, strengthened in the pure bending moment region. They termed this kind of debonding failure as 'flexural peeling'. The ultimate and serviceability characteristic strength, which are based on the 5% probability of failure level, were also proposed for the purpose of design application. That is

$$M_{sp} = \frac{E_c I_{trc,c} f_{ct}}{0.827 E_p t_p} \tag{1.24}$$

$$M_{up} = \frac{E_c I_{trc,c} f_{ct}}{0.474 E_p t_p} \tag{1.25}$$

where M_{sp} and M_{up} are, respectively, predicted serviceability and ultimate peeling moment; f_{ct} the cylinder splitting tensile strength of concrete, and can be taken as $0.5\sqrt{f_c'}$, where f_c' is the concrete cylinder compressive strength in MPa, if it is not determined from tests.

In the case of practical designing, the external moment at a distance of 1.2 d from the end of the plate does not exceed the following serviceability M_{sc} and ultimate M_{uc} characteristic strengths, i.e.

$$M_{sc} = \frac{E_c I_{trc,c} f_{ct}}{1.86 E_p t_p} \tag{1.26}$$

$$M_{uc} = \frac{E_c I_{trc,c} f_{ct}}{0.901 E_p t_p} \tag{1.27}$$

It was suggested that in design, this moment needed only to be compared to the additional moment applied to the beam at the plate end after the plate is bonded.

(b) Ziraba et al's Models (1994)

Ziraba et al. (1994) proposed an interfacial debonding strength model for steel plated RC beams, and the also referred to Baluch et al. 's (1995) shear strength model to predict the debonding strength for plate end debonding.

In this model, the Mohr-Coulomb failure criterion is used to define the critical stress state at plate end interfacial debonding:

$$\tau + \sigma_y \tan\phi \le C \tag{1.28}$$

where τ and σ_y are the peak interfacial shear and normal stresses at the plate end; C the coefficient of cohesion; and ϕ the angle of internal friction. The peak interfacial shear and normal stresses are given by

$$\tau = \alpha_1 f_{ct} \left(\frac{C_{R1} V_0}{f_c'} \right)^{\frac{5}{4}} \tag{1.29}$$

$$\sigma_y = \alpha_2 C_{R2} \tau \tag{1.30}$$

where C_{R1} and C_{R2} are obtained from Equation 1.5 and Equation 1.6 respectively; α_1 and α_2 are empirical multipliers calibrated from numerical studies for RC beams retrofitted with steel plates.

Substitution of Equations 1.29 and 1.30 into Equation 1.28 gives an expression for the shear force at the plate end of the beam

$$V_d = \frac{f_c'}{C_{R1}} \left[\frac{C}{\alpha_1 f_{ct} (1 + \alpha_2 C_{R2} \tan\phi)} \right]^{\frac{4}{5}} \tag{1.31}$$

where V_d is the critical shear force in the RC beam at the plate end to cause debonding. This relationship is subject to the constraint of $a/h < 3$, where h is the overall depth of the RC beam. The following values for α_1, α_2 and ϕ were specified in Ziraba et al. (1994): $\alpha_1 = 35$, $\alpha_2 = 1.1$ and $\phi = 28^\circ$. In Ziraba et al. (1994) two values of C were used in different numerical examples, namely 2.68 MPa and 5.36 MPa, although the criteria used for the selection of these values were not made clear. Ziraba et al. (1994) suggested that C lie between 4.80 MPa and 9.50 MPa based on experimental and numerical findings.

(c) Varastehpour and Hamelin's Model (1997)

Varastehpour and Hamelin (1997) also developed a plate end interfacial debonding strength model based on the Mohr-Coulomb failure criterion. In their model, the coefficient of cohesion C was calibrated from single lap shear tests and the angle of internal friction ϕ determined from small-scale FRP-plated beam tests that failed by debonding. Details of the particular mode of debonding exhibited by these test beams were not specified by them. An average value of 5.4 MPa was suggested for C, while a value of 33° was suggested for ϕ.

The shear stress required in the Mohr-Coulomb equation is given by

$$\tau = \frac{1}{2}(\beta)^{0.5}(\lambda V_0)^{1.5} \tag{1.32}$$

This equation was modified from the following expression for the shear stress between a steel soffit plate and an RC beam originally proposed by Jones *et al* (1988) using the classical shear stress method:

$$\tau = \lambda V_0 \tag{1.33}$$

where λ is the rigidity of the section defined by

$$\lambda = \frac{t_p E_p}{I_{trc,c} E_c}\left(h_p - h_{trc,c}\right) \tag{1.34}$$

where $I_{trc,c}$ is the cracked transformed second moment of area of the plated section transformed to concrete. In Equation 1.32, the factor β was introduced to account for the effect of various variables that have a significant influence on the interfacial shear stress between the RC beam and the soffit plate, such as the rigidity and thickness of the plate, geometry of the section, and nature of loading based on a parametric study using a numerical model which considered slip between the plate and the RC beam. The following expression was developed by them for β:

$$\beta = \frac{1.26\times10^5 B}{h^{0.7} t_p E_p} \tag{1.35}$$

The normal stress σ_y is related to the shear stress as derived by Roberts (1989)

$$\sigma_y = C_{R2}\tau \tag{1.36}$$

The shear force in the beam, at the plate end to cause debonding, can then be determined by

$$V_d = \frac{1.6\tau_{\max}^{\frac{2}{3}}}{\lambda\beta^{\frac{1}{3}}} \tag{1.37}$$

where

$$\tau_{\max} = \frac{5.4}{1 + C_{R2}\tan 33^o} \tag{1.38}$$

(d) Saadatmanesh and Malek's Model (1998)

Saadatmanesh and Malek (1998) developed a debonding strength model to predict plate end debonding in FRP-plated beams based on the assumption that PED failure is

related to high stresses at the plate end. Of the three stresses present at the end of the soffit plate, the shear stress τ and the normal stress σ_y are from a closed-form solution derived by Malek et al. (1998) while the longitudinal stress is from a section bending analysis, all based on an uncracked section. This closed-form solution was derived assuming the following quadratic distribution for the bending moment, which can accommodate both point and uniformly-distributed loads:

$$M = a_1(x+a)^2 + a_2(x+a) + a_3 \tag{1.39}$$

where x is the distance along the soffit plate from its left end. For a simply supported beam subjected to three or four point bending, the bending moment at the plate end (M_0) for a soffit plate terminated in the shear span is given by $M_0 = a_2 a + a_3$. Under this bending moment distribution (Equation 1.39), the interfacial shear stress τ at the plate end is given as

$$\tau = t_p\left(b_3\sqrt{A} + b_2\right) \tag{1.40}$$

where

$$A = \frac{G_a}{t_a t_p E_p} \tag{1.41}$$

$$b_2 = \frac{E_p}{I_{tru,c}E_c}\left(h_p - h_{tru,c}\right)\left(2a_1 a + a_2\right) \tag{1.42}$$

$$b_3 = E_p\left[\frac{1}{I_{tru,c}E_c}\left(h_p - h_{tru,c}\right)\left(a_1 a^2 + a_2 a + a_3\right) + 2\frac{a_1 E_p}{I_{tru,c}E_c}\left(h_p - h_{tru,c}\right)\frac{t_a t_p}{G_a}\right] \tag{1.43}$$

where $I_{tru,c}$ is the uncracked second moment of area of the plated section transformed to concrete, and $h_{tru,c}$ is the neutral axis depth of this transformed section. The normal stress σ_y at the plate end is

$$\sigma_y = \frac{K_n}{2b_a\beta^{*3}}\left(\frac{V_p}{E_p I_p} - \frac{V_0^* + \beta^* M_0}{E_c I_c}\right) + \frac{qE_p I_p}{b_p E_c I_c} \tag{1.44}$$

where

$$V_0^* = V_0 - 0.5hb_p t_p\left(b_3\sqrt{A} + b_2\right) \tag{1.45}$$

$$V_p = -0.5b_p t_p^2\left(b_3\sqrt{A} + b_2\right) \tag{1.46}$$

and

$$\beta^* = \left(\frac{K_n b_p}{4b_a E_p I_p}\right)^{\frac{1}{4}} \tag{1.47}$$

where I_c is the second moment of area of the beam and q is a uniformly distributed load if such a load exists.

The longitudinal stress σ_x at the base of the RC beam, at the end of the soffit plate, due to a bending moment M_0 can be determined from a bending analysis of an uncracked section. The bending moment in the concrete beam at the plate end is increased by an amount M_m, defined as follows and attributed to the peak interfacial shear stress:

$$M_m = 0.5hab_p\tau \tag{1.48}$$

Once all three stress components at the plate end are determined, the maximum principal stress can be found as follows

$$\sigma_1 = \left(\frac{\sigma_x + \sigma_y}{2}\right) + \sqrt{\left(\frac{\sigma_x - \sigma_y}{2}\right)^2 + \tau^2} \tag{1.49}$$

At the plate end, the concrete is generally subjected to biaxial tension. Plate end debonding is deemed to occur when the maximum principal stress (in MPa) reaches the concrete splitting tensile strength, that is, when

$$\sigma_1 = f_{ct} = 0.295\left(f_c'\right)^{2/3} \tag{1.50}$$

(e) Tumialan et al's Model (1999)

Tumialan et al. (1999) developed a plate end debonding strength model for FRP-plated beams. Their model is in principle similar to Saadatmanesh and Malek's model (1998) reviewed above, in which the stresses acting on a concrete element at the plate end are determined and checked against a failure criterion of the concrete. The differences lie in how these stresses are evaluated. In Tumialan et al's model (1999), the peak interfacial shear and normal stresses at the plate end are determined from the solution of Roberts (1989) as follows:

$$\tau = \overline{C}_{R1}\frac{E_p}{E_c}V_0 \tag{1.51}$$

$$\sigma_y = C_{R2}\tau \tag{1.52}$$

where C_{R2} is defined by Equation 1.6, while $\overline{C}_{R1}$ is given by

$$\overline{C}_{R1} = \left[1 + \left(\frac{K_s}{E_p b_p t_p}\right)^{0.5}\frac{M_0}{V_0}\right]\frac{b_p t_p}{I_{tru,c} b_a}\left(h_p - h_{tru,c}\right) \tag{1.53}$$

The factor $\overline{C}_{R1}$ here differs from C_{RI} in Roberts (1989) in that the neutral axis and corresponding second moment of area are here based on an uncracked section transformed to concrete as opposed to a cracked section transformed to the plate material. As a result, the modular ratio of E_p/E_c is included in Equation 1.51. The longitudinal stress at the base of the RC beam σ_x, at the plate end, is also determined from a bending analysis of an uncracked section. However, the additional component induced by the interfacial shear stress as considered by Saadatmanesh and Malek (1998) in Equation 1.48 is not included here.

Once the stresses at the plate end are determined, the maximum principal stress σ_1 can be easily determined using Equation 1.49. Failure by plate end debonding is deemed to occur when this maximum principal stress σ_1 reaches the modulus of rupture of the concrete f_r which is taken as $0.689\sqrt{f_c'}$ (MPa) ($8.3\sqrt{f_c'}$ psi, [Mirza et al (1979)]).

(f) Ei-Mihilmy and Tedesco's Model (2001)

Ei-Mihilmy and Tedesco (2001) reviewed some existing interfacial stress based strength models, including Jones et al's model (1988), Roberts' model (1989), Ziraba et al's model (1994), Quantrill, Hollaway and Thorne's model (1996), Taljsten's model (1997) and Malek and Saadatmanesh's model (1998). Jones et al.'s model (1988) was here categorized as the empirical model in the Section 1.2.2.3-(1). Apart from the models already been reviewed in preceding section, Ei-Mihilmy and Tedesco (2001) utilized some other failure criteria of concrete in conjunction with the various stress formulas. For instance, the limiting shear stress was setting between 3 and 5 MPa for steel soffit plates in Roerts's (1989) stress equations; in Quantrill et al.'s (1996) equations, the peak interfacial shear stress was limited under 8 MPa, and a normal stress was in the range of 5 to 7.4MPa for GFRP, and the limiting shear stress was 11.15 MPa with a normal stress 6.4MPa for CFRP; in Taljsten's (1997) equations, Tasuji et al.'s (1978) failure criteria was used. Inconsistency was found in these strength models, which either overestimate or underestimate the failure loads. Thus Ei-Mihilmy and Tedesco (2001) proposed an improved model, which modified and simplified Roberts' equations (1989) and accounted for the nonlinearity that exist at the concrete-adhesive interface.

The maximum shear stress at plate cut-off points τ_{max} is

$$\tau_{max} = \tau + \alpha_f \sigma_x \tag{1.54}$$

In Equation 1.54, τ is the classical (Jourawski) shear stress given as

$$\tau = \frac{V_0 t_p (h_p - h_{trc,c})}{I_{trc,c}} \tag{1.55}$$

where σ_x is the longitudinal normal stress in the soffit plate, that is

$$\sigma_x = \frac{M_0 \psi_f^2 (h_p - c)}{I_{trc,c}} \tag{1.56}$$

where M_0 is the bending moment at plate cut-off point, ψ_f is the moment factor:

$$\psi_f = 1.35 - 12.5\frac{a}{L}, \ \frac{a}{L} \le 0.1 \tag{1.57}$$

where L is the total span of the soffit plate.

The maximum peeling stress at plate cut-off point $\sigma_{y,max}$ is

$$\sigma_{y,max} = 1.3\sqrt{\alpha_f \tau_{max}} \tag{1.58}$$

in which

$$\alpha_f = 0.28\sqrt{\frac{E_a t_p}{E_p}} \tag{1.59}$$

Then Tasuji et al.'s (1978) failure criterion was used to predict the failure load. As far as the biaxial tension state is conserned, failure occurs if the principal stress (in MPa) reaches the concrete splitting tensile strength that is when

$$\sigma_1 = f_{ct} = k(f_c')^{1/2} \tag{1.60}$$

where the factor k is set to 0.53 for normal-strength concrete ($f_c' < 55$ MPa) while it is 0.59 for high-strength concrete. It is noted that in Models (a), (d) and (f), the concrete splitting tensile strength f_{ct} is obtained by using various formulas which are taken from different references cited in their original papers.

(3) Concrete Tooth Model

Raoof and his associates (Zhang et al. 1995, Raoof and Zhang 1997) developed a debonding model for the steel plated RC beams based on the formation of 'teeth' along a shear span which is similar to the 'comb' model suggested by Kani (1964) for

the transfer of shear. The width of a tooth in the shear span, which is a very important parameter in the model, is determined by the stabilized minimum crack spacing that depends on the bond strength of the reinforcing bars which is assumed to be constant along the shear span and here was modified to accommodate the effect of the bonded plate. A tooth is then assumed to act as a cantilevered beam that is subjected to horizontal shear flow forces at its free end (Figure 1.4). The shear flow stresses, on the other hand, are stresses acting at the interface between the externally bonded plate and the concrete, based on the maximum direct stress in the plate that is located at the position of maximum bending moment at the end of the shear span remote from the plate end. Debonding is deemed to occur when these shear stresses lead to tensile stresses at the root of the "tooth" that exceeds the tensile strength of the concrete. A lower bound and upper bound to steel plate normal tensile stress were obtained and based on these stresses, the bounds of the ultimate peeling bending moments were predicted by using the method with the assumption of plane-section bending. Wang and Ling (1998) and Raoof and Hassanen (2000) extended this model to cases where FRP plates are used for upgrading RC beams in flexure. Recently Zhao et al. (2001) conducted some experiments to investigate the applicability of tooth model. Experimental results indicated the reasonability of tooth model in term of the failure mechanism.

(a) Raoof and Zhang's Model

The tooth model was first proposed in Zhang et al. 1995. They assumed that the interfacial stresses were distributed uniformly throughout the shear spans. Raoof and Zhang (1997) extended it catering for non-uniform distribution of shear stress throughout the bonded length of plate in the shear spans. Minimum and maximum crack spaces ($l_{\min}$ and $l_{\max}$ respectively) are determined, which lead to a lower and an upper bound stress in the plate to cause debonding respectively. The spaces of these cracks differ by a factor of two ($l_{\max} = 2l_{\min}$). The minimum space of a crack $l_{\min}$, termed the minimum stabilized crack spacing (see Zhang et al. 1995), is given by

$$l_{\min} = \frac{A_e f_{ct}}{u\left(\sum O_{bars} + b_p\right)} \tag{1.61}$$

where A_e is the area of concrete in tension, u the steel-to-concrete average bond strength, ΣO_{bars} the total perimeter of the tension reinforcing bars. It is assumed that $u = 0.28\sqrt{f_{cu}}$ (in MPa) and $f_{ct} = 0.36\sqrt{f_{cu}}$ (in MPa). In the case of an RC beam with a

single layer of steel tension reinforcement, A_e is twice the distance from the centroid of the tension reinforcement to the base of the RC beam multiplied by the width of the RC beam.

Ignoring interaction between adjacent teeth and assuming elastic behaviour, the required shear stress to cause failure of a tooth can be determined. Failure of the tooth occurs when the stress at point A (Figure 1.4b) exceeds the tensile strength of the concrete. The tensile stress at point A, σ_A, can be determined from

$$\sigma_A = \frac{M_A}{I_A}\left(\frac{l}{2}\right) \tag{1.62}$$

where $M_A = \tau l b_p h'$ and $I_A = b_p l^3/12$. Here, l is the crack spacing (minimum or maximum), h' is the net height of concrete cover measured from the base of the steel tension reinforcement to the base of the concrete beam, τ is the shear stress at the interface between the concrete and the soffit plate, I_A is the second moment of area of the tooth, and M_A is the moment at the base of the tooth.

Substitution of M_A and I_A into Equation 1.62 and assuming that at the instant of plate debonding, $\sigma_A = f_{ct}$, the shear stress at the interface between the concrete and the steel plate based on a minimum stabilized crack spacing can be determined. In this tooth theory, all teeth in the end anchorage zone are assumed to fail simultaneously at debonding.

$$\tau_{\min} = \frac{f_{ct} l_{\min}}{6h'} \frac{b_c}{b_p} \tag{1.63}$$

The minimum stress in the soffit plate $\sigma_{s,min}$ required to cause flexural cracking and failure of a tooth covering the minimum stabilized crack spacing can then be determined as follows:

$$\sigma_{s(\min)} = 0.154 \frac{L_p h_1 b_c^2 \sqrt{f_{cu}}}{h' b_p t_p \left(\sum O_{bars} + b_p\right)} \tag{1.64}$$

where L_p is an effective length of soffit plate for end anchorage, and h_1 is the distance from the centroid of the tension reinforcement to the base of the RC beam.

In Zhang et al. (1995), the effective length for end anchorage was taken as the length of the soffit plate in the shear span (in Figure 1.4a this is indicated as L_{p1}). In Raoof and Zhang (1997), it was recommended that the effective length for end anchorage be the smaller of the length of the soffit plate in the shear span L_{p1} and the following lengths L_{p2}, which were calibrated against test data of steel, plated RC beams that failed by plate end debonding:

$$L_{p2} = l_{\min}\left(21 - 0.25 l_{\min}\right) \quad l_{\min} \le 72mm \tag{1.65a}$$

$$L_{p2} = 3 l_{\min} \qquad l_{\min} > 72mm \tag{1.65b}$$

Once the stress in the plate is known, the moment to cause debonding of the plate, at the same location as the stress, can be calculated using a conventional section analysis with the assumption of plane section bending in accordance with Zhang et al. (1995) and the tensile strength of concrete taken into account. A lower and an upper bound bending moments are determined as a consequence of the assumed minimum ($l_{\min}$) and maximum ($l_{\max}$) stabilized crack spacings differing by a factor of two.

For a simply supported beam under four point bending with the plate positioned in the constant moment region, Raoof and Zhang (1997) specified that the effective length should be obtained from Equation 1.65b as the length of the plate in the shear span L_{p1} is zero.

(b) Wang and Ling's Model (1998)

Wang and Ling (1998) proposed a modification to Zhang et al.'s tooth model (1995) to make it suitable for FRP-strengthened beams. This involved modifying the average bond strength between the concrete and the plate, leading to the following formula for the minimum crack spacing:

$$l_{\min} = \frac{A_e f_{ct}}{u_s \sum O_{bars} + u_p b_p} \tag{1.66}$$

where $u_s = 0.313\sqrt{f_c'}$ is the average bond strength between the steel tension reinforcement and concrete and is the same as that used by Zhang et al. (1995) assuming $f_c' = 0.8 f_{cu}$. u_p is the average bond shear strength between the FRP and the concrete and was taken as 1.96 MPa.

Once the minimum stabilised crack spacing is determined, the remainder of the analysis is essentially the same as that given in Zhang et al. (1995) although the effective length for end anchorage taken by Wang and Ling (1998) was the total plate length in the shear span. In Wang and Ling's model, the tensile strength of concrete was not included in the section analysis for relating the bending moment in the beam to the stress in the plate. Similar to the model of Zhang et al. (1995), an upper bound solution of Wang and Ling's model is obtainable by replacing their minimum crack spacing (Equation 1.66) with a maximum crack spacing which is twice the former.

(c) Raoof and Hassanen's Model (2000)

Raoof and Hassanen (2000) also modified Zhang et al.'s model (1995) for application to FRP-plated beams. Two expressions were presented for the effective length of the FRP plate for end anchorage, which included two values for the bond strength between the FRP and the concrete. These modifications leaded to two new models. They are referred to herein as Raoof and Hassanen's model I and model II.

In Raoof and Hassanen's model I (2000), Equation 1.65 is retained to calculate the minimum stabilised crack spacing. The effective length of the plate for end anchorage is taken to be the smaller of the plate length in the shear span (L_{p1} in Figure 1.3a) and the following lengths which were calibrated with test data of FRP-plated RC beams reported to have failed by plate end debonding:

$$L_{p2} = l_{\min}\left(24 - 0.5 l_{\min}\right) \quad l_{\min} \le 40\,mm \tag{1.67a}$$

$$L_{p2} = 4 l_{\min} \qquad l_{\min} > 40\,mm \tag{1.67b}$$

In Raoof and Hassanen's model II, the bond strength between the FRP plate and the concrete is specified as 0.8 MPa, while the bond strength between the steel tension reinforcement and the concrete is still the same as that originally specified in Zhang et al. (1995). The effective length of the FRP plate for end anchorage is defined as the smaller of the plate length in the shear span and the following lengths which were calibrated with test data of FRP-plated RC beams reported to have failed by plate end debonding using the new value of FRP-to-concrete bond strength:

$$L_{p2} = l_{\min}\left(11.6 - 0.17 l_{\min}\right) l_{\min} \leq 56.5mm \tag{1.68a}$$

$$L_{p2} = 2l_{\min} \qquad l_{\min} > 56.5mm \tag{1.68b}$$

Once the stabilised crack spacing and the effective length of FRP plate for end anchorage are determined, the remainder of the analysis is the same as that given in Zhang et al. (1995).

(4) Interaction Model

(a) Oehlers' Model (1992)

Oehlers' Model (1992) proposed this model to determine an interaction envelope to describe the combination of shear and flexural peeling in steel plated beams. The work was based on experimentally tested beams plated over their full width, in which the length of plate and the shear span were varied so that the end of the plate was located in positions of varying proportions of bending moment and shear force. The envelope was described by

$$\frac{M}{M_u} + \frac{V}{V_u} \leq 1.17 \tag{1.69}$$

and

$$M \leq M_u,\ V \leq V_u \tag{1.70}$$

Where M and V are respectively the serviceability/ultimate debonding moment and shear force at the cut-off ends of the bonded plate; M_u is the serviceability/ultimate debonding moment for a plate terminated in the constant bending moment region and is given by Equation 1.24 or 1.25; and V_u is the serviceability/ultimate shear strength of the corresponding un-strengthened beam without shear stirrups, which can be found in most codes of practice. When Equations 1.69 and 1.70 are used for designing applications, the characteristic values for M_u and V_u, rather than the nominal ones, should be used, e.g. M_u should be taken as provided by Equation 1.26 or 1.27.

(b) Garden's Model (1997)

Garden (1997) proposed another interaction envelope based on the maximum global shear force and bending moment of the plated beams. This is a modification of Oehlers' (1992) model to consider the ultimate failure of the bonded beams rather than the initial onset of plate debonding. This interaction envelope could include the

transition from local failure modes towards flexural failure modes. It is calibrated from the experiments of the beams bonded with FRP plates. Therefore, it is suitable for FRP bonded beams. The interaction equation is

$$0.38\frac{V_{ult}}{V_{uc}} - \frac{M_{ult}}{M_{ult,a}} = 0.0076 \tag{1.70}$$

where V_{ult} is the ultimate shear force at failure of the beam; M_{ult} is the ultimate bending moment at the loading positions at failure; V_{uc} is the ultimate shear capacity of beam with internal tensile rebars but without internal shear stirrups; $M_{ult,a}$ is the theoretical global bending moment at the loading position corresponding to flexural failure, and can be obtained by the strain compatibility iterative method described in Section 1.2.2.1.

(c) Smith and Teng's Model (2001)

Smith and Teng (2001) also extended Oehlers' (1992) model to predict the debonding strength of RC beams bonded with FRP plates. In their model, they ignored the effect of bending moment and factored the ultimate shear capacity of the unplated beam without shear stirrups. That is

$$V_d = \eta V_u \tag{1.71}$$

where V_u was taken from the Australian Concrete code (AS 3600 1988):

$$V_u = [1.4 - (d/2000)]b_c d[\rho_s f_c']^{\frac{1}{3}} \tag{1.72}$$

where $\rho_s = A_s / b_c d$ is the ratio of steel tension reinforcement and it is required that $1.4 - (d/2000) \geq 1.1$.

(5) Fracture Mechanic-Based Strength Model

In this type of model, stress intensity factors or energy criteria, such as the strain energy release rate (ERR) in the context of linear elastic fracture mechanics (LEFM) and fracture toughness in the context of nonlinear facture mechanics (NLFM), replaces the stress criteria in the prediction of the interfacial crack initiation and growth. Although this approach is commonly used in aerospace and mechanical engineering practice, application of this concept in the analysis and design of RC structures is still limited. The main obstacle to apply this approach lies in the necessity for an accurate and reliable solution of the stress and deformation field near the crack tip or at the delamination front.

(a) Triantafillou and Plevris's Model I (1991)

Triantafillou and Plevris (1991) considered the peeling of a plate at the base of a shear cracks that was influenced by the size of the vertical and horizontal crack opening, '*v*' and '*w*', respectively, at the base of the crack. It was acknowledged that, for a given provision of internal shear reinforcement, these crack openings are controlled by the area fractions of the internal longitudinal steel and the external plate (if the beam is shear strengthened). Thus the applied shear force at which the plate initially separated at the shear crack V_{scd} was related to the crack openings and the shear provision by

$$V_{scd} \propto (v/w)_{cr} \sum GA \tag{1.73}$$

where $\sum GA$ is the total shear stiffness provided by the internal links and the external plate. It was suggested by Triantafillou and Plevris (1991) that shear crack-induced debonding occurs when the ratio, *v/w* reaches a critical value $(v/w)_{cr}$ that is a characteristic value of the plate/concrete bond. This method can only be applied if Equation 1.73 is calibrated with sufficient experimental data. However, it is seen qualitatively that a greater density of shear reinforcement will modify the failure load and/or failure modes by preventing or reducing the vertical step at a shear crack. Therefore, the finding of Oehlers (1992), that the shear reinforcement provision does not influence the ultimate condition, is valid only for cases of plate end debonding rather than shear crack-induced debonding.

(b) Triantafillou and Plevris's Model II (1991)

Triantafillou and Plevris (1991) also investigated the debonding along the bond line due to, for example, the occurrence of flexural cracks. They also attributed the causes which trigger this failure mode to (a) imperfections in the spreading of the adhesive; (b) peeling-off of the composite when the concrete tensile face is not perfectly flat and (c) fatigue loads, though they are rare. They referred to a numerical study undertaken by Anandarajah and Vardy (1985) to investigate interfacial fracture, where a linear elastic fracture mechanics model (LEFM) was based. The crack propagation along the bond-line resembled fracture mode II and the compliance method was used to obtain the strain energy release rate G_{II}, i.e.

$$G_{II} = \frac{P^2}{2b_c}\frac{dC}{da} \tag{1.74}$$

where C is the compliance of the plated beam under applied load P and a is the crack length. The rate of change of compliance, with respect to interfacial crack length, i.e. dC/da, cannot be found directly, but may be determined using a numerical procedure to find the variation of C with a and then to determine dC/da (see Anandarajah and Vardy ,1985). When the strain energy release rate G_{II} reached the critical strain energy release rate G_{IIcr}, the crack propagated catastrophic and the failure progress accelerated.

(c) Neubauer and Rostasy's Model (1999)

Neubauer and Rostasy (1999) extended a fracture mechanics model for bond strength of bonded CFRP-plates, derived from bond test, to beams subjected to bending and shear. In a bonded beam, vertical shear crack mouth displacements can reduce bond strength by reducing the total fracture energy, that failed the local bond. The shear crack mouth displacements for a CFRP strengthened RC beam were calculated, according to the acting forces, the geometry, the reinforcement and the material parameters of the beam. Then a mixed mode fracture mechanics approach was used to quantify the loss of bond strength due to simultaneous action of bending and shear. They found that in most cases, bond strength reduction due to the vertical shear crack displacement would range from 5% to 10%.

(d) Rabinovitch and Frostig's Model (2001)

Rabinovitch and Frostig (2001) conducted a comprehensive stress analysis of the strengthened RC beam using a closed-form high-oreder (CFHO) approach and predicted the interfacial delamination failure using an energy release rate (ERR) criterion. The ERR was calculated by the J-integral formulation. Three critical sections of the strengtheened beam, namely, at the plate end (the edge of the FRP strip), near a flexural crack and in the vicinity of a flexure-shear crack were investigated. Due to the complexity of the stress field as discussed in Section 1.2.1, the J-integral has to be calculated by the numerical methods. Numerical studies showed that the ERR decayed with the delamination growth at the flexural and flexural-shear cracks and the delamination was arrested when the ERR went below the critical fracture energy G_c. While at the plate ends, the ERR increased as the delamination progressed. This suggests that once the delamination reaches a critical length at which the ERR equals to

the critical fracture energy G_c, an unstable delamination growth is developed and a brittle failure of the beam is expected.

(e) FRP EBR Model (2001)

fib Task Group 9.3 EBR sub-group developed a debonding strength model in a unified way for both plate end debonding and intermediate crack-induced debonding based on the interface shear stress-slip law and the envelope line of tensile stresses in the FRP(Niedermeier 2000). The main principle of the method is to compare the maximum possible increase in tensile stress with the external bonded reinforcement (EBR) to the increase resistance according the design assuming full composite action. The basis approach consists of three steps, i.e. (1) determination of the most unfavorable spacing of flexural cracks; (2) determination of the tensile force within the EBR between two subsequent cracks according to the design in bending; and (3) determination of the maximum possible increase in tensile stress in the EBR. According to this method, the most unfavorable spacing of flexural cracks is:

$$s_{rm} = 2l_t = 2\frac{M_{cr}}{z_m}\frac{1}{\left(\sum \tau_{fm} b_p + \sum \tau_{sm} d_s \pi\right)} \tag{1.75}$$

$$\tau_{sm} = 1.85 f_{ctm} \tag{1.76}$$

$$\tau_{fm} = 0.44 f_{ctm} \tag{1.77}$$

$$M_{cr} = \frac{k f_{ct} b_c D^2}{6} \tag{1.78}$$

$$z_m = 0.85\frac{\left(DE_p A_p + dE_s A_s\right)}{\left(E_f A_f + E_s A_s\right)} \tag{1.79}$$

where s_{rm} is the mean value of crack spacing ; l_t is the transferring length; M_{cr} is the cracking moment; z_m is the mean lever arm of internal forces; τ_{sm} is the mean bond stress of steel reinforcement; τ_{fm} is the mean bond stress of FRP; f_{ctm} is the mean value of the concrete tensile strength; d_s is the diameter of steel rebars; k is the reduction factor; D is the overall depth of the RC beam. Using the flexural analysis, the tensile stresses at each cracks are calculated, during which the shift rule according to EC2 should be applied. Then the permitted maximal increases in tensile stresses in the EBR are showed as an envelope line in Figure 1.5 (the solid line) and for each part they are given as :

$$\text{line (1):} \qquad \max \Delta\sigma_{fd}^{(1)} = \max \Delta\sigma_{fd}^{(A)} - \frac{\left(\max \Delta\sigma_{fd}^{(A)} - \max \Delta\sigma_{fd}^{(B)}\right)}{\sigma_f^{(B)}} \sigma_{fd} \tag{1.80}$$

$$\text{line (2):} \qquad \max \Delta\sigma_{fd}^{(2)} = \frac{1}{\gamma_c}\left(\sqrt{\frac{0.0529 E_p \sqrt{f_{ck} f_{ctm}}}{t_p} + \sigma_{fd}^2} - \sigma_{fd}\right) \tag{1.81}$$

$$\text{line (3):} \qquad \max \Delta\sigma_{fd}^{(3)} = f_{fd} - \sigma_{fd} \tag{1.82}$$

where

$$\max \Delta\sigma_{fd}^{(A)} = \begin{cases} \dfrac{0.23}{\gamma_c}\sqrt{\dfrac{E_p \sqrt{f_{ck} f_{ctm}}}{t_p}}, & l_b = l_{b,\max} \\ \dfrac{l_b}{l_{b,\max}}\left(2 - \dfrac{l_b}{l_{b,\max}}\right)\sigma_{fad,\max}, & l_b \le l_{b,\max} \end{cases} \tag{1.83}$$

$$l_{b,\max} = 1.44\sqrt{\frac{E_p t_p}{\sqrt{f_{ck} f_{ctm}}}} \tag{1.84}$$

$$\max \Delta\sigma_{fd}^{(B)} = \frac{1}{\gamma_c}\left(\sqrt{\frac{0.0529 E_p \sqrt{f_{ck} f_{ctm}}}{t_p} + \left(\sigma_f^{(B)}\right)^2} - \sigma_f^{(B)}\right) \tag{1.85}$$

$$\sigma_f^{(B)} = \frac{0.185 E_f}{s_{rm}} - 0.285\sqrt{f_{ck} f_{ctm}}\,\frac{s_{rm}}{4t_f} \tag{1.86}$$

In the above equations, σ_f, σ_{fd} and $\sigma_{fad,\max}$ are respectively nominal stress, design value of stress, and design value of maximum anchorage stress in FRP. f_{ck}, f_{ctm} and f_{fd} are respectively characteristic value of the concrete compressive strength, mean value of the concrete compressive strength, and design value of FRP tensile strength. γ_c is the material safety factor for the concrete. l_b and $l_{b,\max}$ are bond length and maximum anchorage length.

(f) Teng and Chen's Model (2001)

Teng et al. (2001a) indicated that intermediate crack-induced interfacial debonding failures have much in common with debonding failures observed in simple shear test. The simple strength model of Chen and Teng (2001) for steel and FRP plate-to-concrete bonded beams, which was derived based on the NLFM method and then calibrated by experimental data, was modified to predict the intermediate flexural crack-induced debonding by Teng et al (2001c), i.e.

$$\sigma_{dic} = \alpha\beta_p\beta_L\sqrt{\frac{E_p\sqrt{f_c'}}{t_p}} \tag{1.87}$$

where α, β_p and β_L are the calibration coefficients which are given respectively in Teng et al (2001c) and Chen and Teng (2001); σ_{dic} is the stress in the FRP when the intermediate crack-induced debonding occurs. Once the plate stress, σ_{dic} in a critical section is predicted using Equation 1.87, the debonding moment capacity can be calculated by the conventional section analysis. Teng et al. (2000) also recommended this strength model to predict the shear or shear/flexural crack-induced debonding, after they found the predictions were favorably conservative.

1.2.2.4 *Concluding Remarks on the Review of Strength Models*

Table 1.2 shows the applicability of the preceding reviewed strength models. From Table 1.2, we can see that not all the strength models apply to both steel plate and FRP plate strengthening. This is because of the significant differences of the material properties between these two bonded materials. Except for the interfacial stress-based strength models, all the other strength models are concerned with the ultimate debonding loads, at which the ultimate debonding failure occur. Generally speaking, at the ultimate limiting state, it is very difficult to distinguish one debonding mode from the others. However, one common feature of all these failure mechanisms is that cracks occur due to complex stresses, which is the key cause leading to failure. The difference among them is that the cracks from the plate end have different inclinations, which has close relation with the various magnitudes of failure loads and brittleness when failure occurs (Teng et al. 2001a). The degree of the inclination of a crack is believed to relate to the stress state at the crack tip, i.e. the interaction between the stress components. Owing to the complexity of the failure mechanism and affecting factors, most of the existing strength models were calibrated by the experimental data. From Table 1.2, we can see that all the interfacial stress-based strength models are concerned with serviceability strength. However, it is the ultimate failure loads other than the initial debonding loads were recorded in the existing experimental database, since it is very difficult to observe the onset of the debonding by naked eyes when the first fine inside crack occurred. In some literature, the predicted serviceability strength was compared with the experimental ultimate strength, which is arguable. Another point, which should be noted, is that some of the existing analytical stress predictions, either based on the elastic analysis or calibrated by the numerical results taking into account nonlinearity, are not accurate enough. It is one of the reasons that lead to in-

consistent reliability of the strength models. Thus a more reliable stress analysis approach, which is simple but can reflect the real status of the strengthened RC beam, is required.

1.2.3 Some Other Aspects of the EPB Techniques

1.2.3.1 *Effect of the Plate Anchorage Lengths upon the Premature Failure Loads*

Jones et al. (1980) tested some steel bonded beams with a constant span between the two beam supports. The beams were loaded with a variable load span such that the shear span/depth ratio ranged from 1.7 to 3.7. Plated beams with shear span/depth ratios of 1.7 and 2.4 failed in shear while a shear span/depth ratio of 3.7 resulted in flexural failure, with concrete crushing at the top of the beam. Weder and Ladner (1981) tested steel plated beams whose anchorage length varied with plate width to maintain a constant bonded area. The beams strengthened by the plate with the highest aspect ratio while shortest anchorage length failed in flexure, whereby yielding of the steel plate preceded concrete crushing at the top of the beam. This indicated that a high plate aspect ratio might compensate for a low anchorage length, preventing the concrete cover separating from internal reinforcement. Beams with lower plate aspect ratios and greater anchorage lengths failed by separation of the concrete cover layer from the internal rebars, highlighting the inability of long anchorage lengths to prevent this failure mode when the plate was narrow and thick. Johnson and Tait (1981) used a cantilever loading arrangement to apply bending and tension loading to reinforced concrete members strengthened by externally bonded mild steel plates. The length of bonded plate was varied to achieve different ratios of bond length to loaded span. The premature failure occurred at relatively low anchorage lengths. Jansze (1995) tested beams in which steel plates were bonded up to three different distances from a loading point in order to provide three anchorage lengths for comparison. All three specimens failed by separation of the concrete cover layer from the internal longitudinal reinforcement, initiated at the end of the plate. Bond line shear stresses, determined from plate strain data, became greater with reducing anchorage length at a given applied load. Failure loads were found to be lower under shorter anchorage lengths. Garden et al. (1997) carried out an experimental parameter study of the strengthening of reinforced concrete beams by bonded composite plates. Plate geometry and applied load configuration are studied, revealing that bonded plates increase

the ultimate capacity of beams but reduce ductility. Ultimate capacity falls with reducing plate aspect ratio and beam shear span/depth ratio. Failure under low shear span/depth ratios is associated with high plate strains, while this is not always the case for high shear span/depth. Four point bending and cantilever loading are used by Garden et al (1998) to show that the ultimate capacities and failure modes of reinforced concrete beams externally strengthened with bonded composite plates are dependent on the shear span/depth ration. Strengthened members are found to fail by separation of the concrete cover from the internal rebars throughout the whole of one shear span under low shear span/depth ratios, while a thinner concrete layer is separated at higher ratios. Peeling of the plate end is thought to occur under low shear span/depth ratios. The end of the bonded plate in the failed shear span experiences strain increases relatively soon after yield of the internal steel when the shear span/depth ratio is low, but the plate ends are less sensitive to yield under higher ratios, indicating the lower shear transferred into the concrete via the adhesive at the plate ends. Ultimate bending moments are found to reach an upper limit with increasing shear span/depth ratio in the range of ratios studied. Adhesive shear stresses are of great magnitude at the ends of the plate under low shear span/depth ratios. Garden and Hollaway (1998a) conducted an experimental study for the CFRP plated bonded RC beams to investigate the influence of plate end anchorage. Results found that the structural benefit of plate end anchorage diminishes as the shear span/depth ratio of the beam increases. Also influenced by the shear span/depth ratio is the plate anchorage length, which determines the magnitudes of the shear and peel stresses at the ends of the bonded plate.

1.2.3.2 *End Anchorages*

Swamy and Mukhopadhyaya (2000) experimentally investigated the plate-debonding phenomenon when CFRP laminates were used as externally bonded additional reinforcement to strengthen existing RC beams. The test results show that although strengthening with CFRP laminates can impart many structural benefits, in terms of strength and stiffness, to the strengthened member, failures of the strengthened beams invariably occur in a catastrophic manner with much reduced ductility and a sudden loss of load capacity. Test observations also indicated that the complex stress system at the end of the laminates, leading to bond slip and plate separation, and the bond slip of the laminate itself along the span at critical sections of cracking and both of these can be successfully overcome by a judicious combination of end anchorages, addi-

tional intermediate anchorages along the span and lateral confinement of the compression zone. A definition of structural ductility was also put forward in their paper and can form a sound engineering basis to evaluate the structural behavior of beams strengthened by CFRP laminates.

1.2.3.3 *Strengthened with Prestressed FRP Plates*

Triantafillou et al. (1992) established a new method of strengthening and/or reinforcing concrete structures involving external bonding of pretensioned FRP sheets on their tension zones. An analytical model for the maximum achievable prestress developed in an earlier study is summarized and verified with test. Garden and Hollaway (1998b) made an extensive literature review about the previous work on the prestressed composite plates bonding technique. It was found that using prestrssed plate bonding technique could reduce the crack width, improve the shear resistance of concrete beams and change the failure modes compared with the non-prestressed bonding. Then the authors carried out some tests to study the failure modes of FRP prestressed concrete beams. The test results found that the prestressed beams normally failed by plate fracture, which longitudinal splitting developed progressively in the interlaminar interfaces. Quantrill and Hollaway (1998) also studied the advantage from the prestressed bonding to RC beam. After a literature review, they presented an experimental work on the structural behavior of RC beam for which an initial prestress was applied to the external FRP plate prior to bonding. Their findings on the benefit from the prestress bonding included increasing the cracking load, serviceability load in case of steel stress status governing such a load, yield load and maximum load, and, however, the increases of the ductility and the overall member stiffness after cracking of the concrete is not very significant.

1.2.3.4 *Strengthening for Precracked RC Beams*

Sharif et al. (1994) experimentally investigated the repair of initially loaded reinforced concrete beams with epoxy-bonded GFRP plates. The RC beams were initially loaded to 85 percent of the ultimate flexural capacity and developed midspan flexural cracks of which the length was 75 percent of their depth and the width was about 1.5mm under loading and reduced to 0.7 mm after unloading. Various repairing and anchoring schemes were conducted and different failure modes and the corresponding load deflection curves were discussed. Theoretical analysis for predicting the flexural strength (ACI) and the plate separation load (Roberts, 1989) are compared with ex-

periment results. From the test on double overlap FRP/concrete specimens, the maximum sustainable shear stress was to be 3.5 - 4 N/mm^2. The effects of the plate thickness on the separation load and that of the anchoring system on the ductility were studied. The results generally indicate that the flexural strength of the repaired beams is increased. The ductile behavior of the repaired beams is inversely proportional to the plate thickness. The use of an I-jacket plate provided a proper anchorage system and improved the ductility of beams repaired with plates of large thickness.

Hussain et al. (1995) presented some experimental data on the steel plate bonding repairing technique to the precracked RC beam. The effect of plate thickness and end anchorage on ductility, ultimate load and mode of failure was investigated. Test results showed that repairing could increase the strength if the plate thickness did not exceed a certain limiting thickness, and, otherwise, the brittle premature failure would occur. End anchorages to the bonded plates could not prevent the premature failure of the beams but improved ductility and yielded a marginal improvement in ultimate strength. Aruini and Nanni (1997a) presented experimental and analytical results for precracked RC beams and subsequently strengthened with CFRP sheets. Several variables were investigated, including: CFRP materials systems, concrete surface preparations, RC cross section and the number and location of CFRP plies. Also the presence of applied load as well as external prestressing during the adhesion of the CFRP were investigated. Based on the analytical and experimental results, they found that the pre-existing cracks, the CFRP materials systems and post tensioning were not significant while the surface preparation, the carbon fibre stiffness, fibre direction and number of plies have important consequences on performance of strengthened beams. Buyukozturk and Hearing (1998) reviewed the typical failure mechanisms of the precracked RC beam retrofitted with FRP and current analytical techniques for each of the failure modes.

1.2.3.5 *Optimization*

Mukhopadhyaya et al. (1998) tested full-scale beams bonded by GFRP plate externally to enhance the understanding of the flexural behavior of RC beams and then develop a clearer picture of the role and effectiveness of the GFRP plates in the structural performance of the composite beams. A special design technique was adopted to improve the ultimate load capacity of the strengthened composite beam and enhances

its ductility. The techniques include preservation of the plate-adhesive-concrete interface bond and strengthening the compression concrete by confinement through the use of bonded plates onto the beam web. The thickness of the compression plate should limited to prevent the premature bond failure to occur. Spadea et al. (2000) proposed a new criterion, i.e. Performance Factor to evaluate the structural performance of RC beam strengthened by CFRP laminates as well as the efficiency of the external anchorage system. This design criterion incorporates both the deformability and strength of composite beams. The effects of numerous parameters, which influence structural design, are included. External anchorage showed by the test results, play a significant role on optimizing the structure behavior, which is also reflected by the Performance Factor. The test carried out by Spadea et al. (1998) again showed that the provision of adequate external anchorages at the ends of the plates and at critical sections along the span can be essential prerequisites to obtain the maximum benefit from the CFRP plate and enhance the structural ductility of the plated composite beams.

1.2.3.6 *Shear Strengthening*

As an alternative approach to bonding steel plates at the soffit of a RC beam is to bond adhesively steel plates to the sides of reinforced concrete beams, according to the studies of Oehlers and Nguyen (2000a, 2000b). This bonding technique can enhance the shear peeling resistance and can even increase the ductility of the beam. Design rule for preventing premature debonding of the ends of side plates is developed, during which the former paper concentrated on the debonding due to flexural peeling, and the later went for the shear peeling and the interaction between shear peeling and flexural peeling.

Sharif et al. (1994) presented test results and their interpretation for shear-damaged RC beams with deficient shear strength, strengthened by externally bonded steel plates. The strength of all repaired beams was increased and the degraded stiffness of the beams was restored. Different arrangements of steel plates were used. Trantafillou (1998a) compiled some results related to the use of composites as shear strengthening materials for concrete, masonry and wood members. The classical truss analogy was adopted to predict the ultimate shear capacity of the RC beam strengthened by composite laminates or fabrics in shear. A wide range of experimental results on shear strengthening of RC beams with FRP laminates or fabrics were evaluated. Triantafil-

lou (1998b) presented a review of the literatures up to early 1997 for the shear strengthening of the RC beam. It was reported in that study that the effectiveness of the external FRP shear reinforcement and its contribution to the shear capacity of RC members depends on the mode of failure, which may occur either by peeling off through the concrete near the concrete-FRP interface, or by FRP tensile fracture at a stress that may be lower than the FRP tensile strength (e.g., because of stress concentrations at debonded areas or at rounded corners). Whether peeling off or fracture will occur first depends on the bond conditions, available anchorage length, types of attachment at the FRP curtailment, FRP thickness, FRP elastic modulus, concrete strength and other factors. It also was stated that, in many cases, the actual mechanism is a combination of peeling off at certain areas and fracture at others. Based on mostly qualitative arguments, Triantafillou (1998) derived a polynomial function that relates the strain in the FRP at shear failure of the member, defined as effective strain to the axial rigidity of externally bonded strips or sheets. Swamy et al (1999) carried out strengthening towards RC beam by bonding steel and GFRP on the tension face and web of RC beams weak in shear. Test results indicated that external plate bonding could transform the shear failure into flexural failure of RC beams with no, or inadequate, internal shear reinforcement. Also some factors determine the effectiveness of this bonding technique was identified. Tantafillou and Antonopoulos (2000) described an improved, yet simple, modeling approach for the contribution of externally bonded FRP shear reinforcement to the shear capacity of RC flexural members. It was then presented in three design formats: Eurocode, ACI and JCI.

1.2.4 Summary of the Literature Review

External Plate Bonding (EPB) technique applied to RC beams has become popular over the last few years. It is a strengthening procedure by bonding the steel or FRP plates to the soffit of the RC beams. Variations from this basic procedure include additional end anchorage and prestressing of the plates. In this section, some topics such as the stress transfer between the bonded plate and RC beam, and strength models for various failure modes are extensively reviewed. It also highlights some prerequisite work, which needs to be improved.

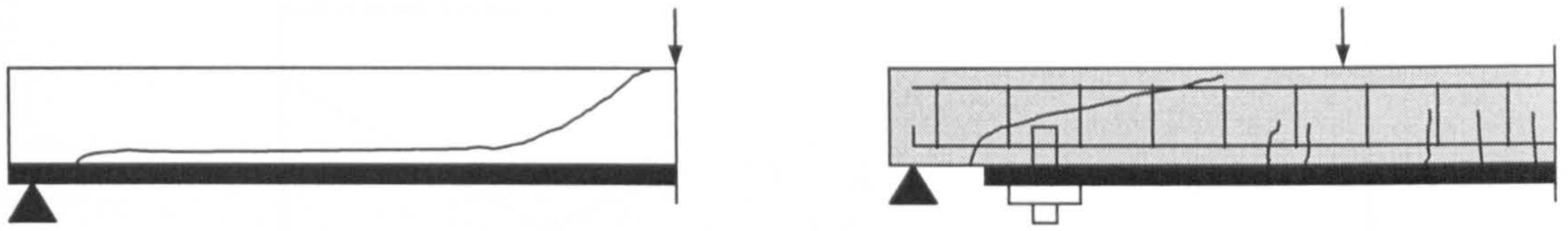

(a) Shear failure by a flexural shear crack in unreinforced beam C5 plated in flexural (I'Hermite and Bresson 1967)

(b) Shear failure by a plate-end shear crack in RC beam P2B plated in flexural and additional bolted for anchorage (Sharif et al 1994)

Fig. 1.2 Examples of the shear failure in the plated RC beams

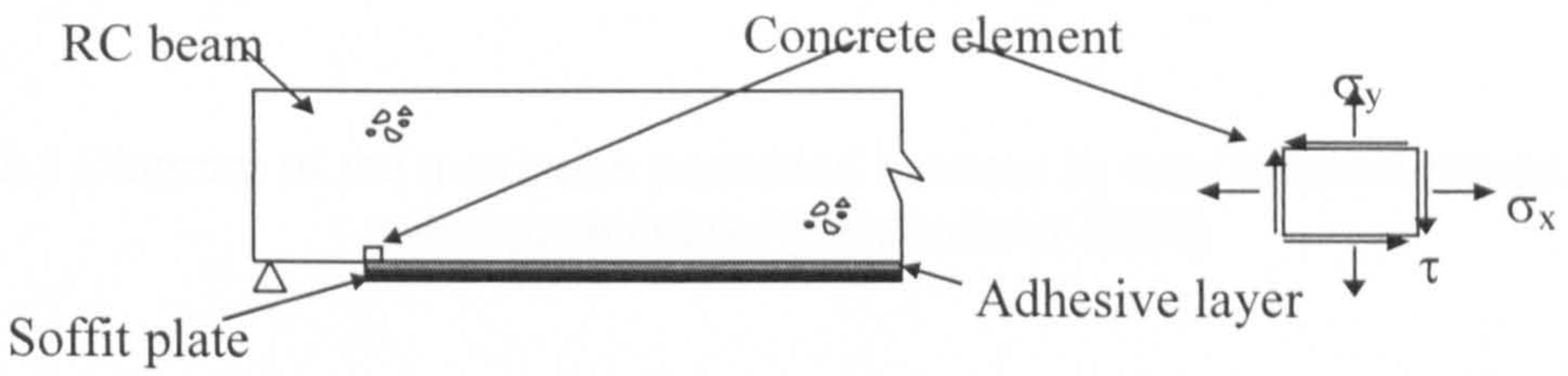

Fig. 1.3 Stresses acting on a concrete element adjacent to the plate end (Teng et al. 2001)

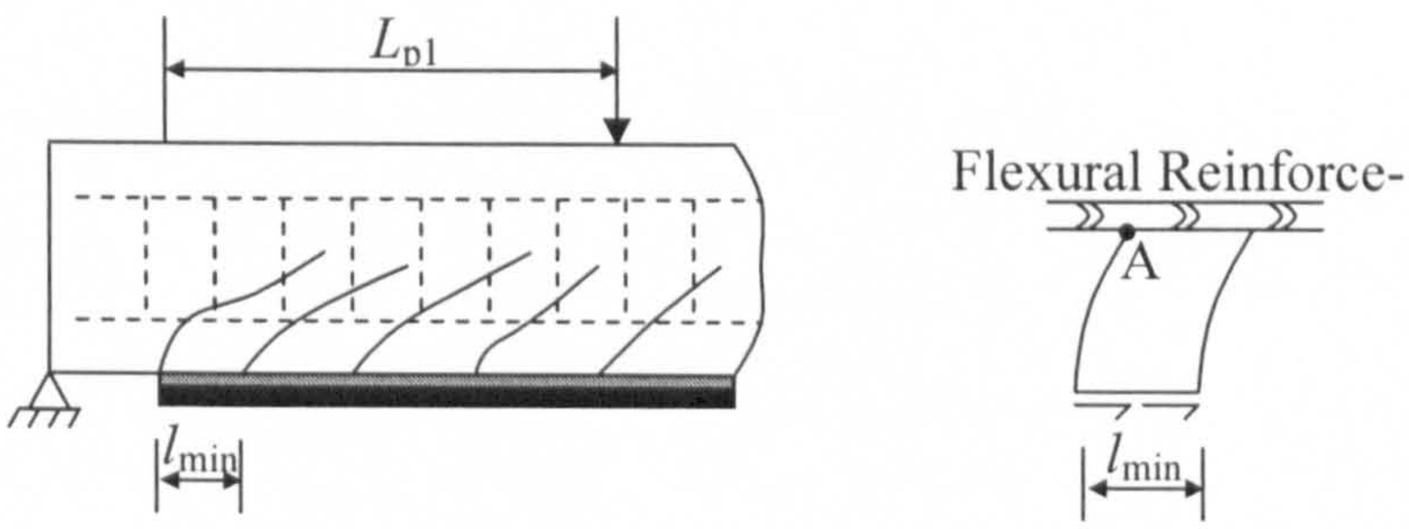

(a) Cracked beam (b) Concrete tooth between two adiacent flexural cracks

Fig. 1.4 Concrete tooth model (Teng et al. 2001)

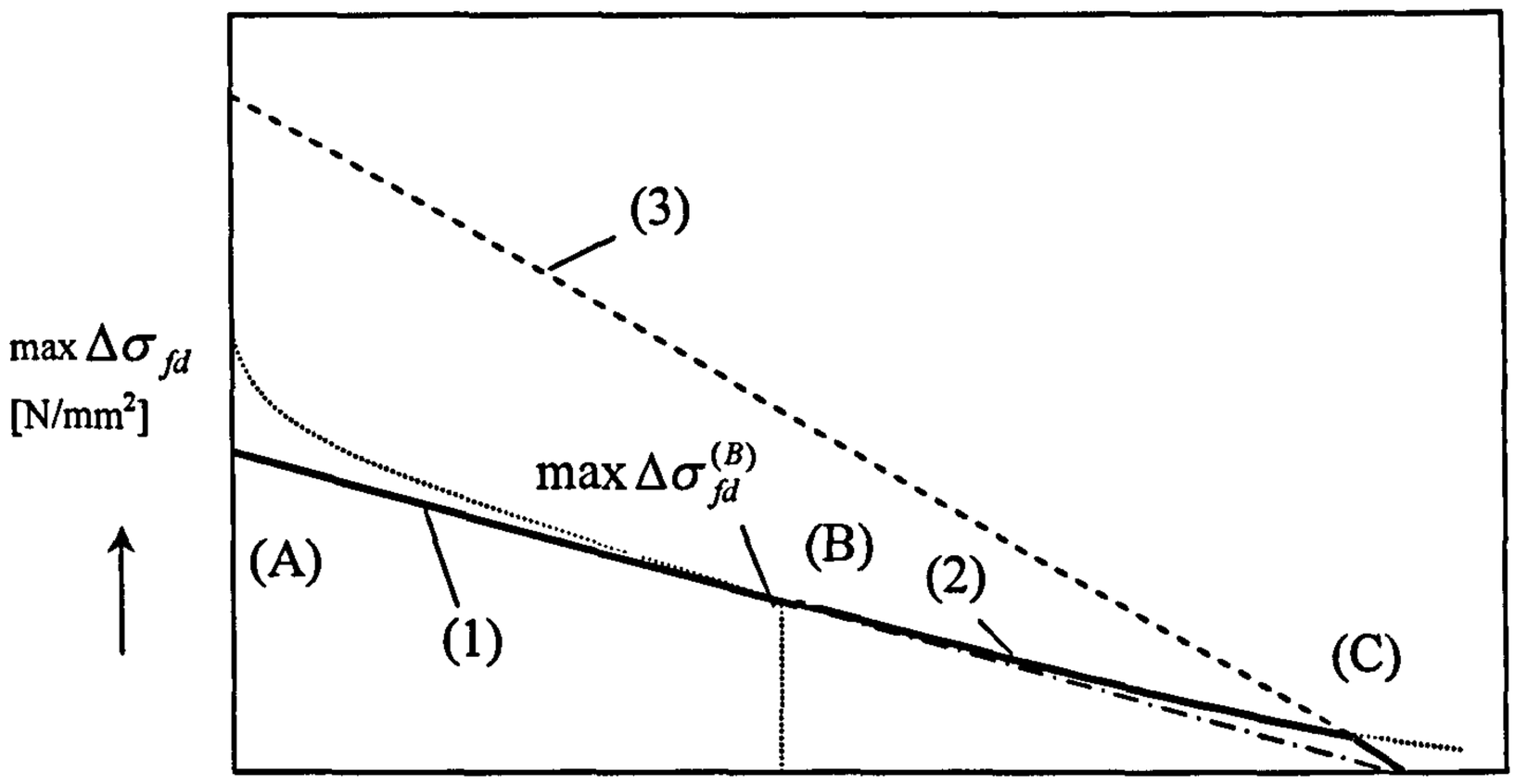

Fig. 1.5 Diagram of the maximum permitted increase in tensile stress between two subsequent cracks (Niedermeier 2000)

Table 1.1 Comparison in approximate closed-form solutions (Smith and Teng 2001)

Source		Vilnay (1988)	Roberts(1989)	Roberts and Haji-Kazemi (1989)	Liu and Zhu (1994)	Taljsten (1997)	Malek et al. (1998)	Smith and Teng (2001)
Load Cases		Point Load at mid-span	General	UDL	UDL, Point load at mid-span, two symmetric point loads	Single point load	General with some limitations	General*
Shear Stress	Axial deformations of beam	No	Partially considered*	Yes	No	Yes	Partially considered*	Yes
	Bending deformations of plate	No	Partially considered*	Yes	No	No	Partially considered*	Yes
	Shear deformations	No	No	No	Yes but incorrectly	No	No	Yes(in governing equations only)
	Boundary/continuity conditions at point load	Zero shear stress	-	-	Continuity in shear stress and its first derivative	Zero shear stress	Zero shear stress	Continuity in shear stress and its first derivative
	Other remarks	-	*Considered in stage 1 analysis which is for a fully composite section	-	Only general soluitons are given with boundary conditions	-	*Extreme fiber stress of the original beam base on fully composite action	*Specific interfacial stress expressions developed only for three load cases
Normal Stress	Bending deformations of beam	No	No	No	Yes	Yes	Yes	Yes
	Shear deformation	No	No	No	Yes but incorrectly	No	No	Yes (in governing equations only)
	Additional plate bending deformations due to interfacial shear stresses	Yes	No	Yes	Yes	Yes	No	Yes

Table 1.2 Applicability of various strength models

Model	Steel(S) or FRP	Failure Modes	Serviceability (S) or Ultimate (U)
Baluch et al.'s Model (1994)	S	SF, PED	U
Jansze's Model (1997)	S	SF, PED	U
Ahmed et al's Model (2001)	FRP	SF, PED	U
Colotti and Spadea's Model (2001)	S, FRP	SCD, PED	U
Ali et al's Model (2001)	S	SF, SCD, PED	U
Oehlers and Moran's Model (1990)	S	PED	S, U
Ziraba et al's Models (1994)	S	PED	S
Varastehpour and Hamelin's Model (1997)	FRP	PED	S
Saadatmanesh and Malek's Model (1998)	S, FRP	PED	S
Tumialan et al's Model (1999)	S, FRP	PED	S
Ei-Mihilmy and Tedesco's Model (2001)	S, FRP	PED	S
Raoof and Zhang's Model (1995, 1997)	S	PED, SCD	U
Wang and Ling's Model (1998)	FRP	PED, SCD	U
Raoof and Hassanen's Model (2000)	S, FRP	PED, SCD	U
Oehlers' Interaction Model (1992)	S	SF, PED	U
Garden' Interaction Model (1997)	FRP	SF, PED, F	U
Smith and Teng' Interaction Model (2001)	FRP	SF, PED	U
Triantafillou and Plevris's Model I (1991)	FRP	SCD	U
Triantafillou and Plevris's Model II (1991)	FRP	FCD	U
Neubauer and Rostasy's Model (1999)	FRP	PED, SCD, FCD	U
Rabinovitch and Frostig's Model (2001)	S, FRP	PED, SCD, FCD	U
FRP EBR Model (2001)	FRP	PED, SCD, FCD	U
Teng and Chen's Model (2001)	FRP	SCD, FCD	U

Note: SF denotes shear failure; PED denotes plate end debonding; SCD denotes shear/flexural crack-induced debonding; FCD denotes flexural crack-induced debonding and F denotes flexural failure.

1.3 Research Objective

The main objectives of this research are to carry out a systematic study on the stress behavior of plated RC beams and its application in predicting the serviceability and ultimate debonding loads. The stress solutions, mainly for those along the interfaces, are sought in both linear and nonlinear context. The aim of the linear stress analysis is to develop a simplified solution of the interfacial stresses with adequate accuracy. To this end, a series of logically ordered linear solutions are derived, which include linear finite element analysis (LEFEA), complete numerical solution, closed-form rigorous solution and simplified solution. Allowing for the nonlinearity, a nonlinear finite element analysis (NLFEA) and a nonlinear fracture mechanics analysis (NLFM) are performed respectively. These solutions, in conjunction with some failure criteria, are exploited to predict both the serviceability and ultimate loads and the results are compared with those obtained from the experiments. Some recommendations are offered with regards to the application of the EPB technique to RC beams on the basis of the research findings.

1.4 Scope of the Thesis

Figure 1.6 shows the schematic representation of the main structure of the thesis. We can see that three modules compose the main body of this thesis, that is, the linear stress analyses, the nonlinear stress analyses and the applications and parametric studies.

As a first step of the linear analysis, the LEFEA simulation is carried out using the commercial general purpose FEA package ABAQUS in Chapter 2. To cater for the aforementioned singularity feature of the problem, a linear fracture method (LEFM) analysis is performed, in which a sub-modelling technique is used to avoid the cumbersome meshing procedure and improve the calculation accuracy. A special singular element is selected in the modelling process. The stress results show that an improved accuracy has been achieved compared with the conventional LEFEA analysis. In addition, the J integral is also calculated, which potentially can act as a criteria for the onset of the first plate end crack. This solution may be deemed as the benchmark of the following derived analytical solutions.

Chapter 3 presents a linear elastic complete solution. Unlike some other analytical solutions, no major assumptions are introduced prior to the solution derivation and hence the stress fields in the adhesive are achieved using a complete and accurate approach. The principle of complementary energy is adopted to derive the stress solutions, which are expressed in Fourier series. A limited number of the terms are taken and the algebraic equation system has to be solved by numerical programming. A wide range of load cases is included in the solutions such as symmetrical loadings, antisymmetrical loadings and other arbitrary loadings. To the best of the author's knowledge, this is the first analytical solutions which have correctly predicted the drastic difference in the interfacial normal stress between the plate-adhesive (PA) and adhesive-concrete (AC) interfaces and achieved a rather good agreement with the FEA results obtained by very fine meshes. Another significant feature of this solution is that it is versatile and may be easily adopted to other composite materials/structures under thermal/mechanical load.

Chapter 4 presents a closed-form rigorous elastic solutions using a two-stage method. This is a spreadsheet-based solution and the numerical results can be obtained without cumbersome coding. In the first stage of the derivation, the shear stress is derived with high degree of accuracy and in the second stage the normal stress at the middle horizontal section across the adhesive layer is obtained by utilizing the shear stress from stage one as the known variable. The assumption that the shear stress is constant across the adhesive thickness is used and this leads to the implication that the normal stress is varied linearly. However, the comparison with the complete solution suggests that this assumption does not incur great loss of accuracy. This solution forms the basis to develop a simplified solution in the following chapter.

As mentioned in the preceding section, one of the main targets of the present work is to develop a simple and reliable stress solution, which can be potentially used in the engineering practice and be exploited to develop some robust strength models. In Chapter 5, the closed-form rigorous elastic solutions derived in Chapter 4 is further investigated. One of the important findings is that the bending moment value at the plate end section is the dominant factor determining the stress concentration, and whereas the shear force only contributes to the interfacial shear stress in the classic way and it does not induce any interfacial normal stresses. On the basis of this find-

ing, some numerically minor terms are omitted in the original solutions with the only presence of the end moments. The simplified versions of both shear and normal stresses are then derived. The shear stress consists of two parts, i.e. the simplified shear stress solution for the plated beam under end moment and the classic shear stress solution for laminated beam. Also proposed is the equation of development length. By the adoption of the concept of development length, we may extend the solution to a plated RC beam from subjected to symmetric loads to arbitrary loads. This substantially broadens the applicability of this simplified solution.

None of the previous solutions allows for the nonlinear material property for the concrete, the nonlinear behaviour of the interface and the impact due to the presence of reinforcements. A complicated nonlinear FEA modelling is performed in Chapter 6 using the ABAQUS package again. In this modelling, the full features of the concrete material are taken into account and the reinforcements and shear links are modelled separately. Tested beams including the virgin (unplated) and plated beam are modelled. And the results show good agreement with the experimental data in terms of cracking loads, yielding loads, ultimate loads and deflections. Extensive results are presented to show the structural behaviour of the plate beam in detail, which is believed to be the first one in the published literature.

As the last analytical stress solution, a Nonlinear Fracture Mechanics (NLFM) solutions is developed in Chapter 7. The interfacial behaviours are sophisticatedly considered which include both pre-cracking and post-cracking features. The interaction between Mode I fracture and Mode II fracture are considered in the solution. The interaction reflects in the determination of the peak shear and transverse normal stress and the corresponding post-cracking behaviours. This solution may predict both serviceability load, which is defined as the load level at the onset of the first plate end crack, and the ultimate load, which is defined as the load level when the cracking surfaces start to separate. To the best of the author's knowledge, this is the first solution considering both the post-cracking behaviour and the interactions between two fracture modes.

Each solution is coherent and relatively independent. In principle, the more completed and rigorous solutions may be used to verify the relative simpler ones; and the nonlin-

ear analyses can become the linear ones when the applied load is low and material behaviour is in the elastic region.

In the second to last chapter, the solutions are further compared with the experimental data and the serviceability and ultimate loads are predicted based on some of the solutions in conjunction with two failure criteria of the concrete materials. A series of extensive parametric analysis are carried out to show the effect of various variables on the stress distributions.

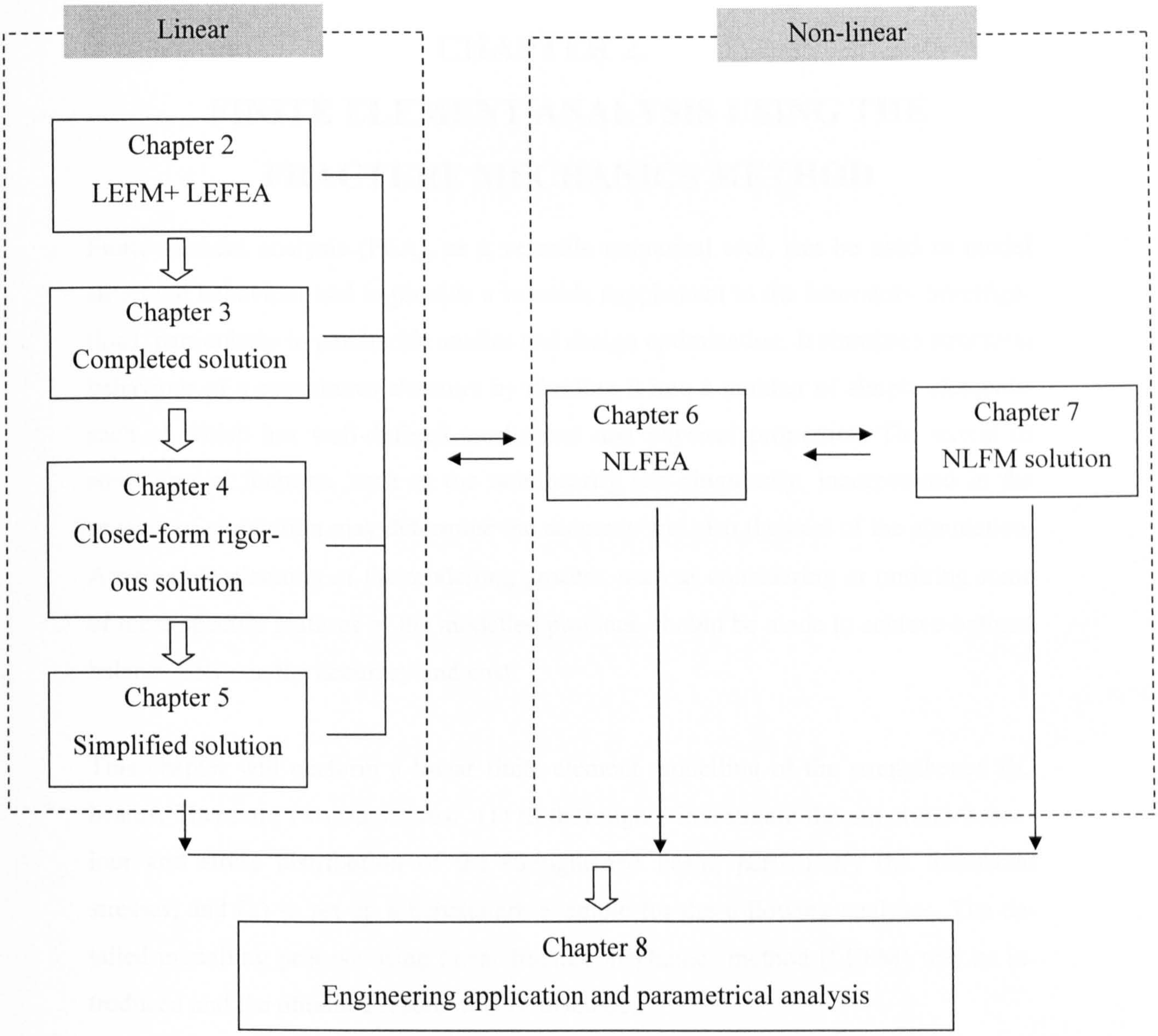

Fig.1.6 Diagram of the solution strategy

CHAPTER 2.
FINITE ELEMENT ANALYSIS USING THE FRACTURE MECHANICS METHOD

Finite element analysis (FEA), as a versatile numerical tool, can be used to model structural behaviour and to provide a valuable supplement to the laboratory investigations, particularly in parametric studies and design optimisation. It simulates structural behaviour of a continuous structure by dividing it into a number of simple elements, each of which has well-defined mechanical and physical properties. The extent of some special features, such as the nonlinearity and singularity, incorporated in the process of simulation may determine the accuracy and also the cost of the simulation. Appropriate planning of the modelling process, such as considering or omitting some of these specific features of the modelled problem, should be made to achieve optimal balance between the accuracy and cost.

This chapter will perform a linear finite element modelling of the strengthened RC beams. There are two objectives: (1) to thoroughly investigate the structural behaviour and stress distribution of the strengthened beam, particularly the interfacial stresses; and (2) to set up a benchmark example for the following analyses. The detailed modelling process using linear fracture mechanics method (LEFM) will be introduced and the obtained results will be discussed.

2.1 Introduction

There are many cases where stress singularity occurs, i.e., one or some of the stress components approach infinity within a material in the context of elastic theory. It occurs when crack tips, interfacial cracks; free edges, corners and wedges of single material or multiple materials are present. Each case may have different degrees of singularity. For instance, the stress is inversely proportional to the square root of the distance from a crack tip, while in the vicinity of an interfacial crack, the stresses oscillate when they approach infinity. Hein and Erdogan (1971) investigated two material wedges with an arbitrary angle. The stress singularity was studied and, quantitatively defined by the strength of singularity λ that shows the rate of stress increase

towards the singular point. The relationship between the magnitude of a stress component σ_i and the strength of singularity can be express as

$$\sigma_i = \alpha r^{-\lambda} \tag{2.1}$$

where r is the distance from the singular point. α is a term including the stress intensity factor, or/and the oscillation term, depending on the nature of problem. For example:

1. for Mode I and II crack tips in a homogeneous material:

$$\sigma_n = \frac{K_I}{\sqrt{2\pi}} r^{-1/2};\ \sigma_s = \frac{K_{II}}{\sqrt{2\pi}} r^{-1/2} \tag{2.2a, b}$$

where, σ_n and σ_s are the transverse normal and shear stress along the crack line, K_I and K_{II} are the stress intensity factors for the mode I and mode II cracks. They can be found from fracture mechanics hand-books e.g. Murakami (1987);

2. for a singular point at a bi-material free edge,

$$\sigma_n = Hr^{-\lambda} \tag{2.3}$$

where, σ_n is the transverse normal stress along the interface. λ can be calculated from the relative material properties through a characteristic equation and H is called H factor and denotes singularity strength, that is normally calculated by numerical method (Bogy, 1968);

3. for the case of interfacial cracks, it is difficult to decouple Mode I and Mode II cracks. The transverse normal stress σ_n and shear stress σ_s along the interface can then be expressed by a complex form as

$$\sigma_n + i\sigma_s = \frac{(K_I + iK_{II}) r^{-1/2+i\varepsilon}}{\sqrt{2\pi}} \tag{2.4}$$

where $r^{i\varepsilon}$ is the oscillation term near the crack tip (Willams 1959);

4. for the general dissimilar wedges, the situation is more complex. Under different circumstances, we may have the following cases: (a) there is no singularity, (b) there are multiple singularity strength values, and(c) oscillation phenomena may or may not exist. (Hein and Erdogan 1971).

The bonded beam problem includes two types of singular points if the internal concrete cracks are not included. As depicted in Figure 2.5(b), they are, respectively, the

end of the interface between the concrete and adhesive (point A; type 4) and between the adhesive layer and bonded plate (point B; type 2). Obviously, in the vicinity of these singular points, the strength of singularity depends on the properties of surrounding materials, and the geometrical configuration. The finite element analysis is performed in the following sections using the general purpose FEA package ABAQUS.

Apparently, very fine mesh is needed in the local areas near the singular points. Away from these points, coarse mesh can be used in order to save the computing time. In general, using triangular elements and/or adjacent elements with significant size difference may lose accuracy of analysis, while using advanced elements with smooth change of size will increase computing cost significantly. To overcome this difficulty, sub-modelling is used in this analysis.

Sub-modelling is a technique that is utilized for localized stress with refined meshes, based on interpolation of the solutions from an initial, global model onto the nodes on the appropriate parts of the boundary of the sub-model. The method is most useful when it is necessary to obtain an accurate, detailed solution in the local region and the detailed modelling of that local region has negligible effect on the overall solution. The response at the boundary of the local region is defined by the solution for the global model and it, together with any loads applied to the local region, determines the solution in the sub-model.

Two steps are carried out using the sub-modelling technique:

1. A global analysis with coarse mesh pattern are performed first and the displacement at each nodes are saved in a result file;
2. The local areas containing singular points are separated and divided into very fine meshes. The displacement fields calculated in the first step are interpolated and imposed to the boundary nodes of the sub-model.

Linear elastic fracture mechanics analysis (LEFM) is conducted to calculate the stress distribution and predict the onset of cracking by using contour integrals. As one of significant measures, the J-integral is also calculated by ABAQUS in the sub-model.

The J-integral is to characterize the energy release associated with crack growth. It is equal to the energy release rate for elastic material (Rice, 1968) and defined as

$$J = \int_{\Gamma} \mathbf{n}.(W - \boldsymbol{\sigma}.\frac{\delta \mathbf{u}}{\delta x}).\mathbf{q}d\Gamma \tag{2.5}$$

where Γ is any closed contour followed counter clockwise surrounding the crack tip in a stressed body as shown in Figure 2.1; $\mathbf{n}$ is the outward normal of Γ and $\mathbf{q}$ is a unit vector in direction of the virtual crack extension; W denotes strain energy density. The J integral is suitable for both linear and nonlinear elastic materials, as well as for monotonic loading of elastic-plastic materials.

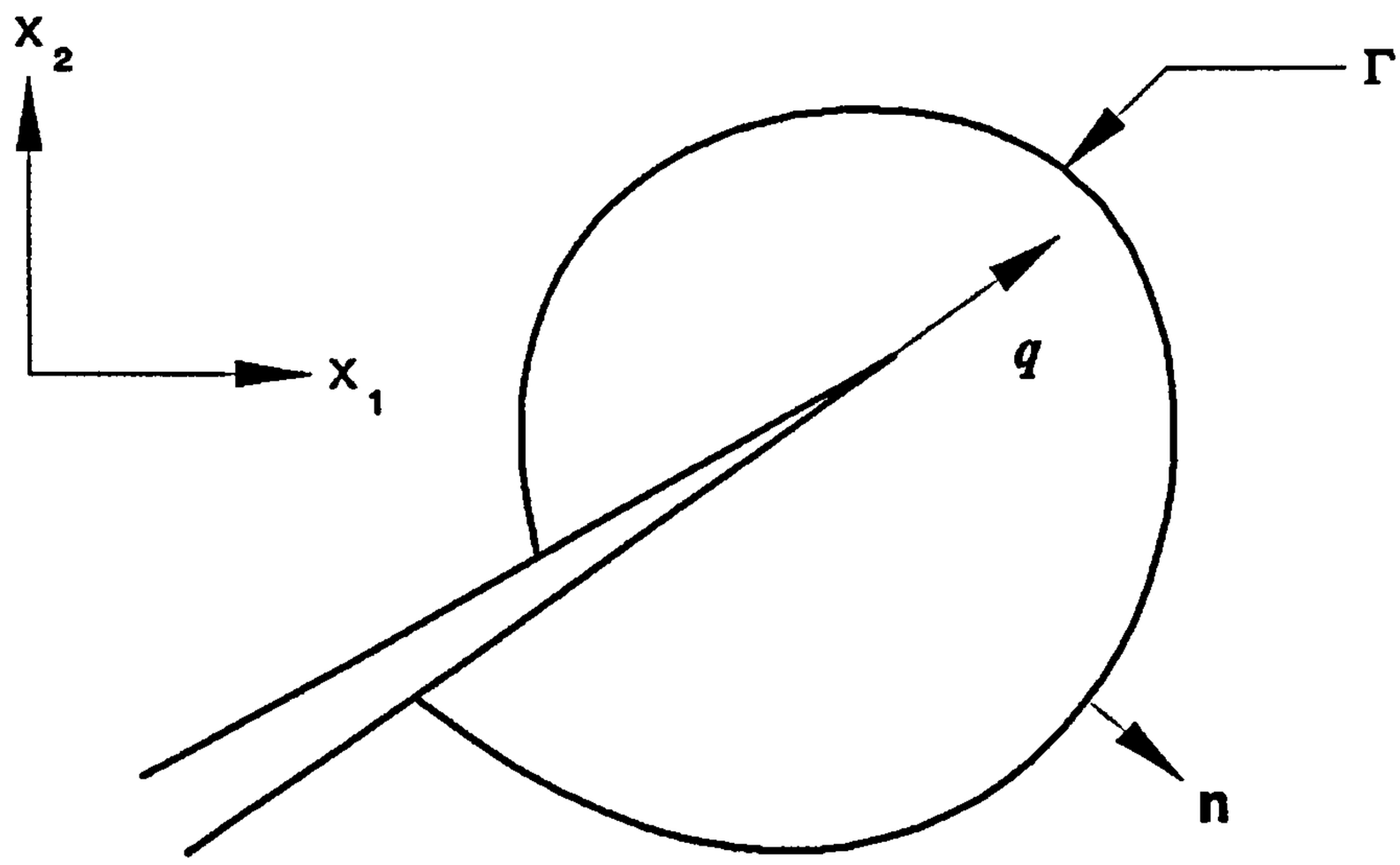

Fig. 2.1 Schematic diagram of J-integral

In ABAQUS, the contour is defined by a ring of elements completely surrounding the singular points from one traction free face to the opposite one and the contour integral is evaluated as an area integral over a finite domain bounded by the contour (ABAQUS, 2000).

2.2 Modelling Process

2.2.1 Problem Description

In order to compare the results with those in the published literature, the examples in Teng et al. (2002) are adopted in this modelling. It is a steel plated bonded reinforced concrete (RC) beam first investigated by Roberts and Haji-Kazemi (1989). The span

of the RC beam is 2400mm, the length of the plate is 1800mm and the UDL is 15N/mm. The geometric and material properties of the RC beam, the adhesive layer and the plate are given in Table 1.

Table 2.1 Geometric and material properties

Component	Width(mm)	Height(mm)	Length (mm)	Young's modulus(MPa)	Poisson's ratio
Concrete	100	150	2400	20,000	0.17
Adhesive	100	4	1800	2,000	0.25
Steel plate	100	4	1800	200,000	0.30

The problem is modelled as a 2-D plane stress one in the following section. The dimension in the width direction is input as the properties of the element.

2.2.2 Element Type

A 8-node biquadratic isoparametric plane stress element CPS8 (Figure 2.2 a) is used to model the concrete, adhesive layer and bonded sheet, respectively. Each node has two active degrees of freedom, i.e. u_x and u_y. Full integration scheme are numerically implemented, and the integration points are shown in Figure 2.2 b.

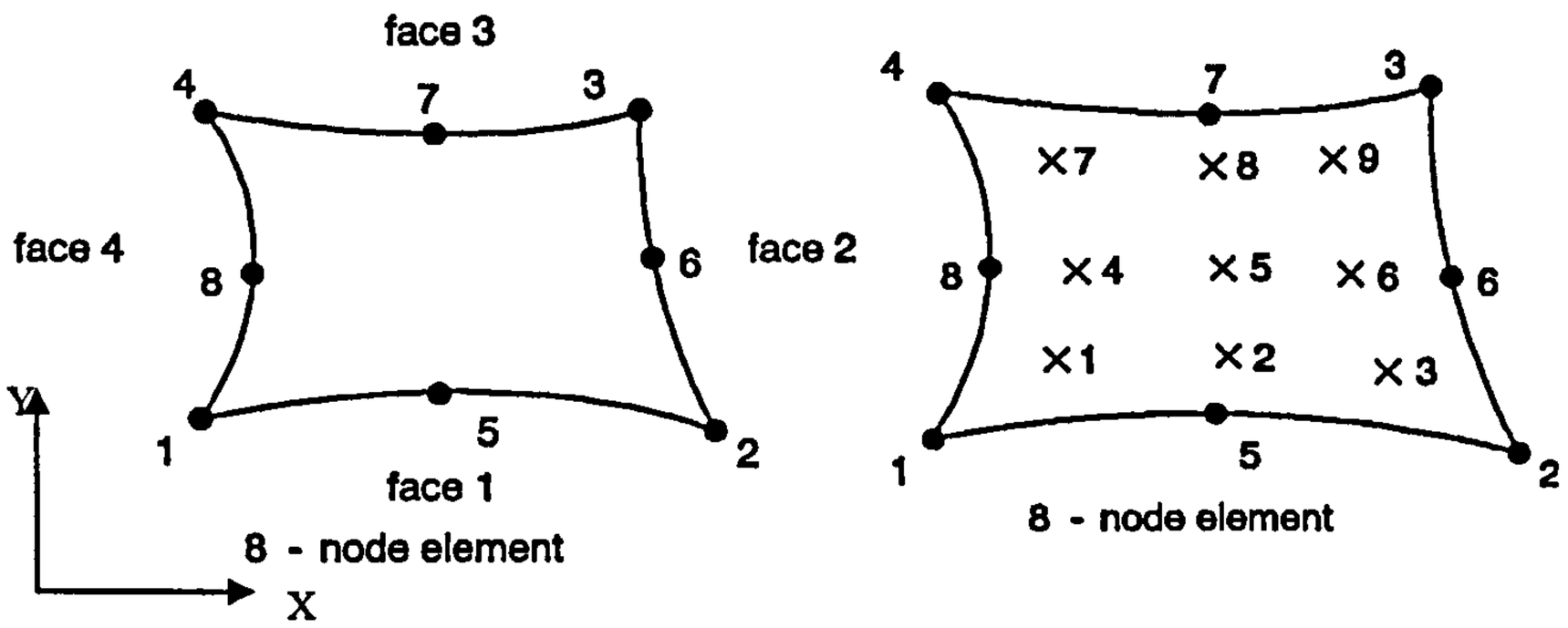

(a) Nodes in the element (b) the integrating points

Fig. 2.2 CPS8 element (ABAQUS 2000)

In order to simulate the stress/strain singularity at interface ends, one of the conventional methods is to use a special refined mesh pattern. However, the singularity of the stress/strain components near the singular point significantly affects the accuracy of

the numerical results even when very fine meshes are used. In this analysis, elements with special nodes layout are used to accommodate the stress/strain singularity by collapsing one side of the standard element CPS8. This results in a new element with all three nodes along the collapsed side having the same geometric location at the singular point. In addition to this, the midside nodes on the two sides connected to the singular point are relocated to the 1/4 point near the singular point. The SINGULAR parameter on the NFILL option can be used to create "quarter point" spacing. Using these type of elements can favourably improve the accuracy of the J-integral and stress/strain calculations.

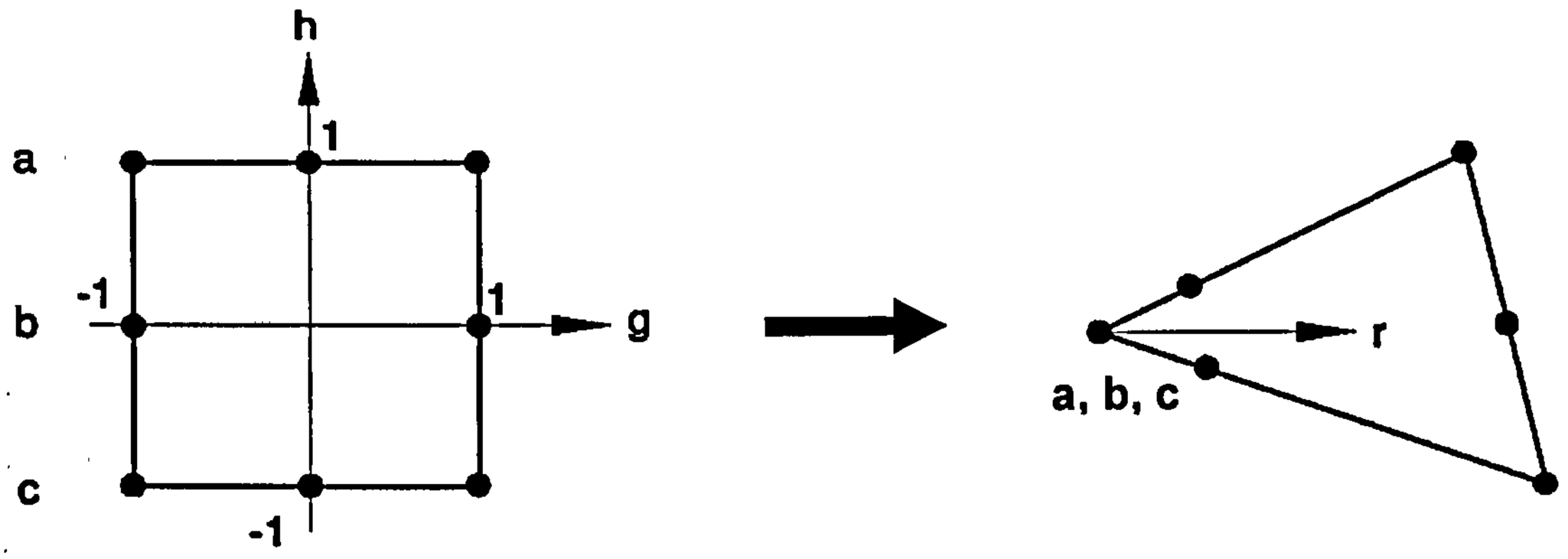

Fig. 2.3 Collapsed 8-node plane stress element

The SOLID SECTION option is used to define the properties of the section such as geometrical dimension in the thickness direction and material properties.

2.2.3 Material Properties

Elastic isotropic material properties are assigned to concrete, adhesive materials and steel material. The Elastic option is used to input the values for the elastic modulus and Poisson's ratio.

2.2.4 Modelling

A global modelling is firstly performed to attain the displacements and stress/strain distributions in the bonded beam without focusing on the singular points, i.e. without using fine mesh near the singular points. By taking advantage of the symmetry of the structure, half of the bonded beam is used in the modelling. This reduced computa-

tional time and computer disk space requirements significantly. The half span is shown in Figure 2.4.

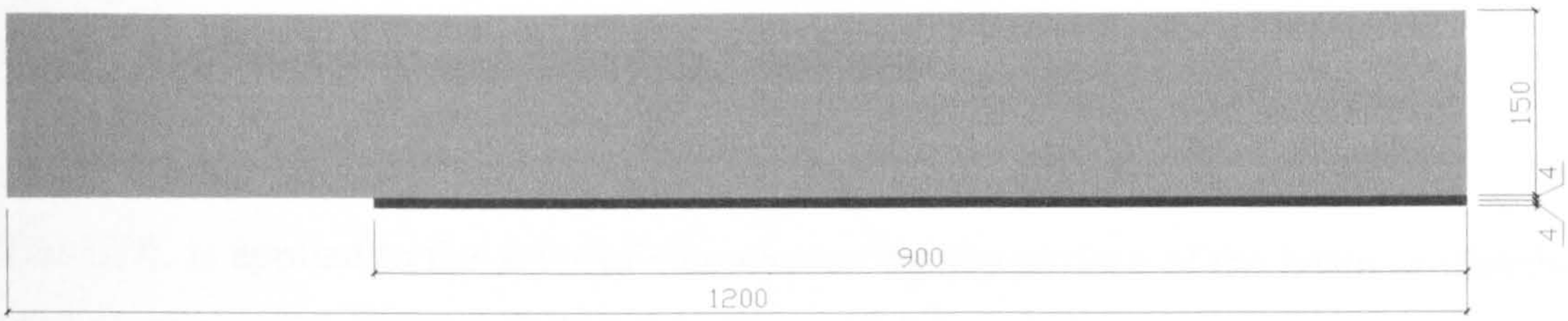

Fig. 2.4 Half span of the beam

As an essential step, a finite element analysis requires discretizing the geometrical model into a number of small elements and this process is called as meshing of model. The freedoms at each node are sought by solving the system equations obtained with some global-featured method, such as energy method. The loading, stress, strain are calculated at integration points of these small elements. Generally there are two methods of meshing the model, i.e. build the geometrical body and then mesh it in a specified pattern, or create the elements directly. The latter is used in this study. Input file is compiled to build up the analysis model where nodes and elements are input directly. The option SOLID SECTION with its data lines provides the input of the thickness of the elements, which is 100mm herein. The overall mesh is rather coarse except those at the two singular points, where the refined mesh has been established. By doing so, the displacement at the boundary, which will build the sub-model can be rather accurately predicted. Figure 2.5 (a) shows the mesh pattern in the overall view and Figure 2.5 (b) shows the enlarged detailed view at the singular points.

Ideally, the bond stress and displacement between the concrete and adhesive layer (AC interface) and adhesive layer and bonded sheet (PA interface) should be considered individually. However, in this analysis, perfect bond between materials is assumed, i.e., it is assumed that the elements share the same nodes at the same geometric location.

In the vicinity of point A and point B, two sub-models are established in the predefined domains, where the further fine meshing takes place and the collapsed elements are used. Figures 2.5 (c) and (d) display the detailed meshes for the sub-models.

2.2.5 Applied Loads and Boundary Conditions

2.2.5.1 *Global Model*

The UDL is applied to the sides of elements on the top surface of the beam as distributed pressure of $0.15N/mm^2$. The boundary conditions include simply supported end condition and symmetry about the central line. The simply supported boundary condition can be implemented in the simulation by restraining the degree of freedoms in the *y*-direction at the lowest left corner node and the symmetric one is easily input by adding the 'symmetrical' parameter to the nodes on the central line in the BOUNDARY option.

2.2.5.2 *Sub-models*

The displacements of the nodes along the boundary of the sub-models are derived from the displacement fields calculated in the global model. To use the global results in the sub-model analysis, a necessary step in the global analysis is to save all nodal displacements required for the interpolation of the driven displacements to the boundary of the sub-model. NODE FILE option is used to write the results to a results file. For convenience, displacements of all the nodes in the global model are saved in this study. The actual driven displacements are defined in the input file of the sub-model by the BOUNDARY option with the SUBMODEL parameters. No applied loads are applied in the sub-model area.

2.2.6 Solving Process

Linear analysis procedure is carried out to analyse the displacement field and stress/strain field with the STATIC option in the input file. A small-strain assumption is used in this analysis.

When the global analysis is performed, three mesh patterns are adopted to investigate its impact to the results of the sub-models. Table 2.2 shows the dimensions for the

mesh refined area and the number of elements at all edges in this area. The dimension l_1, and l_2 and the numbers of division n_i (i = 1..5) are shown in Figure 2.6.

Figure 2.7 shows the number of element along all edges in two sub-models. The black dots represent singular points and the thicker lines denote driven boundary. The boundary is 2mm away from the singular point in sub-model A. In sub-model B, the upper and lower boundaries are 2mm and the right-hand boundary are 2mm + 4mm.

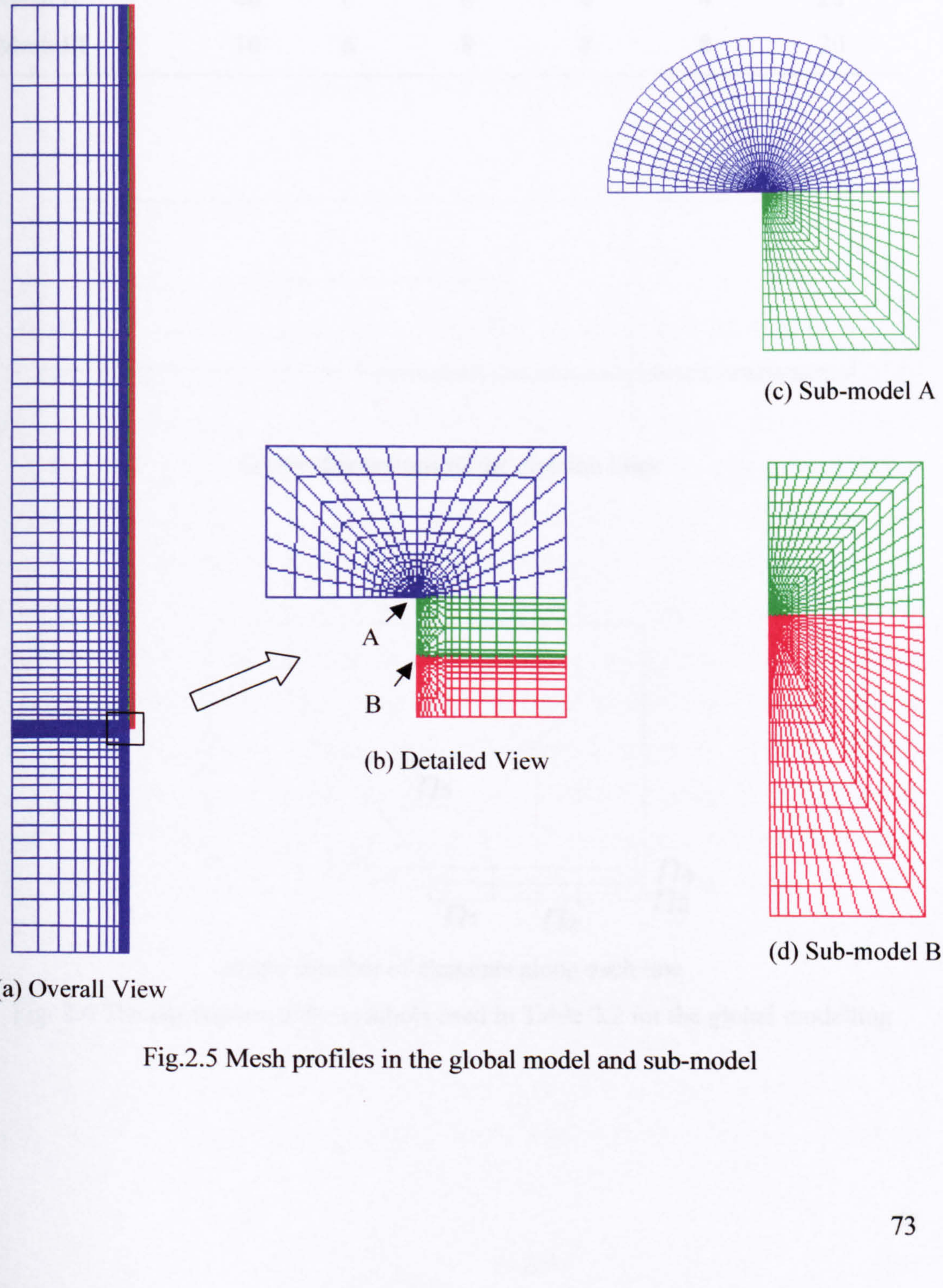

(a) Overall View

(b) Detailed View

(c) Sub-model A

(d) Sub-model B

Fig.2.5 Mesh profiles in the global model and sub-model

The size of the elements in both global model and sub-model increases progressively as they are away from the singular locations by a ratio of 1.25 using the parameter of 'BIAS' and 'TWO STEP' in creating the nodes.

Table 2.2 Dimensions of the division lines and the number of elements along each line in the global modelling

	l_1 (mm)	l_2 (mm)	n_1	n_2	n_3	n_4	n_5
Mesh I	8	80	6	6	2	4	20
Mesh II	5	40	6	6	4	4	20
Mesh III	2	10	6	8	8	8	20

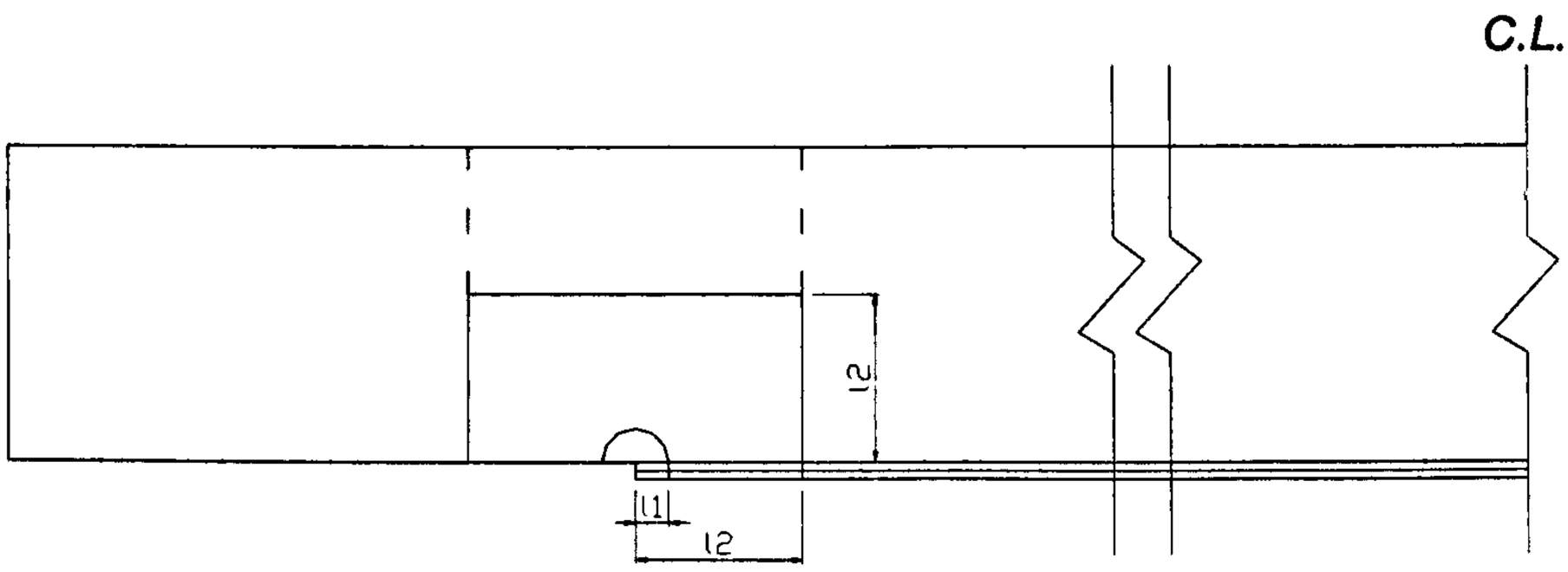

(a) the dimensions of the division lines

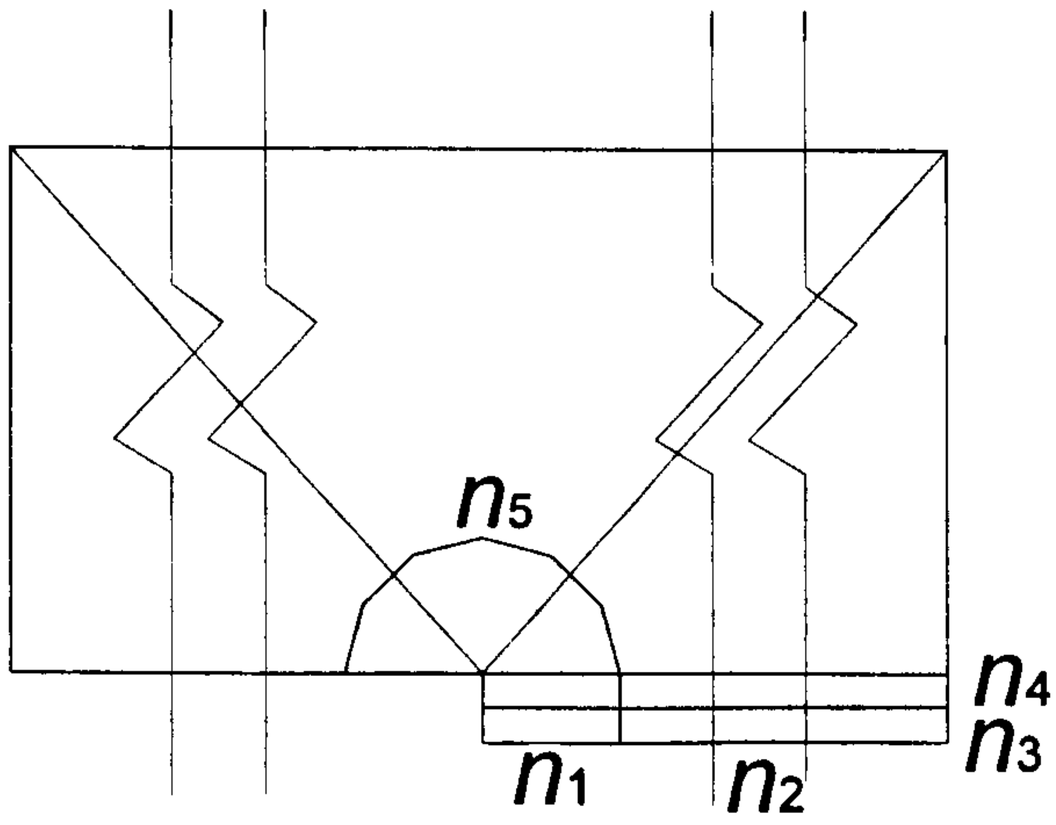

(b) the number of elements along each line

Fig. 2.6 The denotation of the symbols used in Table 2.2 for the global modelling

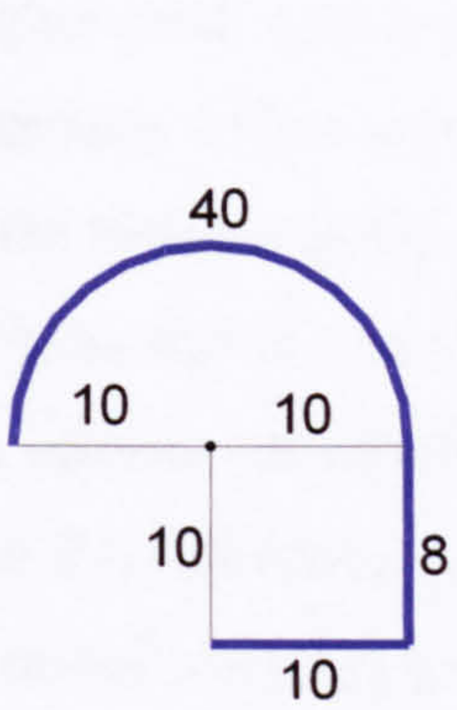

(a) sub-model at point A

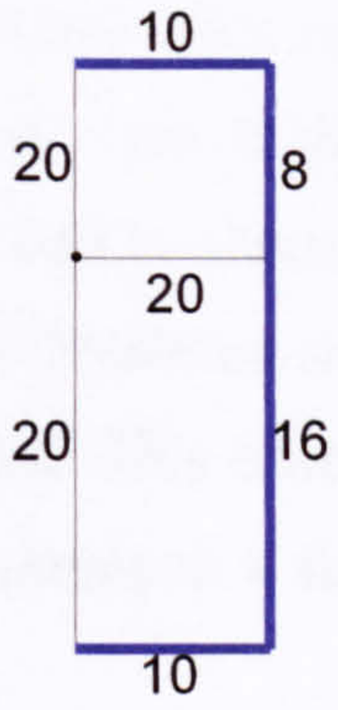

(b) sub-model at point B

Fig. 2.7 The number of elements for the sub-modellings

2.2.7 Analysis Results

2.2.7.1 *Convergence Analysis*

Figure 2.8 (a)-(f) show the variation of the interfacial normal and shear stresses at the AC interface, MA section, and PA interface, respectively, using the mesh pattern presented in the preceding section. Apart from the interfacial shear stress in the PA interface, the stresses are generally converged very well. We only see discrepancy in the elements at the singular points. This is expected as the stress level should approach infinity in theory in these elements. The stress components in the middle section of the adhesive layer (MA section) show best convergence. The shear stress therein equals zero at the plate end, which satisfies the traction free boundary conditions. The corresponding normal stress increases monotonically when approaching the plate end, and then starts to reduce its magnitude at about 2mm from the plate end. We can see from the figure that the interfacial shear stresses show oscillation in the global modelling region using Meshes I and II. The adoption of Mesh III almost eliminates the oscillation. Hence in the following study, Mesh III is used unless otherwise stated.

2.2.7.2 *Result Comparison and Analysis*

Figures 2.9 shows two comparisons of the interfacial stresses between the present analysis and Teng et al. 's (2002) elastic analysis. They meshed the model with a smallest size of 0.1mm. Figure 2.9 reveals that in general, both results agree with each other only except those in the vicinity of the singular points. The present analysis

achieves much higher peak values at the singular points. This implies a fact that the elastic analysis unlikely offers convergent solutions, even if the finest meshes are used. Apart from the singular points, both methods lead to almost identical solutions. The present result also shows that the magnitude of interfacial shear stress in the PA interface will also increase drastically at the plate end. This observation suggests the conclusion that the PA interfacial shear stress converges to a fixed value drawn by Teng et al. (2002) doesn't have general meaning.

The comparisons of the results are also made between the global modelling and sub-modelling in Figure 2.9. The submodelling presents much higher stress levels for both stress components near the ends, which are about twice of their global counterparts. In the regions away from singular points, both results are almost identical, which suggests the driven boundary is adequate to apply the displacement from the global model analysis to the sub-model one.

Figure 2.10 shows the displacement contour plot in the adhesive from the global model analysis and sub model analyses. It shows that the distribution of displacement fields from the two modellings are essentially the same. This can be explained by the fact that the displacements do not have singularity.

Figure 2.11 shows the stress contour plots (shear stress and transverse normal stress) for the sub-model 1 and sub-model 2, in which two innermost rings of elements are excluded as the extremely large magnitude will affect the display of the stress distribution in the whole domains. Figure 2.11 (a) shows the shear stress contour plot at point A. It presents a clear pattern that two sets of similar contour line loop bunches surround the singular point A. It becomes denser and denser when they approach the singular point, which show a large stress gradient over the region. Figure 2.11 (b) is the normal stress contour plot at point A, which shows a single set of contour loop bunch which tends to converge to Point A. The principal stress contour is depicted as the initiation of cracks usually occur in the concrete material near the singular point and the principal stress provide an important measure to the occurrence of the first crack. As we expect, the maximum principal stress occurs in concrete immediately above the singularity point in a diagonal direction. This agrees with the observation that concrete crack initiates at the end of the bonding line and extends upwards with

an angle. From Figure 2.12 (a), the shear stress contour plot for sub-model B, we can see that there exists a low shear stress area near the singular point. In the adhesive layer, shear stresses are mainly positive in contrast to steel plate where the shear stresses are mainly negative. The contour plot of the normal stress in sub-model B is depicted in Figure 2.12 (b), in which we can see the contour lines scatter out of Point B and they are bent near the singular point as if they were dragged by a force over there.

The J integral estimation, as introduced in the preceding section, is a very important measure to investigate the initiation of the cracks. Table 2.3 lists the J integral estimations at point A and point B from the global modelling and the sub-modelling, respectively. The first row in the table lists the number of the element ring within the J integral contour lines. In the sub-models, four contour lines are used to estimate the J integrals and investigate the convergence. The second row is the *x*-coordinates of the intersection points between the J integral contour lines and the AC interface. We can easily see from Table 2.3 that the estimations are very close by using the different contour lines. It also proves that the J integral is route independent. The last column in the table is the average values from the four estimations. The estimations from global modelling and sub-modelling are very close at both point A and point B, which implies that the J integral estimation is less affected by the stress/strain at the singular points predicted by the FEA analysis, which as we discussed early, are not very reliable.

Table 2.3 The J integral estimation in the global model and sub-model analyses

		Global Model	Sub-Model				
Number of element ring		6	17	18	19	20	Average
x-coordinate in the interfaces		2.0	1.445	1.62	1.805	2.0	
J-integeral estimates	Point A	**9.38E-02**	9.18E-02	9.30E-02	9.39E-02	9.45E-02	**9.33E-02**
	Point B	**1.55E-02**	1.54E-02	1.54E-02	1.55E-02	1.56E-02	**1.55E-02**

2.3 Conclusion

A finite element analysis (FEA) in the framework of the linear elastic fracture mechanics (LEFM) is performed in this chapter. Compared with conventional linear elastic element analysis, the present one is featured in the following aspect:

1 Use some advanced techniques to tackle the singular stress problem, e.g. sub-modelling technique and singular element type;
2 Attain the fracture mechanics fracture parameter J-integral, which potentially can be used to investigate the first crack occurrence instead of the strength criteria;
3 Avoid the cumbersome meshing over the whole domain and save the computing cost;
4 Provide much higher peak stresses, which suggests a rather accurate trend for the stress distribution around the peak stress.

The current solutions, however, also show some inherent disadvantages, including exclusion of nonlinear material properties of the concrete, contribution of the reinforcement and their interaction between two material phase, and not suitable for simulating the post-cracking behaviour. To solve this problem, a thorough nonlinear FEA needs to be carried out and is introduced in Chapter 6.

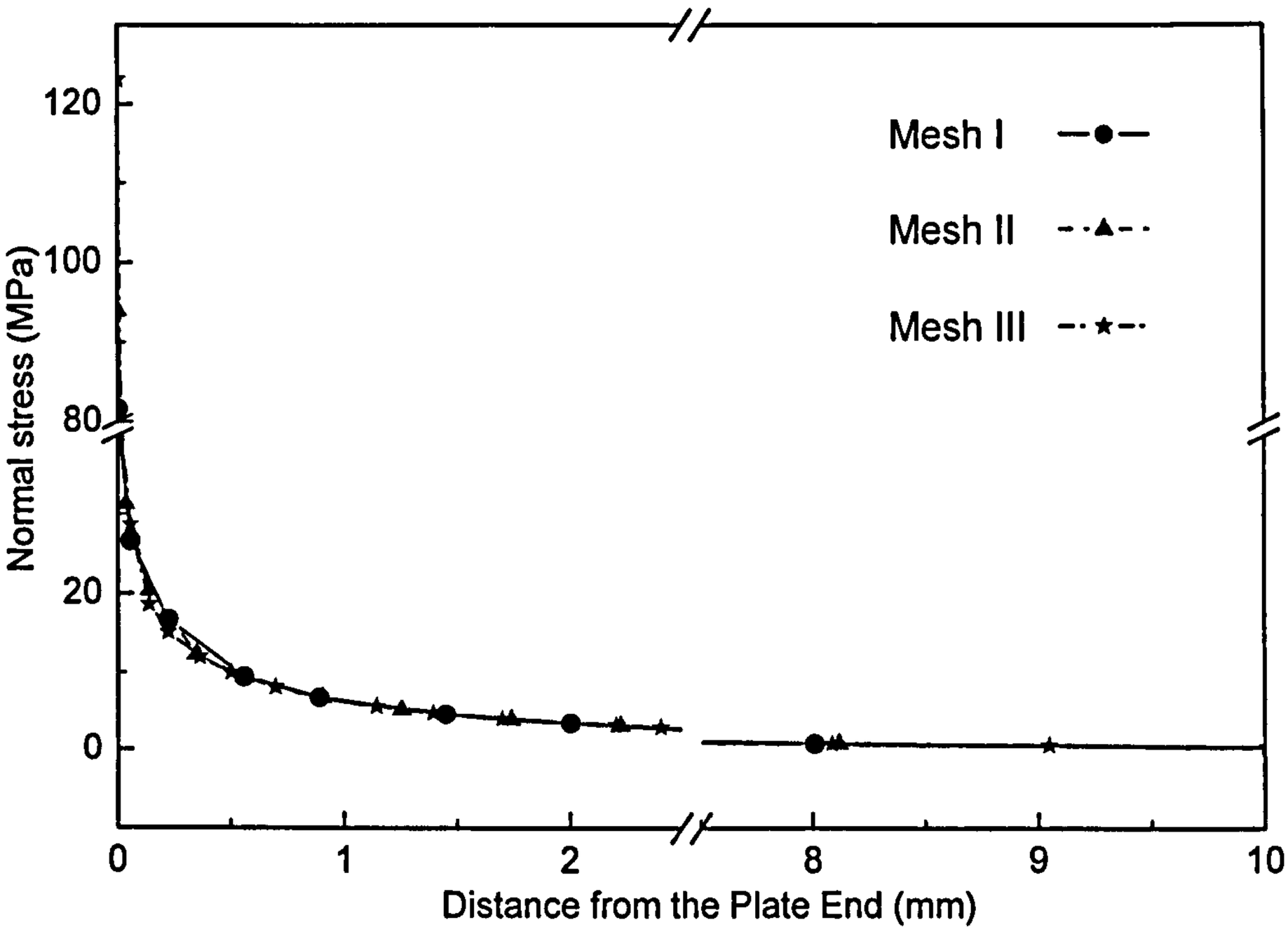

(a) Normal stress in the AC interface

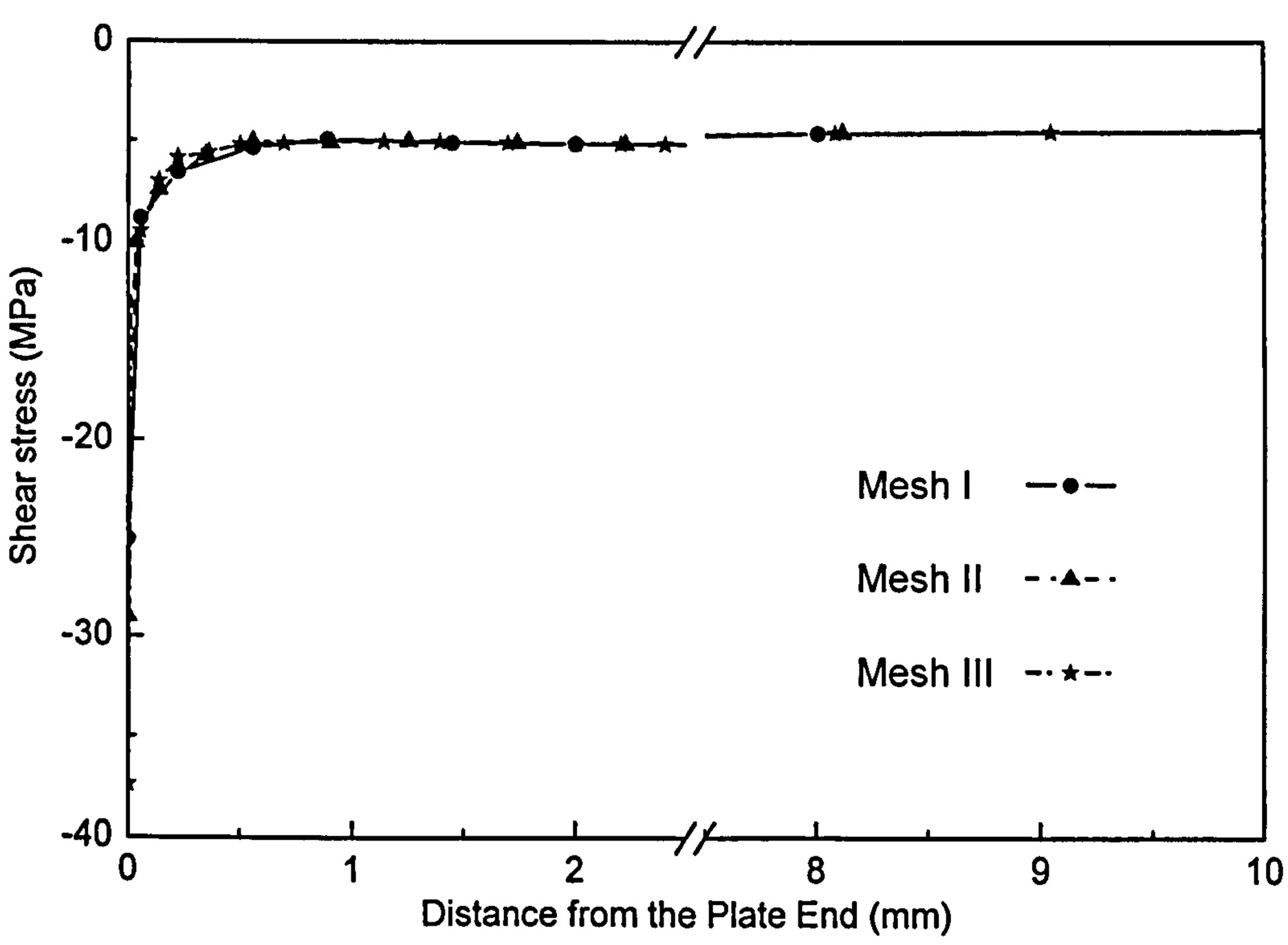

(b) Shear stress in AC interface

Fig. 2.8 Convergence analysis

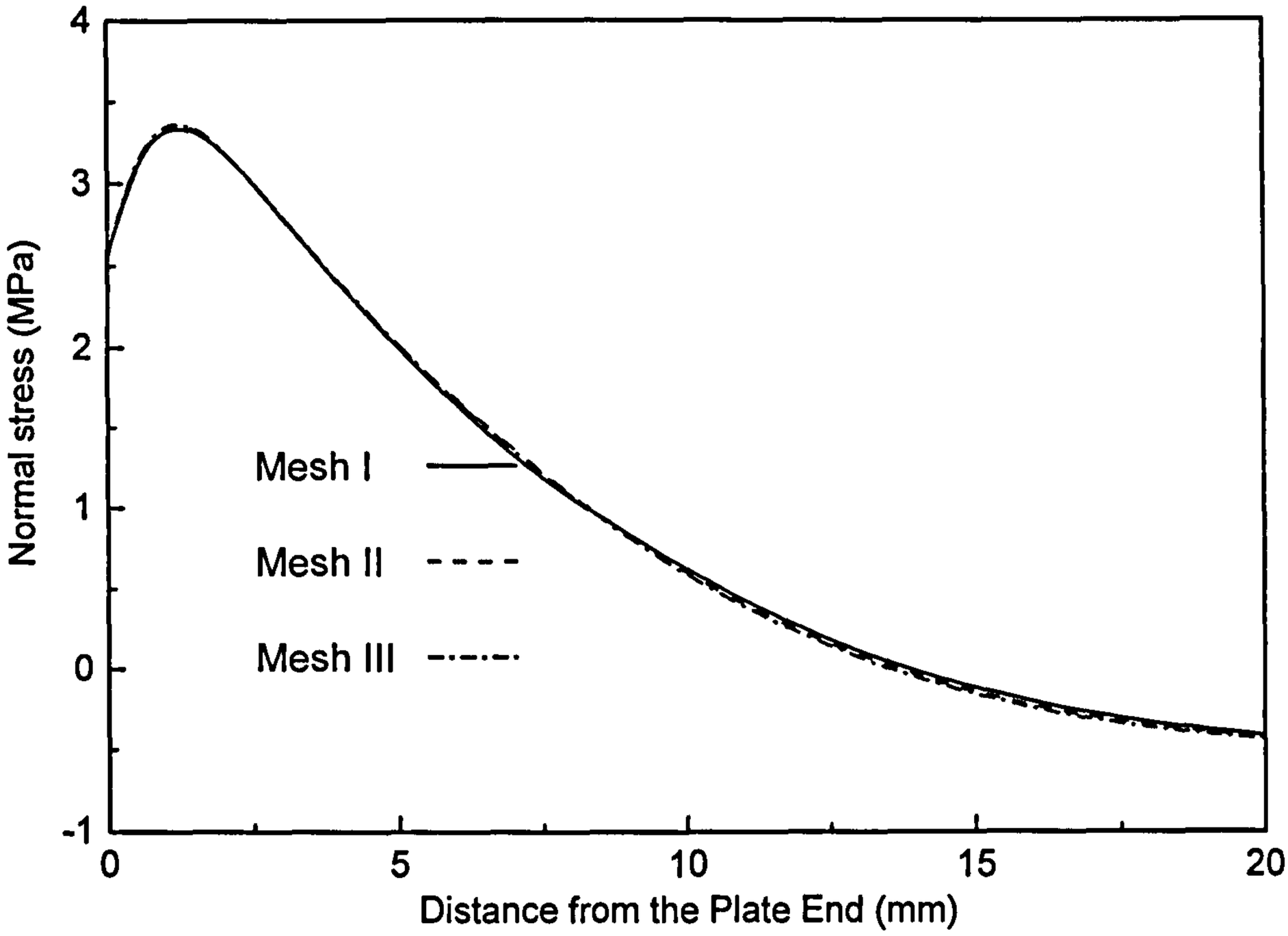

(c) Normal stress in MA section

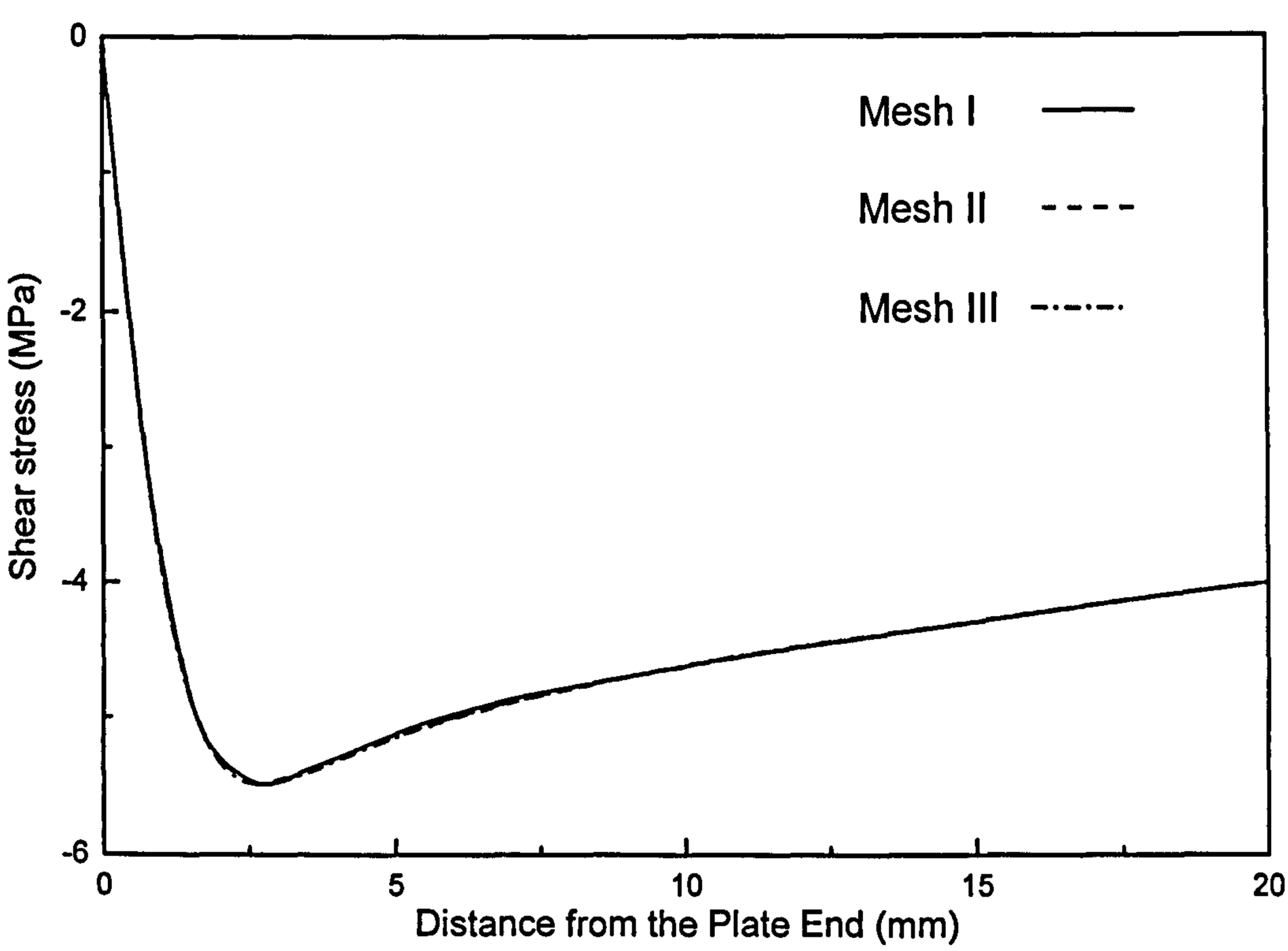

(d) Shear stress in MA section

Fig. 2.8 Convergence analysis

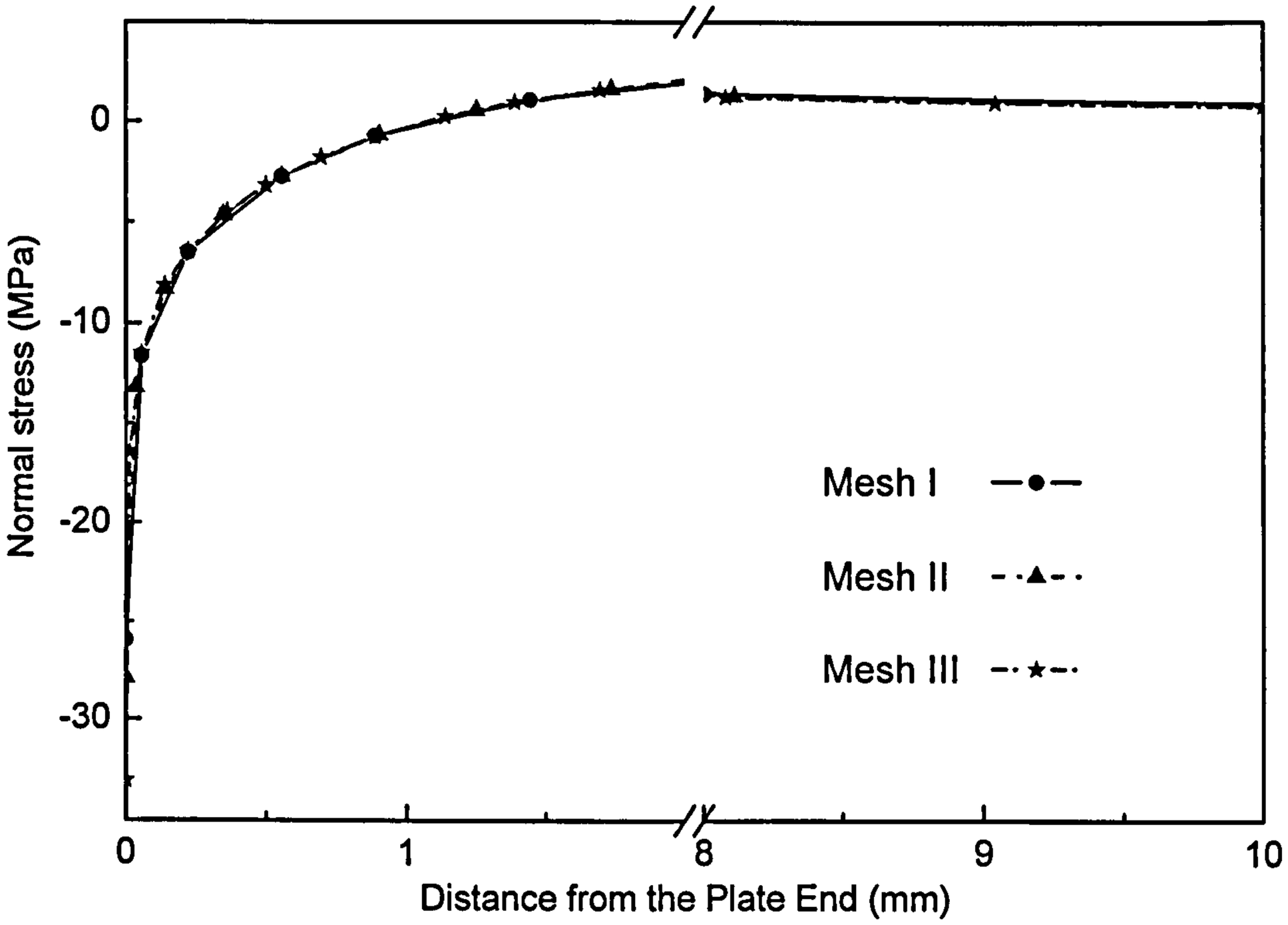

(e) Normal stress in PA interface

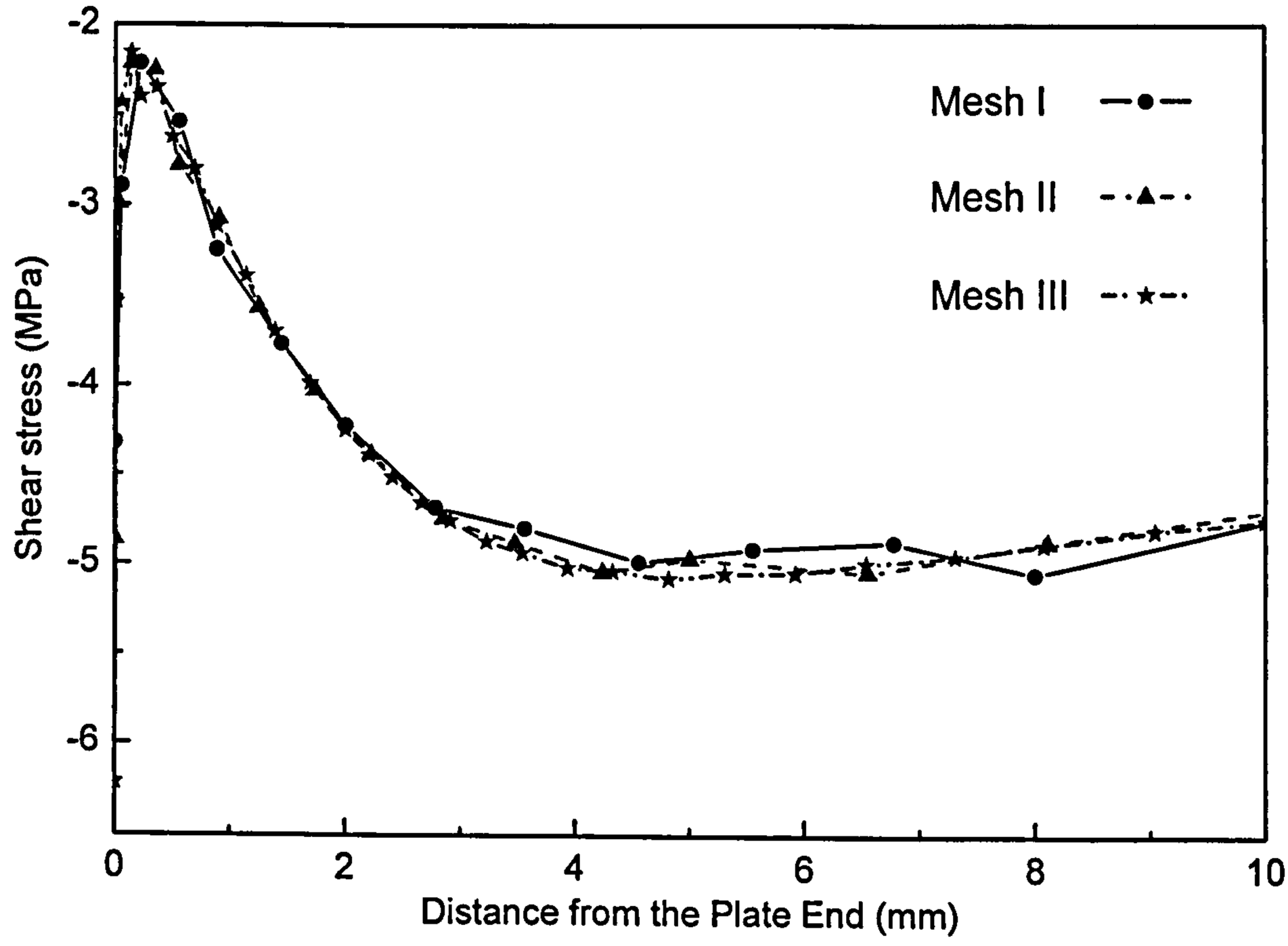

(f) Shear stress in PA interface

Fig. 2.8 Convergence analysis

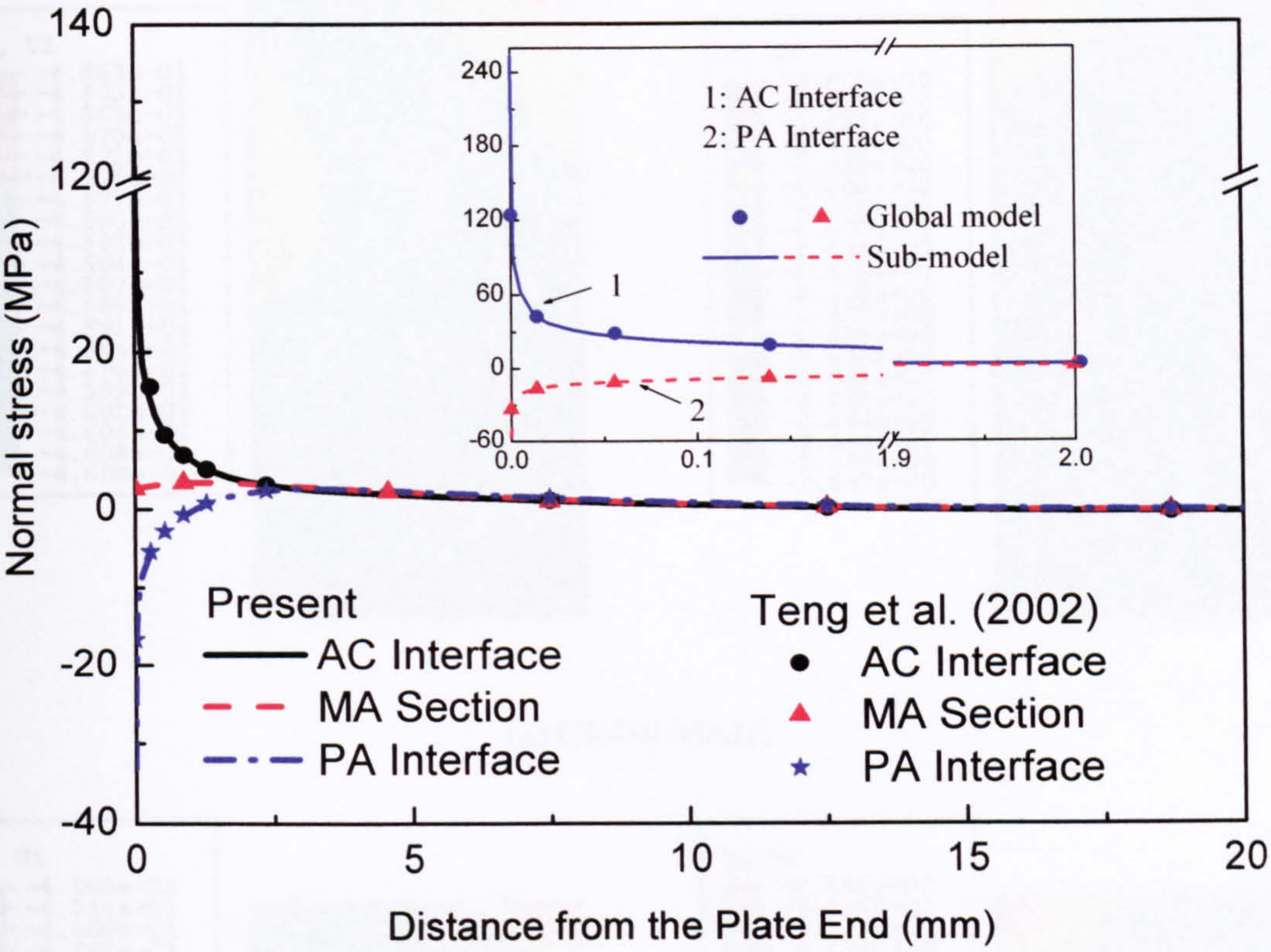

(a) Interfacial normal stresses

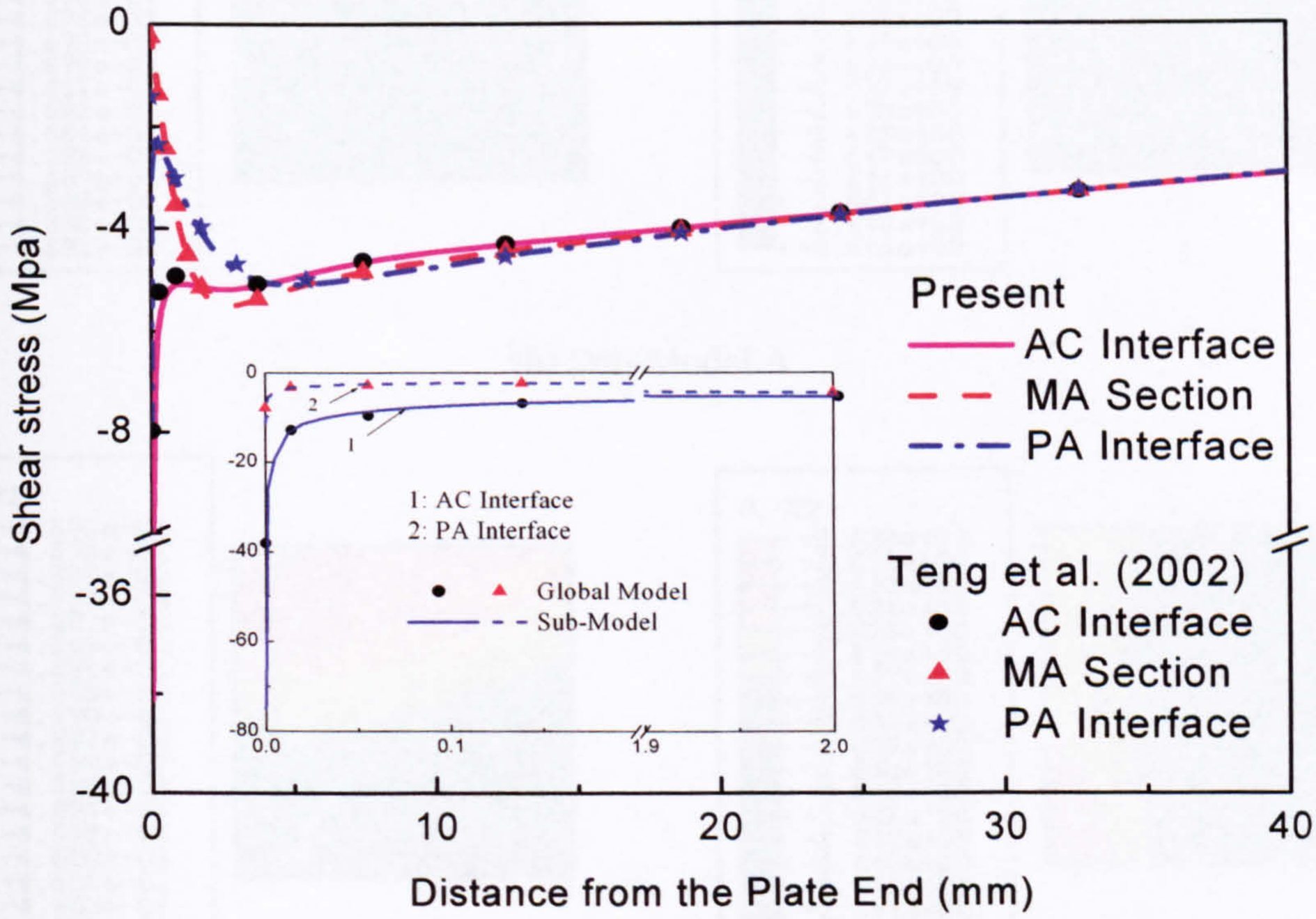

(b) Interfacial shear stresses

Fig. 2.9. The comparisons between the present solution and Teng et al.'s (2002) and that between the global model and sub-model

(1)

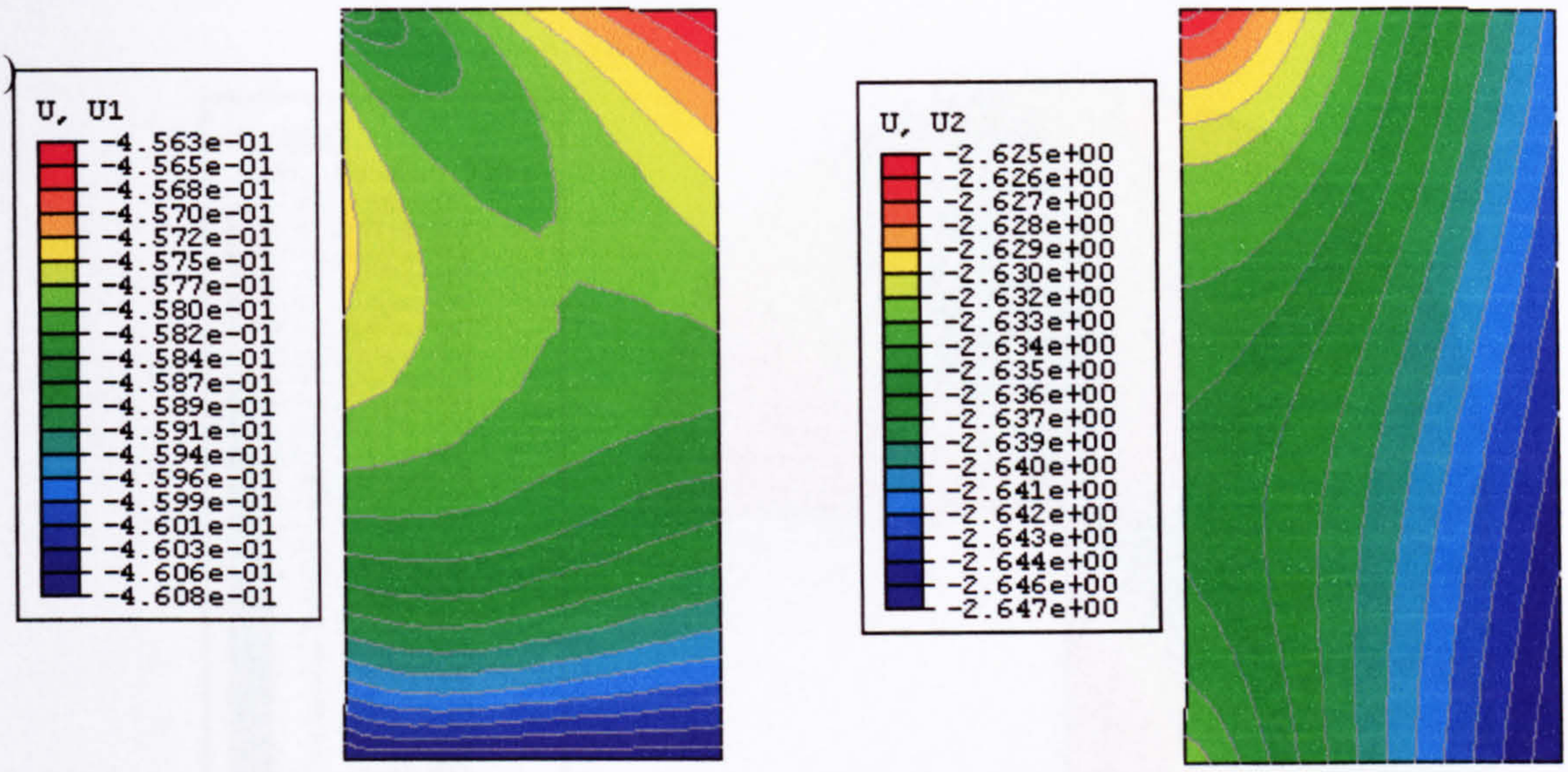

(a) Global Model

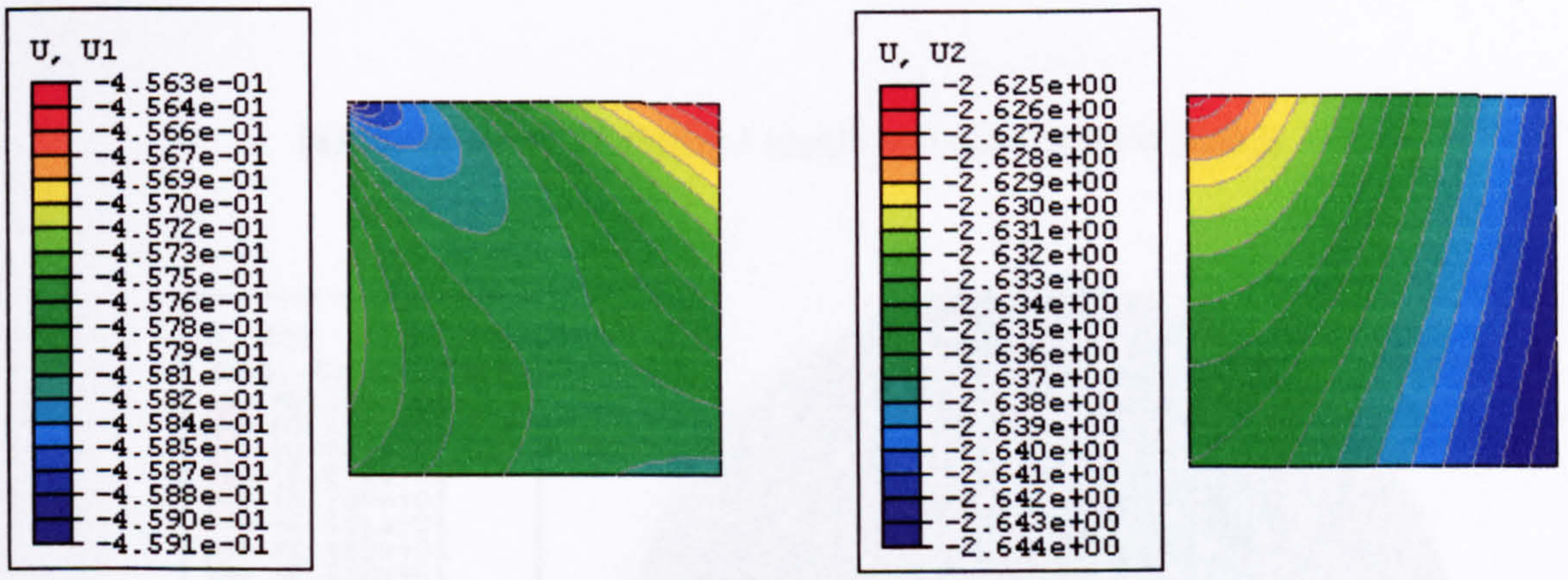

(b) Sub-Model A

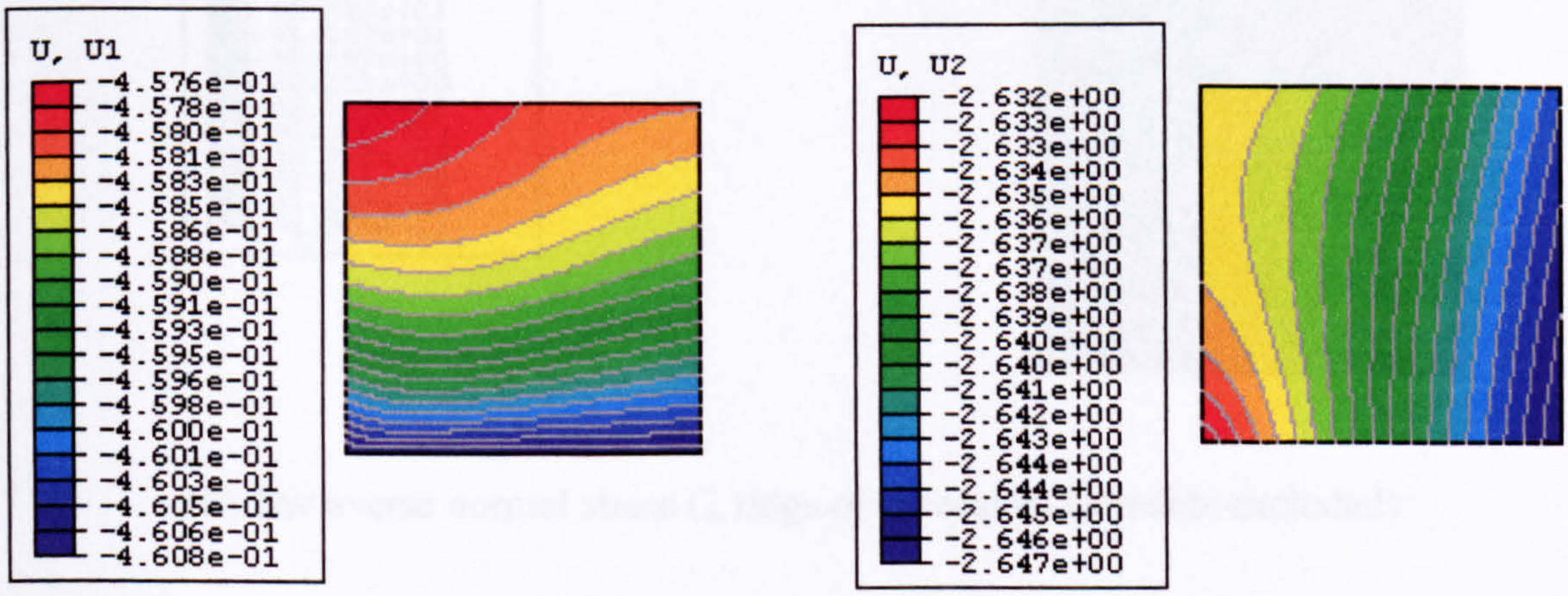

(c) Sub-Model B

Fig. 2.10 Displacement contour plots of the adhesive in the global and sub-models

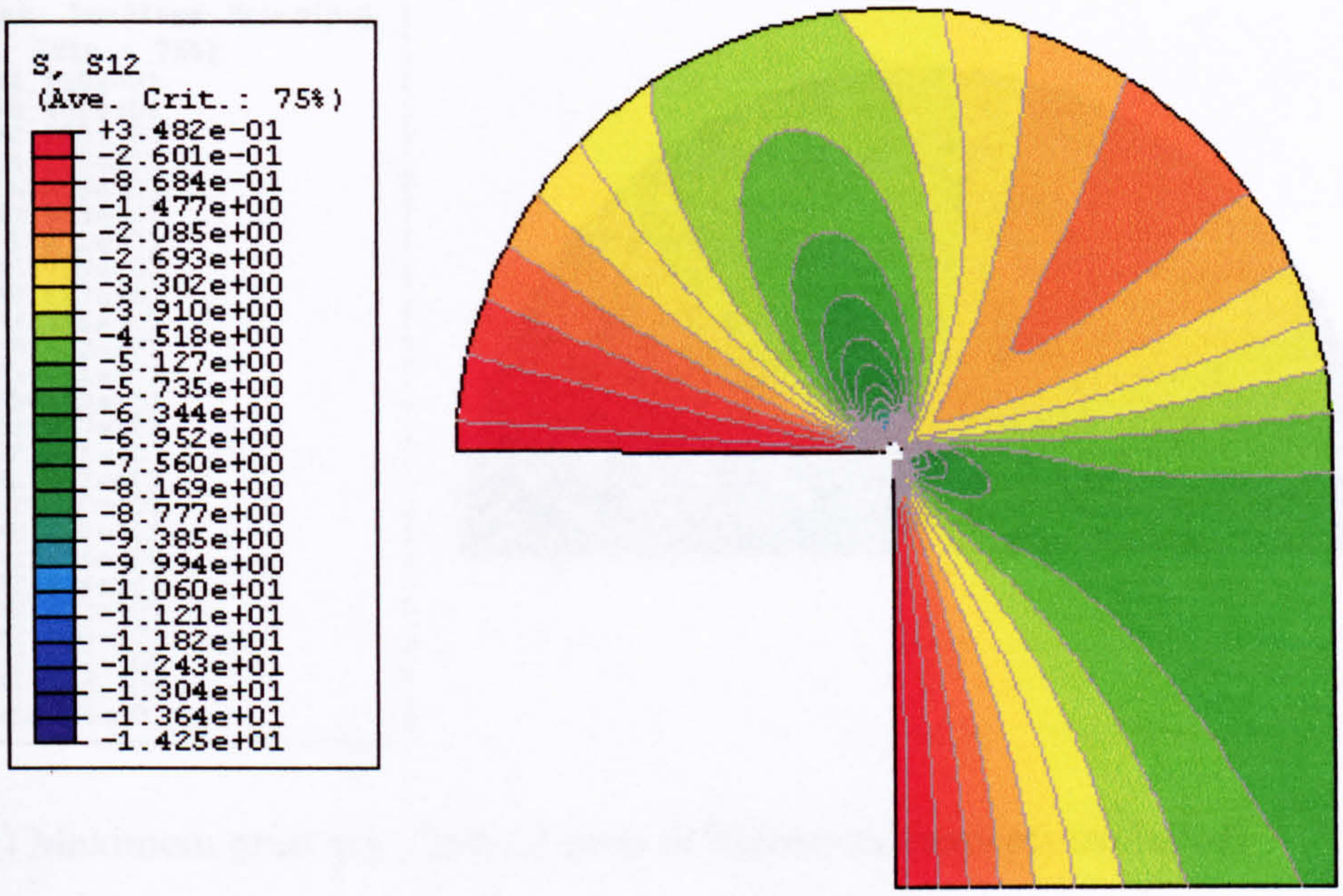

(a) Shear stress (2 rings of innermost elements excluded)

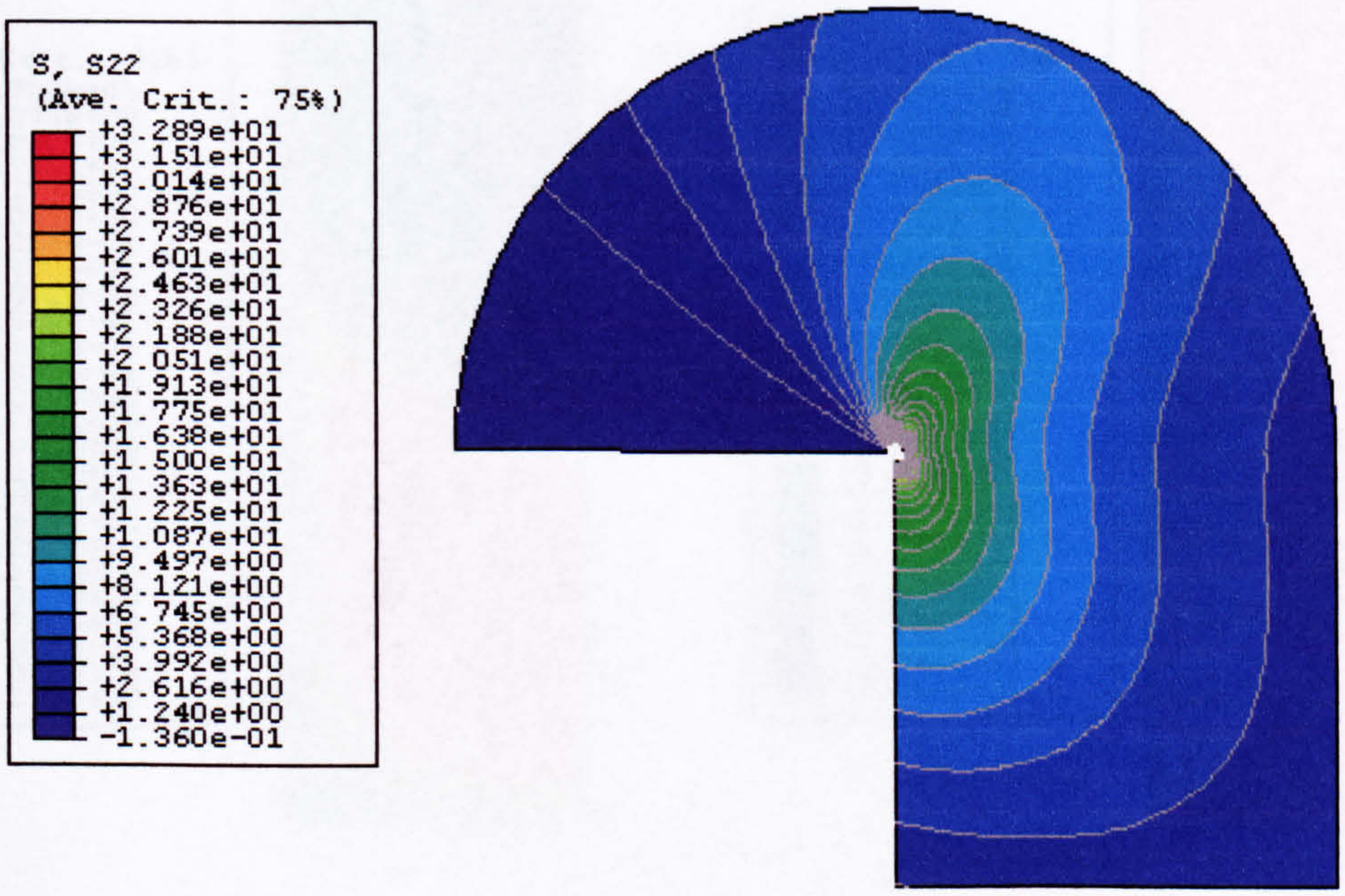

(b) Transverse normal stress (2 rings of innermost elements excluded)

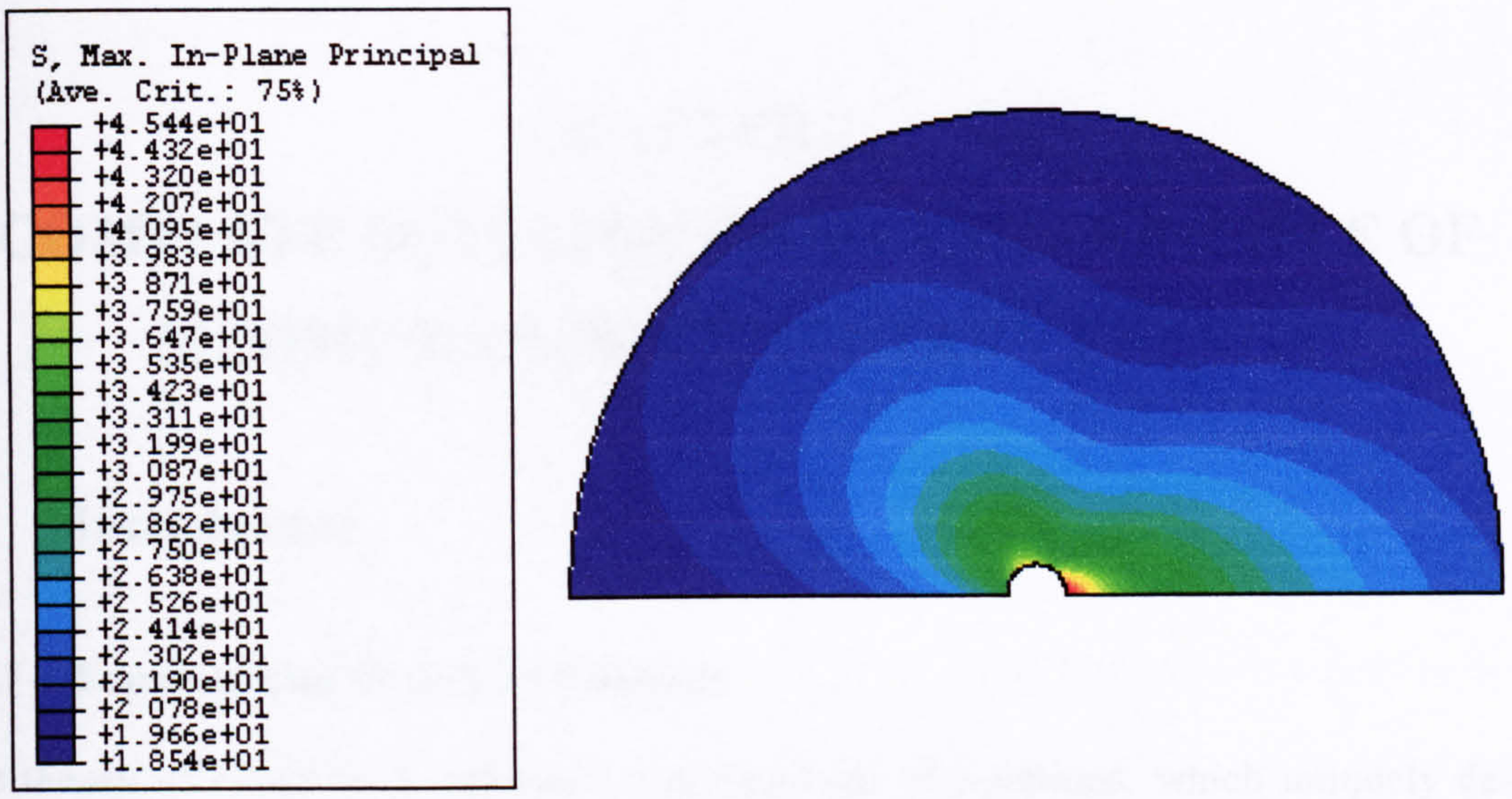

(c) Maximum principle stress (2 rings of innermost elements excluded)

Fig. 2.11 The stress contour plots at point A

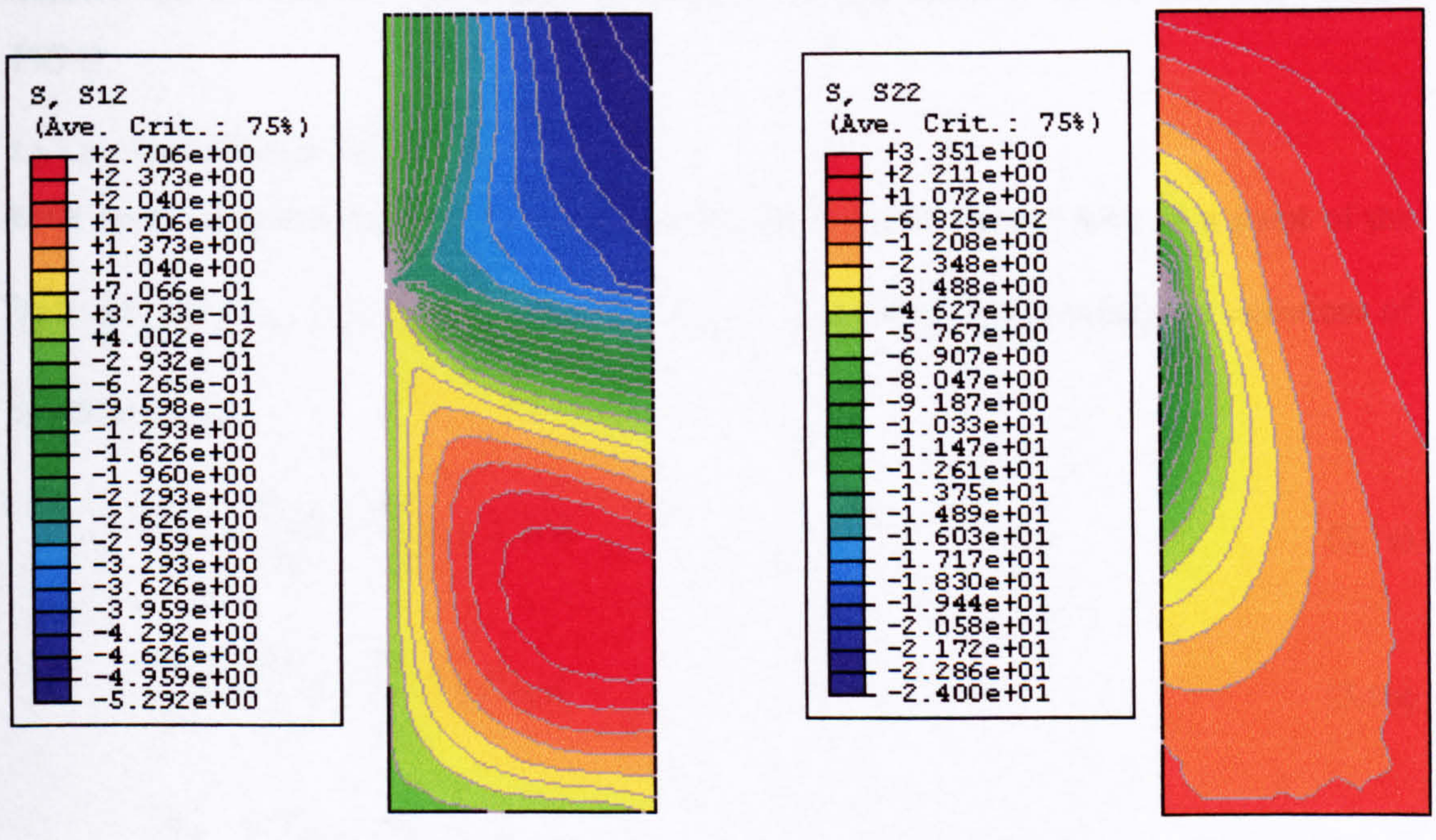

(a) Shear stress (b) Transverse normal stress

Fig. 2.12 The stress contour plots at point B

CHAPTER 3.

COMPLETE SOLUTION USING THE PRINCIPLE OF MINIMUM COMPLEMENTARY ENERGY

3.1 Introduction

3.1.1 Fundamental Theory of Elasticity

The theory of elasticity comprises a consistent set of equations, which uniquely describe the state of stress, strain and displacement at each point within an elastic deformable body. The theory of elasticity contains *equilibrium* equations relating the stresses; *kinematic* equations relating the strains and displacements; *constitutive* equations relating the stresses and strains; *boundary* conditions relating to the physical domain and *uniqueness* constraints relating to the applicability of the solution (Gould 1994).

3.1.1.1 *Equilibrium Equations*

Nine stress components are defined to describe the state of internal force at a point of the body, i.e. σ_x, τ_{yx}, τ_{zx}, τ_{xy}, σ_y, τ_{zy}, τ_{xz}, τ_{yz}, σ_z, and they should satisfy the equations of equilibrium, i.e.

$$\frac{\partial \sigma_x}{\partial x}+\frac{\partial \tau_{yx}}{\partial y}+\frac{\partial \tau_{zx}}{\partial z}+\overline{X}=0 \tag{3.1a}$$

$$\frac{\partial \tau_{xy}}{\partial x}+\frac{\partial \sigma_y}{\partial y}+\frac{\partial \tau_{zy}}{\partial z}+\overline{Y}=0 \tag{3.1b}$$

$$\frac{\partial \tau_{xz}}{\partial x}+\frac{\partial \tau_{yz}}{\partial y}+\frac{\partial \sigma_z}{\partial z}+\overline{Z}=0 \tag{3.1c}$$

$$\tau_{yz}=\tau_{zy},\ \tau_{zx}=\tau_{xz},\ \tau_{xy}=\tau_{yx} \tag{3.1d-f}$$

where $\overline{X}$, $\overline{Y}$ and $\overline{Z}$ are components of the body forces per unit volume. By adopting Equations (3.1 d-f), only six stress components are independent, and they have the following relationships

$$\frac{\partial \sigma_x}{\partial x}+\frac{\partial \tau_{xy}}{\partial y}+\frac{\partial \tau_{zx}}{\partial z}+\overline{X}=0 \tag{3.2a}$$

$$\frac{\partial \tau_{xy}}{\partial x}+\frac{\partial \sigma_y}{\partial y}+\frac{\partial \tau_{yz}}{\partial z}+\overline{Y}=0 \tag{3.2b}$$

$$\frac{\partial \tau_{zx}}{\partial x}+\frac{\partial \tau_{yz}}{\partial y}+\frac{\partial \sigma_z}{\partial z}+\overline{Z}=0 \tag{3.2c}$$

3.1.1.2 *Kinematic Equations*

Corresponding to the six independent stress components, the state of strain at a point is defined by six components of strain, i.e. ε_x, ε_y, ε_z, γ_{yz}, γ_{zx}, γ_{xy} and their relationship with the displacement are given as follows

$$\varepsilon_x=\frac{\partial u}{\partial x},\ \varepsilon_y=\frac{\partial v}{\partial y},\ \varepsilon_z=\frac{\partial w}{\partial z},$$

$$\gamma_{yz}=\frac{\partial w}{\partial y}+\frac{\partial v}{\partial z},\ \gamma_{zx}=\frac{\partial u}{\partial z}+\frac{\partial w}{\partial x},\ \gamma_{xy}=\frac{\partial v}{\partial x}+\frac{\partial u}{\partial y} \tag{3.3a-f}$$

where u, v, w are the displacement components of a point of the body in the x-, y- and z- directions, respectively.

3.1.1.3 *Constitutive Relations*

The stress-strain relations are given in linear, homogeneous form as:

$$\begin{bmatrix}\sigma_x\\ \sigma_y\\ \sigma_z\\ \tau_{yz}\\ \tau_{zx}\\ \tau_{xy}\end{bmatrix}=\begin{bmatrix}a_{11} & a_{12} & a_{13} & a_{14} & a_{15} & a_{16}\\ a_{21} & a_{22} & a_{23} & a_{24} & a_{25} & a_{26}\\ a_{31} & a_{32} & a_{33} & a_{34} & a_{35} & a_{36}\\ a_{41} & a_{42} & a_{43} & a_{44} & a_{45} & a_{46}\\ a_{51} & a_{52} & a_{53} & a_{54} & a_{55} & a_{56}\\ a_{61} & a_{62} & a_{63} & a_{64} & a_{65} & a_{66}\end{bmatrix}\begin{bmatrix}\varepsilon_x\\ \varepsilon_y\\ \varepsilon_z\\ \gamma_{yz}\\ \gamma_{zx}\\ \gamma_{xy}\end{bmatrix} \tag{3.4}$$

The coefficients of these equations are called elastic constants. Among them, there exist relations of the form:

$$a_{pq}=a_{qp}\ (p,q=1,2,\ldots,6) \tag{3.5}$$

Equation 3.4 may be inverted to yield:

$$\begin{bmatrix} \varepsilon_x \\ \varepsilon_y \\ \varepsilon_z \\ \gamma_{yz} \\ \gamma_{zx} \\ \gamma_{xy} \end{bmatrix} = \begin{bmatrix} b_{11} & b_{12} & b_{13} & b_{14} & b_{15} & b_{16} \\ b_{21} & b_{22} & b_{23} & b_{24} & b_{25} & b_{26} \\ b_{31} & b_{32} & b_{33} & b_{34} & b_{35} & b_{36} \\ b_{41} & b_{42} & b_{43} & b_{44} & b_{45} & b_{46} \\ b_{51} & b_{52} & b_{53} & b_{54} & b_{55} & b_{56} \\ b_{61} & b_{62} & b_{63} & b_{64} & b_{65} & b_{66} \end{bmatrix} \begin{bmatrix} \sigma_x \\ \sigma_y \\ \sigma_z \\ \tau_{yz} \\ \tau_{zx} \\ \tau_{xy} \end{bmatrix} \tag{3.6}$$

where

$$b_{pq} = b_{qp} \ (p, q = 1, 2, \ldots, 6) \tag{3.7}$$

For an isotropic material, the number of the independent elastic constants reduced to 2, and the stress-strain relations are given by

$$\sigma_x = 2G\left[\varepsilon_x + \frac{\nu}{1-2\nu}\left(\varepsilon_x + \varepsilon_y + \varepsilon_z\right)\right],\ \tau_{yz} = G\gamma_{yz},$$

$$\sigma_y = 2G\left[\varepsilon_y + \frac{\nu}{1-2\nu}\left(\varepsilon_x + \varepsilon_y + \varepsilon_z\right)\right],\ \tau_{zx} = G\gamma_{zx},$$

$$\sigma_z = 2G\left[\varepsilon_z + \frac{\nu}{1-2\nu}\left(\varepsilon_x + \varepsilon_y + \varepsilon_z\right)\right],\ \tau_{xy} = G\gamma_{xy} \tag{3.8a-f}$$

or, inversely,

$$\varepsilon_x = \frac{1}{E}\left[\sigma_x - \nu\left(\sigma_y + \sigma_z\right)\right],\ \gamma_{yz} = \frac{\tau_{yz}}{G},$$

$$\varepsilon_y = \frac{1}{E}\left[\sigma_y - \nu\left(\sigma_z + \sigma_x\right)\right],\ \gamma_{zx} = \frac{\tau_{zx}}{G},$$

$$\varepsilon_z = \frac{1}{E}\left[\sigma_z - \nu\left(\sigma_x + \sigma_y\right)\right],\ \gamma_{xy} = \frac{\tau_{xy}}{G} \tag{3.9a-f}$$

where E, G and ν are Young's modulus, shear modulus and Poisson's ratio respectively, and they hold the relationship as

$$G = \frac{E}{2(1+\nu)} \tag{3.10}$$

3.1.1.4 *Boundary Conditions*

The surface of the bodies can be divided into two parts from the viewpoint of the boundary conditions: part S_1 over which boundary conditions are prescribed in terms of external forces and part S_2 over which boundary conditions are prescribed in terms of displacements. Obviously $S = S_1 + S_2$. Denoting the components of the prescribed external forces per unit area of the boundary surface by $\overline{X}_\nu$, $\overline{Y}_\nu$ and $\overline{Z}_\nu$, the mechanical boundary conditions are given by

$$X_\nu = \overline{X}_\nu,\ Y_\nu = \overline{Y}_\nu,\ Z_\nu = \overline{Z}_\nu \qquad \text{on } S_1 \tag{3.11}$$

where

$$X_\nu = \sigma_x l + \tau_{xy} m + \tau_{zx} n$$

$$Y_\nu = \tau_{xy} l + \sigma_y m + \tau_{yz} n$$

$$Z_\nu = \tau_{zx} l + \tau_{yz} m + \sigma_z n \tag{3.12a-c}$$

l, m, n are the direction cosines of the unit normal ν drawn outwards on the boundary, i.e. $l = \cos(x,\nu)$, $m = \cos(y,\nu)$ and $n = \cos(z,\nu)$. On the other hand, denoting the components of the prescribed displacement by $\overline{u}$, $\overline{v}$ and $\overline{w}$, the geometrical conditions are given by

$$u = \overline{u}\ ,\ v = \overline{v},\ w = \overline{w} \qquad \text{on } S_2 \tag{3.13}$$

3.1.1.5 *Two-dimensional Elasticity*

An 3-D elasticity problem may be reduced to a 2-D one if there is no traction on one plane passing through the body, which typically includes the cases of plane stress and plane strain. To confine the study into the realm of isotropic elasticity, we have the following, which may be easily extended to more complex material laws.

For plane stress with the z-axis stress-free, we have

$$\tau_{xz} = \tau_{yz} = \sigma_z = 0 \tag{3.14}$$

Also, it is assumed that the remaining stresses do not vary with z, but are only function of x and y. This reduces the equilibrium equations to

$$\frac{\partial \sigma_x}{\partial x} + \frac{\partial \tau_{xy}}{\partial y} + \overline{X} = 0 \tag{3.15a}$$

$$\frac{\partial \tau_{xy}}{\partial x}+\frac{\partial \sigma_y}{\partial y}+\bar{Y}=0 \tag{3.15b}$$

Only three kinematic equations are involved in the case of plane stress

$$\varepsilon_x=\frac{\partial u}{\partial x},\ \varepsilon_y=\frac{\partial v}{\partial y},\ \gamma_{xy}=\frac{\partial v}{\partial x}+\frac{\partial u}{\partial y} \tag{3.16a-b}$$

and the constitutive equation become

$$\varepsilon_x=\frac{1}{E}\left[\sigma_x-\nu\sigma_y\right],\ \varepsilon_y=\frac{1}{E}\left[\sigma_y-\nu\sigma_x\right],\ \varepsilon_z=-\frac{\nu}{E}\left(\sigma_x+\sigma_y\right),\ \gamma_{xy}=\frac{\tau_{xy}}{G} \tag{3.17a-d}$$

In terms of the plane strain, we only need to substitute the constant in Equation 3.17, i.e.

$$E \text{ by } \frac{E}{1-\nu^2}\text{; and } \nu \text{ by } \frac{\nu}{1-\nu} \tag{3.18a-b}$$

3.1.2 Principle of Virtual Work and Principle of Minimum Potential Energy (Washizu, 1974)

Consider the body in equilibrium under prescribed body force and boundary condition, the equilibrium Equations 3.2a-c hold in the volume and the mechanical boundary conditions 3.12 and 3.13 are valid on S_1. The body is assumed to experience an arbitrary set of infinitesimal virtual displacement δu, δv and δw from the equilibrating configuration, we have

$$-\iiint_V\left[\left(\frac{\partial \sigma_x}{\partial x}+\frac{\partial \tau_{yx}}{\partial y}+\frac{\partial \tau_{zx}}{\partial z}+\bar{X}\right)\delta u+(\cdots)\delta v+(\cdots)\delta w\right]dV+\iint_{S1}\left[(X_\nu-\bar{X}_\nu)\delta u+(\cdots)\delta v+(\cdots)\delta w\right]dS=0 \tag{3.19}$$

where $dV = dx\,dy\,dz$ and dS are the elementary volume and the elementary area of the surface of the body, respectively. The arbitrary sets of virtual displacement are so chosen that the geometrical boundary conditions on S_2 be not violated, namely, they satisfy

$$\delta u=0\ ,\ \delta v=0,\ \delta w=0 \text{ on } S_2 \tag{3.20a-c}$$

Using the integration by parts together with the kinematic relationship, Equation 3.19 becomes

$$\iiint_V\left(\sigma_x\delta\varepsilon_x+\sigma_y\delta\varepsilon_y+\sigma_z\delta\varepsilon_z+\tau_{yz}\delta\gamma_{yz}+\tau_{zx}\delta\gamma_{zx}+\tau_{xy}\delta\gamma_{xy}\right)dV$$

$$-\iiint_V (\bar{X}\delta u + \bar{Y}\delta v + \bar{Z}\delta w)dV - \iint_{S1} (\bar{X}_v \delta u + \bar{Y}_v \delta v + \bar{Z}_v \delta w)dS = 0 \tag{3.21}$$

Equation 3.21 is the principle of virtual work, which holds valid for arbitrary infinitesimal virtual displacement satisfying the prescribed geometrical boundary conditions.

If we construct state functions which satisfy the following conditions

$$\delta A = \sigma_x \delta\varepsilon_x + \sigma_y \delta\varepsilon_y + \sigma_z \delta\varepsilon_z + \tau_{yz}\delta\gamma_{yz} + \tau_{zx}\delta\gamma_{zx} + \tau_{xy}\delta\gamma_{xy}$$

$$-\delta\Phi = \bar{X}\delta u + \bar{Y}\delta v + \bar{Z}\delta w$$

$$-\delta\Psi = \bar{X}_v \delta u + \bar{Y}_v \delta v + \bar{Z}_v \delta w \tag{3.22a-c}$$

For instance, in the case of isotropic material, we let

$$A = \frac{E\nu}{2(1+\nu)(1-2\nu)}\left(\frac{\partial u}{\partial x}+\frac{\partial v}{\partial y}+\frac{\partial w}{\partial z}\right)^2 + G\left[\left(\frac{\partial u}{\partial x}\right)^2 + \left(\frac{\partial v}{\partial y}\right)^2 + \left(\frac{\partial w}{\partial z}\right)^2\right]$$

$$+\frac{G}{2}\left[\left(\frac{\partial v}{\partial z}+\frac{\partial w}{\partial y}\right)^2 + \left(\frac{\partial w}{\partial x}+\frac{\partial u}{\partial z}\right)^2 + \left(\frac{\partial u}{\partial y}+\frac{\partial v}{\partial x}\right)^2\right]$$

$$-\Phi = \bar{X}u + \bar{Y}v + \bar{Z}w$$

$$-\Psi = \bar{X}_v u + \bar{Y}_v v + \bar{Z}_v w \tag{3.23a-c}$$

The principle of virtual work (Equation 3.21) can be transformed into

$$\delta\Pi = 0 \tag{3.24}$$

where

$$\Pi = \iiint_V [A(u,v,w) + \Phi(u,v,w)]dV + \iint_{S1} \Psi(u,v,w)dS \tag{3.25}$$

being the total potential energy.

Equation 3.24 is the principle of minimum potential energy, which states that among all the admissible displacement functions, the actual displacement make the total potential energy an absolute minimum.

3.1.3 Principle of Complementary Virtual Work and Principle of Minimum Complementary Energy (Washizu, 1974)

As the complementary to the principle of virtual work, we consider the body in equilibrium under the prescribed body forces and boundary conditions to take an arbitrary set of infinitesimal virtual variations of the stress components $(\delta\sigma_x, \delta\sigma_y, \ldots, \delta\tau_{xy})$ from the equilibrating configuration. The kinematic equations and the geometric boundary conditions lead to

$$\iiint_V \left[\left(\varepsilon_x - \frac{\partial u}{\partial x}\right)\delta\sigma_x + (\cdots)\delta\sigma_y + \cdots + \left(\gamma_{xy} - \frac{\partial u}{\partial y} - \frac{\partial v}{\partial x}\right)\delta\tau_{xy}\right]dV + \int_{S2}\iint[(u-\bar{u})\delta X_v + (v-\bar{v})\delta Y_v + (w-\bar{w})\delta Z_v]dS = 0 \tag{3.26}$$

If we choose the arbitrary set of virtual stresses satisfying the equilibrium equations and mechanical boundary conditions, i.e.

$$\frac{\partial\delta\sigma_x}{\partial x} + \frac{\partial\delta\tau_{xy}}{\partial y} + \frac{\partial\delta\tau_{zx}}{\partial z} = 0$$

$$\frac{\partial\delta\tau_{xy}}{\partial x} + \frac{\partial\delta\sigma_y}{\partial y} + \frac{\partial\delta\tau_{yz}}{\partial z} = 0$$

$$\frac{\partial\delta\tau_{zx}}{\partial x} + \frac{\partial\delta\tau_{yz}}{\partial y} + \frac{\partial\delta\sigma_z}{\partial z} = 0 \qquad \text{in } V, \text{ and}$$

$$\delta X_v = \delta\sigma_x l + \delta\tau_{xy} m + \delta\tau_{zx} n = 0$$

$$\delta Y_v = \delta\tau_{xy} l + \delta\sigma_y m + \delta\tau_{yz} n = 0$$

$$\delta Z_v = \delta\tau_{zx} l + \delta\tau_{yz} m + \delta\sigma_z n \qquad \text{on } S_1 \tag{3.27a-f}$$

The integration by parts transforms equation (3.26) into

$$\iiint_V (\varepsilon_x\delta\sigma_x + \varepsilon_y\delta\sigma_y + \varepsilon_z\delta\sigma_z + \gamma_{yz}\delta\tau_{yz} + \gamma_{zx}\delta\tau_{zx} + \gamma_{xy}\delta\tau_{xy})dV$$

$$- \int_{S_2}\iint(\bar{u}\delta X_v + \bar{v}\delta Y_v + \bar{w}\delta Z_v)dS = 0 \tag{3.28}$$

Equation 3.28 is the principle of complementary virtual work. The principle holds valid for arbitrary infinitesimal virtual stress variations satisfying the equations of equilibrium and prescribed mechanical boundary conditions.

Using the similar procedure as the last section, one of the state function B is defined so that

$$\delta B = \varepsilon_x \delta\sigma_x + \varepsilon_y \delta\sigma_y + \varepsilon_z \delta\sigma_z + \gamma_{yz} \delta\tau_{yz} + \gamma_{zx} \delta\tau_{zx} + \gamma_{xy} \delta\tau_{xy} \tag{3.29}$$

For the case of isotropic material, we let

$$B = \frac{1}{2E}\left[(\sigma_x + \sigma_y + \sigma_z)^2 + 2(1+\nu)(\tau_{yz}^2 + \tau_{zx}^2 + \tau_{xy}^2 - \sigma_y\sigma_z - \sigma_z\sigma_x - \sigma_x\sigma_y)\right] \tag{3.30}$$

The principle of complementary virtual work can be transformed into

$$\delta\Pi_c = 0 \tag{3.31}$$

where

$$\Pi_c = \iiint_V \left[B(\sigma_x, \sigma_y, \cdots, \sigma_{xy})\right] dV - \iint_{S_2} (\bar{u}\delta X_v + \bar{v}\delta Y_v + \bar{w}\delta Z_v) dS \tag{3.32}$$

being the total complementary energy.

Equation 3.31 is the principle of minimum complementary energy, which states that among all the admissible stresses, which satisfy the equilibrium and the prescribed mechanical boundary conditions on S_1, the set of actual stress components make the total complementary energy an absolute minimum.

3.2 Interfacial Stresses in Bonded RC Beams under Symmetric Loads

3.2.1 Geometry and Loading

Consider a simply supported beam with a span of $2L$. The bonded plate has a length of $2l$ (Figure 3.1). The beam is subjected to an axial force N_0, a pair of end moments M_0 and a symmetrically distributed arbitrary transverse load $q(x)$. The applied loading causes the internal forces N_l, Q_l and M_l at the beam sections where the bonded plate ends [Figure 3.2(a)]. The sign convention for the applied loadings and the internal forces are shown in Figure 3.2(a).

A global Cartesian co-ordinate system x-y is used with its origin being at the middle of the top surface of the beam (Figure 3.1). The bonded part of the beam consists of three layers: the concrete beam, the adhesive layer and the plate. A local coordinate

system $x^{[i]}$ - $y^{[i]}$ is adopted for each of the three layers, with the origin being at the geometrical centre of each layer (Figure 3.2a). For ease of reference, these three layers are denoted by superscripts $^{[1]}$, $^{[2]}$ and $^{[3]}$ respectively (e.g. the thicknesses of the three layers are denoted by $h^{[1]}$, $h^{[2]}$ and $h^{[3]}$ respectively). Similarly, superscripts $^{(0)}$, $^{(1)}$, $^{(2)}$ and $^{(3)}$ are used to denote the surfaces and interfaces (e.g. the widths the surfaces/interfaces are $b^{(0)}$, $b^{(1)}$, $b^{(2)}$ and $b^{(3)}$ respectively) (Figure 3.2b). Note $b^{(0)} = b^{(1)} = b^{(2)}$ from physical observation.

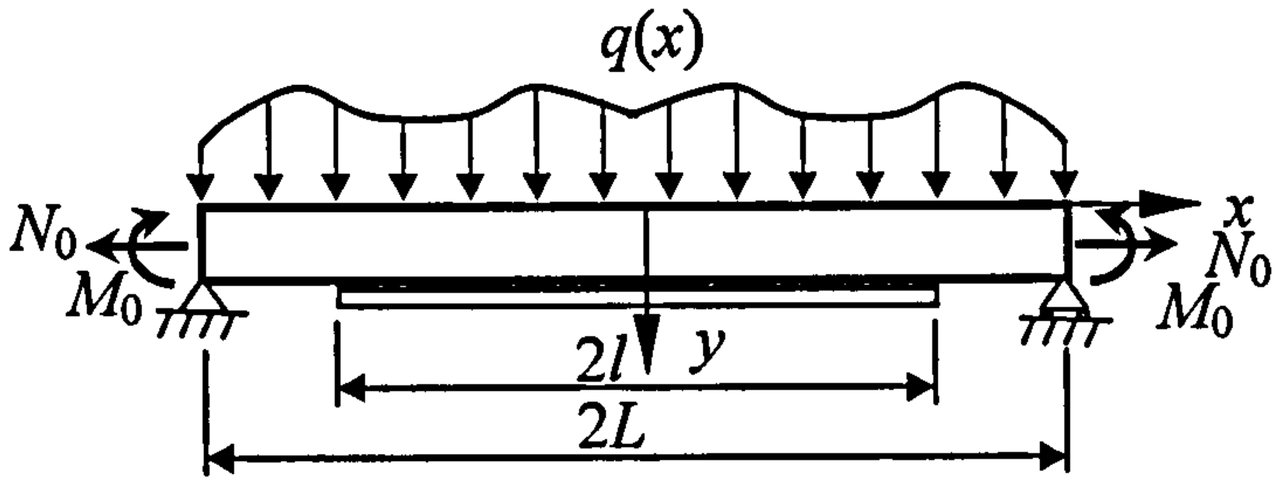

Fig. 3.1 A plated beam under symmetric loads

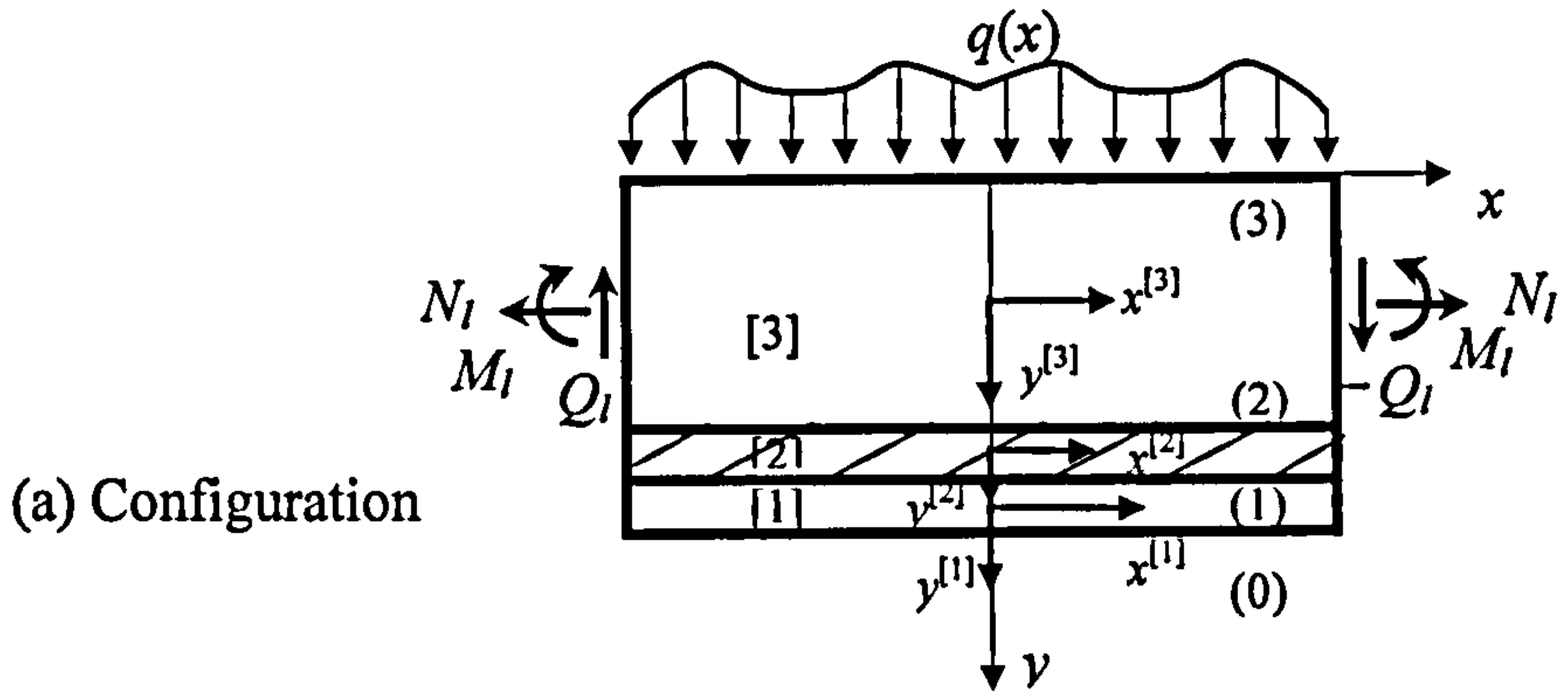

Fig. 3.2 Notations

3.2.2 Assumptions

The present analysis takes into consideration the transverse shear stress and strain in the beam and the plate but ignores the transverse normal stress in them. Additionally, the following four assumptions are adopted:

1. Each individual layer is elastic, homogeneous and orthotropic. Note that the assumption of orthotropic behaviour has implications only for the shear moduli of the materials for the existing beam and the bonded plate;
2. The three layers are perfectly bonded (no slips or opening-up at the interfaces);
3. The Euler-Bernoulli beam theory is adopted for the beam and the plate, whereas the adhesive layer is considered to be in a plane stress state; and
4. The longitudinal stress in the adhesive is assumed to vary linearly across its thickness.

3.2.3 Equilibrium Equations of Beam and Plate

For the beam and plate (i^{th} layer, $i = 1, 3$, see Figure 3.2c), equilibrium considerations lead to the following relations between the interfacial stresses and the stress resultants acting on the layer :

$$\frac{dN^{[i]}(x)}{dx} = b^{(i)}\sigma_{xy}^{(i)}(x) - b^{(i-1)}\sigma_{xy}^{(i-1)}(x) \tag{3.33a}$$

$$\frac{dQ^{[i]}(x)}{dx} = b^{(i)}\sigma_{y}^{(i)}(x) - b^{(i-1)}\sigma_{y}^{(i-1)}(x) - \begin{cases} 0 & (i \neq 3) \\ q(x) & (i = 3) \end{cases} \tag{3.33b}$$

$$\frac{dM^{[i]}(x)}{dx} = Q^{[i]}(x) - \frac{h^{[i]}}{2}\left[b^{(i-1)}\sigma_{xy}^{(i-1)}(x) + b^{(i)}\sigma_{xy}^{(i)}(x)\right] \tag{3.33c}$$

where $N^{[i]}(x)$, $Q^{[i]}(x)$ and $M^{[i]}(x)$ are the axial force, shear force and bending moment respectively in the i^{th} layer and $\sigma_{xy}^{(i)}(x)$ and $\sigma_{y}^{(i)}(x)$ are the shear and transverse normal stresses respectively at the i^{th} interface. In Equations 3.33 and the rest of this paper, the superscript in $x^{[i]}$ is omitted because the global and the three local co-ordinate systems share the same horizontal axis.

3.2.4 Boundary Conditions at Ends of Plate

The boundary conditions at the ends of the plate are

$$N^{[i]}(\pm l) = \begin{cases} 0 & (i \neq 3) \\ N_l & (i = 3) \end{cases} \tag{3.34a}$$

$$Q^{[i]}(\pm l) = \begin{cases} 0 & (i \neq 3) \\ \mp Q_l & (i = 3) \end{cases} \tag{3.34b}$$

$$M^{[i]}(\pm l) = \begin{cases} 0 & (i \neq 3) \\ M_t & (i = 3) \end{cases} \tag{3.34c}$$

3.2.5 Representation of Stress Fields

3.2.5.1 *Stress Field in the Adhesive Layer*

The adhesive layer is treated as an elastic continuum without any body force. The equilibrium equations in its local coordinate system are

$$\frac{\partial \sigma_x^{[2]}}{\partial x} + \frac{\partial \sigma_{xy}^{[2]}}{\partial y^{[2]}} = 0 \tag{3.35a}$$

$$\frac{\partial \sigma_{xy}^{[2]}}{\partial x} + \frac{\partial \sigma_y^{[2]}}{\partial y^{[2]}} = 0 \tag{3.35b}$$

where $\sigma_x^{[2]}$, $\sigma_{xy}^{[2]}$ and $\sigma_y^{[2]}$ denote the longitudinal, shear and transverse stresses respectively.

The longitudinal stress in the adhesive layer is assumed to be a linear function of $y^{[2]}$ and it then follows from Equation 3.35a, that the shear stress distribution is parabolic. Equating the shear and normal stresses at lower and upper faces to the appropriate interfacial stresses, $\sigma_{xy}^{(i)}(x)$ and $\sigma_y^{(i)}(x)$ (i=1, 2) and adopting the equilibrium conditions of Equations 3.35a and b lead to

$$\sigma_x^{[2]} = \int_x^l \left\{ \frac{\sigma_{xy}^{(1)} - \sigma_{xy}^{(2)}}{h^{[2]}} + \frac{4y^{[2]}}{\left(h^{[2]}\right)^2} \left[\sigma_{xy}^{(1)} + \sigma_{xy}^{(2)} + \int_0^x \left[\frac{3\left(\sigma_y^{(1)} - \sigma_y^{(2)}\right)}{h^{[2]}} + \frac{\left(\sigma_{xy}^{(1)'} + \sigma_{xy}^{(2)'}\right)}{2} \right] dx \right] \right\} dx \tag{3.36a}$$

$$\sigma_{xy}^{[2]} = \int_0^x \left[\frac{3\left(\sigma_y^{(2)} - \sigma_y^{(1)}\right)}{2h^{[2]}} - \frac{\left(\sigma_{xy}^{(1)'} + \sigma_{xy}^{(2)'}\right)}{4} \right] dx + \frac{y^{[2]}\left(\sigma_{xy}^{(1)} - \sigma_{xy}^{(2)}\right)}{h^{[2]}} + \frac{\left(y^{[2]}\right)^2}{\left(h^{[2]}\right)^2} \left\{ 2\left(\sigma_{xy}^{(1)} + \sigma_{xy}^{(2)}\right) + \int_0^x \left[\frac{6\left(\sigma_y^{(1)} - \sigma_y^{(2)}\right)}{h^{[2]}} + h^{[2]}\left(\sigma_{xy}^{(1)'} + \sigma_{xy}^{(2)'}\right) \right] dx \right\} \tag{3.36b}$$

$$\sigma_y^{[2]} = \frac{\sigma_y^{(1)} + \sigma_y^{(2)}}{2} + \frac{h^{[2]}\left(\sigma_{xy}^{(1)} - \sigma_{xy}^{(2)}\right)}{8} + y^{[2]}\left[\frac{\left(\sigma_{xy}^{(1)'} + \sigma_{xy}^{(2)'}\right)}{4} + \frac{3\left(\sigma_y^{(1)} - \sigma_y^{(2)}\right)}{2h^{[2]}}\right]$$

$$+\frac{\left(y^{[2]}\right)^2}{2h^{[2]}}\left(\sigma_{xy}^{(2)'} - \sigma_{xy}^{(1)'}\right) + \frac{\left(y^{[2]}\right)^3}{\left(h^{[2]}\right)^2}\left[\frac{2\left(\sigma_y^{(2)} - \sigma_y^{(1)}\right)}{h^{[2]}} - \left(\sigma_{xy}^{(1)'} + \sigma_{xy}^{(2)'}\right)\right] \quad (3.36c)$$

in which a prime denotes differentiation with respect to x.

3.2.5.2 *Stress Fields in the Plate and the Beam*

Using assumption 3, the longitudinal and shear stresses in the plate and the beam can be expressed as

$$\sigma_x^{[i]} = \frac{N^{[i]}(x)}{b^{(i)}h^{[i]}} + \frac{12M^{[i]}(x)y^{[i]}}{b^{(i)}\left(h^{[i]}\right)^3} \qquad (i = 1, 3) \quad (3.37a)$$

$$\sigma_{xy}^{[i]} = -\frac{6Q^{[i]}(x)}{b^{(i)}\left(h^{[i]}\right)^3}\left[\left(y^{[i]}\right)^2 - \frac{\left(h^{[i]}\right)^2}{4}\right] + \frac{1}{b^{(i)}h^{[i]}}\begin{cases}\sigma_{xy}^{(1)}\left(\dfrac{h^{[1]}}{2} - y^{[1]}\right) & i = 1\\ \sigma_{xy}^{(2)}\left(\dfrac{h^{[3]}}{2} + y^{[3]}\right) & i = 3\end{cases} \quad (3.37b)$$

As assumed, $\sigma_y^{[i]}$ $(i = 1, 3)$ is neglected in both the beam and the plate.

3.2.6 Solution Procedure

The interfacial normal and shear stresses may be expressed as Fourier series

$$\sigma_y^{(i)}(x) = \sum_m a_m^{(i)} \cos\frac{m\pi x}{l} \quad (3.38a)$$

$$\sigma_{xy}^{(i)}(x) = \sum_m b_m^{(i)} \sin\frac{m\pi x}{l} \quad (3.38b)$$

where i =1, 2; $a_m^{(i)}$ and $b_m^{(i)}$ are unknown Fourier coefficients; and m = 1, 2, …∞. The constant term in Equation 3.38a has been set to zero to satisfy the equilibrium requirement that the integration of the interfacial normal stress over the entire length of the interface must be equal to zero. It may be noted that $\sigma_y^{(0)} = \sigma_y^{(3)} = \sigma_{xy}^{(0)} = \sigma_{xy}^{(3)} = 0$ because no interfacial stresses exist on the top and bottom surfaces of the strengthened beam.

Substituting Equations 3.6a and b into Equations 3.33 yields

$$N^{[i]}(x)=\sum_m\left(\frac{l}{m\pi}\right)\left[b^{(i)}b_m^{(i)}-b^{(i-1)}b_m^{(i-1)}\right]\left[(-1)^m-\cos\frac{m\pi x}{l}\right]+\begin{cases}0 & i=1\\ N_l & i=3\end{cases} \tag{3.39a}$$

$$Q^{[i]}(x)=\sum_m\left(\frac{l}{m\pi}\right)\left[b^{(i)}a_m^{(i)}-b^{(i-1)}b_m^{(i-1)}\right]\sin\frac{m\pi x}{l}+\begin{cases}0 & i=1\\ Q^a(x) & i=3\end{cases} \tag{3.39b}$$

$$M^{[i]}(x)=\sum_m\left(\frac{l}{m\pi}\right)\left\{\frac{l}{m\pi}\left[b^{(i)}a_m^{(i)}-b^{(i-1)}a_m^{(i-1)}\right]-\frac{h^i}{2}\left[b^{(i)}b_m^{(i)}+b^{(i-1)}b_m^{(i-1)}\right]\right\}\left[(-1)^m-\cos\frac{m\pi x}{l}\right]$$
$$+\begin{cases}0 & i=1\\ M^a(x) & i=3\end{cases} \tag{3.39c}$$

where $Q^a(x)$ and $M^a(x)$ are stress resultants in the corresponding un-strengthened beam caused by the same applied loads:

$$Q^a(x)=-\int_0^x q(x)dx \tag{3.40a}$$

$$M^a(x)=L\int_0^L q(x)dx-\int_x^L xq(x)dx-x\int_0^x q(x)dx+M_0 \tag{3.40b}$$

Substituting Equations 3.39 and 3.40 into Equations 3.37 and substituting Equations 3.38a and 3.40 into Equation 3.36s lead to the following stress components expressed in terms of the unknown coefficients $a_m^{(1)}$, $b_m^{(1)}$, $a_m^{(2)}$ and $b_m^{(2)}$:

$$\sigma_x^{[i]}=-\sum_m\frac{l}{m\pi}\left\{\frac{\left(b_m^{(i-1)}-b_m^{(i)}\right)}{h^{[i]}}+\frac{12ly^{[i]}}{\left(h^{[i]}\right)^3}\left[\frac{a_m^{(i-1)}-a_m^{(i)}}{m\pi}+\frac{h^{[i]}\left(b_m^{(i-1)}+b_m^{(i)}\right)}{2l}\right]\right\}\left[(-1)^m-\cos\frac{m\pi x}{l}\right]$$
$$+\begin{cases}0 & (i=1,2)\\ \sigma_x^a & (i=3)\end{cases} \tag{3.41}$$

$$\sigma_{xy}^{[i]}=-\sum_m\left\{\frac{3l\left(a_m^{(i-1)}-a_m^{(i)}\right)}{2m\pi h^{[i]}}+\frac{\left(b_m^{(i-1)}+b_m^{(i)}\right)}{4}-\frac{y^{[i]}\left(b_m^{(i-1)}-b_m^{(i)}\right)}{h^{[i]}}\right.$$
$$\left.-\frac{6l\left(y^{[i]}\right)^2}{\left(h^{[i]}\right)^3}\left[\frac{a_m^{(i-1)}-a_m^{(i)}}{m\pi}+\frac{h^{[i]}\left(b_m^{(i-1)}+b_m^{(i)}\right)}{2l}\right]\right\}\sin\frac{m\pi x}{l}+\begin{cases}0 & (i=1,2)\\ \sigma_{xy}^a & (i=3)\end{cases} \tag{3.42}$$

$$\sigma_y^{[i]}=\begin{cases}0 & (i=1,3)\\ \sum_m\zeta_m(y^{[2]})\cos\frac{m\pi x}{l} & (i=2)\end{cases} \tag{3.43}$$

in which

$$\zeta_m(y^{[2]}) = \left\{ \frac{\left(a_m^{(1)} + a_m^{(2)}\right)}{2} - \frac{h^{[2]} m\pi \left(b_m^{(1)} - b_m^{(2)}\right)}{8l} + \frac{3y^{[2]}}{2h^{[2]}} \left[\left(a_m^{(1)} - a_m^{(2)}\right) + \frac{m\pi \left(b_m^{(1)} + b_m^{(2)}\right)}{6l} \right] \right.$$

$$\left. + \frac{\left(y^{[2]}\right)^2 m\pi \left(b_m^{(1)} - b_m^{(2)}\right)}{2lh^{[2]}} - \frac{3\left(y^{[2]}\right)^3}{\left(h^{[2]}\right)^3} \left[\left(a_m^{(1)} - a_m^{(2)}\right) + \frac{h^{[2]} m\pi \left(b_m^{(1)} + b_m^{(2)}\right)}{2l} \right] \right\} \tag{3.44}$$

and σ_x^a and σ_{xy}^a are longitudinal and shear stresses in the un-strengthened beam caused by the same applied loads:

$$\sigma_x^a = \frac{N_1}{b^{(3)} h^{[3]}} + \frac{12y^{[3]}}{b^{(3)} \left(h^{[3]}\right)^3} M^a(x) \tag{3.45}$$

$$\sigma_{xy}^a = \frac{3y^{[3]}}{2b^{(3)} \left(h^{[3]}\right)^3} \left[\left(h^{[3]}\right)^2 - 4\left(y^{[3]}\right)^2 \right] Q^a(x) \tag{3.46}$$

The unknown coefficients may now be determined by minimising the complementary energy of the composite beam in the strengthened part. Only one half of the beam is considered here owing to symmetry. The total complementary energy in half of the strengthened portion is

$$\Pi_c = \frac{1}{2} \sum_{i=1}^{3} b^{(i)} \int_{-h^{[i]}/2}^{+h^{[i]}/2} \int_0^l \left[\frac{1}{E_x^{[i]}} \left(\sigma_x^{[i]}\right)^2 + \frac{1}{E_y^{[i]}} \left(\sigma_y^{[i]}\right)^2 - \frac{2\nu_{xy}^{[i]}}{E_x^{[i]}} \sigma_x^{[i]} \sigma_y^{[i]} + \frac{1}{G_{xy}^{[i]}} \left(\sigma_{xy}^{[i]}\right)^2 \right] dx dy^{[i]} \tag{3.47}$$

where $E_x^{[i]}$ and $E_y^{[i]}$ are the Young's moduli in x- and y-directions respectively; and $G_{xy}^{[i]}$ and $\nu_{xy}^{[i]}$ are the shear modulus and Poisson's ratio in the x-y plane of the i^{th} layer.

Minimising Π_c by setting $\partial U / \partial c_{m,i} = 0$, where $c_{m,i}$ is an element of the sub-vector $\mathbf{c}_m = \left[a_m^{(1)}, b_m^{(1)}, a_m^{(2)}, b_m^{(2)}\right]^T$, leads to

$$\mathbf{C}\ \mathbf{c}\ = \mathbf{P} \tag{3.48}$$

where

$$\mathbf{C} = \begin{bmatrix} \mathbf{C}_{11} & \cdots & \cdots & \cdots & \cdots & \cdots \\ & \ddots & \vdots & \vdots & \vdots & \vdots \\ & & \mathbf{C}_{mm} & \cdots & \mathbf{C}_{mn} & \cdots \\ & & & \ddots & \vdots & \vdots \\ & \textit{sym.} & & & \ddots & \vdots \\ & & & & & \mathbf{C}_{MM} \end{bmatrix} \tag{3.49}$$

$$\mathbf{c} = \begin{bmatrix} \mathbf{c}_1 & \cdots & \mathbf{c}_m & \cdots & \mathbf{c}_M \end{bmatrix}^T \tag{3.50}$$

$$\mathbf{P} = \begin{bmatrix} \mathbf{P}_1 & \cdots & \mathbf{P}_m & \cdots & \mathbf{P}_M \end{bmatrix}^T \tag{3.51}$$

in which M is the number of term of the Fourier series; $\mathbf{C}_{mm}$ and $\mathbf{C}_{mn}$ are sub-matrices of $\mathbf{C}$; and $\mathbf{P}_m$ is the sub-vector of $\mathbf{P}$. The elements of $\mathbf{C}_{mm}$, $\mathbf{C}_{mn}$ and $\mathbf{P}_m$ are given in Appendix A.

The interfacial stresses are obtained by solving Equation 3.48 and substituting the resulting coefficients into Equations 3.38a and b. All symmetrical loading cases can be considered by properly including various forms of the transverse load $q(x)$, axial force N_0 and end bending moment M_0 in the loading vector $\mathbf{P}$.

3.3 Interfacial Stresses in FRP-Bonded RC Beams under Antisymmetric Loads

3.3.1 Solution Procedure

Consider the same bonded beam subjected to a pair of anti-symmetric end moments M_0 and an anti-symmetrically distributed arbitrary transverse load $q(x)$. To facilitate the representation of the interfacial solutions using the Fourier series, we move the origins of the global and local Cartesian co-ordinate system to the left end of the bonded plate and denote the length of the beam by L and that of the bonded plate by l (Figures 3.3 and 3.4). We should distinguish the co-ordinate systems from those used in the preceding section. Apart from that, it is also worth noting that there are different denotations for L and l between the symmetric solution and anti-symmetric solution. The other signs take the same definition as the preceding section [Figure 3.2(b) and (c)].

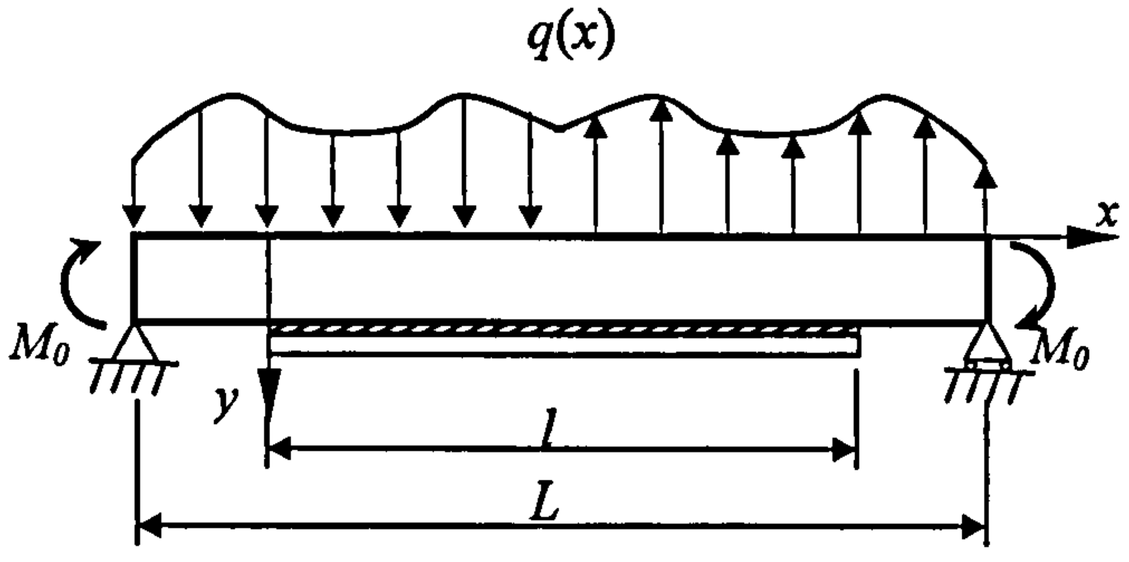

Fig. 3.3 A plated beam under antisymmetric loads

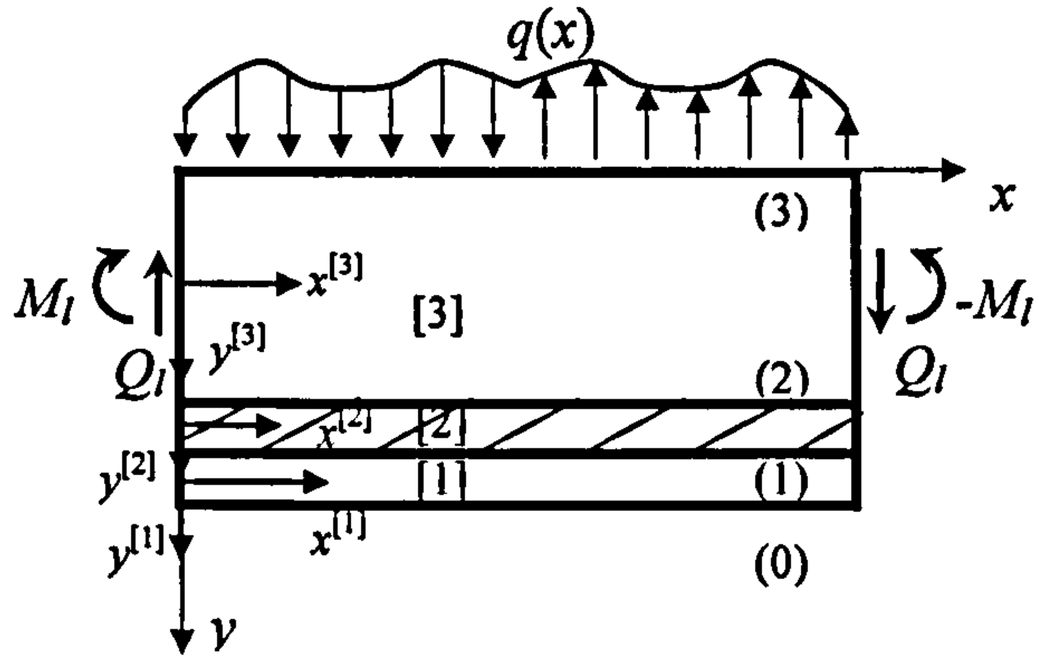

Fig. 3.4 Configurations and local coordinate system

The same equilibrium equation can be adopted as Equations 3.33, but with different boundary conditions due to the change of co-ordinate system, i.e.

$$Q^{[i]}(0;l)=\begin{cases}0 & (i\neq 3)\\ Q_l & (i=3)\end{cases};\quad M^{[i]}(0;\ l)=\begin{cases}0 & (i\neq 3)\\ \pm M_l & (i=3)\end{cases} \tag{3.52a-b}$$

where Q_l and M_l are the shear force and bending moment in the RC beam at the ends of the strengthened part (see Figure 3.4), which are given by

$$Q_l=\frac{2}{L}\left[\int_{\frac{l-L}{2}}^{\frac{l}{2}} q(x)\left(\frac{l}{2}-x\right)dx-M_0\right]-\int_{\frac{l-L}{2}}^{0} q(x)dx \tag{3.53a}$$

$$M_l=\int_0^{\frac{l}{2}} q(x)\left(x-\frac{l}{2}\right)dx+\frac{Q_l l}{2} \tag{3.53b}$$

Following the same procedure as that in Section 3.2.5.1 and 3.2.5.2, the stress components in the adhesive layer can be given by Equations 3.36 and those in the plate and RC beam can be given by Equations 3.37.

Allowing for the nature of interfacial stress, we can express them using the following Fourier series

$$\sigma_y^{(i)}(x)=\sum_m a_m^{(i)}\cos\frac{m\pi x}{l};\ \sigma_{xy}^{(i)}(x)=\sum_m b_m^{(i)}\sin\frac{m\pi x}{l}\qquad (i=1,2)\qquad (3.54a, b)$$

where $a_m^{(i)}$ and $b_m^{(i)}$ are unknown Fourier coefficients, and $m = 1, 3, 5,\ldots\infty$. Global condition of equilibrium for the bonded plate and the adhesive layer requires

$$\int_0^l \sigma_{xy}^{(i)}dx=0;\qquad \int_0^l x\sigma_y^{(i)}dx=0 \qquad (3.55a, b)$$

Substitution Equations 3.55a, b into Equations 3.54a, b leads to

$$\sum_m \frac{b_m^{(i)}}{m}=0;\qquad \sum_m \frac{a_m^{(i)}}{m^2}=0 \qquad (3.56a, b)$$

Substituting Equations 3.54a and b into 3.33 and 3.34. yields

$$N^{[i]}(x)=-\sum_m\left(\frac{l}{m\pi}\right)\left[b^{(i)}b_m^{(i)}-b^{(i-1)}b_m^{(i-1)}\right]\left[1+\cos\frac{m\pi x}{l}\right] \qquad (3.57a)$$

$$Q^{[i]}(x)=\sum_m\left(\frac{l}{m\pi}\right)\left[b^{(i)}a_m^{(i)}-b^{(i-1)}b_m^{(i-1)}\right]\sin\frac{m\pi x}{l}+\begin{cases}0 & i=1\\ Q^a(x) & i=3\end{cases} \qquad (3.57b)$$

$$M^{[i]}(x)=-\sum_m\left(\frac{l}{m\pi}\right)\left\{\frac{l}{m\pi}\left[b^{(i)}a_m^{(i)}-b^{(i-1)}a_m^{(i-1)}\right]-\frac{h^i}{2}\left[b^{(i)}b_m^{(i)}+b^{(i-1)}b_m^{(i-1)}\right]\right\}\left[1+\cos\frac{m\pi x}{l}\right]$$
$$+\begin{cases}0 & i=1\\ M^a(x) & i=3\end{cases} \qquad (3.57c)$$

where $Q^a(x)$ and $M^a(x)$ are stress resultants in the un-strengthened beam subjected to the same applied loads which are

$$Q^a(x)=-\int_0^x q(x)dx+Q_l \qquad (3.58a)$$

$$M^a(x)=-x\int_0^x q(x)dx+\int_0^x xq(x)dx-M_l+Q_l x \qquad (3.58b)$$

Accordingly the stress components in all three layers can be expressed by the Fourier series as follows

$$\sigma_x^{[i]}=\sum_{m=1,3,\ldots}\frac{l}{m\pi}\left\{\frac{\left(b_m^{(i-1)}-b_m^{(i)}\right)}{h^{[i]}}+\frac{12ly^{[i]}}{\left(h^{[i]}\right)^3}\left[\frac{a_m^{(i-1)}-a_m^{(i)}}{m\pi}+\frac{h^{[i]}\left(b_m^{(i-1)}+b_m^{(i)}\right)}{2l}\right]\right\}\left[1+\cos\frac{m\pi x}{l}\right]$$

$$+\begin{cases} 0 & (i=1,2) \\ \sigma_x^a & (i=3) \end{cases} \tag{3.59}$$

$$\sigma_{xy}^{[i]} = -\sum_m \left\{ \frac{3l\left(a_m^{(i-1)} - a_m^{(i)}\right)}{2m\pi h^{[i]}} + \frac{\left(b_m^{(i-1)} + b_m^{(i)}\right)}{4} - \frac{y^{[i]}\left(b_m^{(i-1)} - b_m^{(i)}\right)}{h^{[i]}} \right.$$

$$\left. - \frac{6l\left(y^{[i]}\right)^2}{\left(h^{[i]}\right)^3}\left[\frac{a_m^{(i-1)} - a_m^{(i)}}{m\pi} + \frac{h^{[i]}\left(b_m^{(i-1)} + b_m^{(i)}\right)}{2l} \right] \right\} \sin\frac{m\pi x}{l} + \begin{cases} 0 & (i=1,2) \\ \sigma_{xy}^a & (i=3) \end{cases} \tag{3.60}$$

$$\sigma_y^{[i]} = \begin{cases} 0 & (i=1,3) \\ \sum_m \zeta_m(y^{[2]}) \cos\frac{m\pi x}{l} & (i=2) \end{cases} \tag{3.61}$$

where

$$\zeta_m(y^{[2]}) = \left\{ \frac{\left(a_m^{(1)} + a_m^{(2)}\right)}{2} - \frac{h^{[2]} m\pi\left(b_m^{(1)} - b_m^{(2)}\right)}{8l} + \frac{3y^{[2]}}{2h^{[2]}}\left[\left(a_m^{(1)} - a_m^{(2)}\right) + \frac{m\pi\left(b_m^{(1)} + b_m^{(2)}\right)}{6l} \right] \right.$$

$$\left. + \frac{\left(y^{[2]}\right)^2 m\pi\left(b_m^{(1)} - b_m^{(2)}\right)}{2lh^{[2]}} - \frac{3\left(y^{[2]}\right)^3}{\left(h^{[2]}\right)^3}\left[\left(a_m^{(1)} - a_m^{(2)}\right) + \frac{h^{[2]} m\pi\left(b_m^{(1)} + b_m^{(2)}\right)}{2l} \right] \right\} \tag{3.62}$$

and σ_x^a and σ_{xy}^a are given by Equation 3.45 and 3.46.

In the process of using the principle of complementary energy, we note that Equations 3.56 a and b impose the constrain conditions to the unknown coefficients. It suggests that $a_m^{(1)}$, $b_m^{(1)}$, $a_m^{(2)}$ and $b_m^{(2)}$, m = 1, 3, 5, ..., are not all independent. If we assumed that $a_1^{(1)}$, $b_1^{(1)}$, $a_1^{(2)}$ and $b_1^{(2)}$ are dependent on the other unknown coefficients and the complementary energy Π_c is a composite function, which can be written as $\Pi_c\left[a_1^{(1)}, b_1^{(1)}, a_1^{(2)}, b_1^{(2)}; a_m^{(1)}, b_m^{(1)}, a_m^{(2)}, b_m^{(2)}\right]$. Minimizing Π_c by setting its first-order partial derivative in terms of $a_m^{(1)}$, $b_m^{(1)}$, $a_m^{(2)}$ and $b_m^{(2)}$, (m = 3, 5, ...) equal to zero, and using the chain rule of partial derivative of the composite function gives

$$\frac{\partial U}{\partial a_m^{(i)}} = \frac{\partial U}{\partial a_1^{(i)}}\frac{\partial a_1^{(i)}}{\partial a_m^{(i)}} + \frac{\partial U}{\partial a_m^{(i)}} \qquad m = 3, 5, \ldots, i = 1, 2 \tag{3.63a}$$

$$\frac{\partial U}{\partial b_m^{(i)}} = \frac{\partial U}{\partial b_1^{(i)}}\frac{\partial b_1^{(i)}}{\partial b_m^{(i)}} + \frac{\partial U}{\partial b_m^{(i)}} \qquad m = 3, 5, \ldots, i = 1, 2 \tag{3.63b}$$

In their compact forms, Equations 3.63 can be written as

$$\mathbf{C}\ \mathbf{c} = \mathbf{P} \tag{3.64}$$

where

$$\mathbf{C} = \begin{bmatrix} \mathbf{C}_{11} & \cdots & \cdots & \cdots & \cdots & \cdots \\ \vdots & \ddots & \vdots & \vdots & \vdots & \vdots \\ \cdots & \cdots & \mathbf{C}_{ss} & \cdots & \mathbf{C}_{st} & \cdots \\ \vdots & \vdots & \vdots & \ddots & \vdots & \vdots \\ \cdots & \cdots & \mathbf{C}_{ts} & \cdots & \ddots & \cdots \\ \vdots & \vdots & \vdots & \vdots & \vdots & \mathbf{C}_{MM} \end{bmatrix} \tag{3.65}$$

$$\mathbf{c} = \begin{bmatrix} \mathbf{c}_1 & \cdots & \mathbf{c}_s & \cdots & \mathbf{c}_M \end{bmatrix}^T \tag{3.66}$$

$$\mathbf{P} = \begin{bmatrix} \mathbf{P}_1 & \cdots & \mathbf{P}_s & \cdots & \mathbf{P}_M \end{bmatrix}^T \tag{3.67}$$

where M is the term number of the Fourier series. $\mathbf{C}_{ss}$ and $\mathbf{C}_{st}$ are respectively the sub-matrix of $\mathbf{C}$ in the diagonal place and non-diagonal place and $\mathbf{c}_s$ and $\mathbf{P}_s$ are the sub-vector of $\mathbf{c}$ and $\mathbf{P}$, which are given in Appendix B.

Solving Equation 3.64, and substituting them into Equations 3.56a and b to obtain $a_1^{(1)}$, $b_1^{(1)}$, $a_1^{(2)}$ and $b_1^{(2)}$, and then into Equations 3.54a and b, the interfacial stresses can be obtained.

3.4 Interfacial Stresses in Bonded RC Beams under Arbitrary Loads using the Principle of Superposition

Based on the theory of elasticity, we can decompose any arbitrary load into a symmetric component and an anti-symmetric component. The solutions for the symmetric load case and antisymmetric load case derived in the preceding sections are applied and superimposed to obtain the solutions for the bonded beam under an arbitrary load. The detailed decomposition of an arbitrary load is illustrated in Figure 3.5.

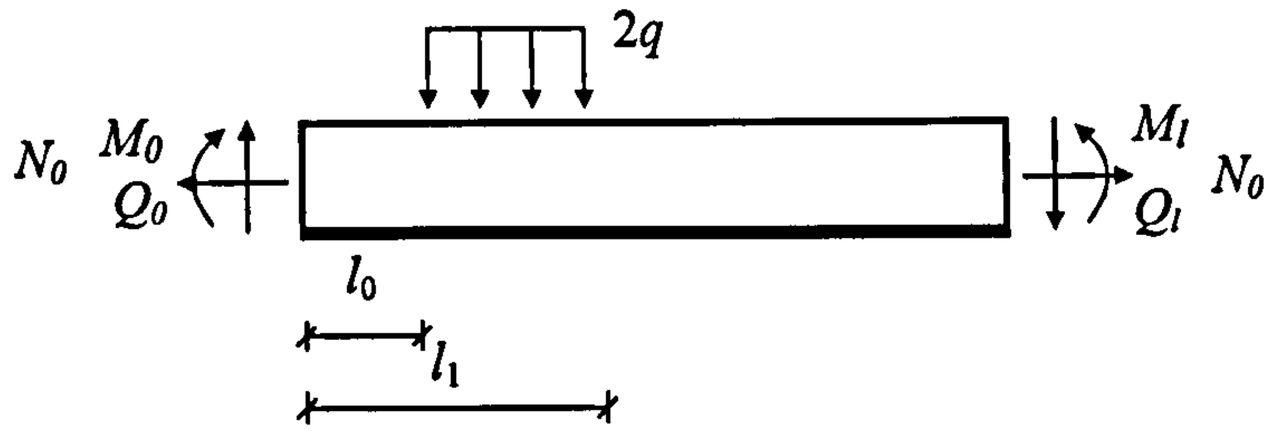

a) General loading

=

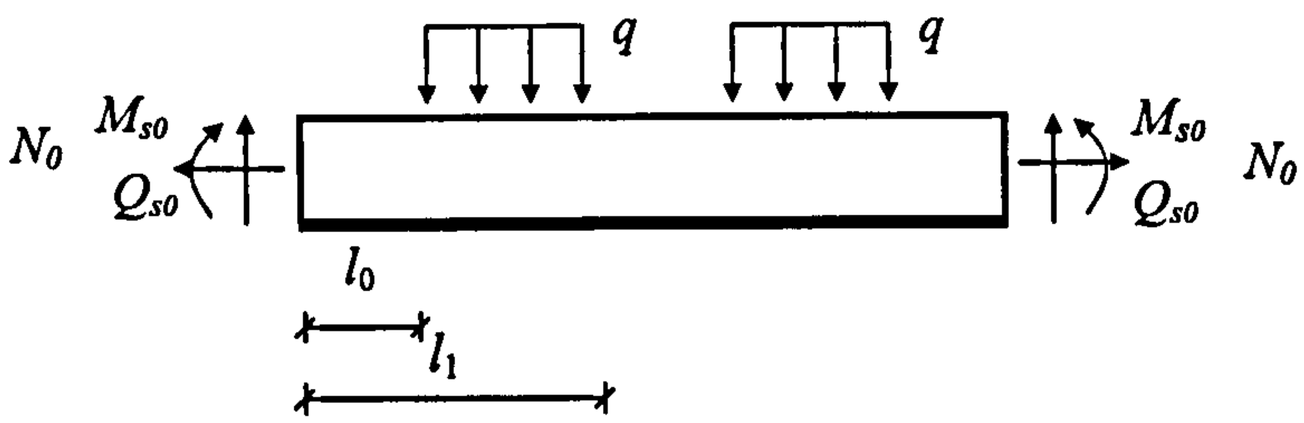

b) Symmetric loading

+

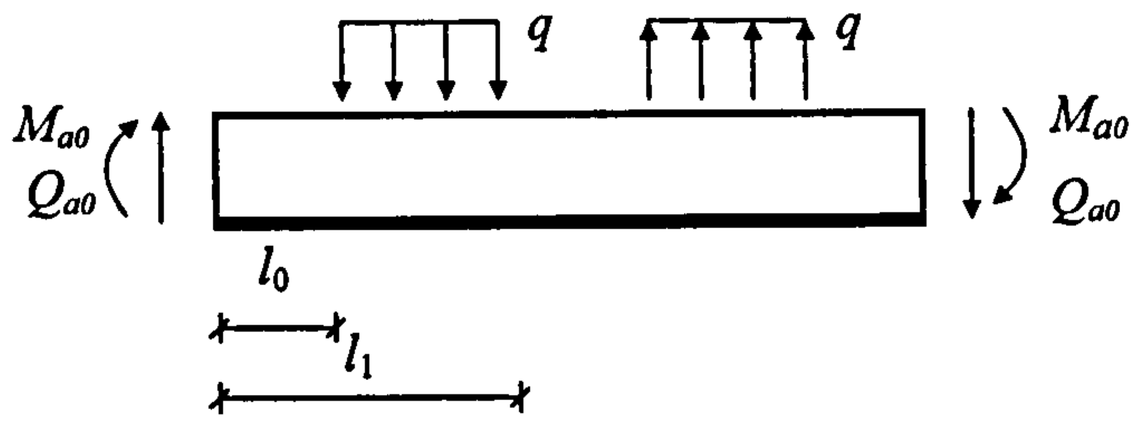

c) Antisymmetric loading

Fig. 3.5 Decomposition of loading

3.5 Numerical Examples

3.5.1 Uniformly Distributed Load (UDL)

For a uniformly distributed load (UDL), which fall into the category of symmetric load, the components of the applied loadings are $N_0 = 0$, $M_0 = 0$, $q(x) = q$ and $M_l = q\left(L^2 - l^2\right)/2$.

The example analysed in the preceding chapter is reanalysed here. For ease of reading, the parameters are relisted as follows:

q = 15N/mm; L = 1200 mm, l = 900 mm, $h^{[1]} = h^{[2]} = 4$ mm, $h^{[3]} = 150$ mm; $b^{(1)} = b^{(2)} = b^{(3)} = 100$ mm; $E_x^{[1]} = E_y^{[1]} = 200$ GPa, $E_x^{[2]} = E_y^{[2]} = 2$ GPa, $E_x^{[3]} = E_y^{[3]} =$ 20GPa, and $\nu_{xy}^{[2]} = 0.25$.

Due to the singularity of the stresses at the plate ends, the solutions represented by the Fourier series converge slowly because of the Gibbs-Phenomenon Gibbs (1899). An example is shown in Figure 3.6 for the number of Fourier series terms m = 800. For sufficiently large number of Fourier series term m, the solution tends to converge to the mean value of the upper and lower bounds, which is in accordance with the theory of Fourier series as explained by Hobson (1926). Figure 3.7 shows the curves of the average values of the interfacial stresses for m = 400, 600, 800 and 1000 respectively. It is seen that the curves from m = 1000 are very close to those from m = 800. A number of Fourier series terms m = 800 is used in this example.

To verify the present solution, Figure 3.7 compares the present predictions with those obtained by FEA in the preceding chapter. The interfacial normal stresses at the plate-to-adhesive (PA) interface, the mid-adhesive (MA) section and the adhesive-to-concrete (AC) interface are small and almost identical to each other away from the vicinities of the plate ends. Near the plate ends, the interfacial normal stress at the MA section is larger than that away from the plate ends but the value is still limited. This stress at the PA and AC interfaces diverges dramatically towards the plate end and large compressive stresses are experienced at the PA interface. Clearly, the present predictions agree very closely with the FE results (Figure 3.7a). It may be noted that this is the first analytical solution, which correctly predicts the drastic difference in the interfacial normal stress between the PA and AC interfaces, as demonstrated by its close agreement with FE predictions (Figure 3.7a).

The interfacial shear stress (Figure 3.7b) increases towards the plate end and then reduces rapidly to zero at the free edge, complying with the stress-free boundary condition there. Both the peak value and its corresponding location are slightly different at PA interface, the MA section and the AC interface. The present solution is

again in close agreement with the FE results, except for the interfacial shear stress at the AC interface near the very end of the plate (within 1 mm), where the FE analysis predicts a rather large shear stress level.

3.5.2 Mid-span Point Load (MPL)

For a beam under a point load at the mid-span which is the symmetric case, the components of the applied loading are: $N_0 = 0$, $M_0 = 0$, $q(x) = p\delta(x)$ and $M_l = p(L-l)/2$. Here $\delta(x)$ is the Dirac delta function used to represent the MPL in the context of Schwarz's distributed theory (Schwarz 1966, Yavari *et al.* 2000).

An RC beam bonded with a CFRP plate and subjected to a mid point load p = 150 KN is used here as the second example. The RC beam has a span 3000 mm, a width $b^{(3)} = 200$ mm, a depth $h^{[3]} = 300$ mm, Young's moduli $E_x^{[3]} = E_y^{[3]} = 30$ GPa and a Poisson's ratio $\nu_{xy}^{[3]} = 0.17$. The orthotropic FRP plate has a length 2400 mm, a width $b^{(1)} = 200$ mm, a thickness $h^{[1]} = 4$ mm, a Young's modulus in the x-direction $E_x^{[1]} =$ 100 GPa and a shear modulus in x-y plane $G_{xy}^{[1]} = 5$ GPa. The isotropic adhesive layer has a width $b^{(2)} = 200$ mm, a thickness $h^{[2]} = 2$ mm, Young's moduli $E_x^{[2]} = E_y^{[2]} = 2$ GPa, and a Poisson's ratio $\nu_{xy}^{[2]} = 0.35$. All these geometric and material properties, except the Poisson's ratios for the RC beam and the adhesive layer and the shear modulus for FRP plate, which are assumed common values here, were given by Smith and Teng (2001).

Figure 3.9 shows the present predictions of interfacial normal and shear stresses. Approximate analytical results from Smith and Teng (2001) and Täljsten (1997) are also shown for comparison. Both Smith and Teng (2001) and Täljsten (1997) assumed invariable normal and shear stresses across the thickness of the adhesive layer. The interfacial normal stresses from the two approximate analytical solutions agree well with the present solution away from the plate ends and in the vicinity of the point load (Figure 3.9a). At the plate end, the present solution predicts a much higher stress (approximately 3 times) at the AC interface than both approximate solutions. This is an inevitable consequence that the assumption of uniform shear and transverse normal stresses in the adhesive layer adopted by these approximate solutions alleviates the

stress singularity near the plate end. The present solution also predicts significant compressive interfacial stresses at the PA interface in the vicinity of the point load.

For the interfacial shear stress (Figure 3.9b), very significant differences exist between the present solution and the two approximate solutions. The approximate solutions predict monotonically increasing shear stresses towards the plate end, which does not satisfy the traction-free boundary condition there. This traction-free boundary condition is satisfied by the present solution. Consequently, the peak shear stresses predicted by the present solution are only about half of those predicted by the two approximate solutions. The approximate solutions are also unable to predict the significant interfacial shear stresses in the vicinity of the concentrated load.

3.5.3 Two-Point Load (TPL)

For a beam under two symmetrical point loads, the components of the applied loading are as follows: $q(x) = p[\delta(x-l_0)+\delta(x-l_0)]$, $N_0 = 0$, $M_0 = 0$ and $M_l = p(L-l)$. Here l_0 is the distance from the mid-span of the beam to either of the two point loads.

The same CFRP plated RC beam as in Section 2.7.2 is used here. The beam is subjected to TPL with $p = 75$ KN and $l_0 = 600$ mm. This same example was also calculated by Shen et al. (2001).

Figure 3.10 compares the present solution with Shen et al.'s (2001) high-order solution. The interfacial shear stresses from Shen et al.'s (2001) high-order solution are in close agreement with those of the present solution (Figure 3.10b). However, significant differences exist between the two solutions for the interfacial normal stress. Near the plate end, Shen et al.'s (2001) solution predicts tensile stresses at both the PA and AC interfaces, in contrast to tensile stresses at the AC interface and compressive stresses at the PA interface as predicted by the present solution (Figure 3.10a). Shen et al.'s (2001) solution also yields considerably different predictions for the peak values at both the plate end and directly below the concentrated load. This is believed to be due to the partial use of the plane section assumption in their solution process.

3.5.4 Antisymmetric Point Loads (APL)

If two point loads are symmetrically applied to the strengthened RC beam with opposite directions, which is the antisymmetric load case, i.e. $M_0 = 0$, $q(x) = p\left[\delta(x-l_0)-\delta(x-l+l_0)\right]$, where l_0 is the distance between the applied load and plate ends.

Using the same geometrical and material parameters as those in 3.5.3, so do the load magnitude and load location, i.e. p = 75KN and $l_0 = 600$, with the only difference that the RHS point load is changed the direction pointing upwards.

Convergence analysis suggests that the term number of Fourier series is also taken as 800 for this example problem. Figure 3.11 shows the interfacial normal stresses and shear stresses along PA interface and the AC interface, respectively. It is noted that the origin of coordinate system is located at the left plate end, unlike the symmetric case with the origin located at the middle point, and the stresses is plotted for the right half beam. As can be seen in Figure 3.11, both the normal stresses and shear stresses show significant concentration at the plate ends and slight concentration at the loading positions, which is attributed to the stress singularity. This concentration only affects the localized areas, that is, in the region away from plate ends and load positions, the stresses remain the same as are given by the classic laminate beam theory (CLBT). The regions experiencing the stress concentration near the plate ends are development zones through which the FRP starts to work together with RC beam. For the normal stress, the develop length is only about 25 mm, during which the interfacial normal stress in the AC interface increase dramatically to 2.0 MPa, while the normal stress in the PA interface increases before it reduces to low value and then even becomes negative at the plate end. That is consistent with the laboratory and practical observations where the debonding exclusively occurs along the AC interface. For the interfacial shear stresses, the develop length is much longer than that for normal stresses, i.e. around 250mm, where the interfacial stress increases greatly before it reduces to zero value at the plate end which satisfies the stress-free condition. As there are no existing published data about the same loading available, we are unable to make any comparisons between the present solution and the others. However, in the next example, we

are going to compare the results with published approximate analytical solution for the bonded RC beam subjected to an arbitrary non-symmetric point load.

3.5.5 Arbitrary Non-symmetric Point Load (PL)

The solution presented in Sections 3.7.3 and 3.7.4 can be superimposed to obtain the interfacial stress solution for the bonded beam subjected to a single arbitrary point load (PL). The point load in the right-hand-side is cancelled out and that in the left-hand-side has been doubled in its magnitude, i.e. p = 150KN. Figure 3.12 shows the interfacial normal and shear stresses for the strengthened beam under a single point load using the present method. Also showed are the comparisons with the approximate analytical method by Smith and Teng (2001), in which both normal stress and shear stress remain uniform in the thickness of the adhesive layer. Similar to the other load cases, both interfacial stresses show concentration at the plate end. The comparison shows that both methods provide favourable agreement in the majority area except the vicinity of the singularity points. For the normal stresses, the approximate analytical results fall in between two values along the PA and AC interface given by the present solution. This is attributed to the assumption of the uniform distribution of the transverse normal stress across the entire thickness of the adhesive layer. This assumption obviously restrains the variation of the normal stress within the thickness. For the shear stresses, the analytical results show its monotonically trends towards the plate ends rather than reduced to zero value, which inevitably enhance the peak value at the plate ends, while the present solution provide almost identical interfacial shear stress in PA and AC interfaces with the peak values at the location slightly away from the plate end, i.e. 1-2 times of the adhesive thickness, where the normal stress in the AC interface is also reduced its magnitude substantially.

3.6 Remarks

In this chapter, a rigorous solution for the interfacial stresses in the plate bonded reinforced concrete beam has been developed using the principle of minimum complementary energy. The solution is so called as completed because there are almost no simplifications introduced in the process of derivation, except that the longitudinal stress in the adhesive is assumed linearly distributed across the adhesive thickness. This assumption is rational as the low Young's modulus of the adhesive leads to a

fairly low longitudinal stress and the assumption of linear variation in the thickness direction is adequate to simulate its real distribution even near the plate end.

Both symmetric and antisymmetric load cases are considered and the appropriate combination of these two may construct any arbitrary load case in the framework of elasticity. The distribution functions provide a generic form to include any loading pattern. This can avoid the painstaking manipulation of the continuous conditions, used in most of the available approximate solutions, at the point load position or the positions where step change of the load occurs.

Verifying examples demonstrate that this solution provides much more accurate results than the approximate solutions and the results are favourably coincident with FEA results using the fracture mechanics approach. But this solution can avoid the cumbersome meshing process and are highly versatile.

The solution not only takes into consideration the non-uniform stress distribution in the adhesive layer and the stress-free boundary condition at the ends of the plate, but also correctly predicts the drastic difference in the interfacial normal stress between the plate-adhesive and adhesive-concrete interfaces revealed by finite element analysis for the first time. The solution methodology is general in nature and may be applied to the analysis of other types of composite structures with thermal-mechanical loads.

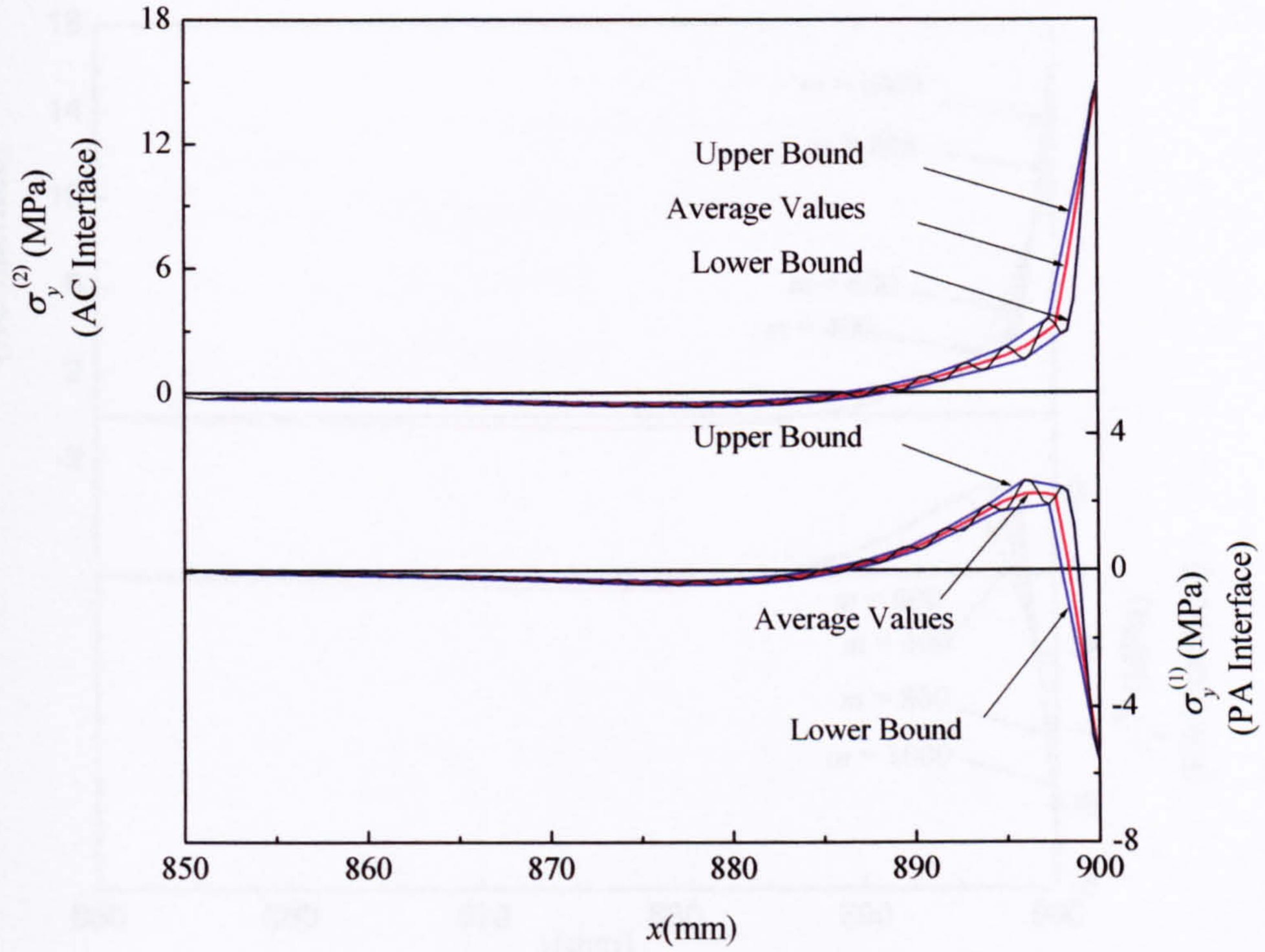

(a) Interfacial normal stress

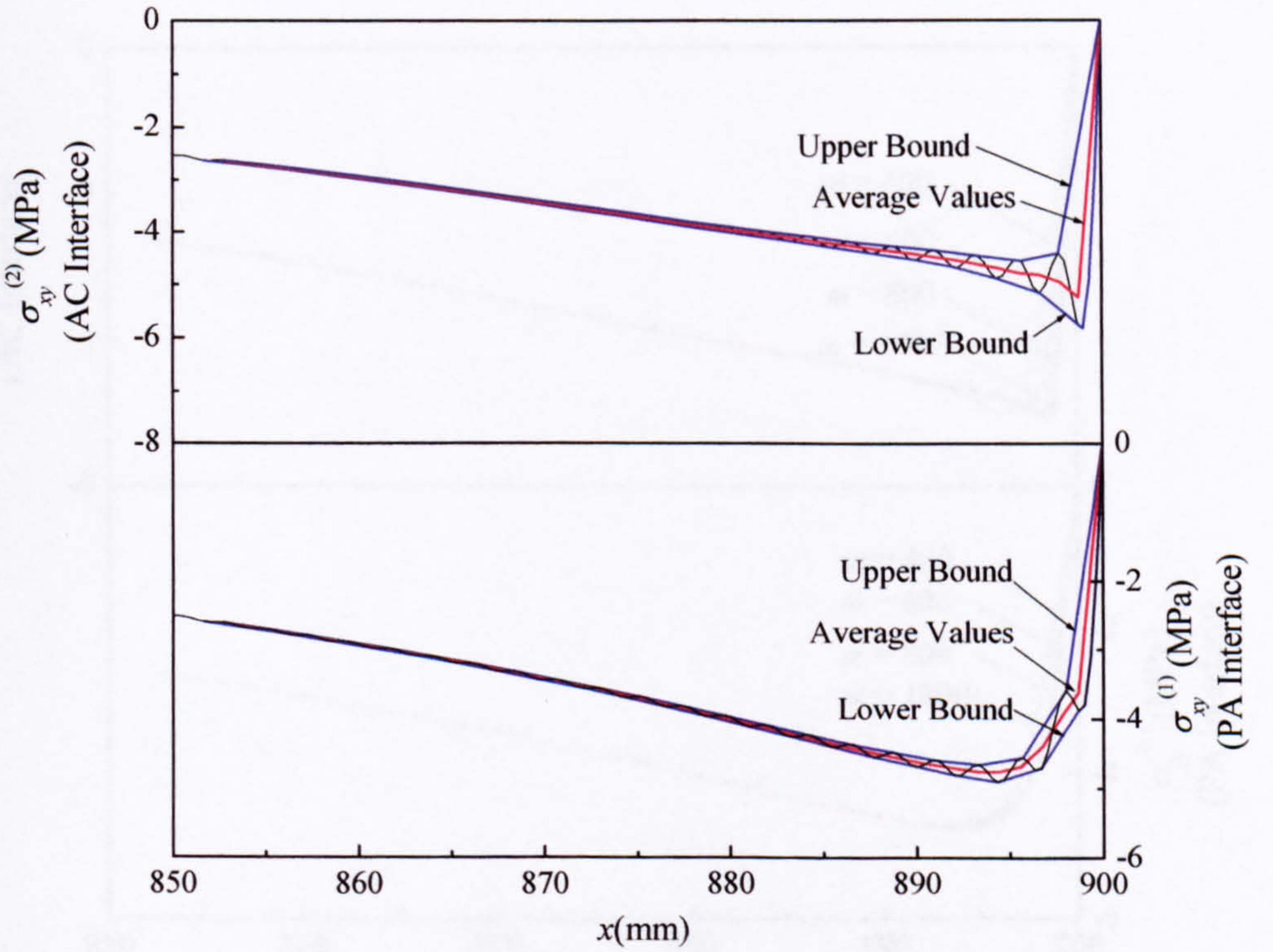

(b) Interfacial shear stress

Fig. 3.6 Fourier series solutions for a steel plated beam under UDL

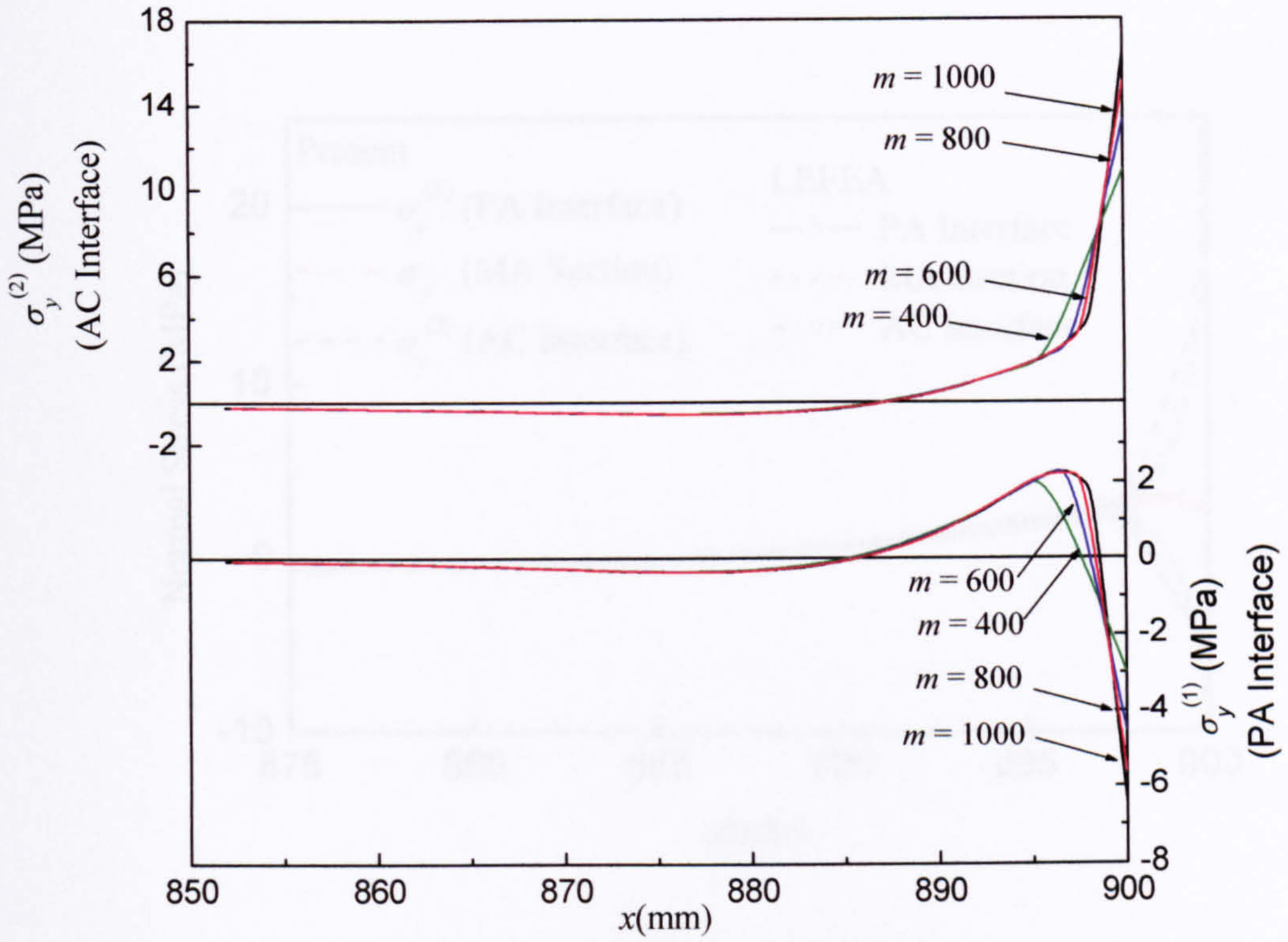

(a) Interfacial normal stress

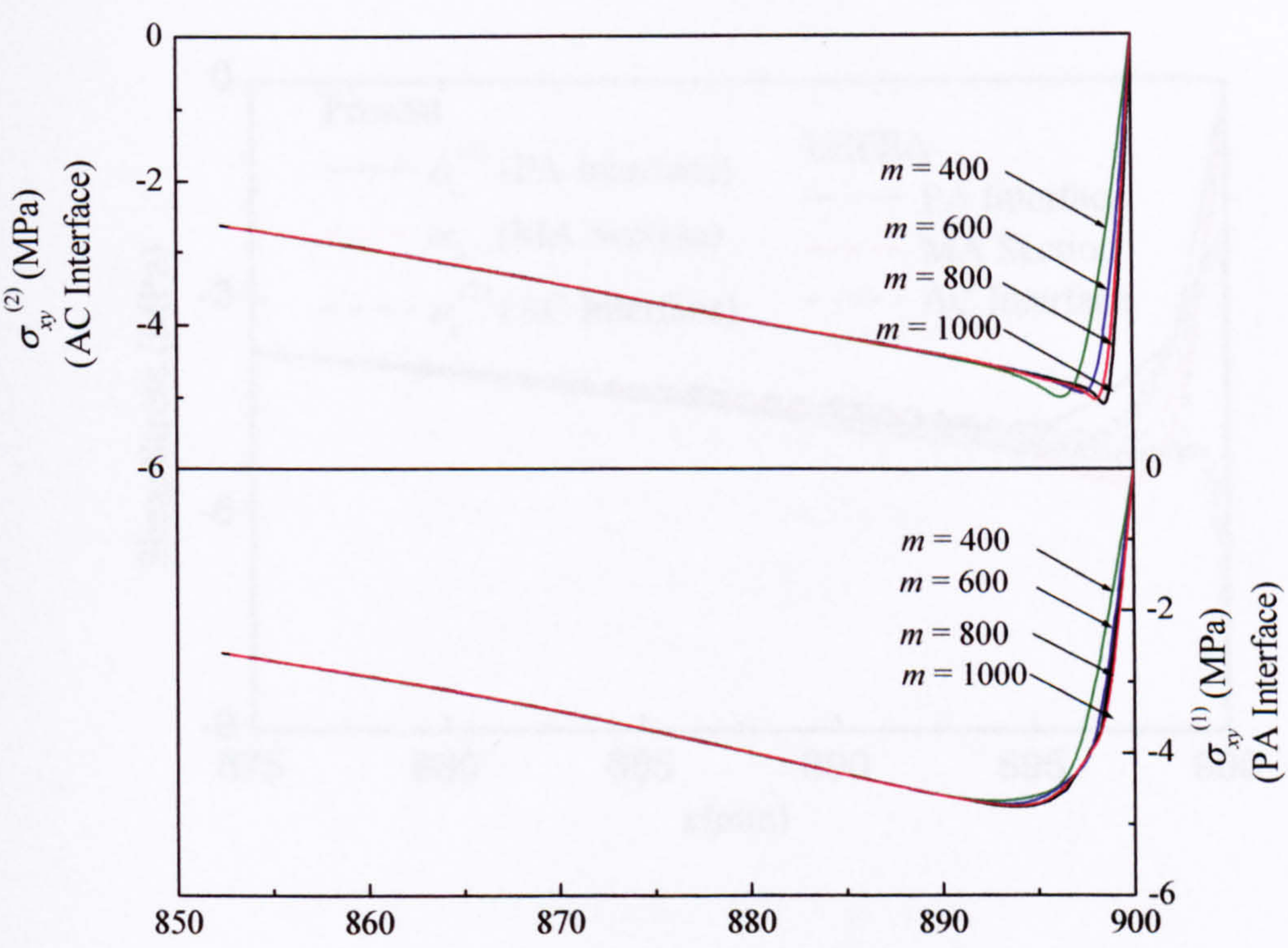

(b) Interfacial shear stress

Fig. 3.7 Convergence of interfacial stress solutions in a steel plated beam under UDL

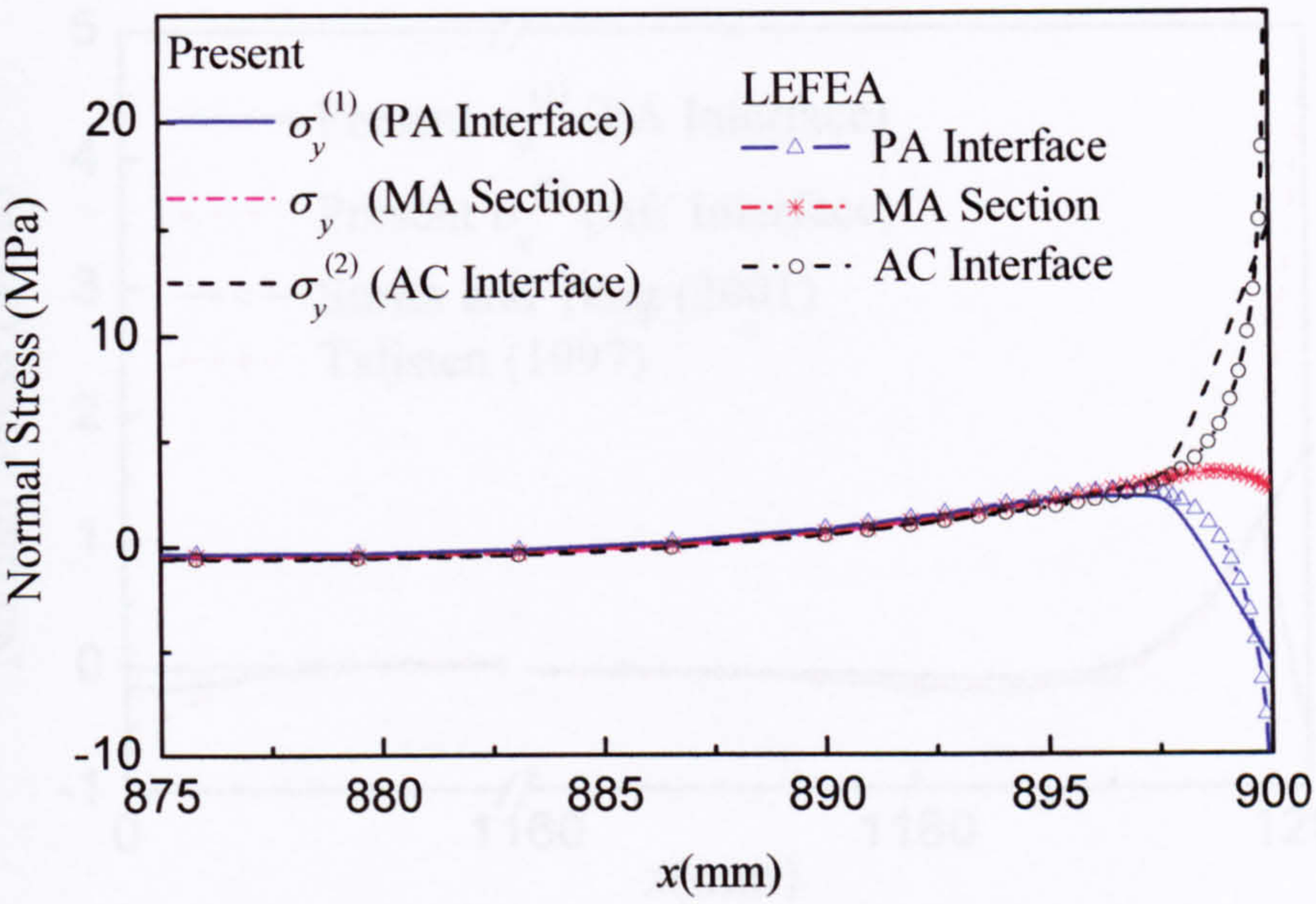

(a) Interfacial normal stress

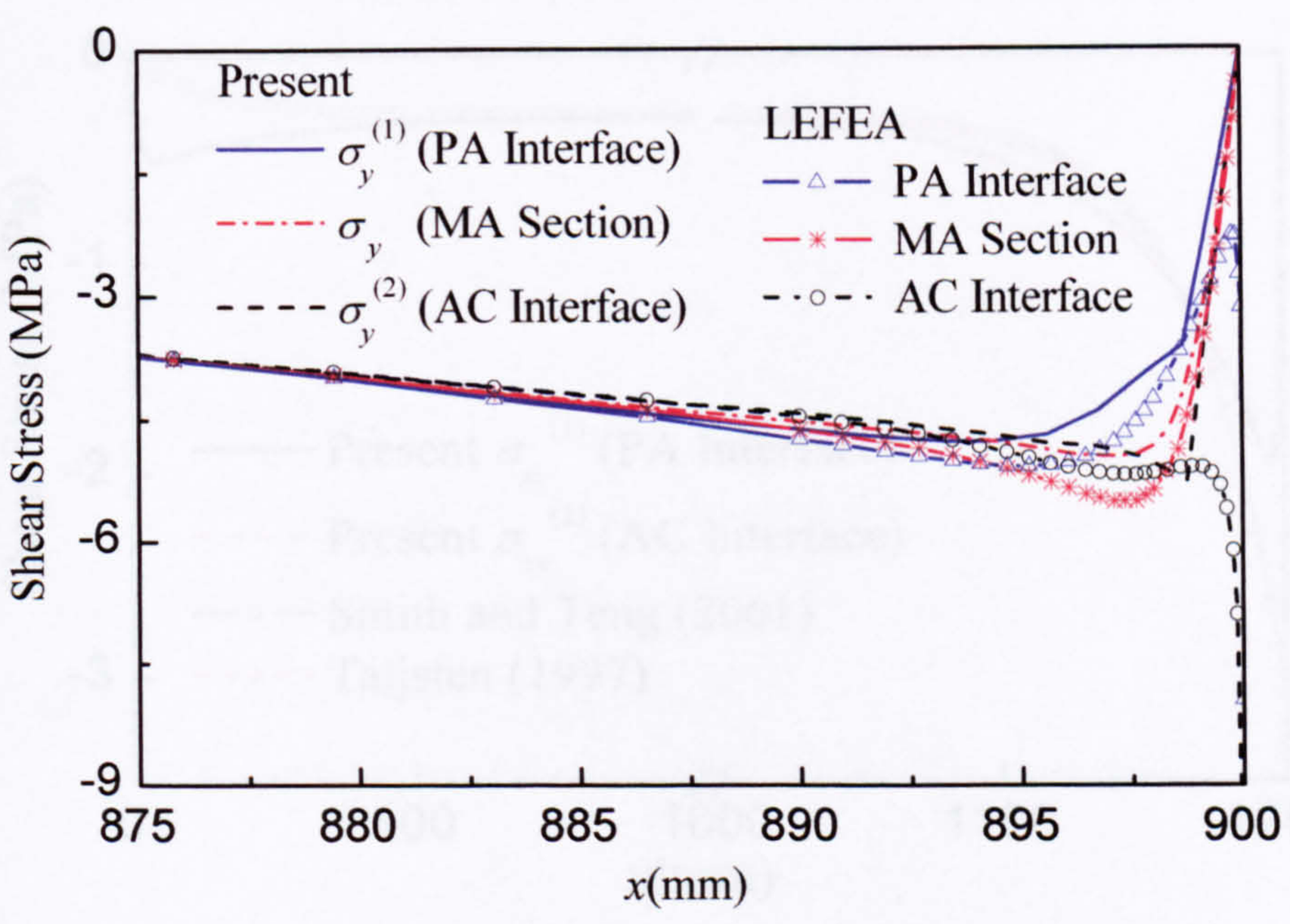

(b) Interfacial shear stress

Fig. 3.8 Steel plated beam under UDL

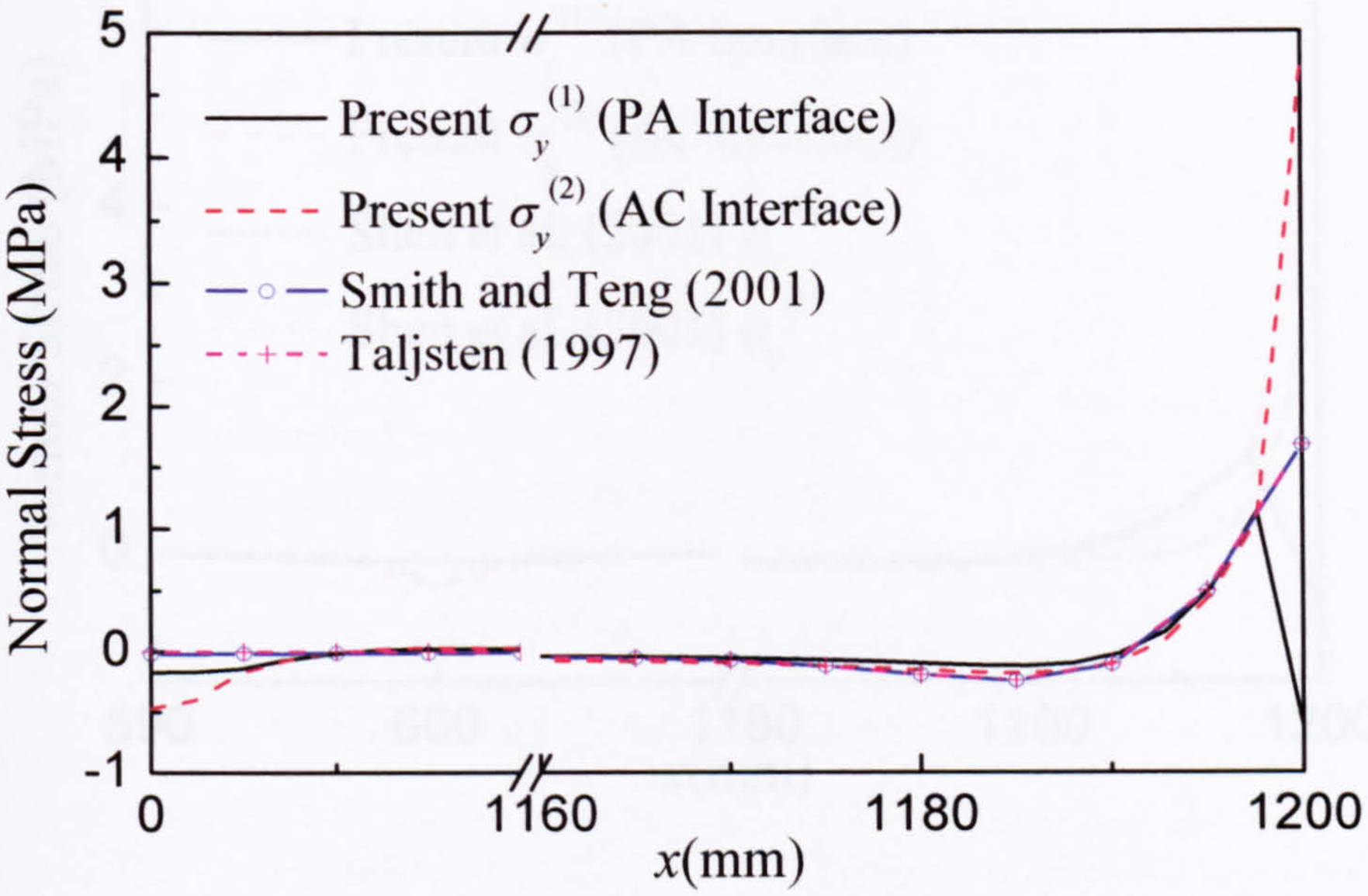

(a) Interfacial normal stresses

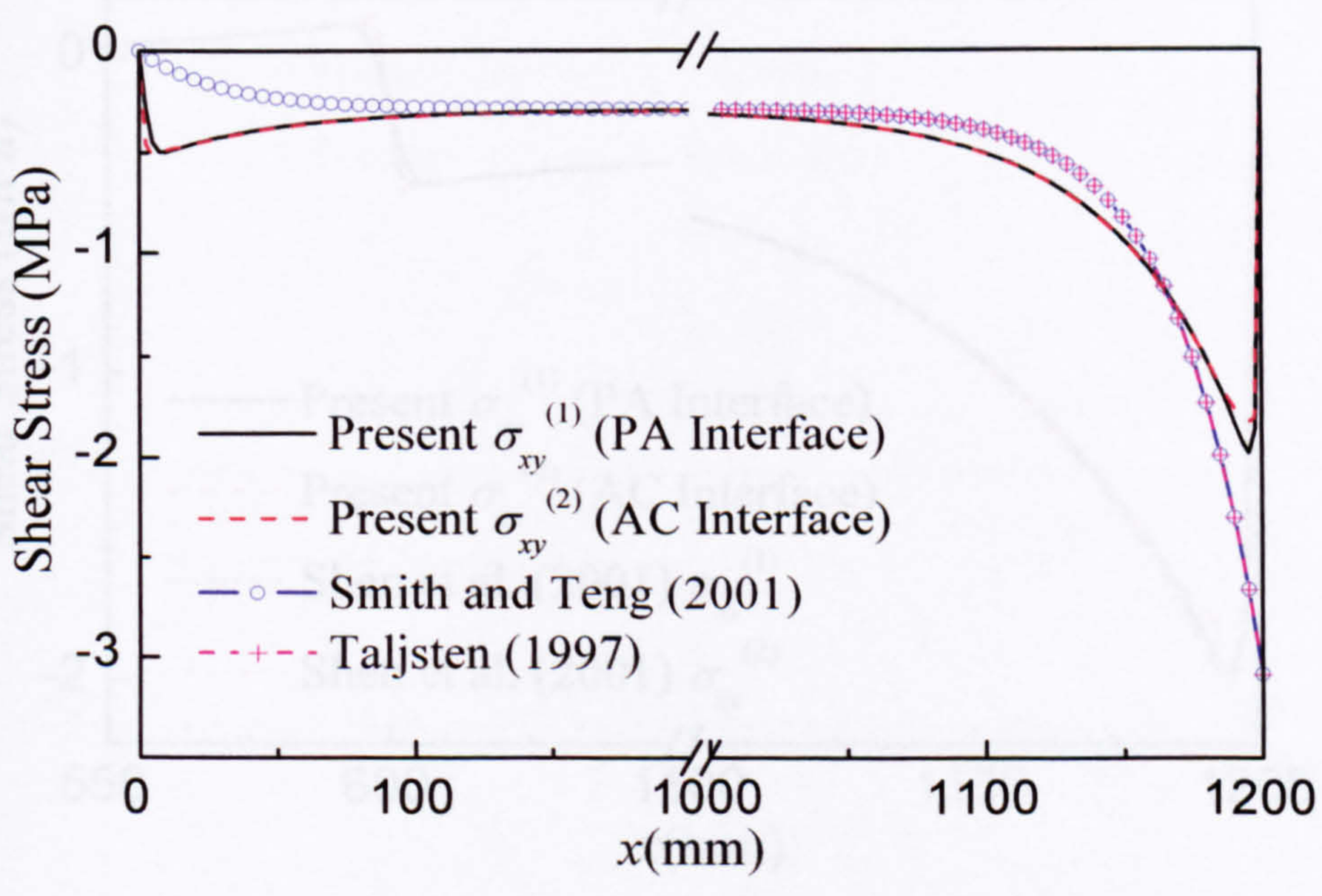

(b) Interfacial shear stresses

Fig. 3.9 CFRP plated beam under middle point load

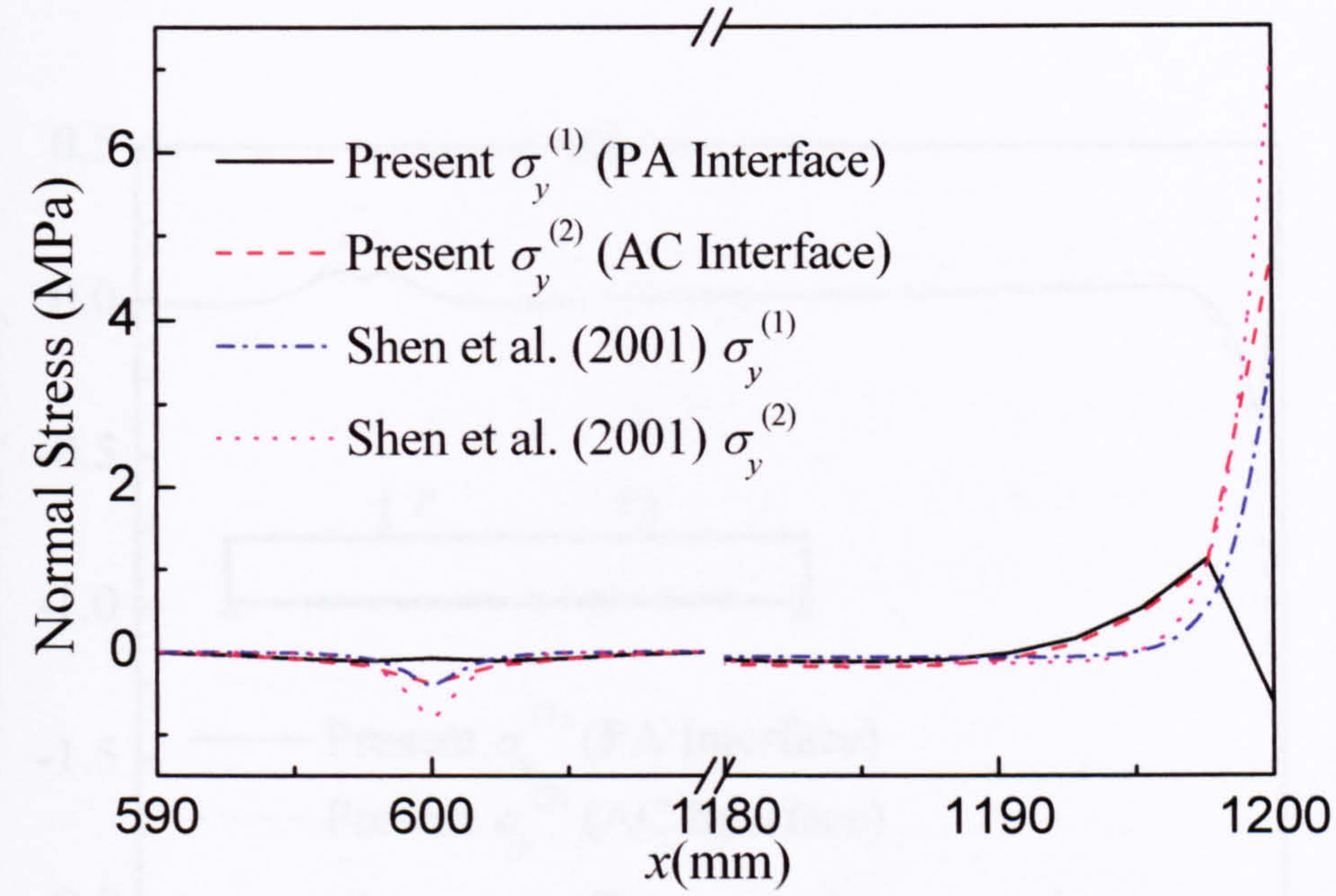

(a) Interfacial normal stress

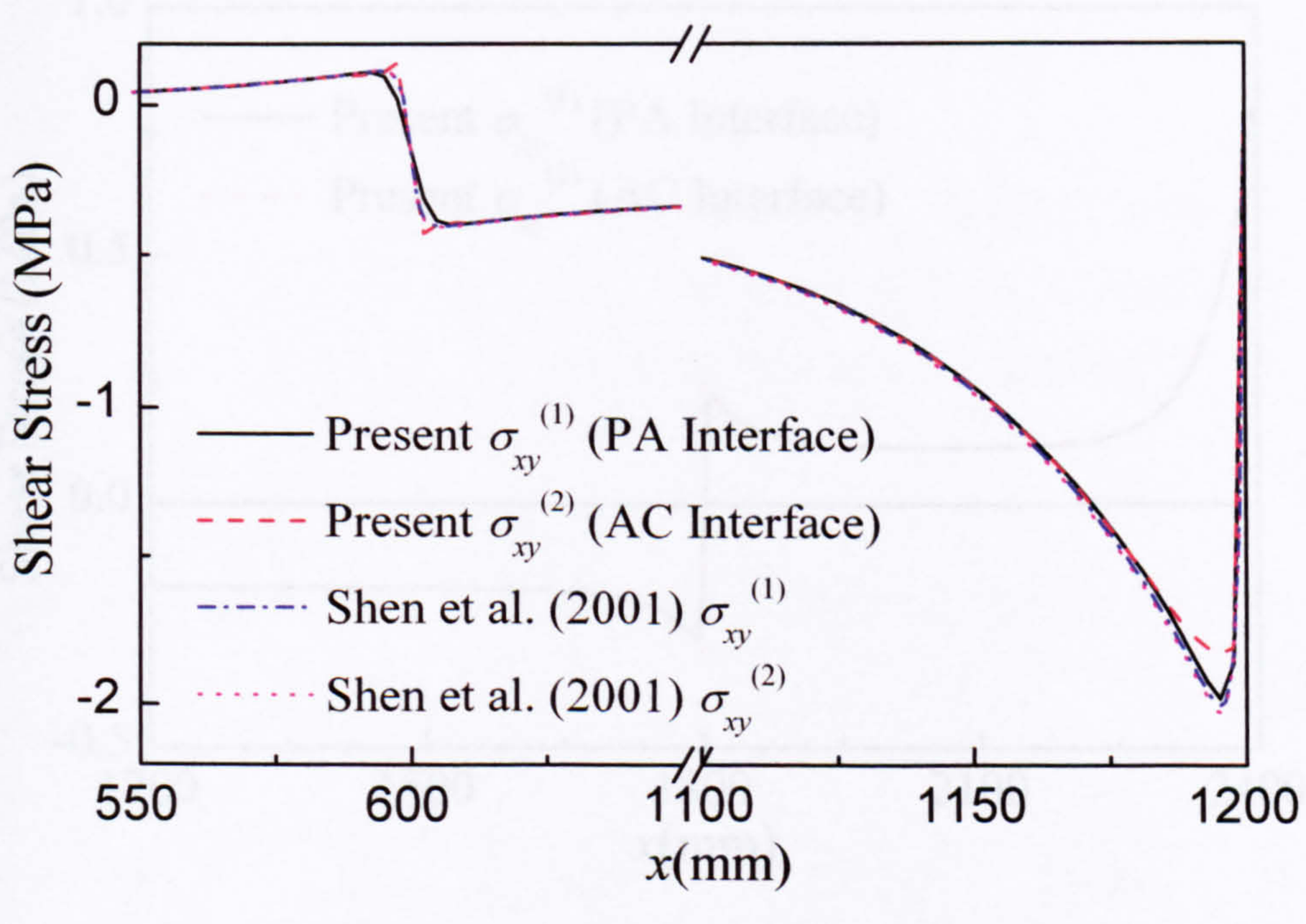

(b) Interfacial shear stress

Fig. 3.10 CFRP plated beam under two point loads

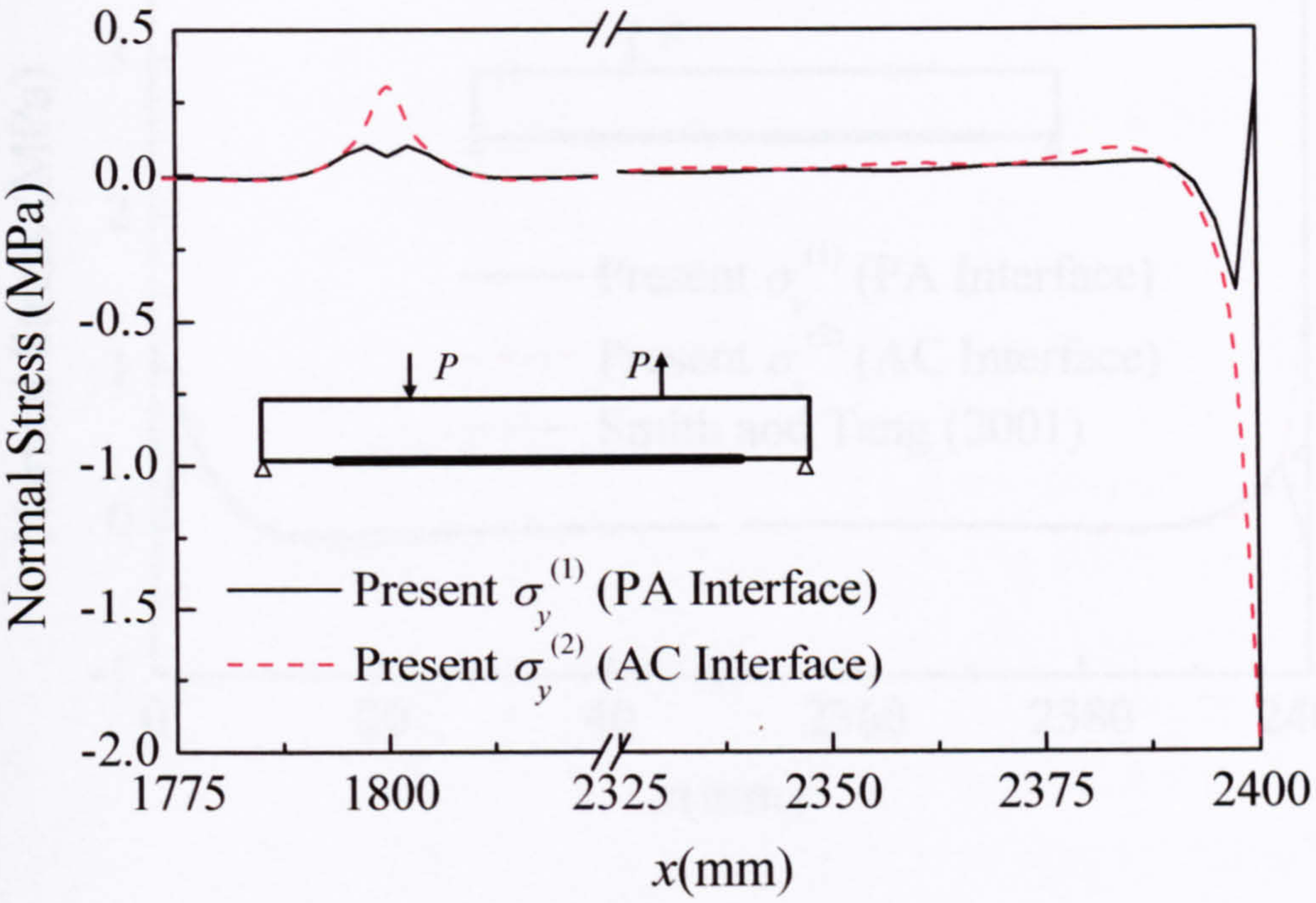

(a) Interfacial normal stress

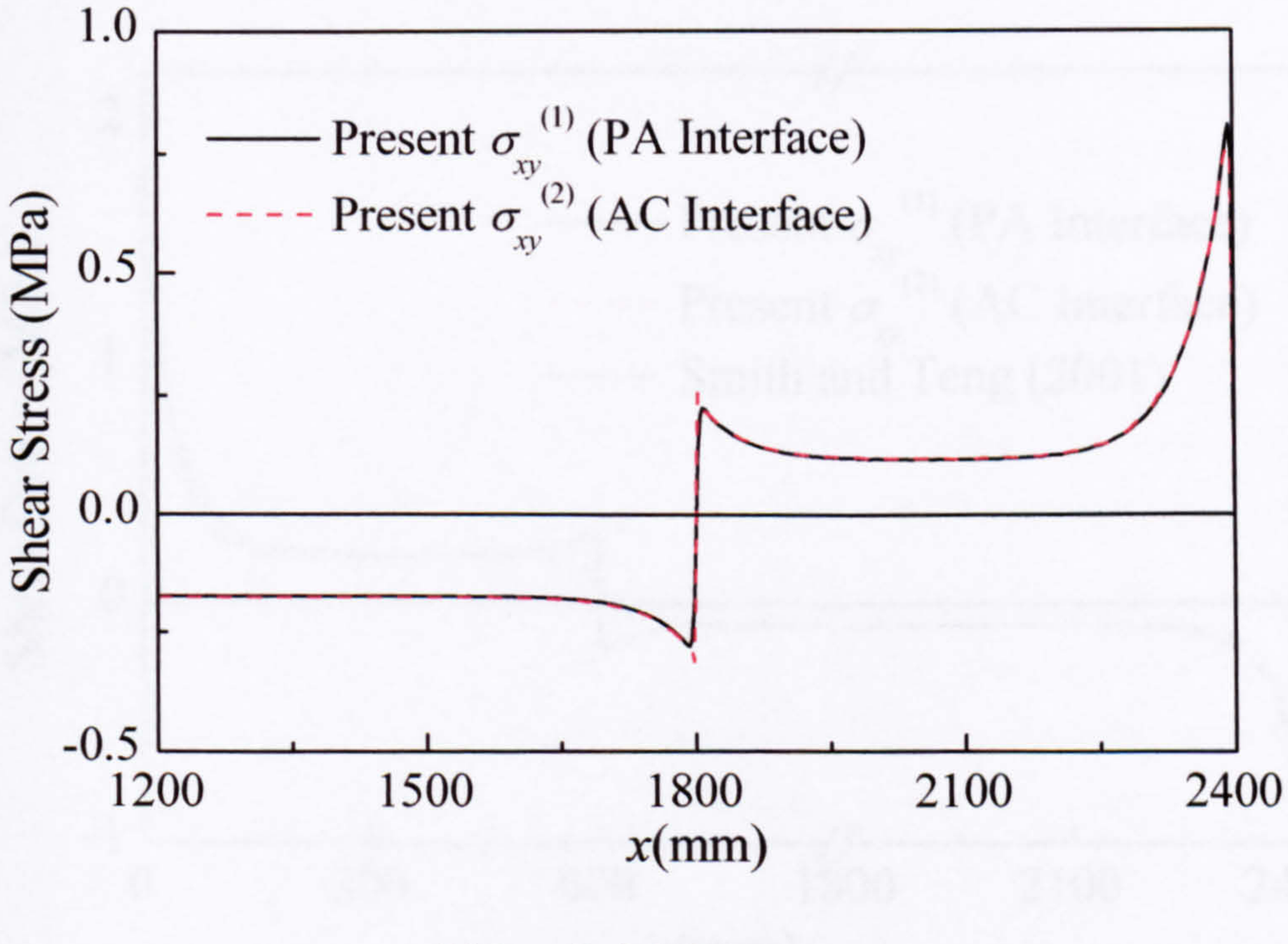

(b) Interfacial shear stress

Fig. 3.11 CFRP plated beam under two antisymmetric point loads

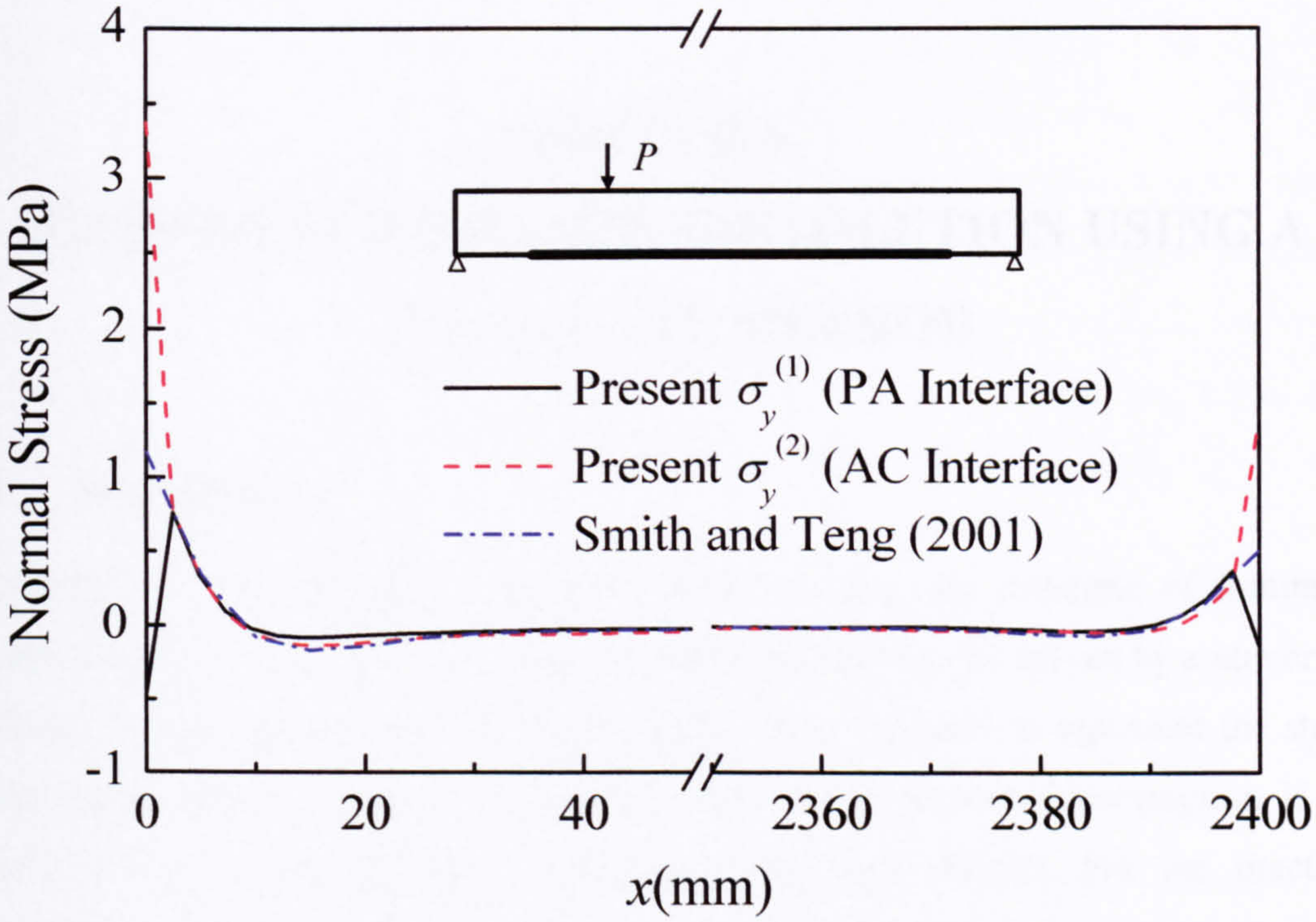

(a) Interfacial normal stress

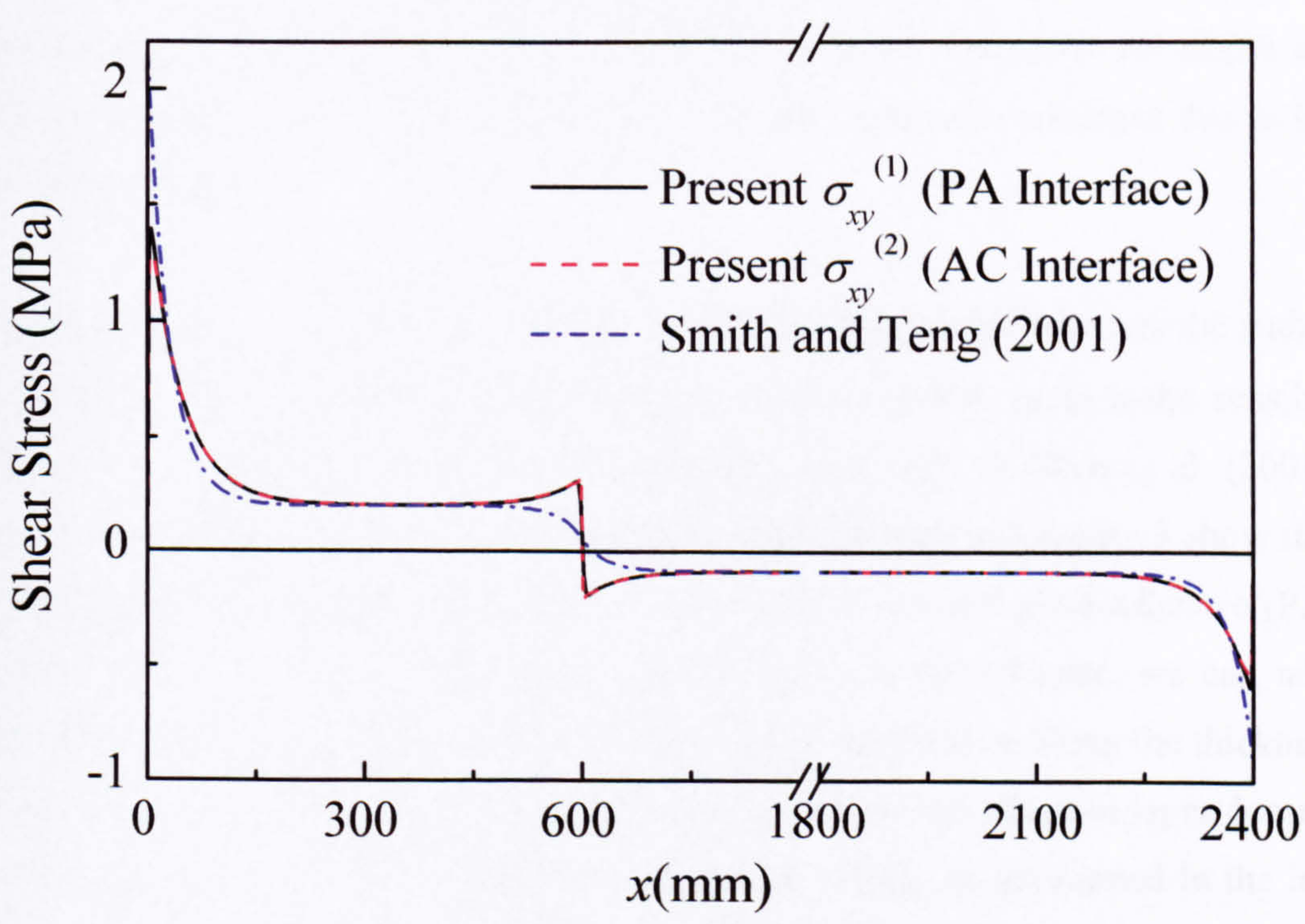

(b) Interfacial shear stress

Fig. 3.12 CFRP plated beam under a single arbitrary point load

CHAPTER 4.
CLOSED-FORM RIGOROUS SOLUTION USING A TWO STAGE METHOD

4.1 Introduction

In Chapter 3, we developed a complete solution using the principle of minimum complementary energy, in which algebraic equations have to be solved by a numerical method. In deriving the solution, the Fourier's series are used to represent the stress components. The solution is exact in the light of the presumed assumption if the number of the terms of Fourier's series could reach infinite. For the practical application, a limited number of terms are adopted and a set of equations in terms of the unknown Fourier coefficients are formed. The numerical solution can only be obtained using computer programming. Gibbs phenomena occurs due to the stress singularity at the plate end. The mean values of the upper and lower envelopes are taken as the correct values since the results show the nature of oscillation due to the Gibbs phenomenon.

Previous studies on the interfacial stresses in the plate bonded RC beam by the author have gained a great deal of useful information, which enables us to make sensible assumptions to improve the solution. For instance, the work by Shen et al. (2001), Yang et al. (2004) and that done by the author and presented in Chapter 3 show that the interfacial shear stresses on the adhesive-concrete (AC) and plate-adhesive (PA) interfaces are very close to each other. Accordingly, in this chapter, we can take advantage of the assumption of a constant shear stress distribution along the thickness of the adhesive layer. In fact, this assumption suggests that the adhesive layer doesn't carry the normal stress in the longitudinal direction, which, as mentioned in the last chapter, attributes to the fact that its Young's modulus is much lower than the adherends. The adoption of this assumption together with those listed in Chapter 3 establish the principle assumption, based on which a closed-form solution for the interfacial stresses in the plated RC beam is to be proposed.

Comparison with the numerical solution, which has to turn to the computer programming, this closed-form solution can be carried out using widely used spreadsheet packages, such as MS Excel. It obviously provides a very useful alternative approach. Furthermore, the closed-form solution can be simplified by omitting terms with small quantities to obtain a compact solution without losing too much accuracy. In this sense, seeking the closed-form rigorous solution becomes rather important without question.

In this chapter, the interfacial stress solution is obtained in two stages. In both stages, Fourier series represent the stress solutions and the principle of the complementary energy is used again. One of the unique features of the solutions is that infinite Fourier series can be taken and the explicit summations of the relevant series can be obtained. In the first stage, two stress distributions along the middle section of the adhesive layer is presumed first, and an approximate relationship between the shear stress and transverse normal stress is introduced based on the assumption of composite action among different materials. This reduces the number of the unknown coefficients and leads to the explicit solutions of both interfacial stresses. However, in this stage, the solution for the transverse normal stress is not deemed ideal as the imposed constraint relationship is used in deriving it. The Fourier coefficients are not independently determined by the principle of the complementary energy. The solution for the interfacial shear stress, however, provides desired accuracy with the absence of the constraints and it is then used as a known condition in the second stage when deriving the transverse normal stress. In the second stage, the other stress components are represented using the interfacial shear stress, and the constraints used in the first stage are discarded. This step largely increase the accuracy of the transverse normal stress.

Compared with other closed-form approximate solutions, the present one takes into consideration the non-uniform transverse normal stress distribution in the adhesive layer and satisfy the stress-free boundary condition for the shear stress at the ends of the plate. It favourably predicts the significant difference of the transverse normal stress between the PA interface and AC interface as revealed by finite element analysis, while none of the analytical solutions can achieve this. Compared with the 'closed-form' high-order solution by Rabinovich and Frostig (2000), the present

solution principally offers the same degree of accuracy. However, Rabinovich and Frostig's solution is not a closed-form solution, where there are eleven integration constants that have to be calculated by a numerical method. Spatial packages, such as Maple, have to be used to avoid the overflow. These problems do not exist in the present solution.

Based on the closed-form rigorous solution, simplified approximate solutions for both shear stress and normal stress are developed in the next chapter. The present solution methodology is general in nature and may be applied to the analysis of other types of composite structures.

4.2 Method of Solution

4.2.1 Geometry and Loading

The same geometric configuration, coordinate systems and sign conventions are used as those for the symmetrical loading case in Chapter 3 (Figures 3.1 and 3.2). The loading components include a pair of symmetric end moment M_0 and a uniformly distributed load (UDL) with a load intensity q. As can be seen in the following sections, only the end moment M_0 plays a significant role in determining the stress concentration at the plate ends. The inclusion of the UDL is for the purpose of validating the present solutions using the existing validated data.

4.2.2 Assumptions

The first three assumptions listed in section 3.2.2 are also used in this part. Apart from those, there are three additional ones as following:

1. The adhesive layer only carries negligible longitudinal stress, which implies that the shear stress is constantly distributed along the thickness of the adhesive layer in a given section.
2. In the first stage, the assumption of plain section remains plain is used to define the relationship between the transverse normal stress and shear stress along the middle section of the adhesive layer.
3. In the second stage, the assumption (2) is discarded.

4.2.3 Stress Fields

Following the similar procedures in Sections 3.2.3 and 3.2.4, the equilibrium equations and the boundary conditions for each layer, i.e. the RC beam, adhesive layer and bonded plate are given in the same forms as Equations 3.33 and 3.34. The similar stress fields in the plate and the beam as given by Equations 3.37 can also be used in this solution. The stress fields in the adhesive layer need to be rederived. Equations 3.35 for the equilibrium equations of the adhesive layer is adopted herein and the integration with respect to $y^{[2]}$ leads to the following transverse normal stress field in the adhesive layer as

$$\sigma_y^{[2]} = \sigma_{y0} - y^{[2]} \frac{d\sigma_{xy}^{[2]}}{dx} \tag{4.1}$$

in which σ_{y0} is the normal stress in the middle section of the adhesive layer. As assumed, the shear stress remains constant in the thickness direction in the adhesive layer, i.e. $\sigma_{xy}^{[2]}$ is only the function of the x coordinate .

4.2.4 Solution Procedure for Shear Stress $\sigma_{xy}^{[2]}$

As the first step of the solution procedure, the shear stress $\sigma_{xy}^{[2]}$ is expressed as Fourier series function, i.e.

$$\sigma_{xy}^{[2]}(x) = \sum_m b_m \sin\frac{m\pi x}{l} \tag{4.2a}$$

And the normal stress in the middle section of the adhesive layer (MA) $\sigma_{y0}(x)$ is expressed as

$$\sigma_{y0}(x) = \sum_m a_m \cos\frac{m\pi x}{l} \tag{4.2b}$$

where a_m and b_m are unknown Fourier coefficients; and $m = 1, 2, \ldots\infty$. Note that the constant term in Equation 4.2b has been set to zero to satisfy the equilibrium requirement that the integration of the interfacial normal stress over the entire length of the middle section must be equal to zero.

In this step, we only focus on the solution of shear stress $\sigma_{xy}^{[2]}$. To facilitate the derivation of the explicit solution, we set up the relationship between the unknown Fourier coefficients a_m and b_m by:

$$a_m = b_m \frac{m\pi}{l}\xi \tag{4.2c}$$

where ξ is the coefficient, which can be derived in the following section. This leaves only one set of unknown coefficient b_m in the equations. Note that the coefficient ξ, given as a constant in Equation 4.10 in the following section, is an approximation in the vicinity of the plate end. Hence, transverse normal stress obtained in this stage is not as accurate as the shear stress due to the reason mentioned above. An improved normal stress solution will be presented at the second stage.

4.2.5 Derivation of the Coefficient ξ

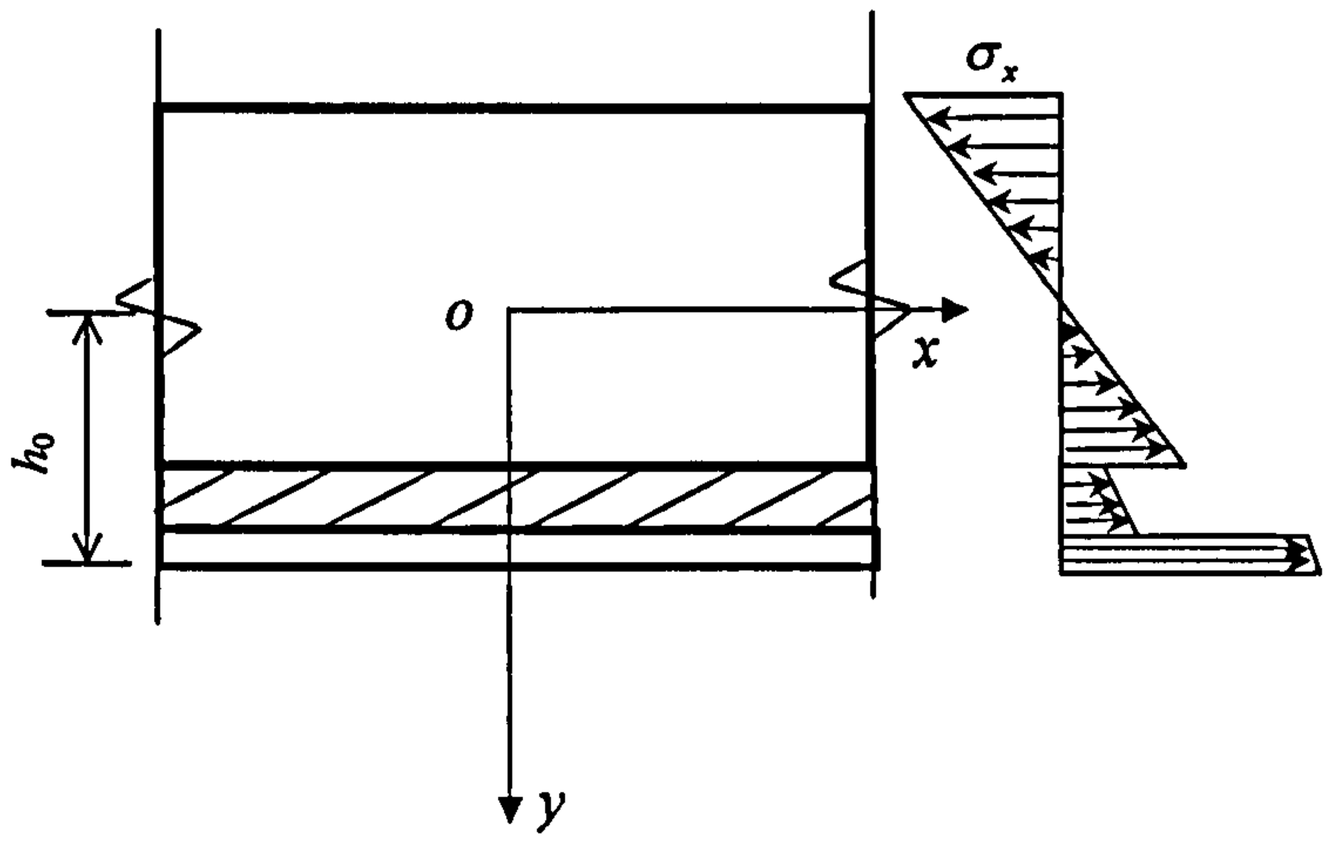

Fig. 4.1 The longitudinal normal stress along the composite cross section of the bonded beam using CLBT

The longitudinal normal stress of the bonded beam along the composite cross section, σ_x can be obtained by the classical laminate beam theory (CLBT; Gere and Timoshenko, 1999) (see Figure 4.1) as

$$\sigma_x = \frac{M_z}{I_0} y \tag{4.3}$$

where M_z is the internal bending moment in an arbitrary cross section, y is the vertical coordinate, for which the origin located in the neutral axis, and I_0 is the

second moment of area of the cross-section transferred to the plate material which is given as

$$I_0 = \frac{1}{12}\left[b^{(1)}\left(h^{[1]}\right)^3 + \frac{b^{(2)}E_x^{[2]}}{E_x^{[1]}}\left(h^{[2]}\right)^3 + \frac{b^{(3)}E_x^{[3]}}{E_x^{[1]}}\left(h^{[3]}\right)^3 \right]$$

$$+ b^{(1)}h^{[1]}\left(\frac{h^{[1]}}{2} - h_0\right)^2 + \frac{b^{(1)}E_x^{[2]}}{E_x^{[1]}}h^{[2]}\left(h^{[1]} + \frac{h^{[2]}}{2} - h_0\right)^2 + \frac{b^{(3)}E_x^{[3]}}{E_x^{[1]}}h^{[3]}\left(h^{[1]} + h^{[2]} + \frac{h^{[3]}}{2} - h_0\right)^2 \tag{4.4}$$

where h_0 is the distance from the neutral axis to the lower edge of the cross-section transferred the plate material, i.e.

$$h_0 = \frac{\frac{b^{(1)}\left(h^{[1]}\right)^2}{2} + \frac{b^{(2)}E_x^{[2]}}{E_x^{[1]}}h^{[2]}\left(h^{[1]} + \frac{h^{[2]}}{2}\right) + \frac{b^{(3)}E_x^{[3]}}{E_x^{[1]}}h^{[3]}\left(h^{[1]} + h^{[2]} + \frac{h^{[3]}}{2}\right)}{A} \tag{4.5}$$

in which A is the transformed cross sectional area with regards to the plate material, i.e.

$$A = bh^{[2]} + \frac{bE_x^{[2]}}{E_x^{[1]}}h^{[2]} + \frac{BE_x^{[3]}}{E_x^{[1]}}h^{[3]} \tag{4.6}$$

The stress results due to $\sigma_x = \frac{M_z}{I_0}y$ in the bonded plate in respect of its own neutral axis are

$$N^{[1]} = \int_{h_0 - h^{[1]}}^{h_0} \sigma_x dy = \frac{M_z h^{[1]}\left(2h_0 - h^{[1]}\right)}{2I_0} \tag{4.7a}$$

$$M^{[1]} = \int_{h_0 - h^{[1]}}^{h_0} \sigma_x \left(y - h_0 + \frac{h^{[1]}}{2}\right)dy = \frac{M_z\left(h^{[1]}\right)^3}{12I_0} \tag{4.7b}$$

These two stress results can also be obtained from Equations 3.33 by substituting the stress components with the Fourier series in Equations 4.2 as follows

$$N^{[1]} = \sum_m \frac{lb^{(1)}b_m}{m\pi}\left[(-1)^m - \cos\frac{m\pi x}{l}\right] \tag{4.8a}$$

$$M^{[1]} = \sum_m \frac{lb^{(1)}b_m}{2m\pi}\left[(-1)^m - \cos\frac{m\pi x}{l}\right]\left(2\xi - h^{[1]} - h^{[2]}\right) \tag{4.8b}$$

Equating Equation 4.7a divided by Equation 4.7b to Equation 4.8a divided by Equation 4.8b yields

$$\frac{\left(h^{[1]}\right)^2}{3}\sum_m \frac{b_m}{m}\left[(-1)^m-\cos\frac{m\pi x}{l}\right]=\left(2h_0-h^{[1]}\right)\left(2\xi-h^{[1]}-h^{[2]}\right)\sum_m \frac{b_m}{m}\left[(-1)^m-\cos\frac{m\pi x}{l}\right] \tag{4.9}$$

To remain the equality of the summation of the series functions on both sides of Equation 4.9, we equalize them termwisely, and that results in

$$\xi=\frac{\left(h^{[1]}\right)^2}{6\left(2h_0-h^{[1]}\right)}+\frac{\left(h^{[1]}+h^{[2]}\right)}{2} \tag{4.10}$$

4.2.6 Stress Representation in Three Layers with Fourier Series

Substituting Equations 4.2a-c into Equations 3.36 yields

$$\sigma_x^{[1]}=\left\{\frac{1}{h^{[1]}}-\frac{6y^{[1]}}{\left(h^{[1]}\right)^3}\left[h^{[1]}+h^{[2]}-2\xi\right]\right\}\sum_m \frac{l}{m\pi}b_m\left[(-1)^m-\cos\frac{m\pi x}{l}\right] \tag{4.11a}$$

$$\sigma_{xy}^{[1]}=\left\{-\frac{1}{4}+\frac{3\left[2\xi-h^{[2]}\right]}{4h^{[1]}}-\frac{y^{[1]}}{h^{[1]}}+\frac{3\left(y^{[1]}\right)^2}{\left(h^{[1]}\right)^3}\left[h^{[1]}+h^{[2]}-2\xi\right]\right\}\sum_m b_m\sin\frac{m\pi x}{l} \tag{4.11b}$$

$$\sigma_x^{[3]}=\frac{b^{(2)}}{b^{(3)}}\left\{-\frac{1}{h^{[3]}}-\frac{6y^{[1]}}{\left(h^{[3]}\right)^3}\left[h^{[2]}+h^{[3]}+2\xi\right]\right\}\sum_m \frac{l}{m\pi}b_m\left[(-1)^m-\cos\frac{m\pi x}{l}\right]+\frac{6y^{[1]}}{b^{(3)}\left(h^{[3]}\right)^3}\left(2M_1+ql^2-qx^2\right) \tag{4.11c}$$

$$\sigma_{xy}^{[3]}=\frac{b^{(2)}}{b^{(3)}}\left\{-\frac{1}{4}-\frac{3\left[2\xi+h^{[2]}\right]}{4h^{[3]}}+\frac{y^{[3]}}{h^{[3]}}+\frac{3\left(y^{[3]}\right)^2}{\left(h^{[3]}\right)^3}\left[h^{[2]}+h^{[3]}+2\xi\right]\right\}\sum_m b_m\sin\frac{m\pi x}{l}+\frac{3qx}{2b^{(3)}\left(h^{[3]}\right)^3}\left(4\left(y^{[3]}\right)^2-\left(h^{[3]}\right)^2\right) \tag{4.11d}$$

Substituting Equations 4.2 to Equation 4.1 leads to

$$\sigma_y^{[2]}=\left(\xi-y^{[2]}\right)\sum_m \frac{m\pi}{l}b_m\cos\frac{m\pi x}{l} \tag{4.12}$$

The unknown coefficients b_m may now be determined by minimising the total complementary energy of the composite beam in the strengthened part written in Equation 3.47 by nullifying the first-order partial derivative about b_m, i.e.

$$\partial\Pi_c/\partial b_m=0 \tag{4.13}$$

which yields

$$S_1\left(\frac{l}{m\pi}\right)(-1)^m \sum_{j=1,2,\cdots}\left(\frac{l}{j\pi}\right)b_j(-1)^j + \left[\frac{S_1}{2}\left(\frac{l}{m\pi}\right)^2 + S_2 + S_3\left(\frac{m\pi}{l}\right)^2\right]b_m = P_m \quad (4.14)$$

where

$$S_1 = \frac{b^{(1)}}{E_x^{[1]}\left(h^{[1]}\right)^3}\left[3\left(h^{[1]}+h^{[2]}\right)^2 + 12\xi\left(\xi - h^{[1]} - h^{[2]}\right) + \left(h^{[1]}\right)^2\right]$$

$$+ \frac{\left(b^{(2)}\right)^2}{b^{(3)}E_x^{[3]}\left(h^{[3]}\right)^3}\left[3\left(h^{[2]}+h^{[3]}\right)^2 + 12\xi\left(\xi + h^{[2]} + h^{[3]}\right) + \left(h^{[3]}\right)^2\right] \quad (4.15a)$$

$$S_2 = \frac{b^{(1)}}{20G_{xy}^{[1]}}\left[\frac{3\left(h^{[2]}-2\xi\right)^2}{h^{[1]}} + \left(h^{[1]}+h^{[2]}-2\xi\right) - \frac{h^{[1]}}{3}\right] + \frac{h^{[2]}b^{(2)}}{2G_{xy}^{[2]}}$$

$$+ \frac{\left(b^{(2)}\right)^2}{20b^{(3)}G_{xy}^{[3]}}\left[\frac{3\left(h^{[2]}+2\xi\right)^2}{h^{[3]}} + \left(h^{[2]}+h^{[3]}+2\xi\right) - \frac{h^{[3]}}{3}\right] \quad (4.15b)$$

$$S_3 = \frac{b^{(2)}h^{[2]}}{24E_y^{[2]}}\left[\left(h^{[2]}\right)^2 + 12\xi^2\right] \quad (4.15c)$$

$$P_m = A\frac{(-1)^m}{m} + B\frac{(-1)^m}{m^3} \quad (4.15d)$$

where

$$A = \frac{lb^{(2)}}{\pi b^{(3)}h^{[3]}}\left[\frac{2\left(3M_0 + l^2q\right)\left(h^{[2]}+h^{[3]}+2\xi\right)}{E_x^{[3]}\left(h^{[3]}\right)^2} + \frac{q\left(6h^{[2]}+h^{[3]}+12\xi\right)}{10G_{xy}^{[3]}}\right] \quad (4.15e)$$

$$B = \frac{6b^{(2)}ql^3}{24b^{(3)}\pi E_x^{[3]}\left(h^{[3]}\right)^3}\left[h^{[2]}+h^{[3]}+2\xi\right] \quad (4.15f)$$

To facilitate the simplification, we introduce the following parameters

$$R = \sum_m\left(\frac{l}{m\pi}\right)b_m(-1)^m;\ \beta = \left(\frac{l}{\pi}\right)^2\frac{S_2}{2S_3};\ \alpha = \left(\frac{l}{\pi}\right)^2\sqrt{\frac{S_1}{2S_3}} \quad (4.16a\text{-}c)$$

where $\beta > \alpha$ for practical cases.

Equation 4.14 can be re-written as

$$b_m = \frac{m^4}{m^4 + 2\beta m^2 + \alpha^2}\left[P_m - \left(\frac{l}{m\pi}\right)(-1)^m RS_1\right]\frac{1}{S_3} \quad (4.17)$$

Substitution of Equation 4.17 into Equation 4.16a yields

$$R = \frac{l^2 \pi^2 \overline{\Theta}}{\pi^4 S_3 + l^4 S_1 \Theta} \tag{4.18}$$

where

$$\Theta = \sum_m \frac{1}{m^4 + 2\beta m^2 + \alpha^2} \tag{4.19a}$$

$$\overline{\Theta} = \sum_m \frac{(-1)^m m P_m}{m^4 + 2\beta m^2 + \alpha^2} = A\Theta + B\Theta' \tag{4.19b}$$

$$\Theta' = \sum_m \frac{1}{m^2\left(m^4 + 2\beta m^2 + \alpha^2\right)} \tag{4.19c}$$

The infinite summation of Equations 4.19a and 4.19b are derived using the following procedure.

Each term of the summation function can be converted into a series of partial fraction functions and the constant terms can be moved out of the summation sign. For instance,

$$\sum_m \frac{1}{m^4 + 2\beta m^2 + \alpha^2} = \sum_m \frac{1}{\left(m^2 + \gamma_1^2\right)\left(m^2 + \gamma_2^2\right)} = \frac{1}{\gamma_1^2 - \gamma_2^2}\left[\sum_m \frac{1}{\left(m^2 + \gamma_2^2\right)} - \sum_m \frac{1}{\left(m^2 + \gamma_1^2\right)}\right] \tag{4.20a}$$

$$\sum_m \frac{1}{m^2\left(m^4 + 2\beta m^2 + \alpha^2\right)} = \sum_m \frac{1}{m^2\left(m^2 + \gamma_1^2\right)\left(m^2 + \gamma_2^2\right)}$$

$$= \frac{1}{\gamma_1^2 - \gamma_2^2}\left[\frac{1}{\gamma_1^2}\sum_m \frac{1}{\left(m^2 + \gamma_1^2\right)} - \frac{1}{\gamma_2^2}\sum_m \frac{1}{\left(m^2 + \gamma_2^2\right)}\right] + \frac{1}{\gamma_1^2 \gamma_2^2}\sum_m \frac{1}{m^2} \tag{4.20b}$$

where $\gamma_1 = \sqrt{\beta + \sqrt{\beta^2 - \alpha^2}}$ and $\gamma_2 = \sqrt{\beta - \sqrt{\beta^2 - \alpha^2}}$. By adopting the summation of the Fourier series functions listed as follows, we can easily obtain the explicit functions for Equations 4.20a and b.

The summations of Fourier series functions are,

$$\sum_m \frac{1}{m^2 + a^2}\cos(mx) = \frac{\pi}{2a}\frac{\cosh a(\pi - x)}{\sinh a\pi} - \frac{1}{2a^2},\ 0 \le x \le 2\pi \tag{4.21a}$$

$$\sum_m \frac{(-1)^m}{m^2 + a^2}\cos(mx) = \frac{\pi}{2a}\frac{\cosh ax}{\sinh a\pi} - \frac{1}{2a^2},\ 0 \le x \le 2\pi \tag{4.21b}$$

$$\sum_m \frac{m}{m^2+a^2}\sin(mx)=\begin{cases}-\dfrac{\pi}{2}\dfrac{\sinh a(\pi+x)}{\sinh a\pi}, & -\pi\le x<0\\ 0 & x=0\\ \dfrac{\pi}{2}\dfrac{\sinh a(\pi-x)}{\sinh a\pi}, & 0<x\le\pi\end{cases} \tag{4.21c}$$

$$\sum_m \frac{(-1)^m m}{m^2+a^2}\sin(mx)=\begin{cases}-\dfrac{\pi}{2}\dfrac{\sinh ax}{\sinh a\pi}, & -\pi<x<\pi\\ 0, & \pm\pi\end{cases} \tag{4.21d}$$

where a is an arbitrary real constant, and m is a non-negative integer, i.e., $m = 0, 1, 2, 3, \ldots$ The summation functions are given in one periodical region for the trigonometric functions. For the x values out of the regions, we can conduct some simple transformation to move these values into the defined region. For example, if x belongs to the region of $-2\pi \le x \le 0$ in Equation 4.21a, we introduce another variable X and let $X = x - 2\pi$. Thus

$$\sum_m \frac{1}{m^2+a^2}\cos(mx)=\sum_m \frac{1}{m^2+a^2}\cos(mX)$$

$$=\frac{\pi}{2a}\frac{\cosh a(\pi-X)}{\sinh a\pi}-\frac{1}{2a^2}=\frac{\pi}{2a}\frac{\cosh a(x-\pi)}{\sinh a\pi}-\frac{1}{2a^2}, -2\pi\le x\le 0 \tag{4.21d}$$

Using the above summation functions, by substituting appropriate values, we can easily obtain the summation values involved in Equation 4.20. For instance, by substituting x = 0 and $\gamma_1 = a$ into Equation 4.21a, we have

$$\sum_m \frac{1}{\left(m^2+\gamma_1^2\right)}=\frac{\pi}{2\gamma_1}\frac{\cosh\gamma_1\pi}{\sinh\gamma_1\pi}-\frac{1}{2\gamma_1^2} \tag{4.22a}$$

The limit value of Equation 4.22 (a) when $\gamma_1 \to 0$ is

$$\sum_m \frac{1}{m^2}=\frac{\pi^2}{6} \tag{4.22b}$$

Obvious, the summation in Equations 4.22a and b are both constant.

Substituting Equation 4.18 to Equation 4.17 and then Equation 4.12 to 3.2(a) , the shear stress can be rewritten as

$$\sigma_{xy}^{[2]}=\frac{l^2}{\pi^2 S_3}\left\{\left(A-\frac{lS_1R}{\pi}\right)\sum_m \frac{(-1)^m m}{m^4+2\beta m^2+\alpha^2}\sin\left(\frac{m\pi}{l}x\right)+B\sum_m \frac{(-1)^m}{m\left(m^4+2\beta m^2+\alpha^2\right)}\sin\left(\frac{m\pi}{l}x\right)\right\}$$

$$= C_1 \sinh\left(\frac{\gamma_1 \pi}{l} x\right) + C_2 \sinh\left(\frac{\gamma_2 \pi}{l} x\right) + C_3 x \tag{4.23}$$

where the summation functions have been calculated using the method described above .

The coefficients, C_1, C_2 and C_3, are given as

$$C_1 = \frac{c_1}{c_0};\ C_2 = -\frac{c_2}{c_0};\ C_3 = -\frac{B}{2\pi S_3 \alpha^2} \tag{4.24a-c}$$

$$c_1 = \frac{l^2}{6\pi S_3 \gamma_2^2 \sinh \pi\gamma_1}\left\{Bl^4 S_1\left[\pi\gamma_2(3\coth \pi\gamma_2 - \pi\gamma_2) - 3\right] + 6\pi^4 S_3 \gamma_2^4\left(A\gamma_1^2 - B\right)\right\} \tag{4.24d}$$

$$c_2 = \frac{l^2}{6\pi S_3 \gamma_1^2 \sinh \pi\gamma_2}\left\{Bl^4 S_1\left[\pi\gamma_1(3\coth \pi\gamma_1 - \pi\gamma_1) - 3\right] + 6\pi^4 S_3 \gamma_1^4\left(A\gamma_2^2 - B\right)\right\} \tag{4.24e}$$

$$c_0 = l^4 S_1\left[\pi\gamma_1\gamma_2(\gamma_1 \coth \pi\gamma_2 - \gamma_2 \coth \pi\gamma_1) - 2\sqrt{\beta^2 - \alpha^2}\right] + 4\pi^4 S_3 \alpha^2 \sqrt{\beta^2 - \alpha^2} \tag{4.24f}$$

Note that c_2 is obtained by exchanging γ_1 and γ_2 in c_1.

4.2.7 Solution Procedure for Normal Stress σ_{y0}

Based on the shear stress in Equation 4.23 obtained in section 4.2.6 and the Fourier representation of $\sigma_{y0}(x)$ in Equation 4.2b, Equation 4.12 becomes

$$\sigma_y^{[2]} = \sum_m a_m \cos\frac{m\pi x}{l} - y\left(C_1 \frac{\gamma_1 \pi}{l} \cosh\frac{\gamma_1 \pi}{l} x + C_2 \frac{\gamma_2 \pi}{l} \cosh\frac{\gamma_2 \pi}{l} x + C_3\right) \tag{4.25}$$

Using the same procedure as described in the preceding section, the stress components are obtained as the following

$$\sigma_x^{[1]} = \frac{12 y^{[1]}}{\left(h^{[1]}\right)^3} \sum_m \left(\frac{l}{m\pi}\right)^2 a_m \left[(-1)^m - \cos\frac{m\pi x}{l}\right] + \sigma_{xa}^{[1]} \tag{4.26a}$$

$$\sigma_{xy}^{[1]} = \frac{3}{2\left(h^{[1]}\right)^3}\left[\left(h^{[1]}\right)^2 - 4\left(y^{[1]}\right)^2\right] \sum_m \frac{l}{m\pi} a_m \sin\frac{m\pi x}{l} + \sigma_{xya}^{[1]} \tag{4.26b}$$

$$\sigma_x^{[3]} = -\frac{b^{(2)}}{b^{(3)}} \frac{12 y^{[3]}}{\left(h^{[3]}\right)^3} \sum_m \left(\frac{l}{m\pi}\right)^2 a_m \left[(-1)^m - \cos\frac{m\pi x}{l}\right] + \sigma_{xa}^{[3]} + \sigma_{xb}^{[3]} \tag{4.26c}$$

$$\sigma_{xy}^{[3]} = \frac{3b^{(2)}}{2b^{(3)}}\left\{\frac{3}{\left(h^{[3]}\right)^3}\left[\left(h^{[3]}\right)^2 - 4\left(y^{[3]}\right)^2\right]\right\} \sum_m a_m \sin\frac{m\pi x}{l} + \sigma_{xya}^{[3]} + \sigma_{xyb}^{[3]} \tag{4.26d}$$

where

$$\sigma_{xa}^{[1]} = C_1\left\{\left[1-\frac{6y^{[1]}\left(h^{[1]}+h^{[2]}\right)}{\left(h^{[1]}\right)^2}\right]\left[\cosh\frac{\gamma_1\pi}{l}x-\cosh\gamma_1\pi\right]+\frac{6h^{[2]}y^{[1]}(x-l)}{\left(h^{[1]}\right)^3}\sinh\gamma_1\pi\right\}$$

$$+C_2\left\{\left[1-\frac{6y^{[1]}\left(h^{[1]}+h^{[2]}\right)}{\left(h^{[1]}\right)^2}\right]\left[\cosh\frac{\gamma_2\pi}{l}x-\cosh\gamma_2\pi\right]+\frac{6h^{[2]}y^{[1]}(x-l)}{\left(h^{[1]}\right)^3}\sinh\gamma_2\pi\right\}$$

$$+C_3\left[\frac{\left(l^2-x^2\right)\left(6y^{[1]}-h^{[1]}\right)}{2\left(h^{[1]}\right)^2}-\frac{3y^{[1]}h^{[2]}(l-x)^2}{\left(h^{[1]}\right)^3}\right] \qquad (4.27a)$$

$$\sigma_{xya}^{[1]} = C_1\left\{\left[\frac{3\left(y^{[1]}\right)^2\left(h^{[1]}+h^{[2]}\right)}{\left(h^{[1]}\right)^3}-\frac{4y^{[1]}+3h^{[2]}}{4h^{[1]}}-\frac{1}{4}\right]\sinh\frac{\gamma_1\pi}{l}x+\frac{3h^{[2]}\left[\left(h^{[1]}\right)^2-4\left(y^{[1]}\right)^2\right]}{4\left(h^{[1]}\right)^3}\sinh\gamma_1\pi\right\}$$

$$+C_2\left\{\left[\frac{3\left(y^{[1]}\right)^2\left(h^{[1]}+h^{[2]}\right)}{\left(h^{[1]}\right)^3}-\frac{4y^{[1]}+3h^{[2]}}{4h^{[1]}}-\frac{1}{4}\right]\sinh\frac{\gamma_2\pi}{l}x+\frac{3h^{[2]}\left[\left(h^{[1]}\right)^2-4\left(y^{[1]}\right)^2\right]}{4\left(h^{[1]}\right)^3}\sinh\gamma_2\pi\right\}$$

$$+C_3\left\{x\left[\left(\frac{y^{[1]}}{h^{[1]}}\right)^2\left(\frac{3h^{[2]}}{h^{[1]}}+3\right)-\frac{4y^{[1]}+3h^{[2]}+h^{[1]}}{4h^{[1]}}\right]-\frac{3h^{[2]}l}{h^{[1]}}\left(\frac{1}{4}-\left(\frac{y^{[1]}}{h^{[1]}}\right)^2\right)\right\} \qquad (4.28b)$$

$$\sigma_{xa}^{[3]} = C_1\frac{b^{(2)}}{b^{(3)}}\left\{\left[1+\frac{6y^{[3]}\left(h^{[2]}+h^{[3]}\right)}{\left(h^{[3]}\right)^2}\right]\left[\cosh\gamma_1\pi-\cosh\frac{\gamma_1\pi}{l}x\right]+\frac{6h^{[2]}y^{[3]}(x-l)}{\left(h^{[3]}\right)^3}\sinh\gamma_1\pi\right\}$$

$$+C_2\frac{b^{(2)}}{b^{(3)}}\left\{\left[1-\frac{6y^{[3]}\left(h^{[2]}+h^{[3]}\right)}{\left(h^{[3]}\right)^2}\right]\left[\cosh\frac{\gamma_2\pi}{l}x-\cosh\gamma_2\pi\right]+\frac{6h^{[2]}y^{[3]}(x-l)}{\left(h^{[3]}\right)^3}\sinh\gamma_2\pi\right\}$$

$$+C_3\frac{b^{(2)}}{b^{(3)}}\left[\frac{\left(l^2-x^2\right)\left(6y^{[3]}-h^{[3]}\right)}{2\left(h^{[3]}\right)^2}-\frac{3y^{[3]}h^{[2]}(l-x)^2}{\left(h^{[3]}\right)^3}\right] \qquad (4.29c)$$

$$\sigma_{xya}^{[3]} = C_1\frac{b^{(2)}}{b^{(3)}}\left\{\left[\frac{3\left(y^{[3]}\right)^2\left(h^{[2]}+h^{[3}\right)}{\left(h^{[3]}\right)^3}+\frac{4y^{[3]}-3h^{[2]}}{4h^{[3]}}-\frac{1}{4}\right]\sinh\frac{\gamma_1\pi}{l}x+\frac{3h^{[2]}\left[\left(h^{[3]}\right)^2-4\left(y^{[3]}\right)^2\right]}{4\left(h^{[3]}\right)^3}\sinh\gamma_1\pi\right\}$$

$$+C_2\frac{b^{(2)}}{b^{(3)}}\left\{\left[\frac{3\left(y^{[3]}\right)^2\left(h^{[2]}+h^{[3]}\right)}{\left(h^{[3]}\right)^3}-\frac{4y^{[3]}+3h^{[2]}}{4h^{[3]}}-\frac{1}{4}\right]\sinh\frac{\gamma_2\pi}{l}x+\frac{3h^{[2]}\left[\left(h^{[3]}\right)^2-4\left(y^{[3]}\right)^2\right]}{4\left(h^{[3]}\right)^3}\sinh\gamma_2\pi\right\}$$

$$+C_3\frac{b^{(2)}}{b^{(3)}}\left\{x\left[\left(\frac{y^{[3]}}{h^{[3]}}\right)^2\left(\frac{3h^{[2]}}{h^{[3]}}+3\right)+\frac{4y^{[3]}-3h^{[2]}-h^{[3]}}{4h^{[3]}}\right]-\frac{3h^{[2]}l}{h^{[3]}}\left(\frac{1}{4}-\left(\frac{y^{[3]}}{h^{[3]}}\right)^2\right)\right\}$$

(4.29d)

$$\sigma_{xb}^{[3]} = \frac{6y^{[3]}}{b^{(3)}\left(h^{[3]}\right)^3}\left(2M_0 + ql^2 - qx^2\right) \tag{4.29e}$$

$$\sigma_{xyb}^{[3]} = \frac{3qx}{2b^{(3)}\left(h^{[3]}\right)^3}\left(2y^{[3]} - h^{[3]}\right)\left(2y^{[3]} + h^{[3]}\right) \tag{4.29f}$$

Minimizing Π_c in terms of a_m by requiring $\partial\Pi_c/\partial a_m = 0$ leads to

$$S_1'\left(\frac{l}{m\pi}\right)^2(-1)^m \sum_{j=1,2,\ldots}\left(\frac{l}{j\pi}\right)a_j(-1)^j + \left[\frac{S_1'}{2}\left(\frac{l}{m\pi}\right)^4 + S_2'\left(\frac{l}{m\pi}\right)^2 + S_3'\right]a_m = P_m' \tag{4.30}$$

where

$$S_1' = \frac{12b^{(1)}}{E_x^{[1]}\left(h^{[1]}\right)^3} + \frac{12\left(b^{(1)}\right)^2}{b^{(3)}E_x^{[3]}\left(h^{[3]}\right)^3} \tag{4.31a}$$

$$S_2' = \frac{3b^{(1)}}{5G_{xy}^{[1]}h^{[1]}} + \frac{3\left(b^{(2)}\right)^2}{5b^{(3)}G_{xy}^{[3]}h^{[3]}} \tag{4.31b}$$

$$S_3' = \frac{b^{(2)}h^{[2]}}{2E_y^{[2]}} \tag{4.31c}$$

$$P_m' = \frac{F_1}{m^4} + \frac{F_2}{m^2} + (-1)^m\left(\frac{F_3}{m^4} + \frac{F_4}{m^2} + \frac{F_5}{m^2+\gamma_1^2} + \frac{F_6}{m^2+\gamma_2^2}\right) \tag{4.31d}$$

where F_i ($i = 1..6$) are:

$$F_1 = \frac{6l^3h^{[2]}}{\pi^4}T_{11}\left(C_1\sinh\gamma_1\pi + C_2\sinh\gamma_2\pi + C_3l\right) \tag{4.32a}$$

$$F_2 = \frac{l}{5\pi^2}\left[\frac{3T_{21}}{h^{[2]}}\left(C_1\sinh\gamma_1\pi + C_2\sinh\gamma_2\pi + C_3l^2 - 2C_2\right) - C_2T_{22}\right] \tag{4.32b}$$

$$F_3 = \frac{6l^3}{\pi^4}\left\{T_{11}\left[h^{[2]}\left(C_1\sinh\gamma_1\pi + C_2\sinh\gamma_2\pi\right) - C_3l\right] + \frac{2b^{(2)}ql}{b^{(3)}E_x^{[3]}\left(h^{[3]}\right)^3}\right\} \tag{4.32c}$$

$$F_4 = \frac{l}{\pi^2}\left\{\frac{6l^2}{\pi}\left(T_{12} + h^{[2]}T_{11}\right)\left(C_1\frac{\cosh\gamma_1\pi}{\gamma_1} + C_2\frac{\cosh\gamma_2\pi}{\gamma_2}\right) - \frac{3h^{[2]}}{5}\left(T_{21} + 5l^2T_{11}\right)\left(C_1\sinh\gamma_1\pi + C_2\sinh\gamma_2\pi\right)\right.$$
$$+ C_2\left[\frac{\left(T_{22} + 6h^{[2]}T_{21}\right)}{5} - \frac{12l^2\left(T_{12} + h^{[2]}T_{11}\right)}{\pi\gamma_2}\right] + C_3l\left[2l^2T_{12} + \frac{T_{22}}{10} - l^2h^{[2]}T_{11}\right]$$
$$\left. + \frac{2b^{(2)}ql}{b^{(3)}}\left[\frac{2l^2}{E_x^{[3]}\left(h^{[3]}\right)^3} + \frac{3}{5G_{xy}^{[3]}h^{[3]}}\right] + \frac{12b^{(2)}M_0l}{b^{(3)}}\frac{1}{E_x^{[3]}\left(h^{[3]}\right)^3}\right\} \tag{4.32d}$$

$$F_5 = \frac{l}{\pi^2}C_1\sinh\gamma_1\pi\left[\frac{1}{5}\left(\frac{T_{22}}{2} + 3h^{[2]}T_{21}\right) - \frac{6l^2\left(T_{12} + h^{[2]}T_{11}\right)}{\pi(\gamma_1)^2}\right] \tag{4.32e}$$

$$F_6 = \frac{l}{\pi^2} C_2 \sinh \gamma_2 \pi \left[\frac{1}{5} \left(\frac{T_{22}}{2} + 3h^{[2]} T_{21} \right) - \frac{6l^2 \left(T_{12} + h^{[2]} T_{11} \right)}{\pi (\gamma_2)^2} \right] \tag{4.32f}$$

$$T_{11} = \frac{\left(b^{(2)}\right)^2}{b^{(3)} E_x^{[3]} \left(h^{[3]}\right)^3} - \frac{b^{(1)}}{E_x^{[1]} \left(h^{[1]}\right)^3} \tag{4.32g}$$

$$T_{12} = \frac{\left(b^{(2)}\right)^2}{b^{(3)} E_x^{[3]} \left(h^{[3]}\right)^2} - \frac{b^{(1)}}{E_x^{[1]} \left(h^{[1]}\right)^2} \tag{4.32h}$$

$$T_{21} = \frac{\left(b^{(2)}\right)^2}{b^{(3)} G_{xy}^{[3]} h^{[3]}} - \frac{b^{(1)}}{G_{xy}^{[1]} h^{[1]}} \tag{4.32i}$$

$$T_{22} = \frac{\left(b^{(2)}\right)^2}{b^{(3)} G_{xy}^{[3]}} - \frac{b^{(1)}}{G_{xy}^{[1]}} \tag{4.32j}$$

Introducing

$$\beta' = \left(\frac{l}{\pi} \right)^2 \frac{S_2'}{2S_3'}; \quad \alpha' = \left(\frac{l}{\pi} \right)^2 \sqrt{\frac{S_1'}{2S_3'}} \tag{4.33}$$

where $\beta' < \alpha'$ for most practical cases, and following the same procedure as section 2.6

$$\begin{aligned} \sigma_{y0} = {} & H_1 \sum_m \frac{(-1)^m}{m^2 + (\gamma_1)^2} \cos\left(\frac{m\pi}{l} x \right) + H_2 \sum_m \frac{(-1)^m}{m^2 + (\gamma_2)^2} \cos\left(\frac{m\pi}{l} x \right) \\ & + H_3 \sum_m \frac{(-1)^m}{m^2 + (\eta_1 + i\eta_2)^2} \cos\left(\frac{m\pi}{l} x \right) + H_4 \sum_m \frac{(-1)^m}{m^2 + (\eta_1 - i\eta_2)^2} \cos\left(\frac{m\pi}{l} x \right) \\ & + H_5 \sum_m \frac{1}{m^2 + (\eta_1 + i\eta_2)^2} \cos\left(\frac{m\pi}{l} x \right) + H_6 \sum_m \frac{1}{m^2 + (\eta_1 - i\eta_2)^2} \cos\left(\frac{m\pi}{l} x \right) \end{aligned} \tag{4.34}$$

where the dimensionless parameters $\eta_1 = \sqrt{\frac{\alpha' + \beta'}{2}}$ and $\eta_2 = \sqrt{\frac{\alpha' - \beta'}{2}}$. Note that H_i (i = 1..6), which are too complex to list herein, are normally complex. The summation functions in Equations 4.21 also apply to the case when a is a complex, e.g. the substitution of a by $c + id$ in Equations 4.21a and b, yields

$$\sum_m \frac{1}{m^2 + (c + id)^2} \cos mx = G_{1R} + iG_{1I} \tag{4.35a}$$

$$\sum_m \frac{(-1)^m}{m^2 + (c + id)^2} \cos mx = G_{2R} + iG_{2I} \tag{4.35b}$$

$$G_{1R}=\frac{1}{2(c^2+d^2)}\left\{\pi\left[\frac{c(\sinh cx\cos d(x-2\pi)-\sinh c(x-2\pi)\cos dx)+d(\cosh cx\sin d(x-2\pi)-\cosh c(x-2\pi)\sin dx)}{\cos 2\pi c-\cos 2\pi d}\right]-\frac{c^2-d^2}{c^2+d^2}\right\}$$

$$G_{1I}=\frac{1}{2(c^2+d^2)}\left\{-\pi\left[\frac{c(\cosh cx\sin d(x-2\pi)+\cosh c(x-2\pi)\sin dx)+d(\sinh cx\cos d(x-2\pi)+\sinh c(x-2\pi)\cos dx)}{\cos 2\pi c-\cos 2\pi d}\right]+\frac{cd}{c^2+d^2}\right\}$$

$$G_{2R}=\frac{1}{2(c^2+d^2)}\left\{\pi\left[\frac{c(\sinh c(x+\pi)\cos d(x-\pi)-\sinh c(x-\pi)\cos d(x+\pi))+d(\cosh c(x+\pi)\sin d(x-\pi)-\cosh c(x-\pi)\sin d(x+\pi))}{\cos 2\pi c-\cos 2\pi d}\right]-\frac{c^2-d^2}{c^2+d^2}\right\}$$

$$G_{2I}=\frac{1}{2(c^2+d^2)}\left\{-\pi\left[\frac{c(\cosh c(x+\pi)\sin d(x-\pi)+\cosh c(x-\pi)\sin d(x+\pi))+d(\sinh c(x+\pi)\cos d(x-\pi)+\sinh c(x-\pi)\cos d(x+\pi))}{\cos 2\pi c-\cos 2\pi d}\right]+\frac{cd}{c^2+d^2}\right\}$$

(4.36a-d)

By simplifying Equation 4.34, the imagine components will automatically vanish, leaving the real components representing the normal stress in the MA section as

$$\sigma_{y0}=\frac{1}{S_3'}\{G_{1R}F_2+G_{1I}\frac{F_2\beta'-F_1}{2\eta_1\eta_2}+G_{2R}\left(F_4+\frac{\delta_0}{\delta_{11}\delta_{12}}F_5+\frac{\delta_0}{\delta_{21}\delta_{22}}F_6-\frac{l^2}{\pi^2}S_1'R'\right)$$

$$+\frac{G_{2I}}{2\eta_1\eta_2}\left[F_4(\beta'-F_3)+\frac{\delta_0\gamma_1^2}{\delta_{11}\delta_{12}}F_5+\frac{\delta_0\gamma_2^2}{\delta_{21}\delta_{22}}F_6-\frac{l^2}{\pi^2}S_1'R'\beta'\right]+G_1'\frac{\gamma_1^4}{\delta_{11}\delta_{12}}+G_2'\frac{\gamma_2^4}{\delta_{21}\delta_{22}}\}$$

(4.37)

where G_{1R}, G_{1I}, G_{2R}, G_{2I} are obtained by substituting c with η_1, d with η_2, x with $\pi x/l$ in Equations 4.35 and 4.36, respectively, G_1', G_2' are obtained by substituting x with $\pi x/l$, a with γ_1 and γ_2 respectively in Equations 4.32b. Thus

$$\delta_0=\alpha'^2-2\beta'\gamma_1^2 \quad (4.38a)$$

$$\delta_{11}=\gamma_1^2-2\eta_1\gamma_1+\alpha' \quad (4.38b)$$

$$\delta_{12}=\gamma_1^2+2\eta_1\gamma_1+\alpha' \quad (4.38c)$$

$$\delta_{21}=\gamma_2^2-2\eta_1\gamma_2+\alpha' \quad (4.38d)$$

$$\delta_{22}=\gamma_2^2+2\eta_1\gamma_2+\alpha' \quad (4.38e)$$

$$R'=\frac{l^3\pi\bar{\Psi}}{\pi^4S_3+l^4S_1\Psi} \quad (4.38f)$$

$$\Psi=\sum_m\frac{1}{m^4+2\beta'm^2+\alpha'^2} \quad (4.28a)$$

$$\bar{\Psi}=\sum_m\frac{(-1)^m m^2P_m}{m^4+2\beta'm^2+\alpha'^2} \quad (4.38b)$$

Using Equation 4.25, the interfacial normal stress can be obtained by substituting $y^{[2]}$ with $h^{[2]}/2$ and $-h^{[2]}/2$, respectively.

$$\sigma_y^{(1)} = \sigma_{y0} - \frac{h^{[2]}}{2}\left(C_1 \frac{\gamma_1 \pi}{l}\cosh\frac{\gamma_1 \pi}{l}x + C_2 \frac{\gamma_2 \pi}{l}\cosh\frac{\gamma_2 \pi}{l}x + C_3\right) \tag{4.39a}$$

$$\sigma_y^{(2)} = \sigma_{y0} + \frac{h^{[2]}}{2}\left(C_1 \frac{\gamma_1 \pi}{l}\cosh\frac{\gamma_1 \pi}{l}x + C_2 \frac{\gamma_2 \pi}{l}\cosh\frac{\gamma_2 \pi}{l}x + C_3\right) \tag{4.39b}$$

4.3 Solution Verification by Numerical Examples

The example used in Section 3.7.1 in Chapter 3 is used again herein to verify the present closed-form solution. Figure 4.2 shows the results of normal stress and shear stress. Figure 4.2 (a) displays the transverse normal stress in PA interface, MA section and AC interfaces, respectively. Two groups of results are compared, one from the present solution, the other from complete solution introduced in the preceding chapter. As the figure shows, the present solution shows the difference of the transverse normal stress along the PA interface and AC interface. But the peak values are lower than those obtained by complete solution. It is believed that this is attribute to the assumption that the shear stress keeps constant along the transverse direction in the adhesive.

The shear stress is plotted in Figure 4.2 (b) where only one curve appears as they are assumed to be constant across the thickness of the adhesive layer. Again, the peak stress predicted by the present solution is slightly lower than those given by the complete solution. In fact, the present solutions show a reduced order of the shear stress. However, the relative difference is within 10% and the present is actually very close to that in the MA section predicted by the complete solution.

The second verification example is taken from Shen et al. (2001). An RC beam bonded with a GFRP plate and subjected to UDL. The RC beam has a span 3000 mm, a width $b^{(3)} = 200$ mm, a cross-sectional height $h^{[3]} = 300$ mm, Young's moduli $E_x^{[3]} = E_y^{[3]} = 30$ GPa and a Poisson's ratio $\nu_{xy}^{[3]} = 0.18$. The orthotropic FRP plate has a length 2400 mm, a width $b^{(1)} = 200$ mm, a thickness $h^{[1]} = 2$ mm, a Young's modulus in the x-direction $E_x^{[1]} = 100$ GPa and a shear modulus in x-y plane $G_{xy}^{[1]} = 5$ GPa. The isotropic adhesive layer has a width $b^{(2)} = 200$ mm, a thickness $h^{[2]} = 2$ mm, Young's moduli $E_x^{[2]} = E_y^{[2]} = 3$ GPa, and a Poisson's ratio $\nu_{xy}^{[2]} = 0.35$.

The stress results are presented in the dimensionless format in the plots as shown in Figure 4.3, i.e. the x coordinate is normalized by the half length of GFRP l, and stress values are normalized by the concrete maximum tensile stress experienced by the concrete particle in the bottom of the RC beam at midspan. It can be calculated in this case as $qL^2h_c/2I_c$, where q is the intensity of UDL, Ic is the second moment of area about the neutral axis of the composite cross-section with all the materials transferred to concrete, h_c is the distance between this neutral axis to the concrete tensile furthermost fibre. As the dimensionless value is independent of the applied load magnitude, the value of q is not specified herein.

Figures 4.3 show the dimensionless normal stress and shear stress and their counterparts from Shen et al. (2001)'s solution. Shen's results show greater peak normal stress at the AC interface, and the normal stress at the PA interface near the plate end is tensile as well. The present solution offers only about half of that peak value at the AC interface and a compressive stress at PA interface. The transverse normal stress in the MA section from the present solution is in between them. From Shen's results, the normal stresses are zero when the shear stresses arrive at their peak values, but the present solution shows that normal stress occurs at this position with limited magnitude.

From the shear stress showed in Figure 4.2b, we can see both solutions provided fairly consistent results and Shen's results suggest that there is little different in terms of the interfacial shear stresses between the AC interface and PA interface. This conclusion can be used to validate the assumption adopted in deriving the present solution that the shear stress is constant along the thickness direction.

By observing the dimensionless magnitude for both stress components, we can see that the peak normal stress can reach about 25 percent of the maximum tensile fibre stress in the concrete and the peak shear stress can reach about 10 percent. It is also accompanied with a simultaneous transverse normal stress. This highly complex stress field is believed to result in plate end cracks when the magnitude reaches certain level.

4.4 Conclusions

In this chapter, a closed-form rigorous stress solution is proposed for a plated beam in the context of linear elasticity. The main advantages of these solutions are as follows:

1. It provides highly accurate results compared with some other approximate solutions;
2. The closed-form solutions enable the application of the simple spreadsheet package to calculate the numerical results;
3. They are the first closed-form solutions that predict the compressive stress at the PA interface;
4. They can be further exploited to develop a simplified version, so that the design-oriented strength model can be proposed based on the compact stress solution;
5. The float-point accuracy problem encountered in some other solutions can be avoided;
6. They are versatile and can be used to analyze other composite structures such as strengthened cast iron beams.

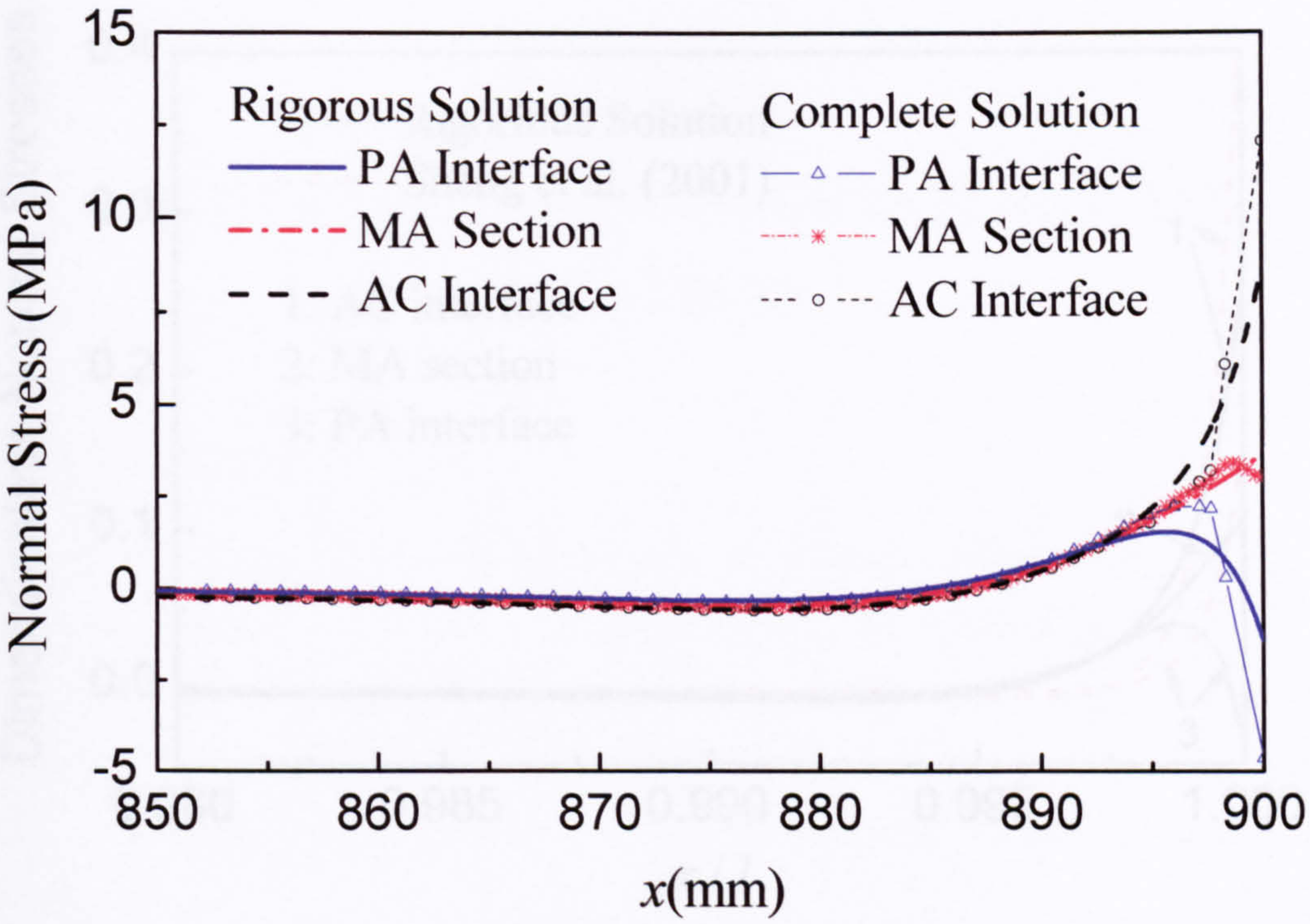

(a) Normal stress

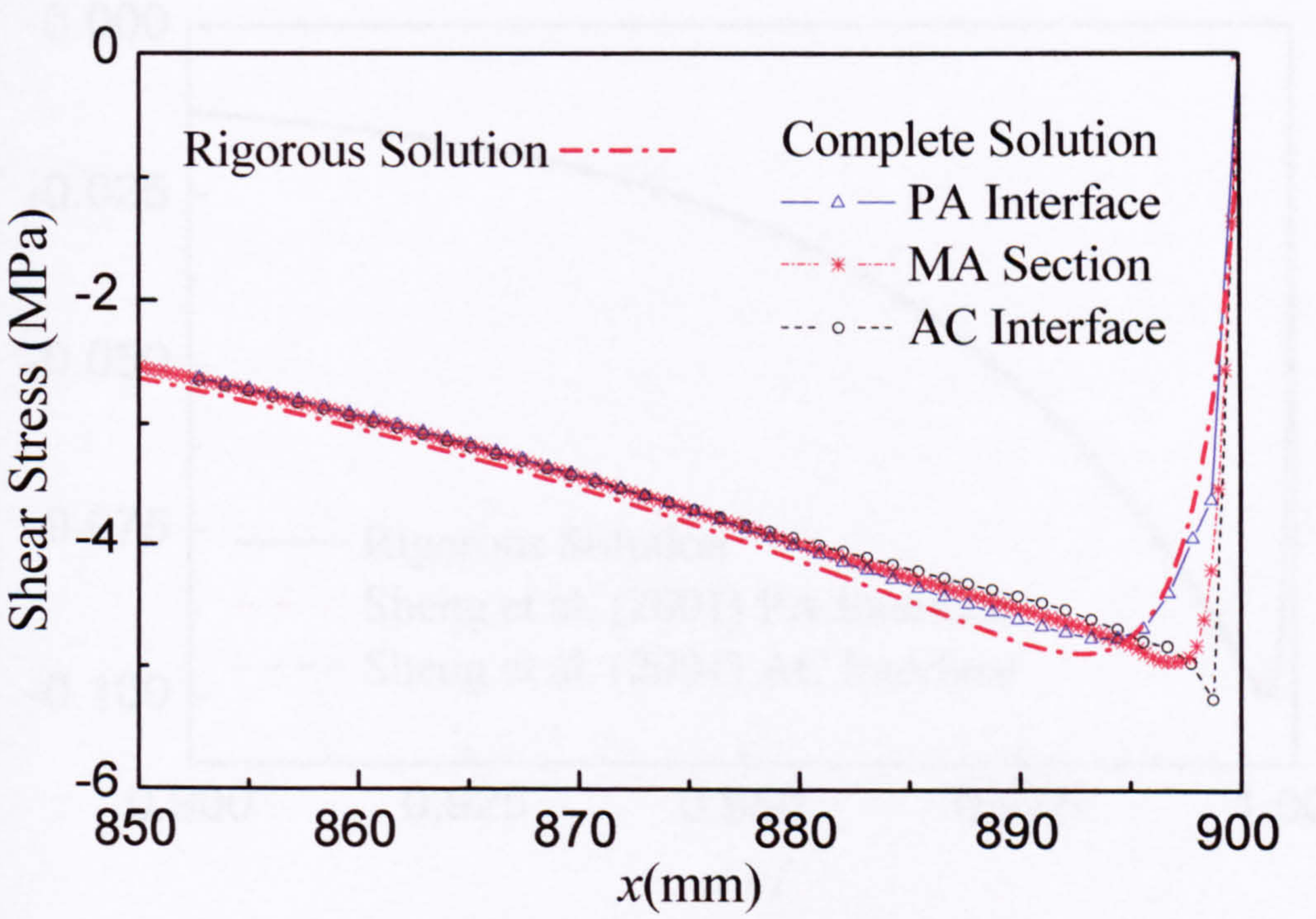

(b) Shear stress

Fig. 4.2 Steel plate beam

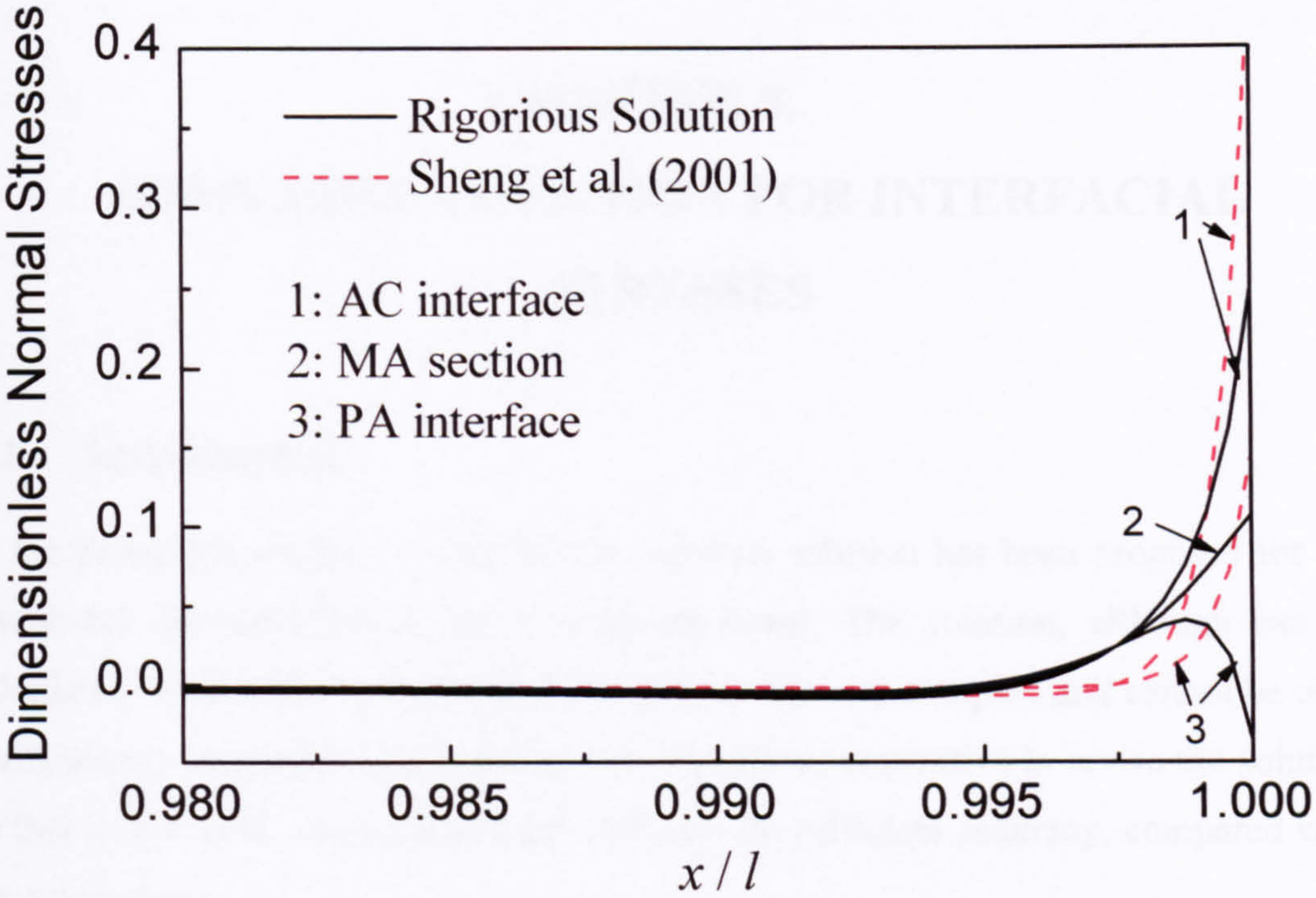

(a) Transverse normal stress

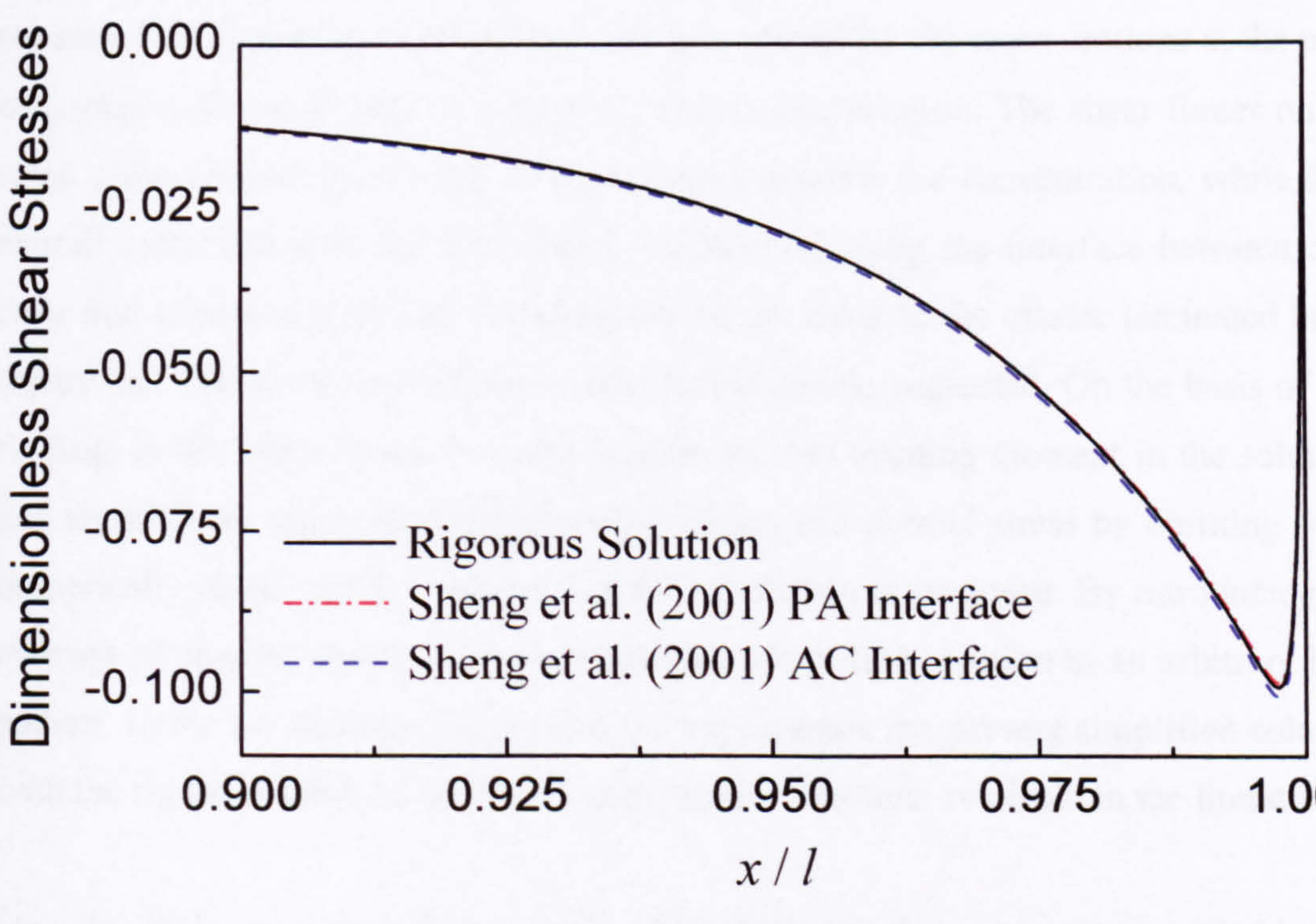

(b) Shear stress

Fig. 4.3 GFRP plated beam

CHAPTER 5.
SIMPLIFIED SOLUTION FOR INTERFACIAL STRESSES

5.1 Introduction

In the preceding chapter, a closed-form rigorous solution has been proposed for the interfacial structural behaviour in a plated beam. The solution, although can be calculated using some spreadsheet packages, is still very complex and cannot be used conveniently in engineering practice. It is, therefore, imperative to revise the solution so that it is simple, practical and can still provide sufficient accuracy, compared with the original one.

To this end, this chapter first studies the impact of applied loads on the interfacial stresses. It is found that the bending moments carried by the cross sections at the plate ends play a dominant role in generating stress concentration. The shear forces on the same cross sections have little to contribution towards the concentration, while their overall contribution to the shear stress distribution along the interface between concrete and adhesive layer can be calculated on the basis of the classic laminated beam theory and that to the normal stress distribution can be neglected. On the basis of this finding, in the second step, we only include the end bending moment in the solution, and simplify the rigorous interfacial shear stress and normal stress by omitting some numerically small terms. Finally a simplified solution is proposed. By introducing the concept of transfer length, we can extend this simplified solution to an arbitrary load pattern. In the numerical example section, we compare the present simplified solution with the rigorous solution and other approximate solutions available in the literature.

Due to their compact feature, the simplified solutions are more suitable for engineering applications using a portable calculator and to be possibly adopted as a design equation if suitably experiment data is compared and the solution is further calibrated.

5.2 The Impact of the End Bending Moment to the Interfacial Stresses

Yang and Ye (2004) numerically validated the dominant load component that causes shear stress concentration is the internal bending moment carried by the beam at the end of the plate. To demonstrate that the end bending moment also dominates the normal stress concentration, a numerical example is studied. In this example, the simply supported beam is bonded by a CFRP sheet and the corresponding parameters are as follows:

L = 1500mm, l =1200mm, $b^{(0)} = b^{(2)}$ = 200mm, $h^{[1]}$=4mm, $h^{[2]}$=2mm, $h^{[3]}$ = 300mm, $E_x^{[1]}$ = 100GPa, $E_x^{[2]} = E_y^{[2]}$ = 2GPa, $E_x^{[3]} = E_y^{[3]}$ =30GPa, $G_{xy}^{[1]}$ =5GPa, $\nu_{xy}^{[2]}$ = 0.35 and $\nu_{xy}^{[3]}$ = 0.17.

For a strengthened RC beam subjected to symmetric loadings [Figure 5.1 (a)], only the strengthened part is considered, the applied loads incur two groups of internal load at the cut-off cross sections, i.e. a pair of equal bending moments and shear forces respectively [Figure 5.1 (b)]. The equivalent form of the strengthened part is the combination of two fictitious beams with the same lengths as the strengthened part and subjected to, respectively, a pair of equal bending moment $q\left(L^2 - l^2\right)/2$ [Figure 5.1 (c)] and the UDL with load intensity q acting only in the strengthened part [Figure 5.1 (d)]. It is noted that these two fictitious beams are fully bonded. These two beams and the original one are calculated using the closed-form rigorous solutions developed in Chapter 4. The calculated stresses are normalized by the maximum tensile concrete fiber stress in the original beam. The dimensionless results for the three cases are plotted in Figures 5.2.

Figures 5.2a and 5.2b show the dimensionless shear stress in the adhesive layer and the normal stress at the AC interface, MA section, PA interface respectively. These stress distributions are for the original plated beam and regarded as the reference results. Figures 5.2c and 5.2d show the same stress distributions for Beam I. Figures 5.2e and 5.2f are for Beam II. In Figure 5.2e, the interfacial shear stress obtained by the classical laminate beam theory (CLBT) is also shown.

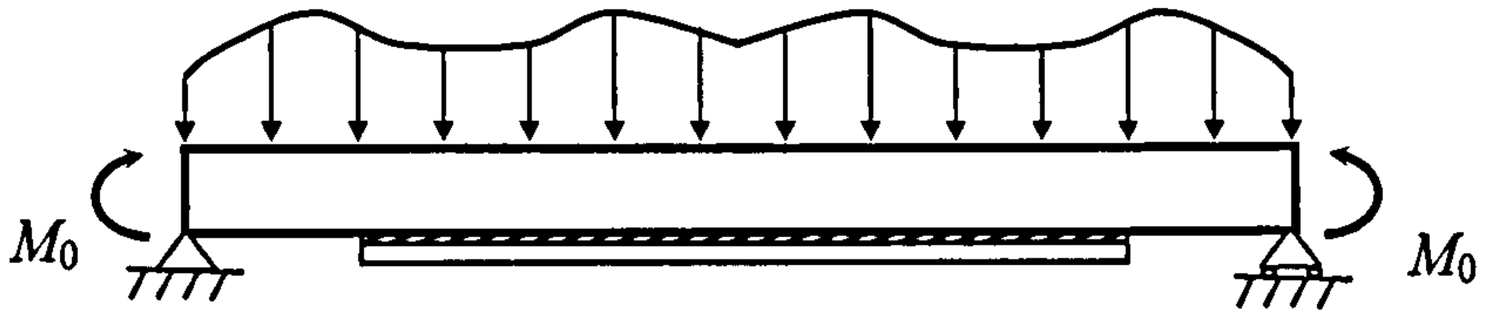

(a) A plated beam under symmetric loads

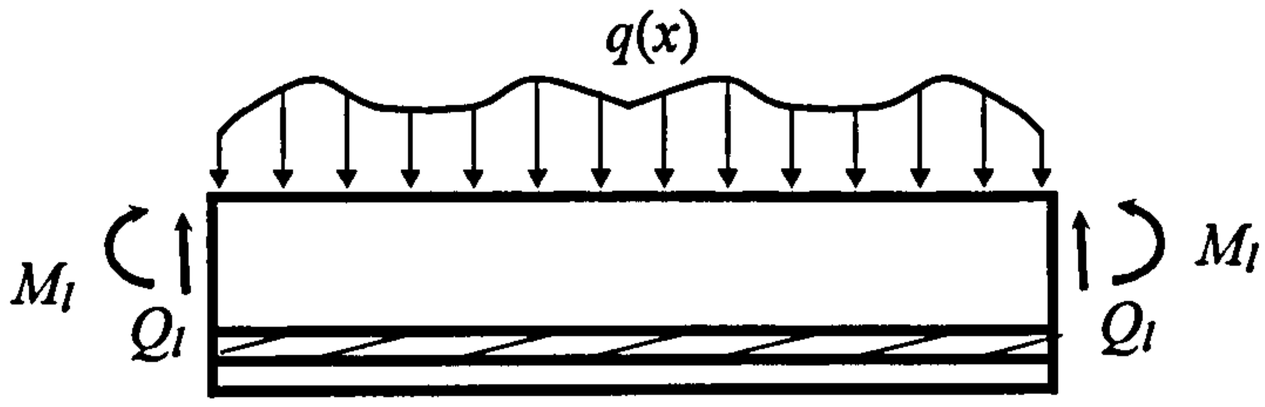

(b) The strengthened part

=

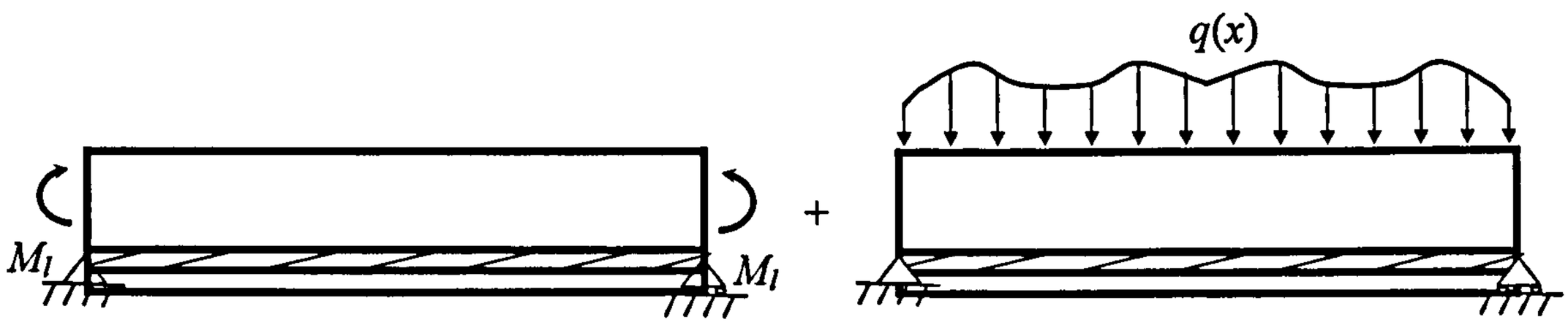

(c) Beam I (d) Beam II

Fig. 5.1 Diagrammatic representation of the strengthened beam subjected to symmetric loadings

From the figures, we can see that the UDL hardly introduce any stress concentration. The interfacial shear stress is almost coincident to the CLBT solution and the transverse normal stress at the plate end is negligible. In contrast, the bending moment induces significant increase in shear and normal stresses at the plate end.

In light of the numerical results, the following observation can be obtained:

1 The bending moment in the cross section at the plate end is the key cause of the stress concentration;

2 The transversely applied load and the corresponding internal shear forces play a negligible impact to the stress concentration. This contribution to the shear stresses can be computed on the basis of CLBT ;

3 The interfacial stresses in a plated beam subjected to any symmetric load can be obtained approximately using the following steps: (a) calculate the internal bending moment carried by the cross sections at the plate ends and the resulting interfacial stresses; (b) calculate the interfacial shear stress using CLBT; (c) calculate the normal stress from (a) and the shear stress by adding the shear stresses from (a) to (b).

In the next section, we will focus on the interfacial structural behavior for a plated beam subjected to a pair of symmetric bending moments. The related rigorous solutions will be re-investigated and the numerically small terms will be omitted so that a simple version of the solution will be proposed without losing much accuracy.

5.3 Solution Simplification

In the rigorous solutions present in Chapter 4, we let $q = 0$ in all the corresponding equations to represents the case of the plated beam subjected to end bending moment only. Some terms in the solutions, which are numerically small in practical engineering applications, can be omitted.

5.3.1 Solution Simplification for Shear Stress

Equation 4.10 can be rearranged as

$$\xi = h^{[1]}\left(\frac{1}{12h_0/h^{[1]} - 6} + \frac{h^{[2]}}{2h^{[1]}} + \frac{1}{2}\right) \tag{5.1}$$

Due to the fact that the thickness of both the plate and the adhesive layer are far smaller than the RC beam, i.e. the $h_0/h^{[1]}$ can be deemed far greater than the unit, making the first term in the bracket of Equation 4.1 negligibly smaller than the other two terms. Hence it can be omitted and ξ is then simplified as

$$\xi = \frac{h^{[1]} + h^{[2]}}{2} \tag{5.2}$$

Taking into account the above simplification, we can further simplify the coefficients of S_1, S_2 and S_3 of Equations 4.15a – c into

$$S_1 = b\left[\frac{4}{E_x^{[3]}h^{[3]}}\frac{b}{B}+\frac{1}{E_x^{[1]}h^{[1]}}\right] \tag{5.3a}$$

$$S_2 = b\left[\frac{h^{[3]}}{15G_{xy}^{[3]}}\frac{b}{B}+\frac{h^{[2]}}{2G_{xy}^{[2]}}+\frac{h^{[1]}}{6G_{xy}^{[1]}}\right] \tag{5.3b}$$

$$S_3 = \frac{h^{[2]}b}{E_y^{[2]}}\left[\frac{\left(h^{[1]}\right)^2}{8}+\frac{h^{[1]}h^{[2]}}{4}+\frac{\left(h^{[2]}\right)^2}{6}\right] \tag{5.3c}$$

where B and b denote the width of the beam and bonded plate respectively. Note that $B = b^{(3)}$ and $b = b^{(0)} = b^{(1)} = b^{(2)}$ in relation to the notations of Chapters 3 and 4.

Representing γ_1 and γ_2 in terms of S_1, S_2 and S_3 directly yields

$$\gamma_1 = \sqrt{\frac{S_2+\sqrt{S_2^{\,2}-2S_1S_3}}{2S_3}}\;;\;\gamma_2 = \sqrt{\frac{S_2-\sqrt{S_2^{\,2}-2S_1S_3}}{2S_3}} \tag{5.4a, b}$$

By observing the Equation 43.23 in connection with 4.21d, shear stress $\sigma_{xy}^{[2]}$ in Equation 4.23 can be written as

$$\sigma_{xy}^{[2]} = K\left[\frac{\sinh\gamma_1 x}{\sinh\gamma_1 l}-\frac{\sinh\gamma_2 x}{\sinh\gamma_2 l}\right] \tag{5.5}$$

The coefficient K actually determines the peak value of $\sigma_{xy}^{[2]}$ in the adhesive layer. Representing the hyperbolic functions in Equation 5.5 with the form of exponential ones, we obtain

$$\frac{\sinh\gamma_1 x}{\sinh\gamma_1 l} = e^{\gamma_1(l-x)}\frac{e^{2\gamma_1 x}-1}{e^{2\gamma_1 l}-1} = e^{\gamma_1(l-x)}\frac{1-e^{-2\gamma_1 x}}{e^{2\gamma_1(l-x)}-e^{-2\gamma_1 x}} \approx e^{\gamma_1(x-l)} \tag{5.6}$$

the second equation above is valid because $e^{-2\gamma_1 x}$ is close to zero for most x values in the domain.

Thus, Equation 4.5 can be further simplified as

$$\sigma_{xy}^{[2]} = K\left[e^{\gamma_1(x-l)}-e^{\gamma_2(x-l)}\right] \tag{5.7}$$

Thus Equation 5.7 has only one unknown coefficient K that can be determined by equalizing the resultant of the shear stress over the PA interface to the sum of the lon-

gitudinal tensile stress result acting on its cross section at the middle span of the bonded plate. The required tensile force can be easily computed from the classical laminated beam theory, using the similar procedure in Section 4.2.5. After some algebraic manipulation, K can be obtained as

$$K = \frac{M_0}{I_0}\frac{h_0 h^{[1]}}{\left[\dfrac{e^{-\gamma_1 l}-1}{\gamma_1} - \dfrac{e^{-\gamma_2 l}-1}{\gamma_2}\right]} \approx \frac{M_0}{I_0}\frac{\gamma_1\gamma_2 h_0 h^{[1]}}{(\gamma_1-\gamma_2)} \tag{5.8}$$

in which $e^{-\gamma_1 l}$ approximately equals zero. Thus the shear stress becomes

$$\sigma_{xy}^{[2]} = \frac{M_0}{I_0}\frac{\gamma_1\gamma_2 h_0 h^{[1]}}{(\gamma_1-\gamma_2)}\left[e^{\gamma_1(x-l)} - e^{\gamma_2(x-l)}\right] \tag{5.9}$$

Nullifying the first-order derivative of $\sigma_{xy}^{[2]}$, the interfacial shear stress approaches its peak value at (l-x^*), where

$$x^* = \frac{\ln\gamma_1 - \ln\gamma_2}{\gamma_1-\gamma_2} \tag{5.10}$$

The substitution of Equation 5.10 into Equation 5.9 leads to

$$[\sigma_{xy}^{[2]}]_{\max} = -\frac{M_0}{I_0}\gamma_1 h_0 h^{[1]}\left(\frac{\gamma_1}{\gamma_2}\right)^{\frac{\gamma_1}{\gamma_1-\gamma_2}} \tag{5.11}$$

The interfacial shear stress induced by the imposed transverse load $q(x)$ along with its corresponding shear forces is obtained using the classic laminated beam theory (CLBT) as (Gere and Timoshenko, 1999)

$$\sigma_{xy}^{'} = -\frac{\int_0^x q(x)dx}{I_0} h_0 h^{[1]} \tag{5.12}$$

For the sake of simplicity, its value at $x = l - x^*$ is computed approximately by introducing $x = l$ into Equation 4.12, i.e.

$$[\sigma_{xy}^{'}]_{\max} = -\frac{\int_0^l q(x)dx}{I_0} h_0 h^{[1]} \tag{5.13}$$

Thus, the complete solution of the interfacial shear stress for the beam subjected to a combined action of end moment and transverse load is

$$\sigma_{xy} = \sigma_{xy}^{[2]} + \sigma_{xy}^{'} = \frac{h_0 h^{[1]}}{I_0}\left[M_0 \frac{\gamma_1\gamma_2\left[e^{\gamma_1(x-l)} - e^{\gamma_2(x-l)}\right]}{(\gamma_1 - \gamma_2)} - \int_0^x q(x)dx \right] \tag{5.14}$$

and the maximum shear stress is

$$[\sigma_{xy}]_{\max} = -\frac{h_0 h^{[1]}}{I_0}\left[M_0\gamma_1\left(\frac{\gamma_1}{\gamma_2}\right)^{\frac{\gamma_1}{\gamma_1-\gamma_2}} + \int_0^l q(x)dx \right] \tag{5.15}$$

where M_0 denotes the internal bending moment carried by the cross sections at the plate end.

5.3.2 Solution Simplification for Normal Stress

We rewrite α' and β' in terms of S_1', S_2' and S_3' directly

$$\alpha' = \sqrt{\frac{S_1'}{2S_3'}}; \quad \beta' = \frac{S_2'}{2S_3'} \tag{5.16}$$

and η_1 and η_2 become

$$\eta_1 = \sqrt{\frac{\sqrt{2S_1'S_3'} + S_2'}{4S_3'}} \text{ and } \eta_2 = \sqrt{\frac{\sqrt{2S_1'S_3'} - S_2'}{4S_3'}} \tag{5.17}$$

As $\sinh x$ and $\cosh x$ are very close to $e^x/2$ when x is greater than 2.5, it is sensible that we simplify all the hyperbolic functions into the exponential ones. As a result, the solution of normal stress in Equation 4.37 can be simplified as

$$\sigma_{y0}^{[2]} = K_1 \sin\eta_2(x-l)e^{\eta_1(x-l)} + K_2\cos\eta_2(x-l)e^{\eta_1(x-l)} + K_3e^{\gamma_1(x-l)} + K_4e^{\gamma_2(x-l)} \tag{5.18}$$

where

$$K_1 = \frac{l}{4\alpha'\eta_2S_3'}\left\{\left[\beta' + 2(\eta_2)^2\right]f_1 + \frac{h_{21}}{\delta_{11}'\delta_{12}'}f_{21} + \frac{h_{22}}{\delta_{21}'\delta_{22}'}f_{22} - \left[\beta' + 2(\eta_2)^2\right]S_1'R\right\}$$

$$K_2 = \frac{l}{32\alpha'\eta_1S_3'}\left\{4\left[\alpha' - \beta' + 2(\eta_1)^2\right]f_1 + \frac{h_{31}}{\delta_{11}'\delta_{12}'}f_{21} + \frac{h_{32}}{\delta_{21}'\delta_{22}'}f_{22} - 4\left[\alpha' - \beta' + 2(\eta_1)^2\right]S_1'R\right\}$$

$$K_3 = \frac{l(\gamma_1)^3}{2S_3'\delta_{11}'\delta_{12}'}f_{21}$$

$$K_4 = \frac{l(\gamma_2)^3}{2S_3'\delta_{21}'\delta_{22}'}f_{22}$$

$$f_1 = 6M_0 b\left[\frac{2}{\left(h^{[3]}\right)^3 E_x^{[3]} B} - \frac{\left(h^{[1]}+h^{[2]}\right)h_0}{I_0\left(h^{[1]}\right)^2 E_x^{[1]}}\right]$$

$$f_{21} = \frac{b}{l}\left[\frac{3\left(h^{[1]}+h^{[2]}\right)}{(\gamma_1)^2\left(h^{[1]}\right)^3 E_x^{[1]}} - \frac{h^{[1]}+6h^{[2]}}{20G_{xy}^{[1]}h^{[1]}} + \frac{b}{20G_{xy}^{[3]}B}\right]C$$

$$f_{22} = \frac{b}{l}\left[\frac{3\left(h^{[1]}+h^{[2]}\right)}{(\gamma_2)^2\left(h^{[1]}\right)^3 E_x^{[1]}} - \frac{h^{[1]}+6h^{[2]}}{20G_{xy}^{[1]}h^{[1]}} + \frac{b}{20G_{xy}^{[3]}B}\right]C$$

$$R = \frac{\left(1-\frac{2\eta_1}{l\alpha'}\right)f_1 + \frac{h_{11}}{\delta'_{11}\delta'_{12}}f_{21} + \frac{h_{12}}{\delta'_{21}\delta'_{22}}f_{22}}{\left(1-\frac{2\eta_1}{l\alpha'}\right)S'_1 + \frac{4\eta_1\alpha'}{l}S'_3}$$

$$C = \frac{2M_0}{I_0}\frac{\gamma_1\gamma_2 h_0 h^{[1]}}{(\gamma_1-\gamma_2)}$$

$$h_{11} = \left[2(\eta_1)^2-\beta'\right]\left[(\gamma_1)^2-\beta'\right] + 2\eta_1\alpha'(\eta_1-\gamma_1)$$

$$h_{12} = \left[2(\eta_1)^2-\beta'\right]\left[(\gamma_2)^2-\beta'\right] + 2\eta_1\alpha'(\eta_1-\gamma_2)$$

$$h_{21} = (\gamma_1)^2\left[2(\eta_2)^2(\alpha'-\beta') - (\beta')^2\right] + 2(\eta_2)^2\left[(\alpha')^2+\alpha'\beta'+(\beta')^2\right] + (\beta')^3$$

$$h_{22} = (\gamma_2)^2\left[2(\eta_2)^2(\alpha'-\beta') - (\beta')^2\right] + 2(\eta_2)^2\left[(\alpha')^2+\alpha'\beta'+(\beta')^2\right] + (\beta')^3$$

$$h_{31} = (\gamma_1)^2\left[2(\alpha'-\beta')^2 - 4(\eta_1)^2(5\alpha'+\beta')\right] + 2(\eta_1)^2\left[7(\alpha')^2 - 4\alpha'\beta' + (\beta')^2\right] + (\alpha'-\beta')^3$$

$$h_{32} = (\gamma_2)^2\left[2(\alpha'-\beta')^2 - 4(\eta_1)^2(5\alpha'+\beta')\right] + 2(\eta_1)^2\left[7(\alpha')^2 - 4\alpha'\beta' + (\beta')^2\right] + (\alpha'-\beta')^3$$

(5.19a-o)

where δ'_{11}, δ'_{12}, δ'_{21} and δ'_{22} take the similar forms of Eq. (4.38b-e).

$$\delta'_{11} = \gamma_1^2 - 2\eta_1\gamma_1 + \alpha' \tag{5.20a}$$

$$\delta'_{12} = \gamma_1^2 + 2\eta_1\gamma_1 + \alpha' \tag{5.20b}$$

$$\delta'_{21} = \gamma_2^2 - 2\eta_1\gamma_2 + \alpha' \tag{5.20c}$$

$$\delta'_{22} = \gamma_2^2 + 2\eta_1\gamma_2 + \alpha' \tag{5.20d}$$

Note that the variables α', β', γ_1, γ_2, η_1 and η_2 used in this simplified solution must take should take their simplified forms defined in Equations 5.16, 5. 4 and 5.17, respectively. The interfacial normal stress on PA and AC interfaces are as follow:

$$\sigma_y^{(1)} = \sigma_{y0}^{[2]} - \frac{h_0 h^{[1]} h^{[2]}}{2I_0}\left\{M_0\frac{\gamma_1\gamma_2\left[\gamma_1 e^{\gamma_1(x-l)} - \gamma_2 e^{\gamma_2(x-l)}\right]}{(\gamma_1-\gamma_2)} - q(x)\right\} \tag{5.21a}$$

$$\sigma_y^{(2)} = \sigma_{y0}^{[2]} + \frac{h_0 h^{[1]} h^{[2]}}{2I_0}\left\{M_0\frac{\gamma_1\gamma_2\left[\gamma_1 e^{\gamma_1(x-l)} - \gamma_2 e^{\gamma_2(x-l)}\right]}{(\gamma_1-\gamma_2)} - q(x)\right\} \tag{5.21b}$$

The maximum values for the normal stresses which are obtained when $x = l$ are:

$$\left[\sigma_{y0}^{[2]}\right]_{\max} = K_2 + K_3 + K_4 \tag{5.22a}$$

$$\left(\sigma_y^{(1)}\right)_{\max} = K_2 + K_3 + K_4 - \frac{h_0 h^{[1]} h^{[2]}}{2I_0}\left[M_0\gamma_1\gamma_2 - q(x)\right] \tag{5.22b}$$

$$\left(\sigma_y^{(2)}\right)_{\max} = K_2 + K_3 + K_4 + \frac{h_0 h^{[1]} h^{[2]}}{2I_0}\left[M_0\gamma_1\gamma_2 - q(x)\right] \tag{5.22c}$$

5.3.3 The Simplified Solution for Arbitrary Loads

From Section 5.3.2, we can see that there are two parts of calculation involved in seeking the stress distribution under the symmetric loadings. One of them is to calculate the interfacial shear stress using the classic laminate beam theory (CLBT), which is very straightforward and applicable to any loading patterns. The main challenge is to calculate the shear and normal stresses due to the end bending moment. Figures 5.2 c and d reveal that the stress concentration is virtually occuring in a local region near the plate ends, and the length of the region is only 20 percent of the half length of the bonded plate for the shear stress and 2 percent for the normal stress. In this region, the bonded plate is developing the stress transferred by the adhesive up to its full composite commission, so we call this region a transition zone. Beyond the transition zone, the full composite action takes place among the three material phases, in which CLBT is applicable. The length of the transition zone is called development length, and it is defined as the distance from the end of the plate to the point where full composite action occurs (Nguyen et al. 2001). Brosens and Gemert (1998) defined the development length as the length needed to attain 97% of the maximum force. Based on this definition together with Equation 5.9, we can calculate the development length l' using the following procedures

$$\int_{l-l'}^{l} \sigma_{xy}^{[2]}(x)dx = 0.97\Sigma_p \tag{5.21}$$

where Σ_p is the stress results in a cross section of the bonded plate under the end bending moment M_0. Hence

$$l' = \frac{\ln(\gamma_1) - \ln(\gamma_1 - \gamma_2) + 3.55}{\gamma_2} \tag{5.22}$$

In practical engineering, the bonded plate is always long enough to develop the full stress, that is, the bonded length $l > 2l'$.

The concept of development length also provides a tool to extend the present simplified solution to those beams subjected to an arbitrary loading. We can use the conclusion, that the end bending moment only affect the interfacial stress within the development length. So the solution of Eqautions 5.9 and 5.18 can be utilized to calculate the stress solutions within the development length associated with any plate end provided that the cross section at the plate end experiences a bending moment M_0. As a result, the interfacial stresses for a plated beam subjected to an arbitrary loading can be achieved in two steps:

1 Calculate the interfacial shear stress using the CLBT;
2 Find the development length of the given beam configuration;
3 Calculate the bending moment in the cross sections at both plate ends;
4 Calculate the interfacial shear and normal stresses using Equation 5.9 and 5.18 for the transition zones at both ends using the bending moment from (3);
5 The final interfacial normal stresses in the two transition zones are from (4) and zero for the other regions;
6 The final interfacial shear stresses in the two transition zones are those from (4) superposed by those from (1) and in the other regions is from (1) only.

5.4 Verification Examples and Applicability Study

The verification examples in Section 4.3.3 of Chapter 4 are used here to verify the simplified solutions by comparing them with the rigorous solutions and/or the other approaches. Figures 5.3 show the stress distributions for the first verification example, i.e. the steel plated beam, in which both the simplified solution, rigorous solutions, and an approximate solution from Smith and Teng (2001) are displayed for comparison. In Figure 5.3 (a), which shows the normal stresses in the AC interface, MA section and PA interface, we can observe that Smith and Teng's solution predicts much lower normal stress that is close to that for the MA section predicated by the present solutions. The simplified solution predicts slightly lower normal stress, more significant in the AC interface. However, the discrepancy between the rigorous and the simplified one is very limited, say, below 10% for the peak value.

Figure 5.3 (b) plots the shear stress. Only a single value has been developed as both the present and the approximate solution assume a constant distribution of shear stress

in the adhesive layer. Smith and Teng (2001)'s approximate solution predicts the shear stress in a monotonic trend in contrast to the present solution achieving a zero-valued shear stress at the plate end. As a result, the present solution yields a much lower peak stress. Like the normal stress, both rigorous and simplified solution show a very good agreement.

The stress distribution for the second example are plotted in Figures 5.4, where three groups of results are compared, i.e. Shen et al. 's (2001) high-order solution, present rigorous and simplified ones. The same dimensionless form is used as that in Section 4.3.3 of Chapter 4. For the simplified solution, only the stress in the AC interface is plotted. From the figures, we can see that in general the shear stresses from the stress solution are very closed (see Figures 5.4b). There is a clear discrepancy for the interfacial normal stresses (see Figures 5.4a) between Shen et al.'s and present results. That is due to the applied assumption with regards to the relationship between the interfacial shear and normal stress in Shen et al.'s solution. Another encouraging observation is that the predictions based on the rigorous and the simplified solutions are very close, which again provides verification of the present simplified solution.

As an additional verification example, we re-visit the example in Section 3.5.5 in Chapter 3, where its results was achieved using the approach of superposition. In Figures 5.5, The present simplified solution is compared with Smith and Teng (2001) and Yang et al. (2004).

Selected distributions for both normal and shear stresses are plotted in the figures. In Figure 5.5(a), two stress distributions are presented, in the AC interface and the MA section. The normal stress in the AC interfaces is predicted by present simplified solution and Yang et al's (2004) solution. Clearly, Yang et al.'s solution leads to a much higher peak stress value as it always does. Quantitively, the former is more than twice the later. The stress in the MA section is given by the present simplified solution, and in the figure this curve is actually very close to the results predicted by Smith and Teng. It is reasonable, because Smith and Teng (2001) assumed that the normal stress remains constant along the whole adhesive layer, which imposes an average stress distribution along the thickness direction.

In Figures 5.5(b), the three curves are, respectively, related to the present simplified solution, Yang et al's (2000) solution and Smith and Teng's (2002) approximate solution. As Yang et al. pointed out that the shear stress along the AC interface and PA interface is very close, only one of them is plotted in the figures. The large figure in Figures 5.5 (b) focuses on the details at both ends and the small one in the upper right area gives the overall distribution. Again, Smith and Teng predicted a higher peak shear stress. Yang et al. and present simplified results are rather close; they provide comparable peak stresses. However, the present simplified solution leads to a peak position closer to the plate end.

As seen in the derivation of the simplified solution, we neglected the stress concentration due to the transverse load. To investigate the applicability of this assumption, we compare the results between the rigorous and simplified solution for three different ratios of the plate end bending moment and plate end shear force (see Table 5.1). This is implemented by changing the length of the bonded plate for a given beam. We use the same geometrical and material properties as those used in Section 5.2 except the half-span of bonded plate l, which are now designed as 800mm, 1000mm and 1200mm respectively. This leads to three different ratios of the internal bending moment to the internal shear force at the plate end and the data are summarized in Table 5.1. It is noted that for the three-point bending and four-point bending, the ratio of bending moment to the shear force at the plate end is, in fact, the length between the support and the adjacent plate end.

Table 5.1 Various ratios of bending moments to the shear forces

	Case I	Case II	Case III
l (mm)	800	1000	1200
M_l / Q_l (mm)	1006	625	338

Figure 5.6 show the normal and shear stress distributions for the above three cases. The same dimensionless parameters are used as those in Figure 5.2, i.e. the stresses are normalized by the maximum stress in the concrete that is the same for all three cases.

From Figure 5.6 (a), we can see that the smaller the ratio is, the larger the discrepancy between the two solutions emerges. This is attributed to the fact that when the end shear force or the transverse load is relatively greater, their contribution to the stress concentration is more profound. However, the largest relative discrepancy is within 5%, which suggests that the simplified solution may be used for any bonded ration. Figures 5.6(b) further suggests that the simplified solution provides a satisfactory approximation to the rigorous one.

5.5 Conclusions

Based on the rigorous solution developed in Chapter 4, a simplified version has been proposed by omitting the numerically small terms. Due to the simplicity, the solution can be computed using a portable calculator, which is more practical in industrial practice. Comparing with other methods as well as the rigorous solution, this solution shows high accuracy. The wide applicability demonstrated by the example suggests that the solution can be applied for most bonded ratio. Furthermore, by introducing the concept of the development length, this method can be extended to analyse beams subjected to arbitrary loading pattern. Thus, the present study provides a potentially useful solution that can be further exploited to investigate the problem of end debonding and conduct parametric studies with highly reduced computational efforts.

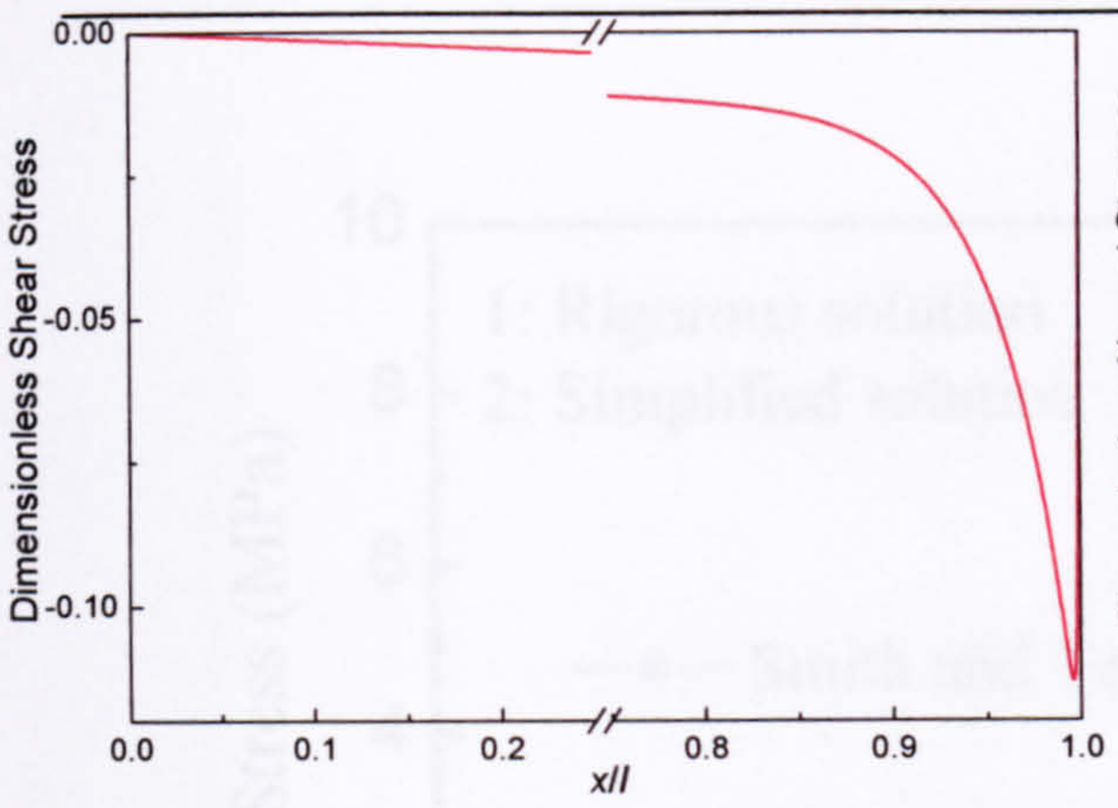

(a) Shear stress for the original beam

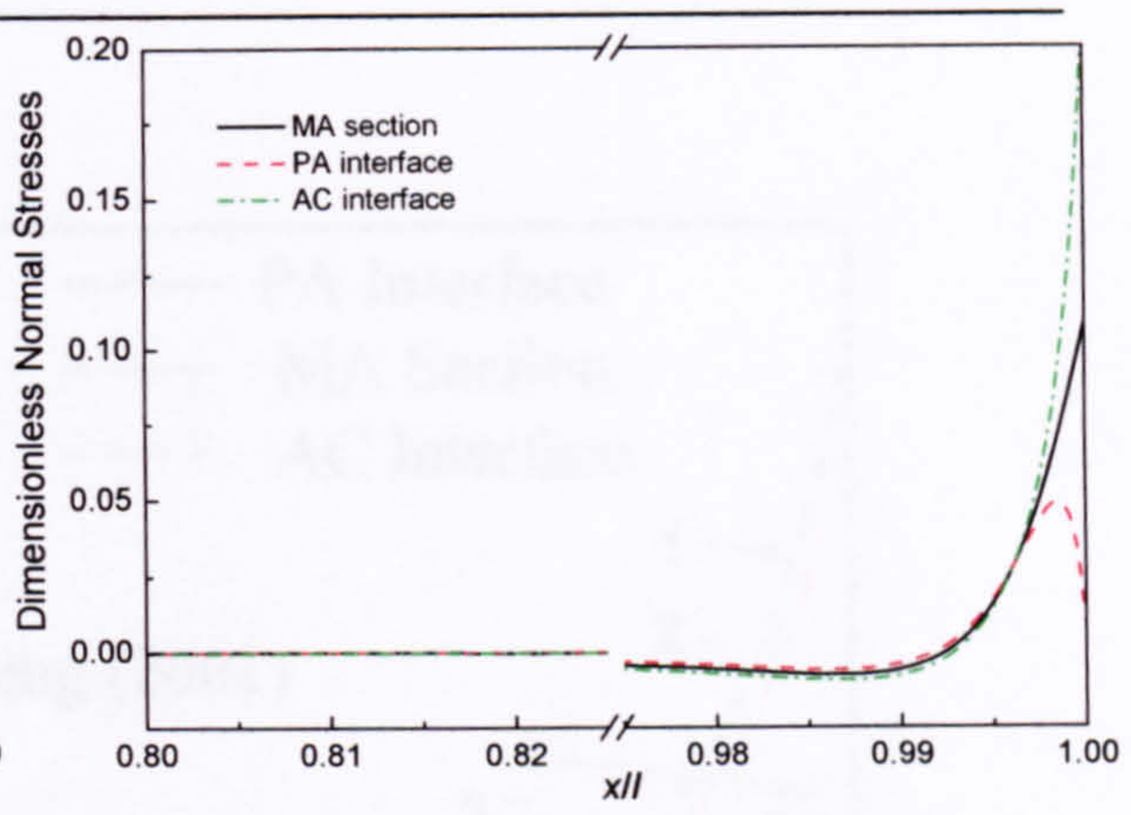

(b) Normal stress for the original beam

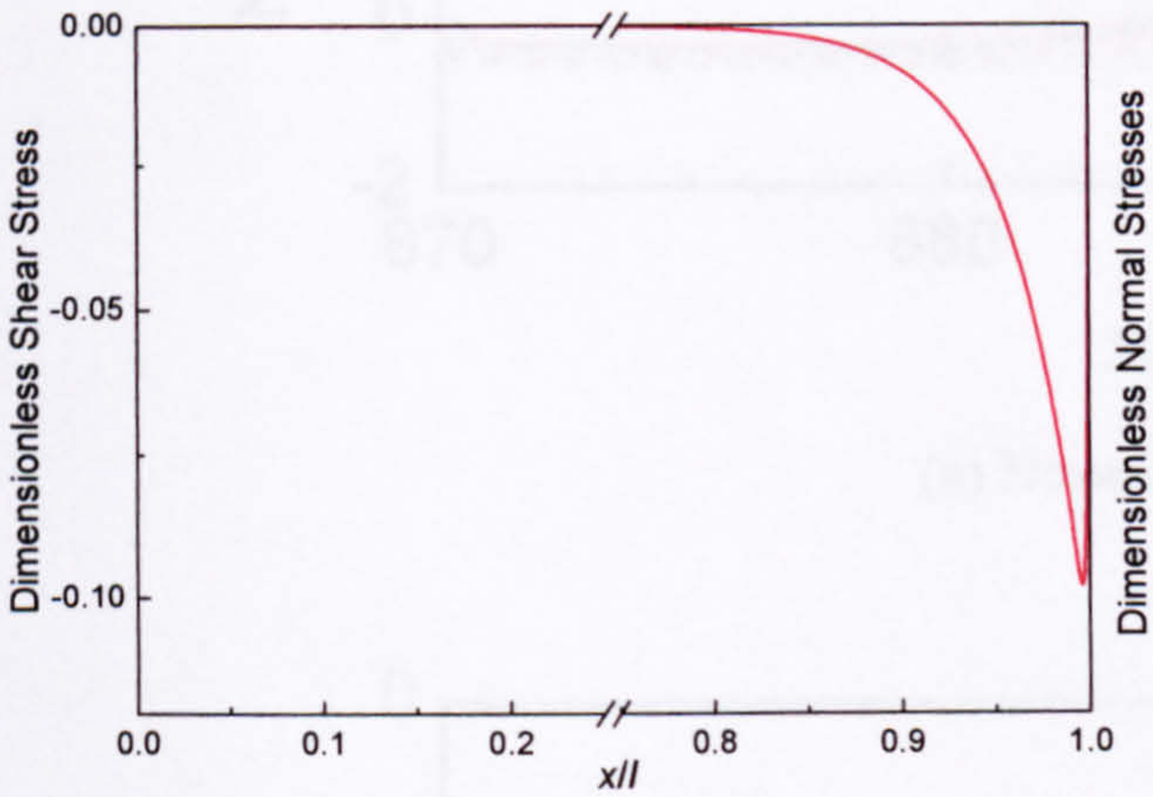

(c) Shear stress for Beam I

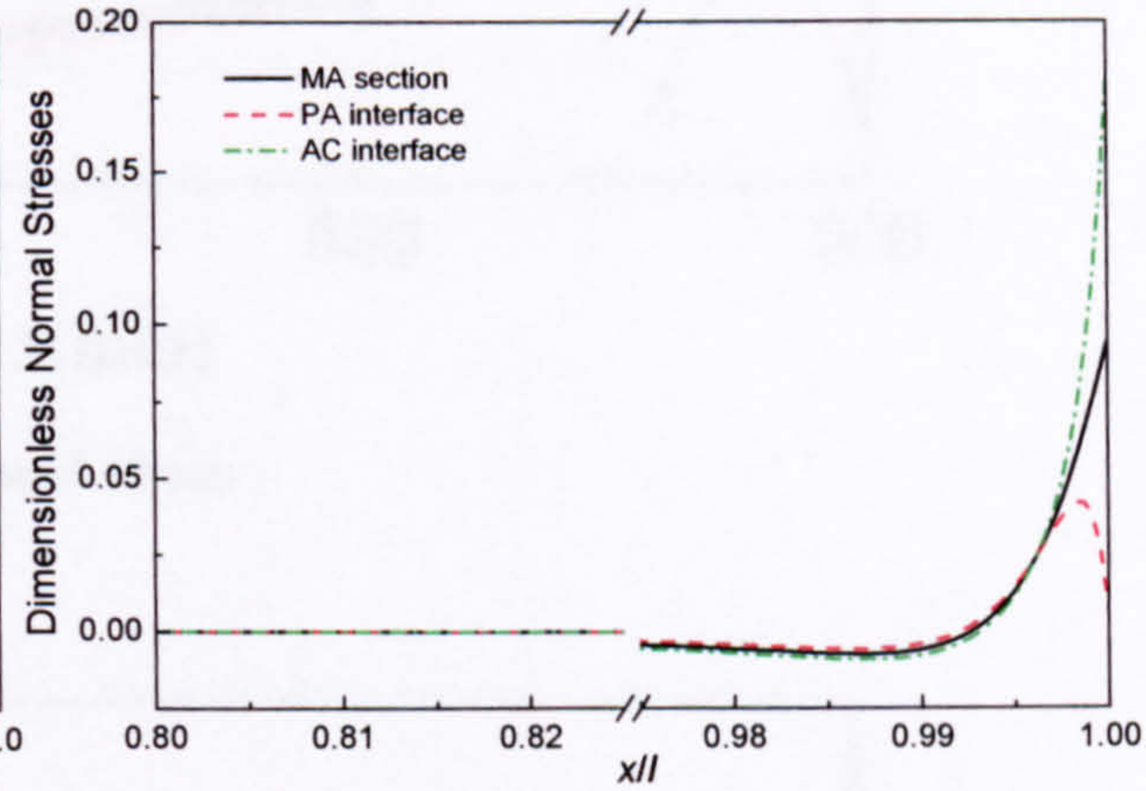

(b) Normal stress for Beam I

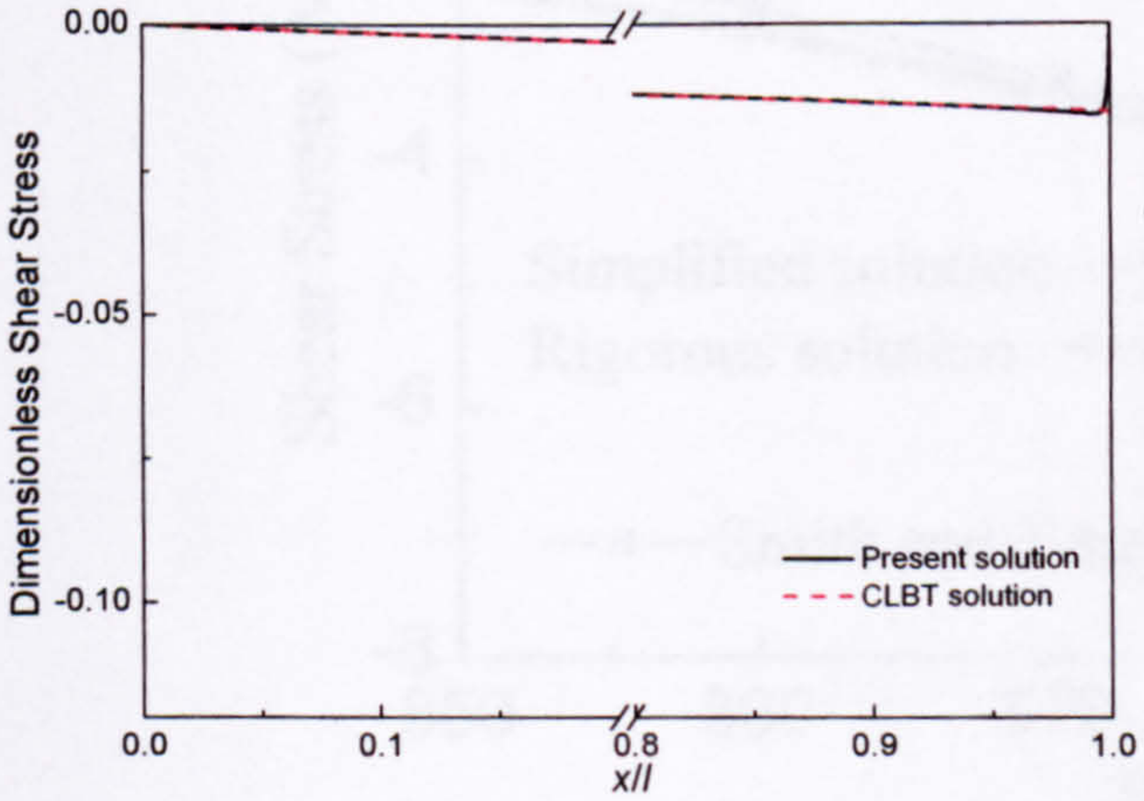

(e) Shear stress for Beam I I

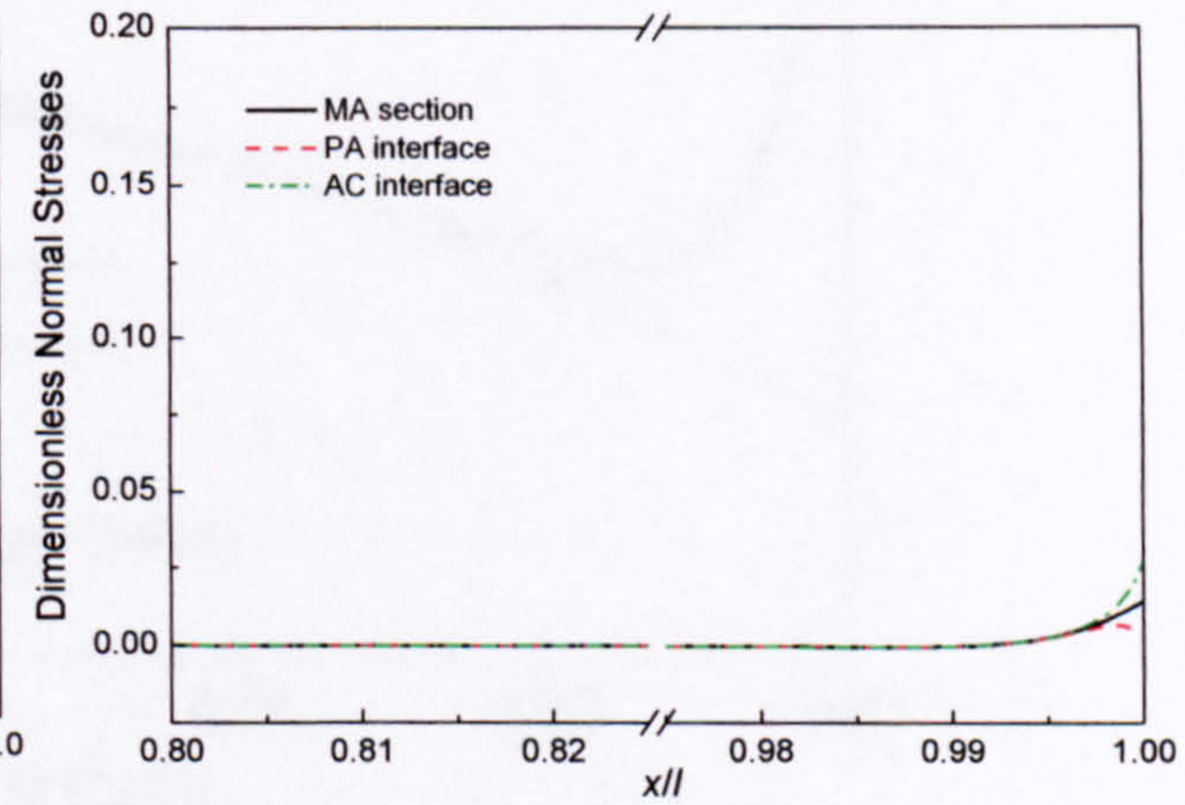

(f) Normal stress for Beam II

Fig. 5.2 Dimensionless interfacial shear and normal stresses

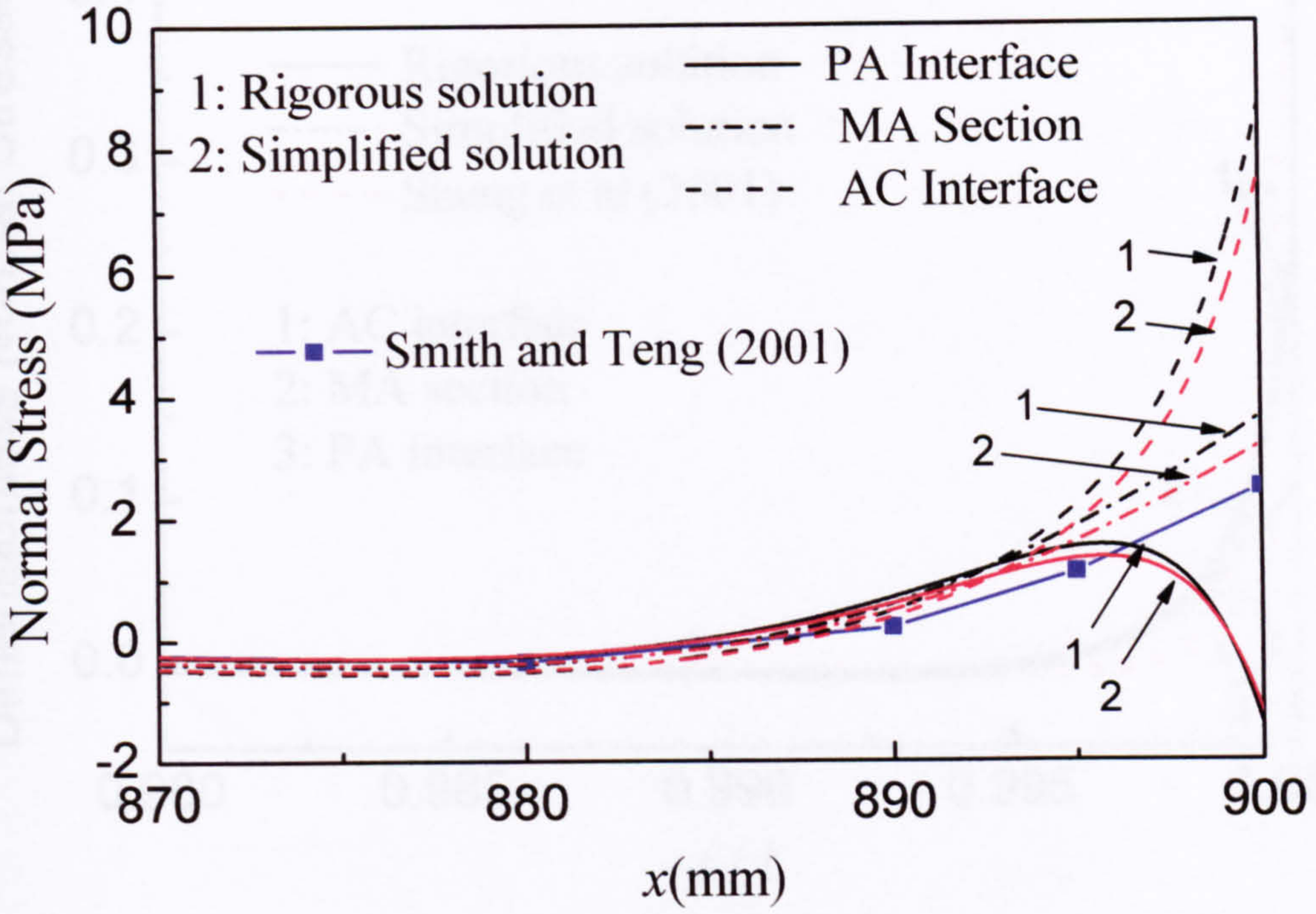

(a) Normal stress

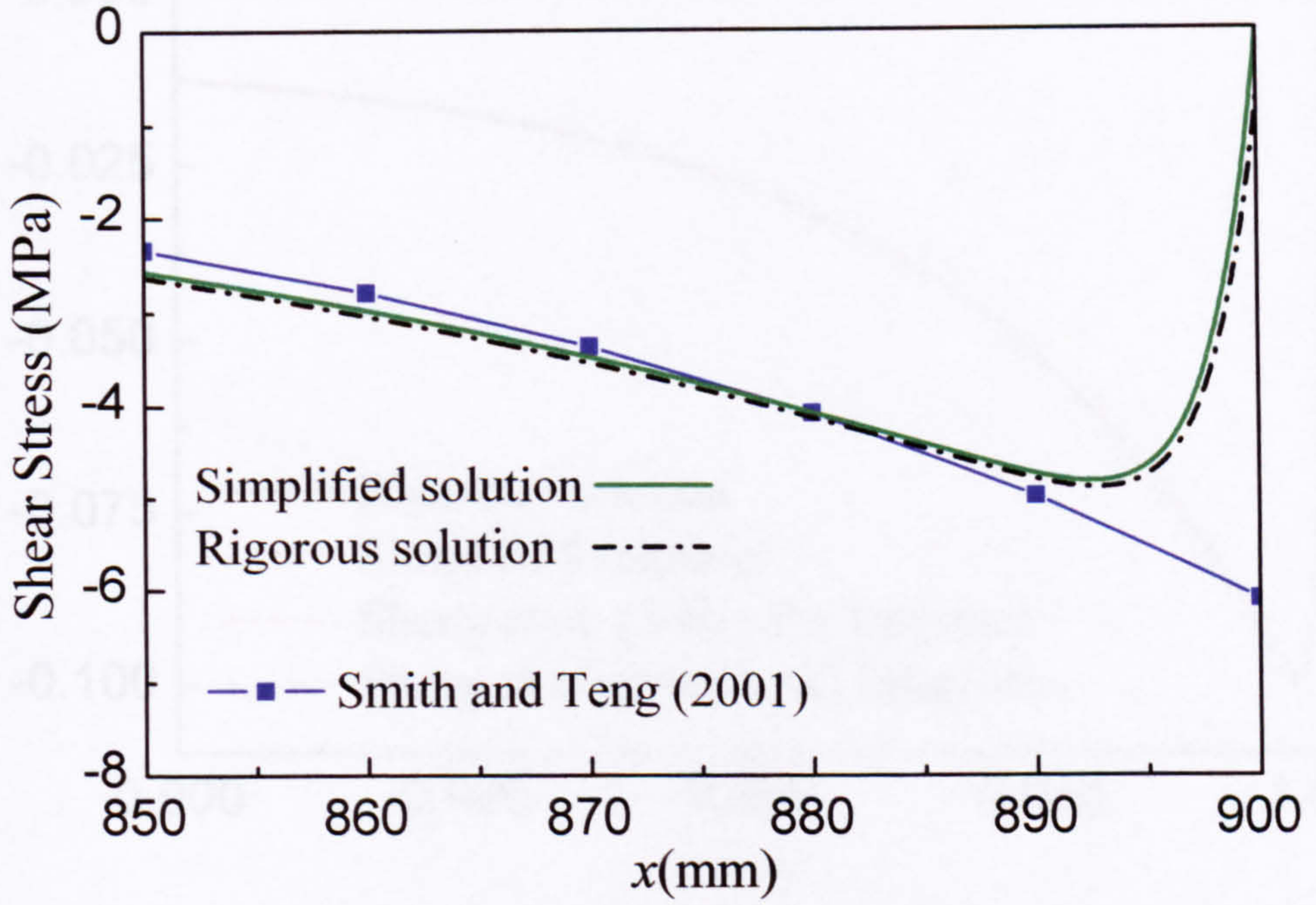

(b) Shear stress

Fig. 5.3 Comparison of the stress solutions for steel plated beam

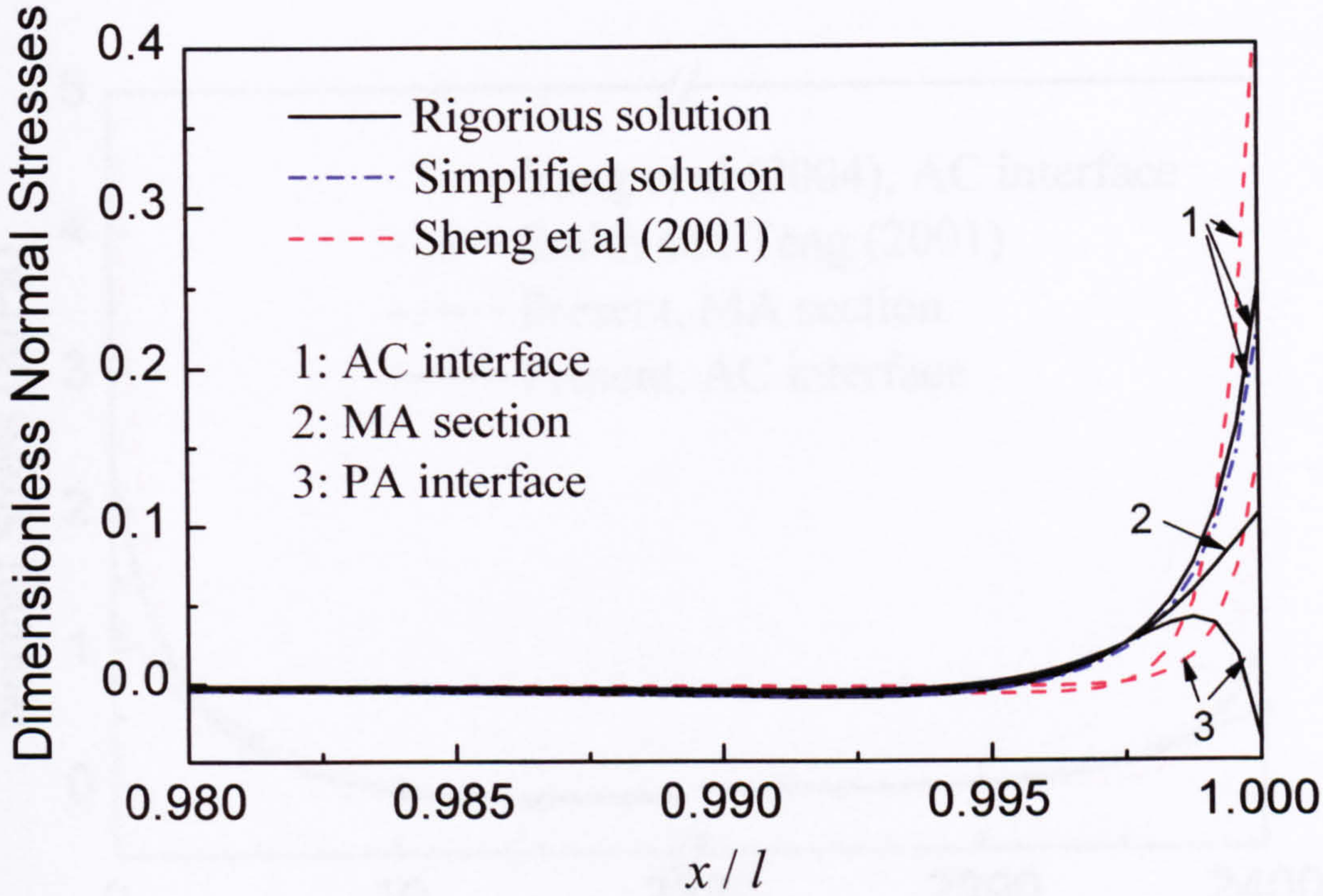

(a) Normal stress

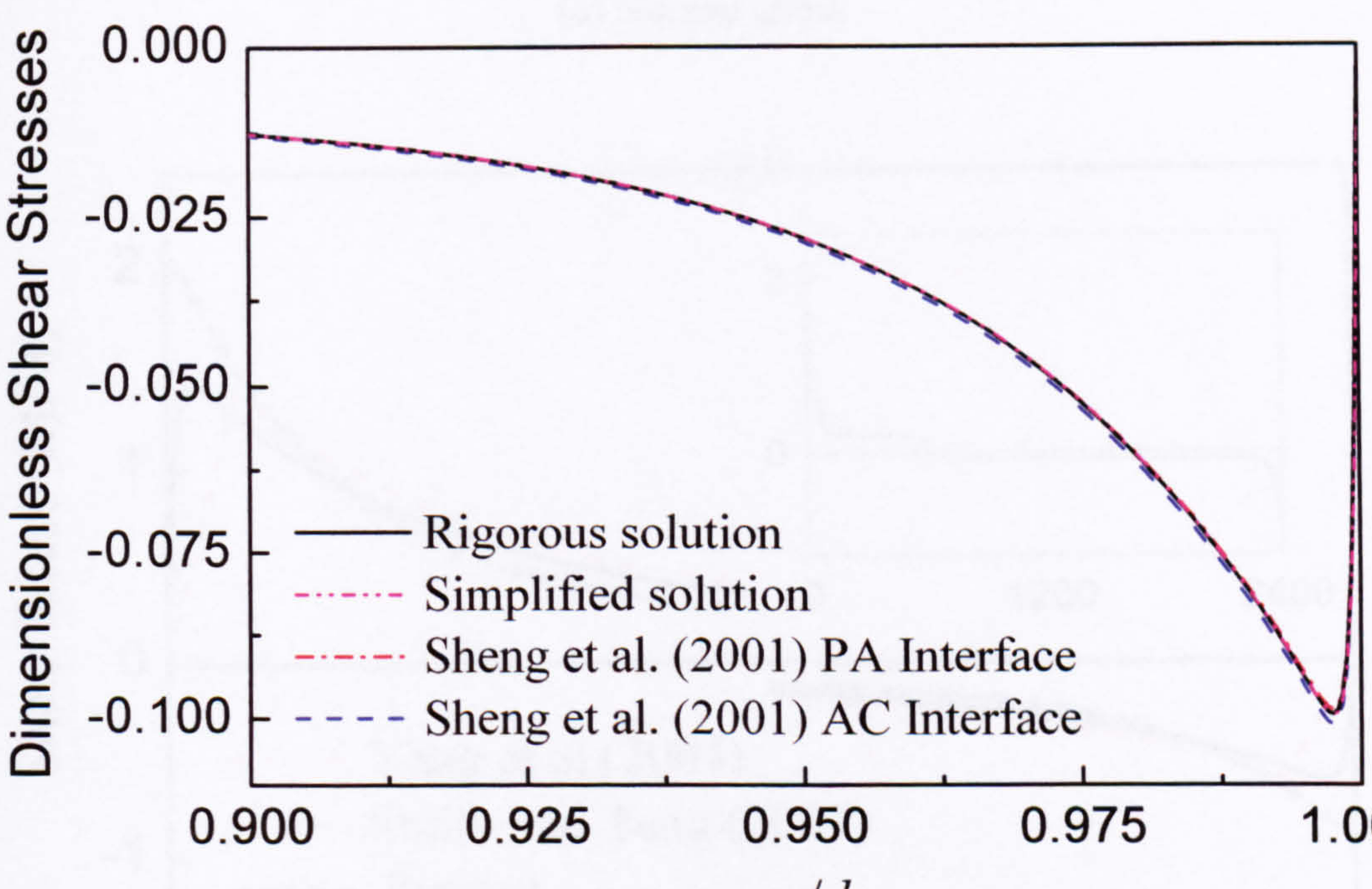

(b) Shear stress

Fig. 5.4 Comparison of the stress solutions for GFRP plated beam

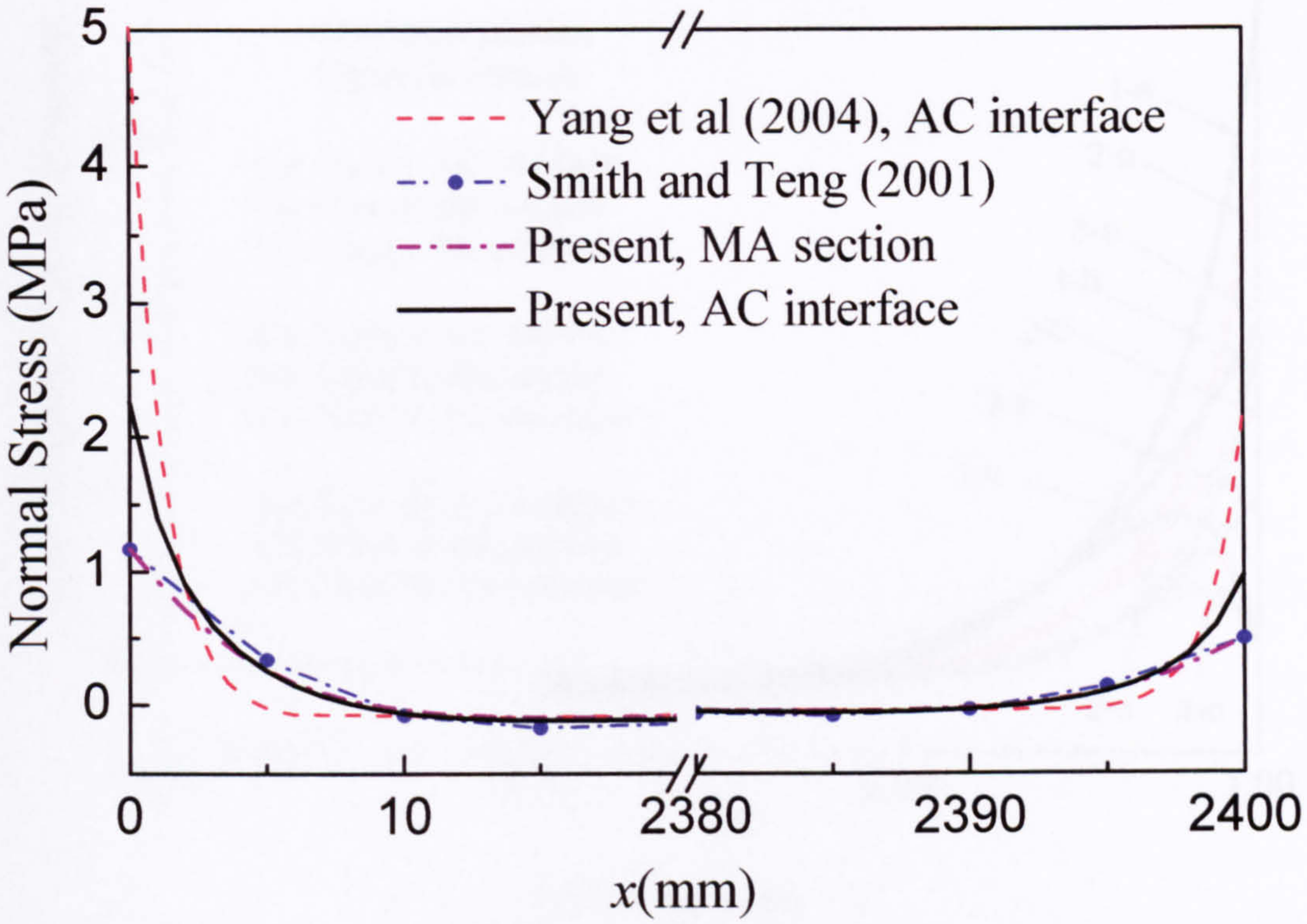

(a) Normal stress

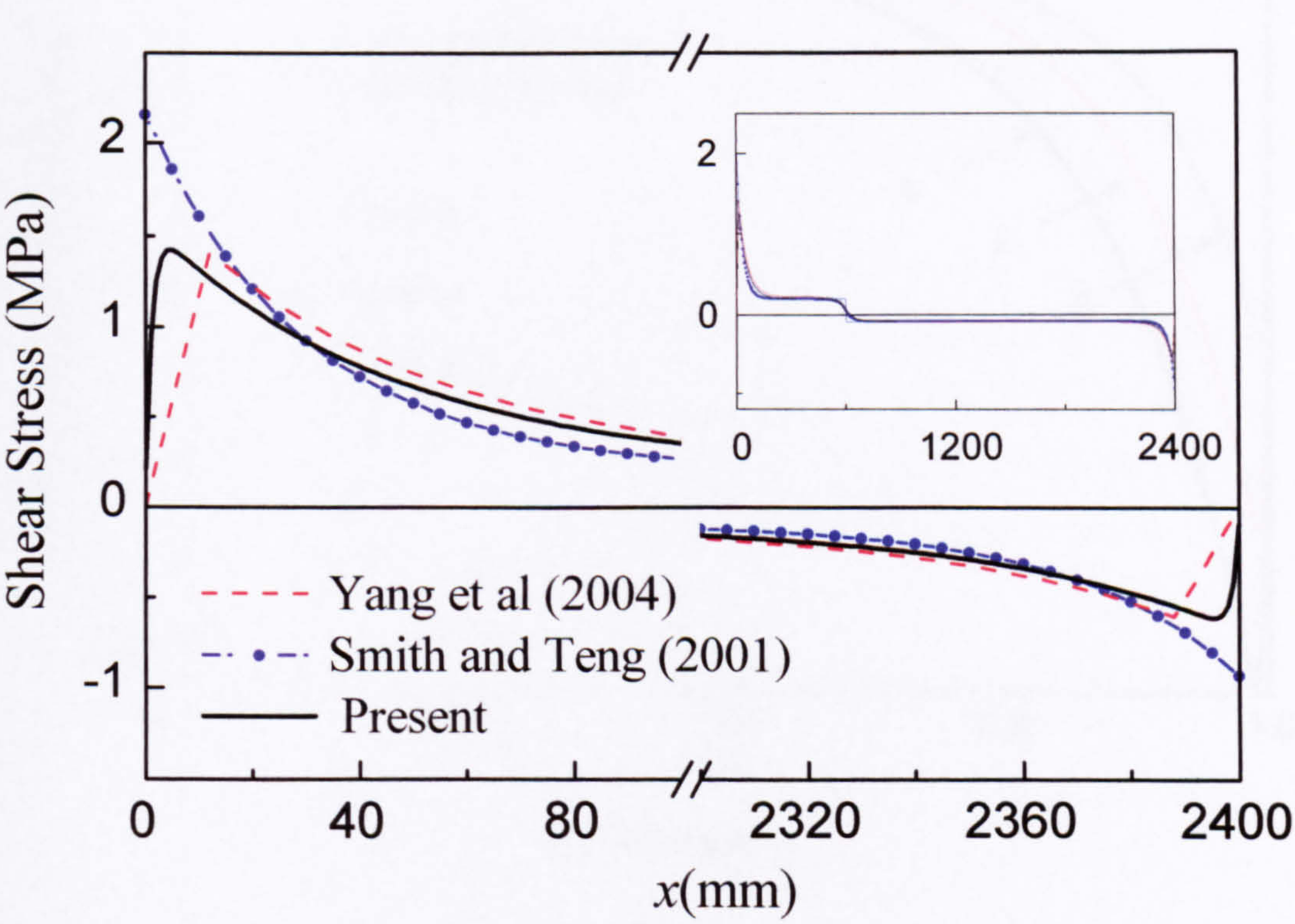

(b) Shear stress

Fig. 5.5 Comparison of the stress solutions for CFRP plated beam under a single point load

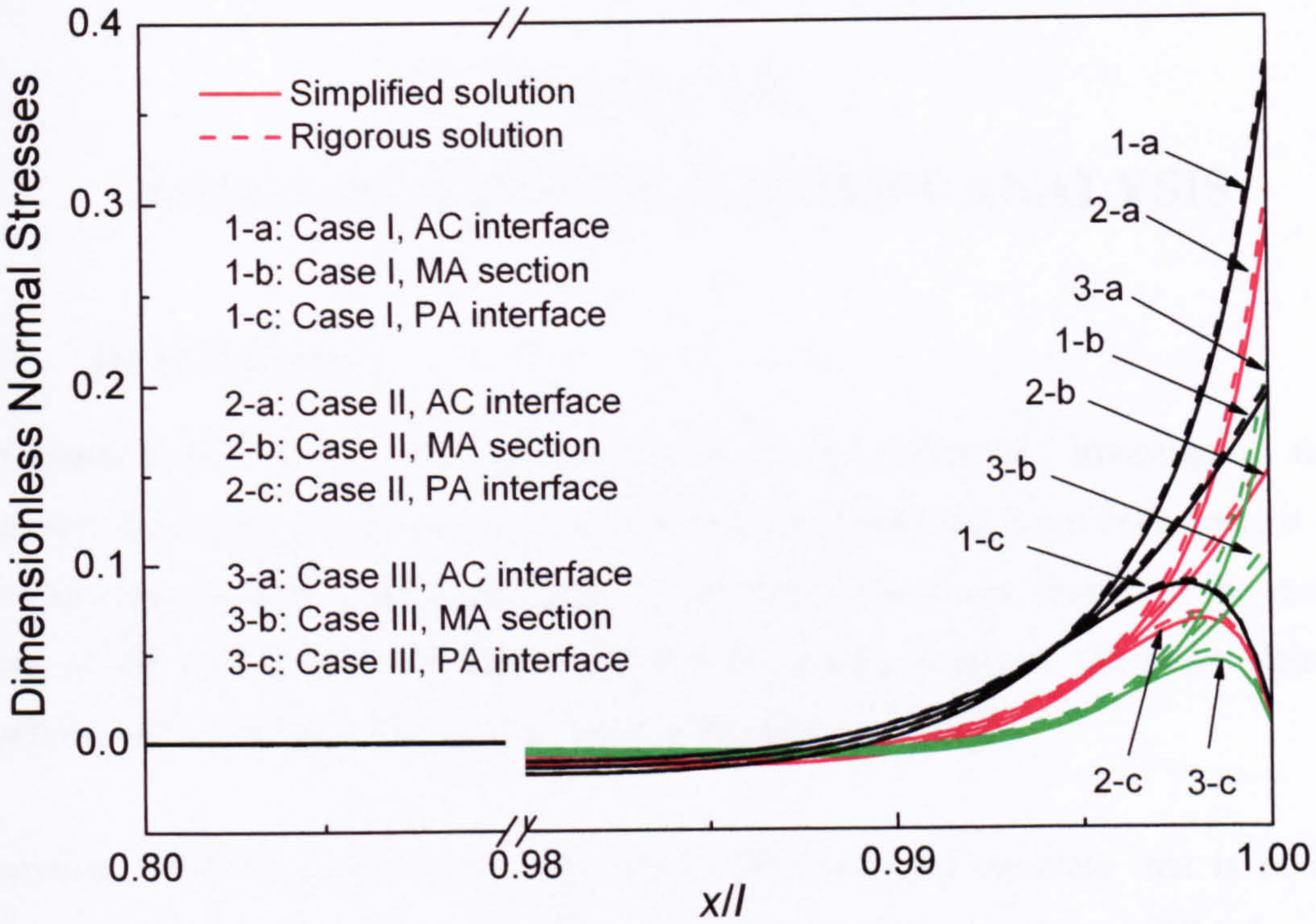

(a) Normal stress

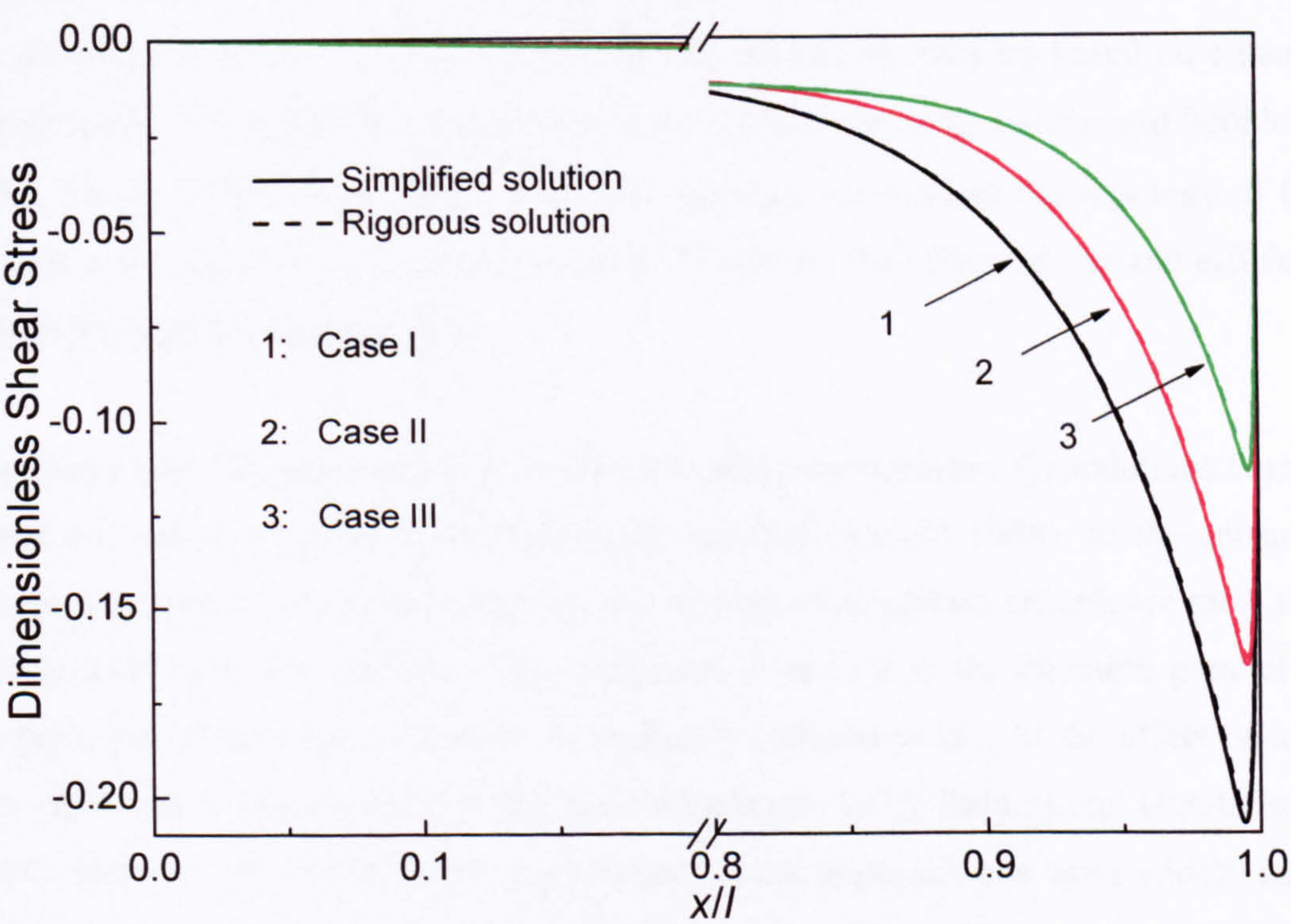

(b) Shear stress

Fig. 5.6 The comparisons between the simplified and rigorous solutions under various ration of bending moment to shear force

CHAPTER 6.

NONLINEAR FINITE ELEMENT ANALYSIS

6.1 Introduction

Structural behaviour of concrete elements has been extensively investigated since concrete materials came into use. Most of the investigations have been carried out through experiments, particularly in the early time. Nowadays, thanks to the inventions of the powerful computing station and personal computers, the finite element analysis (FEA) has provided a very useful alternative approach.

However, modelling the complex behaviour of reinforced concrete that is nonhomogeneous and anisotropic, is a difficult challenge in the applications of FEA for civil engineering structures. Most early finite element models of reinforced concrete used the discrete crack approach, which included the effects of cracking based on either a pre-defined crack pattern or strength-determined crack occurrence (Ngo and Scordelis 1997; Nilson 1968; Yang 2003). With this approach, changes in the topology of the models were required as the load increased. Therefore, the effectiveness and efficiencies of the analysis were limited.

A smeared cracking approach was introduced using isoparametric formulations to represent a cracked concrete as an orthotropic material (Rashid 1968). In the smeared cracking approach, cracking of the concrete occurs when certain criteria are met. The elastic modulus of the material is then assumed to be zero in the direction parallel to the principal tensile stress direction or gradually reduced to zero if the effect of tension stiffening is considered (Suidan and Schnobrich, 1973; Rahimi and Hutchinson, 2001). Because of its simplicity, the smeared crack approach has been widely used and is available in many general purpose commercial FEA package (e.g. ABAQUS, ANSYS) despite its inherent disadvantages such as mesh sensitivity. It will also encounter convergence difficulty due to the local instability when part of the concrete crushes or cracks and hence the simulation fails to obtain the ultimate load.

Due to the nature of feasibility, FEA is also used to verify the laboratory investigation (Arduini, et al. 1997, Tedesco, el al. 1999). Some modern FEA packages such as ABAQUS, can simulate the complicated material properties of the concrete, from pre-failure to post-failure, and various failure mechanisms, from ductile to brittle.

In this chapter, numeral analyses are carried out and comparisons with experimental cases reported in existing publications (Fanning and Kelley, 2001) are made. The tested beams include a virgin RC beam and some RC beams strengthened by CFRP sheets. The geometrical dimensions are shown in Figure 6.1. The length of the beam is 3000 mm; it has a rectangular cross section with 155mm in width and 240mm in height. Three 12mm diameter high yield steel bars with an effective depth of 203mm are included for the tensile reinforcement and two 12mm diameter bars at a depth of 37mm were specified in the compression zone. Shear links are provided by 6mm mild steel bars at 125mm centre to centre. Two of the beams are strengthened by CFRP composite plates bonded to its soffit with a two-part epoxy resin adhesive. The geo-metrical dimensions are: 2050 mm and 1700mm in length, 120mm in width and 1.2mm in thickness. The thickness of the adhesive layer is 3mm.

(a) Virgin RC beam

(b) Strengthened RC beam

Fig. 6.1 Geometrical dimensions of virgin and strengthened beams

6.2 Element Type

6.2.1 Concrete, Adhesive Layer and Bonded Sheet

A 4-node bilinear isoparametric plane stress element CPS4 (Figures 6.2 a and b) is used to model the concrete, adhesive layer and bonded sheet. Like CPS8, each node has two active degrees of freedom, i.e. u_x and u_y. Full integration schemes are numerically implemented, and the integration points are showed in Figure 6.2 b. The SOLID SECTION option is used to define the properties of the section including geometrical dimension in the thickness direction and material properties.

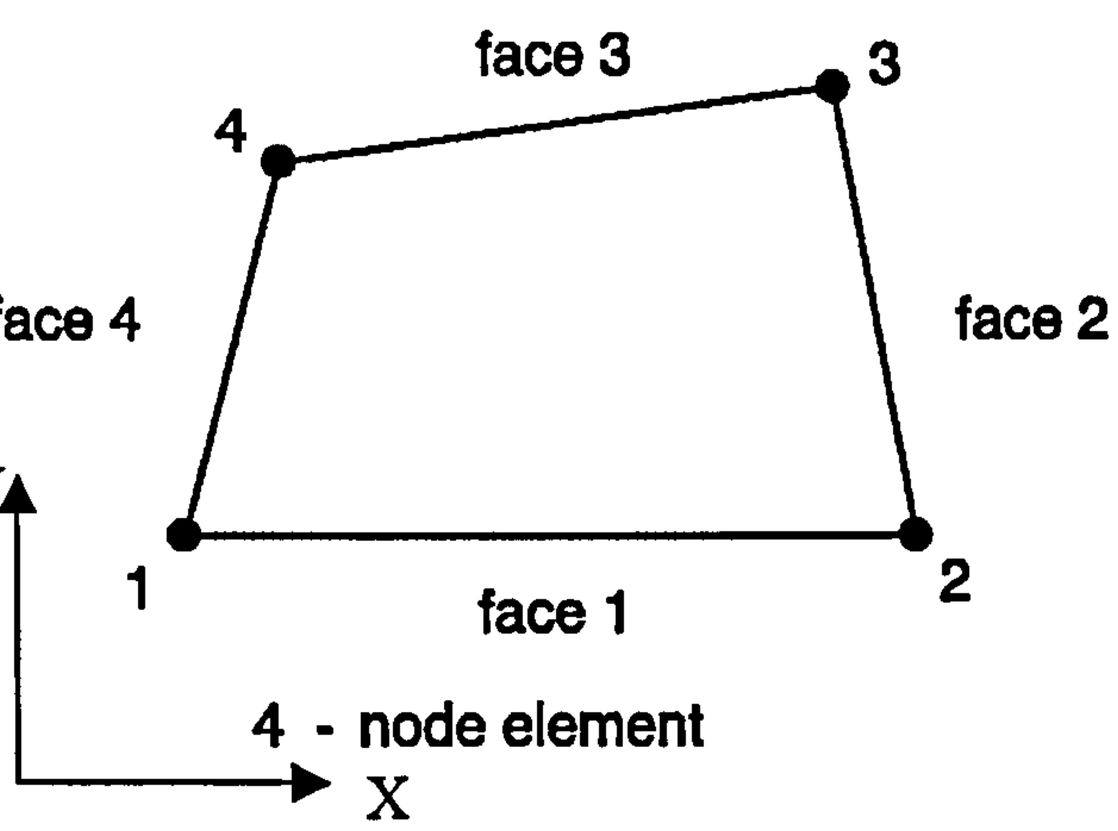

(a) Nodes for CPCS4

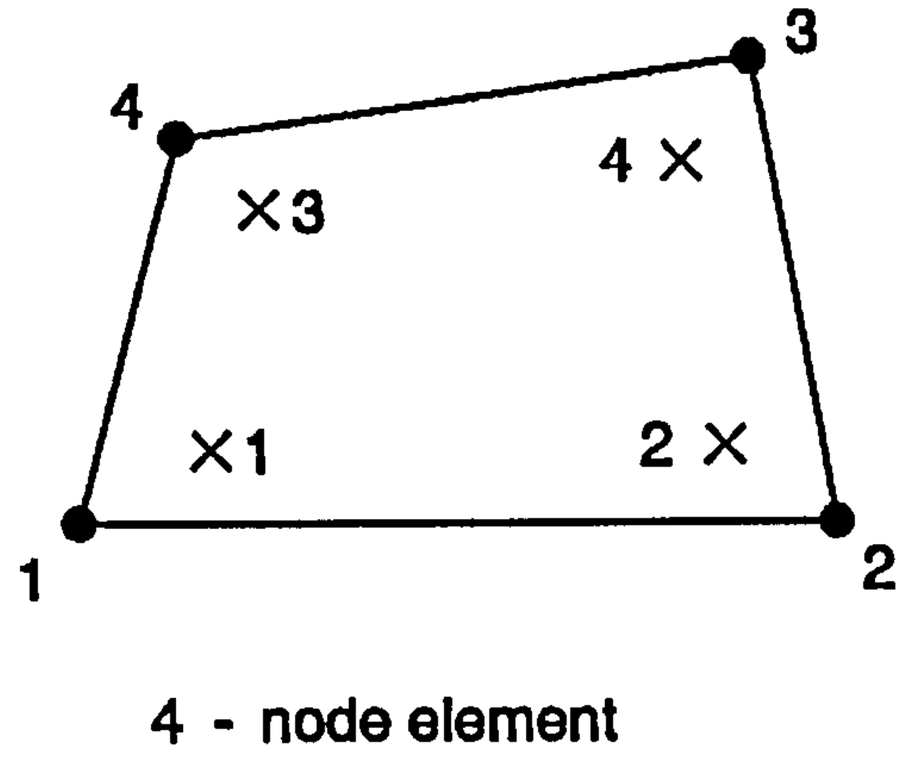

(b) Integration points for CPCS4

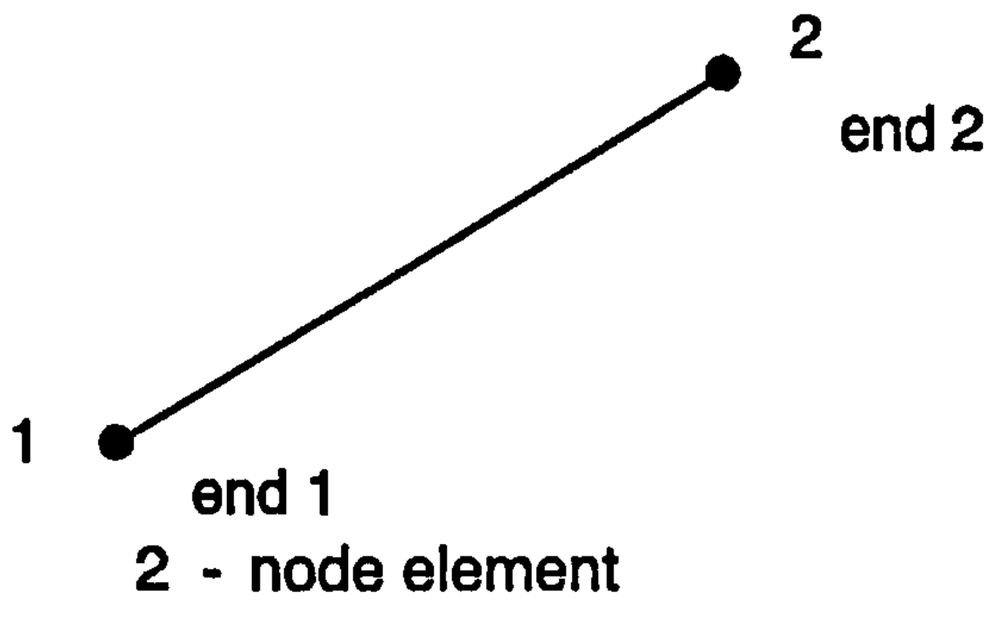

(c) Nodes for T2D2

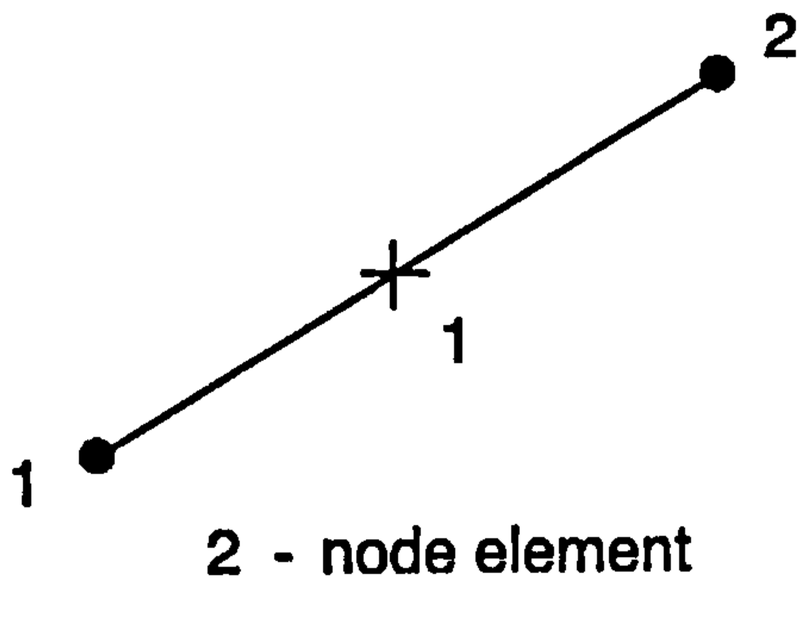

(d) Integration point for T2D2

Fig. 6.2 Element types for the modelling

6.2.2 Reinforcement

A 2-D stress/displacement truss element T2D2 is used to model the tensile/compressive rebars and shear links which are assumed to deform only in the directions of either axial extension or shortening. They are rigidly jointed at their nodes and only the translation displacements, i.e. u_x and u_y, at each node are considered. The SOLID SECTION option is used to define the cross-sectional area of the elements and the MATERIAL option is used to define their materials properties.

6.3 Materials

6.3.1 Concrete

6.3.1.1 *The Characteristics of Uniaxial Stress - Strain*

Development of a model for the behaviour of concrete is a challenging task. Concrete is a quasi-brittle material and has different properties in compression and tension. The uniaxial tensile strength of concrete is typically 8-15% of the compressive strength (Shah el al. 1995). Figure 6.3 (a) shows a typical uniaxial stress-strain curve for normal weight concrete (Bangash 1989). As we can see from the curve, in compression, the stress-strain curve for concrete is linearly elastic up to about 30 percent of the maximum compressive strength. Above this point, the stress increases nonlinearly up to the maximum compressive strength. After it reaches the maximum compressive strength f_c', the curve descends into a softening region, and eventually crushing failure occurs at an ultimate strain ε_{cu}. In tension, the stress-strain curve for concrete is approximately linear elastic up to the maximum tensile strength. After this point, the concrete cracks and the strength decreases gradually to zero.

6.3.1.2 *Cracking and Cracking Behavior Modeling*

In this study, the concrete is assumed to be an isotropic material prior to cracking. The smeared crack model is used which does not track individual "macrocracks". Constitutive calculation is performed independently at each integration point of the FE model. The presence of cracks enters into the calculations in which the cracks affect the stress and material stiffness associated with the integration points.

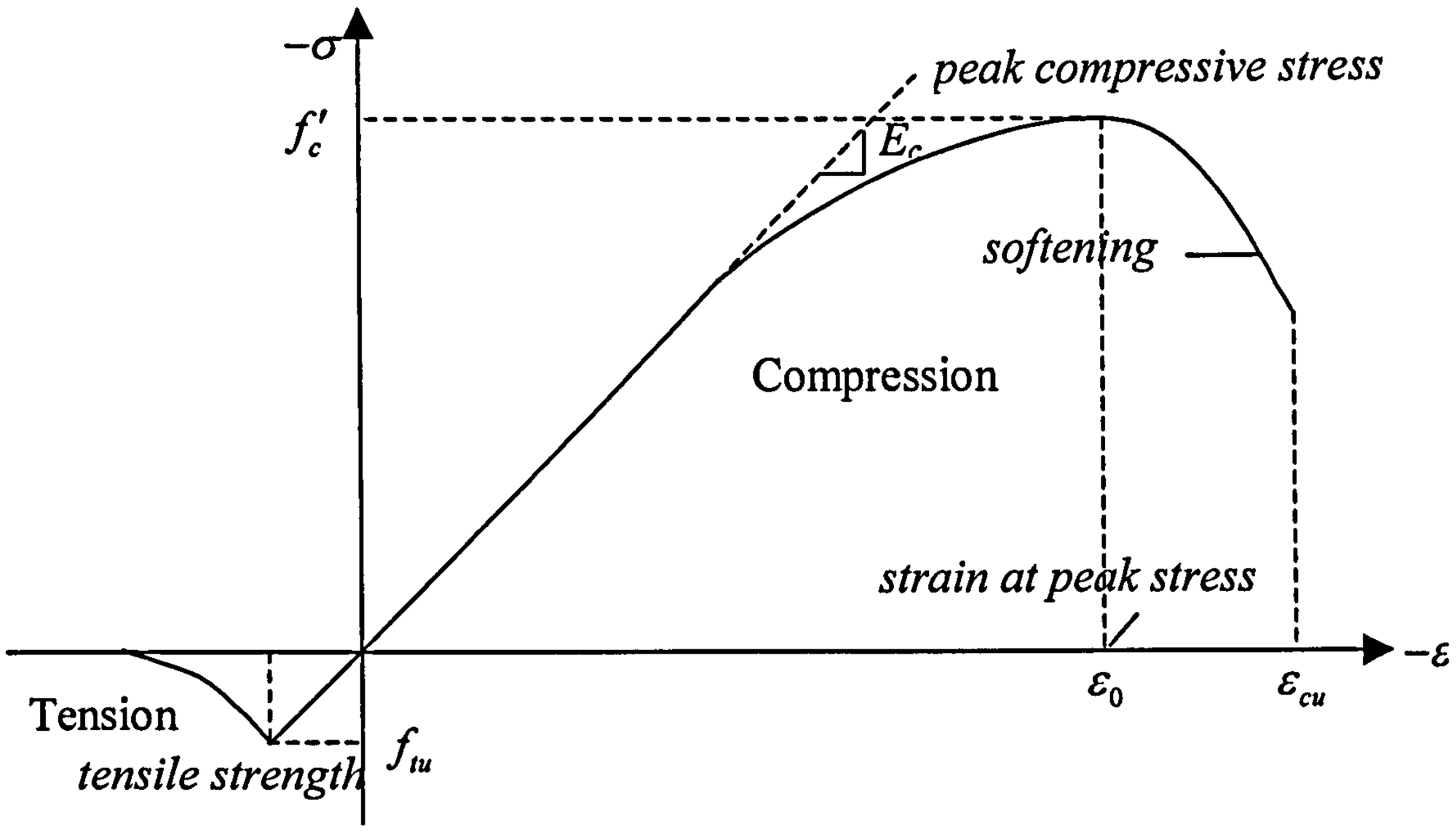

(a) Typical stress strain curve for concrete

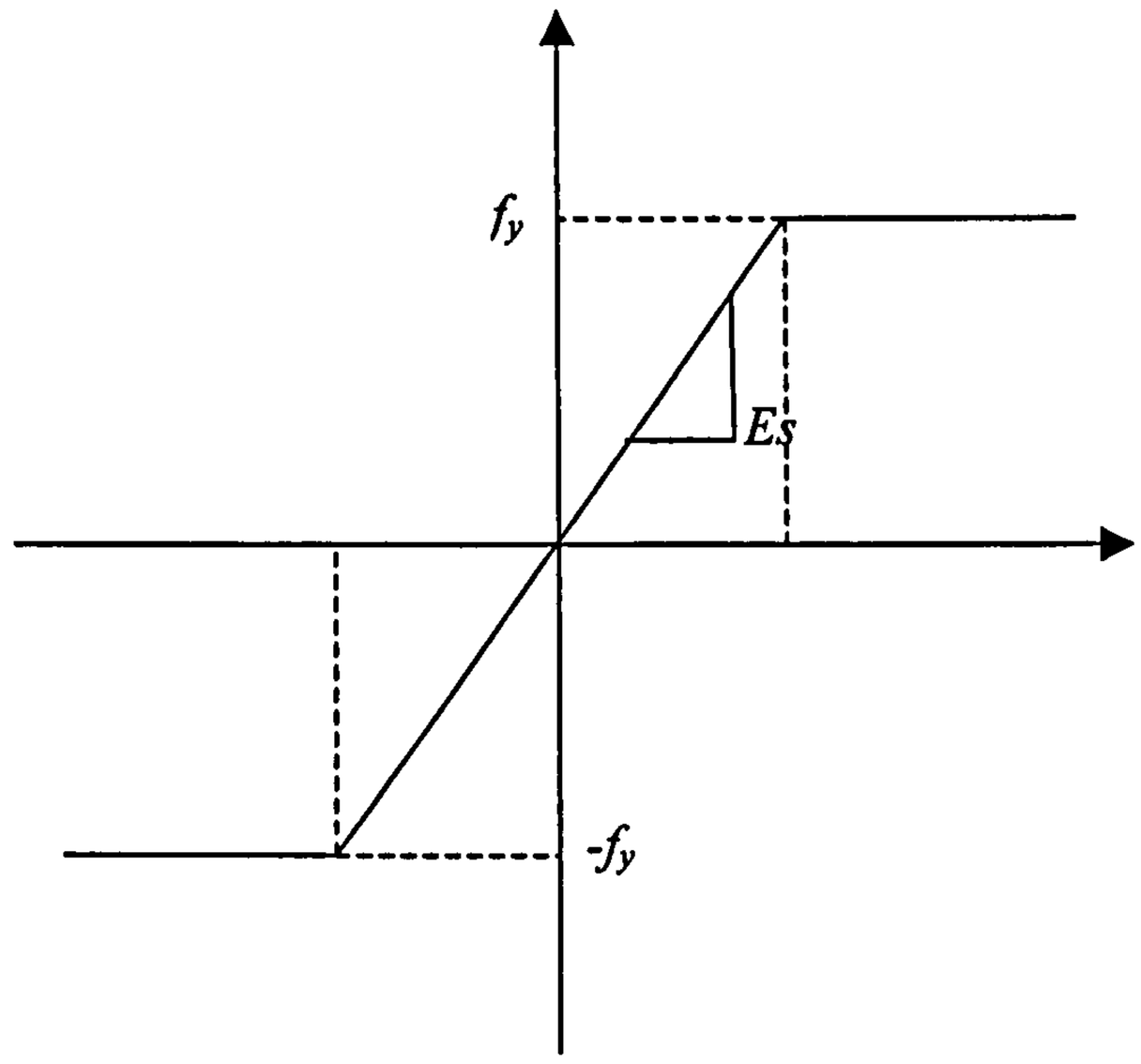

(b) Elastic perfectly plastic material model for structural steel

Fig. 6.3 Material models

Cracking is assumed to occur when the stress reaches a failure surface that is called the "crack detection surface" (see Figure 6.4). This failure surface is a linear relationship between the equivalent pressure stress, p and the Mises equivalent deviatoric stress, q. When a crack is detected, its orientation is stored for subsequent calculations. Further cracking at the same point is restricted to being orthogonal to this direc-

tion since the stress components associated with an open crack are not included in the direction of the failure surface used for detecting the additional cracks. There are three methods determining the crack directions in general, i.e. fixed orthogonal cracks, rotating crack, and fixed multidirectional cracks. ABAQUS uses the fixed orthogonal direction for the cracks. This model will result in some unrealistic results as shown in the following discussion. It also allows the orthogonal crack model to be used with the option to consider shear retention by modifying the shear modulus in the presence of the cracks either in open or closed status. The ABAQUS model defines the total shear stress in relation with the total shear strain, whereas the traditional shear retention model defines the shear stress-strain relationship by incremental form. In this way, it is possible to achieve a shear retention model which will tent to zero shear stress when crack opening occurs. In the state of closed crack, the shear stiffness is degraded as well. The shear retention feature can be implemented by the option SHEAR RETENTION following by CONCRETE in the concrete material data block. Therefore, the orthogonal cracks are allowed with the shear retention model. These cracks are irrecoverable and they will remain either open or closed for the rest of the calculations. No more than two cracks can occur at any point for plane problems. Following crack detection, a damaged elasticity model is used to take into account the effect of the cracks.

6.3.1.3 *Tensile Behavior*

Concrete in tension is considered as a linear-elastic material until the uniaxial tensile strength, f_{tu}, at which concrete cracks and the softening behaviour follows. A linear softening model is used to present the post-failure behaviour in tension. The post-failure behaviour for direct straining across cracks is modelled with a TENSION STIFFENING option, which allows definition of the strain-softening behaviour for cracked concrete. ABAQUS offers two methods to model the tensile post-failure behaviour, i.e. a postfailure stress-strain relation or a fracture energy cracking criterion (ABAQUS 2000). As the former may introduce unreasonable mesh sensitivity into the results (Crisfield, 1986), the later is utilised in this study, in which the Hilleborg's (1976) proposal is adopted. It can be implemented by defining a displacement u_0 at which a linear approximation to the postfailure strain softening gives zero using stress-displacement relationship. This can be done by using the TYPE=DISPLACEMENT parameter on the TENSION STIFFENING option.

6.3.1.4 *Compressive Behavior*

Concrete in compression is considered to be a linear-elastic, plastic and strain-hardening material. When the principal stress components are dominantly compressive, the response of concrete is modelled by an elastic-plastic theory using a simple form of yield and failure surface written in terms of the equivalent pressure stress, p, and the Mises equivalent deviatoric stress, q (see Figure 6.4) by the adoption of the three-parameter model (William and Warnke 1975). Associated flow and isotropic hardening will be used in concrete modelling. The CONCRETE option is used to define the stress-strain behaviour of plain concrete in uniaxial compression outside the elastic range. Compressive stress data can be provided as a tabular function of plastic strain. The stress-strain curve can be defined beyond the ultimate stress, into the strain-softening regime.

6.3.1.5 *Shear Retention*

The decrease of shear transfer capability across an existing crack is taken into account by introducing a factor ρ, a function of tensile strain across the crack. The shear retention model assumes that the stiffness of open cracks reduces linearly to zero as the cracking opening increases. The factor is defined as unit when the opening strain over the crack band is zero and as zero when it reaches the maximum value, ε_{max} and in between them, the linear variation takes place. Beyond the maximum value, the ρ factor keeps zero valued and for negative strains, a constant ρ_{close} is defined.

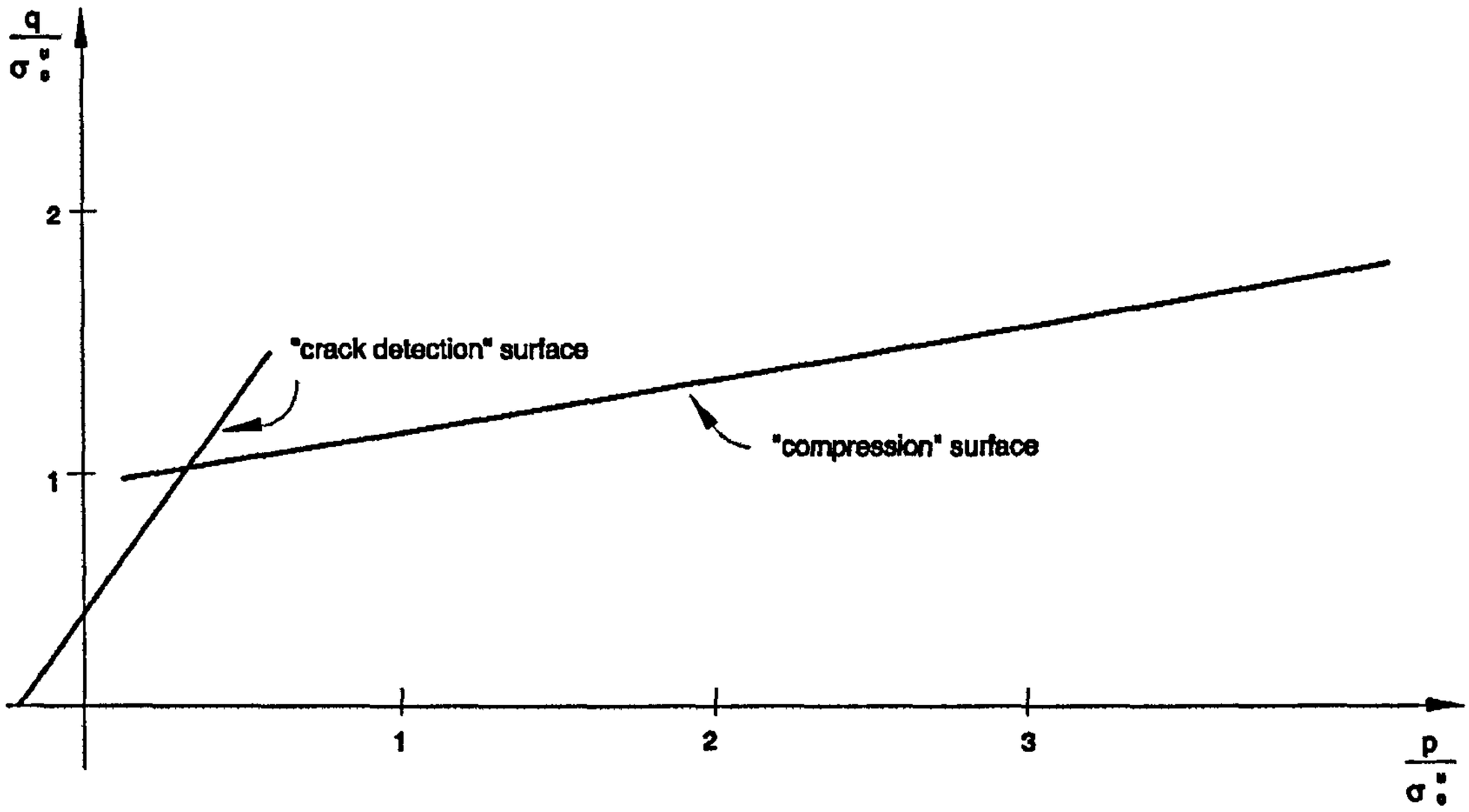

Fig. 6.4 Yield and failure surface in *p*-*q* plane

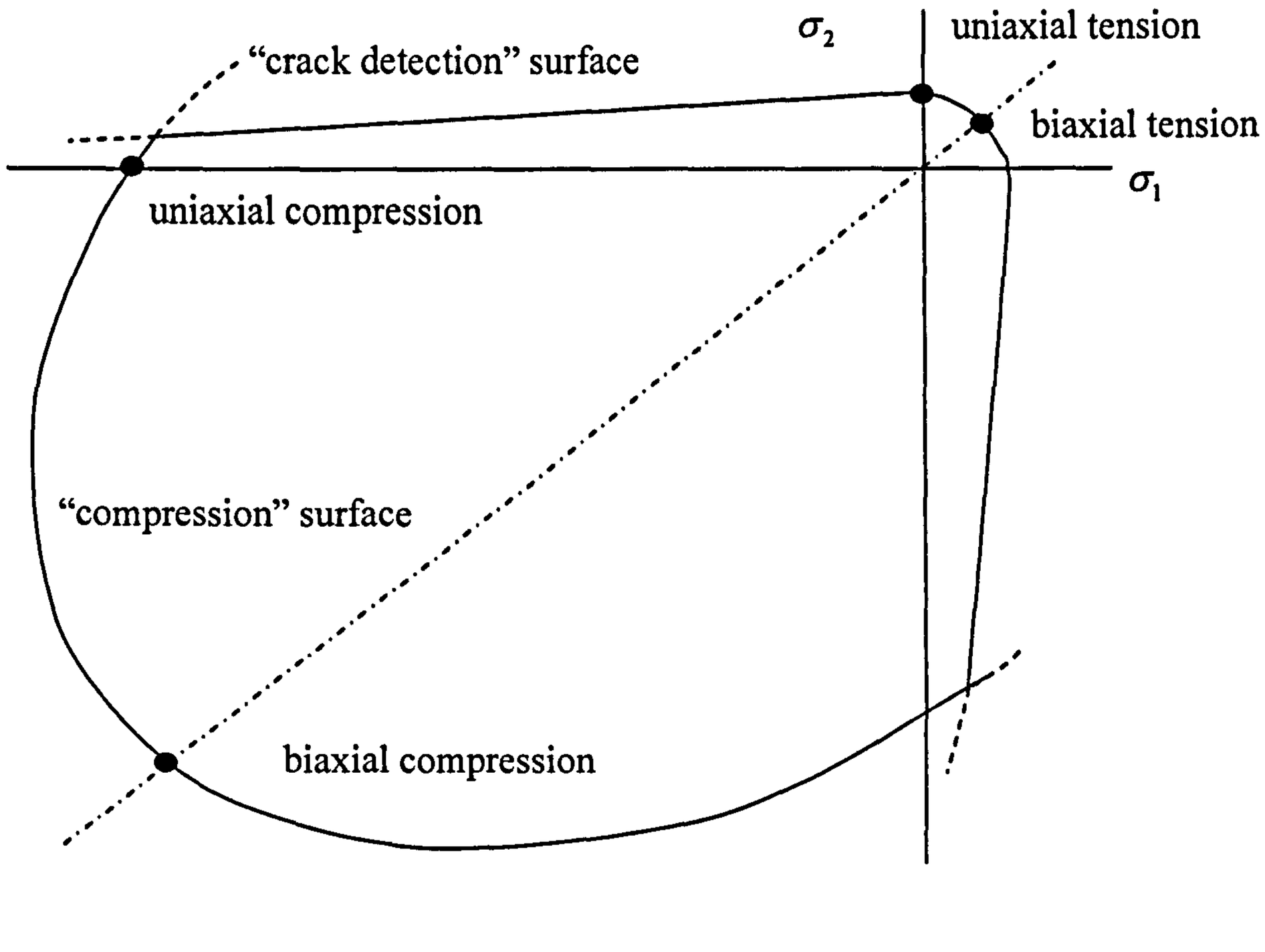

Fig. 6.5 Yield and failure surface in plane stress

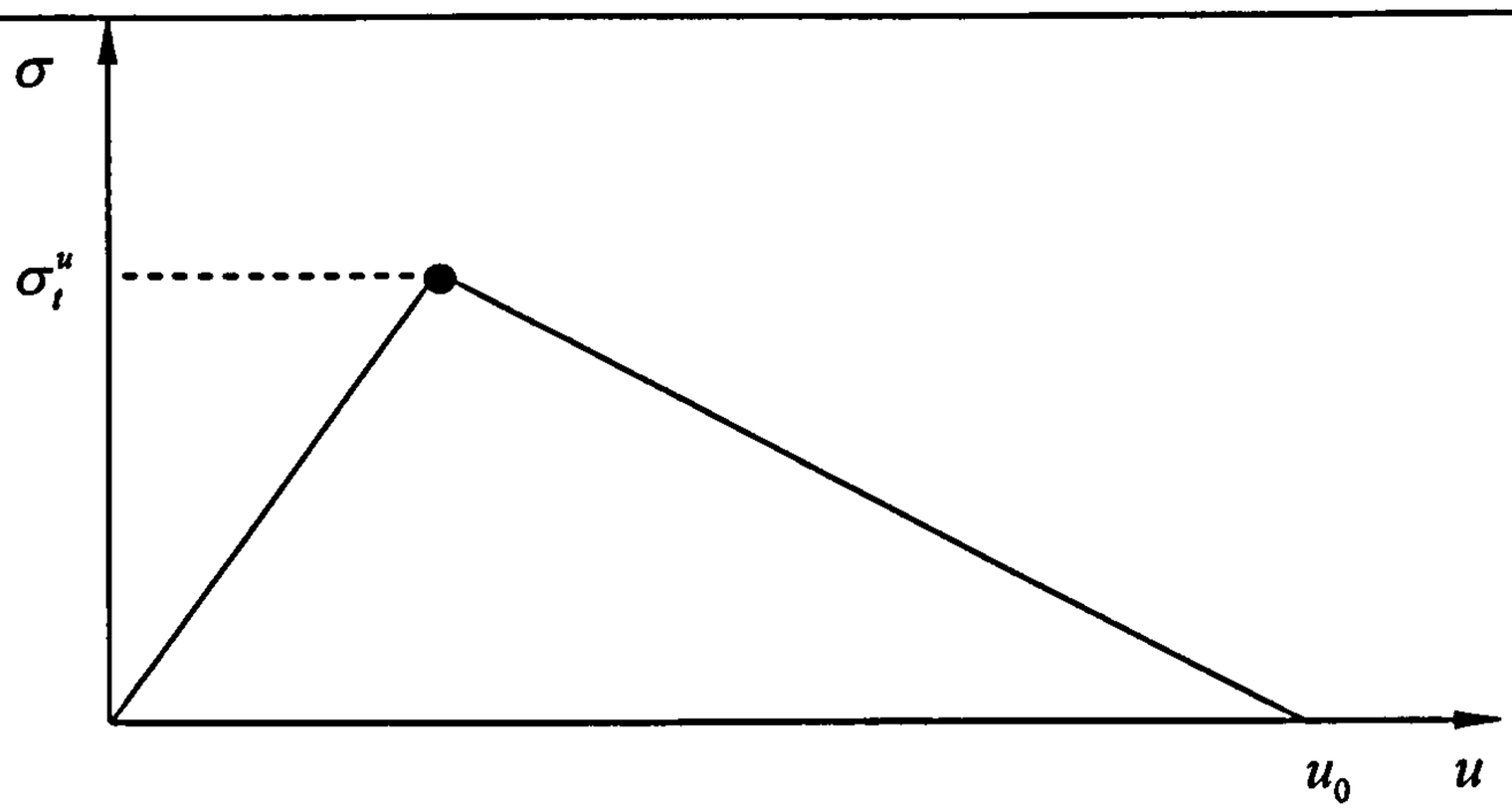

Fig. 6.6 post-cracking stress-displacement of concrete

6.3.2 Steel Reinforcement and Steel Plate

The rebars, shear links and other structural steel components, are modelled as an elastic-perfectly plastic material in both tension and compression. The assumed uniaxial stress-strain curve is shown in Figure 6.3b. The value of Young's modulus is taken as 205 GPa as the standard one.

6.3.3 FRP Composite

FRP composites are materials that consist of two constituents. The constituents are combined at a macroscopic level and are not soluble in each other. One constituent is the reinforcement, which is embedded in the second constituent, a continuous polymer called the matrix. The reinforcing materials is in the form of fibers, e.g. carbon or glass, which are typically stiffer and stronger than the matrix. Figure 6.7 shows a schematic FRP composites. As shown in the figure, the unidirectional lamina has three mutually orthogonal planes of material properties, i.e. *xy*, *xz* and *yz* planes. The *xyz* coordinate axes are refereed to as the principal material coordinates where the *x* direction is the same as the fiber direction and the *y* and *z* directions are perpendicular to the *x* direction. It is a so-called orthotropic materials (Gibson 1994). In this analysis, a further simplified assumption is made, i.e. the bonded sheet is regarded as transversely isotropic where the properties of the FRP composites are nearly the same in any direction perpendicular to the fibres, i.e. the properties in the y direction are the same as those in the z direction. For the plane stress analysis, only 4 material parameters are needed in the FEA input, i.e. E_1, E_2, ν_{12} and G_{12}, which denote, respectively, the Young's modulus in the direction of fibre, Young's modulus in the transverse di-

rection of fibre, Poisson's ratio in the *x-y* plane and shear modulus in the *x-y* plane. The ELASTIC option including the parameter of TYPE = LAMINA is used to define the material properties of FRP composites for the plane stress problem. It is noted that the limiting case, when $E_1 = E_2$, is for isotropic materials.

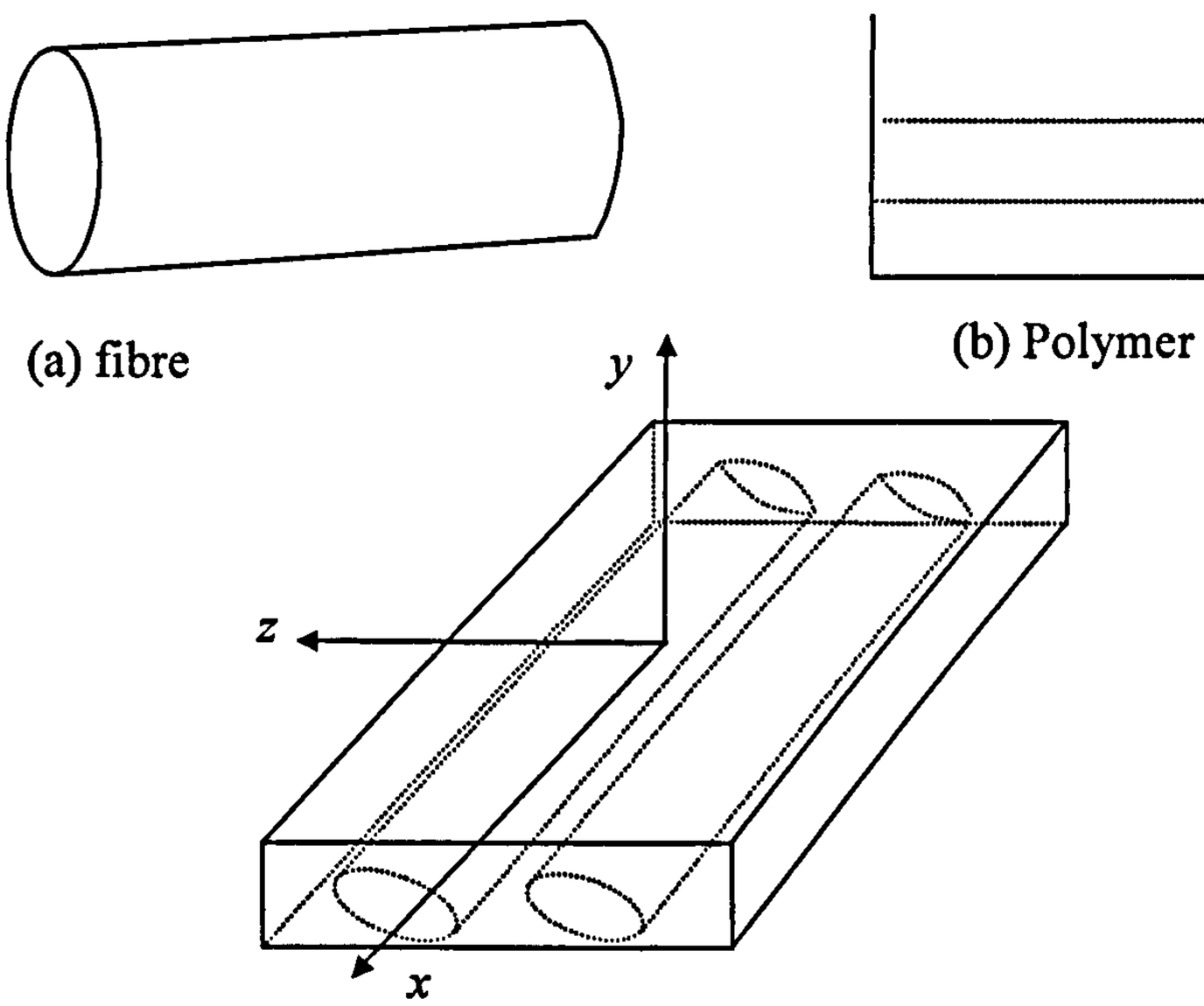

Fig. 6.7 The illustration of the composite material (Kachlakev et al. 2001)

6.3.4 The Input for the Modelling

In this example, the concrete cylinder compressive strength $f_c' = 20\text{MPa}$ and the Young's modulus $E = 21.5$ MPa. The uniaxial compressive stress-strain curve is assumed to be linear up to $0.3 f_c'$. Beyond this point, it is represented by using the equation proposed by Desayi and Krishnan (1964).

$$\sigma = \frac{E\varepsilon}{1+\left(\frac{\varepsilon}{\varepsilon_0}\right)^2} \tag{6.1}$$

it yields

$$\varepsilon_0 = \frac{2f_c'}{E} \tag{6.2}$$

The ultimate compressive strain ε_{cu} is taken as 0.0035.

The ratio of the ultimate biaxial compressive stress to the uniaxial compressive ultimate stress is defined as 1.16 and the absolute value of the ratio of uniaxial tensile stress at failure to uniaxial compressive stress at failure is set as 0.1. The other data are taken as the default values of ABAQUS.

The displacement u_0, at which the concrete material completely loses its tensile stress, varies at different positions, e.g.

(1) in the cover layer where relatively smaller aggregates are located, a small value 0.035 is defined;
(2) in the core concrete material, it is set as 0.04.
(3) in the concrete close to the rebars or shear links, the stiffening effect is more pronounced in the presence of steel reinforcement, and hence a larger value of 0.06 is set.

The reduction factor for the shear modulus when the cracks close is set as 0.95 and the maximum opening strain when the zero shear modulus commences is defined as 0.01.

The summery of other material parameters are tabulated in Table 6.1.

Table 6.1 Material properties

Material	Young's moduli (GPa)	Poisson's ratio	Shear moduli (GPa)	Tensile strength (GPa)	Compressive strength (GPa)	Yield Strength (GPa)
Concrete	21.5	0.17		2	20	
High yield steel	210	0.3				460
Mild steel	210	0.3				250
Adhesive	11.6	0.3				
CFRP	155 (Long.) 10 (Trans.)	0.3 (Major)	4.78			

6.4 Meshing

This example can be analysed as a 2-D plane stress problem due to the fact that the stress variation along the width direction is not significant. Like the LEFM analysis, in this study only half of the structure is modelled due to symmetry. Input file is compiled to define nodes and elements of the concrete, the adhesive layer and the FRP sheet for both the virgin RC beam and the strengthened RC beam. Two different element types are adopted in this modelling. The interface connections between various material phases are defined as perfect bond, i.e. there is no slippage assumed in the modelling. The bond and slippage interaction between the concrete and rebars is included in the tension stiffening effect of the concrete material as introduced in the material section. The interfacial interaction between the FRP and concrete is believed to be presented by the adhesive layer, as the relative compliance of the adhesive material is adequate to absorb the interfacial relative displacement in its own deformation.

An important step in FEA is to mesh the model appropriately. Convergent results are obtained when an adequate number of elements is used in a model. This is practically observed when an increase in the mesh density has a negligible effect on the results. (Adams and Askenazi 1998). However, it is worth noting that, unlike the elastic material, concrete material shows different requirements to the mesh refines, that is, the excessively refined mesh will lead to the convergence failure in the equation iteration and it would prevent the analysis continuing before it reaches the failure loads. Moreover, the heterogeneous feature of concrete in the micro scale normally requires that the size of the minimum element should be at least larger than that of the course aggregate. Consequently, the experiment data is usually a good index to determine the appropriate element size in the nonlinear FEA analyses for concrete structures.

Figure 6.8 and 6.9 show three schemes of meshing for the virgin RC model and the strengthened RC model. Table 6.2 lists the number of element for each meshing scheme.

Table 6.2 Number of elements in various meshing scheme

	Case I	Case II	Case III
Reinforced beam	452	872	766
Strengthened beam	842	942	1056

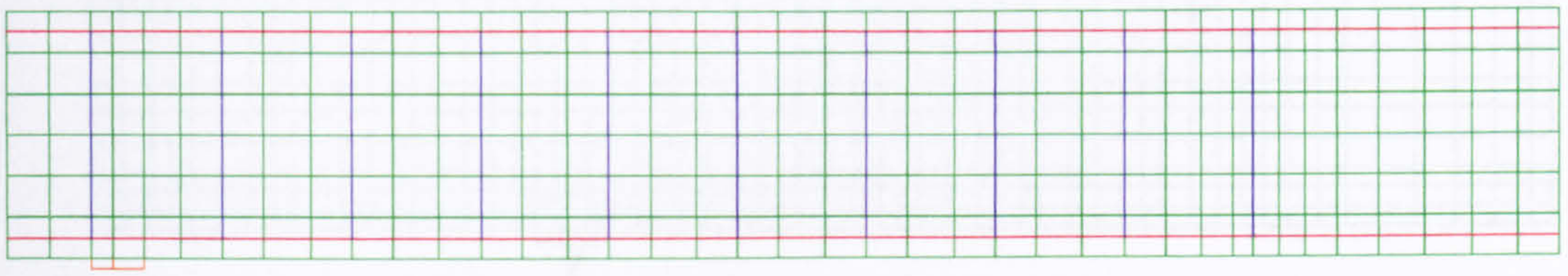

(a) Case I (number of elements = 452)

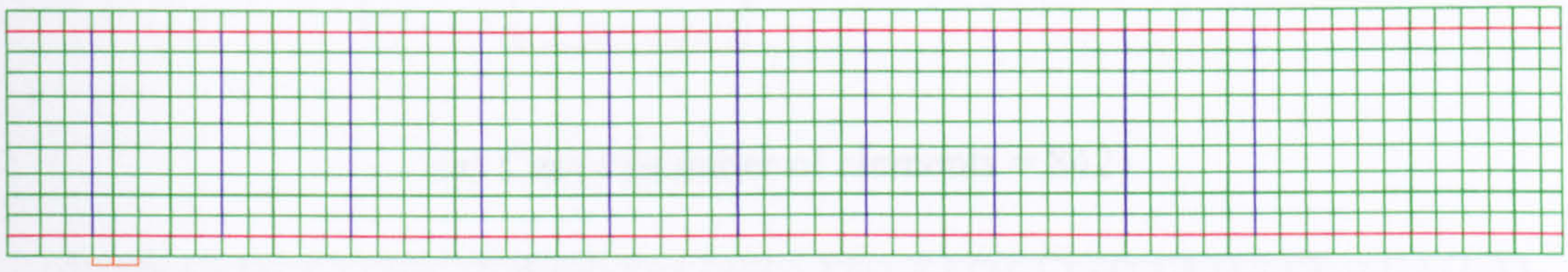

(b) Case II (number of elements = 872)

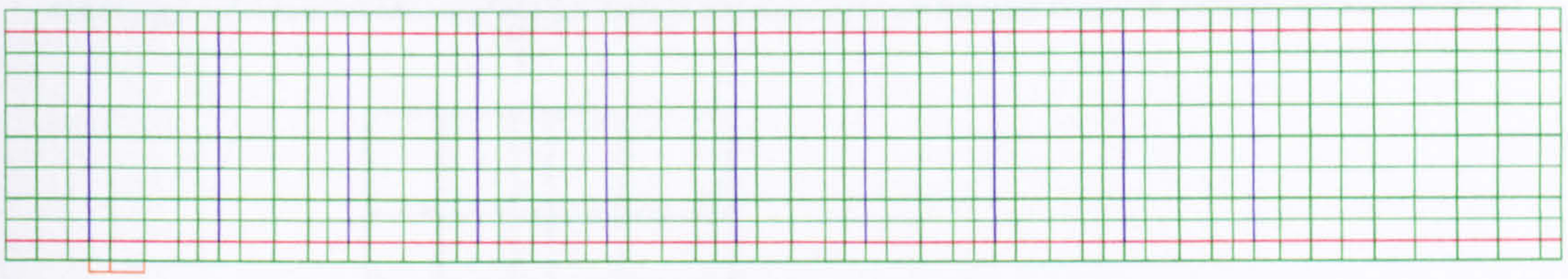

(c) Case II (number of elements = 766)

Fig. 6.8 Mesh schemes for the virgin reinforced concrete model

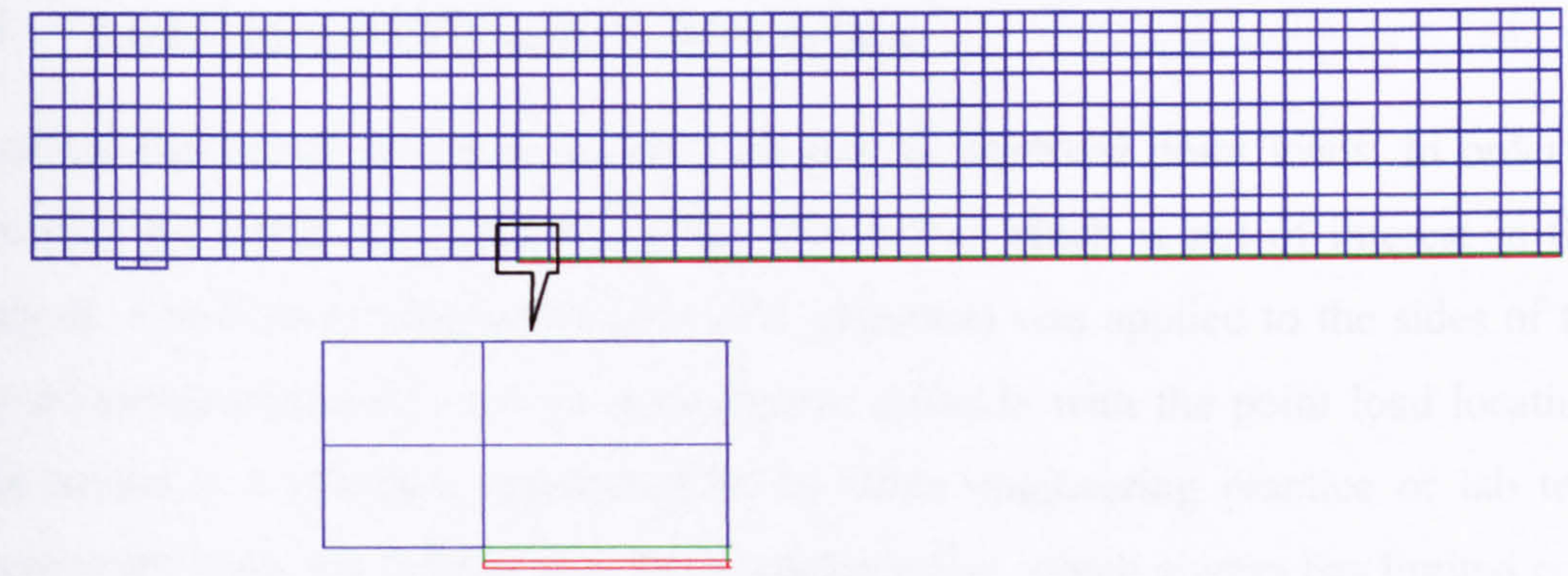

(a) Case I (number of elements = 842)

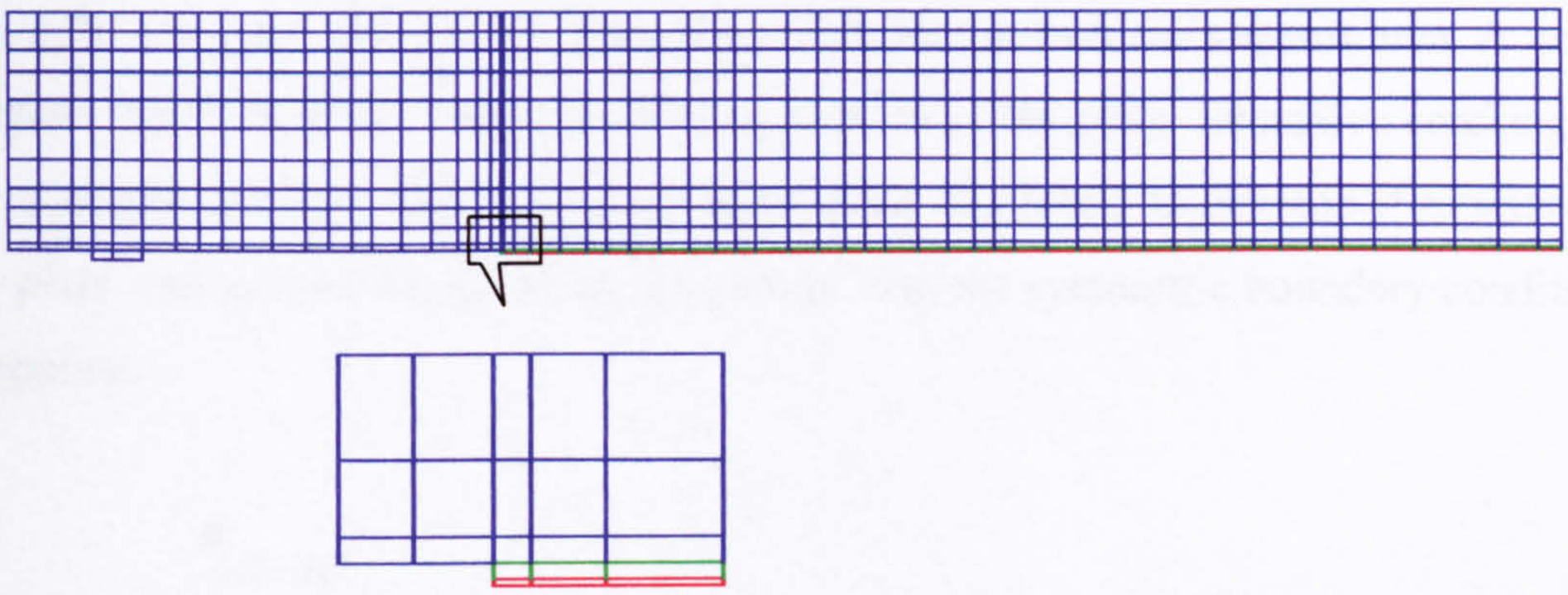

(b) Case II (number of elements = 942)

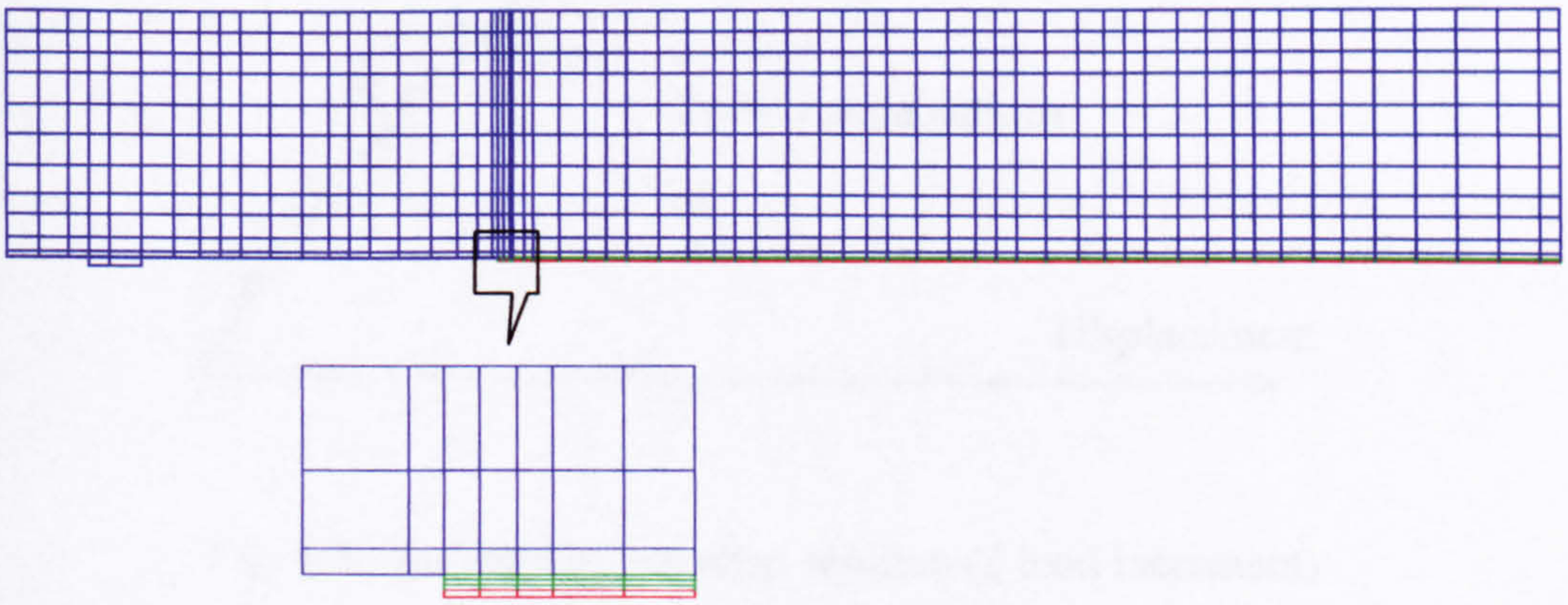

(c) Case III (number of elements = 1056)

Fig. 6.9 Mesh schemes for the strengthened reinforced concrete model

6.5 Loading and Boundary Conditions

Consider the beams in Figure 6.1carrying two symmetrical point loads. In order to eliminate the stress concentration at the load point, which is not of interest in this analysis, a uniformly distributed local load (pressure) was applied to the sides of the two adjoining elements, with its central point coincide with the point load location. This model is a practical approximation to either engineering practice or lab test, where point loads are applied through a bearing roller, which always has limited connect area at the loading points. Similarly, a small support plate with elastic materials is added at the support location in order to avoid stress concentration (see Figures 6.8 and 6.9). This provides a more even stress distribution over the support area. A point support is placed under the plate allowing rotation of the plate. Excessive cracking of the concrete elements above the supporting plate was found to develop if rotation of the plate was not permitted. Along the central line, the symmetric boundary condition is applied.

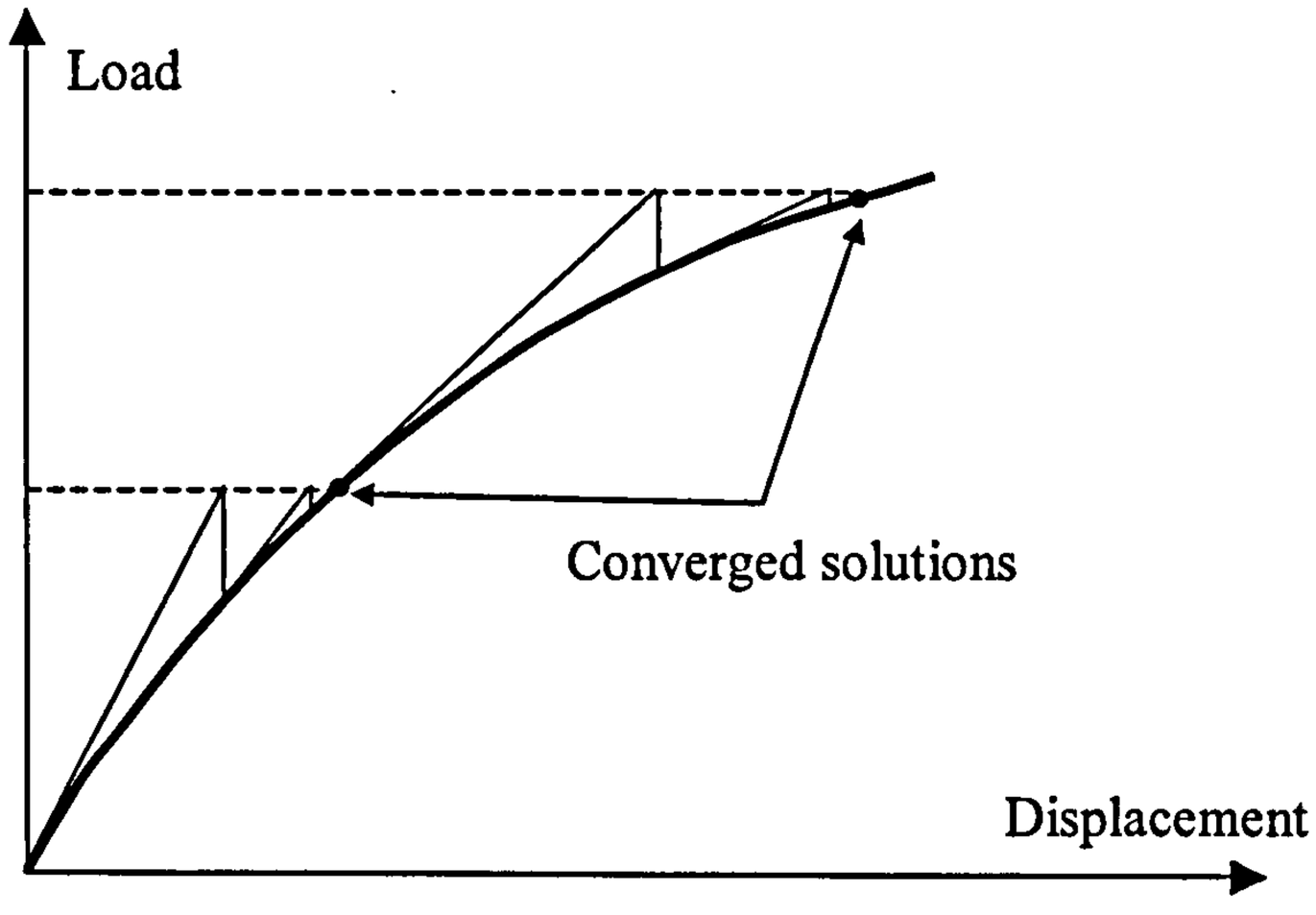

Fig. 6.10 the Newton Iteration solution (2 load increment)

6.6 Nonlinear Analysis Procedures

In nonlinear analysis, the total load applied to a finite element model is divided into a series of load increments called load steps. At the completion of each incremental solution, the stiffness matrix of the model is adjusted to reflect the nonlinear changes in structural stiffness before proceeding to the next load increment. In ABAQUS, the

Newton method is used and successive iterations are followed to determine an accept solution for each time increment. (ABAQUS manual 2000) The Newton equilibrium iterations provide convergence at the end of each load increment within tolerance limits. Figure 6.10 shows the use of the Newton method in a single degree of freedom nonlinear analysis. Prior to each solution, the Newton method assesses the out-of-balance load vector, which is the difference between the restoring forces (the loads corresponding to the element stresses) and the applied loads. Subsequently, the program carries out a linear solution, using the out-of-balance loads, and checks for convergence. If convergence criteria are not satisfied, the out-of-balance load vector is re-evaluated, the stiffness matrix is updated and a new solution attained. The iterative procedure continues until the problem converges.

In this study, the convergence criteria is set to the displacement, which is defined as the ratio of the largest residual to the corresponding average displacement norm. Herein, the tolerance limits 2% is used for both modelling.

As the concrete material may crack or crush, this will cause the structure to lose their stiffness locally and that part of the structure must release some strain energy to remain in equilibrium. In the event of this unstable point, the iteration may become divergent and the modelling fails to approach the ultimate loads or close to the ultimate loads. Some techniques can help to solve this problem, such as, using the displacement control, or using the dashpots to stabilize the structure during a static analysis. One of the efficient methods, called 'modified Riks method' was used in this study. This method uses the load magnitude as an additional unknown and solves simultaneously for loads and displacements. Therefore, another quantity, 'arc length' was used to measure the progess of the solution (ABAQUS manual 2000).

Other techniques to accelerate the convergence include: (a) set the appropriate displacement value as the convergence criteria; (b) use the ANALYSIS=DISCONTINUOUS parameter on the CONTROLS option to avoid premature cutbacks of the time increment; (c) activate the 'line search' algorithm to scale down the solution correction in each iteration.

6.7 Results from the Finite Element Analysis

Figure 6.11 shows load-deflection plot of the reinforced beam using the aforementioned three meshing patterns. It reveals that there are characteristic points along each of the loading path curve, which divides the curve into three stages, that is, zero loading to initial concrete cracking, initial concrete cracking to the reinforcement yielding, the reinforcement yielding to numerous cracking emerging and then ultimate failure. From Figure 6.11, we can see generally a quite good agreement between the FEA and the experimental results from Fanning and Kelly (2000). The FEA results give a slightly higher first-cracking load and the reinforcement yield load than the experiment does, but slightly lower ultimate loads. The most pronounced difference is the deflection at the ultimate state. The FEA results are only about half of the experiment results. That can be attributed to the numerous cracks results in premature termination of the calculation. Some other information exhibited by the plot is that all the three meshing patterns give almost identical load-deflection curves before the yielding points. Case I give rather higher ultimate loads but smaller deflection. Case I and Case II show very similar results, while Case III has slightly larger deflection. This discrepancy is attributed to the fact that over-refined meshing results in a large amount of cracks and hence brings in severe convergence difficulty and eventually terminates the analysis. Mesh III is deemed as the most efficient meshing scheme and most of the following results are present only for this scheme.

Figure 6.12 shows the load-strain plot for the tensile and compressive reinforcements in all three cases. From this figure, we can see that Case I attains the largest strain under the same load before the curves are levelled out. Case II and Case III offer very coincident results. Apart from these, we can observe that the occurrence of yielding of the tensile rebar does not result in an abrupt change of the slope in the load-deflection curve immediately. The accelerated global deflection commences when the yielding of the tensile rebar has developed farther.

Figure 6.13 shows the load stress plot for the concrete at the top and bottom fibres at the midspan of the beam. The impact of the mesh pattern on the concrete stress is very similar to that on the rebar. We also can see that the bottom concrete starts to crack under the applied load of 10KN, which is the first slope changing point of the global

load-deflection curves. After the concrete cracks, its stress starts to reduce, rather slowly first, and then dramatically rapid when a certain part of the tensile reinforcement start to yield. Meanwhile the width of the cracks starts to increase quickly. It is noted that when the damaged mechanics theory is used to model the post-cracking behaviour of the concrete, the tensile strain of the concrete is virtually obtained by dividing the fictitious concrete cracks by the characteristics length, the length allocated to each calculated integration point. This explains the observation of mesh sensitivity of the tensile stress after cracking. The compressive stress of the concrete at the top of the beam is increased gradually until reaching its compressive strength.

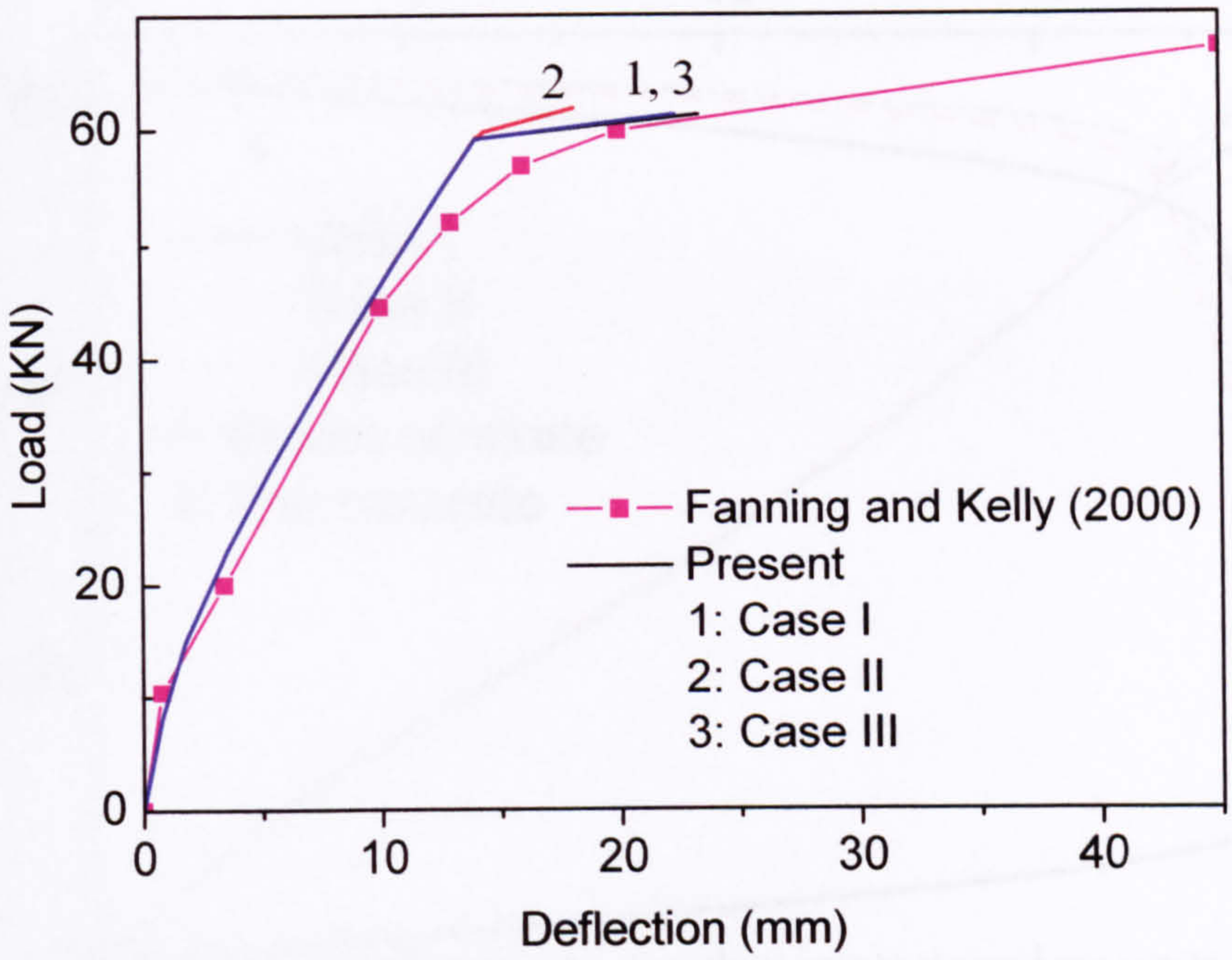

Fig. 6.11 Loads against deflections for various meshing patterns

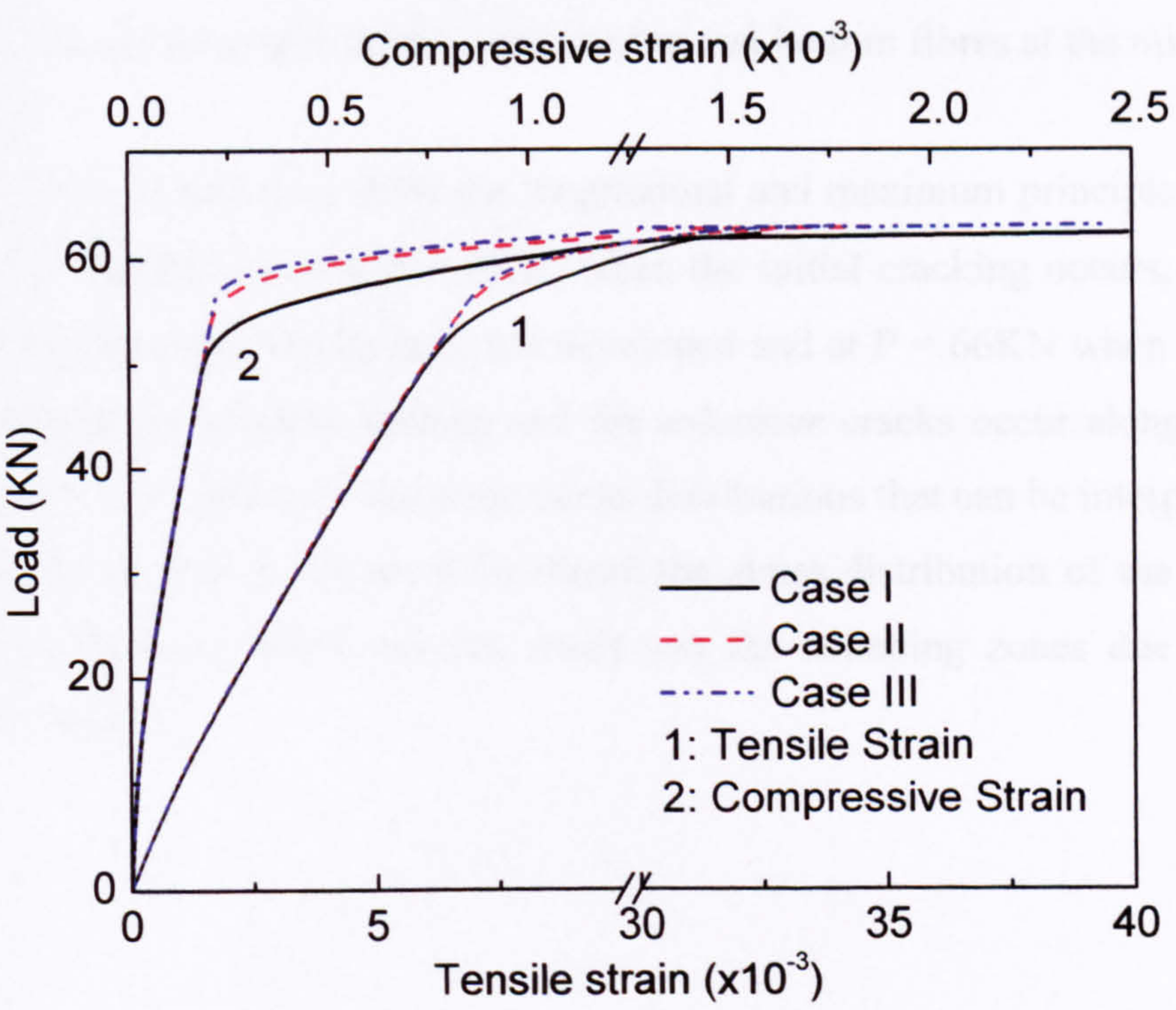

Fig. 6.12 Load-strain plot for tensile and compressive reinforcement at midspan

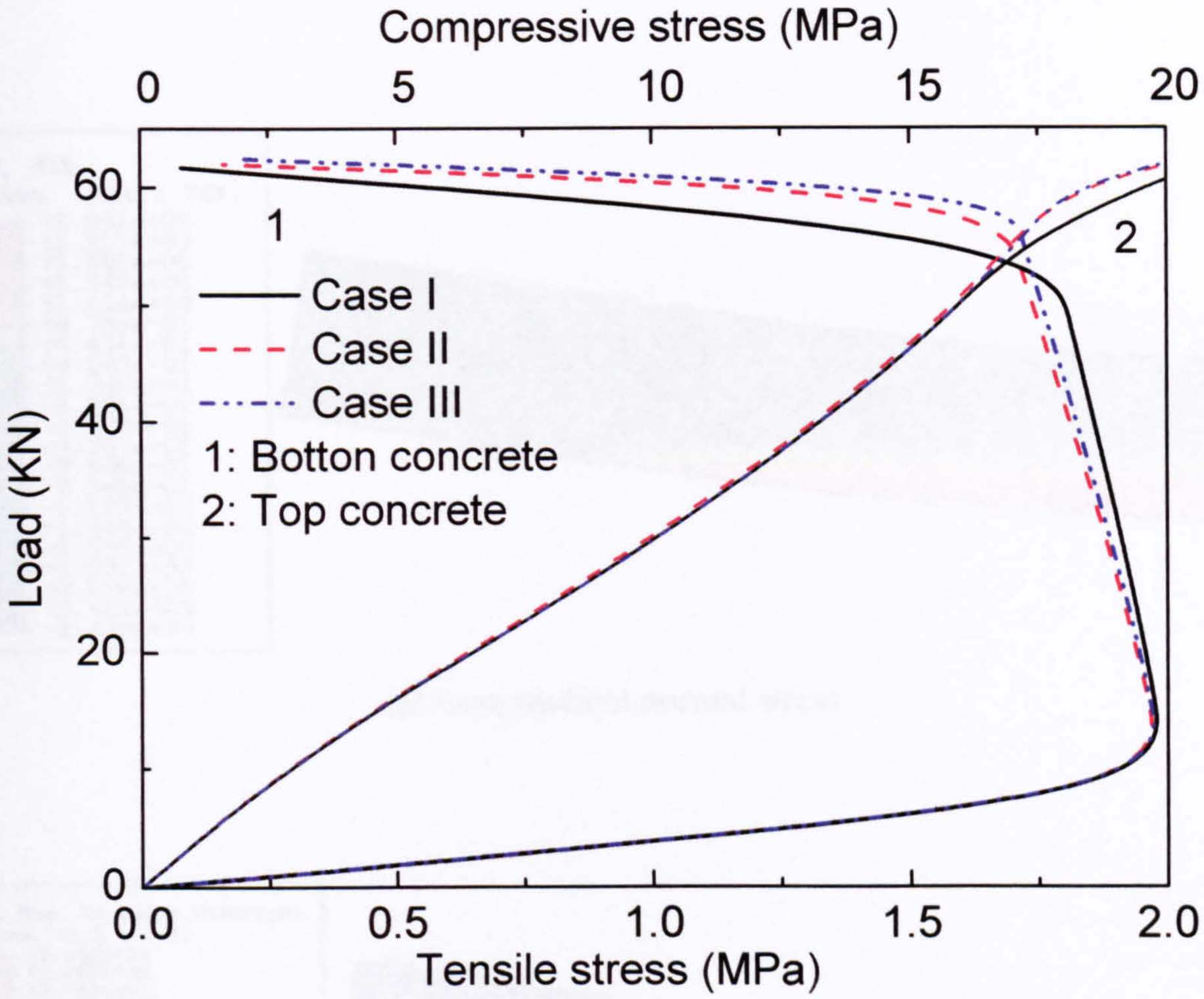

Fig. 6.13 Load-stress plot for the concrete top and bottom fibres at the middle span

Figures 6.14, 6.15 and 6.16 show the longitudinal and maximum principle stress contour plots of the RC beam at P = 8KN, when the initial cracking occurs, and at P = 62KN when numerous cracks have not developed and at P = 66KN when the loading is approaching the ultimate loading and the extensive cracks occur along the whole beam. Figures 6.14 and 6.15 show the stress distributions that can be interpreted using the classic beam theory. Figure 6.16 shows the stress distribution of the beam with massive cracks from which we can easily see the softening zones due to the micro/macro cracks.

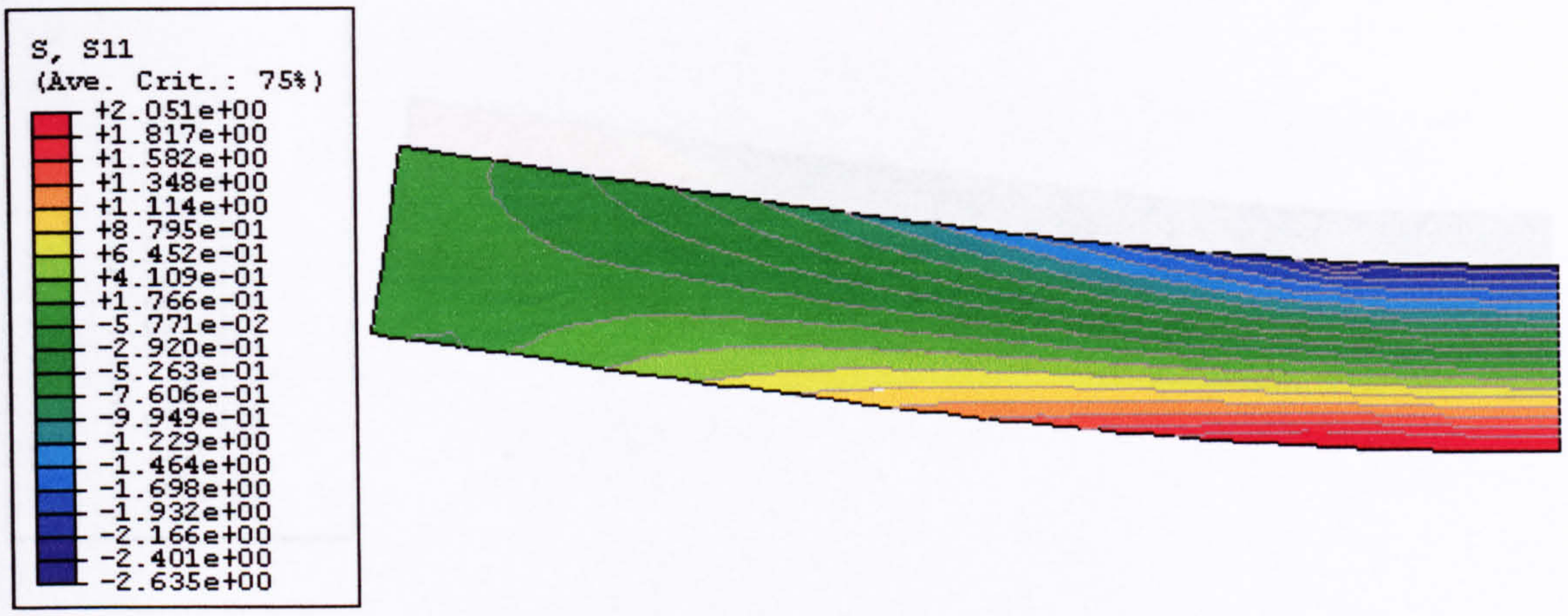

(a) Longitudinal normal stress

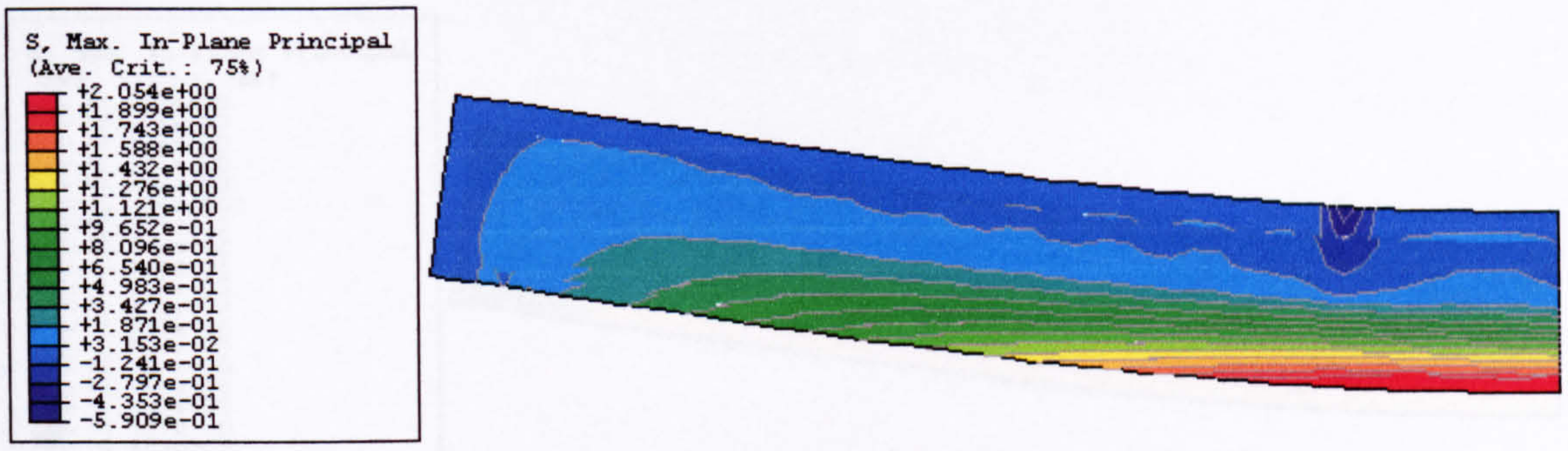

(b) Maximum principle stress

Fig. 6.14 Stress contour plots of the reinforced beam at P = 8KN

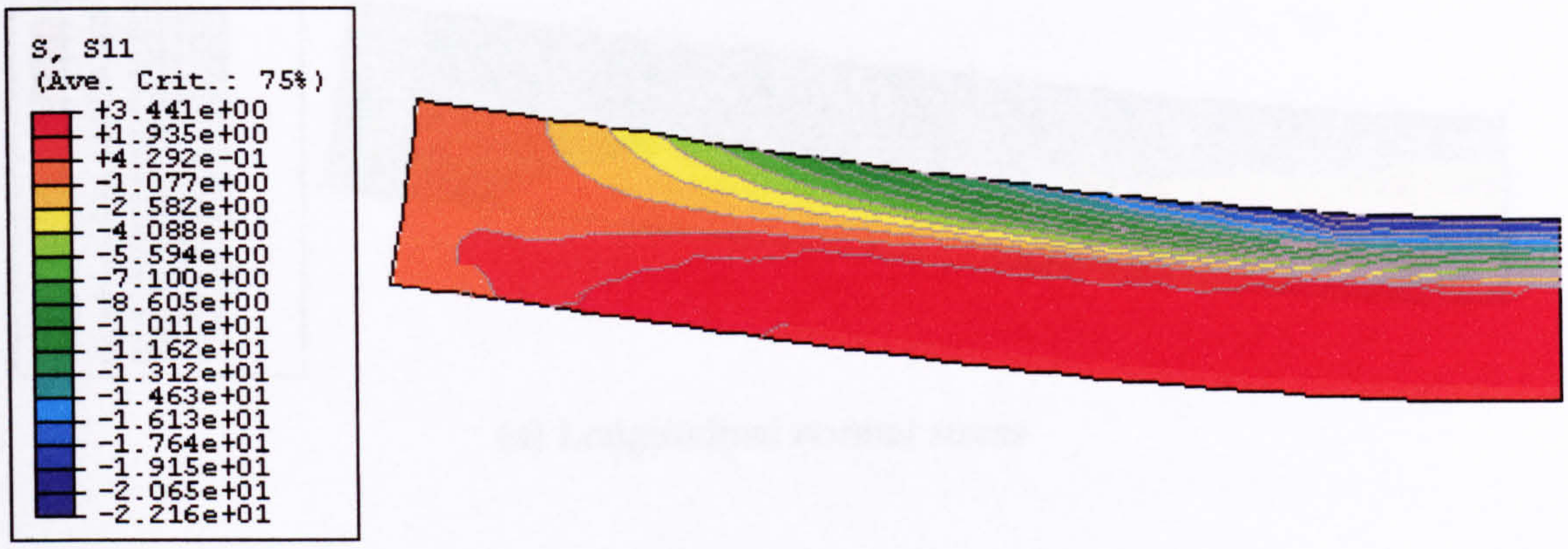

(a) Longitudinal normal stress

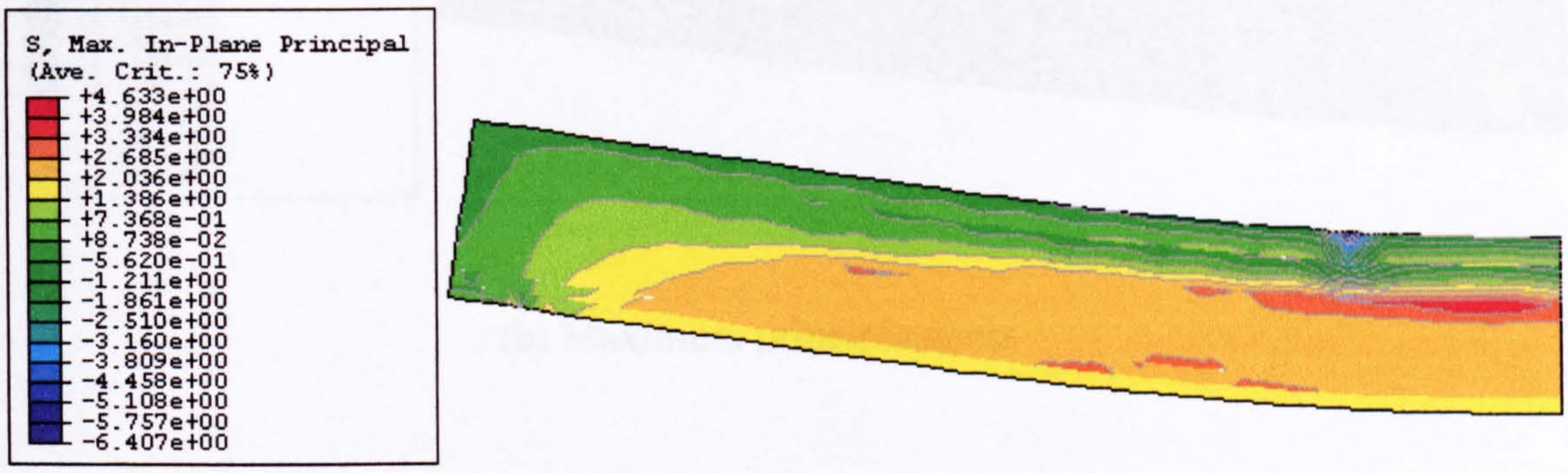

(b) Maximum principle stress

Fig. 6.15 Stress contour plots of the reinforced beam at P = 62KN

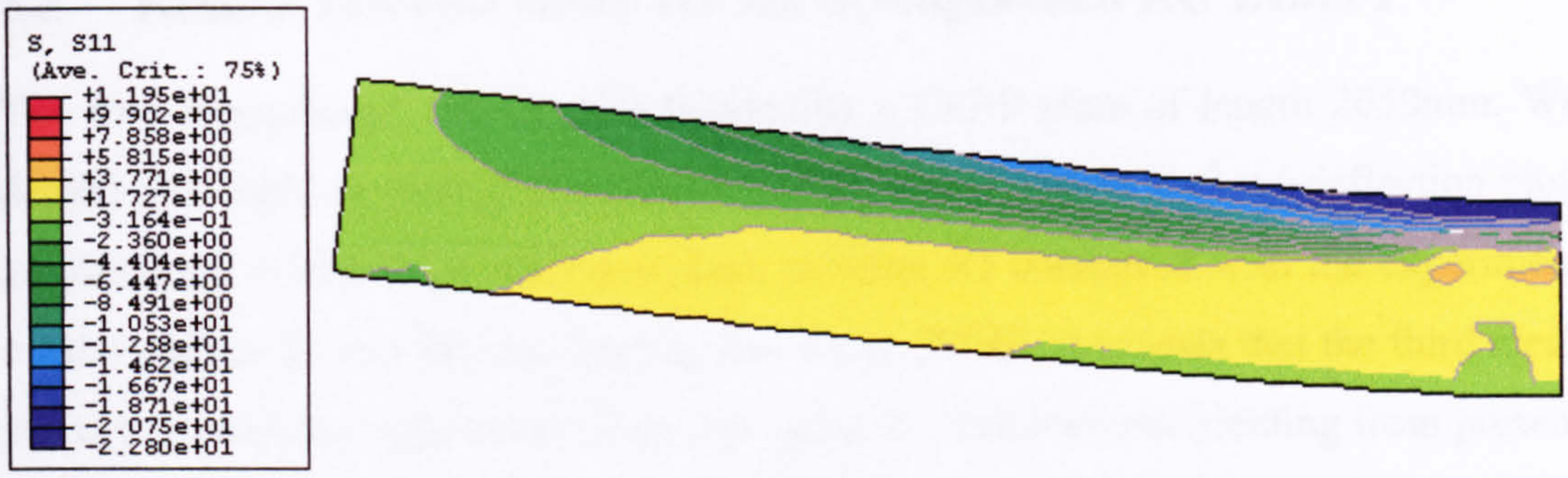

(a) Longitudinal normal stress

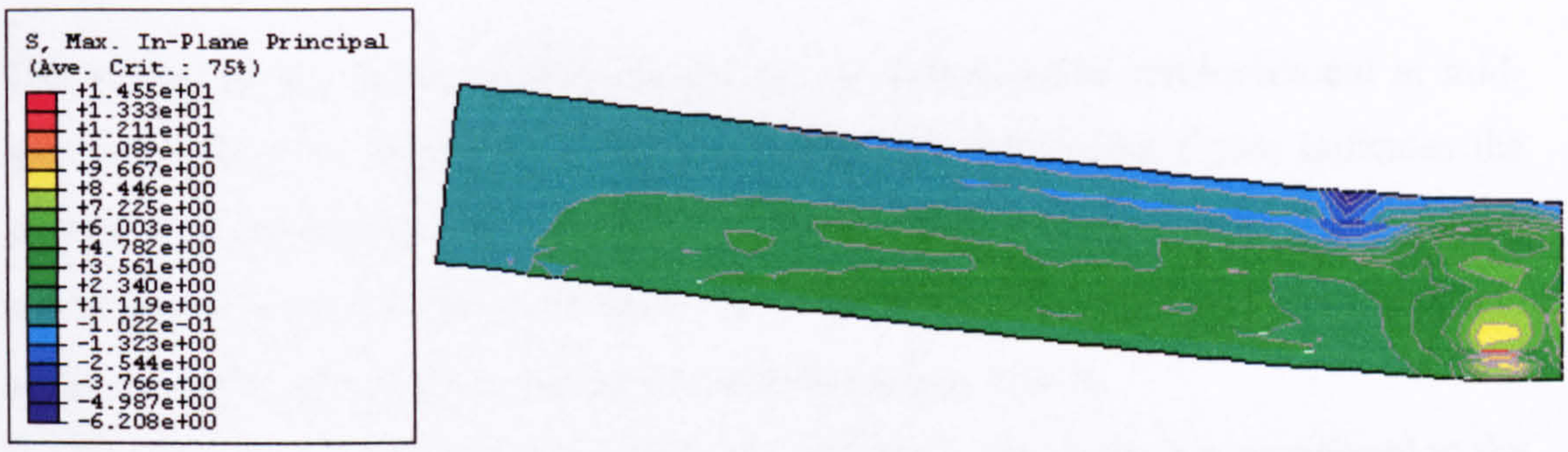

(b) Maximum principle stress

Fig. 6.16 Stress contour plots of the reinforced beam at P = 66KN

6.8 Results Interpretation for the Strengthened RC Beam I

The first strengthened RC beam is bonded by a CFRP plate of length 2050mm. We denote this beam as strengthened Beam I. Figure 6.17 shows its load-deflection plot, in which the results from the three mesh patterns are compared with the experiment results (Beam B5 and B6) by Fanning and Kelly (2000). It reveals that the third mesh patter provided best agreement. The load value at reinforcement yielding from present analysis is 81.5KN while the experimental values are 85.6KN. The ultimate load obtained by this analysis is 101KN while the experimental ones are 100KN and 103KN respectively.

The strains in the tensile reinforcement and the compressive reinforcement at mid-span are plotted in Figure 6.18. The top horizontal axis in the figure indicates the compressive strain from the compressive reinforcements and the bottom axis is for the tensile strain in the tensile reinforcements. It can be seen from the plot that the tensile strain in the rebars is clearly featured by four segments, that is,

(a) from zero loading to the first crack occurrence, the strain is proportional to the applied load;
(b) from the first crack occurrence to the steel yielding, a reduced slope of the curves occurs, due to the partial loss of the global stiffness as the consequence of the crack;
(c) from the steel yielding to the numerous cracks maturely developed, the strain keeps increasing while the load is almost constant;
(d) from the numerous cracks to the ultimate failure, the neutral axis shifts up and both the applied load and the strain keep increasing.

The compressive strain in the top reinforcement behaves differently. They are shortened by the surrounding concrete under compression. It increases proportionally up to the yielding point, after which the strain starts to increase with a higher rate.

The CFRP plate strain and the concrete top fibre strain at the mid-span are plotted in Figure 6.19. It can be seen that both strains show quite similar characteristics except

that the CFRP plate strain is affected more significantly by the first crack occurrence than is the concrete strain.

In the figure, the results from the other two cases are plotted for comparisons. It is obvious that the third meshing scheme yields the best results.

Figure 6.20 shows the load- CFRP strain plot at three different locations near the plate end. In the figure, L_e denotes the distance between the recorded position and the plate end. The strain plotted in the figure is for Le = 5mm, 15mm and 35mm, respectively. It can be observed that the strain for the outermost position is small, and tends to reduce to zero when the load is approaching the ultimate value. It is the debonding cracks that releases the strain near the plate end. Position 2 shows a similar trend but is less profound. The strain in position 3 has very similar characteristics to the mid-span one, except that it is less affected by the yielding of the rebars, as the reinforcement near the position has yet yielded.

Figure 6.21 (a) shows the longitudinal normal stresses experienced by the concrete near the AC interface at Le = 1.25mm, 3.75mm 6.25mm and 8.75mm respectively. It shows that the concrete at the plate end starts to crack in the vertical direction when the applied load is about 16KN and after that the longitudinal stress is gradually reduced at different degrees.

Figure 6.21 (b) shows the shear stress in these four positions, where we can see that the shear stress is less affected by the occurrence of end vertical cracks. However, it is affected by the horizontal cracks. The occurrence of the horizontal cracks near the plate end can be seen in Figure 6.21 (c). The transverse normal stress shown in Figure 6.21(c) reveals that they are not significantly affected by the vertical cracks. When they are increased to a certain level, horizontal cracks are initiated from the outmost position. This is reflected in the plot by the instantaneous drop of the transverse normal stress, at P = 50KN when Le =1.25mm. This also affects the shear stress due to the effect of shear retention. The horizontal crack extends to Le=3.75mm at P=70KN. The other two positions have hardly experienced any transverse normal stress until the horizontal cracks extends to the second position. Figure 6.21(d) shows the principal stresses at the same positions. When the load is below 16KN, all the principle stresses

are almost proportional to the applied load and after the first vertical crack occurrence at *Le* = 1.25 mm, the stresses at points 2, 3 and 4 start to increase, while the stress at point 1 keeps rising and oddly exceeds the tensile strength. This is the consequence of the material model used by ABAQUS, which can only detect the cracks in the orthogonal direction. Imagine the first crack is in the vertical direction exactly, then the model can only detect the horizontal direction when the transverse normal stress arrives at the tensile strength, even though stresses in other directions may be bigger. That is why the calculated maximum principle stress may exceed the tensile strength. Once the horizontal crack is detected, the principal stress level is dropped immediately.

Figures 6.22 a, b, c, d show the corresponding longitudinal normal strain, shear strain, transverse normal strain and maximum principle strain. In Figure 6.22 (a), the first two positions experience an identical axial strain and so do the other two. This is caused by the linear interpolation of the degrees of freedom in the elements between the adjacent nodes, and the fact that axial strain is the gradient of the horizontal displacement with regards to the position. Unlike the stress, the longitudinal strain increases monotonically. A quite similar trend can be observed for the shear stress in Figure 6.22 (b) except for the first position, which shows a slight resilience at the large applied load. Figure 6.22 (c) shows the transverse normal strain. Under the applied small load, strains at all four positions show small negative values, which is related to the Poisson's effect of plane problem. Transverse normal strain is reduced very quickly along the AC interface towards mid-span of the beam.

Figure 6.23 shows the transverse normal stress under increased applied loads at the interfaces and two other horizontal sections in the adhesive layers respectively. The two horizontal sections equally divide the thickness of the adhesive layer into 1mm each. By observing these curves, we can find the following:

(1) Tensile normal stress is developed in the AC interface and compressive normal stress is at the PA interface. In between them, the stress is gradually transformed from tension to compression;

(2) With the increase of the applied load, the tensile stress ratio, which can be indicated by the ratio of peak stress to the applied load, is reduced from 0.036 MPa/KN to 0.023 MPa/KN. The compressive stress ratio is increased from 0

to 0.013 MPa/KN. It is interesting to notice that the variation for both stress ratios is almost identical.

The second observation can be explained that when the concrete develops some cracks near the plate end, it becomes more compliant and thus alleviates the deformation incompatibility in the bi-material interface. This leads to a less severe singularity at the CA interface.

Similarly, the shear stresses along the same sections are plotted in Figure 6.24 under the same applied loads. The following observation can be made:

(1) The AC interface experiences largest shear stress and the PA interface shows the lowest;

(2) The ratio of the peak AC shear stress to the applied load is almost the same for various loading level;

(3) The position of the peak value moves away from the plate end with the increase of the applied loads.

6.9 Results Analysis for Strengthened Beam II

The second strengthened beam modelled in this chapter is the same RC beam strengthened by a 1700mm long CFRP plate, which is referred here as strengthened beam II. Figure 6.25 shows the load deflection plot of strengthened beam II and its experimental counterparts (Beam B9 and B10) by Fanning and Kelly (2000). The present ultimate load value is 76KN and the experiment one is 62KN and 82KN respectively. The great variation between the two experimental results from two identical beams is believed to be human-caused, especially for B9, which is more questionable as it is weaker than the virgin beam. Again both the numerical and experimental results agree well with each other. There is no obvious yielding point in the load path, as the rebars have yet yielded. This can be easily seen in Figure 6.26 where both tensile and compressive strains of the rebars are plotted. It is worth noting that the strain in the compressive reinforcement is almost linear throughout the entire loading history.

The plate strain and top concrete fibre strain at the mid-span are plotted in Figure 6.27, where the experimental one is also plotted. They show very similar trends as the rebar strains. Again the numerical and experiment results are quite coincident except the low loading range.

The longitudinal normal stress, shear stress and transverse normal stress at the concrete in the vicinity of the AC interface are plotted in Figure 6.28. They show very similar trends to Strengthened Beam I. Figure 6.29 shows the corresponding principal strain of the concrete near the plate end. We can draw the conclusion that the stress/strain behaviour from both strengthened beams near the plate end is very similar. An interesting finding from the transverse normal stress plots for both strengthened beams is shown in Table 6.3.

Table 6.3 The result comparisons between two strengthened beams

	Distance between plate end and support (m)		Load at crack extended to position 1 (KN.m)	Load at crack extended to position 2 (KN.m)	Ultimate load (KN.m)
Strengthened Beam I	0.375	Load	48	69	101
		Product	*1.8*	*2.6*	*3.8*
Strengthened Beam II	0.550	Load	32	55	76
		Product	*1.76*	*2.9*	*4.1*

In Table 6.3, the rows for 'Load' represents three characteristic loading levels, i.e. (a) the loading level when the horizontal crack extends to position 1; (b) the loading level when the horizontal crack extends to position 2; and (c) the ultimate load. The rows for 'Product' are the products of the distance between the plate end and beam support and the corresponding characteristic loads. As seen from the table, the products are very close in the same columns. As a matter of fact, the product is the bending moments that cross-sections at the plate ends experience, and that suggests the observation that the bending moment has a dominant impact on the plate end crack occurrence, crack development and the ultimate load for a given beam.

A similar conclusion can be drawn by comparing the ratio of the peak interfacial normal and shear stress in the AC interfaces for both strengthened beams (see Figures 6.23, 6.24 and Figures 6.30, 6.31). Table 6.4 lists the details of the comparison, in which the 'Moment' stands for the moment at the plate end; and 'Ratio' is the peak stress value to the moment value. It is obvious that the interfacial stresses are closely related to the bending moment at the plate end. This also explains the correlation between the plate end moment and the characteristic loadings mentioned in the above paragraph. It is also noted that there is quite a discrepancy between the ratios at the ultimate loads, which implies that the ultimate failure may also be related to other failure mechanism, such as the conventional shear cracking.

Table 6.4 The comparison of the normal stress and shear stress for both strengthened beams

		Normal stress			Shear stress		
		P=1.4KN	P=51KN	P=75KN	P=1.4KN	P=51KN	P=75KN
Streng-thened Beam I	Moment (KN.m)	0.385	14.025	20.625	0.385	14.025	20.625
	Peak stress (MPa)	0.072	2	1.8	-0.05	-1.73	-3.22
	Ratio	*0.187*	*0.143*	*0.087*	*-0.190*	*-0.185*	*-0.170*
Streng-thened Beam II	Moment (KN.m)	0.2625	9.375	18.938	0.2625	9.375	18.938
	Peak stress (MPa)	0.05	1.59	2.15	-0.07	-2.45	-3.08
	Ratio	*0.190*	*0.1696*	*0.113*	*-0.182*	*-0.175*	*-0.149*

The last figure in Figure 6.32 shows the variations in longitudinal strain along the CFRP plate from the plate end to the midspan, as a function of the externally applied load. The strain is normalized to the applied load to investigate its relationship to the applied loads. The strain in the constant bending moment region is virtually uniform for a given load. Within the shear span, the strain drops almost linearly from the load point to the positions closed to the plate end, where the plate has yet developed its full composite action. The strains drop to zero very quickly further towards the end. The length of the region is defined as the development length as introduced in Chapter 5.

From the figure we can see that the strains increase with a higher rate when a higher level of load is applied. The development length also increases as the load increases correspondingly, from approximately 70mm to 100mm when the load is increased from 1.4KN to 75KN.

6.10 Conclusions

A nonlinear FEA simulation has been conducted in this chapter for a virgin reinforced concrete beam and two strengthened reinforced concrete beams. One of the key features of the present analysis is that it has captured most of the properties shown by concrete material and the interactions between the concrete and the other constituent materials.

The modelling of the virgin reinforced concrete verified the application of the ABAQUS package, including the consideration of complicated concrete material properties and the implementation of the reinforcement separately in the modelling. It also provided results such that the comparisons between the strengthened and unstrengthened beam could be carried out.

Two strengthened beams with different bonding lengths have been simulated. Extensive results have been presented and interpreted. All the results have been either favourably verified by the experimental results or been critically analyzed. As an alternative research method to the strengthened RC beam, the present analysis provides more results that are difficult to measure through experiments. These include the interfacial stresses in the concrete near the plate end. These results are deemed as key information in order to elucidate failure mechanism quantitively.

Another important finding is that the structural behaviour near the plate end is dominantly related to the bending moment carried by the beam cross section at the plate end. This includes the peak stresses and the characteristic loads. It also further confirmed the observation in Chapter 5 that the bending moment at the plate end is the major cause of the stress concentration.

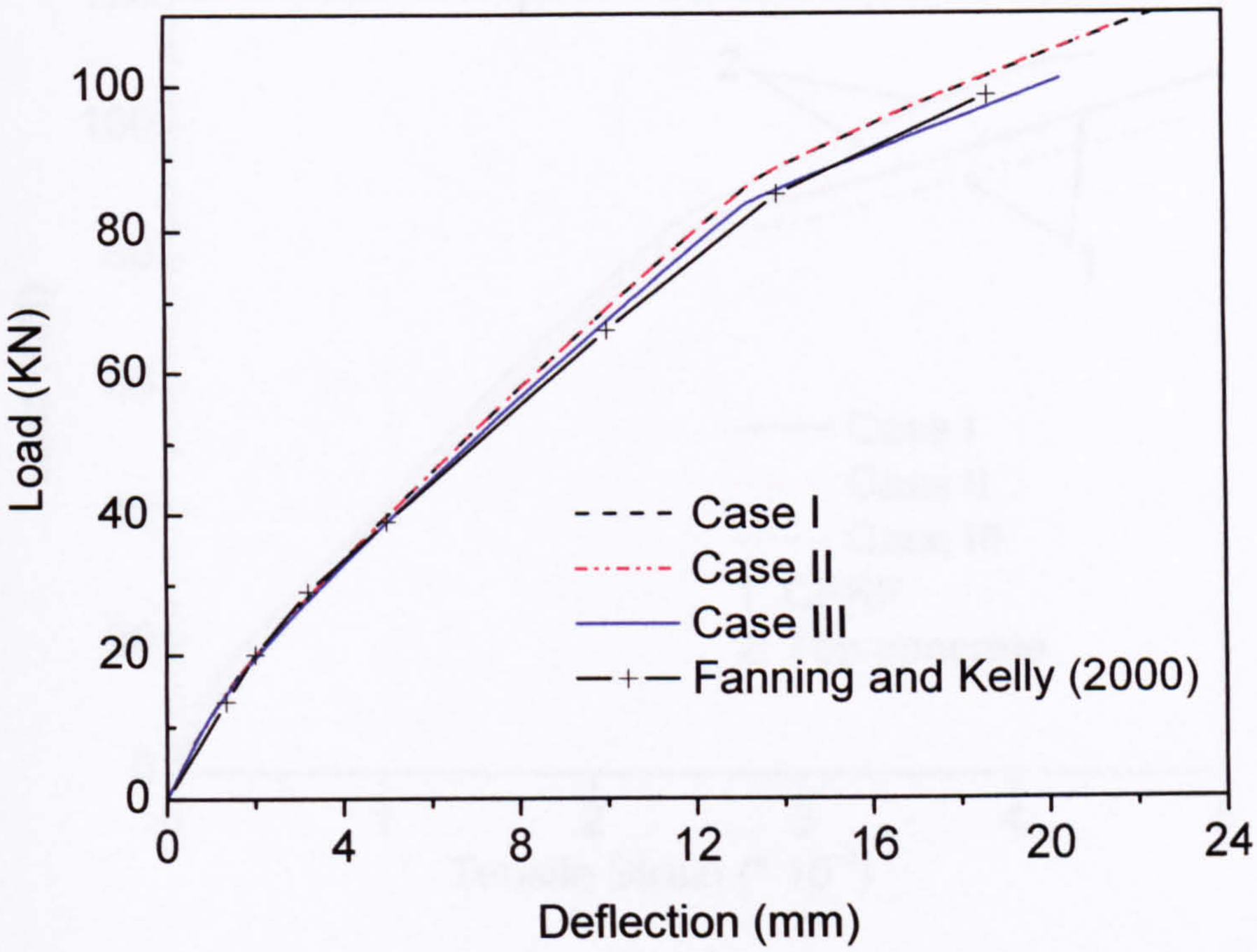

Fig. 6.17 Load-deflection plot for strengthened beam I

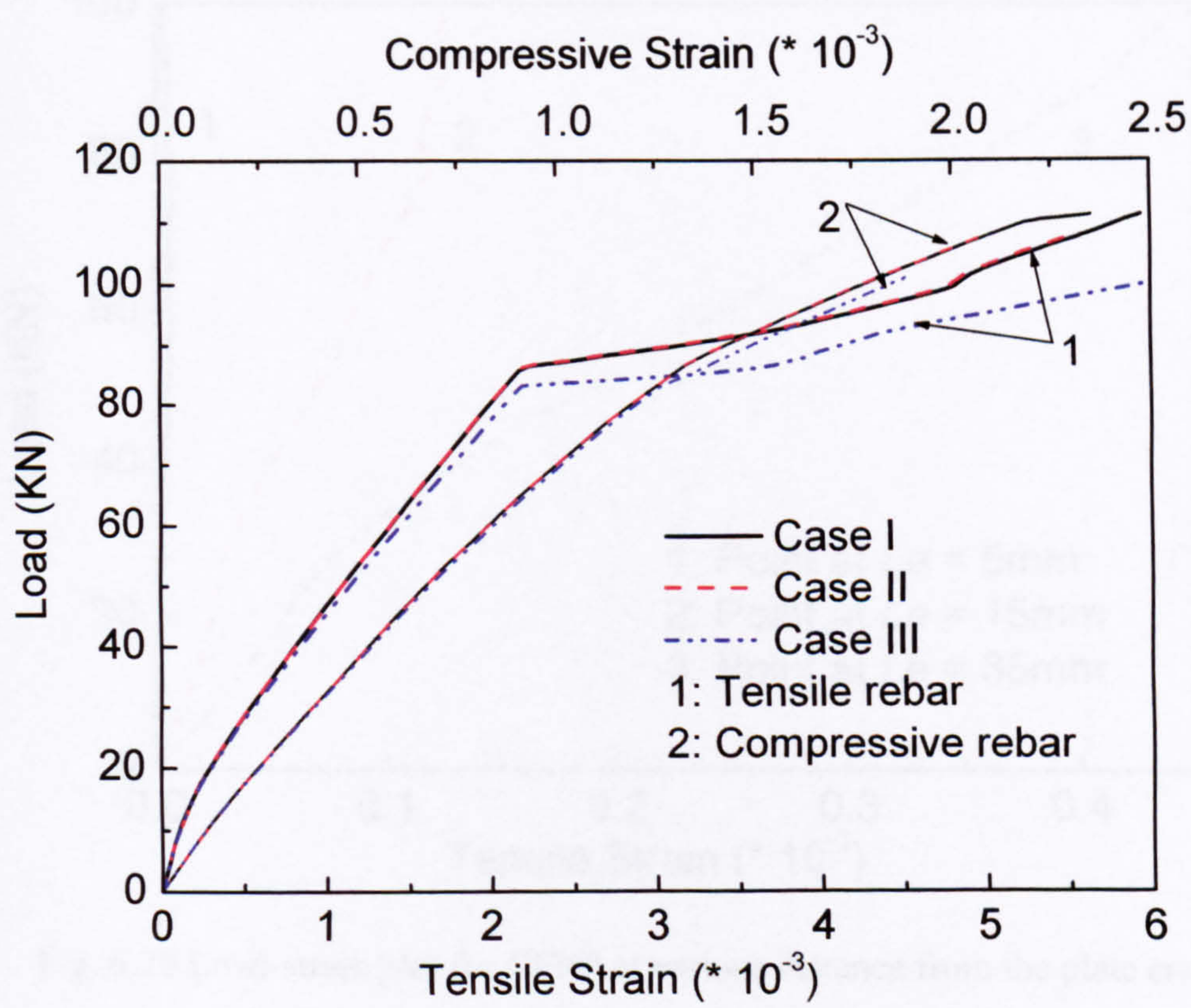

Fig. 6.18 Load-strain plot for the reinforcement

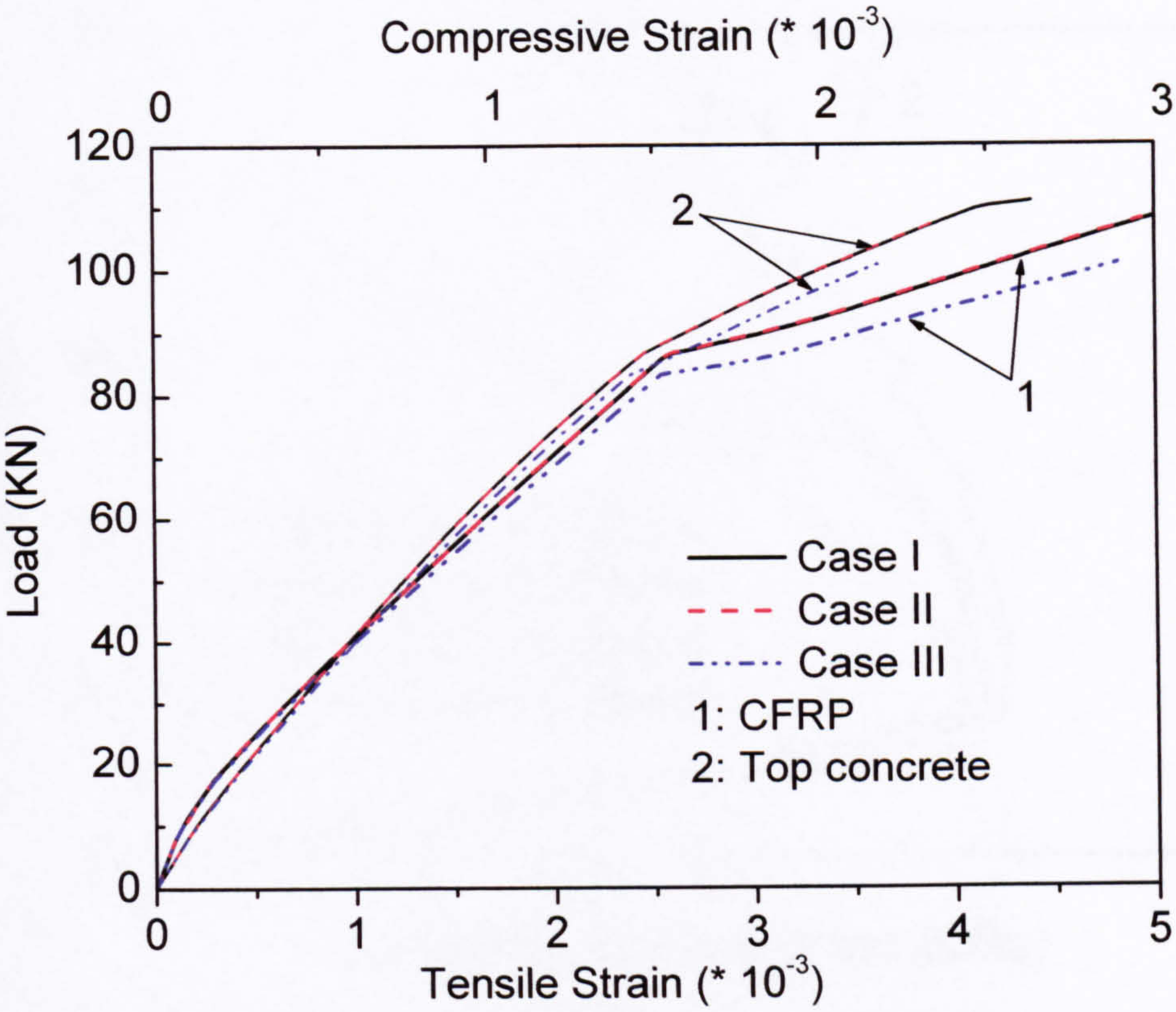

Fig. 6.19 Load-strain plot for CFRP and concrete top fibre at the midplan

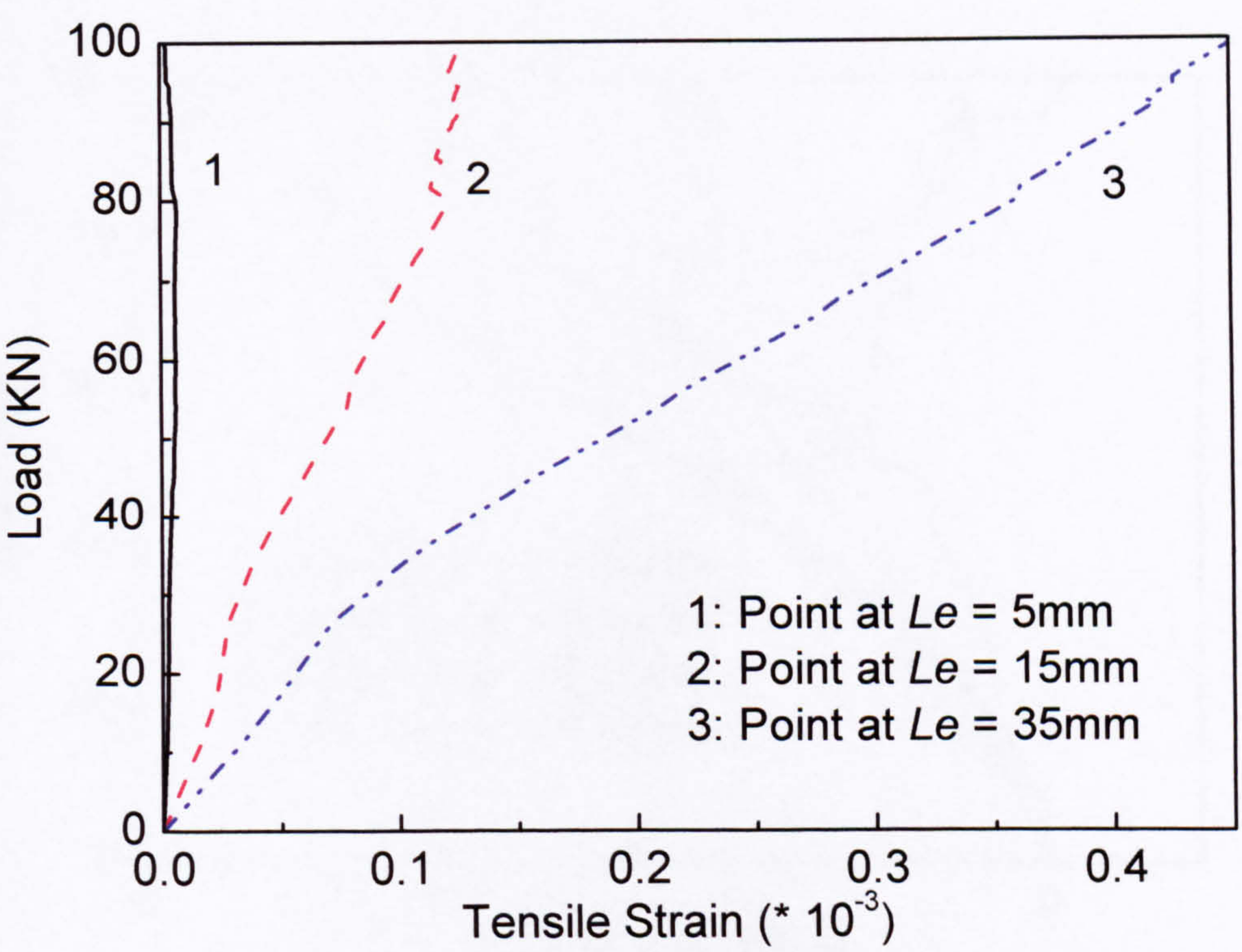

Fig. 6.20 Load-strain plot for CFRP at various distance from the plate end

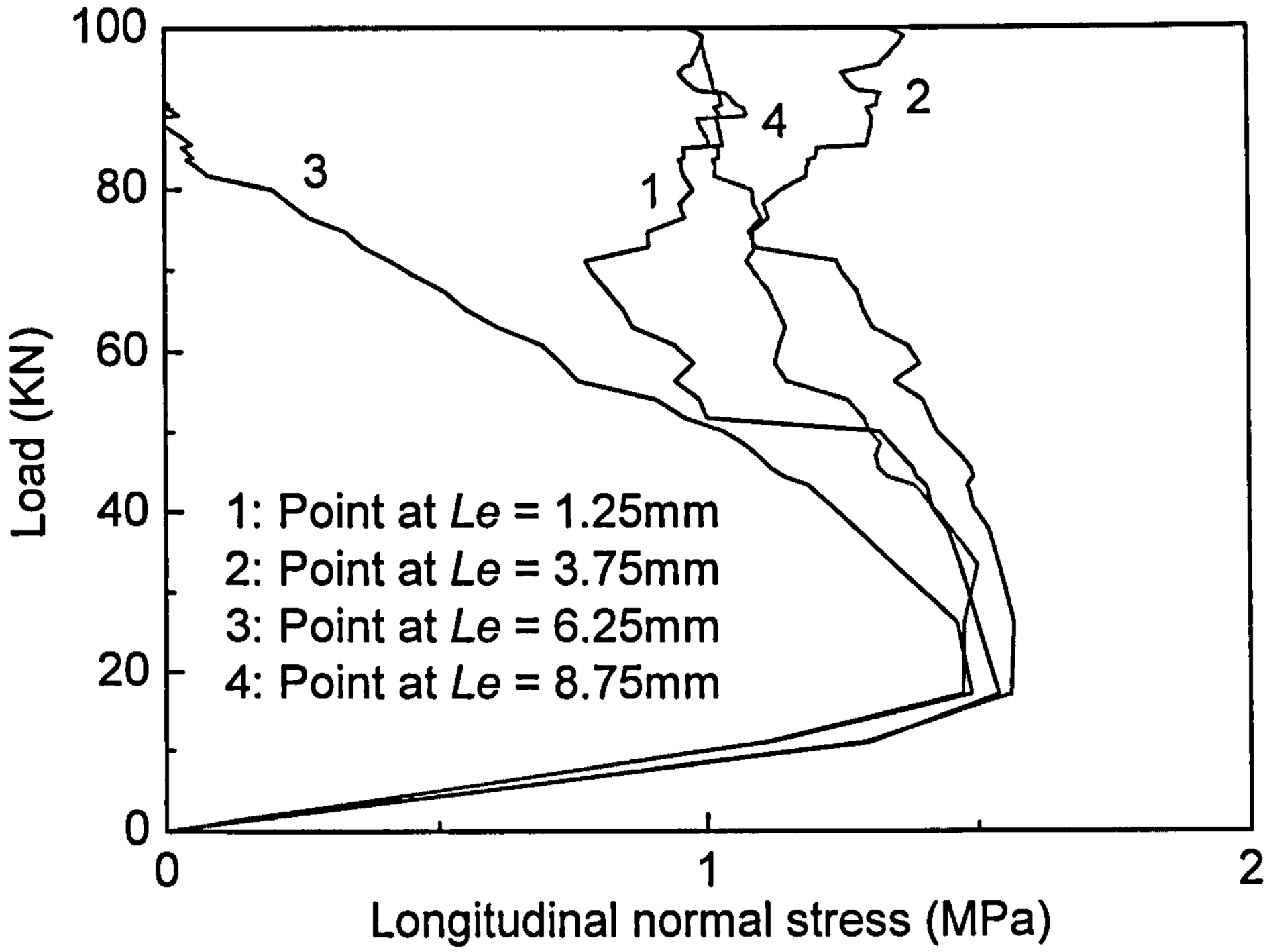

(a) Longitudinal normal stress for the concrete in the beam soffit near the plate end

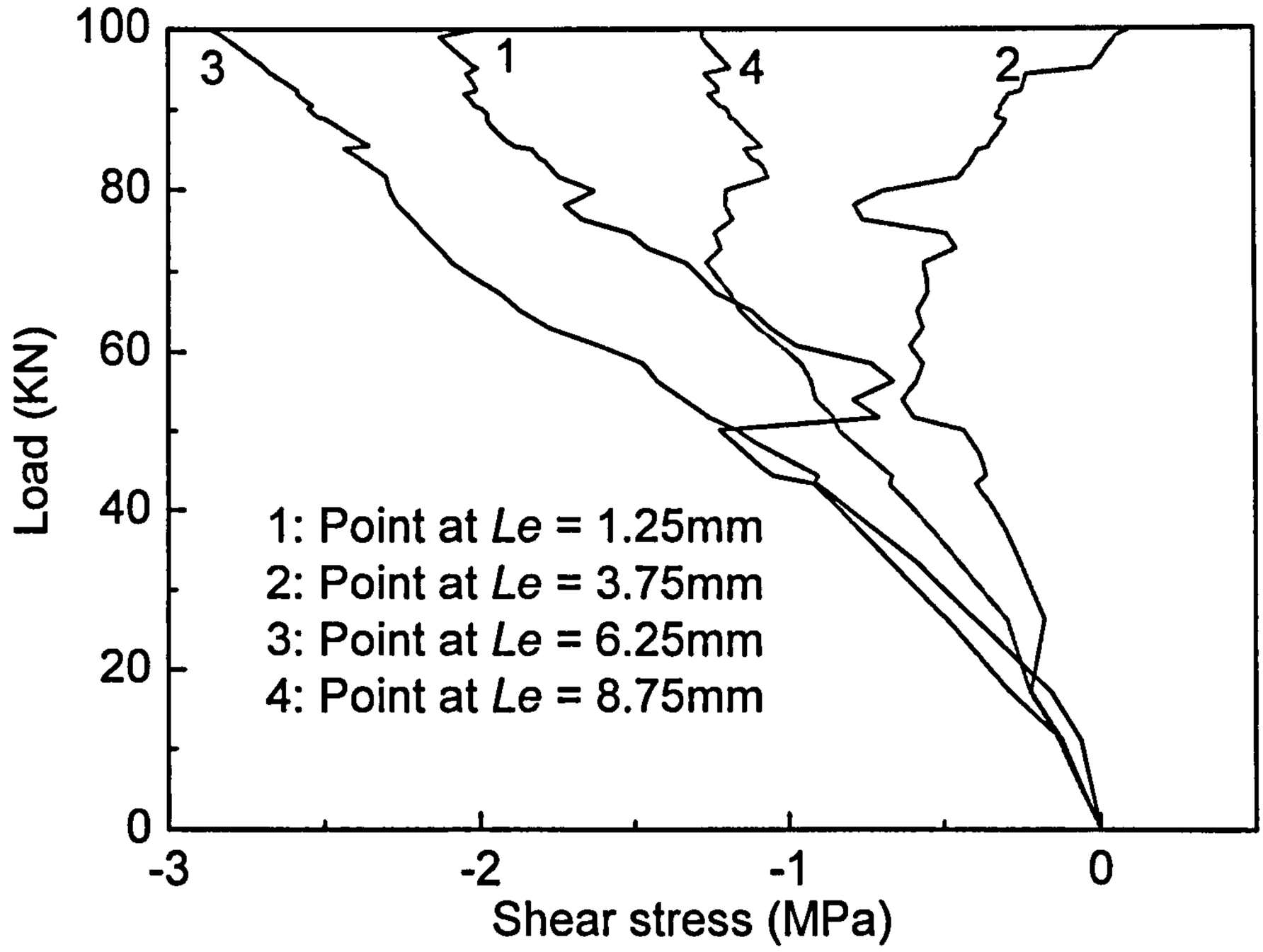

(b) The shear stress for the concrete in the beam soffit near the plate end

Fig. 6.21 The stress component for the concrete in the beam soffit near the plate end

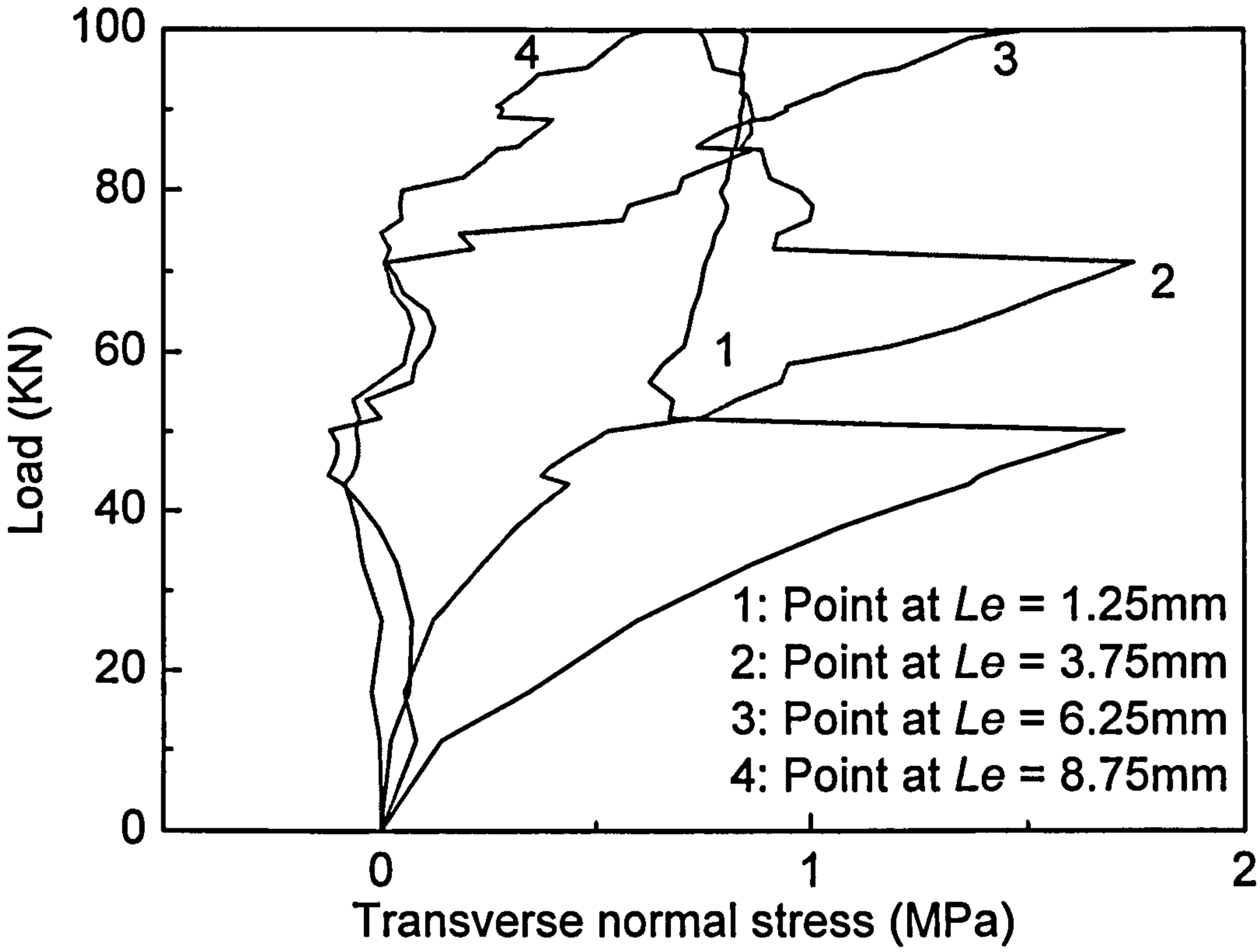

(c) The transverse normal stress for the concrete in the beam soffit near the plate end

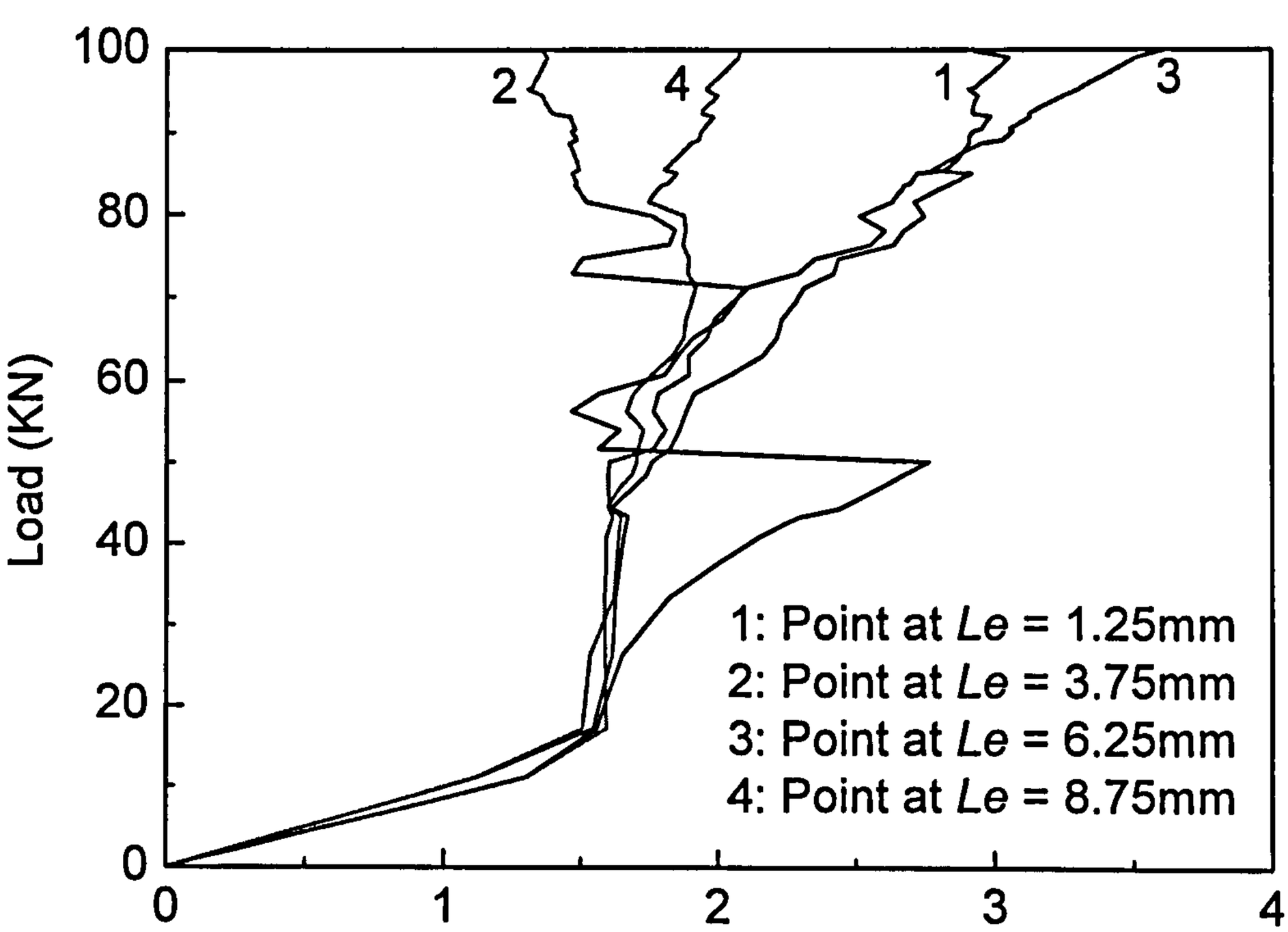

(d) The maximum principle stress for the concrete in the beam soffit near the plate end

Fig. 6.21 The stress component for the concrete in the beam soffit near the plate end

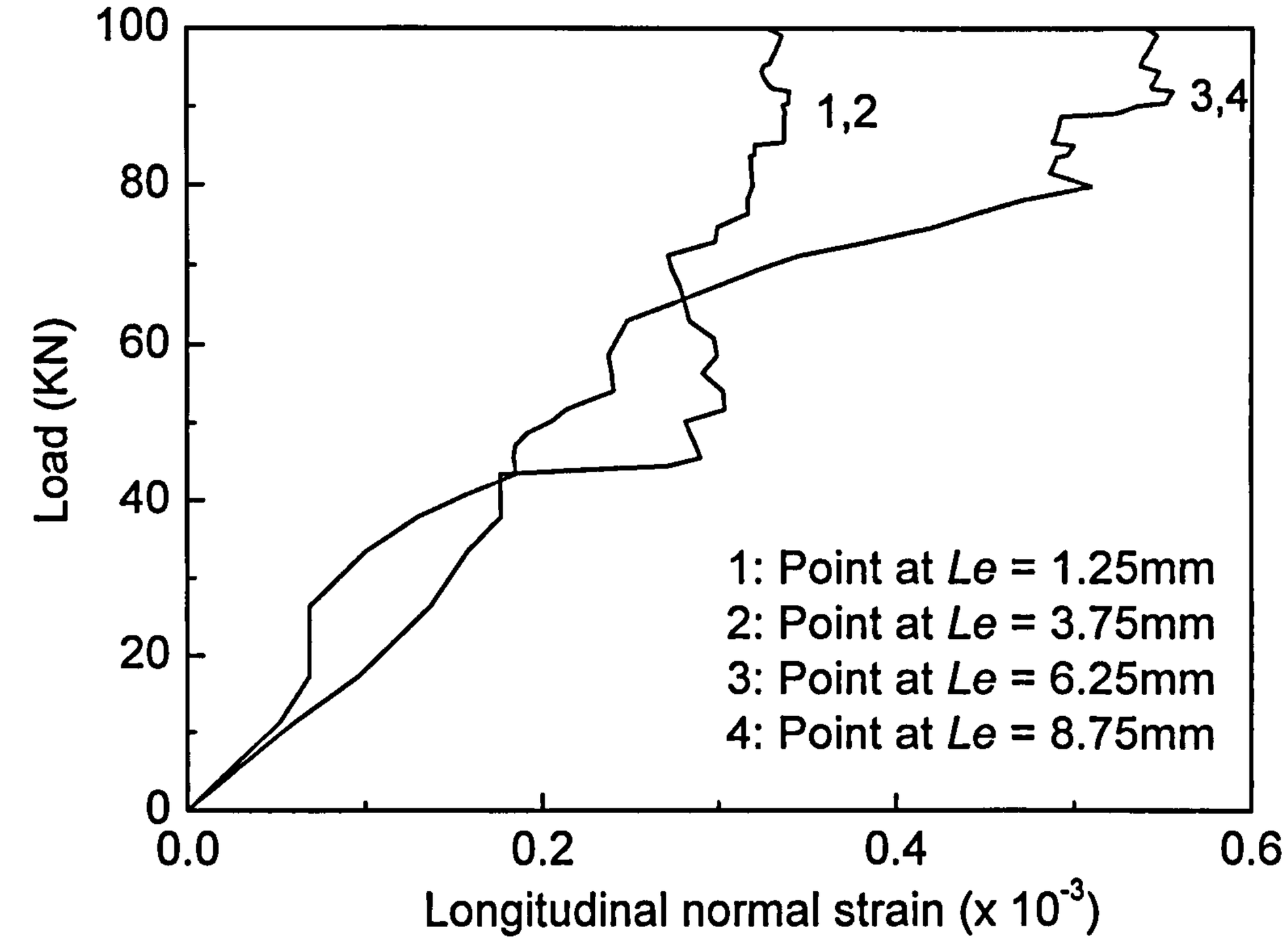

(a) The longitudinal normal strain for the concrete in the beam soffit near the plate end

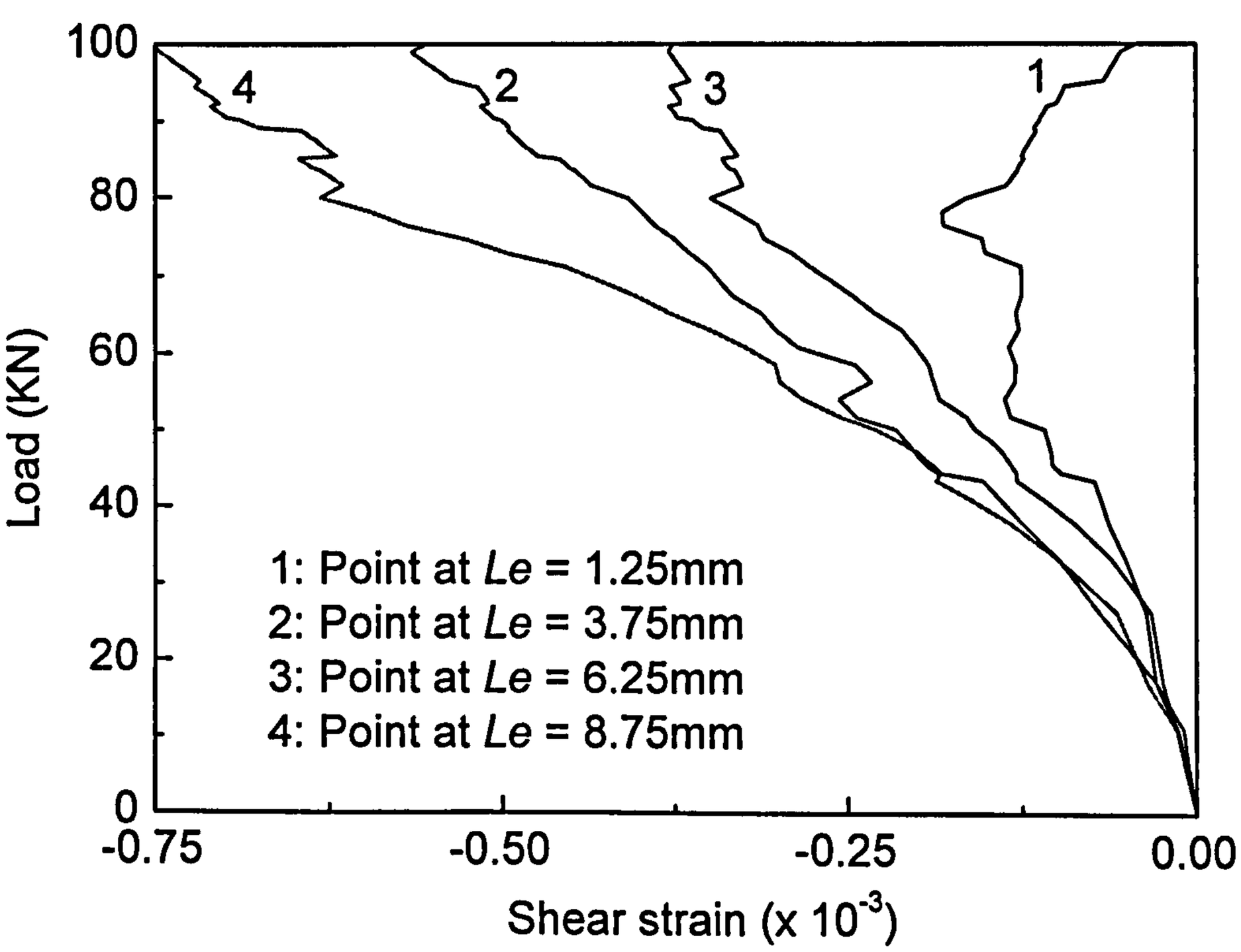

(b) The shear strain for the concrete in the beam soffit near the plate end

Fig. 6.22 The strain components for the concrete in the beam soffit near the plate end

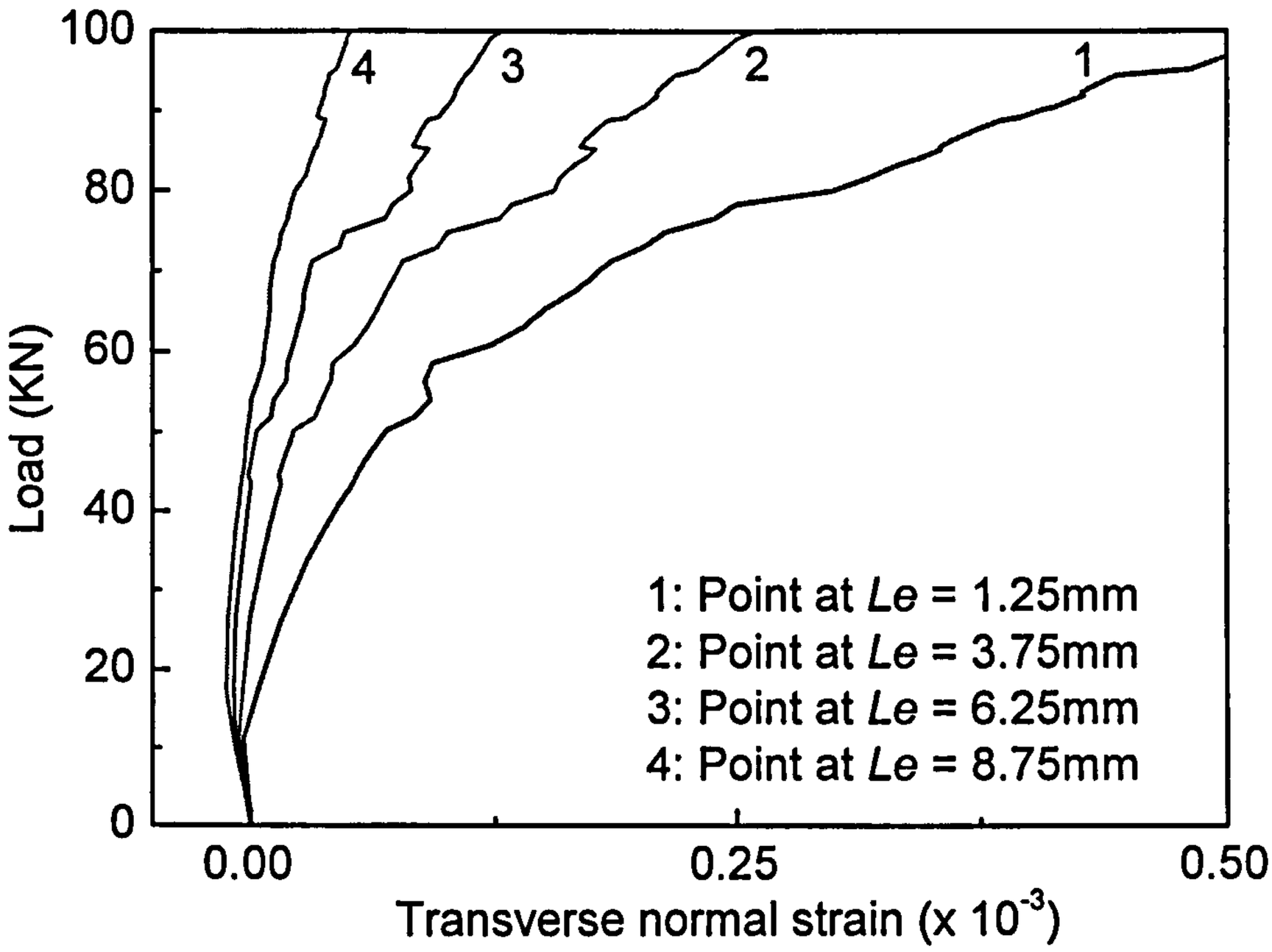

(c) The transverse normal strain for the concrete in the beam soffit near the plate end

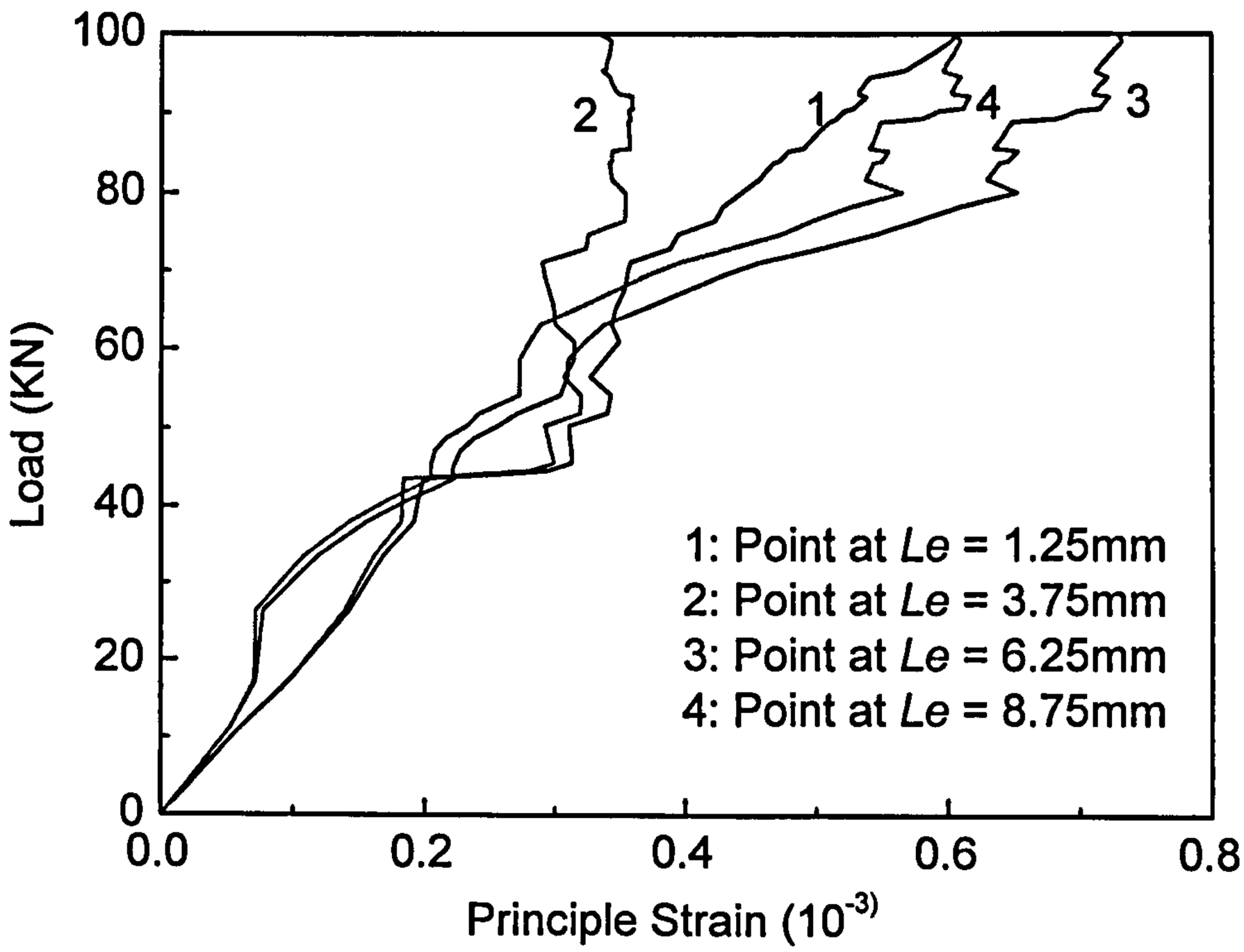

(d) The principle strain for the concrete in the beam soffit near the plate end

Fig. 6.22 The strain components for the concrete in the beam soffit near the plate end

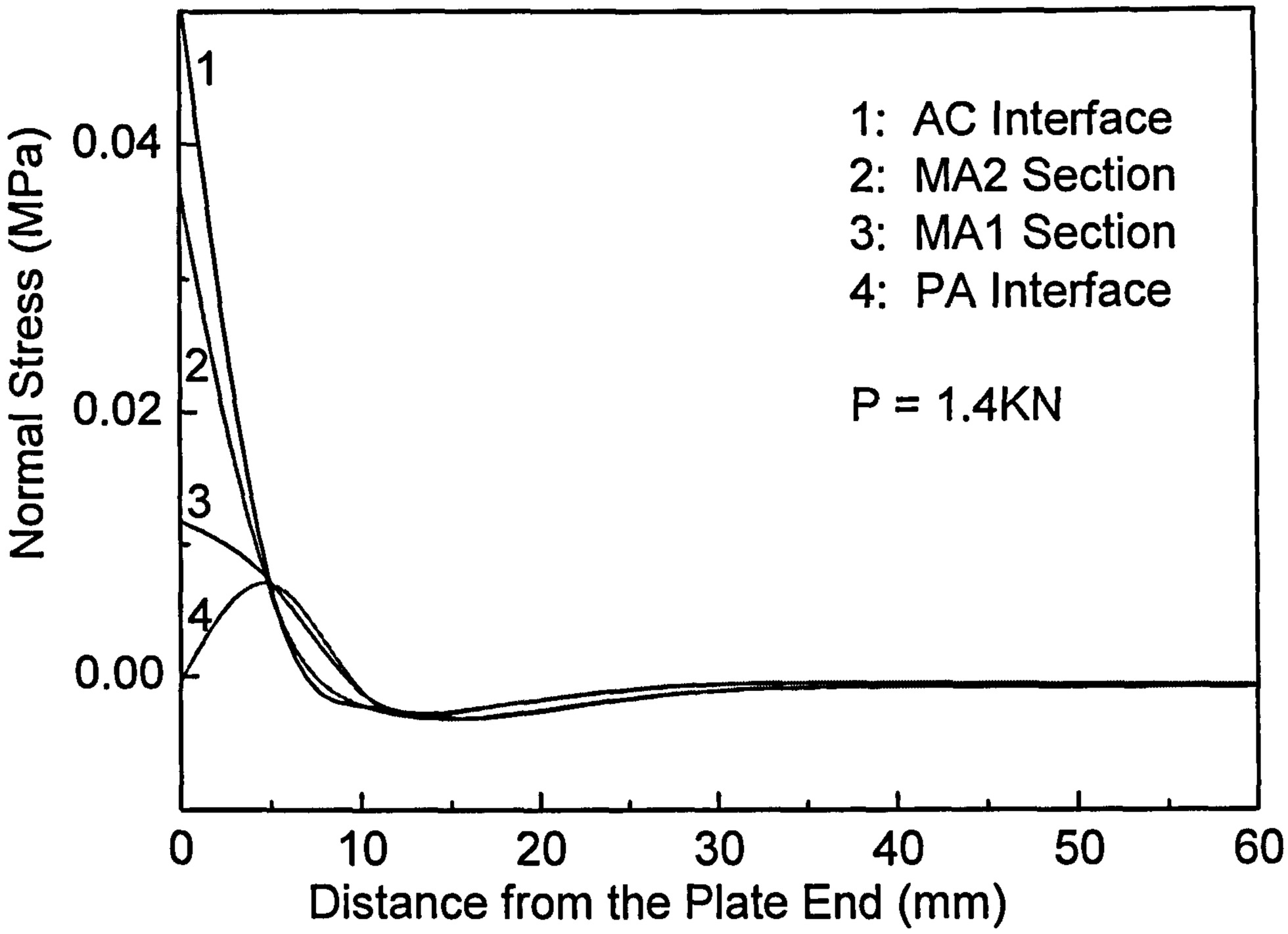

(a)

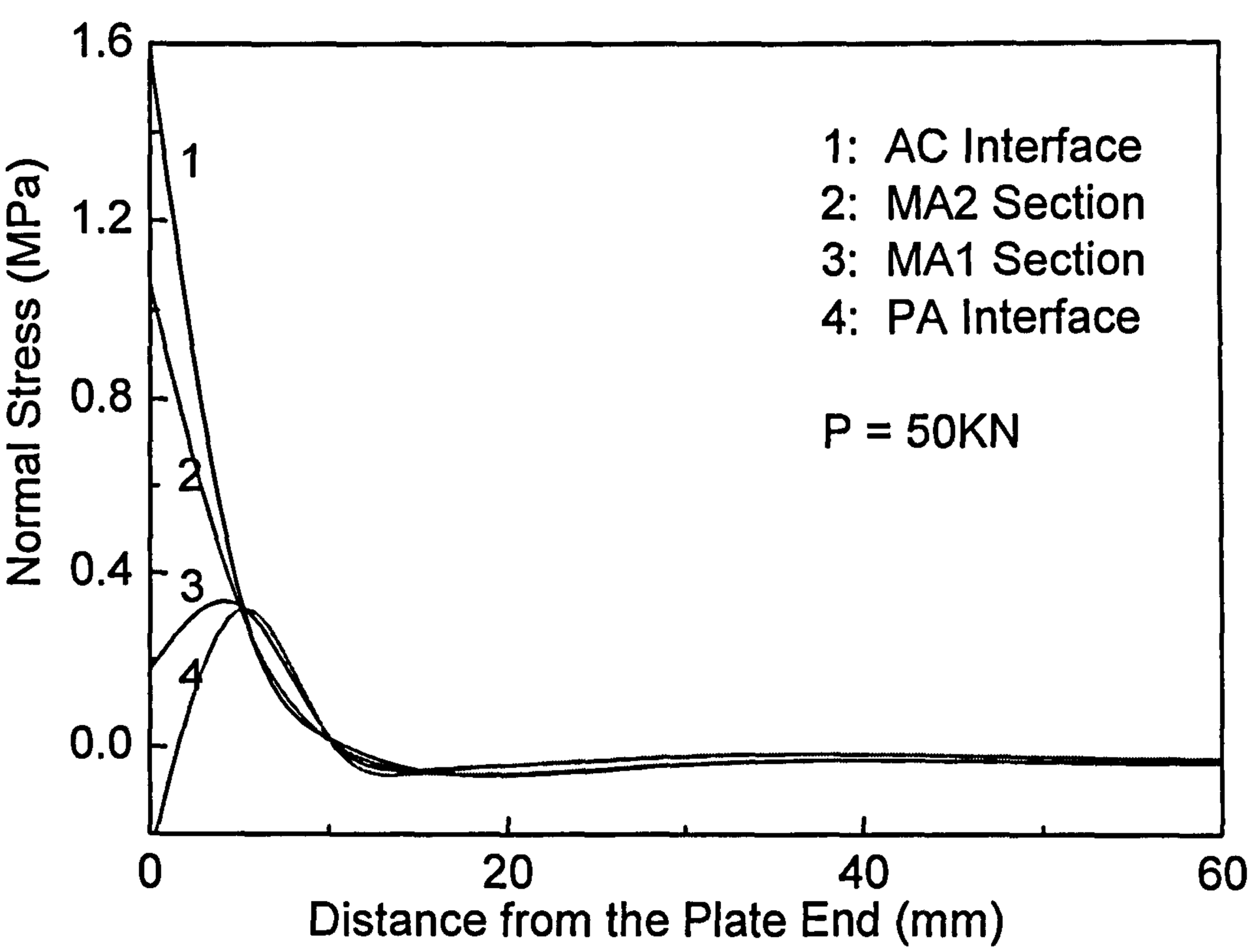

(b)

Fig. 6.23 Normal stresses along the interfaces and two horizontal plane in the adhesive layer

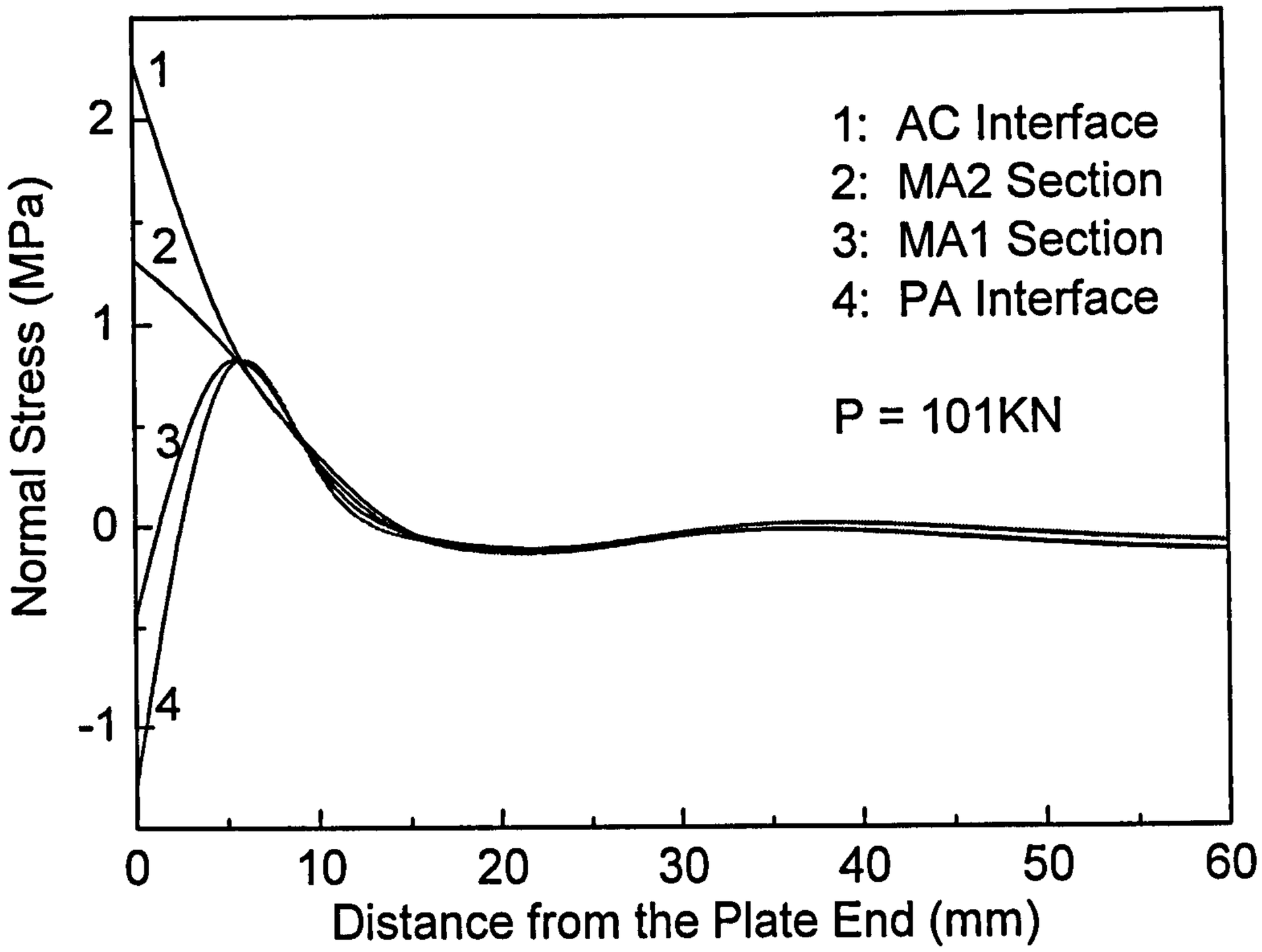

(c)

Fig. 6.23 Normal stresses along the interfaces and two horizontal plane in the adhesive layer

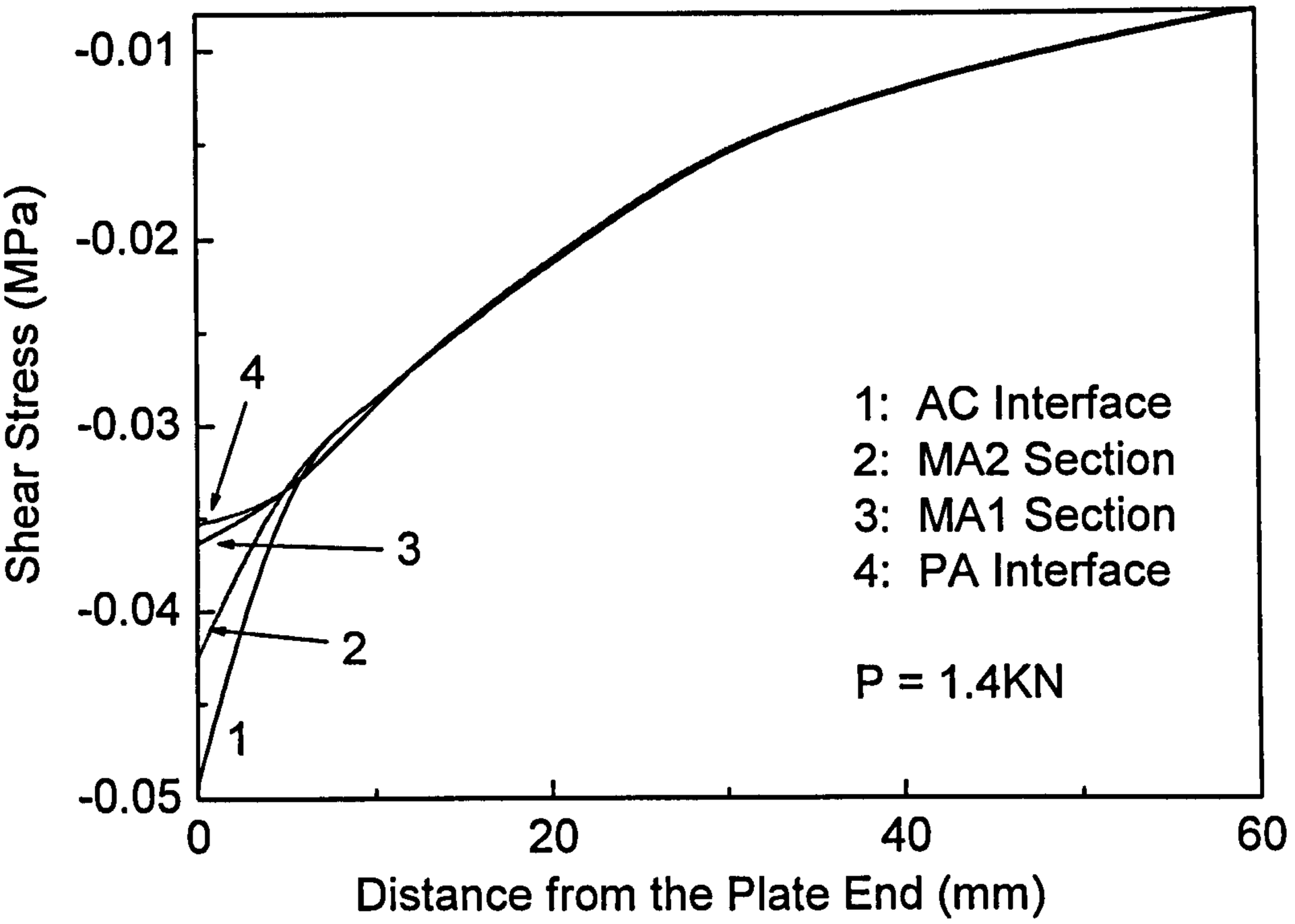

(a)

Fig. 6.24 Normal stresses along the interfaces and two horizontal planes in the adhesive layer

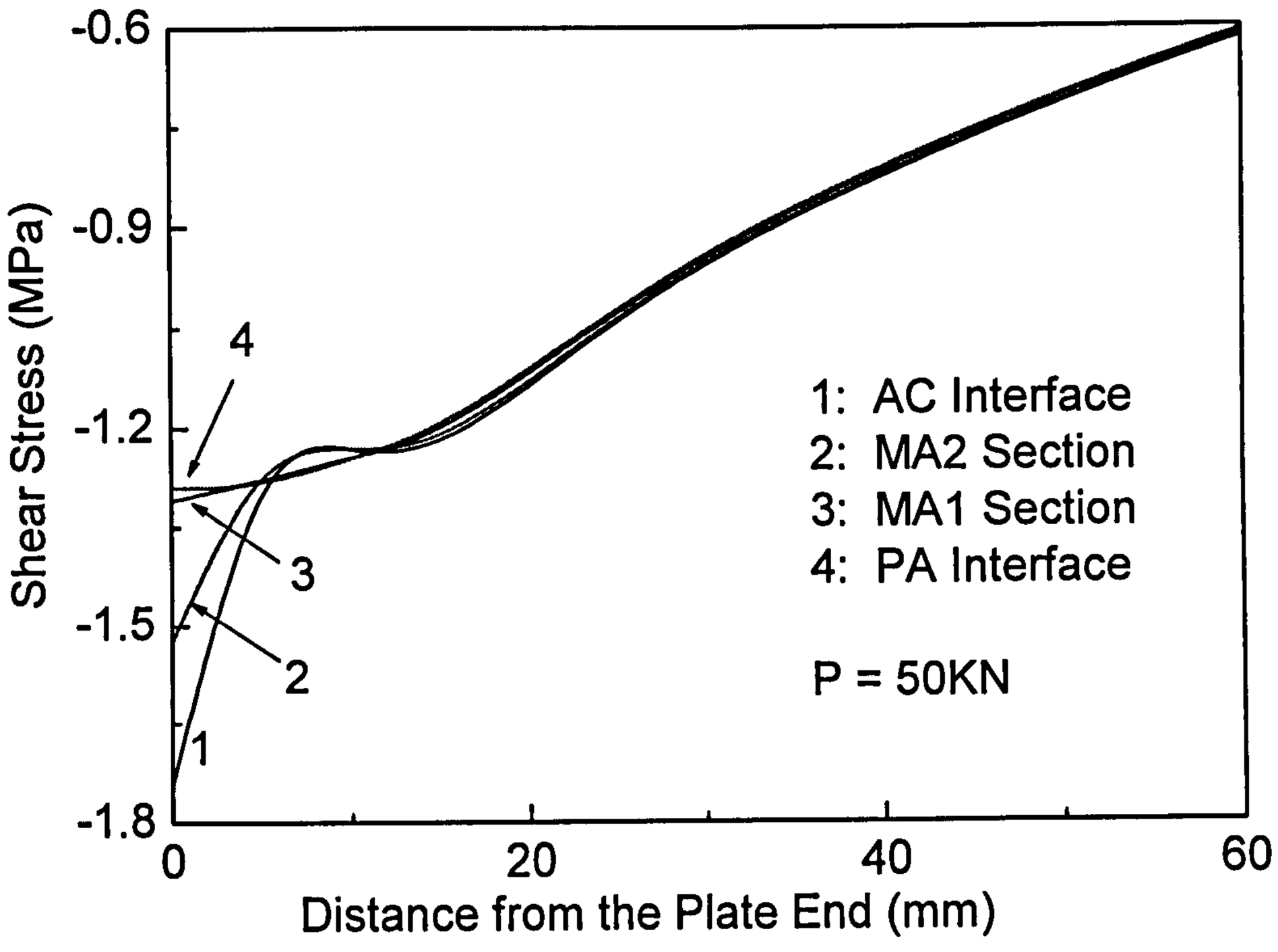

(b)

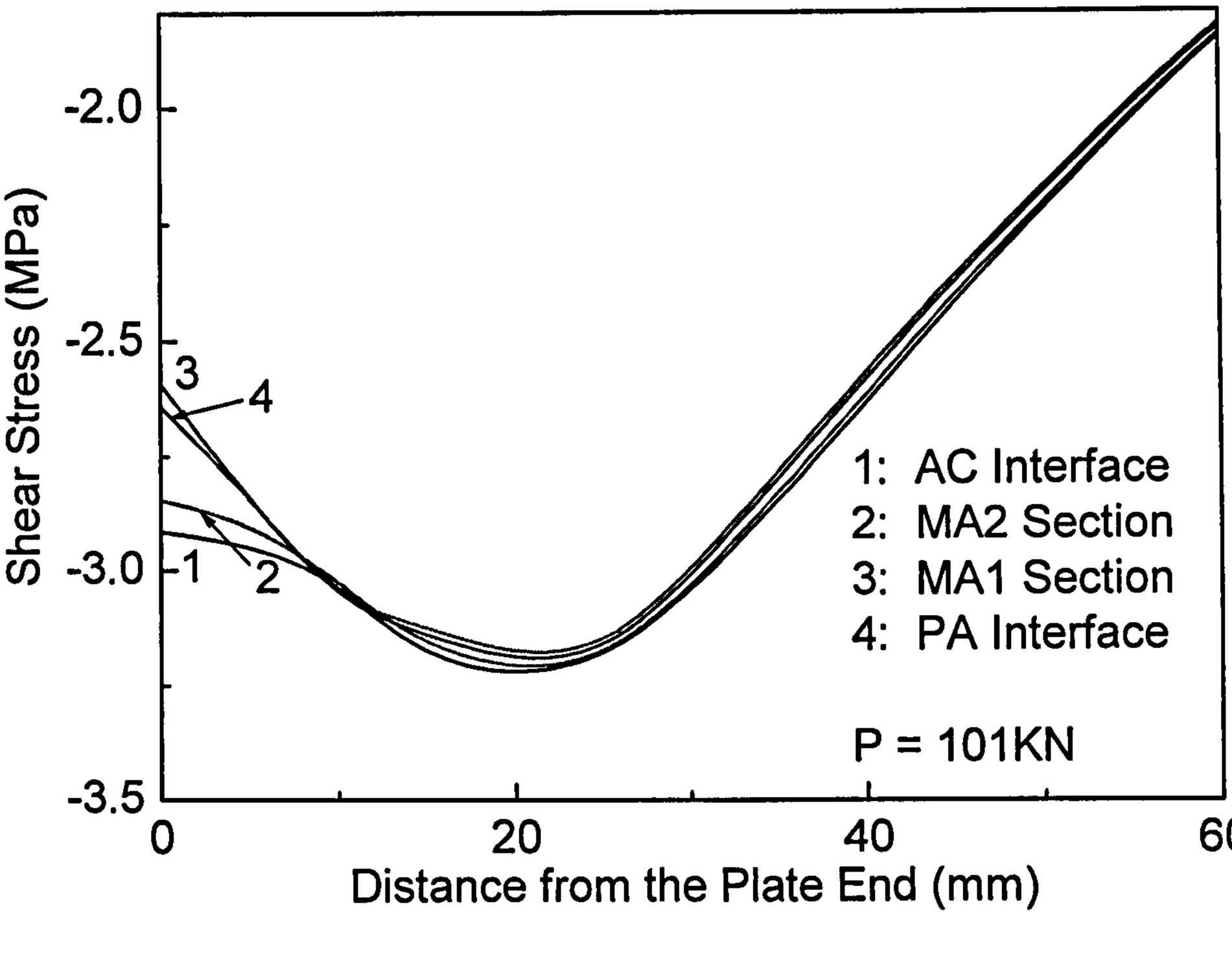

(c)

Fig. 6.24 Normal stresses along the interfaces and two horizontal planes in the adhesive layer

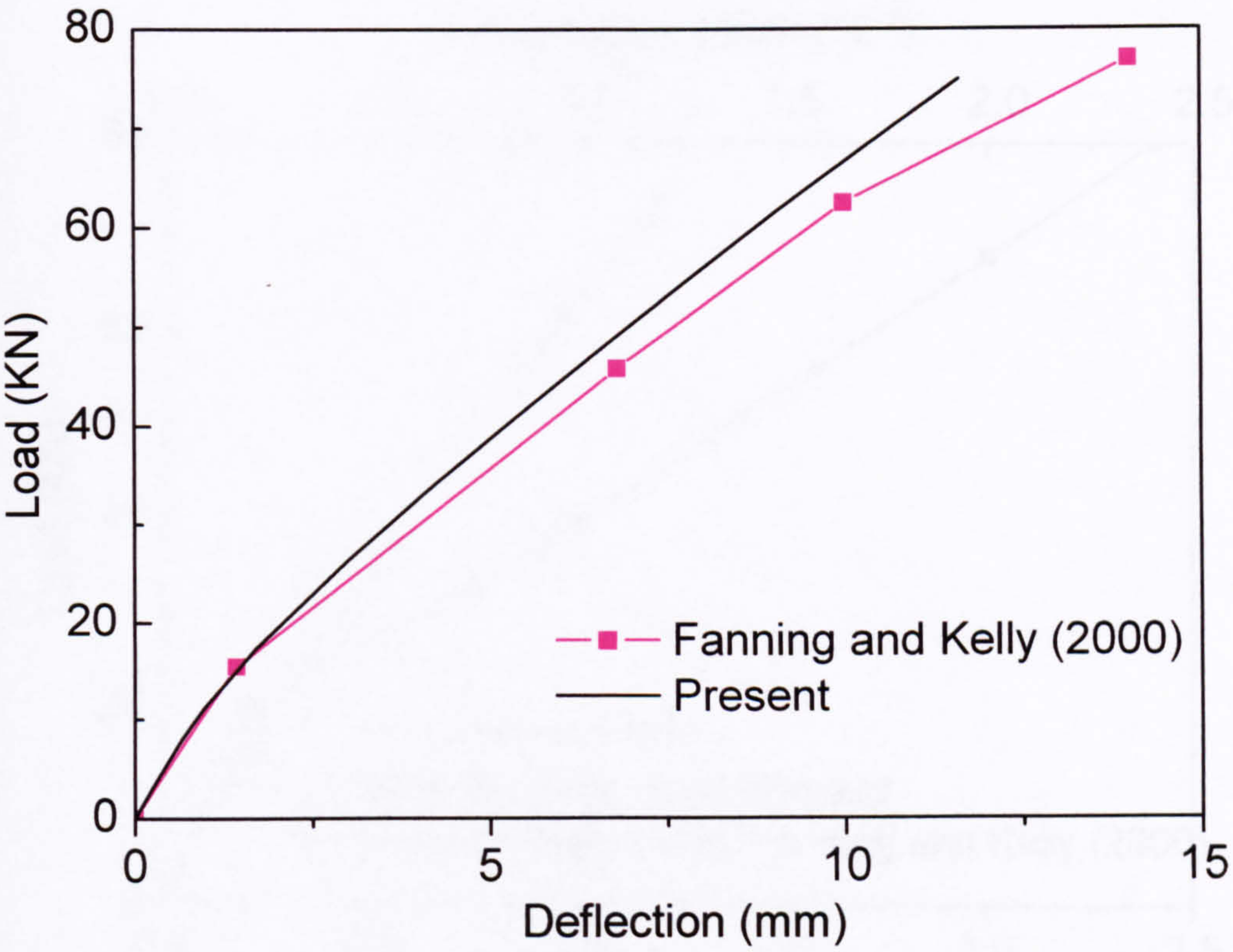

Fig. 6.25 Load-deflection plot of strengthened beam II

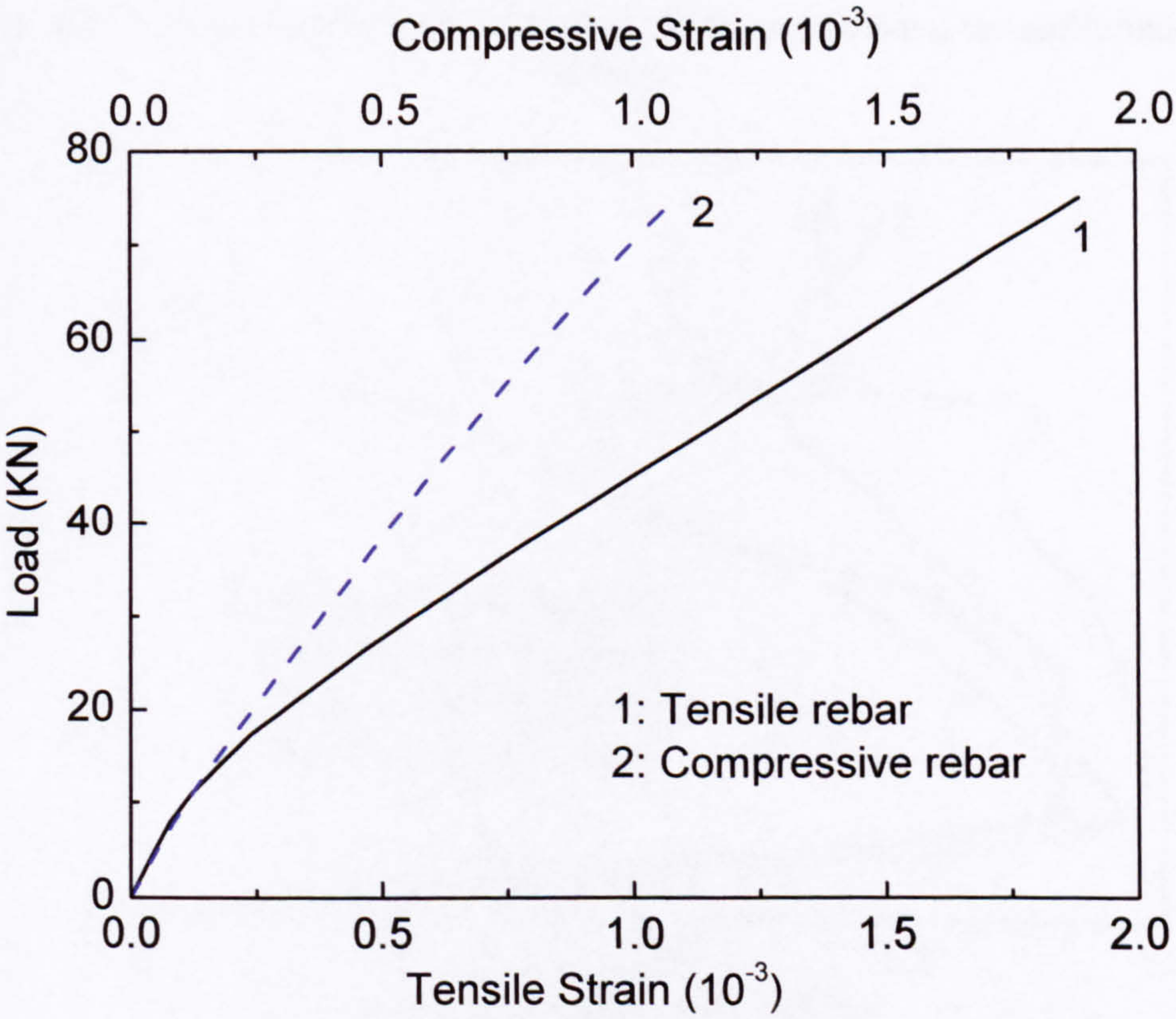

Fig. 6.26 Load-strain plot in the tensile and compressive reinforcement

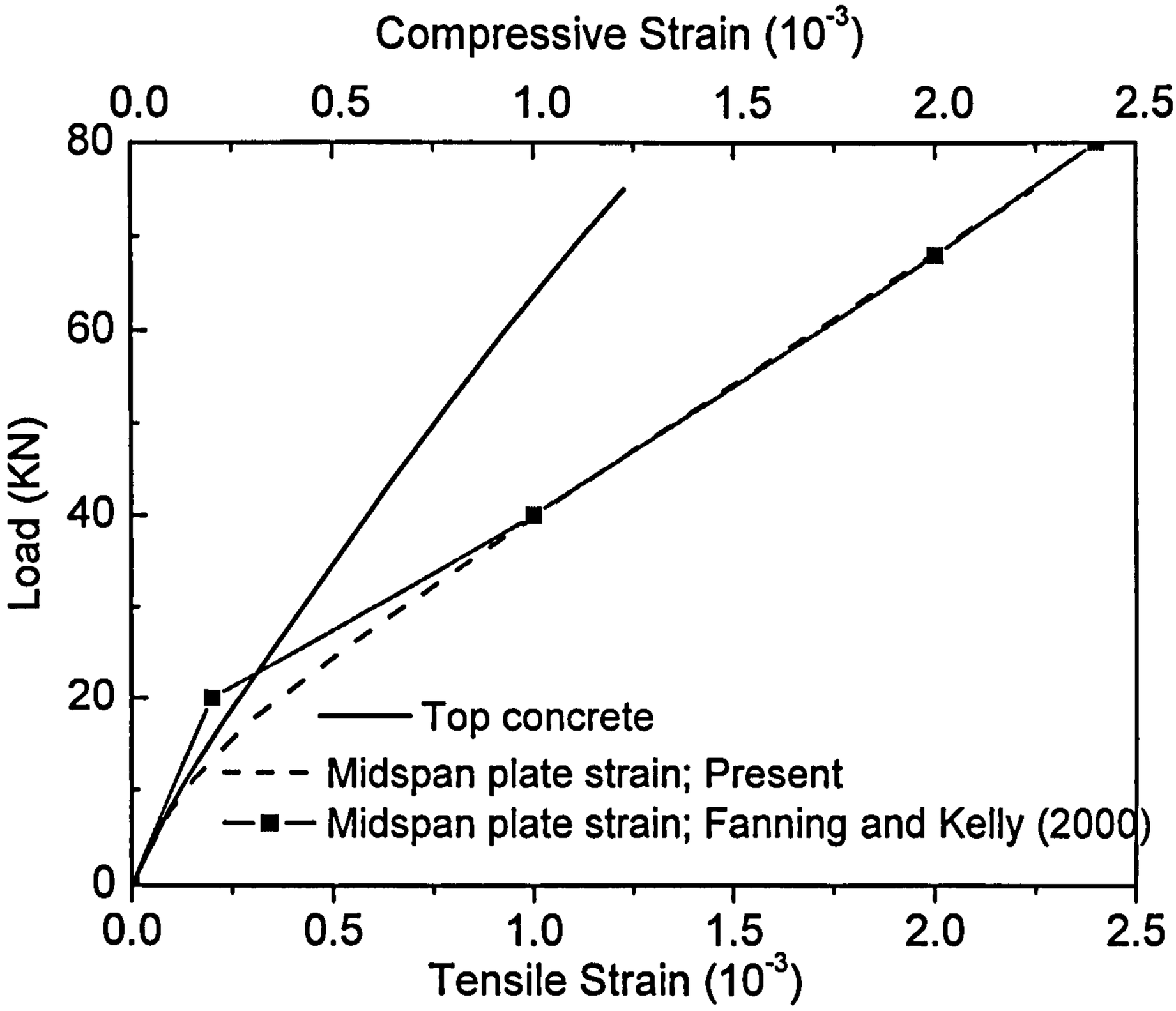

Fig. 6.27 Load-stain plot for the top concrete in midspan and the soffit plate in midspan

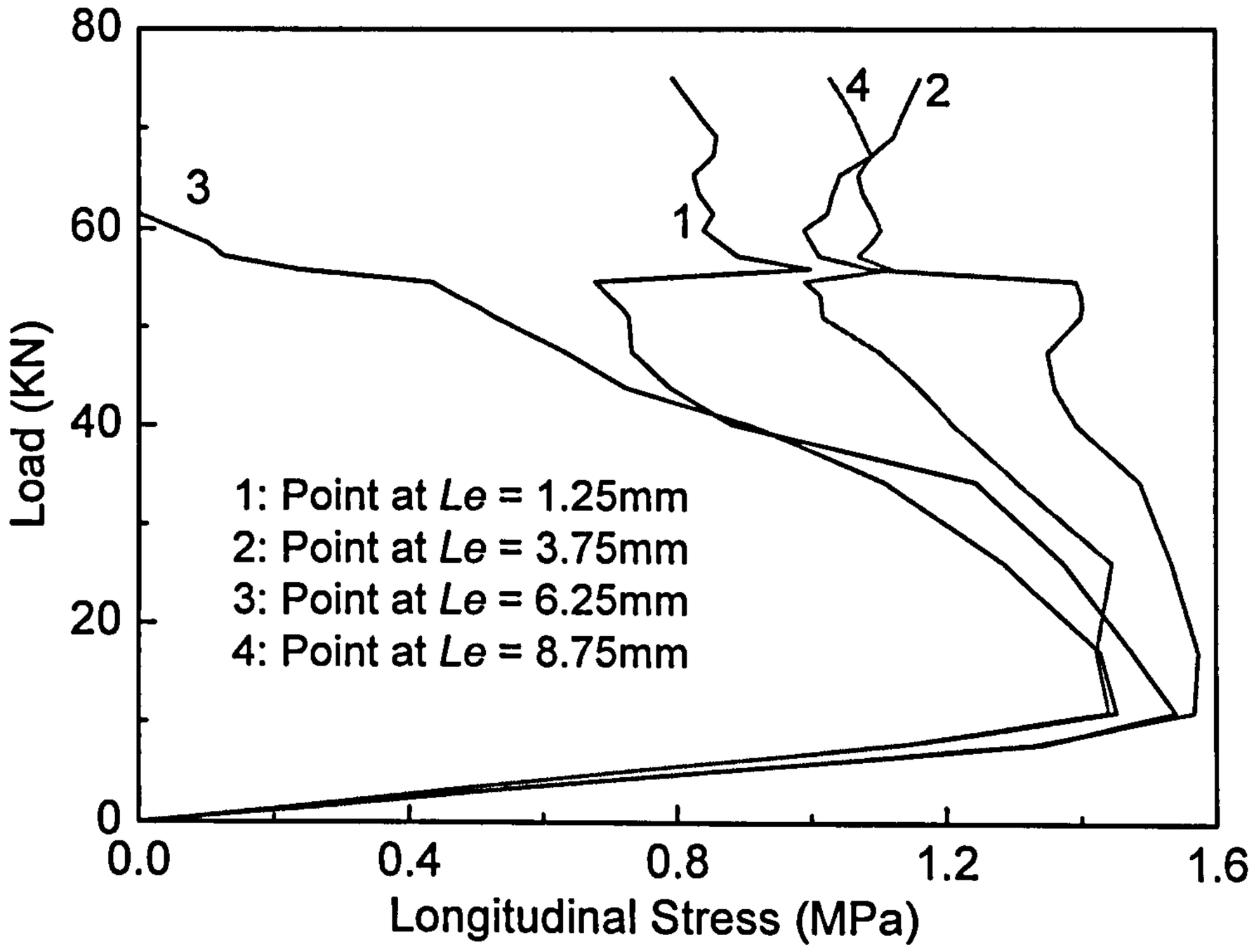

(a) Longitudinal stress

Fig. 6.28 The stress component in the concrete near the plate end

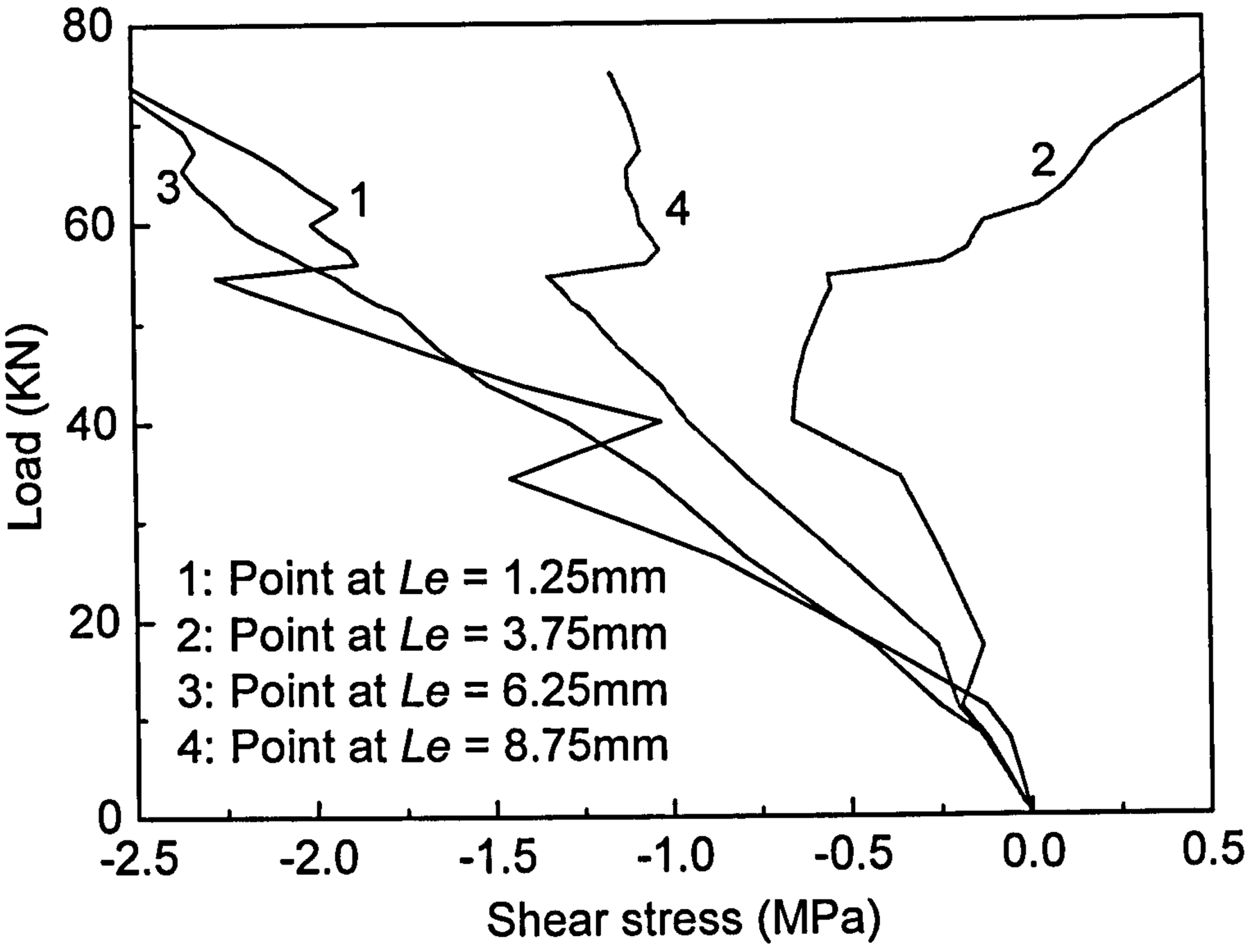

(b) Shear stress

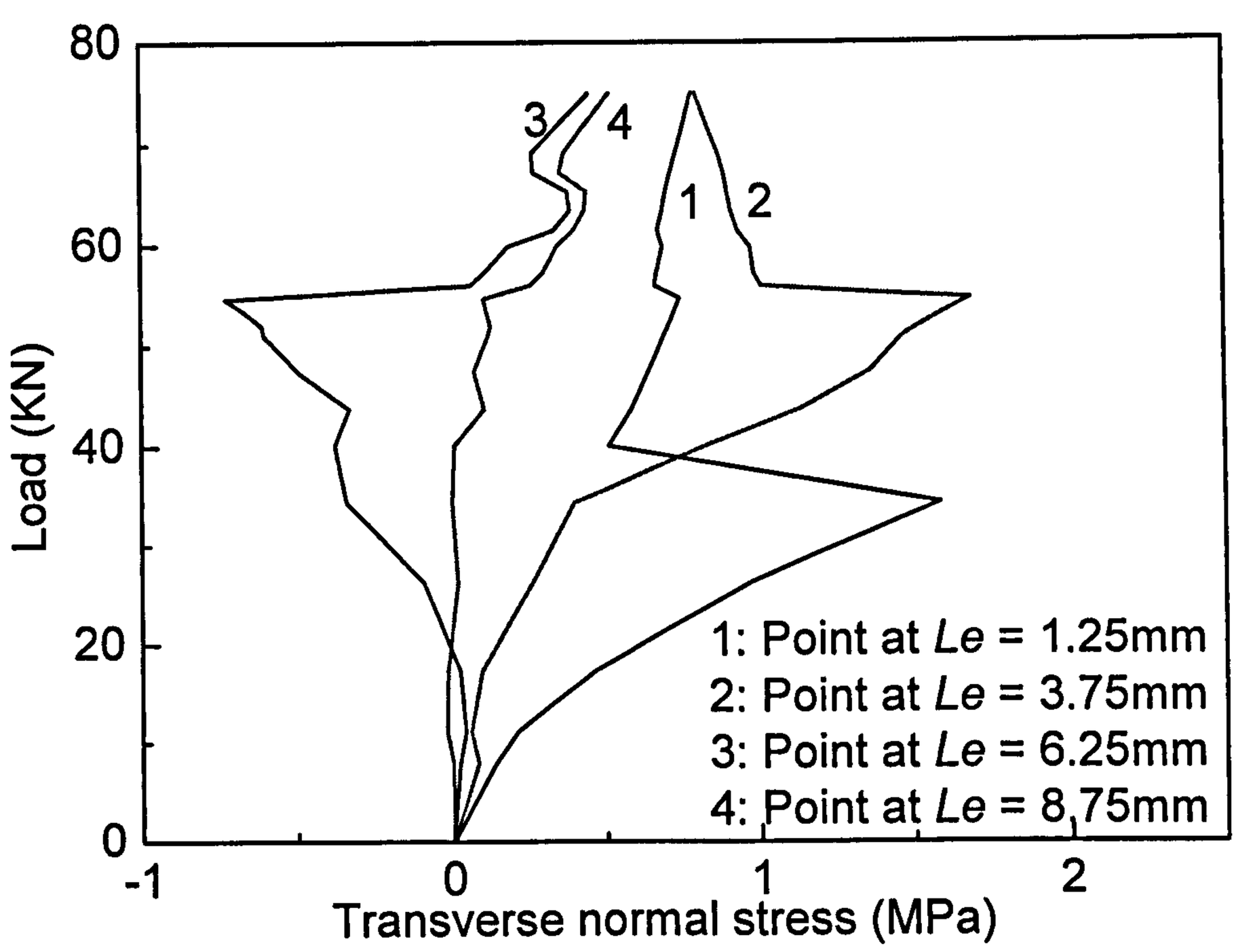

(c) Transverse normal stress

Fig. 6.28 The stress component in the concrete near the plate end

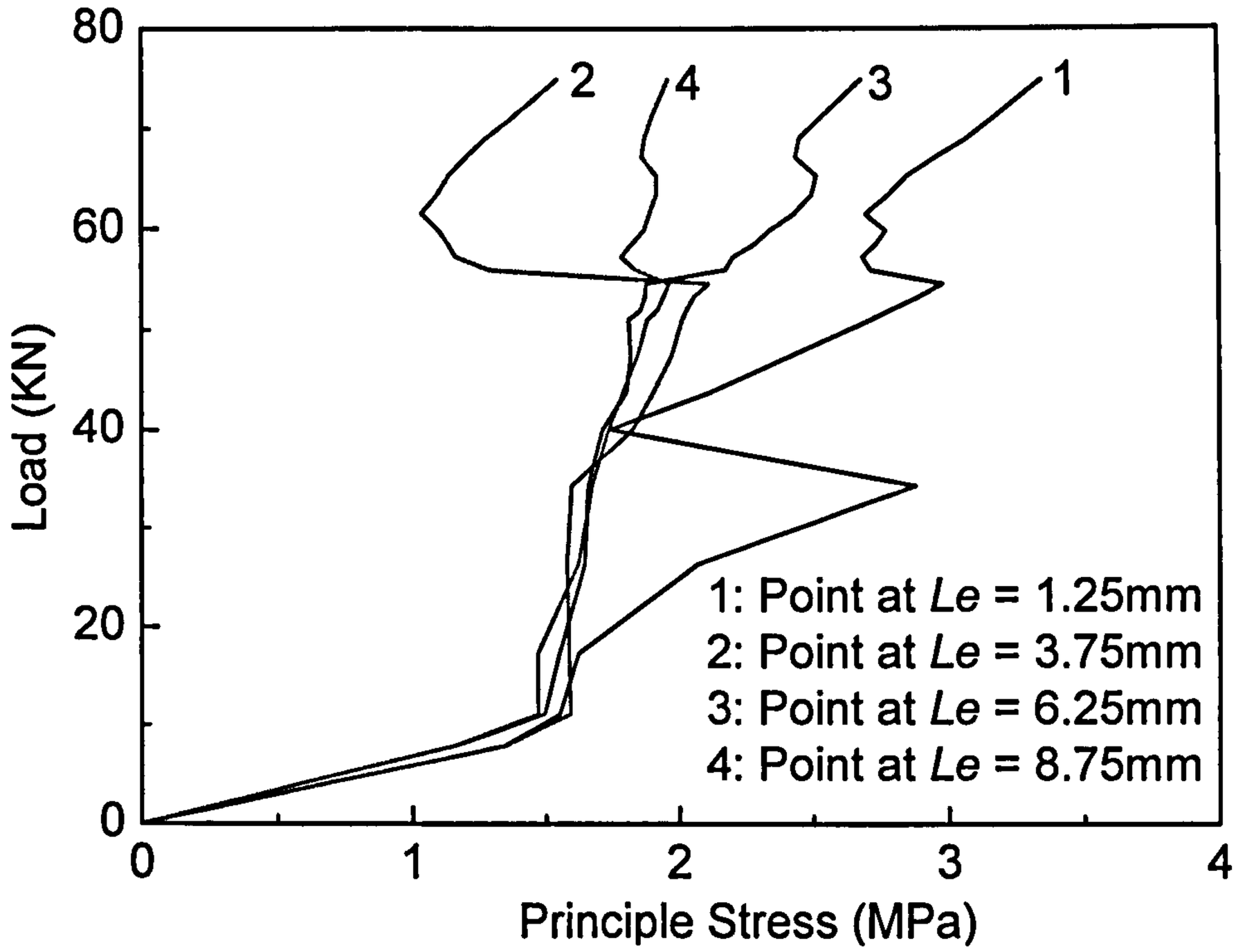

(d) Principle stress

Fig. 6.28 The stress component in the concrete near the plate end

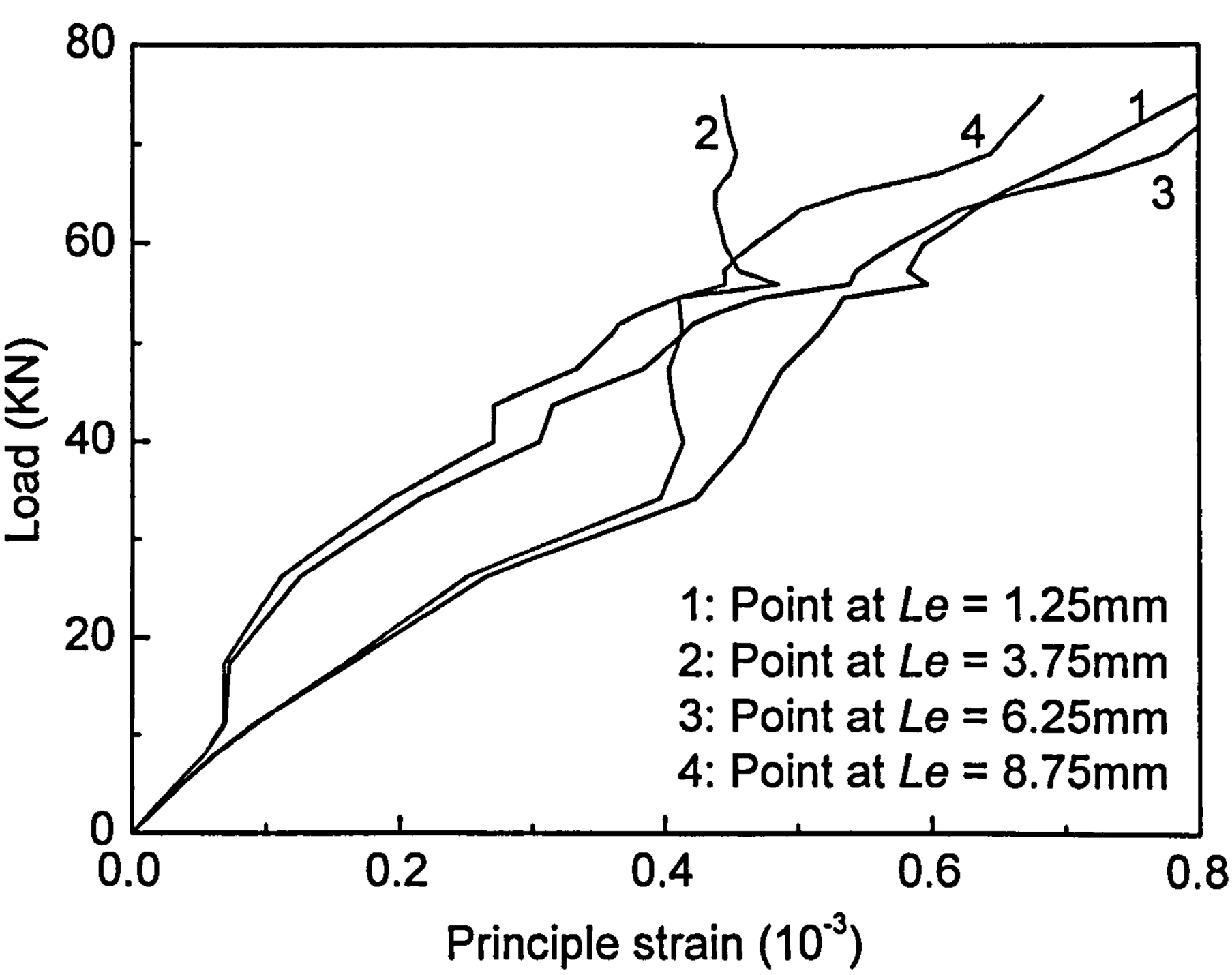

Fig. 6.29 The principle strain in the concrete near the plate end

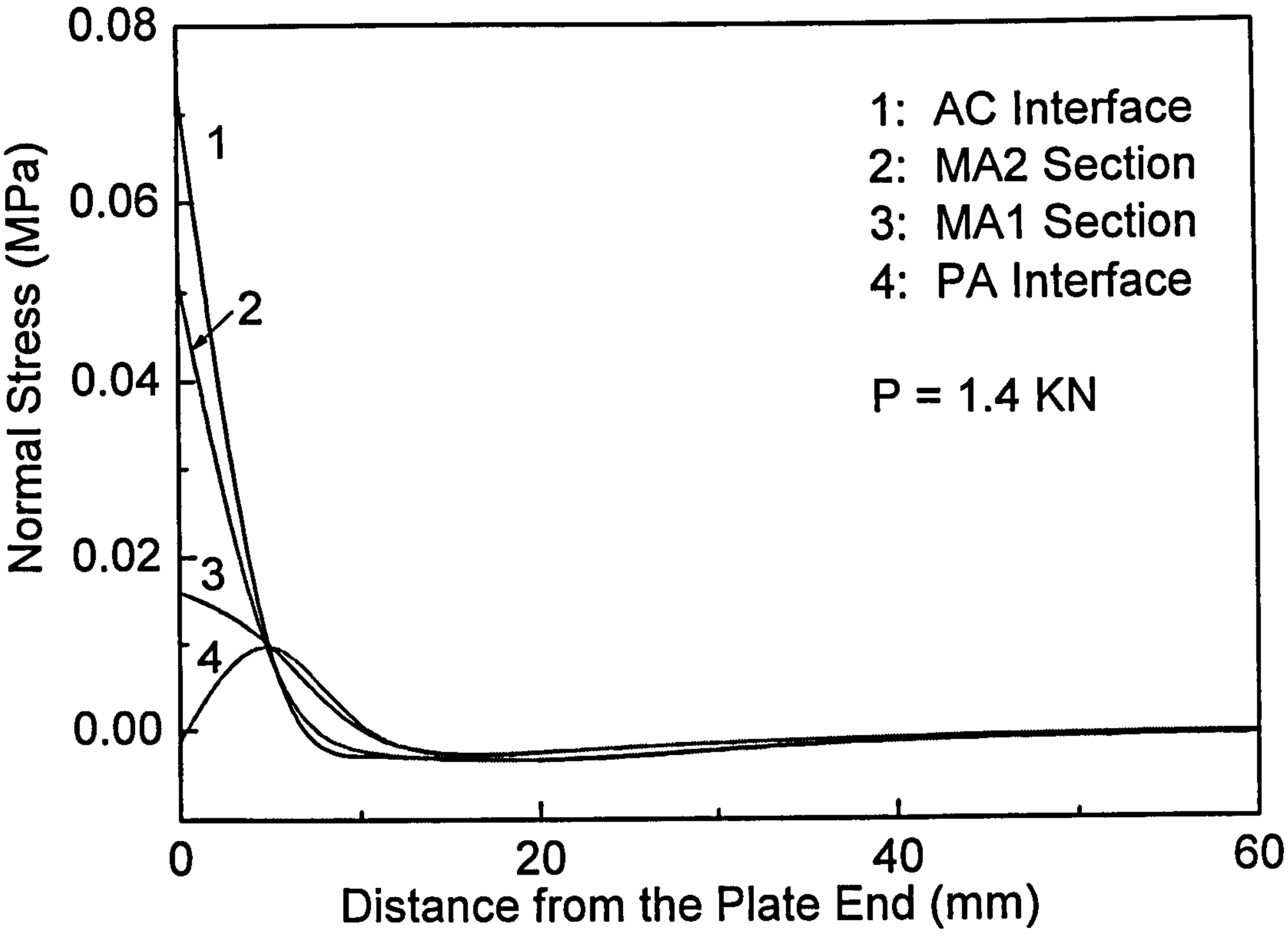

(a)

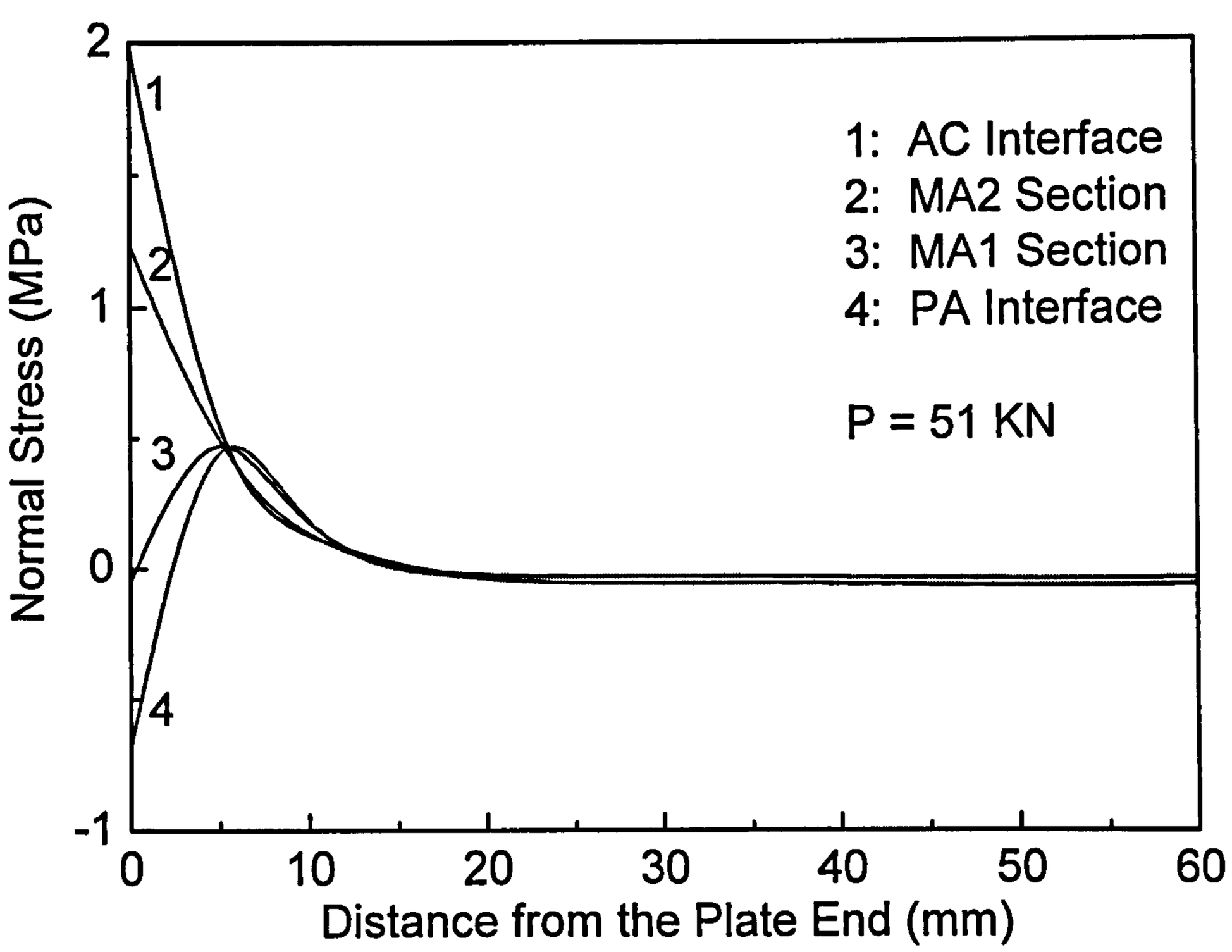

(b)

Fig. 6.30 The transverse normal stress along the interfaces and two horizontal plane in the adhesive layer

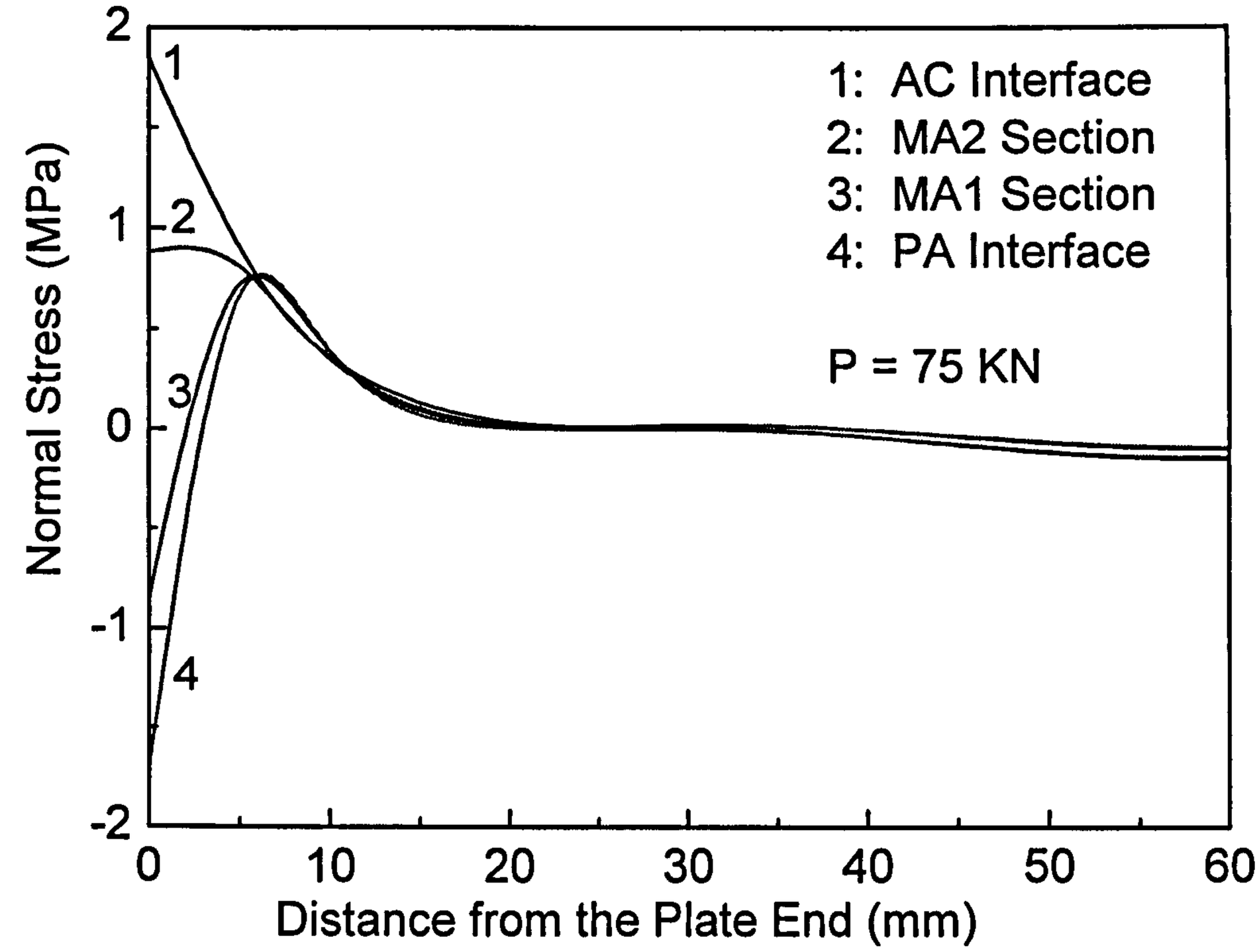

(c)

Fig. 6.30 The transverse normal stress along the interfaces and two horizontal plane in the adhesive layer

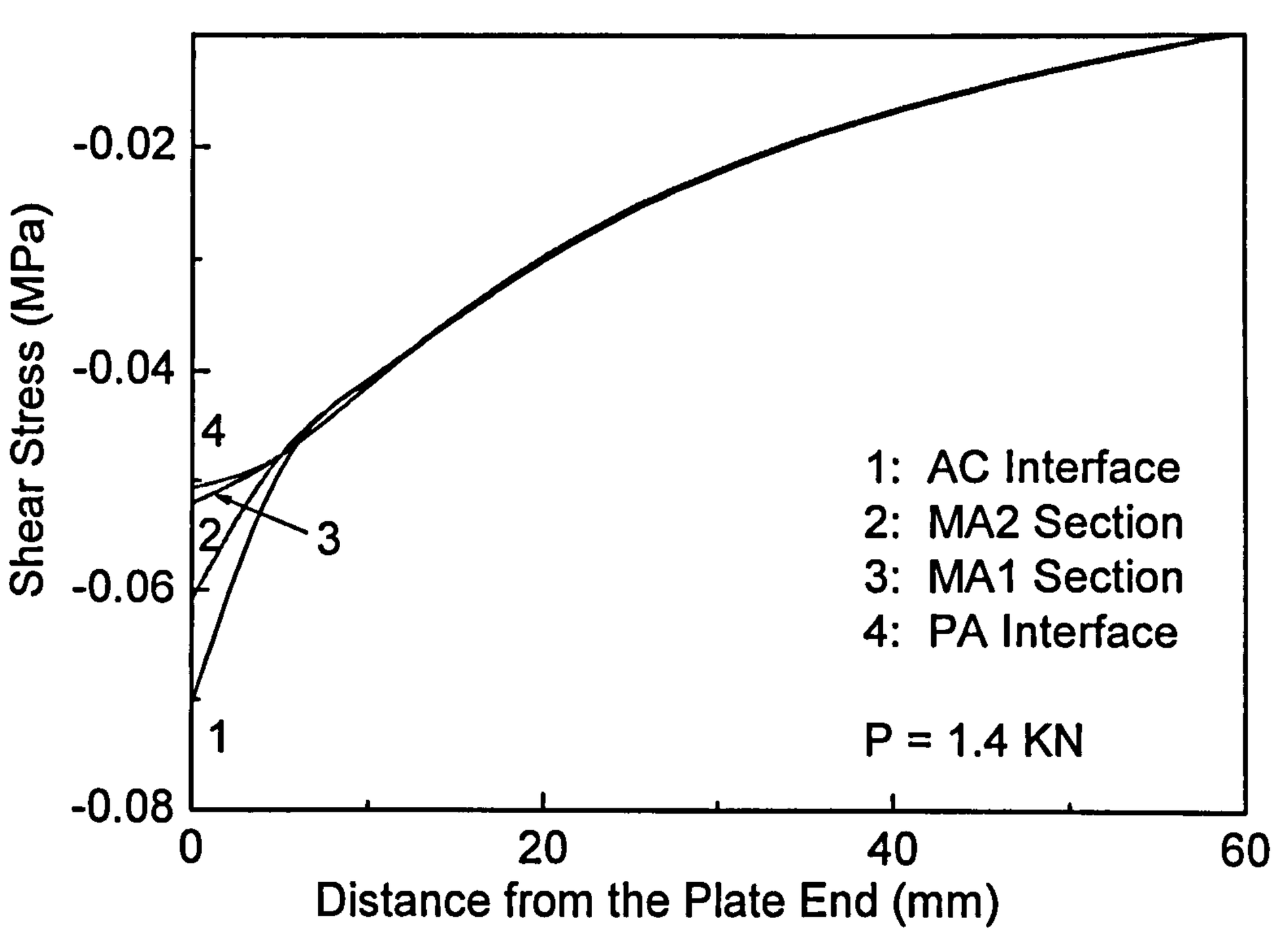

(a)

Fig. 6.31 The shear stress along the interfaces and two horizontal plane in the adhesive layer

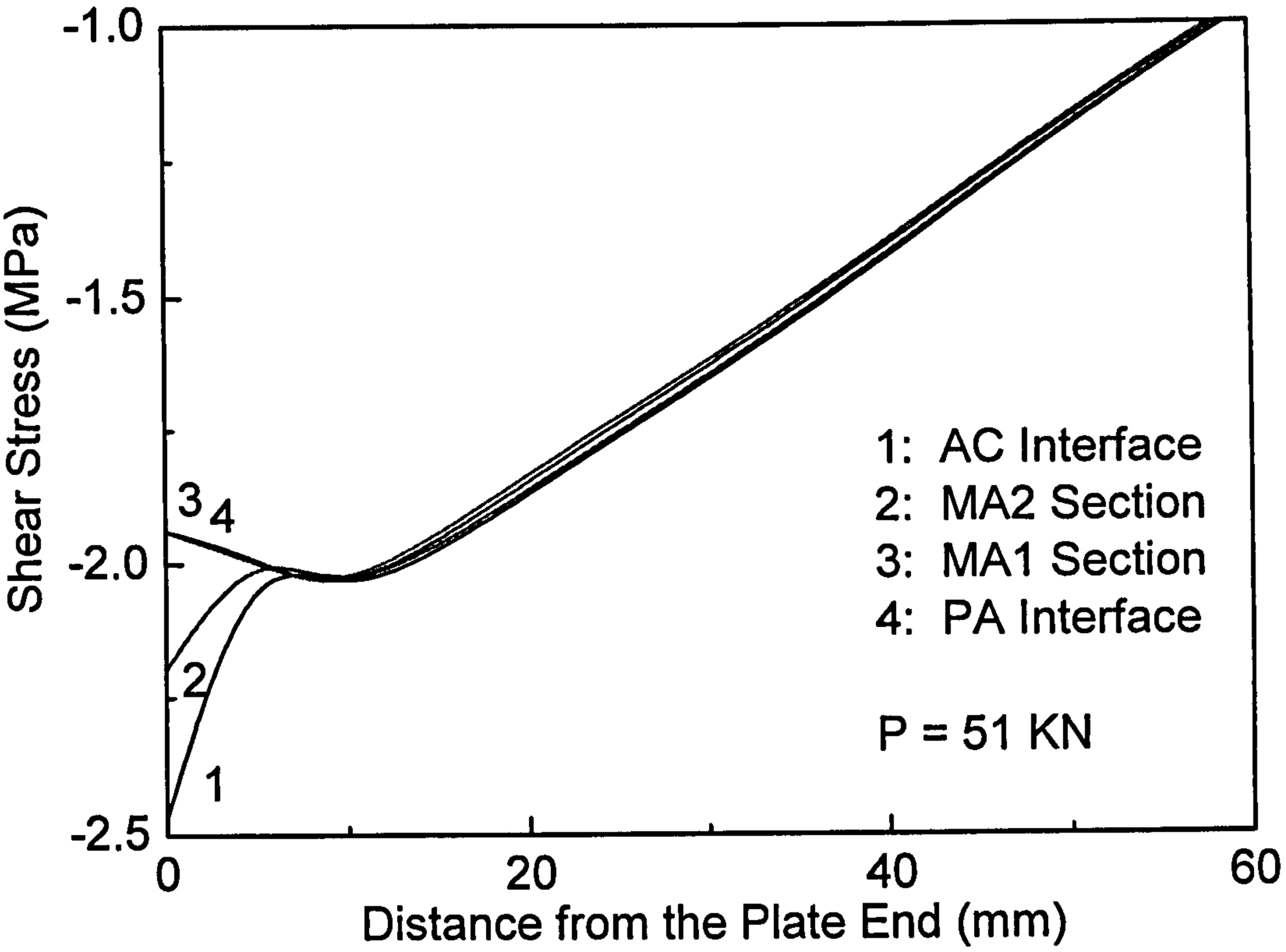

(b)

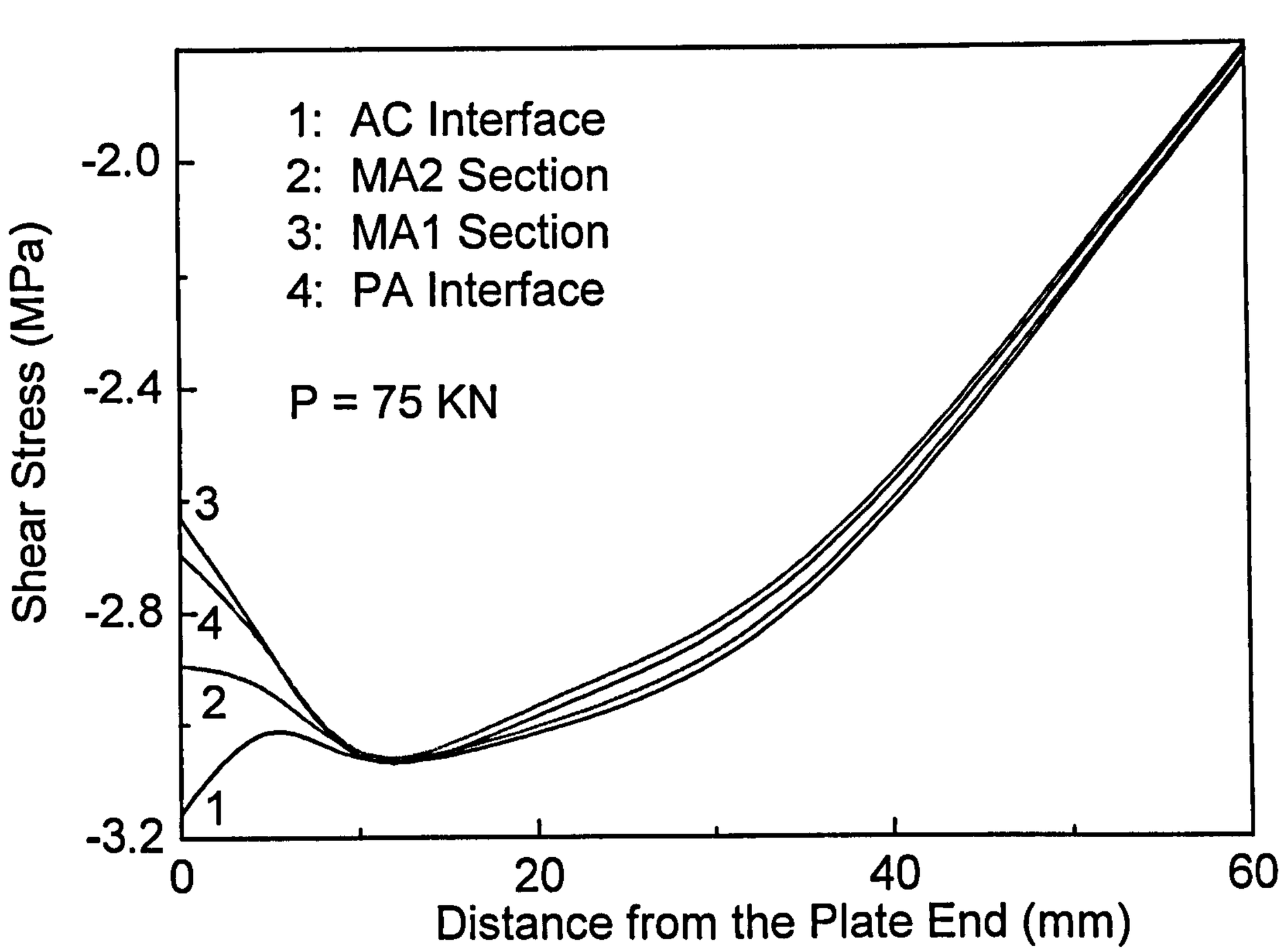

(c)

Fig. 6.31 The shear stress along the interfaces and two horizontal plane in the adhesive layer

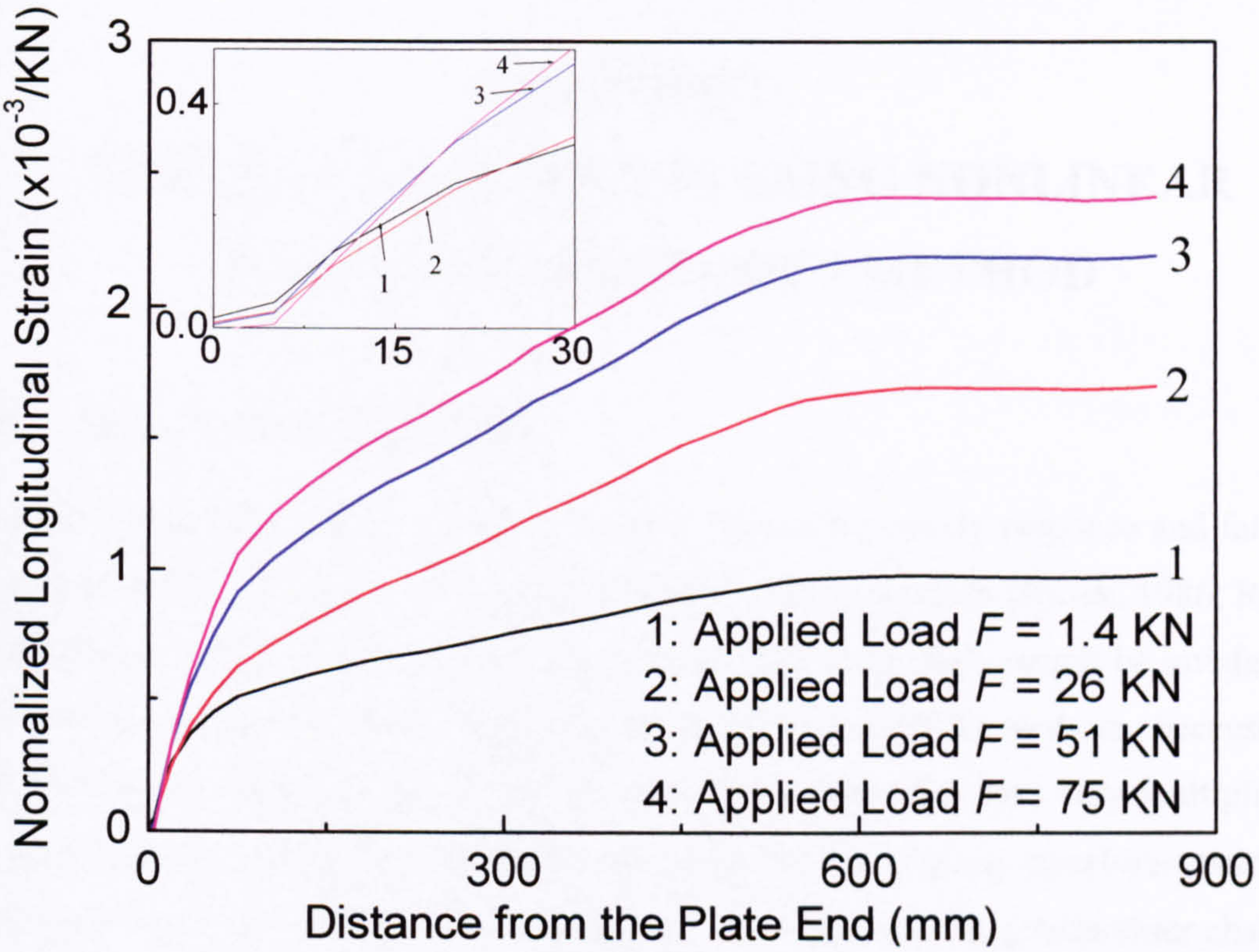

Fig. 6.32 Normalized longitudinal strain in the CFRP plate to the applied load

CHAPTER 7.

INTERFACIAL STRESSES USING NONLINEAR FRACTURE MECHANICS METHOD

7.1 Introduction of NLFM

Fracture mechanics method has been a useful approach to study response and failure of structures as a consequence of crack initiation and propagation (Broek, 1986; Rolfe and Barsom, 1977). However concrete, as a qusi-brittle material, cannot be satisfactorily analysed using the linear elastic fracture mechanics (LEFM) methods, because of the inherent multiplicity of flaws: microcracks or macrocracks. This very multiplicity of cracks actually mitigates against the use of LEFM for concrete structures, particularly small scale structures, and is the cause of the strain-softening behaviour characterized by prepeak and postpeak response of the stress-displacement curve. This is due to a combination of distributed cracking leading to localization of cracking into large fractures that include toughening mechanisms of crack bridging and interlock within the fracture process zone. This phenomenon is termed as *strain localization* (Shah et al 1995), and the nonlinear fracture mechanics (NLFM) is more suitable to this type of materials.

To briefly illustrate the fracture behaviour of the concrete material, we consider a region near a crack in a beam in bending as shown in Figure 7.1 (Shah et al. 1995). The load against crack mouth opening displacement (CMOD) is plotted in Figure 7.2, in which the solid line represents the real crack growth while the dashed one is its simplified form. From the load-CMOD curve, we can see that the CMOD is proportional to the applied load before the load commences its nonlinearity, during which the randomly distributed microcracks in concrete are formed. At a certain point before the peak stress, microckacks begin to be localized into a macrocrack that critically propagates in a stable manner until the peak stress occurs. New crack surfaces are formed at the peak stress along the path of the initial crack tip. The newly formed crack surfaces may be in contact and are tortuous in nature. This leads to toughening mechanisms in the fracture process zone such as aggregate interlocking. The newly formed crack may

continue to sustain some normal tensile stress, which characterises the descending branch in the load-CMOD curve (see Figure 7.2). Very similar mechanisms apply to the Model II fracture, shear-type fracture mode.

Researches has been conducted for the plate end debonding problem by considering only Mode II fracture [Brosens and Van Vemert (1998) and Yuan et al (2004)]. In the early stage, only the ascending branch of the force against slip curve was used. This was followed by a more accurate analysis for the post-cracking behaviour (Taljsten, 1996). In their studies, the bilinear force-slip relationship is

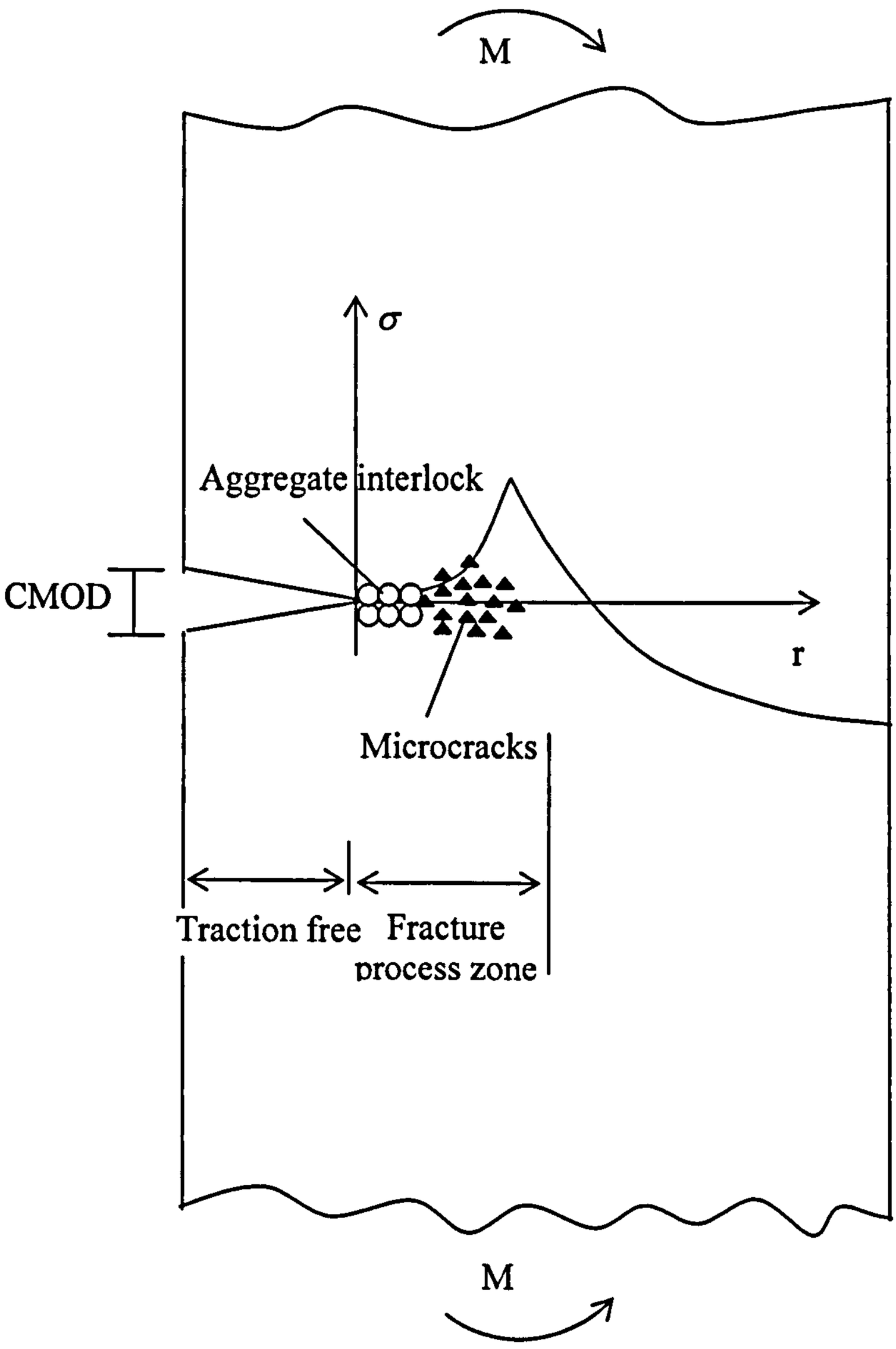

Fig. 7.1 The cracking segment of a concrete beam (Shah et al. 1995)

widely used as an analytical solution (Wu et al. 2002). In the study of the interfacial stresses in the strengthened beam, the high level shear stress is accompanied by a high level tensile normal stress/ peeling stress. It is sensible to consider the plate end crack as a mixed fracture mode, rather than the pure Mode II fracture (Buyukozturk and Hearing 1998).

Numerous experimental observations reveal that debonding occurs within the concrete material in the vicinity of the AC interface (see Wu and Yin 2003, Teng et al. 2001). In this study, it is assumed that the cracks propagate along the AC interface, and both shear stress and tensile normal stress are the driving forces to form the crack. Both pre-cracking and post-cracking are considered in the modelling. The interaction between the simultaneous actions of shear stress and peeling stress are considered. The interaction effect includes two aspects, the critical state when the macrocracks are formed, and the critical state when new crack surface forms. Accodring to Brosens and Van Gemert (1998), the former state is termed as serviceability limit state and the later is termed as ultimate limit state. The relationships for both the normal stress against separation and shear stress against slip are assumed to be bi-linear. A simple linear interaction rule is utilised to describe their interaction. Under this theoretical framework, two coupled governing equations are derived. An iteration approach is used to solve the separation and slip and then the normal stress and shear stress.

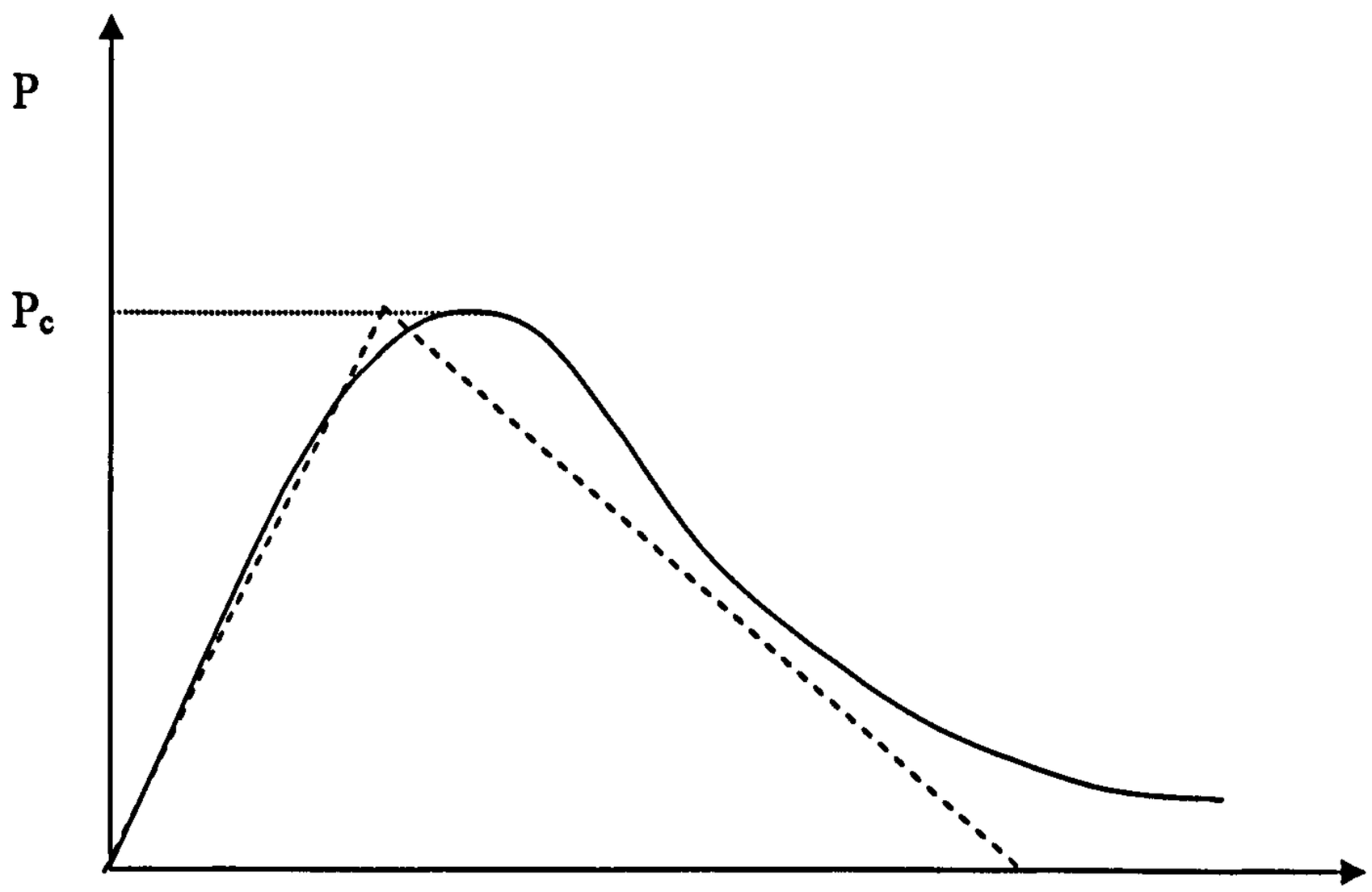

Fig. 7.2 Load-CMOD curve

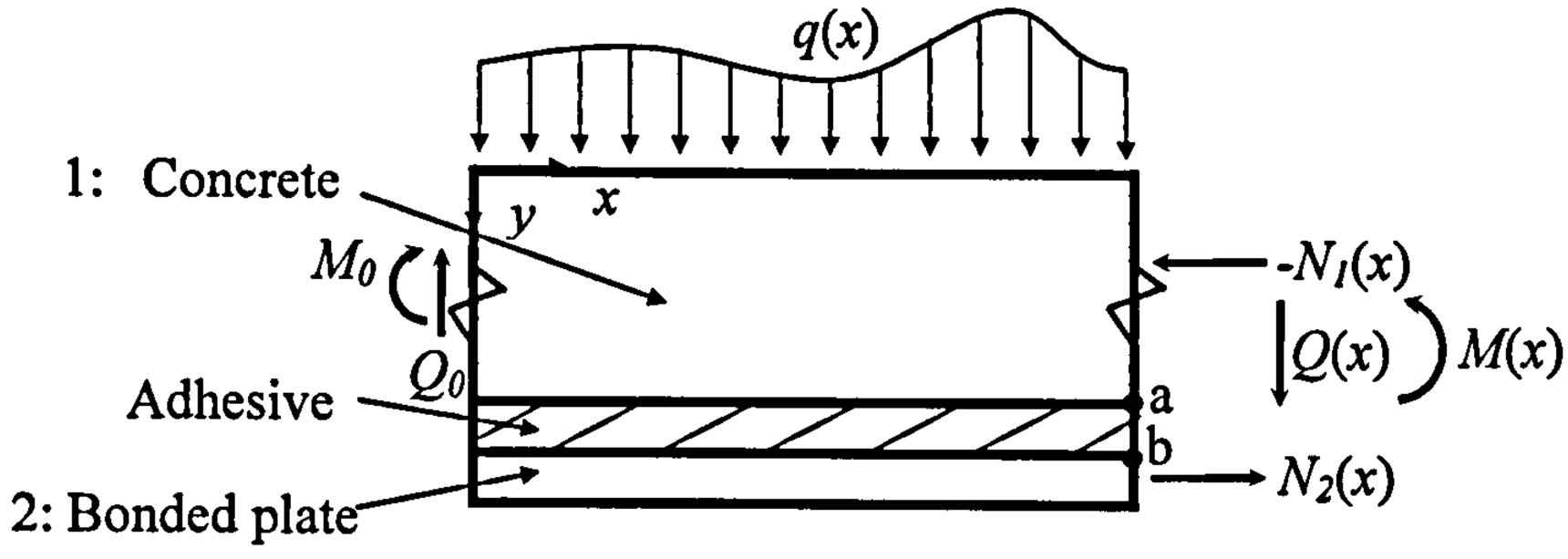

(a) a segment of a strengthened beam

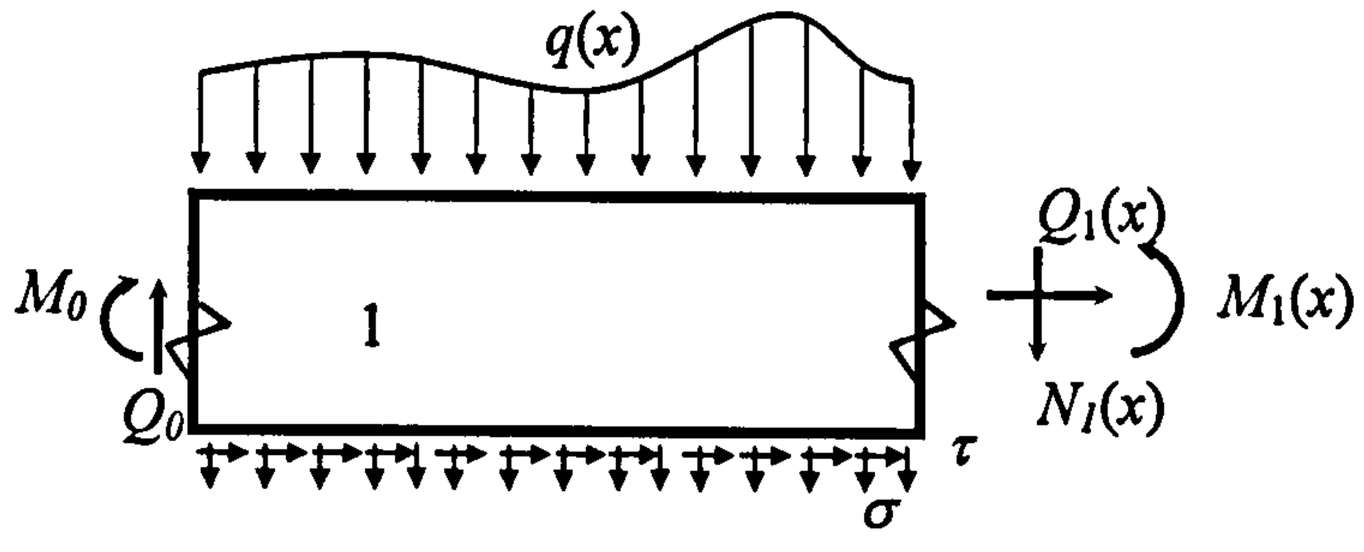

(b) concrete

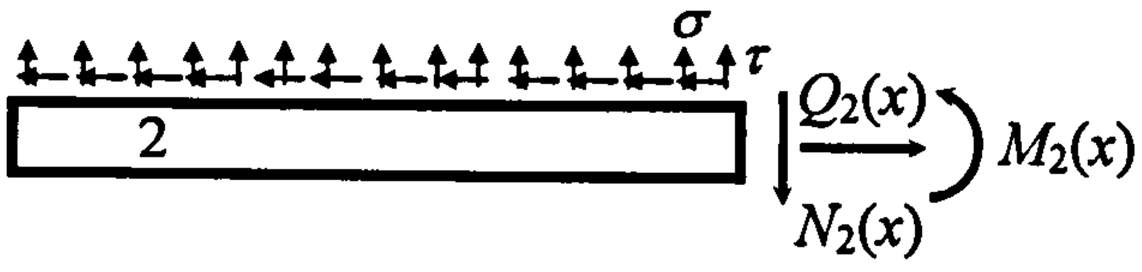

(c) bonded plate

Fig. 7.3 Diagram of the calculation model

7.2 Equations for Interfacial Shear Stress and Slip

Consider a simply supported strengthened RC beam subjected to a transversely distributed load $q(x)$ and end moments (see Figure 7.3). A segment starting from the left plate end with an arbitrary length is plotted in Figure 7.3 (a), in which the internal forces are also plotted. The concrete beam and the bonded plated are denoted by element 1 and 2 respectively (see Figures 7.3 b and c). The coordinate system is designated such that the positive x direction points rightwards, the positive y direction points downwards and the origin located at the upper left corner. The applied load, internal forces and interfacial stresses are also plotted in the figure where their direction are assumed positive.

As shown in the figures, the equilibrium in the longitudinal direction for both elements lead to

$$N_1(x) = N_0 - b\int_0^x \tau(x)dx \tag{7.1}$$

$$N_2(x) = b\int_0^x \tau(x)dx \tag{7.2}$$

where $N_i(x)$ $(i = 1,\ \ 2)$ are axial forces experienced in the sections at an arbitrary distance x of the i-th element respectively and N_0 is the axial force carried by the concrete beam at the left plate end. It is noted that $N_0 = 0$ with the absence of axially applied loads, so it is dropped in the following derivation. $\tau(x)$ is the interfacial shear stress and b is the width of the bonding interface.

In the absence of the axially applied loads, the sum of the two axial forces remains zero at horizontal position, i.e.

$$N_1(x) + N_2(x) = 0 \tag{7.3}$$

That is, the pair of axial forces equal in magnitude with opposite directions, which forms a couple $M_N(x)$ [see Figure 7.3 (a)]) as follows

$$M_N(x) = N_2\left(\frac{h_1 + h_2}{2} + h_a\right) = b\left(\frac{h_1 + h_2}{2} + h_a\right)\int_0^x \tau(x)dx \tag{7.4}$$

where h_1 and h_2 are the heights of the concrete and bonded plate respectively and h_a is the height of the adhesive.

For the un-separated segment (Figure 7.3a), the section at x experiences a total bending moment $M_T(x)$ consisting of three parts, i.e. the internal bending moments carried by 1 and 2, i.e. $M_1(x)$ and $M_2(x)$ respectively, and the couple $M_N(x)$. Applying the equilibrium condition to this composite beam segment, one has

$$M_T(x) = M_0 + Q_0 x - B\int_0^x q(s)(x-s)ds \tag{7.5}$$

where B is the width of the beam and s is an arbitrary coordinate between the origin of the coordinate system and x, $q(s)$ is the distribution of applied pressure.

Using the assumption that two elements have the equal curvature, we can easily allocate bending moment to each element by their related flexural stiffness, e.g.

$$M_1(x) = \frac{E_1 I_1}{E_1 I_1 + E_2 I_2}\left[M_T(x) - M_N(x)\right]$$

$$= \frac{E_1 I_1}{E_1 I_1 + E_2 I_2}\left[M_0 + Q_0 x - B\int_0^x q(s)(x-s)ds - b\left(\frac{h_1+h_2}{2}+h_a\right)\int_0^x \tau(x)dx\right] \tag{7.6a}$$

$$M_2(x) = \frac{E_1 I_2}{E_1 I_1 + E_2 I_2}\left[M_T(x) - M_N(x)\right]$$

$$= \frac{E_2 I_2}{E_1 I_1 + E_2 I_2}\left[M_0 + Q_0 x - B\int_0^x q(s)(x-s)ds - b\left(\frac{h_1+h_2}{2}+h_a\right)\int_0^x \tau(x)dx\right] \tag{7.6b}$$

where $M_1(x)$ and $M_2(x)$ are the bending moment experienced in elements 1 and 2.

By using the relationship that the first-order derivative of $M_1(x)$ and $M_2(x)$ equal to the related shear forces, we obtain

$$Q_1(x) = \frac{dM_1(x)}{dx} \tag{7.7a}$$

$$Q_2(x) = \frac{dM_2(x)}{dx} \tag{7.7b}$$

where $Q_1(x)$ and $Q_2(x)$ are the internal shear forces for elements 1 and 2, respectively.

The relationships between the deflection and the bending moment are

$$E_1 I_1 \frac{d^2 v_1(x)}{dx^2} = -M_1(x) \tag{7.8a}$$

$$E_2 I_2 \frac{d^2 v_2(x)}{dx^2} = -M_2(x) \tag{7.8b}$$

where $v_1(x)$ and $v_2(x)$ are the respective deflections of element 1 and element 2.

The relative horizontal displacement of initially adjacent points is designated as slip s_s and is given as

$$s_s = u_b(x) - u_a(x) \tag{7.9}$$

where $u_a(x)$ and $u_b(x)$ are the horizontal displacements of point a and b, respectively and are

$$u_a(x) = u_1(x) - \frac{h_1}{2}\frac{dv_1(x)}{dx} \tag{7.10a}$$

$$u_b(x) = u_2(x) + \frac{h_2}{2}\frac{dv_2(x)}{dx} \tag{7.10b}$$

where $u_1(x)$ and $u_2(x)$ are the horizontal displacements of the neutral surfaces of elements 1 and 2 and $v_1(x)$ and $v_2(x)$ are their vertical displacements. Substituting Equations 7.10 into Equation 7.9, one obtains

$$s_s = u_2(x) - u_1(x) + \frac{h_2}{2}\frac{dv_2(x)}{dx} + \frac{h_1}{2}\frac{dv_1(x)}{dx} \tag{7.11}$$

As $u_1(x)$ and $u_2(x)$ can be related to the axial forces, $N_1(x)$ and $N_2(x)$, by

$$N_1(x) = A_1\sigma_{x1} = E_1 A_1 \varepsilon_{x1} = E_1 A_1 \frac{du_1(x)}{dx} \tag{7.12a}$$

$$N_2(x) = A_2\sigma_{x2} = E_2 A_2 \varepsilon_{x2} = E_2 A_2 \frac{du_2(x)}{dx} \tag{7.12b}$$

where σ_{xi}, ε_{xi} $(i = 1, \quad 2)$ are the axial normal stresses and strains in the neutral surfaces of elements i. The substitution of Equation 7.8 and 7.12 into the third-order derivatives of Equation 7.11 yields

$$\frac{ds_s^3(x)}{dx^2} = \frac{d^3u_2(x)}{dx^3} - \frac{d^3u_1(x)}{dx^3} + \frac{h_2}{2}\frac{d^4v_2(x)}{dx^4} + \frac{h_1}{2}\frac{d^4v_1(x)}{dx^4}$$

$$= \frac{1}{E_2A_2}\frac{dN_2^2(x)}{dx^2} - \frac{1}{E_1A_1}\frac{dN_1^2(x)}{dx^2} - \frac{h_2}{2E_2I_2}\frac{dM_2^2(x)}{dx^2} - \frac{h_1}{2E_1I_1}\frac{dM_1^2(x)}{dx^2} \tag{7.13}$$

Substituting Equations 7.1, 7.2 and 7.6 to Equation 7.13 and rearranging the resulting equation, one obtains

$$\frac{ds_s{}^3(x)}{dx^2} == b\left[\frac{1}{E_1A_1}+\frac{1}{E_2A_2}+\frac{(h_1+h_2)(h_1+h_2+2h_a)}{4(E_1I_1+E_2I_2)}\right]\frac{d\tau(x)}{dx}+\frac{(h_1+h_2)}{2(E_1I_1+E_2I_2)}q(x) \tag{7.14}$$

7.3 Equations for Interfacial Normal Stress and Separation

Based on the calculated interfacial shear stress, the bending moment can be calculated in a more accurate way, in which $M_1(x)$ and $M_2(x)$ can be re-expressed as

$$M_1(x) = M_0 + Q_0x - B\int_0^x q(s)(x-s)ds - b\int_0^x \sigma(s)(x-s)ds - \frac{bh_1}{2}\int_0^x \tau(x)dx \tag{7.15a}$$

$$M_2(x) = b\int_0^x \sigma(s)(x-s)ds - \frac{bh_2}{2}\int_0^x \tau(x)dx \tag{7.15b}$$

and the shear forces are

$$Q_1(x) = \frac{dM_1(x)}{dx} = Q_0 - B\int_0^x q(s)ds - b\int_0^x \sigma(s)ds - \frac{bh_1}{2}\tau(x) \tag{7.16a}$$

$$Q_2(x) = \frac{dM_2(x)}{dx} = b\int_0^x \sigma(s)ds - \frac{bh_2}{2}\tau(x) \tag{7.16b}$$

where $\sigma(x)$ is the interfacial normal stress along the bonding interface.

The relative vertical displacement of the initially adjacent points is designated as normal separation s_n and it is given as

$$s_n = v_b(x) - v_a(x) = v_2(x) - v_1(x) \tag{7.17}$$

and $v_a(x)$ and $v_b(x)$ are the vertical displacements of points a and b.

Substituting Equations 7.8 to the forth-order derivation of s_n in Equation 7.17, one obtains

$$\frac{ds_n{}^4(x)}{dx^2} = \frac{d^4v_2(x)}{dx^4} - \frac{d^4v_1(x)}{dx^4} = -\frac{1}{E_2I_2}\frac{dM_2^2(x)}{dx^2} + \frac{1}{E_1I_1}\frac{dM_1^2(x)}{dx^2} \tag{7.18}$$

that can be rearranged as,

$$\frac{ds_n{}^4(x)}{dx^2} = -b\left(\frac{1}{E_1I_1}+\frac{1}{E_2I_2}\right)\sigma(x) + \frac{b}{2}\left(\frac{h_2}{E_2I_2}-\frac{h_1}{E_1I_1}\right)\frac{d\tau(x)}{dx} - \frac{B}{E_1I_1}q(x) \tag{7.19}$$

Equations 7.14 and 7.19 are the governing equations from which the shear slip and normal separation can be solved.

7.4 The Bilinear Stress-Slip/Separation Relation under Interaction

Figure 7.4 shows the stress-slip relationship along the bond interface. Figure 7.4(a) shows both ascending and descending branches, representing the pre-cracking and post-crackling behavior.

During the pre-cracking stage, it is characterized that the bonding interface deforms elastically and only microcracks in the concrete near the bonding interface appear and develop, which does not affect the elastic behavior significantly. Up to the peak stress f_{s0}, the structural behaviour is linearly elastic, and the conventional material mechanics theory applies. The slip in this range may be calculated on the basis of the linear stress-strain relationship with a rational characteristic crack bandwidth. Due to the fact that the stiffness of the concrete is much greater than that of the adhesive in the vicinity of the bonding interface, we assume that the characteristic bandwidth equals the height of the adhesive layer h_a. Hence, the slope of the ascending part of the shear stress-slip curve is

$$C_s = \frac{G_a}{h_a} \tag{7.20}$$

and s_{s0y} is obtained as

$$s_{s0y} = \frac{f_{s0}}{C_s} \tag{7.21}$$

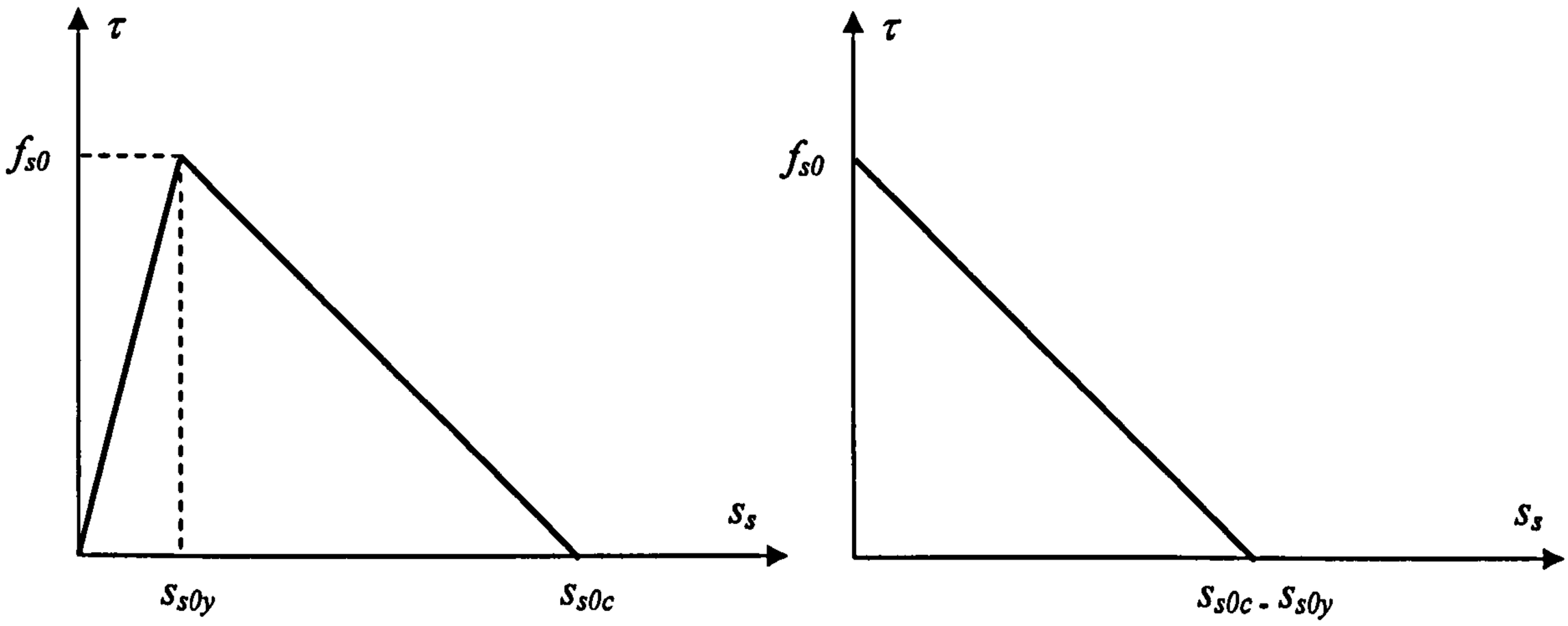

(a) Accending and decending parts (b) Decending parts

Fig. 7.4 Stress-slip relation

After the peak stress, at which the microcracks are localized into a macrocrack, the stress starts to decrease with the increase of the relative displacement. Spatially, a fracturing process zone (FPZ) commences to develop. The so-called fracturing process zone is that where the new crack surfaces are formed but they may still be in contact and are tortuous in nature and hence forms the toughening mechanism (Shah et al. 1995). This material in the FPZ continues to sustain some shear stress after the peak value but the magnitude is reduced to zero when the crack starts to separate. We denote the slip when the shear stress reach zero as the ultimate cracking slip s_{s0c}. If we only plot the curve for the post-cracking stage as shown in Figure 7.4(b), the area under softening stress-slip curve is called fracture toughness G_{II} for mode II cracks and is given by

$$G_{II} = \int_0^{s_{s0c}-s_{s0y}} \tau(s_s) ds_s \tag{7.22}$$

Fracture toughness is property of material. Under the assumption that post-crack shear stress and slip relationship is linear, G_{II} can be solved as

$$G_{II} = \frac{f_{s0}\left(s_{s0c} - s_{s0y}\right)}{2} \tag{7.23}$$

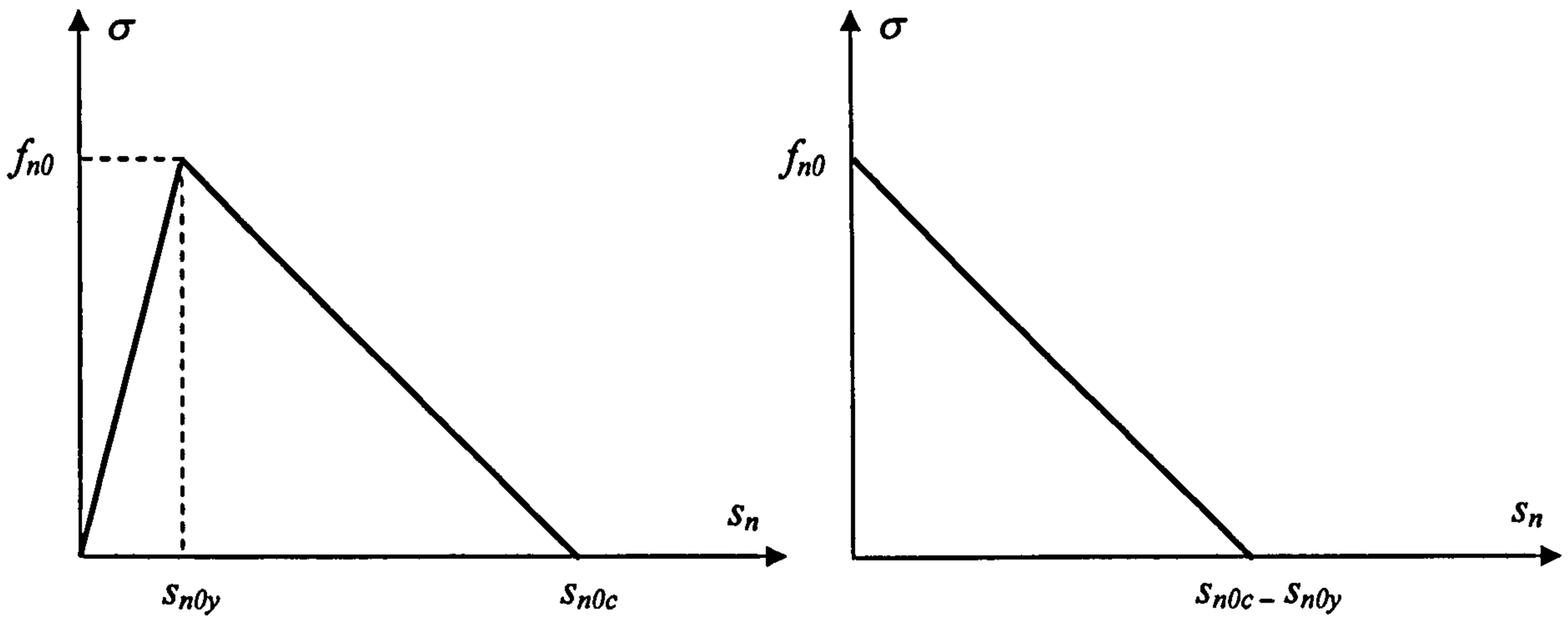

(a) Accending and decending parts (b) Decending parts

Fig. 7.5 Stress-separation relation

Likewisely, the transverse normal stress σ and separation s_n relationship shows the same characteristics as the shear stress and slip. The curves are shown in Figure 7.5 where f_{n0} is the peak transverse normal stress; s_{n0y} is the corresponding separation; and

s_{n0c} is the cracking separation. Thus, the transverse normal stiffness in the elastic stage is

$$C_n = \frac{E_a}{h_a} \tag{7.24}$$

and s_{n0y} is obtained as

$$s_{n0y} = \frac{f_{n0}}{C_n} \tag{7.25}$$

The mode I fracture toughness G_I is given by

$$G_I = \frac{f_{n0}\left(s_{n0c} - s_{n0y}\right)}{2} \tag{7.26}$$

The above stress-displacements relations were proposed to deal with Mode I and Mode II cracks occur separately. In the event that both cracks develop, the interaction between them should be considered.

As mentioned above, two states of interactions are considered in this study, i.e. the peak stress/displacement and the ultimate displacement. A linear interaction theory are adopted for both as follows:

$$\frac{f_s}{f_{s0}} + \frac{f_n}{f_{n0}} = 1 \tag{7.27}$$

where f_s and f_n are the peak shear stress and peak transverse normal stress under the concurrent shear and normal actions.

The ultimate cracking displacement also satisfies the interaction equation, i.e.

$$\frac{s_{sc} - s_{sy}}{s_{sc0} - s_{sy0}} + \frac{s_{nc} - s_{ny}}{s_{nc0} - s_{ny0}} = 1 \tag{7.28}$$

To establish the post-crack stress - displacement relationship under the simultaneous shear stress and transverse normal stress, the following cracking index p_i is defined for an arbitrary combination of shear stress s_{si} and normal stress s_{ni}

$$p_i = \frac{s_{si} - s_{sy}}{s_{sc0} - s_{sy0}} + \frac{s_{ni} - s_{ny}}{s_{nc0} - s_{ny0}} \tag{7.29}$$

The corresponding shear and normal stresses can be written in terms of the cracking index as

$$\tau = f_s\left(1 - p_i\right) \tag{7.30a}$$

$$\sigma = f_n\left(1 - p_i\right) \tag{7.30b}$$

These lead to the fact that when $p_i = 1$, both stresses approach zero and when $p_i = 0$, both stresses approach their peak values. In between these two extreme cases, the stresses remain linear with regards to the cracking index.

Substitute Equation 7.29 into Equations 7.30, we have

$$\tau = f_s\left(1 + \frac{s_{sy}}{s_{sc0} - s_{sy0}} + \frac{s_{ny}}{s_{nc0} - s_{ny0}} - \frac{s_s}{s_{sc0} - s_{sy0}} + \frac{s_n}{s_{nc0} - s_{ny0}}\right) \tag{7.31}$$

$$\sigma = f_n\left(1 + \frac{s_{sy}}{s_{sc0} - s_{sy0}} + \frac{s_{ny}}{s_{nc0} - s_{ny0}} - \frac{s_s}{s_{sc0} - s_{sy0}} + \frac{s_n}{s_{nc0} - s_{ny0}}\right) \tag{7.32}$$

Let

$$C_{s1} = f_s\left(1 + \frac{s_{sy}}{s_{sc0} - s_{sy0}} + \frac{s_{ny}}{s_{nc0} - s_{ny0}}\right);$$

$$C_{s2} = -f_s\left(\frac{1}{s_{sc0} - s_{sy0}}\right);$$

$$C_{s3} = -f_s\left(\frac{1}{s_{nc0} - s_{ny0}}\right);$$

$$C_{n1} = f_n\left(1 + \frac{s_{sy}}{s_{sc0} - s_{sy0}} + \frac{s_{ny}}{s_{nc0} - s_{ny0}}\right);$$

$$C_{n2} = -f_n\left(\frac{1}{s_{sc0} - s_{sy0}}\right); \text{ and}$$

$$C_{n3} = -f_n\left(\frac{1}{s_{nc0} - s_{ny0}}\right) \tag{7.33 a-f}$$

Equations 7.31 and 7.32 become

$$\tau = C_{s1} + C_{s2}s_s + C_{s3}s_n \tag{7.34}$$

$$\sigma = C_{n1} + C_{n2}s_s + C_{n3}s_n \tag{7.35}$$

7.5 Governing Equations

Substitute $\tau = C_s s_s$ and $\sigma = C_n s_n$ into Equations 7.14 and 7.19, we obtain the governing equations for the pre-crack stage as follows:

$$\frac{ds_s^{\,3}(x)}{dx^2} - bC_s\left[\frac{1}{E_1A_1}+\frac{1}{E_2A_2}+\frac{(h_1+h_2)(h_1+h_2+2h_a)}{4(E_1I_1+E_2I_2)}\right]\frac{ds_s(x)}{dx} = \frac{(h_1+h_2)}{2(E_1I_1+E_2I_2)}q(x) \tag{7.36a}$$

$$\frac{ds_n^{\,4}(x)}{dx^2} + bC_n\left(\frac{1}{E_1I_1}+\frac{1}{E_2I_2}\right)s_n(x) + \frac{b}{2}C_s\left(\frac{h_1}{E_1I_1}-\frac{h_2}{E_2I_2}\right)\frac{ds_s(x)}{dx} = -\frac{B}{E_1I_1}q(x) \tag{7.36b}$$

Let

$$\lambda_1^{[1]} = \sqrt{bC_s\left[\frac{1}{E_1A_1}+\frac{1}{E_2A_2}+\frac{(h_1+h_2)(h_1+h_2+2h_a)}{4(E_1I_1+E_2I_2)}\right]}$$

$$\lambda_2^{[1]} = \sqrt[4]{\frac{bC_n}{4}\left(\frac{1}{E_1I_1}+\frac{1}{E_2I_2}\right)}$$

$$K_1^{[1]} = \frac{b}{2}C_s\left(\frac{h_1}{E_1I_1}-\frac{h_2}{E_2I_2}\right)$$

$$k_1 = \frac{(h_1+h_2)}{2(E_1I_1+E_2I_2)}$$

$$k_2 = -\frac{B}{E_1I_1} \tag{7.37a-e}$$

Equations 7.36 can be rewritten as

$$\frac{ds_s^{\,3}(x)}{dx^2} - \left(\lambda_1^{[1]}\right)^2\frac{ds_s(x)}{dx} = k_1q(x) \tag{7.38a}$$

$$\frac{ds_n^{\,4}(x)}{dx^2} + 4\left(\lambda_2^{[1]}\right)^4\sigma(x) + K_1^{[1]}\frac{ds_s(x)}{dx} = k_2q(x) \tag{7.38b}$$

Equations 7.38 are the governing equations for the strengthened beam in the pre-cracking state. It is seen that the first equation is independent of the second. The two equations, therefore, can be solved separately.

Similarly, substitute Equation 7.34 and 7.35 into Equations 7.14 and 7.19, one have the governing equations for the post-crack stage as follows:

$$\frac{ds_s^{\,3}(x)}{dx^2} - b\left[\frac{1}{E_1A_1} + \frac{1}{E_2A_2} + \frac{(h_1+h_2)(h_1+h_2+2h_a)}{4(E_1I_1+E_2I_2)}\right]\left[C_{s2}\frac{ds_s(x)}{dx} + C_{s3}\frac{ds_n(x)}{dx}\right] = \frac{(h_1+h_2)}{2(E_1I_1+E_2I_2)}q(x) \tag{7.39a}$$

$$\frac{ds_n^{\,4}(x)}{dx^2} + b\left(\frac{1}{E_1I_1} + \frac{1}{E_2I_2}\right)\left[C_{n1} + C_{n2}s_s(x) + C_{n3}s_n(x)\right]$$

$$+\frac{b}{2}\left(\frac{h_1}{E_1I_1} - \frac{h_2}{E_2I_2}\right)\left[C_{s2}\frac{ds_s(x)}{dx} + C_{s3}\frac{ds_n(x)}{dx}\right] = -\frac{B}{E_1I_1}q(x) \tag{7.39b}$$

By introducing

$$\lambda_1^{[2]} = \sqrt{-bC_{s2}\left[\frac{1}{E_1A_1} + \frac{1}{E_2A_2} + \frac{(h_1+h_2)(h_1+h_2+2h_a)}{4(E_1I_1+E_2I_2)}\right]}$$

$$\lambda_2^{[2]} = \sqrt[4]{-bC_{n3}\left(\frac{1}{E_1I_1} + \frac{1}{E_2I_2}\right)}$$

$$K_1^{[2]} = -bC_{s3}\left[\frac{1}{E_1A_1} + \frac{1}{E_2A_2} + \frac{(h_1+h_2)(h_1+h_2+2h_a)}{4(E_1I_1+E_2I_2)}\right]$$

$$K_2^{[2]} = \frac{b}{2}C_{s3}\left(\frac{h_1}{E_1I_1} - \frac{h_2}{E_2I_2}\right)$$

$$K_3^{[2]} = \frac{b}{2}C_{s2}\left(\frac{h_1}{E_1I_1} - \frac{h_2}{E_2I_2}\right)$$

$$K_4^{[2]} = bC_{n2}\left(\frac{1}{E_1I_1} + \frac{1}{E_2I_2}\right)$$

$$K_5^{[2]} = bC_{n1}\left(\frac{1}{E_1I_1} + \frac{1}{E_2I_2}\right) \tag{7.40a-g}$$

the post-cracking governing equations can be simplified as

$$\frac{ds_s^{\,3}(x)}{dx^2} + \left(\lambda_1^{[2]}\right)^2\frac{ds_s(x)}{dx} + K_1^{[2]}\frac{ds_n(x)}{dx} = k_1q(x) \tag{7.41a}$$

$$\frac{ds_n^{\,4}(x)}{dx^2} - \left(\lambda_1^{[2]}\right)^4 s_n(x) + K_2^{[2]}\frac{ds_n(x)}{dx} + K_3^{[2]}\frac{ds_s(x)}{dx} + K_4^{[2]}s_s(x) + K_5^{[2]} = k_2q(x) \tag{7.41b}$$

Unlike the pre-cracking equations, these two equations are coupled and it is difficult to solve them analytically.

7.6 Boundary Conditions

7.6.1 Shear Slip

7.6.1.1 *At the Plate End, x = 0,*

In the 1st order derivation of Equation 7.11, i.e.

$$\frac{ds_s(x)}{dx} = \frac{du_2(x)}{dx} - \frac{du_1(x)}{dx} + \frac{h_2}{2}\frac{dv_2^2(x)}{dx^2} + \frac{h_1}{2}\frac{dv_1^2(x)}{dx^2} \tag{7.42}$$

the first two terms are related to the axial forces of elements 1 and 2 and the other two are related to the bending moment. All these terms except the bending moment in element 1 are zero. Hence Equation 7.42 becomes

$$\frac{ds_s(x)}{dx} = -\frac{h_1}{2E_1I_1}M_0 \text{ at } x = 0 \tag{7.43}$$

where M_0 is the bending moment carried by the concrete beam at the plate end. By introducing $j_1 = -\frac{h_1}{2E_1I_1}$, Equations 7.43 can be simplified as

$$\frac{ds_s(x)}{dx} = j_1M_0 \text{ at } x = 0; \tag{7.44}$$

7.6.1.2 *At the Midspan of the Strengthened Beam, x = l*

It is reasonable to assume that the structural behavior at the midspan of the beam is not affected by the stress concentrations at the plate ends. Consequently, the composite behavior follows the classic laminate beam theory.

The shear stress along the bonding interface can be calculated by

$$\tau(x) = \frac{E_2(2y_0 - h_2)}{2E_1I_0}Q(x) \tag{7.45}$$

where $Q(x)$ is the distribution of the shear force along the strengthened beam. For instance, for a UDL, $Q(x) = q(l-x)$, where q is the intensity of the UDL; h_0 denotes the distance between the neutral axis and the plate soffit, i.e.,

$$h_0 = \frac{E_1h_1(h_1 + 2h_a + 2h_2) + E_2h_2^2}{2(E_1h_1 + E_2h_2)} \tag{7.46}$$

and I_0 is the second moment of area about the neutral axis

$$I_0 = \frac{h_1^3}{12} + \frac{E_2 h_2^3}{12E_1} + h_1\left(\frac{h_1}{2} + h_2 + h_a - h_0\right) + \frac{E_2 h_2}{12E_1}\left(h_0 - \frac{h_1}{2}\right)^2 \tag{7.47}$$

Due to symmetry, the shear force at the didspan is zero, thus

$$s_s(x) = 0 \text{ at } x = l \tag{7.48}$$

and

$$\frac{ds_s(x)}{dx} = \frac{d\tau(x)}{C_s dx} = \frac{E_2(2y_0 - h_2)}{2C_s E_1 I_0}\frac{dQ(x)}{dx} \tag{7.49}$$

For UDL,

$$\frac{ds_s(x)}{dx} = j_2 q \text{ at } x = l \tag{7.50}$$

where $j_2 = \frac{E_2(2y_0 - h_2)}{2C_s E_1 I_0}$.

7.6.2 Transverse Normal Separation

7.6.2.1 *At x = 0*

$$\frac{d^2 s_n(x)}{dx^2} = j_3 M_0 \text{ and } j_3 = \frac{1}{E_1 I_1} \tag{7.51}$$

$$\frac{d^3 s_n(x)}{dx^3} = \frac{Q_1(0)}{E_1 I_1} - \frac{Q_2(0)}{E_2 I_2} = \frac{Q_{10}}{E_1 I_1} - \frac{b_1}{2}\left(\frac{h_1}{E_1 I_1} - \frac{h_2}{E_2 I_2}\right)\tau(0) \tag{7.52}$$

If the plate end is still at the pre-crack stage,

$$\frac{d^3 s_n(x)}{dx^3} = \frac{Q_0}{E_1 I_1} - \frac{b_1}{2}\left(\frac{h_1}{E_1 I_1} - \frac{h_2}{E_2 I_2}\right)C_s s_s(0) \tag{7.53}$$

where Q_0 is the shear forces experienced by the concrete beam at the plate end. By introducing $j_3 = \frac{1}{E_1 I_1}$ and $j_4 = -\frac{b_1}{2}\left(\frac{h_1}{E_1 I_1} - \frac{h_2}{E_2 I_2}\right)$, Equation 7.53 becomes

$$\frac{d^3 s_n(x)}{dx^3} = j_3 Q_{10} + j_4 C_s \tau(0) \tag{7.54}$$

If the plate is at the post-crack stage,

$$\frac{d^3 s_n(x)}{dx^3} = j_3 + j_5 \left[C_{s1} + C_{s2} s_s(0) + C_{s3} s_n(0) \right] \tag{7.55}$$

where $j_5 = -\frac{b_1}{2}\left(\frac{h_1}{E_1 I_1} - \frac{h_2}{E_2 I_2} \right)$

7.6.2.2 *At* $x = l$

As mentioned above, the classic laminate beam theory (CLBT) is valid for the region away from the plate ends. Thus

$$s_n(l) = 0 \tag{7.56}$$

Again, due to symmetry,

$$\frac{ds_n(l)}{dx} = 0 \tag{7.57}$$

The above-derived boundary applied to either of the governing equation depending on the actual state the boundary is experienced.

7.6.3 Conditions of Continuity

For beams with both post-cracking and pre-cracking zones, there must exist a transition point. Let l_y denote the length between the plate end and the transition point.

At $x = l_y$, the continuous conditions require

$$\left[S_s(x) \right]_L = \left[S_s(x) \right]_R \tag{7.58a}$$

$$\left[\frac{dS_s(x)}{dx} \right]_L = \left[\frac{dS_s(x)}{dx} \right]_R \tag{7.58b}$$

$$\left[\frac{d^2 S_s(x)}{dx^2} \right]_L = \left[\frac{d^2 S_s(x)}{dx^2} \right]_R \tag{7.58c}$$

where the subscripts L and R denote left and right to the transition point, respectively.

Similarly, for the transverse normal stress, the following equations must be satisfied at $x = l_y$:

$$\left[S_n(x) \right]_L = \left[S_n(x) \right]_R \tag{7.59a}$$

$$\left[\frac{dS_n(x)}{dx} \right]_L = \left[\frac{dS_n(x)}{dx} \right]_R \tag{7.59b}$$

$$\left[\frac{d^2S_n(x)}{dx^2}\right]_L = \left[\frac{d^2S_n(x)}{dx^2}\right]_R \tag{7.59c}$$

$$\left[\frac{d^3S_n(x)}{dx^3}\right]_L = \left[\frac{d^3S_n(x)}{dx^3}\right]_R \tag{7.59d}$$

7.7 Solution Procedure

7.7.1 Linear Solution

When the applied load is small, the entire strengthened beam is in the pre-cracking state. Hence, only linear solutions apply. By solving the governing equations, Equation 7.38a together with boundary conditions 7.44, 7.48 and 7.50, one obtains the linear solutions of the interfacial shear stress as

$$s_{sl}(x) = \delta_1 e^{\lambda_1^{[1]}x} + \delta_2 e^{\lambda_2^{[1]}x} + \delta_3 x + \delta_4 \tag{7.60}$$

where

$$\delta_1 = \frac{q}{\lambda_1^{[1]}}\left[\frac{j_2 e^{\lambda_1^{[1]}l}}{e^{2\lambda_1^{[1]}l}-1} + \frac{k_1}{\left(\lambda_1^{[1]}\right)^2\left(1+e^{\lambda_1^{[1]}l}\right)}\right] - \frac{j_1 M_0}{\lambda_1^{[1]}\left(e^{2\lambda_1^{[1]}l}-1\right)}$$

$$\delta_2 = \frac{q}{\lambda_1^{[1]}}\left[\frac{j_2 e^{\lambda_1^{[1]}l}}{e^{2\lambda_1^{[1]}l}-1} - \frac{e^{\lambda_1^{[1]}l}k_1}{\left(\lambda_1^{[1]}\right)^2\left(1+e^{\lambda_1^{[1]}l}\right)}\right] - \frac{e^{2\lambda_1^{[1]}l}j_1 M_0}{\lambda_1^{[1]}\left(e^{2\lambda_1^{[1]}l}-1\right)}$$

$$\delta_3 = -\frac{k_1 q}{\lambda_1^{[1]2}}$$

$$\delta_4 = \frac{q}{\lambda_1^{[1]}}\left\{-\frac{j_2 e^{\lambda_1^{[1]}l}}{e^{2\lambda_1^{[1]}l}-1} + \frac{k_1\left[1+\lambda_1^{[1]}l - e^{\lambda_1^{[1]}l}\left(1-\lambda_1^{[1]}l\right)\right]}{\lambda_1^{[1]2}\left(1+e^{\lambda_1^{[1]}l}\right)}\right\} - \frac{e^{2\lambda_1^{[1]}l}j_1 M_0}{\lambda_1^{[1]}\left(e^{2\lambda_1^{[1]}l}-1\right)} \tag{7.61a-d}$$

The substitution of $s_{sl}(x)$ into Equation 7.38b and boundary conditions Equations 7.51, 7.52, 7.56, 7.57 leads to

$$s_{nl}(x) = \gamma_1 \sin\lambda_2^{[1]}x \sinh\lambda_2^{[1]}x + \gamma_2 \sin\lambda_2^{[1]}x \cosh\lambda_2^{[1]}x$$

$$+\gamma_3 \cos\lambda_2^{[1]}x \sinh\lambda_2^{[1]}x + \gamma_4 \cos\lambda_2^{[1]}x \cosh\lambda_2^{[1]}x + \gamma_5 e^{\lambda_1^{[1]}x} + \gamma_6 e^{-\lambda_1^{[1]}x} + \gamma_7 \tag{7.62}$$

where

$$\gamma_5 = -\frac{K_1^{[1]}\left[k_1 q\left(e^{\lambda_1^{[1]}l}-1\right)+\lambda_1^{[1]2}\left(j_2 q e^{\lambda_1^{[1]}l}-j_1 M_0\right)\right]}{\lambda_1^{[1]2}\left(e^{2\lambda_1^{[1]}l}-1\right)\left(\lambda_1^{[1]2}+2\lambda_1^{[1]}\lambda_2^{[1]}+2\lambda_2^{[1]2}\right)\left(\lambda_1^{[1]2}-2\lambda_1^{[1]}\lambda_2^{[1]}+2\lambda_2^{[1]2}\right)}$$

$$\gamma_6 = -\frac{K_1^{[1]}e^{\lambda_1^{[1]}l}\left[k_1 q\left(e^{\lambda_1^{[1]}l}-1\right)+\lambda_1^{[1]2}\left(j_1 M_0 e^{\lambda_1^{[1]}l}-j_2 q\right)\right]}{\lambda_1^{[1]2}\left(e^{2\lambda_1^{[1]}l}-1\right)\left[\left(\lambda_1^{[1]}\right)^2+2\lambda_1^{[1]}\lambda_2^{[1]}+2\left(\lambda_2^{[1]}\right)^2\right]\left[\left(\lambda_1^{[1]}\right)^2-2\lambda_1^{[1]}\lambda_2^{[1]}+2\left(\lambda_2^{[1]}\right)^2\right]}$$

$$\gamma_7 = \frac{q\left[K_1^{[1]}k_1+k_2\left(\lambda_1^{[1]}\right)^2\right]}{4\left(\lambda_1^{[1]}\right)^2\left(\lambda_2^{[1]}\right)^4} \qquad (7.63a\text{-}c)$$

the other coefficients γ_i ($i = 1..4$) are not listed herein for the sake of brevity.

7.7.2 The Nonlinear Solutions

As the load increases, the beam starts entering into the post-cracking state. The process starts from the region near the plate end and then extends to the middle of the beam. In this case, different governing equations apply to the different regions. The continuity conditions are imposed at the boundary of the regions. The governing equations of the post-cracking region, Equation 7.41, are coupled with the unknown functions $s_s(x)$ and $s_n(x)$. The traditional method solves these equations by eliminating one of the unknown functions and solves a high order differential equation. Normally an analytical solution cannot be obtained. An alternative method is to convert the coupled equations into a series of first-order differential equations by introducing some dummy functions and a numerical algorithm is adopted to solve them. In this study, an iteration method is used for the post-cracking equations.

To compute the first-order approximate solutions of $s_{s0}(x)$, the terms involving $s_n(x)$ in Equation 7.41a are omitted. This leads to an uncoupled equation

$$\frac{ds_s^{\,3}(x)}{dx^2}+\left(\lambda_1^{[2]}\right)^2\frac{ds_s(x)}{dx}=k_1 q(x) \qquad (7.64)$$

which has the similar form as the first equation of the pre-cracking state, namely, Equation 5.38a. One of the boundary conditions should be applied when solving Equation 7.64, i.e. Equation 7.44.

Equation 7.38a is solved herein again only using the boundary conditions at $x = l$, i.e. Equations 7.48 and 7.50. Connecting both solutions with continuity conditions 5.59 at $x = l_y$, the shear slip can be calculated in entire region as

$$s_{s01}(x) = \delta_{011}\sin\lambda_1^{[2]}x + \delta_{012}\cos\lambda_1^{[2]}x + \delta_{013}x + \delta_{014},\ x \le l_y \tag{7.65a}$$

$$\text{and } s_{s02}(x) = \delta_{021}e^{\lambda_1^{[1]}x} + \delta_{022}e^{\lambda_2^{[1]}x} + \delta_{023}x + \delta_{024},\quad x > l_y \tag{7.65b}$$

where $s_{s01}(x)$ is the solution in the post-cracking region and the $s_{s02}(x)$ is the solution in the pre-cracking region.

Rearrange Equation 7.41b into the following forms

$$\frac{ds_n{}^4(x)}{dx^2} - \left(\lambda_2^{[2]}\right)^4 s_n\ (x) = k_2 q(x) - K_3^{[2]}\frac{ds_s(x)}{dx} - K_4^{[2]}s_s(x) - K_5^{[2]} \tag{7.66}$$

where $-K_2^{[2]}\dfrac{ds_n(x)}{dx}$ was omitted in the first-order approximation.

Introducing the first-order approximate solution $s_{s01}(x)$ into the right-hand side of Equation 7.66 and considering Equation 7.38 b together with the obtained first-order approximation $s_{s02}(x)$, the following solution are obtained from Equation 7.66 using the same procedure as described above

$$s_{n01}(x) = \gamma_{011}e^{\lambda_2^{[2]}x} + \gamma_{012}e^{-\lambda_2^{[2]}x} + \gamma_{013}\sin\lambda_2^{[2]}x + \gamma_{014}\cos\lambda_2^{[2]}x$$
$$+\gamma_{015}\sin\lambda_1^{[2]}x + \gamma_{016}\cos\lambda_1^{[2]}x + \gamma_{017}x + \gamma_{018} \tag{7.67a}$$

$$s_{n02}(x) = \gamma_{021}\sin\lambda_2^{[1]}x\sinh\lambda_2^{[1]}x + \gamma_{022}\sin\lambda_2^{[1]}x\cosh\lambda_2^{[1]}x + \gamma_{023}\cos\lambda_2^{[1]}x\sinh\lambda_2^{[1]}x$$
$$+\gamma_{024}\cos\lambda_2^{[1]}x\cosh\lambda_2^{[1]}x + \gamma_{025}e^{\lambda_1^{[1]}x} + \gamma_{026}e^{-\lambda_1^{[1]}x} + \gamma_{027} \tag{7.67b}$$

Rearranging Equation 7.41(a) yields

$$\frac{ds_s{}^3(x)}{dx^2} + \left(\lambda_1^{[2]}\right)^2\frac{ds_s(x)}{dx} = k_1 q(x) - K_1^{[2]}\frac{ds_n(x)}{dx} \tag{7.68}$$

Substituting $s_{n01}(x)$ into its right-hand side, and following the same procedures, we obtain the second-order approximation, as follows

$$s_{s11}(x) = \delta_{111}x\sin\lambda_1^{[2]}x + \delta_{112}\sin\lambda_1^{[2]}x + \delta_{113}x\cos\lambda_1^{[2]}x + \delta_{114}\cos\lambda_1^{[2]}x$$
$$+\delta_{115}e^{\lambda_2^{[2]}x} + \delta_{116}e^{-\lambda_2^{[2]}x} + \delta_{117}\sin\lambda_2^{[2]}x + \delta_{118}\cos\lambda_2^{[2]}x + \delta_{119}x + \gamma_{1110} \tag{7.69a}$$

and

$$s_{s12}(x) = \delta_{121} e^{\lambda_1^{[1]} x} + \delta_{122} e^{\lambda_2^{[1]} x} + \delta_{123} x + \delta_{124} \tag{7.69b}$$

Rewrite Equation 7.41b as

$$\frac{ds_n{}^4(x)}{dx^2} - \left(\lambda_1^{[2]}\right)^4 s_n\ (x) = k_2 q(x) - K_2^{[2]} \frac{ds_n(x)}{dx} - K_3^{[2]} \frac{ds_s(x)}{dx} - K_4^{[2]} s_s(x) - K_5^{[2]} \tag{7.70}$$

and introducing the shear slip from the previous calculations, the second-order approximation of transverse separation are obtained as

$$s_{n11}(x) = \gamma_{111} e^{\lambda_2^{[2]} x} + \gamma_{112} e^{-\lambda_2^{[2]} x} + \gamma_{113} \sin \lambda_2^{[2]} x + \gamma_{114} \cos \lambda_2^{[2]} x + \gamma_{115} x \sin \lambda_1^{[2]} x$$

$$+\gamma_{116} \sin \lambda_1^{[2]} x + \gamma_{117} x \cos \lambda_1^{[2]} x + \gamma_{118} \cos \lambda_1^{[2]} x + \gamma_{119} x e^{\lambda_2^{[2]} x} + \gamma_{1110} x e^{-\lambda_2^{[2]} x} + \gamma_{1111} x \sin \lambda_2^{[2]} x$$

$$+\gamma_{1112} x \cos \lambda_2^{[2]} x + \gamma_{1113} x^2 + \gamma_{1114} x + \gamma_{1115} \tag{7.71a}$$

and

$$s_{n12}(x) = \gamma_{121} \sin \lambda_2^{[1]} x \sinh \lambda_2^{[1]} x + \gamma_{122} \sin \lambda_2^{[1]} x \cosh \lambda_2^{[1]} x + \gamma_{123} \cos \lambda_2^{[1]} x \sinh \lambda_2^{[1]} x$$

$$+\gamma_{124} \cos \lambda_2^{[1]} x \cosh \lambda_2^{[1]} x + \gamma_{125} e^{\lambda_1^{[1]} x} + \gamma_{126} e^{-\lambda_1^{[1]} x} + \gamma_{127} \tag{7.71b}$$

In the above iteration, $s_{s01}(x)$, $s_{s02}(x)$, $s_{n01}(x)$ and $s_{n02}(x)$ are the first-order approximation to the interfacial displacement and $s_{s11}(x)$, $s_{s12}(x)$, $s_{n11}(x)$ and $s_{n12}(x)$ are the second-order approximation. In both solutions, there is an unknown parameter l_y remains unknown. This parameter can be resolved by letting

$$\frac{s_{s02}(l_y)}{s_{sy0}} + \frac{s_{n02}(l_y)}{s_{ny0}} = 1 \tag{7.72a}$$

for the first-order approximation, and

$$\frac{s_{s12}(l_y)}{s_{sy0}} + \frac{s_{n12}(l_y)}{s_{ny0}} = 1 \tag{7.72b}$$

for the second-order approximation.

7.8 Modelling Parameters

When following the iterative solutions, the shear stress-slip/normal stress-separation relationship must be used. For instance, f_{s0}, s_{s0c}, f_{n0} and s_{n0c} must be defined before calculations. In practical application, the only material parameters, which can easily be found, is the concrete compressive strength. For concrete whose measured values

are not available, CEB-FIP MC90 (1993) has been adopted using the following empirical formulas:

$$f_{cm} = f_{ck} + 8 \tag{7.73}$$

where f_{ck} is the characteristic (5% fractile value) compressive strength of concrete (MPa) which is given by testing standard cylinder specimen. The mean compressive strength f_{cm} considers that the scatter is 8 MPa. In most tests, only the mean strength is attained through testing a limited number of specimens. For those cases, Equation 7.73 can be used to relating the characteristic values and the mean values.

The Young's modulus E_c

$$E_c = 10^4 f_{cm}^{1/3} \tag{7.74}$$

and the mean tensile strength f_{ctm}

$$f_{ctm} = 0.30 f_{ck}^{2/3} \tag{7.75}$$

the model I fracture toughness

$$G_I = a_d f_{cm}^{0.7} \tag{7.76}$$

where a_d is the coefficients related to the maximum aggregate size d, (see Table 7.1).

Table 7.1 Coefficient, a_d, to take into account the effect of maximum aggregate size d on fracture toughness

d (mm)	a_d
8	4
16	6
32	10

The direct shear strength formula in Popovics (1998) is used, i.e.

$$\frac{f_{cs}}{f_{cu}} = 0.25 - \frac{f_{cu}}{8000} \text{ (in kg/cm}^2\text{)} \tag{7.77}$$

or

$$\frac{f_{dsh}}{f_{cu}} = 0.25 - 1.275\times10^{-3} f_{cu} \text{ (in MPa)} \tag{7.78}$$

where f_{cu} is the characteristic compressive cube strength. Utilizing the relationship of the cylinder strength and cube strength (BSI 1985),

$$f_{ck} = 0.79 f_{cu} \tag{7.79}$$

The direct shear strength can be related to the characteristic cylinder strength as

$$f_{dsh} = 0.32 f_{ck} - 2.04 \times 10^{-3} f_{ck}^{\ 2} \tag{7.80}$$

The Mode II fracture toughness is taken as (Neubauer and Rostasy, 1999):

$$G_{II} = k_b^2 C_F f_{ctm} \tag{7.81}$$

where the calibration coefficient k_b is 0.45and C_f is 0.202.

7.9 Numerical Examples

The second verification example used in Section 4.3 of Chapter 4 is studied here again. The parameters required in the calculation are listed as follows. Some of them are the same as those used in Section 4.3 and the others are calculated using the equations as described above.

The geometric parameters are:

concrete: B = 200 mm; h_1 = 300mm; and span is 3000mm;

adhesive: b = 200mm; h_a =2mm;

GFRP plate: b = 200mm; h_2 = 4 mm; l = 2400mm.

The mean compressive cylinder strength f_{cm} = 30MPa. Using Equations 7.74, 7.75 7.76, 7.80 and 7.81, the Young's modulus E = 31GPa, mean tensile strength f_{ctm} = 2.4 MPa, Model I fracture toughness G_I = 0.065 N/mm, direction shear strength f_{cs} = 6.05 MPa, and Model II fracture toughness G_{II} = 0.1 N/mm. Hence, from the above material properties, f_{s0} = 6.05MPa; f_{n0} = 2.4 MPa; s_{s0c}= 0.033mm; and s_{n0c}= 0.054mm.

Except at the bonding interface, the concrete beam is assumed to be elastic. As is well understood, in the normal range of reinforcement ratio, the additional stiffness of the reinforcements in a concrete beam is limited in the elastic state and hence neglected here. The adhesive and the GFRP material are also assumed to be elastic. The Young's modulus of the adhesive E_a = 3 GPa and its Poisson's ratio is 0.35. The Young's modulus of GFRP E_2 = 100 GPa.

Using the terminology of Brosens and Van Gemert (1998), two states are classified, i.e. the serviceability limiting state and the ultimate limiting state. The first state is de-

fined as the state where the stresses reach their peak value at the plate end, and the stresses apart from the plate end are in the elastic state. The results for this state are plotted in Figure 7.6. The second state is defined as the state that the stresses at the plate end reach the ultimate value, i.e. both stresses are dropped to zero. Obviously, the beam has two regions, where the stresses are either in the descending branch or in the ascending branch. The results for this state are plotted in Figure 7.8. In between the two limiting states, there exist intermediate states in which the Fracture Process Zone (FPZ) extends progressively towards the inside of the beam from the plate ends. The results for the intermediate state when q = 0.43N/mm^2 are plotted in Figure 7.7.

Figure 7.6 shows the slip/separation and stress distribution along the bonding interfaces in a short region near the plate end at the serviceability limiting state when q = 0.237 N/mm^2. The stress distribution is also compared with the simplified linear solutions proposed in Chapter 5 and Smith and Teng's (2001) linear results and a good agreement is attained. Figure 7.7 includes four groups of curves, respectively, for the shear slip, transverse separation, shear stress and normal stress. In each group, three curves are presented for comparisons. The linear solution presents the solutions using the linear stress-displacement relationship. The nonlinear solution is for considering both ascending and descending branches in the stress-displacement relationship. The nonlinear solutions are given in the form of first-order and second-order approximation, respectively. The corresponding state is taken between the serviceability state and ultimate state, when q = 0.43 N/mm^2. It is seen that the shear slip given by the three solutions are very close, while the transverse separation shows significant discrepancy between the linear and nonlinear solutions. The nonlinear solution exhibits a sudden drop near the plate end, which is believed to be the consequence of the descending stress-displacement relationship. The region between the plate end and the position where peal stress occurs is the FPZ. The length of the zone is approximately 1.3mm. The nonlinear solution (Figure 7.7 d) also shows a reduced peak normal stress.

Figures 7.8 show the results at the ultimate limiting state when q = 0.86 N/mm^2. One of notable observations is that the transverse separation along the cracking surface becomes negative near the plate end. This is accompanied by a large shear slip and attributed to the interaction between the shear and normal actions. The large shear slip

tends to close up the opening of the cracks. As an intermediate state, a reduction of the shear stress is observed in the FPZ. In respect of the transverse normal stress, it quickly picks up from the maximum compression when approaching the plate end and changes into positive. In the positive range, it increases across a short region, and starts to reduce to zero in the vicinity of the plate end. As Figures 7.8(b) and (c) show, both the shear and normal stresses are zero at the plate end. The length of the FPZ for this case is 2.05 mm. The notably small value of the length of the FPZ may be attributed to the elasticity assumption of the concrete beam and the bonded plate and the assumption of the linear descending part of the stress-displacement relationship at the interface, which, in reality, should have a progressively reducing slope as Figure 7.2 shows. More common values for the length of FPZ in a concrete with 20mm aggregate are in the region of 200mm.

Figures 7.9 a and b, 7.10 and 7.11 show, respectively, the plate end displacements, stresses and the size of the FPZ against the applied loads and the stresses against the relative displacements. It can be seen that the shear slip is monotonically increased with the increase of the applied load. In contrast, the normal separation increases at the early stage and then decreases when the applied load exceeds about 0.25N/mm^2. After that, it is in compression state. The shear slip is much larger than the normal separation. Both the shear stress and the normal stress at the plate end are characterized by a bilinear relationship. They reach this peak value synchronically and the peak stress in shear is about twice of that in tension. However, both of them are lower than the values when they are considered separately. The figure showing size of FPZ against applied load reveals that the FPZ's extension slows down when the applied load is approaching the ultimate limiting state. The curves of stress against displacement in Figure 7.11 look odd. Although the shear stress – slip curves show the typical pattern that includes the ascending and descending branches. The descending branch for the normal stress-separation is in an opposite sense i.e. the separation decreases as the stress is reducing.

7.10 Conclusions

This chapter developed an innovative nonlinear fracture mechanics (NLFM) solution for the interfacial stresses in the plated RC beam. The interaction between the normal

and shear stresses is considered. Two groups of governing differential equations are derived for the pre-cracking and post-cracking stages respectively, along with the boundary conditions and continuity conditions at the transition boundary. For the cases involving the post-cracking stage, the two governing equations are coupled and an iteration approach is proposed. Two approximate solutions are developed in this chapter and the numerical example shows that the second-order approximation gives adequate accuracy.

Based on the NLFM solution, the stress distributions at the serviceability limiting state and ultimate limiting state are studied. Numerical examples reveal that present solutions predict almost the same stress distribution as the linear solution for the serviceability limiting state in which the interaction actions has yet taken place. After the serviceability limiting state, the FPZ starts and extends towards the inside of the beam. As a result, the shear stress starts to reduce its magnitude in the FPZ while the normal stress reduces its slope progressively. When approaching the ultimate state, some parts of the FPZ are in compression and a large slip occurs. By observing the history of the stress/displacement state in the loading process, we find that the shear slip in fact continues to increase while the normal separation starts to reduce once the applied load pass the serviceability state, and the dominant displacement is the shear slip. This is perhaps the reason why many researchers considered only Mode II fracture as the key fracture mode. Nevertheless, the numerical calculations reveal that the interactions between the shear and normal stresses are significant. Both stresses cannot approach their full capacity, when they are present simultaneously.

It is believed that the present solution is the first analytical one to adopt the NLFM theory and consider the interaction between the two stresses.

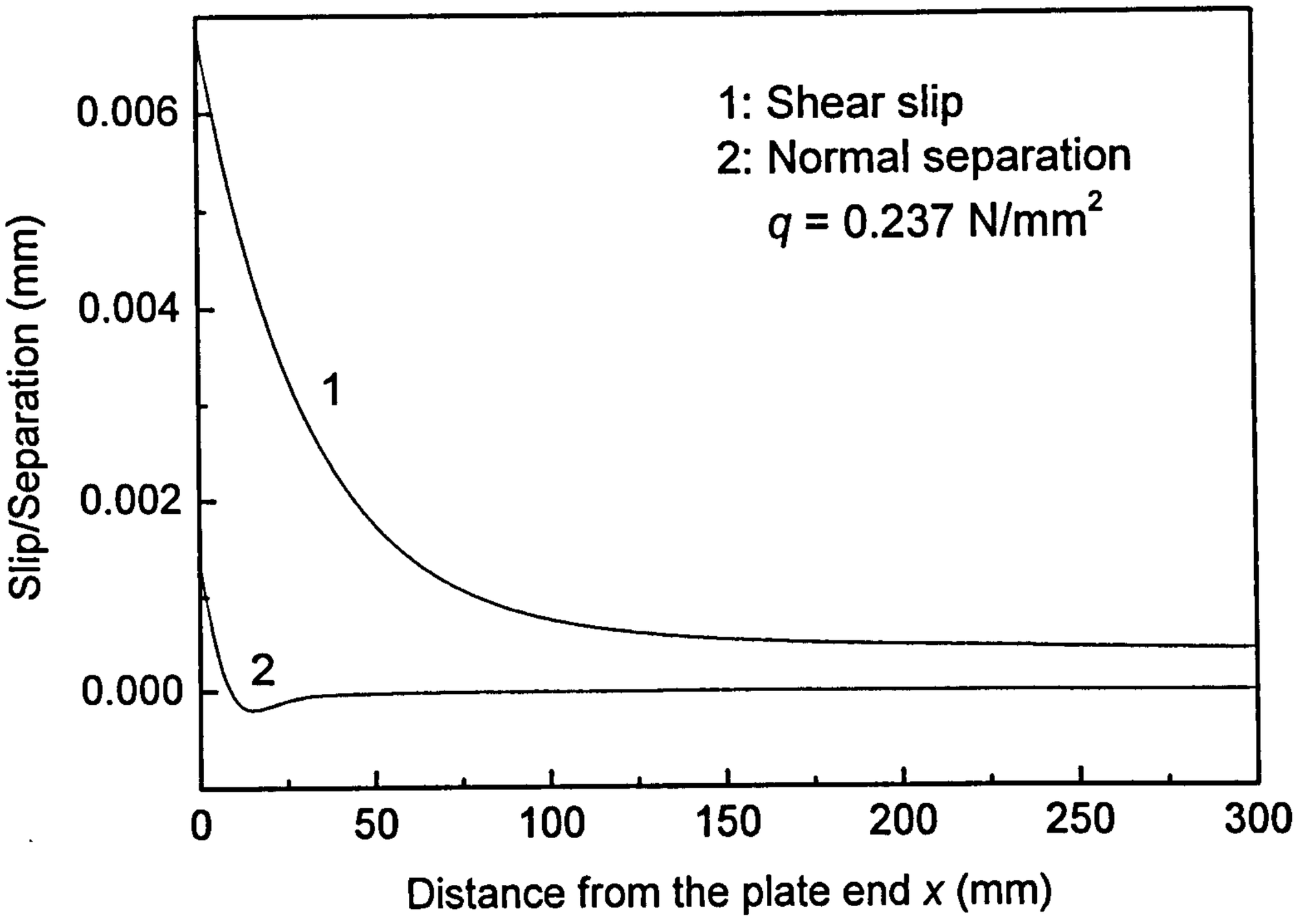

(a) Interfacial slip/separation along the bonding interface

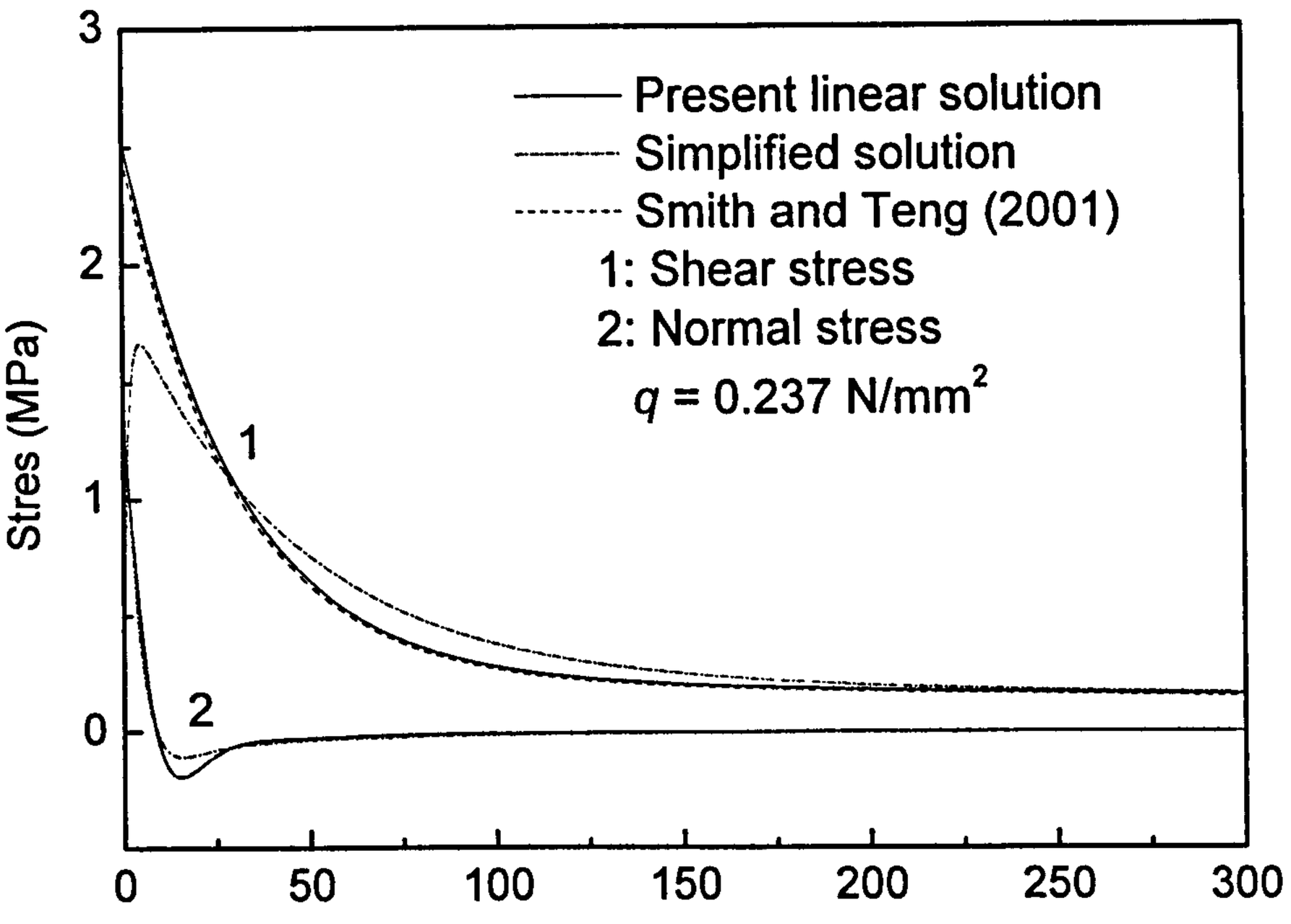

(b) Interfacial stresses along the bonding line

Fig. 7.6 The serviceability limiting state

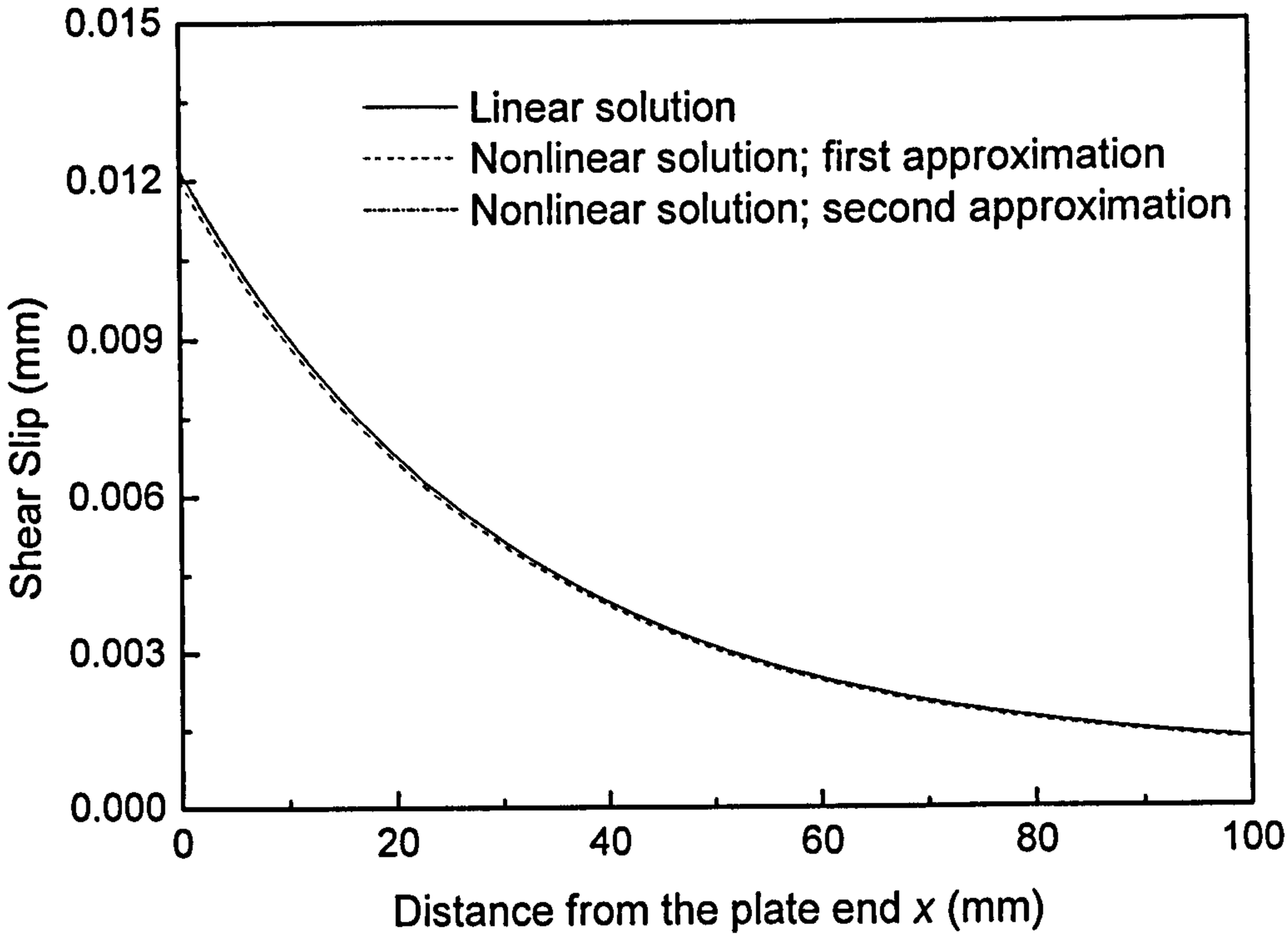

(a) Distribution of the shear slip along the bonding interface

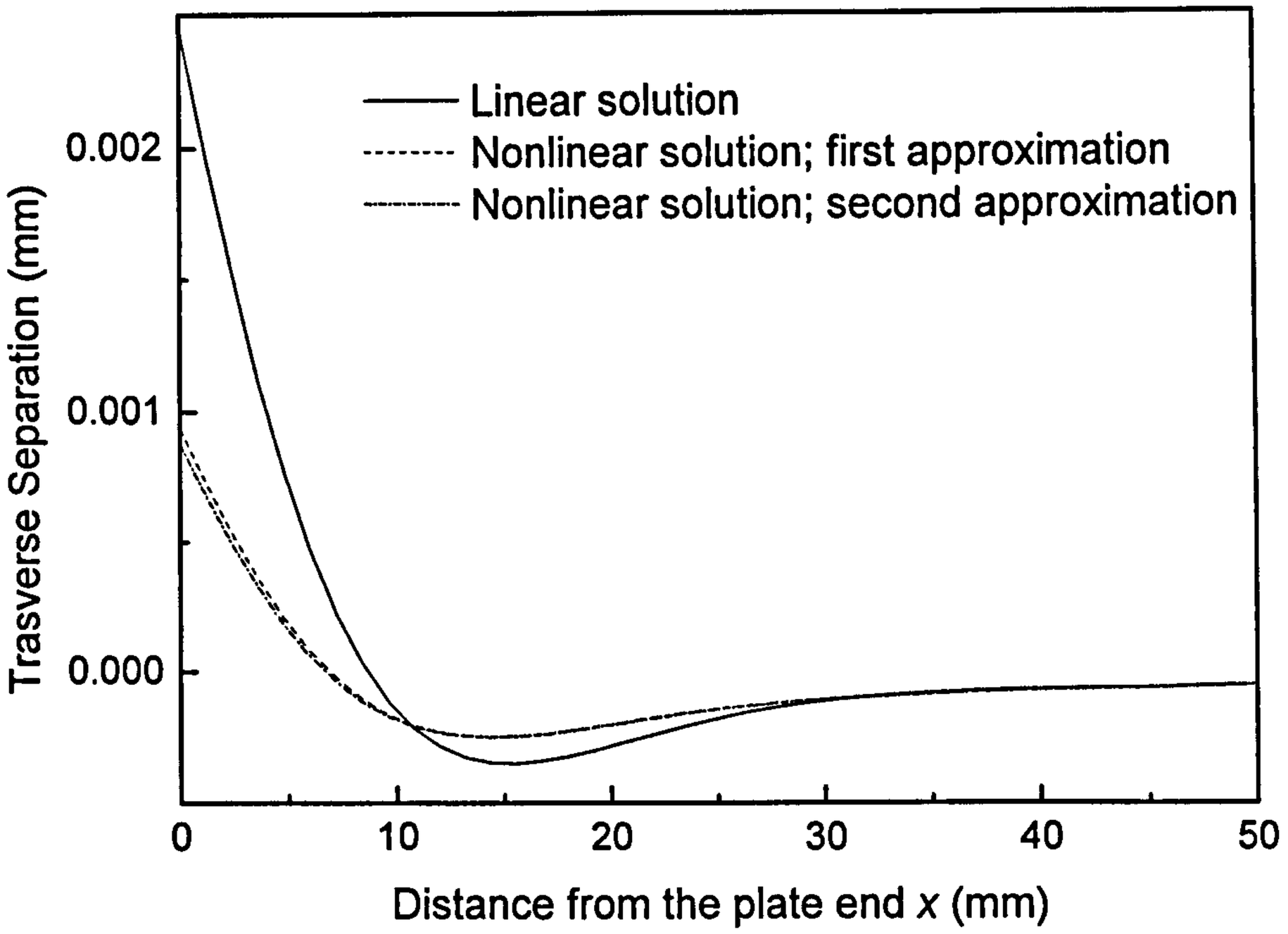

(b) Distribution of the transverse separation along the bonding interface

Fig. 7.7 The intermediate state when $q = 0.43\ N/mm^2$

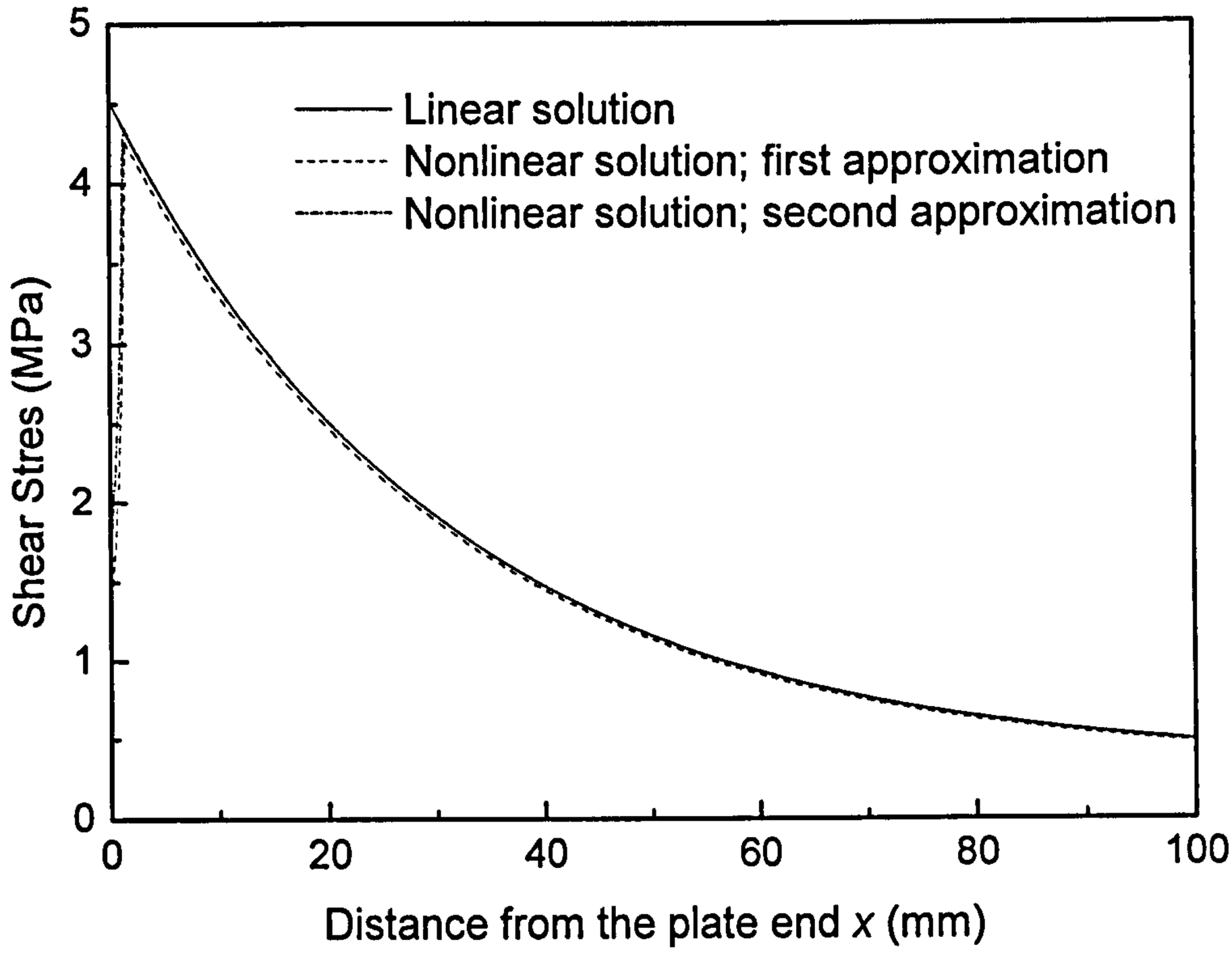

(c) Distribution of the interfacial shear stress along the bonding interface

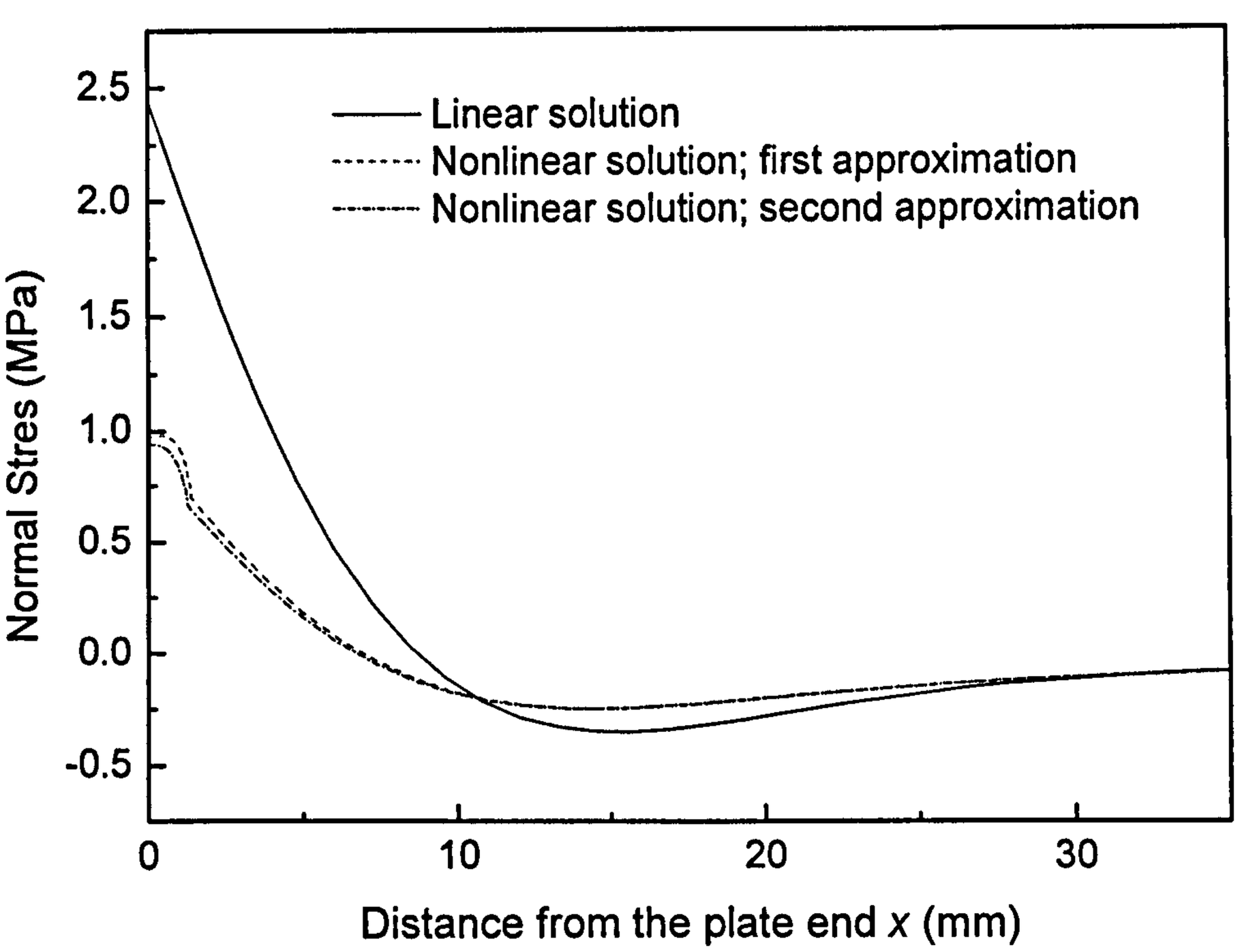

(d) Distribution of the interfacial normal stress along the bonding interface

Fig. 7.7 The intermediate state when q = 0.43 N/mm^2

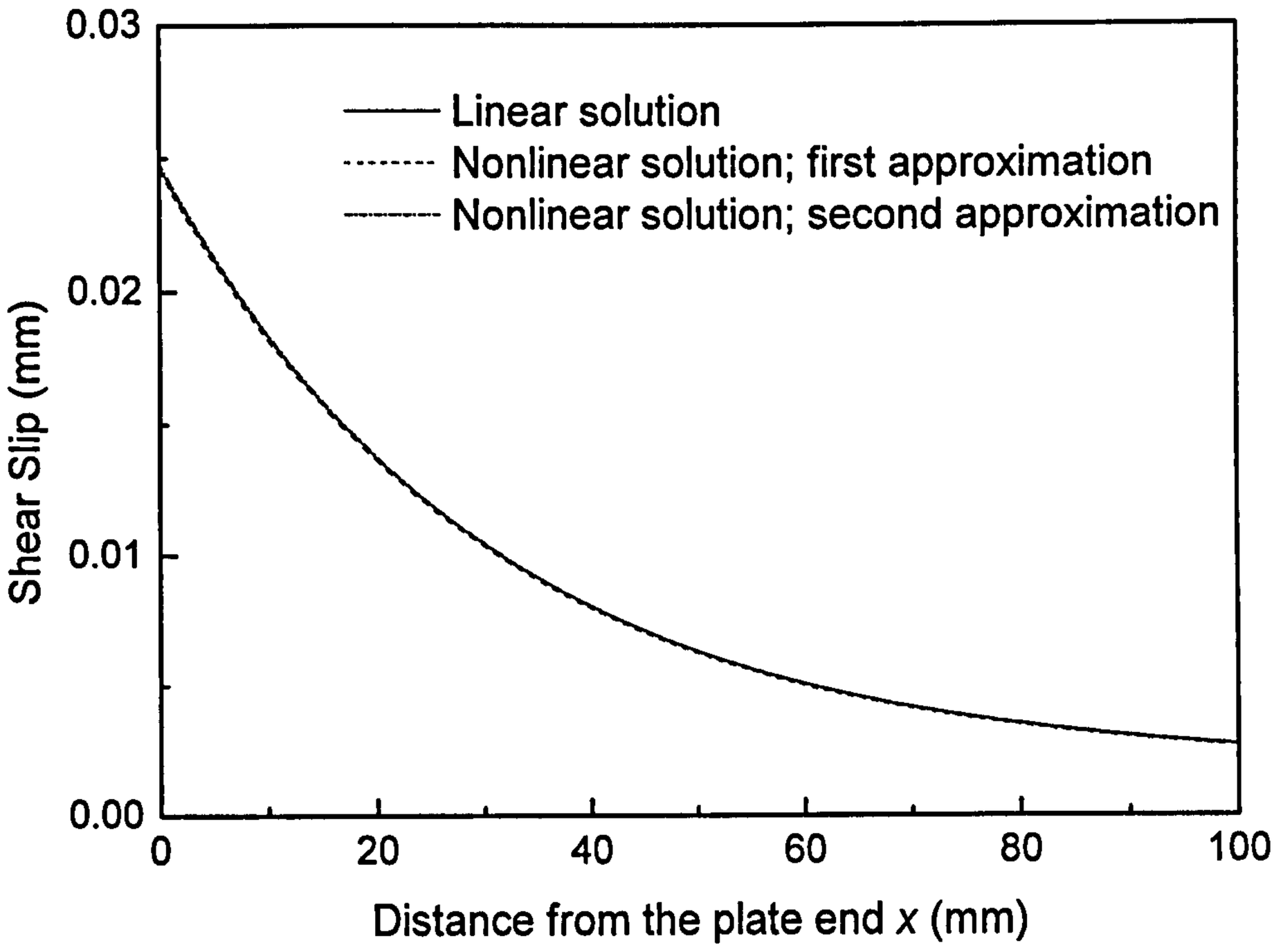

(a) Distribution of the shear slip along the bonding interface

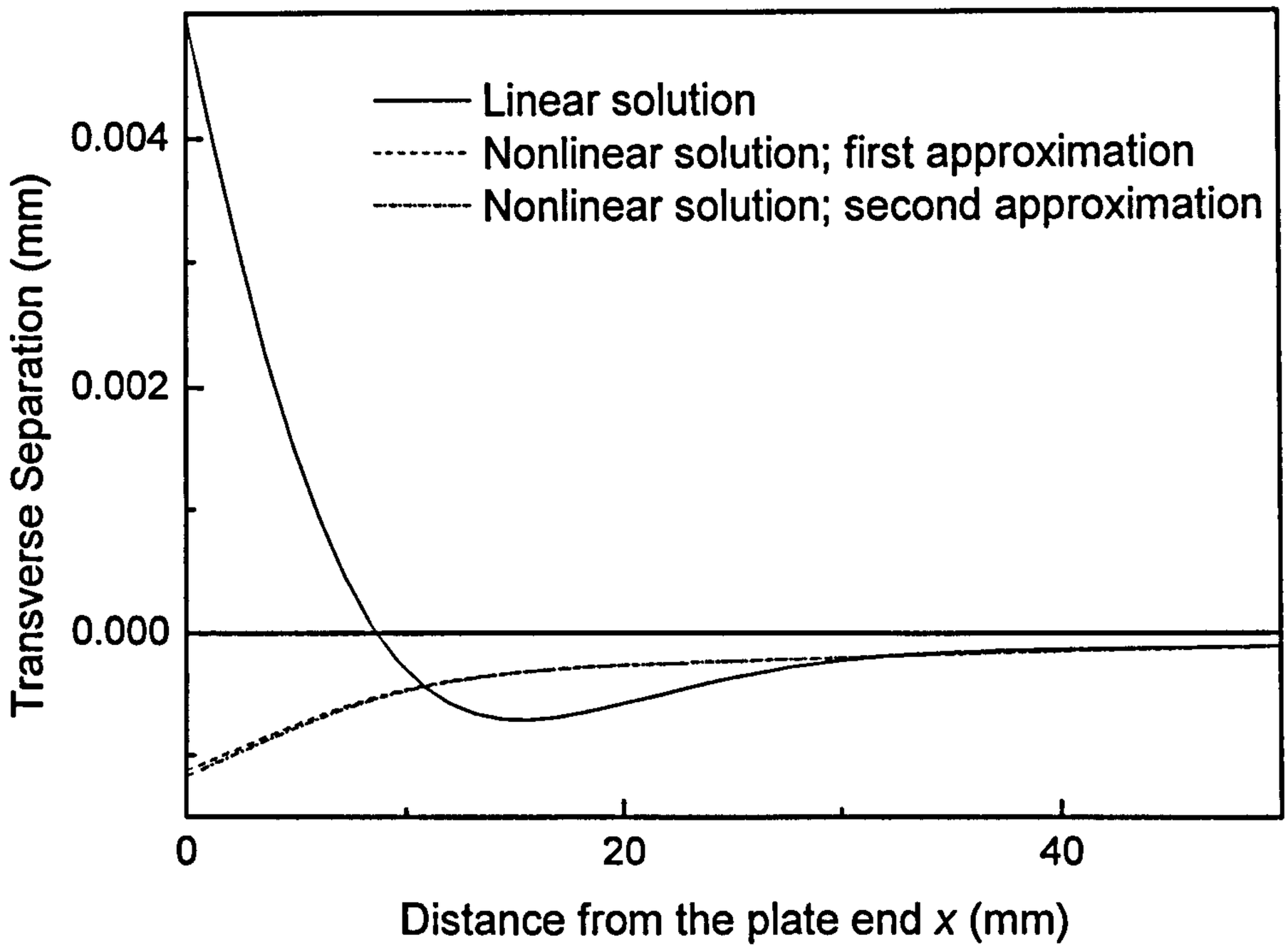

(b) Distribution of the transverse separation along the bonding interface

Fig. 7.8 The ultimate limiting state under $q = 0.86\ N/mm^2$

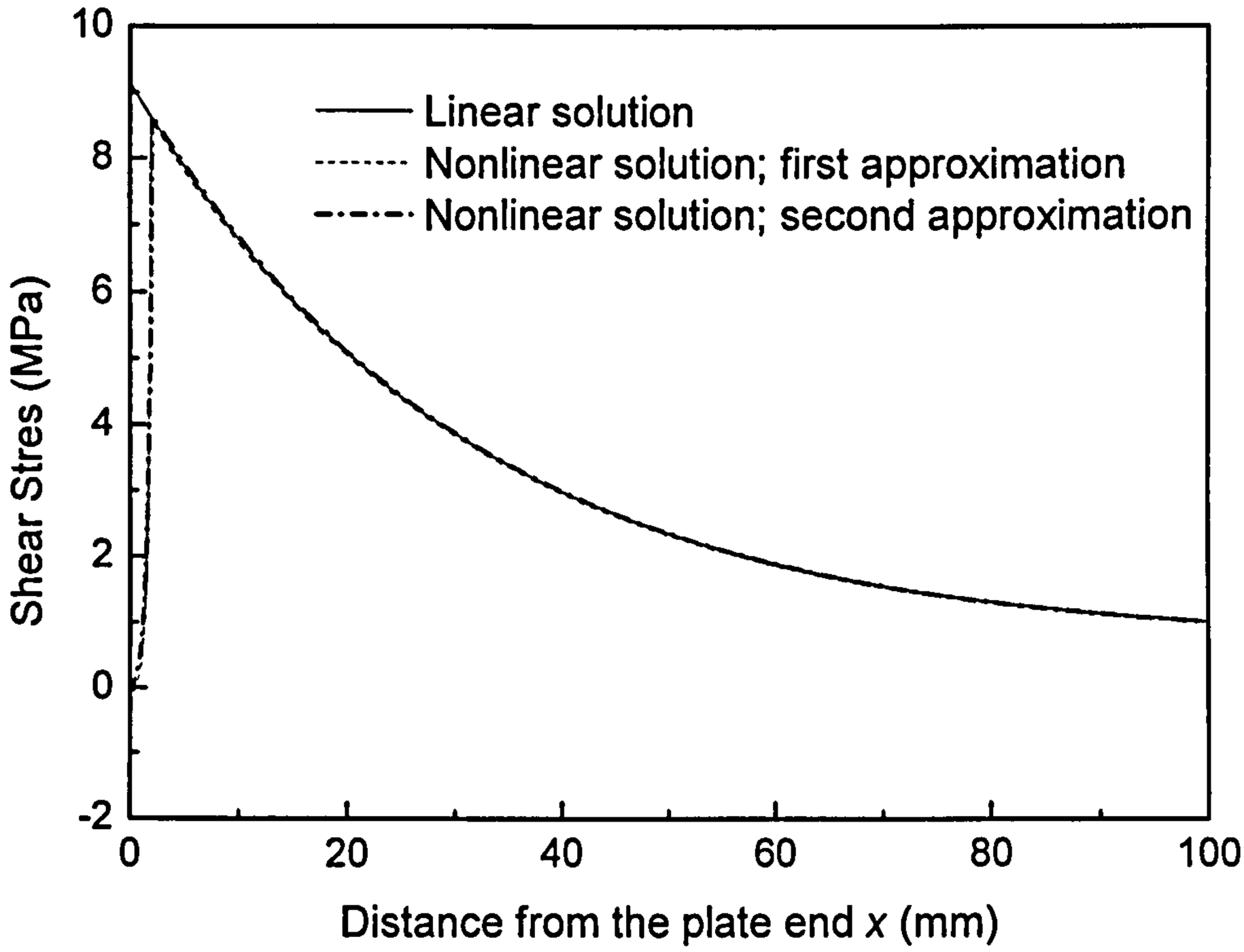

(c) Distribution of the interfacial shear stress along the bonding interface

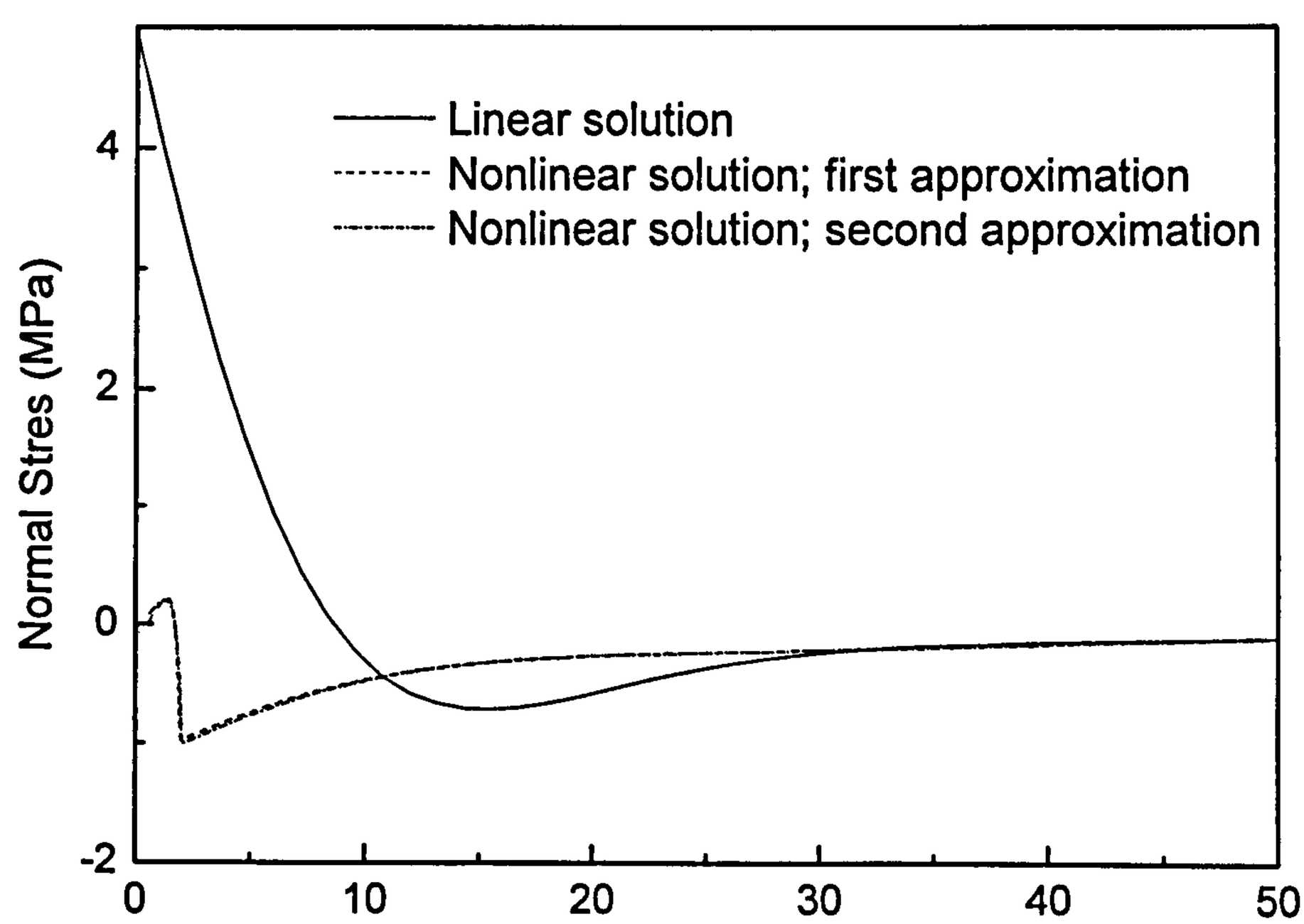

(d) Distribution of the interfacial normal stress along the bonding interface

Fig. 7.8 The ultimate limiting state under $q = 0.86\ N/mm^2$

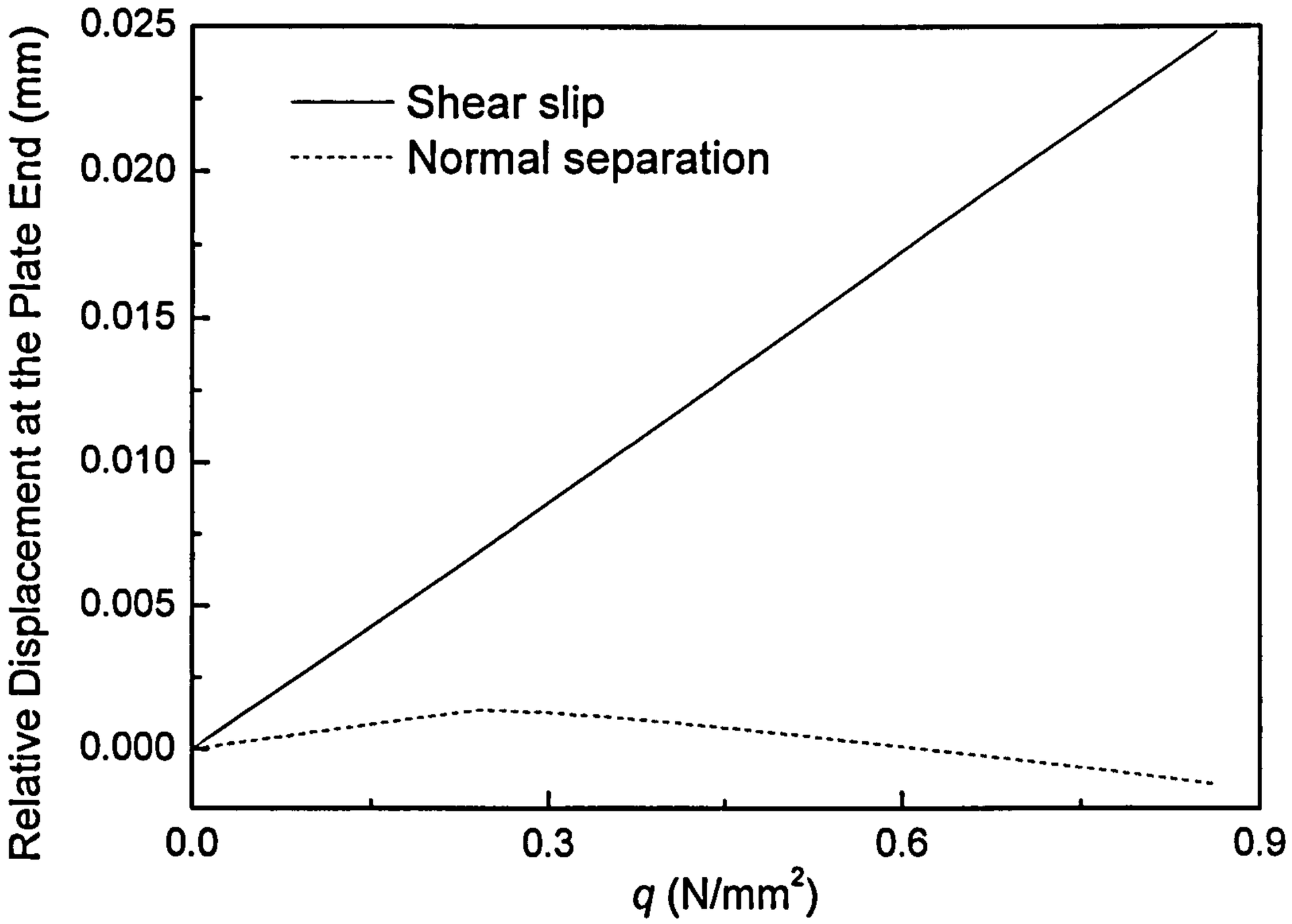

(a) Relative displacements at the plated end against applied load

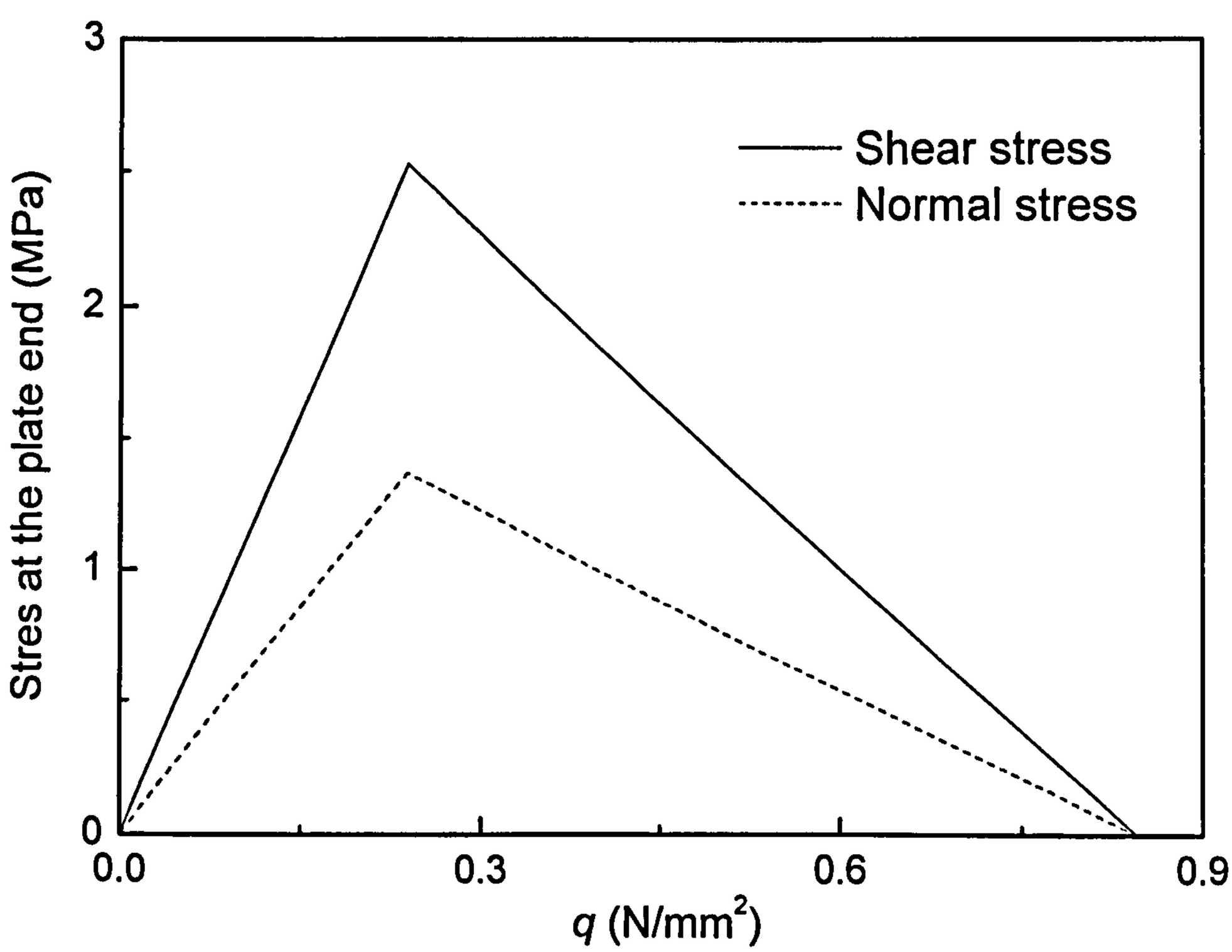

(b) Interfacial stresses at the plated end against applied load

Fig. 7.9 The displacement/stress against applied plot at the plate end

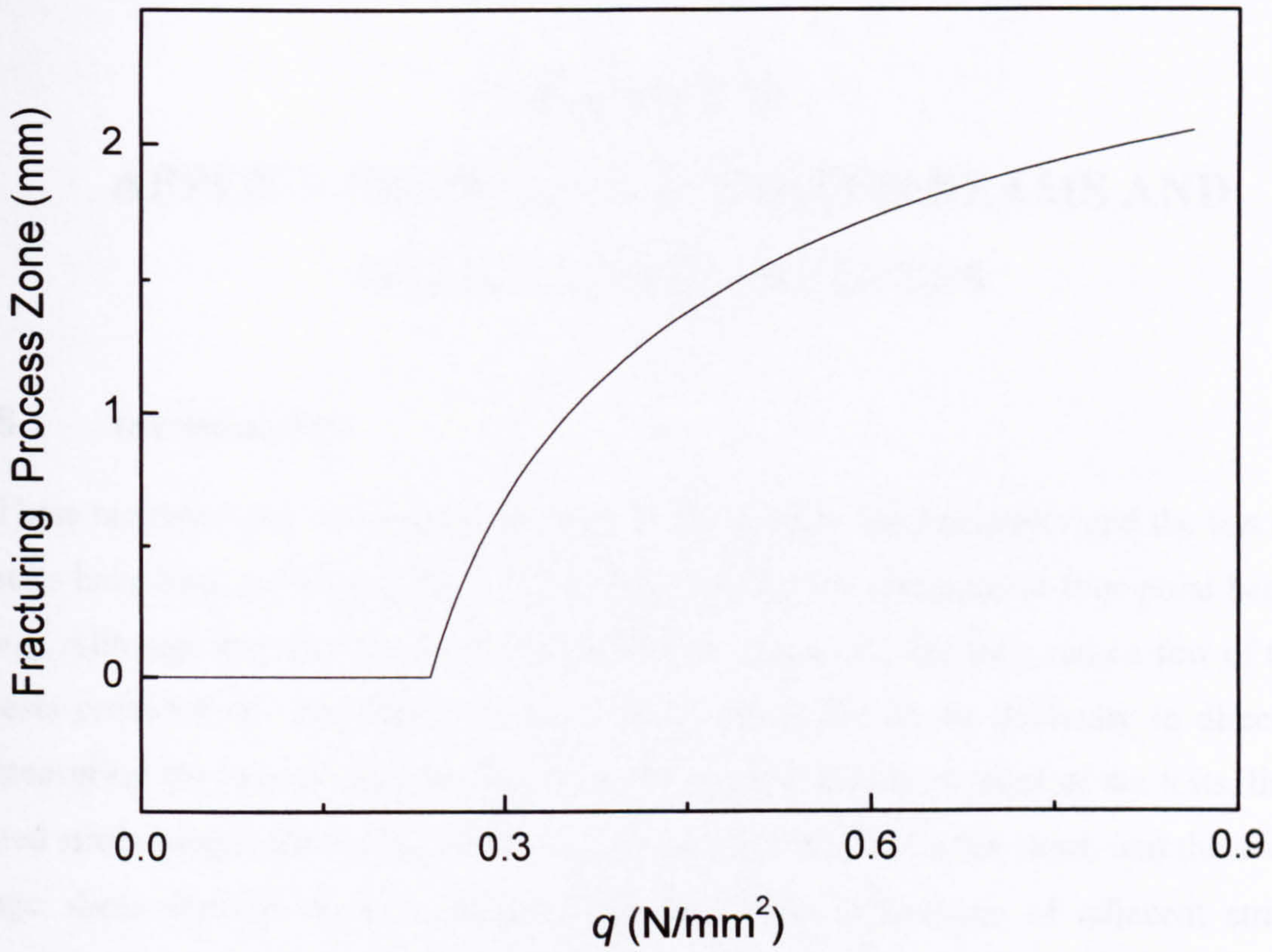

Fig. 7.10 Size of the fracturing process zone against applied load

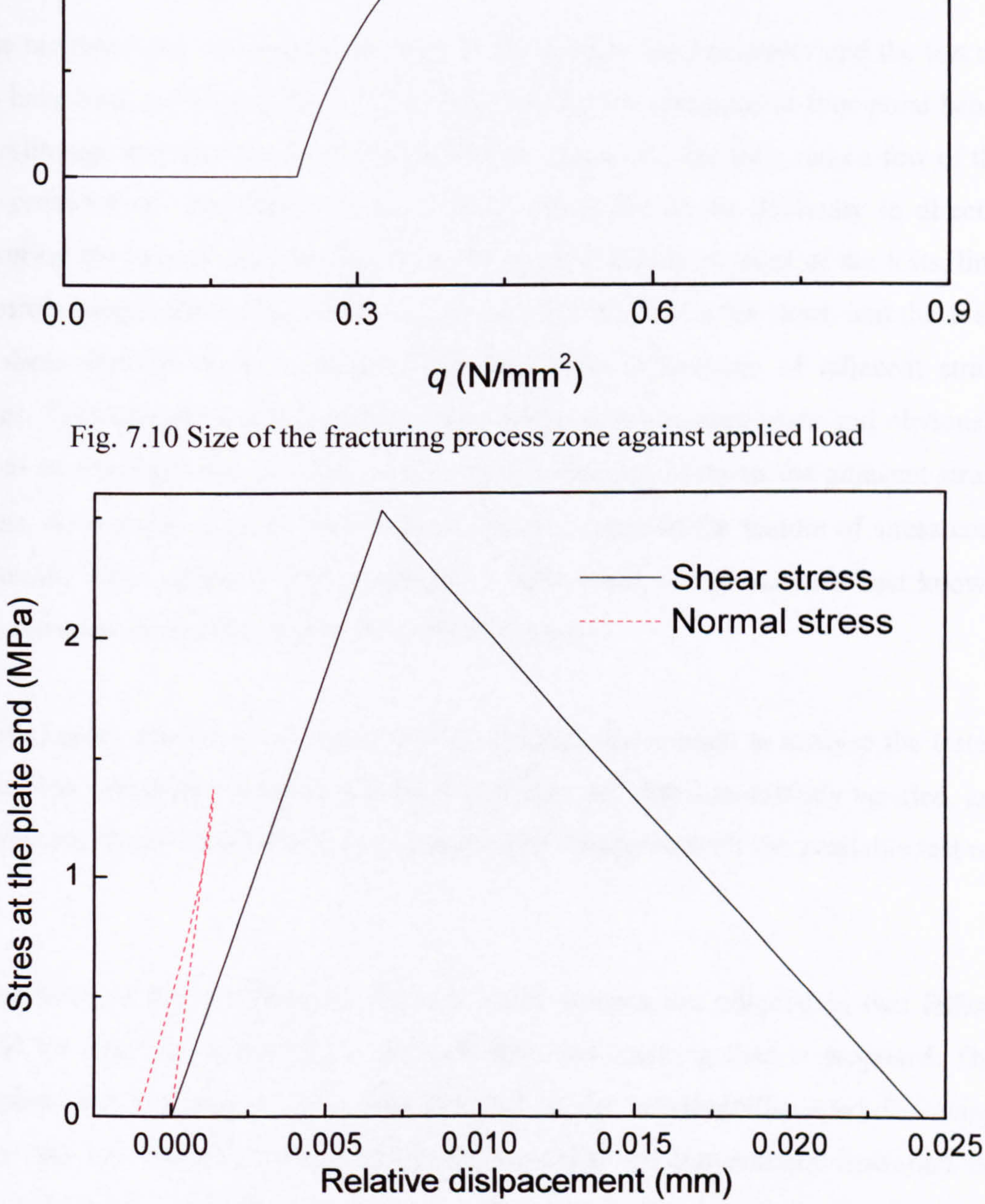

Fig. 7.11 The interfacial stress against relative displacement at the plate end

CHAPTER 8.
APPLICATIONS TO THE TESTED BEAMS AND PARAMETRIC ANALYSES

8.1 Introduction

There are numerous RC beams that have been tested in the laboratory and the test results have been published. Most of the tested beams are subjected to four-point bending. Although the ultimate loads are taken from almost all the tests, only a few of the tests provided the interfacial stresses. That is attributed to the difficulty in directly measuring the interfacial stress/strain for the bonded beams. In most of the tests, limited strain gauges were attached to the external face of the bonded sheet, and the average shear stresses were calculated from the strain differences of adjacent strain gauges. This approach ignored the bending effect on the bonded plate and obviously lead to an average value of shear stress over the interval between the adjacent strain gauges. As a result, most of the test results hardly captured the feature of stress concentration. With regards to the interfacial normal stress, to the author's best knowledge, there are no published results available to date.

In this chapter, the solutions from previous chapters are applied to analyse the tested beams. The completed solution and the simplified one, both successfully verified, are applied, and stress distributions are presented and compared with the available test results.

On the basis of the comparisons, the calculated stresses are adopted in two failure models for concrete materials and the first plate end cracking load is proposed. The first plate end cracking load is also referred as the serviceability load following Brosen and Ven Garment (1998), and it is distinct with the conventional first cracking load in the high bending moment region. The plate end cracking load is normally higher than the conventional first cracking load due to flexure. It is very difficult to be captured in the load-deflection curves, although it can be observed from the load-strain curves of the strain gauge in the very vicinity of the plate end. Few published

test results provided this information. Apart from the serviceability load, the development length is also calculated for the tested beams in this chapter.

The NLFM solution is also used to calculate the serviceability and ultimate loads for the debonding failure and the size of FPZ. These results are compared with other available analytical or experimental results.

The second part of this chapter carries out an extensive parametric analysis on the interfacial stresses using the simplified solution. The parameters discussed include concrete compressive strength, geometrical and material properties of the adhesive and bonded materials. The results are presented in graphic form for each group of parameters.

8.2 Failure Models for the Concrete Materials

Two failure models for the concrete materials are adopted in this chapter to seek the failure load of the concrete under a complex stress state, i.e. Kupfer and Gerstle Model and Mohr-Coulomb strength model.

8.2.1 Kupfer and Gerstle's Model (1973)

The principle stresses are calculated for any critical concrete particle in a complex stress state (see Figure 8.1) and it is checked with this Kupfer and Gerstle's model (1973). This model can be described using the formulas under different stress combination as follows:

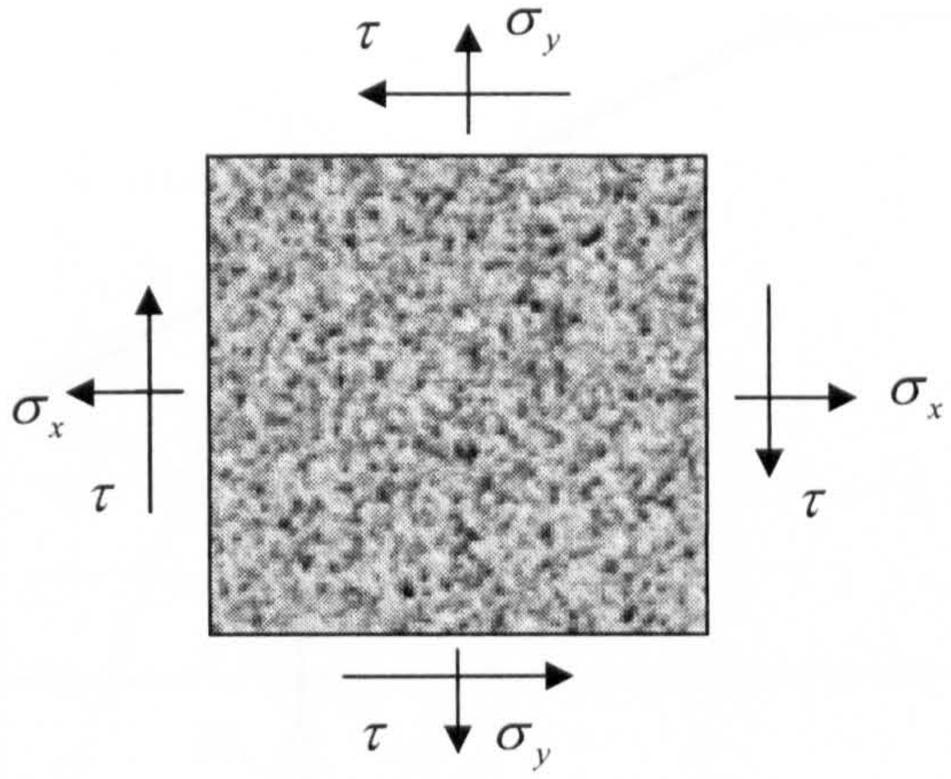

Fig. 8.1 Complex stress state

(1) under compression-compression

$$\left(\frac{\sigma_{\max}}{f_{cu}}+\frac{\sigma_{\min}}{f_{cu}}\right)^2+\frac{\sigma_{\min}}{f_{cu}}+3.65\frac{\sigma_{\max}}{f_{cu}}=0 \tag{8.1a}$$

(2) under compression-tension state

$$\frac{\sigma_{\max}}{f_{tu}}=1+0.8\frac{\sigma_{\min}}{f_{cu}} \tag{8.1b}$$

(3) under tension-tension state

$$\frac{\sigma_{\max}}{f_{tu}}=1 \tag{8.1c}$$

The maximum and minum principl stresses are calculated as

$$\sigma_{\substack{\max\\ \min}}=\frac{\sigma_x+\sigma_y}{2}\pm\sqrt{\frac{\left(\sigma_x+\sigma_y\right)^2}{4}+\tau^2} \tag{8.1d}$$

8.2.2 The Mohr-Coulomb Failure Model (Mohr, 1911)

As Figure 8.2 shows, failure line is the envelope of a series of Mohr circles under the critical stress states. One of the simplifications for the failure line is that it is deemed as a straight line and hence it can be determined by two parameters, which is called as Mohr-Coulomb model. In this model, it is related to two simple strength values, i.e. uniaxial tensile strength f_t and the uniaxial compressive strength $f_{ck,}$ both of which are characteristic values.

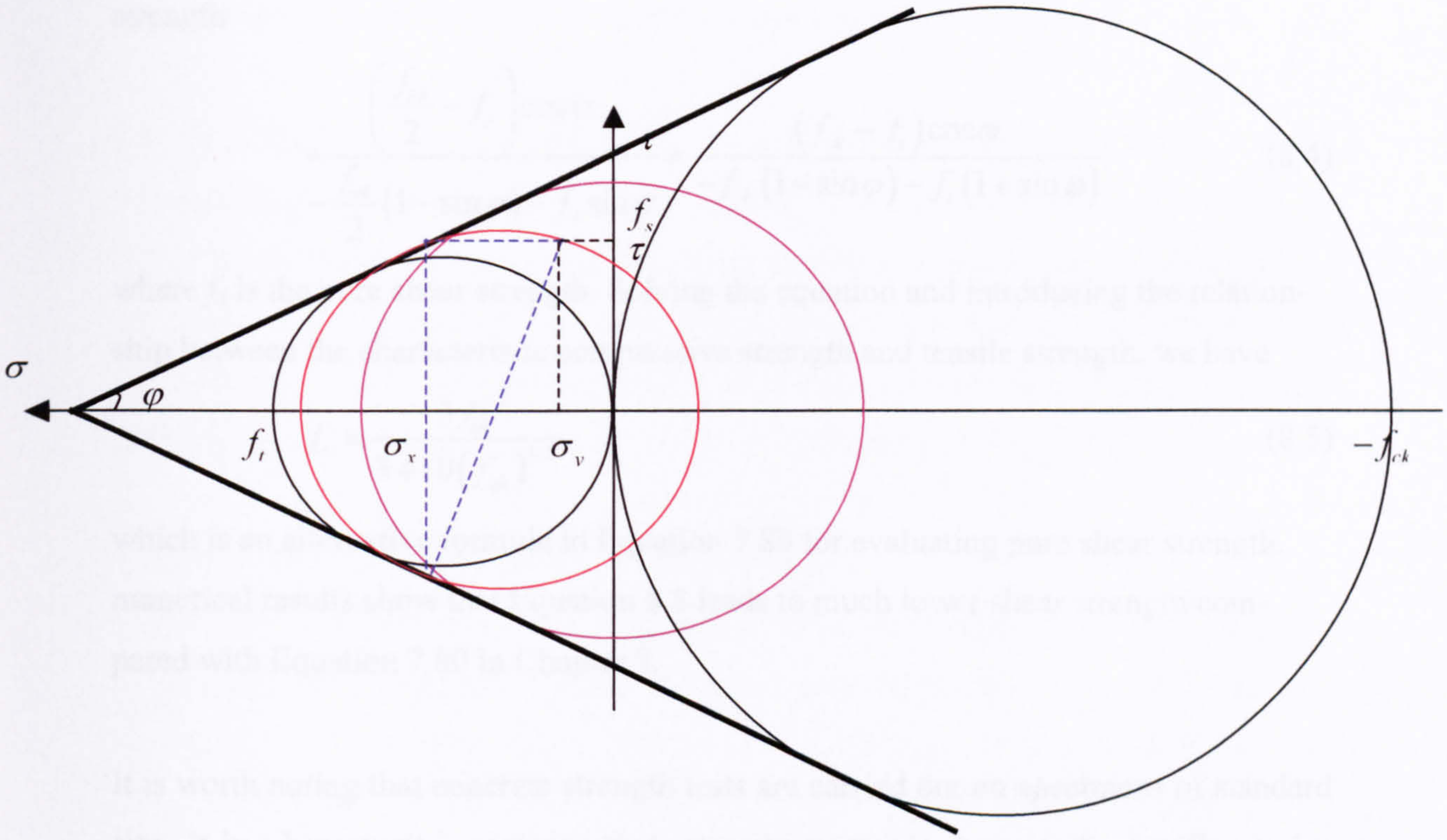

Fig. 8.2 Mohr-Coulomb strength model

In Figure 8.2, the biggest circle is the pure uniaxial compressive Mohr circle and the smallest one is the pure uniaxial tension circle. The failure line is the tangent to both of them. Any other Mohr circle, which is tangent to the line, indicates the critical stress state, and the complex stress state satisfies

$$\frac{\left(\frac{f_{ck}}{2}-r\right)\cos\varphi}{-\frac{f_{ck}}{2}\left(1-\sin\varphi\right)-\left(\frac{\sigma_x+\sigma_y}{2}+r\sin\varphi\right)}=\frac{\left(f_{ck}-f_t\right)\cos\varphi}{-f_{ck}\left(1-\sin\varphi\right)-f_t\left(1+\sin\varphi\right)} \tag{8.2}$$

where

$$\sin\varphi=\frac{f_{ck}-f_t}{f_{ck}+f_t} \tag{8.3a}$$

$$\text{and } r=\sqrt{\frac{\left(\sigma_x+\sigma_y\right)^2}{4}+\tau^2} \tag{8.3b}$$

From this model, we also can derive the pure shear strength formula related to the uniaxial compressive strength. The Mohr circle for pure shear is the one centred at

the origin point. Using the same procedure we have the following equation for shear strength

$$\frac{\left(\frac{f_{ck}}{2}-f_s\right)\cos\varphi}{-\frac{f_{ck}}{2}(1-\sin\varphi)-f_s\sin\varphi}=\frac{(f_{ck}-f_t)\cos\varphi}{-f_{ck}(1-\sin\varphi)-f_t(1+\sin\varphi)} \tag{8.4}$$

where f_s is the pure shear strength. Solving the equation and introducing the relationship between the characteristic compressive strength and tensile strength, we have

$$f_s=\frac{3f_{ck}}{3+10(f_{ck})^{1/3}} \tag{8.5}$$

which is an alternative formula to Equation 7.80 for evaluating pure shear strength. numerical results show that Equation 8.5 leads to much lower shear strength compared with Equation 7.80 in Chapter 7.

It is worth noting that concrete strength tests are carried out on specimens of standard size. It has been well recoginzed that concrete materials show quite significant size effect, which are attributed to the complex heterogeneous natures due to the consitutent materials. To adopt the strength value and strength model approporiately, we study the stress state for an element of limited size, rather than an infinitesimal particle. In this case, we set the size of the critical element to be 1.5 times the maximum coarse aggregate size, which is located in the vicinity of the plate ends.

8.3 Solution Applications

8.3.1 Jones et al. (1988) Steel Plated RC Beam

The first example is a RC beam strengthened by steel plate tested by Jones et al (1988). Seven beams were tested, among which, the first one, Beam F331 is suitable to be re-studied using the methods developed in this study. The RC beam is simply supported with a span 2300mm between the supporting points. It is subjected to four-point bending, each at the third point. The geometrical and material properties are:

Concrete beam:

Cross section size: 155mm x 255mm; Cube strength: 53.6MPa.

Adhesive layer:

Thickness: 1.5mm; Young's modulus: 280MPa; Poisson's ratio: 0.35.

Bonded steel plate:

Length: 2200mm; thickness: 6mm; Young's modulus: 200GPa.

All the above data, except the Poisson's ratio for the adhesive material and the Young's modulus for mild steel, are the original data form the test. The Poisson's ratio for the adhesive material and the Young's modulus for steel material are chosen as the commonly used values of the respective materials. For other material properties of the concrete, which were not specified in the tests, are calculated by the empirical formula listed in Chapter 7 and they are listed in Table 8.1.

Table 8.1. The material properties for the concrete

Young's modulus (GPa)	Direct tensile strength (MPa)	Direction shear strength (MPa)	Fracture toughness for Mode I (N/mm)	Fracture toughness for Mode II (N/mm)
35	3.15	8.5	0.08	0.18

Two solutions, i.e. the completed solution and simplified solution, are adopted to analyse this beam to attain the interfacial stress distribution. Since both solutions are linearly elastic, the computed stresses are proportional to the applied load. As a result, only the solutions for the applied load 60KN are calculated.

Figure 8.3 shows comparisons of the stress distributions obtained from various methods. Figure 8.3a is for the shear stress. Only the stress along the AC interface is plotted. Apart from the analytical results, also listed in Figure 8.3a is the shear stress measured from the experiment (Jones et al. 1988), that were converted from the measured plate strains. As the size of the Demec gauge and the interval between each other, the test results only reflect the average values. As a consequence, there is quite a discrepancy between the experiment and analytical results. The discrepancy is especially distinct in the high stress gradient region. The reason that causes the large discrepancy near the plate end is that the Demec gauge measured the strains at the lower surface of the steel plate. These strains lead to higher interfacial shear stress than the actual value, which should be calculated from the strains in the neutral axis of the plate. Away from the plate end, the experimental results are closer to the analytical

ones. Both analytical results predict quite coincident results, except those near the load point, where the complete solution shows a progressive reduction, whereas the simplified one shows a step change.

Figure 8.3b shows the interfacial normal stress along the AC and PA interfaces. Due to reasons stated in the first section of this chapter, there is no experimental data for comparison. Thus, only the analytical results are presented in the figure. The discrepancy between both results is noticeable, particularly in the vicinity of the plate end. The completed solutions predict a more accurate trend of stress concentration at the plate end, whereas the simplified solution leads to an approximation. As a matter of fact, the stress in the quasi-brittle material cannot reach the infinite value due to the softening mechanism, and the approximate solution may be adequate to represent the real stress distribution in this area. In the following part, the simplified solution is used to predict the serviceability load by utilizing the two strength models as described in Section 8.2.

A concrete element with size 20mm in the vicinity of the plate end is considered as the most onerous element and the stress components are calculated by the simplified solution and used to predict the serviceability load. The results are listed in Table 8.2.

The NLFM solution is also used to predict the serviceability load and ultimate load. As introduced in Chapter 7, the ultimate load is defined as the load, at which the cracking surface starts to separate. The two symmetric point loads are approximately converted to a UDL by equalizing the maximum bending moment at the mid-span between the two loading arrangements. The values for the fracture toughness are given in Table 8.1. The predicted results are given in Table 8.2. The ultimate load is compared with the experimental one. The NLFM method also predicts the size of fracture process zone when the cracking surfaces start to separate. In the last two columns of Table 8.2 is the development length obtained by the simplified solution and Jones et al.'s (1988) analytical solution.

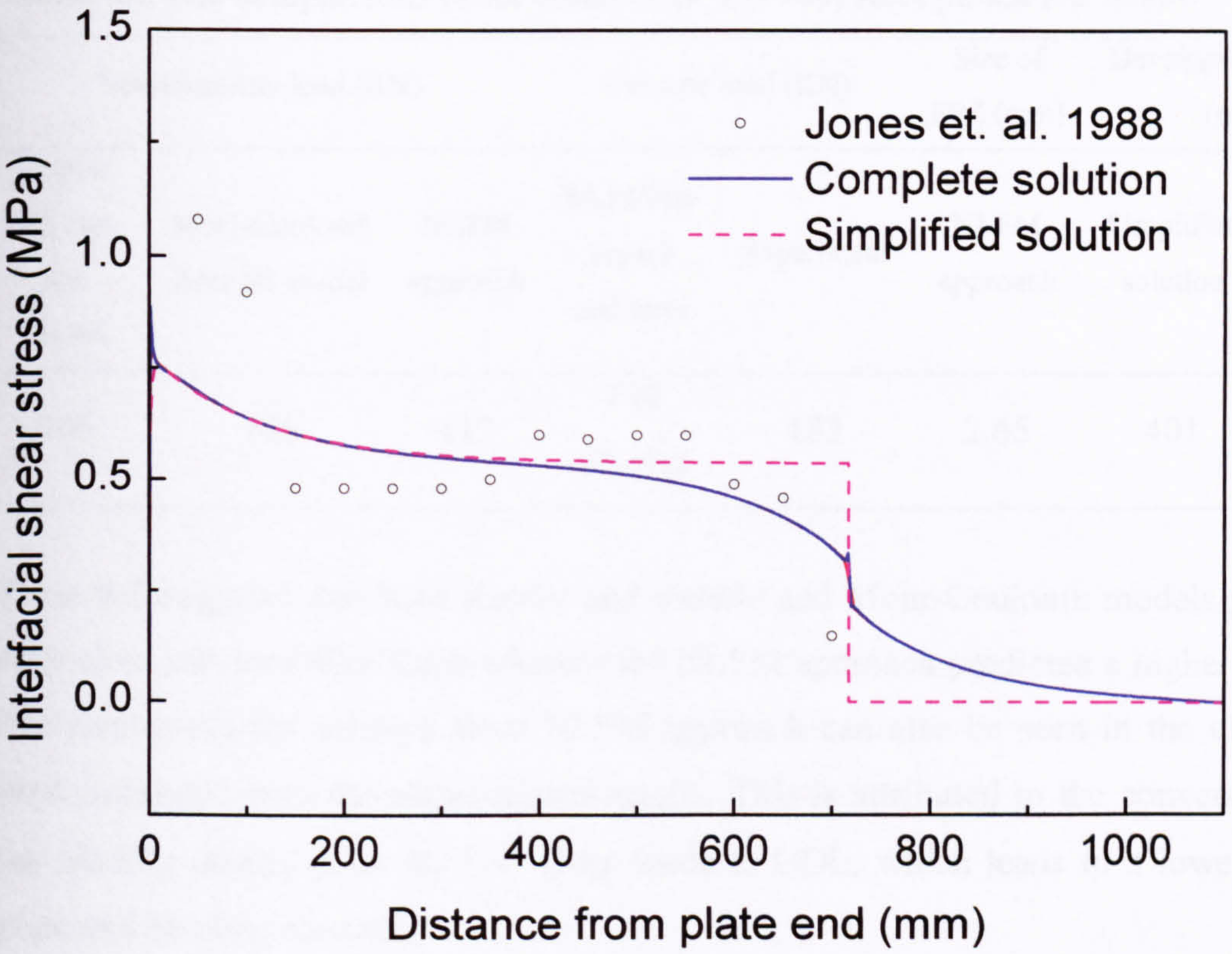

(a) Interfacial shear stress

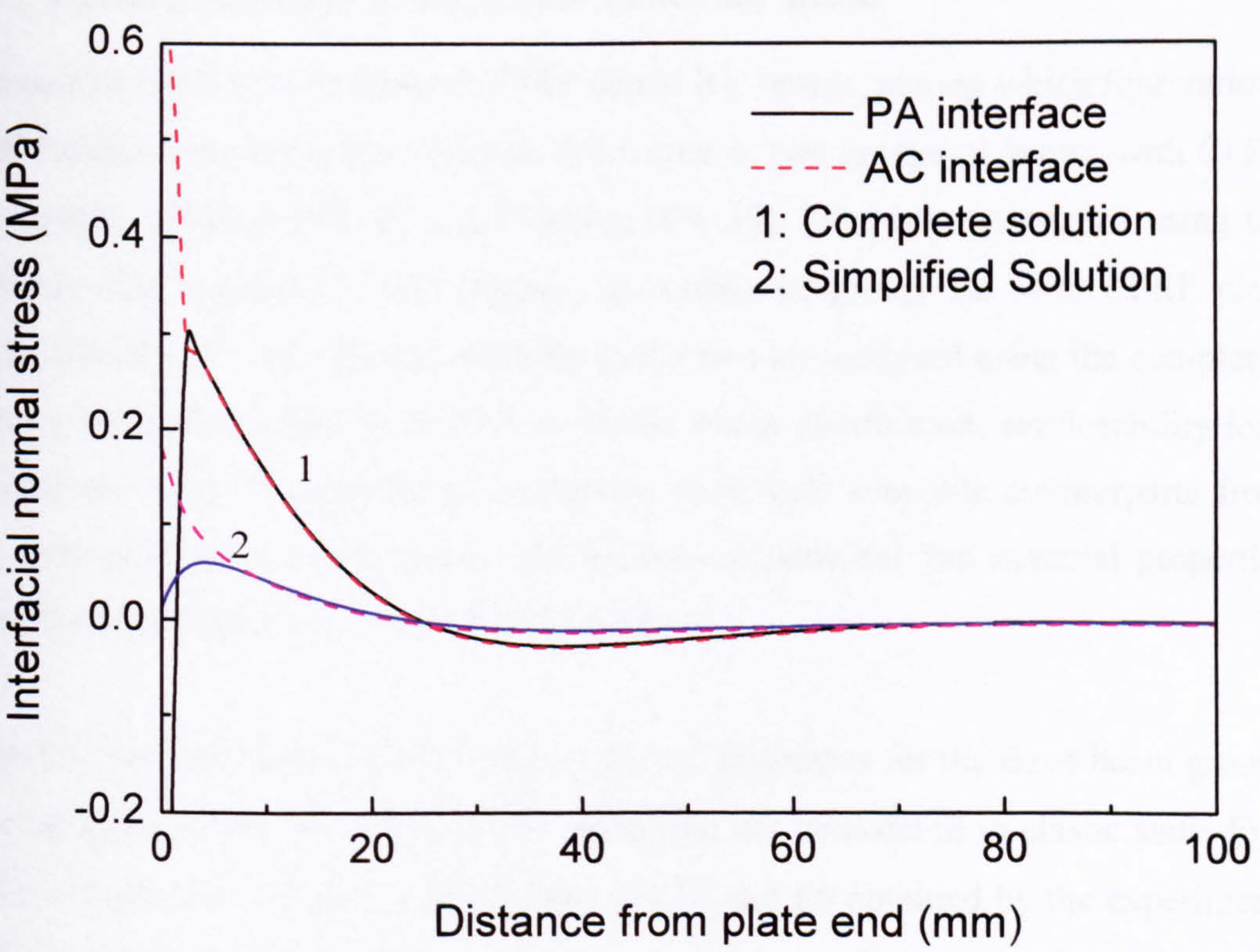

(b) Interfacial normal stress

Fig. 8.3 The comparison of the stress distribution of the steel plated RC beam (Jones et al. 1988)

Table 8.2 The comparisons of for Jones et al.'s (1988) steel plated RC beam

Serviceability load (KN)			Ultimate load (KN)		Size of FPZ (mm)	Development length (mm)	
Kupfer and Gerstle Model	Mohr-Coulomb strength model	NLFM approach	NLFM approach and error	Experiment	NLFM approach	Simplified solution	Jones et al. 1988
106	105	117 (9.3%)	199	182	2.65	401	320

Table 8.2 suggests that both Kupfer and Gerstle and Mohr-Coulomb models predict very close serviceability loads whereas the NLFM approach predicted a higher value. The over-predicted solution from NLFM approach can also be seen in the ultimate load compared with the experimental results. This is attributed to the conversion of the loading pattern from the two point loads to UDL, which leads to a lower level plate end bending moment.

8.3.2 Fanning and Kelly (2001) CFRP Plated RC Beam

Fanning and Kelly (2001) tested 8 CFRP plated RC beams, among which four various CFRP lengths have been investigated. In Chapter 6, two groups of beams with CFRP plate length, 2030mm (F5, 6) and 1700mm (F9, 10), have been simulated using the nonlinear FEA method. In this chapter, an additional group, i.e. with CFRP plate length 1876mm (F7, 8), together with the above two are analysed using the completed solution, simplified solution, NLFM, to obtain stress distribution, serviceability load and ultimate load. The results are compared with their available counterparts from FEA simulations and experiments. The detailed geometrical and material properties can be found in Section 6.1 and 6.3 of Chapter 6.

Figure 8.4 plots the stress distributions in the AC interfaces for the three beam groups under an applied load of 1.4KN. All the materials are considered in elastic state. Figure 8.4 a shows the interfacial shear stress for F5 and F6 obtained by the experiment, Nonlinear FEA simulation (NLFEA), elastic complete solution and simplified solutions, respectively. The experimental results are evaluated from the measured plate strain distribution. As four strain gauges were used over the half of the plate length, only two stress levels can be estimated in the shear span. Hence a large discrepancy is

displayed. Among the other three solutions, the simplified solution predicts the highest peak interfacial shear stress and NLFEA predicts the lowest one. From the curves of the interfacial normal stress presented in Figure 8.4(b), we can see that both complete solution and simplified solution predict almost identical interfacial normal stress while the NLFEA yields a much lower value.

Figures 8.4 (c) and (d) plot the stress distribution for beams F7 and F8, in which only two elastic solutions are presented. Figure 8.4s (e) and (f) are for beams F9 and F10, where the NLFEA results is also plotted. By comparing the interfacial shear stress for the three groups, we can see that the shorter the plate is, the higher the peak shear stress will be. In the event of high shear stress, the simplified solution predicts a relatively lower peak shear stress than the complete solution. However, both methods invariably predict very close interfacial normal stress.

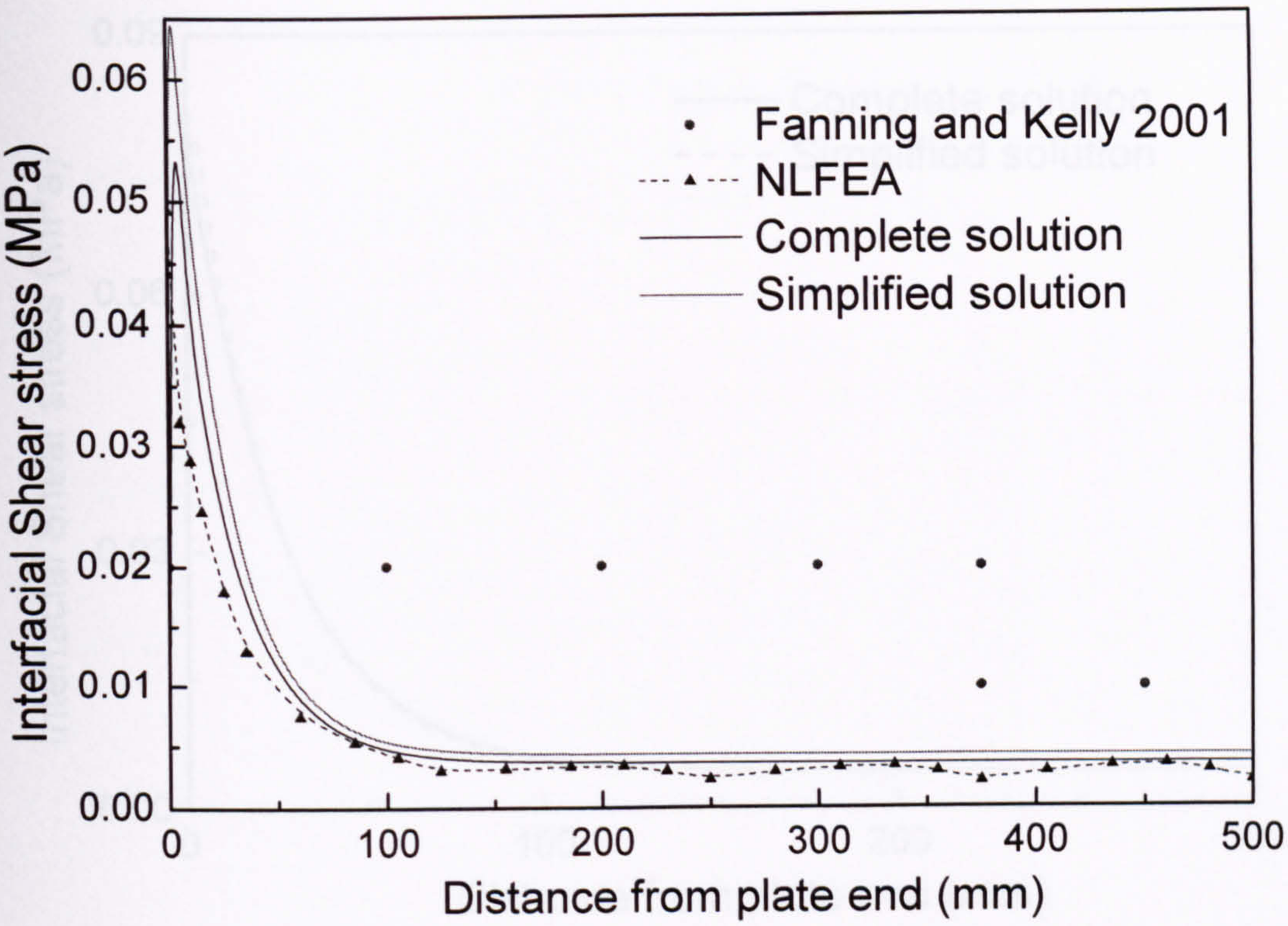

(a) Interfacial shear stress for beam F5, F6

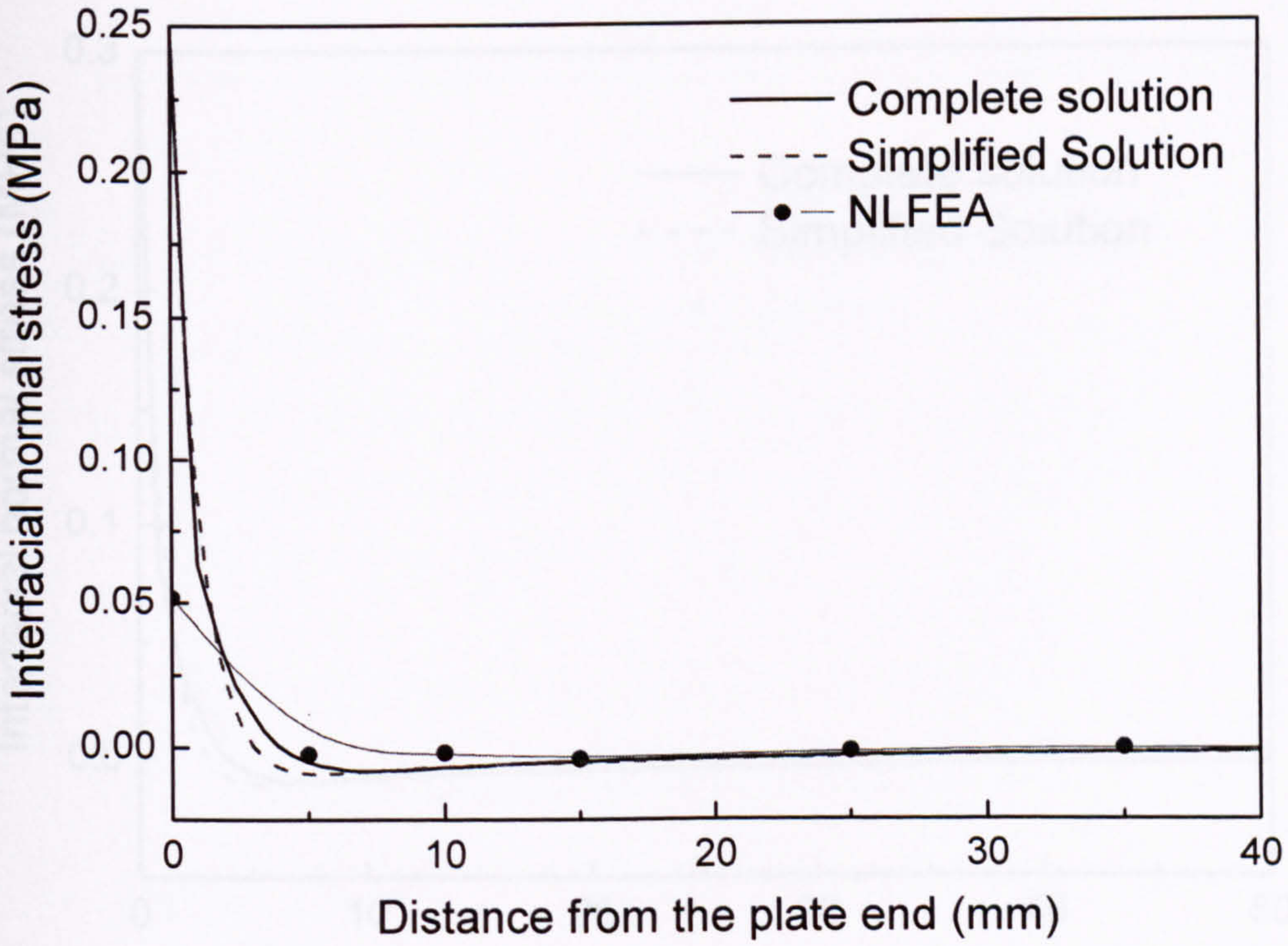

(b) Interfacial normal stress for beam F5, F6

Fig. 8.4 The comparison of the stress distribution of the CFRP plated RC beam (Fanning and Kelly, 2001)

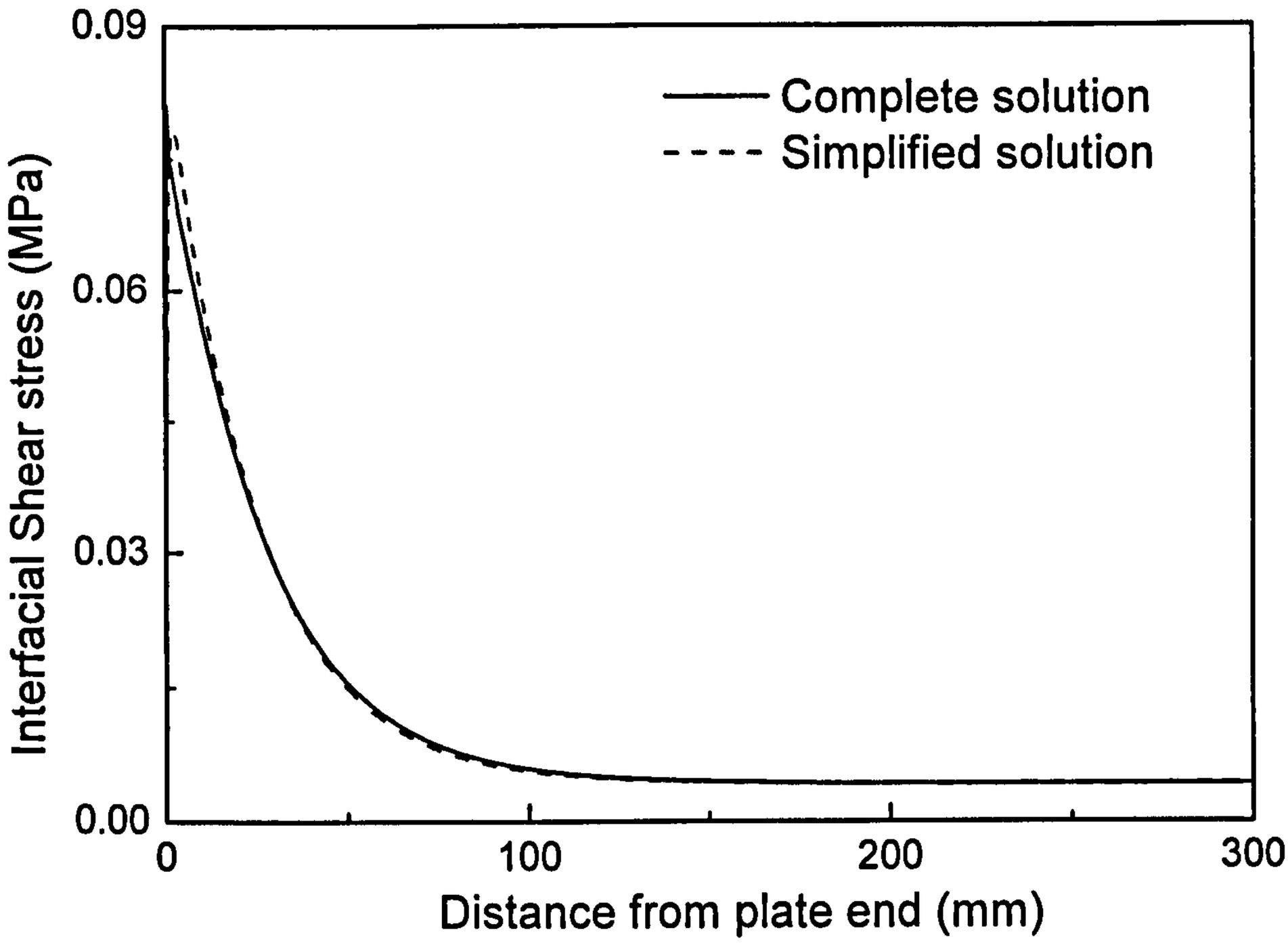

(c) Interfacial shear stress for beam F7, F8

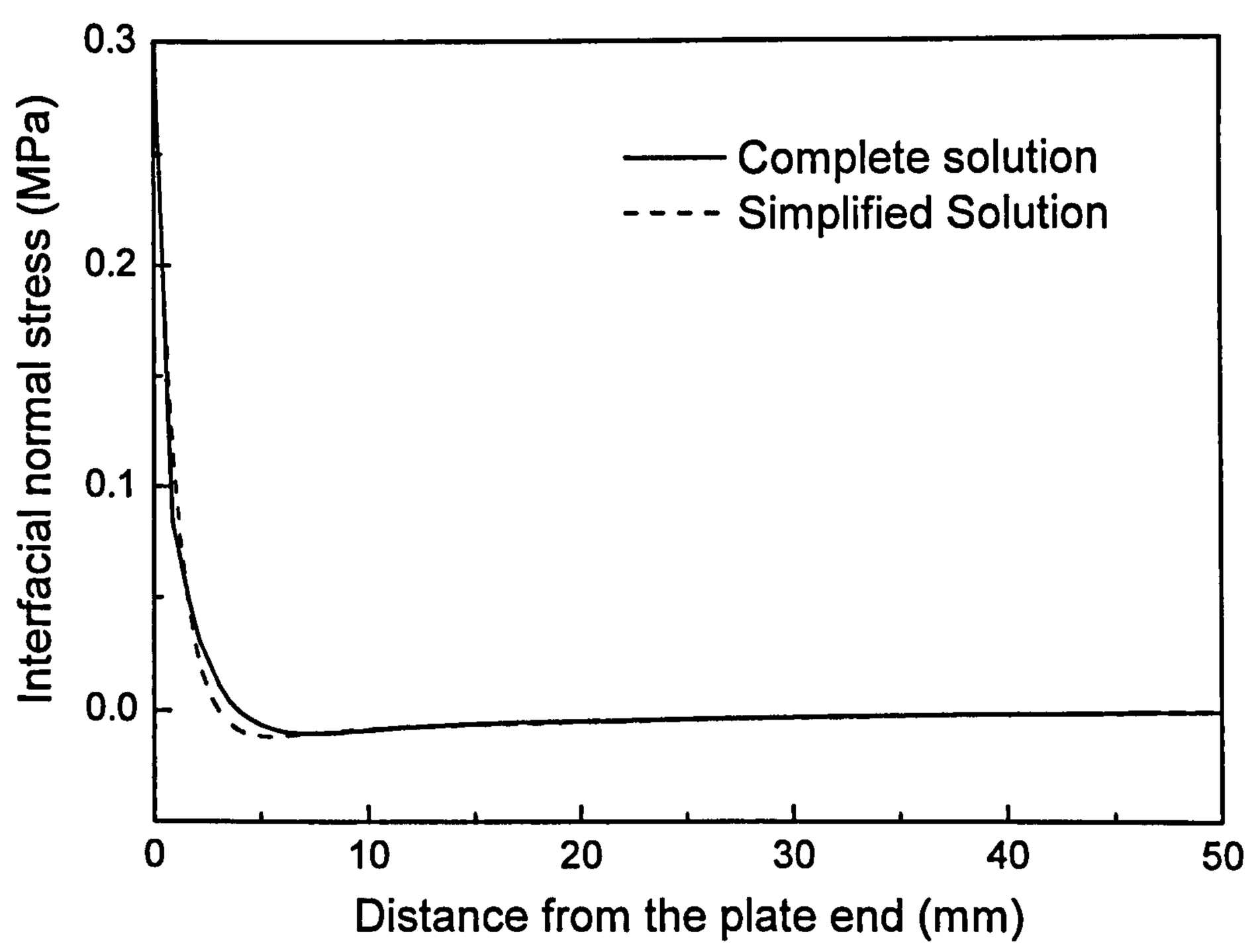

(d) Interfacial normal stress for beam F7, F8

Fig. 8.4 The comparison of the stress distribution of the CFRP plated RC beam (Fanning and Kelly, 2001)

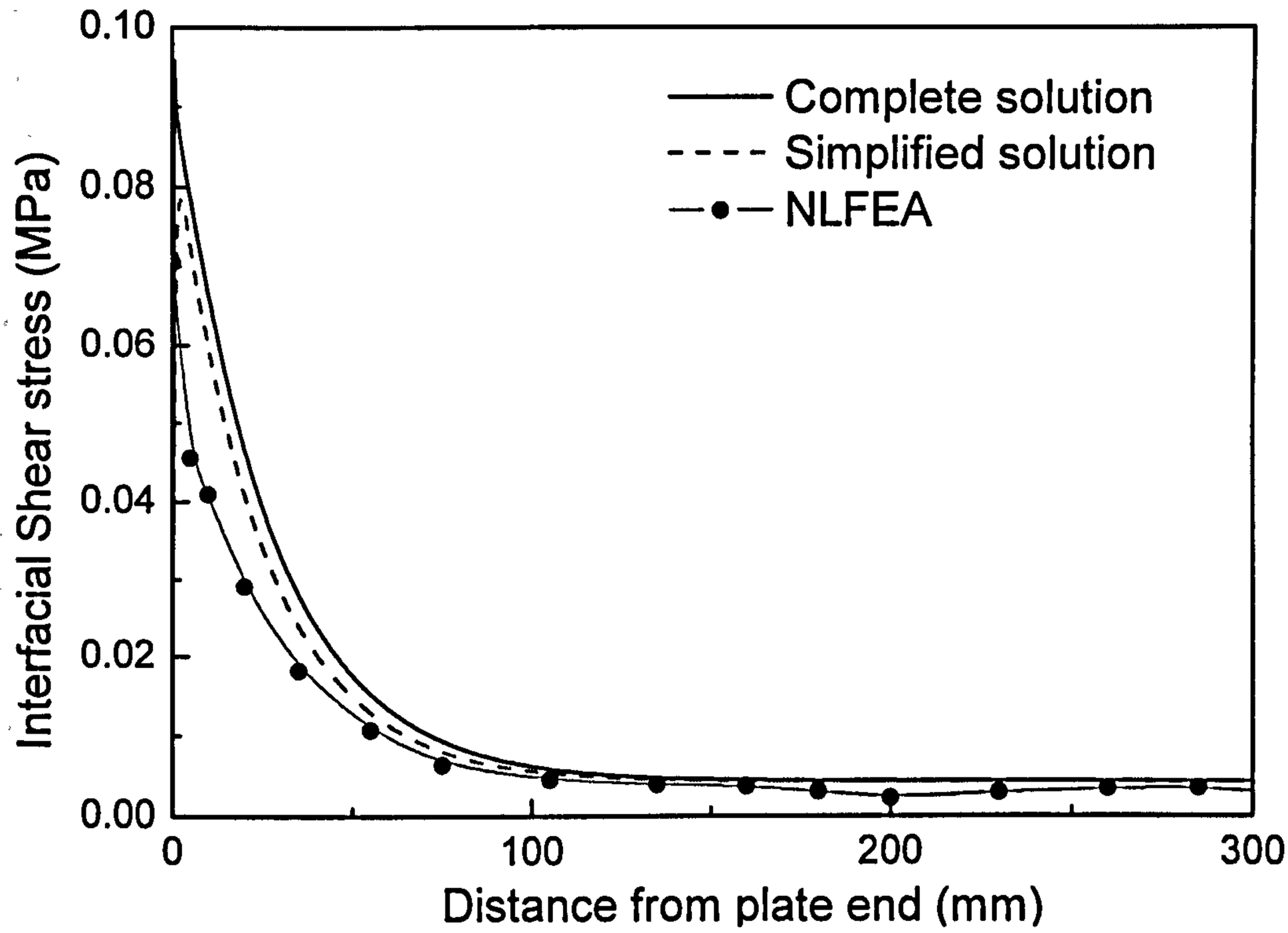

(e) Interfacial shear stress for beam F9, F10

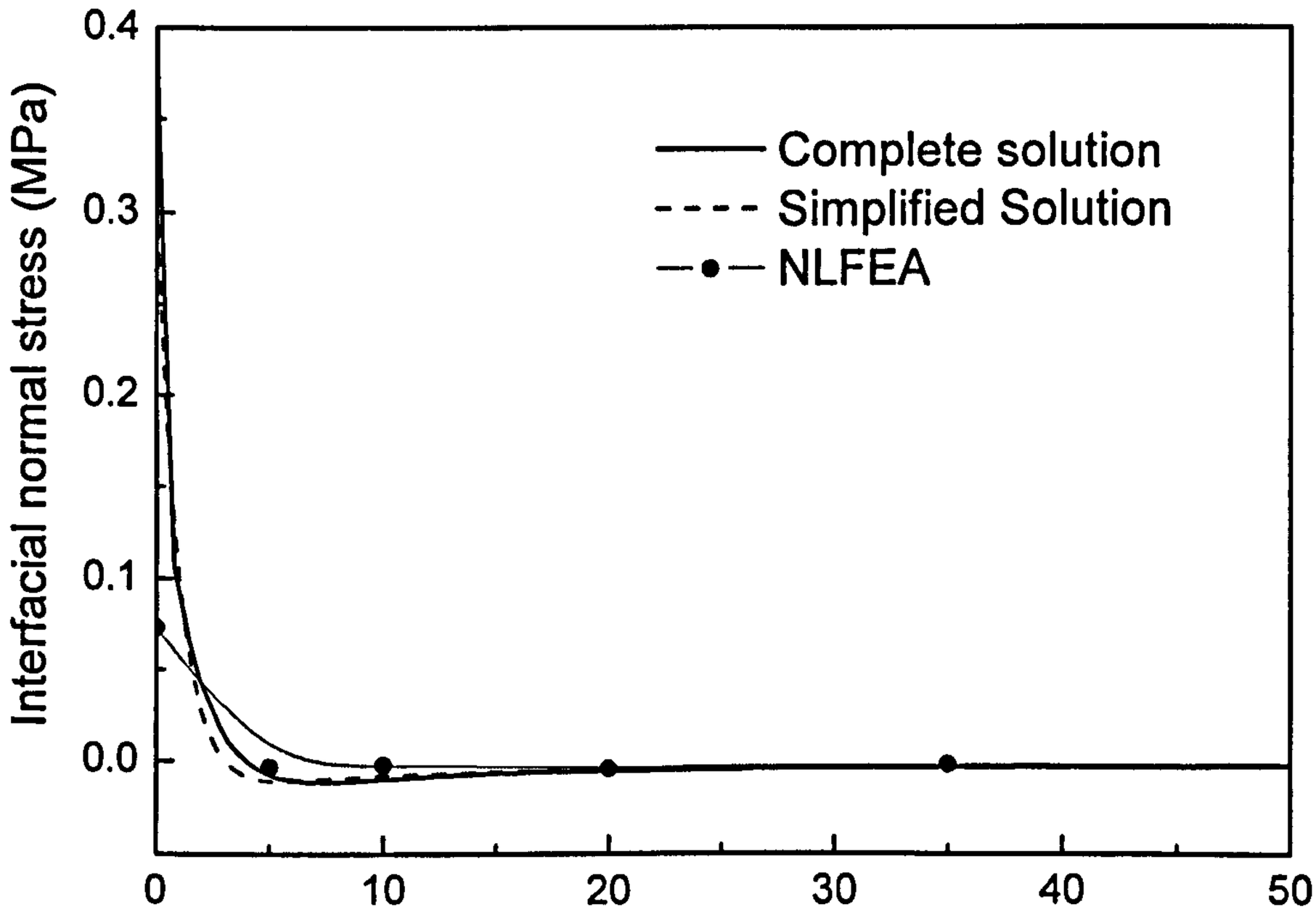

(f) Interfacial normal stress for beam F9, F10

Fig. 8.4 The comparison of the stress distribution of the CFRP plated RC beam (Fanning and Kelly, 2001)

Table 8.3 Summery of the result comparisons for CFRP plated RC beam (Fanning and Kelly 2001)

Beam	Serviceability load (KN)				Ultimate load (KN)			Size of FPZ (mm)	Development length (mm)
	Kupfer and Gerstle Model	Mohr-Coulomb strength model	NLFM approach	NLFEA	NLFM approach and error	NLFEA	Experiment	NLFM approach	Simplified solution
F5,6	12	11	10.5	11	101.4 (1.4%)	100	101.5	5.7	85
F7,8	9.8	9.8	8.2		79.3 (-2%)		81	5.7	85
F9,10	8.3	8.3	6.6	6	63.4 (-17%)	76	72	5.7	85

Table 8.3 shows a summery of the comparisons of serviceability load, ultimate load, size of FPZ and development length. It is evident that the very favorable consistence are show among various approaches.

8.3.3 Etman and Beeby (2000) CFRP Plated RC beam

One of the tested beams from Etman and Beeby (2000) FG1-CF is reinvestigated analytically following the similar procedures. It is a simply supported beam with a span of 1200mm subjected to four-point bending each at the third point. The other parameters for the consistent members are listed as follows.

Concrete beam:

Cross section size: 125mm x 150mm; Mean cube strength: 62MPa.

Adhesive layer:

Thickness: 3mm; Young's modulus: 12.5GPa; Poisson's ratio: 0.33.

Bonded CFRP plate:

Length: 1080mm; thickness: 1.3mm; Young's modulus: 150GPa; and the shear modulus: 5.5 GPa.

Figure 8.5 show comparisons of the stress distribution under the applied load 60 KN. It shows discrepancy between the experimental and analytical results. At the loading

position, the shear stress from the completed solution shows a nature of singularity, which has not been presented by the simplified solution. Also the simplified solutions showed a discrepancy of the interfacial normal stress with the completed solution only in a interval of 1mm from the plate end and it predicts a lower peak normal stress.

Likewise, Table 8.4 shows a summery of comparisons of the serviceability load, ultimate load, size of FPZ and development length. Again, encouraging consistence is exhibited for this beam.

Table 8.4 The comparisons of the results Etman and Beeby (2000 CFRP plated RC beam

Serviceability load (KN)			Ultimate load (KN)		Size of FPZ (mm)	Development length (mm)
Kupfer and Gerstle Model	Mohr-Coulomb strength model	NLFM approach	NLFM approach and error	Experiment	NLFM approach	Simplified solution
44.8	44.8	42.2	89.4 (-10.4%)	99.8	1.5	54

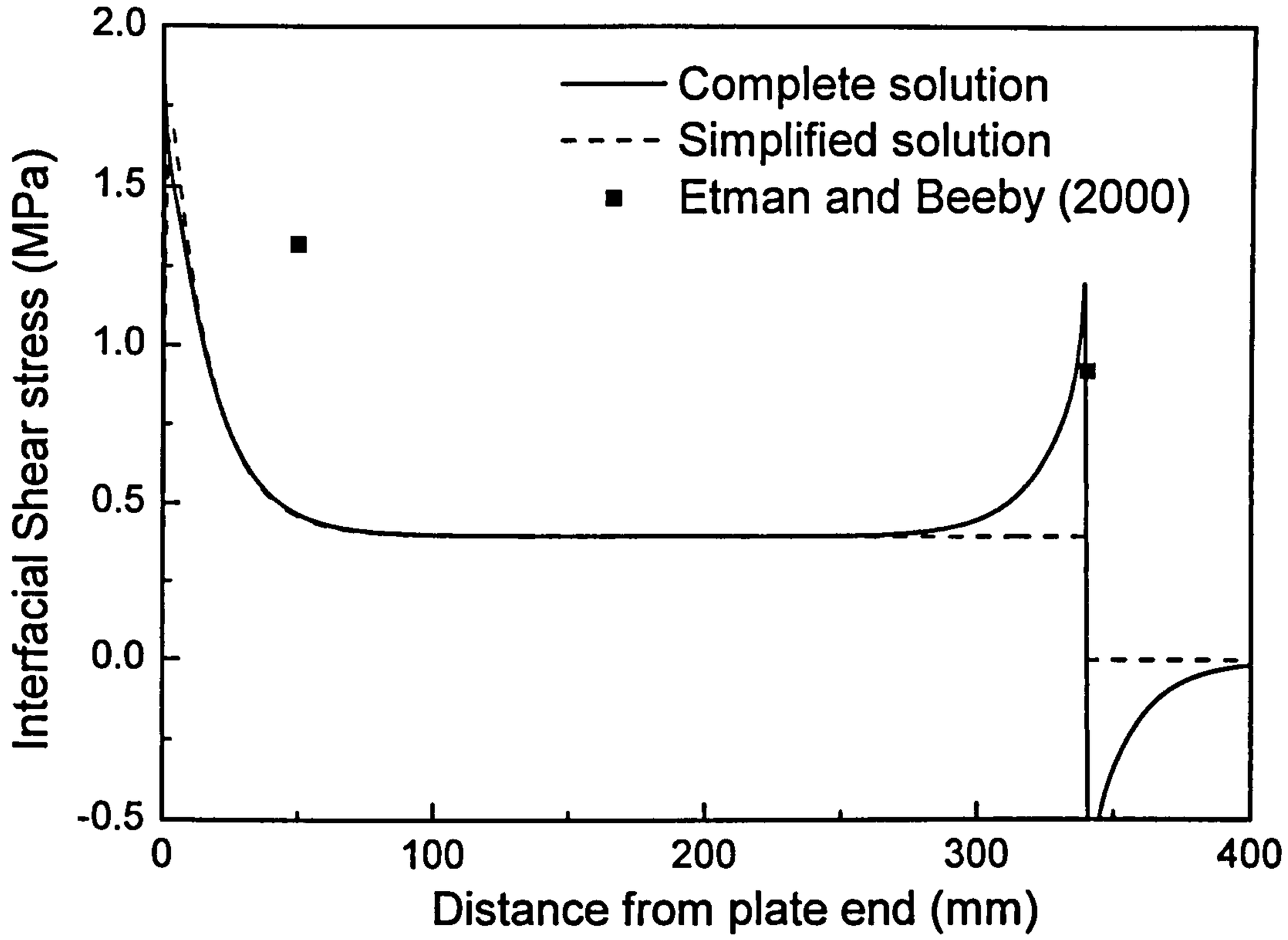

(a) Interfacial shear stress

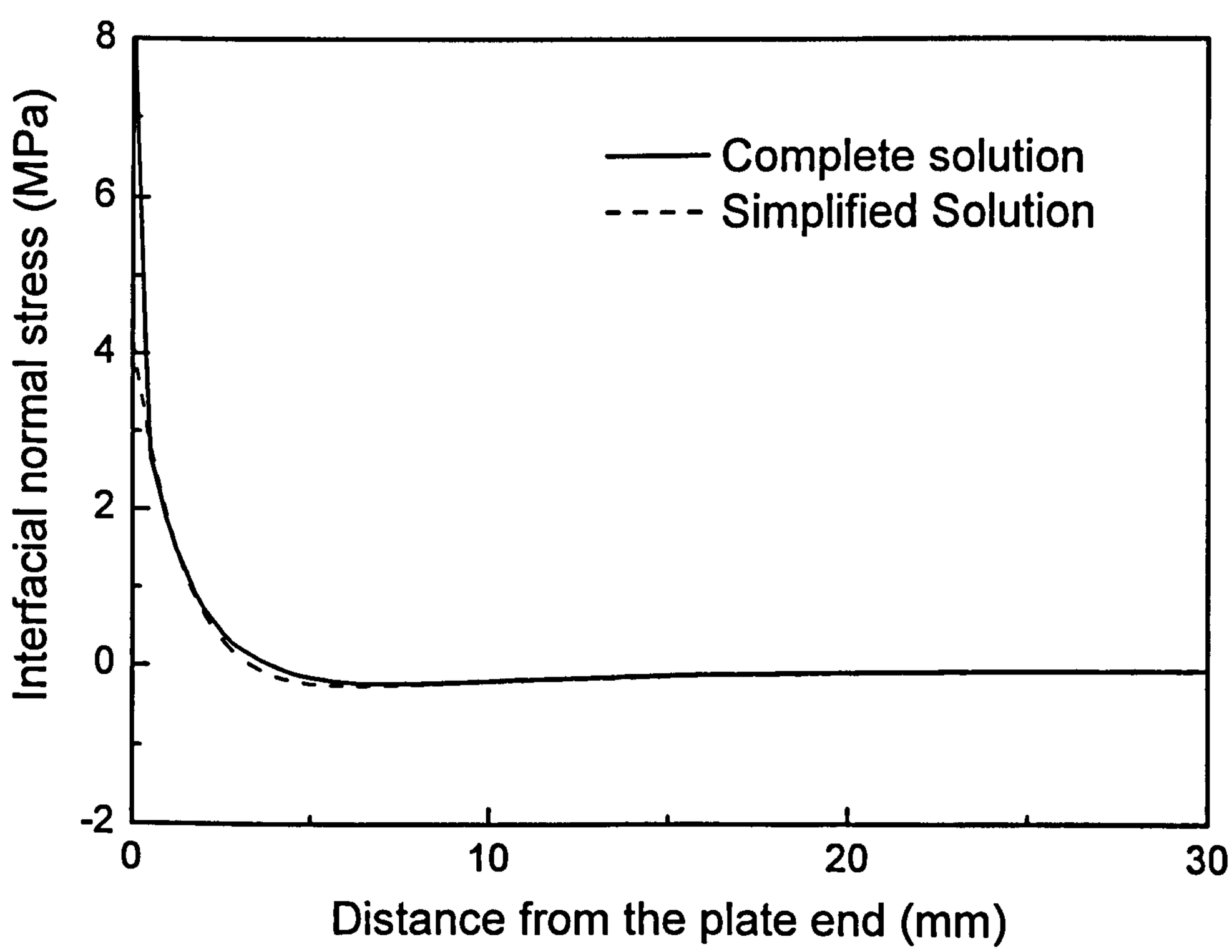

Interfacial normal stress

Fig. 8.5 The comparison of the stress distribution of the CFRP plated RC beam (Etman and Beeby, 2000)

8.3.4 Quantrill et al. (1996) GFRP/CFRP Plated RC Beam

Quantril et al. (1996) carried out extensive tests to investigates the impacts of various parameters to the FRP strengthened beams. The studied parameters include concrete strength, adhesive thickness, plate material, plate size and plate end anchorage system. The tested beams except those with end anchorage system are reanalysed in this chapter and the comparison results are presented.

All the beams are simply supported and spanned over a 900mm distance. Two symmetrical point loads are applied at the third points. The geometrical and material properties are summarized in Table 8.5, in addition to the followings:

Concrete beam:

Cross section size: 100mm x 100mm; maximum coarse aggregate size: 10mm.

Adhesive layer:

Young's modulus:7GPa; Poisson's ratio: 0.3.

Bonded plate:

GFRP with Young's modulus: 49GPa and the shear modulus: 5.8 GPa; CFRP with Young's modulus: 118.5GPa and the shear modulus: 5.5 GPa.

Table 8.5 The summery of the beam parameters (Quantrill et al. 1996)

Beam	Cube strength (MPa)	Adhesive thickness (mm)	Plate material	Plate size (mm)
A1b	70	1.0	GFRP	80 x 1.2 x 860
A1c	70	2.0	GFRP	80 x 1.2 x 860
A2b	42	1.0	GFRP	80 x 1.2 x 860
A2c	42	2.0	GFRP	80 x 1.2 x 860
A2g	42	2.0	GFRP	80 x 1.2 x 600
B2	53	2.0	GFRP	80 x 1.2 x 860
B3	53	2.0	GFRP	30 x 1.2 x 860
B4	53	2.0	GFRP	60 x 1.6 x 600
B6	53	2.0	CFRP	80 x 1.2 x 860

Figure 8.6 plots the interfacial stress at the AC interface for the tested beams under the applied load 1KN using the simplified solutions. Table 8.6 summarizes the result

of comparisons. From the comparisons of the ultimate load with the experimental results, we can see that apart from a few exceptions, they agree with each other very well. Beam A1b experienced an adhesive/concrete interfacial failure, which may be due to the poor workmanship. As a consequence, the beam failed at a relative low load. The same reason applies to beam B3, which failed due to the plate separation along the plate/adhesive interface. This exceptional failure mode gives rise to an error as high as 63%. Another failure mode that Beam A2g has experienced is the shear failure through unplated section. The failure load predicted by NLFM approach is only 7.9KN, while the experimental one is 31.5KN. This implies that the beam did not fail immediately after the plate end crack occurred. In contrast, from test shear cracks appeared within the unplated span, and resulted in the final failure. Beam B6, as the rest of the beams, was tested to show the failure modes of plate and concrete cover separation. The analytical prediction is 30% lower than the tested results. The calculated stress distributions show that the beams bonded by the CFRP plates experienced significantly higher level shear and normal stresses than these counterparts bonded by GFRP plates of the same size (B2 vs. B6). In theory, Beam B6 should have failed at a lower load, which is contradictory to the test result. What caused the odd observation? This unsolved question was also raised in the original paper (Quantrill et al. 1996 b).

Table 8.6 The results comparison (Quantrill et al. 1996)

Beam	Serviceability load (KN)			Ultimate load (KN)		Size of FPZ (mm)	Development length (mm)
	Kupfer and Gerstle Model	Mohr-Coulomb strength model	NLFM approach	NLFM approach and error	Experiment	NLFM approach	Simplified solution
A1b	20.23	20.225	22.35	60.2 (28%)	47.2	0.9	28
A1c	20.19	20.19	22.37	51.17 (16%)	44	0.58	32
A2b	12.675	12.67	12.95	41.5 (13%)	36.7	1	30
A2c	12.64	12.64	12.95	41.5 (11%)	37.3	1	34
A2g	3	2.98	2.25	7.9 (-75%)	31.5	1.4	34
B2	16.1	16.1	16.29	42.25 (24%)	34	0.7	33
B3	16.1	16.095	16.25	40.08 (63%)	24.6	0.7	28
B4	15.99	15.99	13.445	34.4 (1.7%)	35	0.85	36
B6	15.58	15.61	14.63	28.6 (-30%)	40.8	0.74	50

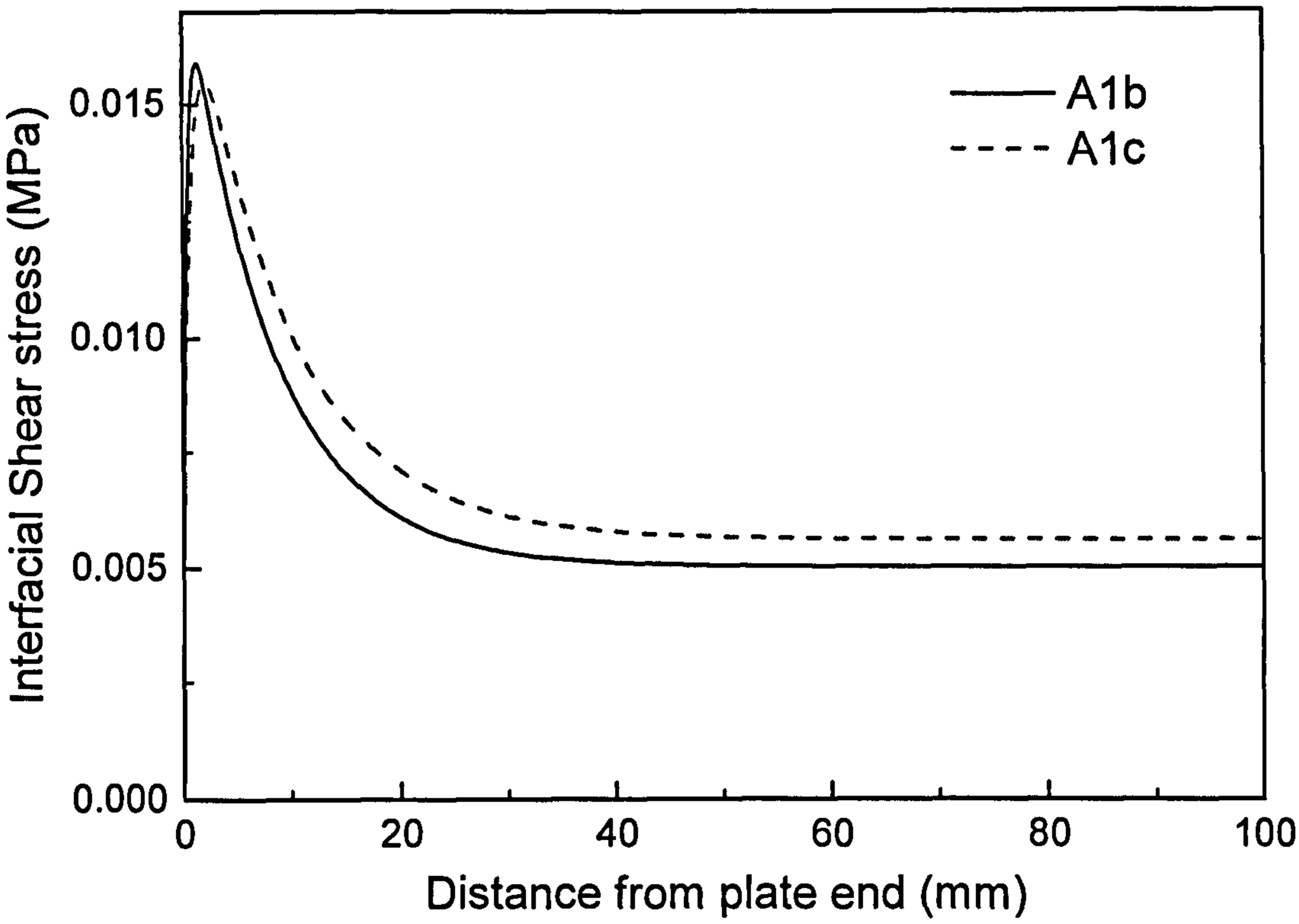

(a) Interfacial shear stress for beam A1 series

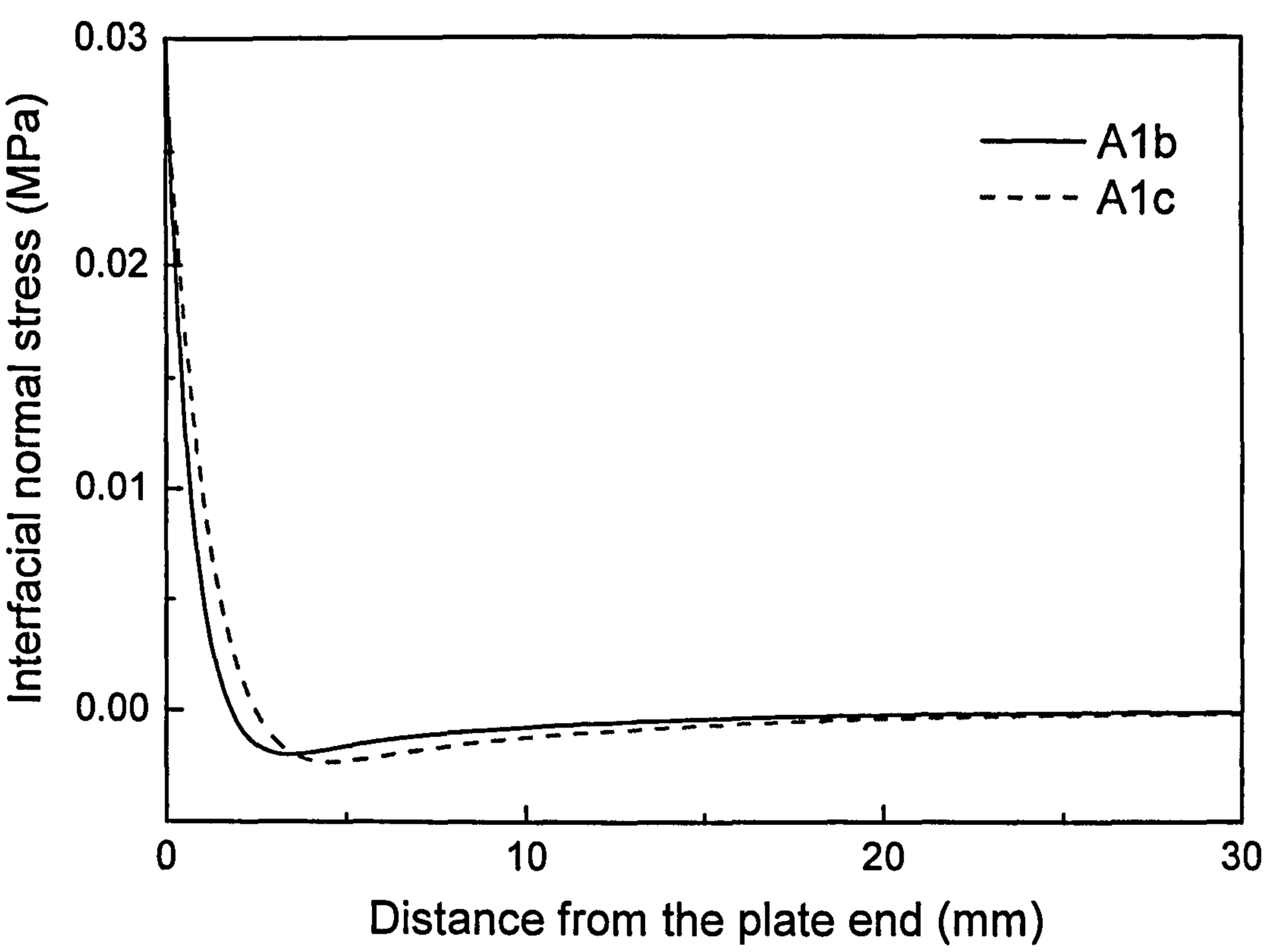

(b) Interfacial normal stress for beam A1 series

Fig. 8.6 The comparison of the stress distribution of the GFRP/CFRP plated RC beam (Quantrill, 1996a, b)

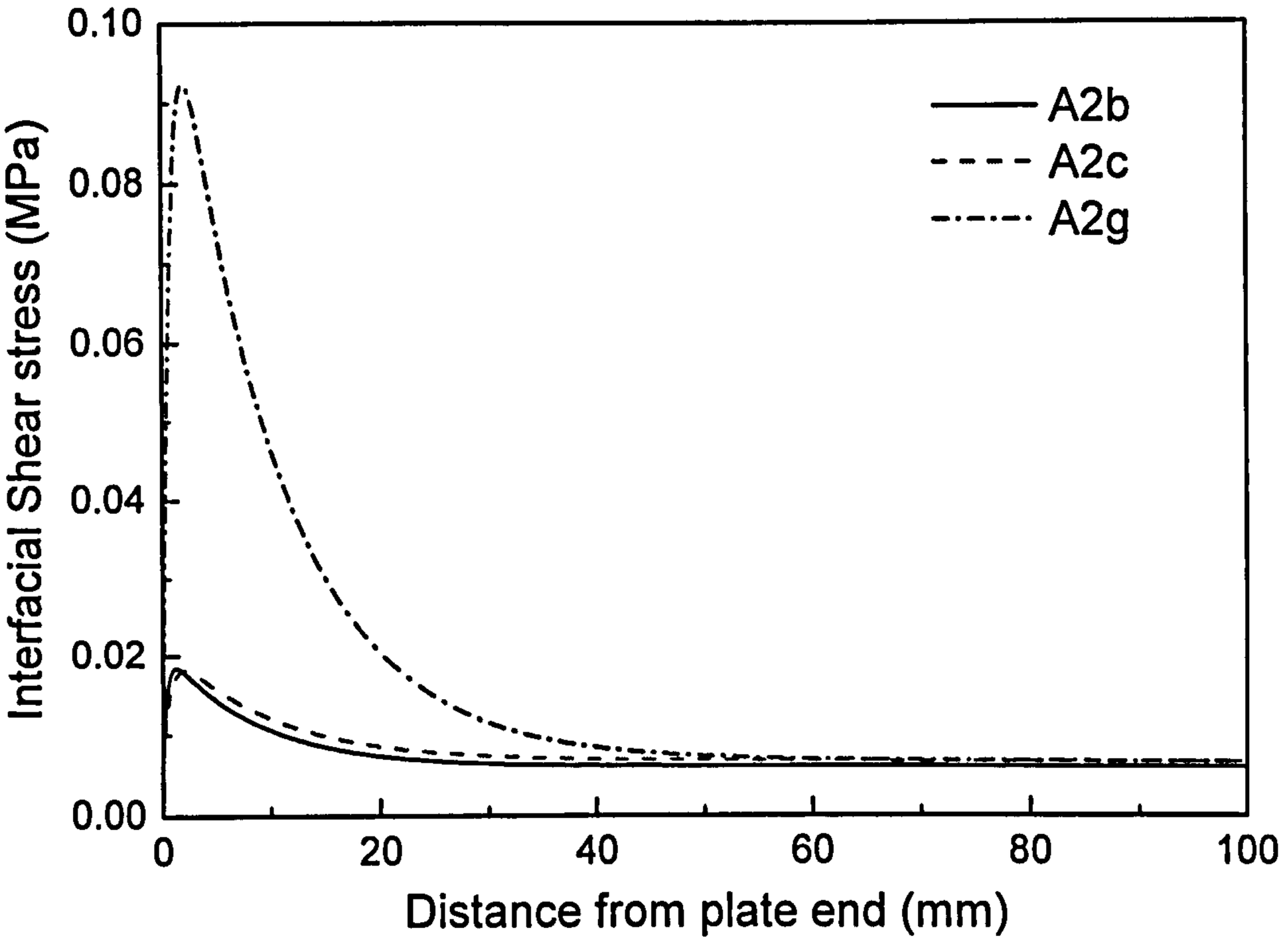

(c) Interfacial shear stress for beam A2 series

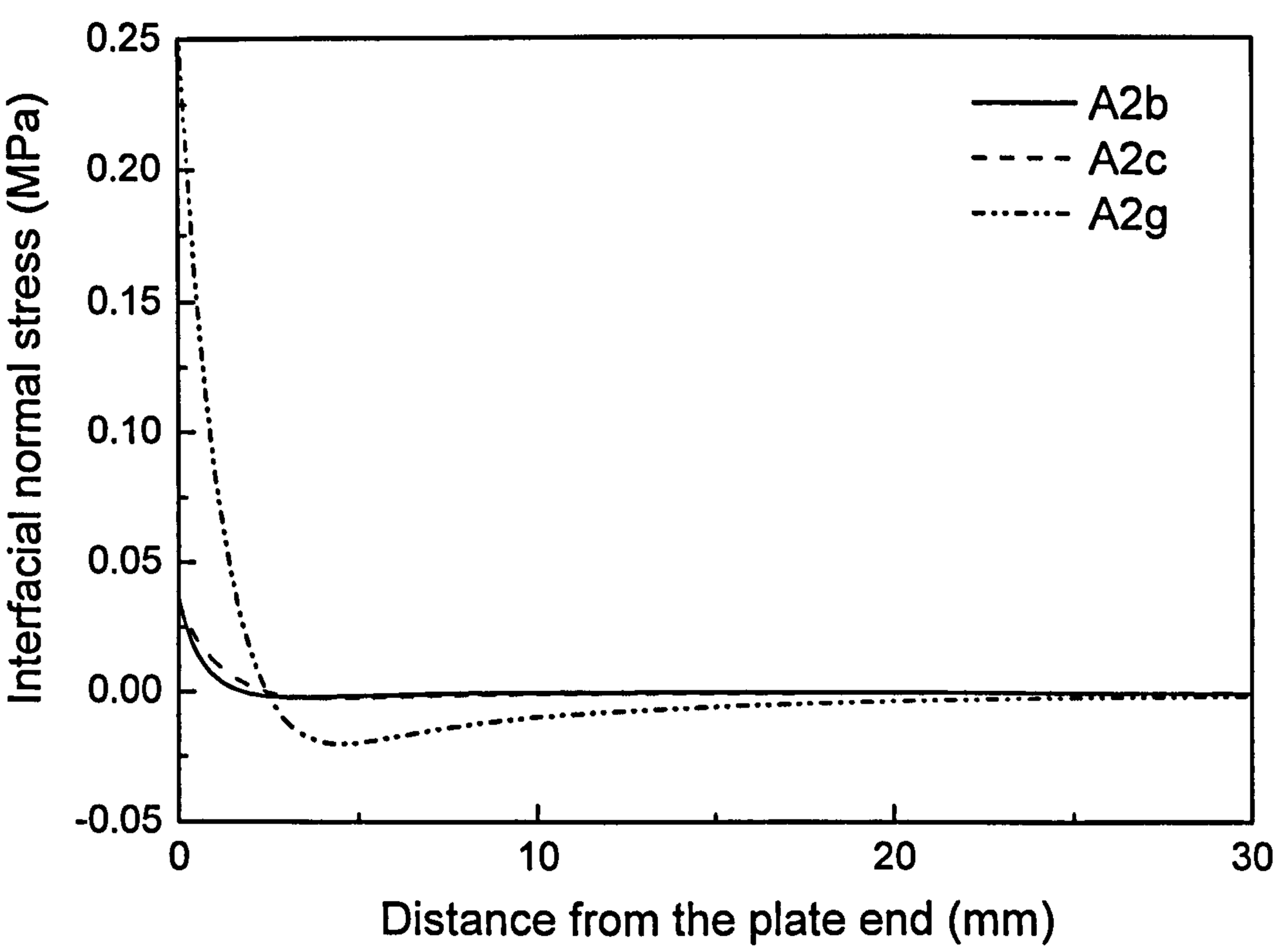

(d) Interfacial normal stress for beam A2 series

Fig. 8.6 The comparison of the stress distribution of the GFRP/CFRP plated RC beam (Quantrill, 1996a, b)

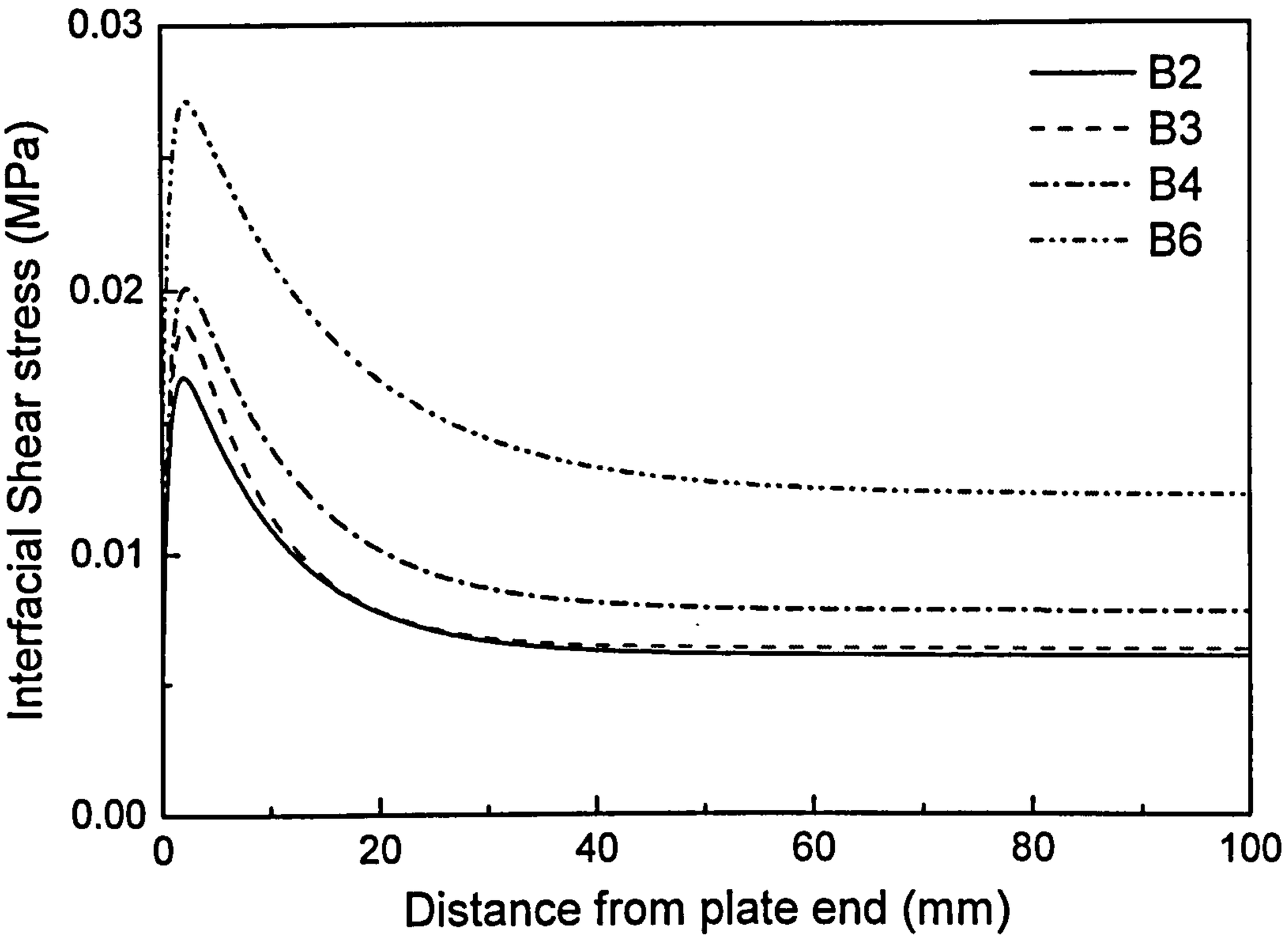

(e) Interfacial shear stress for beam B series

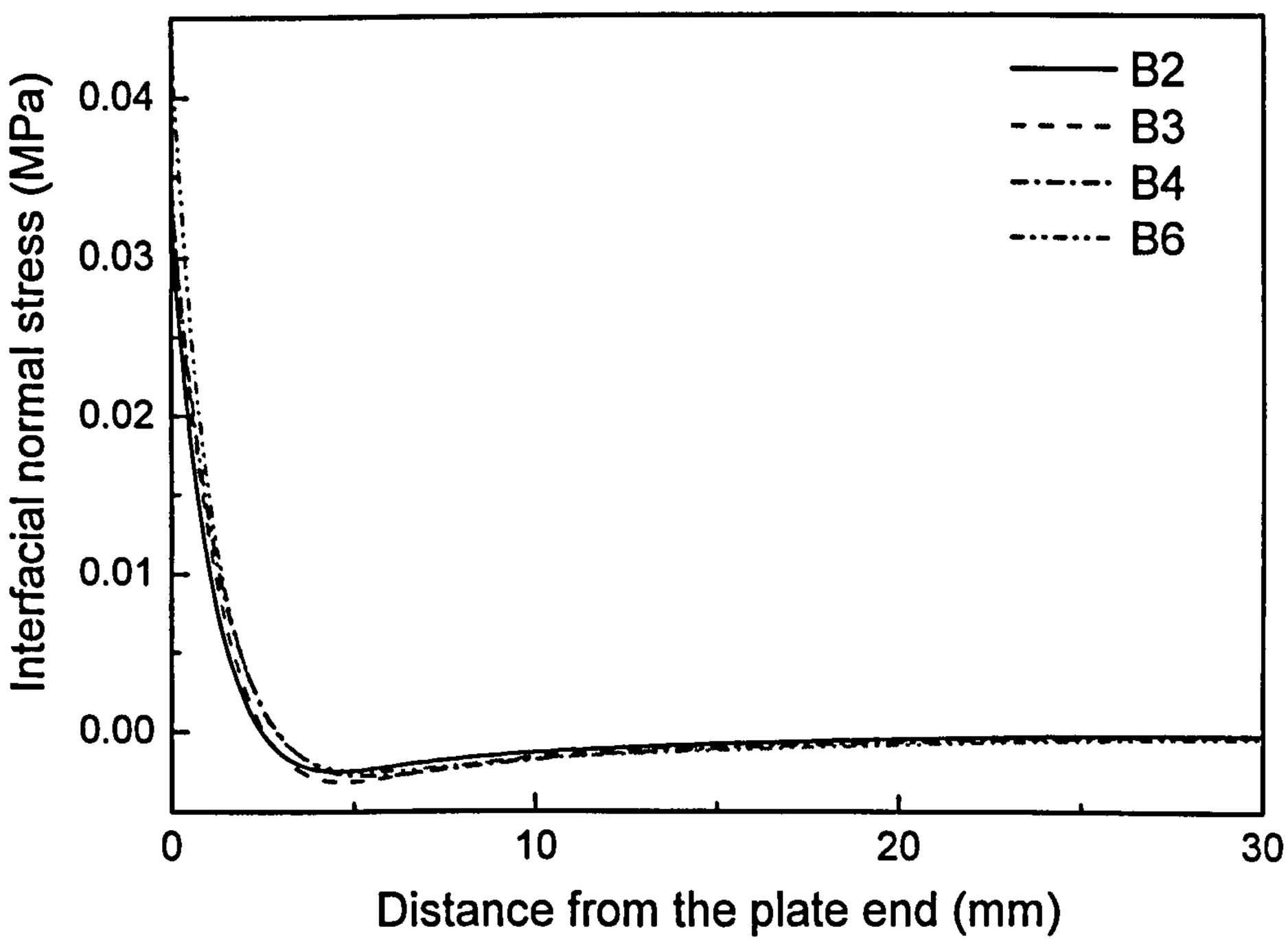

(f) Interfacial normal stress for beam B series

Fig. 8.6 The comparison of the stress distribution of the GFRP/CFRP plated RC beam (Quantrill, 1996a, b)

8.4 Parametric Analyses

As shown in the preceding sections, the stress field in the AC interface, especially near the plate end, is directly related to the failure load. To show a more detailed picture of the stress field and investigate the influencing parameters is of more practical significance in the design and optimisation of the strengthening scheme. In practical applications, there exist various selections of materials and size of the bonded plate and adhesive. The parameters studied in this section include the concrete cylinder strength, adhesive size and material, the bonded plate size and material. Table 8.7 shows the parameters to be used in the analysis. Apart from the parameters listed in the table, the beam to be analysed for all the cases is a 1800mm long RC beam with a rectangular cross section of 150mm x 250mm. The beam is simply supported and subjected to four-point bending each at the third point. The Poisson's ratio for the concrete is 0.2 which takes the standard value from BS8100. The Poisson's ratio of the adhesive layer is 0.35 which is the most typical value for epoxy type adhesive.

In the following parametric study, only one parameter is chosen as the varying parameter each time. Once the varying parameter is chosen, the other parameters shown in Table 8.7 are set as constants taking the values in bold face. For instance, if we discuss the impact of the concrete cylinder strength, i.e. take f_{cm} as the varying parameter, the adhesive thickness is set at 2mm; the adhesive Young's modulus is 6GPa; the bonded plate is 1.6mm x 100mm x 1400mm; the plate Young's modulus is 120GPa, and shear modulus is 5.5 GPa.

The stress distributions are normalized by the tensile fiber stress in concrete at the plate end, which can be calculated by $3P(L-l)/b^{[3]}\left(h^{[3]}\right)^2$ using the classic beam theory. Hence only the dimensionless stress distributions are plotted against the distance from the plate end. These results are plotted in Figures 8.7 to 8. 14. In addition, the development lengths for each case are tabulated in the parenthesis beneath each parameters in Table 8.7.

Table 8.7 Summery of the parameters and the calculated development length (mm)

Concrete	Adhesive		Bonded plate			
Mean cylinder strength f_{cm} (MPa)	Thickness $h^{[2]}$ (mm)	Young's modulus $E^{[2]}$ (GPa)	Length 2 x l (mm)	Width $b^{[1]}$ (mm)	Thickness $h^{[1]}$ (mm)	Young's modulus $E^{[1]}$ and shear modulus $G^{[1]}$ (GPa)
25	1	3	1200	50	1.2	50; 5.5
(74)	*(68.9)*	*(88.5)*	*(76.1)*	*(64.6)*	*(66.1)*	*(50.2)*
40	**2**	**6**	**1400**	**100**	**1.6**	**120; 5.5**
(76)	*(76.1)*	*(76.1)*	*(76.1)*	*(76.1)*	*(76.1)*	*(76.1)*
55	3	12	1600	150	2.0	200; 77
(79.5)	*(82.8)*	*(69.0)*	*(76.1)*	*(85.6)*	*(84.9)*	*(94.6)*

Figure 8.7 presents the interfacial shear and normal stress for strengthened RC beams of various concrete strengths. It can be seen that the beam with the lowest concrete strength has the highest shear and normal stresses near the plate end. As we all know a weaker concrete has a lower Young's modulus and hence is more compliant. The plated material, which is usually stiffer than concrete, will generate larger deformation incompatibility along with the more compliant concrete material, and thus induces higher level interfacial stresses.

Figures 8.8 and 8.9 respectively, show the impact of the adhesive thickness and its Young's modulus to the stress distribution in the AC interface. As Figure 8.8 shows, a change of adhesive thickness does not make significant difference to the interfacial stresses, particularly to the peak normal stress, for which the discrepancy is marginal. However, there is noticeable discrepancy of interfacial normal stress within the interval between 1mm and 3mm from the plate end. From Figure 8.9, it can be seen that the material property of the adhesive layer has greater impact on the interfacial stresses. The figure clearly shows that the stresses at the AC interface near the plate end increases as the stiffness of the adhesive increases. These observations can be explained by the function of the adhesive layer. Adhesive is there to achieve a deformation compatible with both the concrete beam and the bonded plate. Accordingly the thinner it is, the more severe deformation it has. For a given thickness with varying material stiffness, greater stress occurs in a stiffer adhesive, although the strain is similar.

Figure 8.10 shows the dimensionless interfacial stresses when plates with different lengths are bonded to a RC beam. As the stresses are normalized by the concrete fibre stress at the plate end, which also varies with plate length, the dimensionless shear stresses have different levels even away from the plate end. Figure 8.10 shows that a shorter plate generates more severe shear stress concentration at the plate end. Nevertheless, the dimensionless normal stresses from the three cases are almost identical.

Figure 8.11 presents the impact of plate width to the interfacial stresses. As expected, the narrower plate generates higher shear and normal stresses near the plate end. It is worth mentioning here that the present solution uses a 2-D plane analysis, i.e. smear all the variables across the whole width, and the variations in the width direction cannot be captured. More accurate stress fields for the narrow bonded plate can only be obtained in a 3-D analysis.

Figures 8.12 and 8.13 show the effects of plate thickness and plate material properties on the interfacial stresses. It is evident that a thicker plate induces higher shear and normal stresses, though the effect on the normal stress is less significant compared with that on the shear stress. This observation is attributed to the presence of large stiffness in the thick plate, that attracts higher level stress/strain to achieve the compatibility. For the same reason, higher interfacial stresses occur when the bonded plate has a greater Young's Modulus. As Figure 8.13 shows even in the region where a full composite action occurs, a stiffer plate leads to a higher interfacial shear stress. This is due to the presence of the higher tensile stress in the stiffer plate, that induce a higher level shear transfer along the interface. Another important conclusion by observing Figure 8.13 along with Figure 8.7 is that larger difference of Young's moduli between the concrete and bonded plate leads to higher interfacial stresses. Accordingly a very weak concrete strengthened by a steel plate is one of the worst cases.

The development length for each case is tabulated in Table 8.7 (see the values in the parenthesis). It can be seen that larger development length is always accompanied by a lower stress concentrated at the plate end. This observation provides the rationale that some researchers used the average stress in the development length as the criteria to predict failure load (see Swamy et al. 1986).

8.5 Summery

Fourteen RC beams tested by other researchers have been reanalyzed in this chapter in terms of interfacial stresses, serviceability load, ultimate load, size of FPZ and development length. The two elastic interfacial stress solutions developed in this thesis have been applied to analyze the beams and the results were presented and compared with those obtained in the tests. Two concrete strength models, i.e. Kupfer and Gerstle and the Mohr-Coulomb strength models, were utilized together with the stress results and the corresponding serviceability loads were predicted. To the author's best knowledge, there are no published serviceability experimental data available for comparison. Hence, the only comparison was made with the results obtained using the NLFEA.

The NLFM method was also adopted to analyze these beams to predict both serviceability and ultimate loads, in which the four-point bending loads were equivalently converted to a UDL by equalizing their maximum bending moments. Comparisons were made between the analytical ultimate loads predicted by NLFM and the experimental results. Favorable agreements were achieved for the beams that failed due to plate debonding.

Additionally, the size of the FPZ at failure and the development length at the elastic state were calculated and tabulated.

After the comparisons, an extensive parametric analysis was conducted for a series of strengthened RC beams. The parameters include concrete strength, adhesive material property, adhesive thickness, plate size and plate materials. It was found that concrete strength, adhesive material, plate width, plate thickness and plate material had significant impacts on the interfacial stress distributions. In order to maximize the use of the strength of a bonded plate, the plate should be designed using the following optimization principle. Subjected to other restriction, the plate material should have a Young's modulus close to the concrete material, a thin and wide cross section, and be adequately close to the beam supports. The adhesive material should be flexible and thick enough with adequate strength.

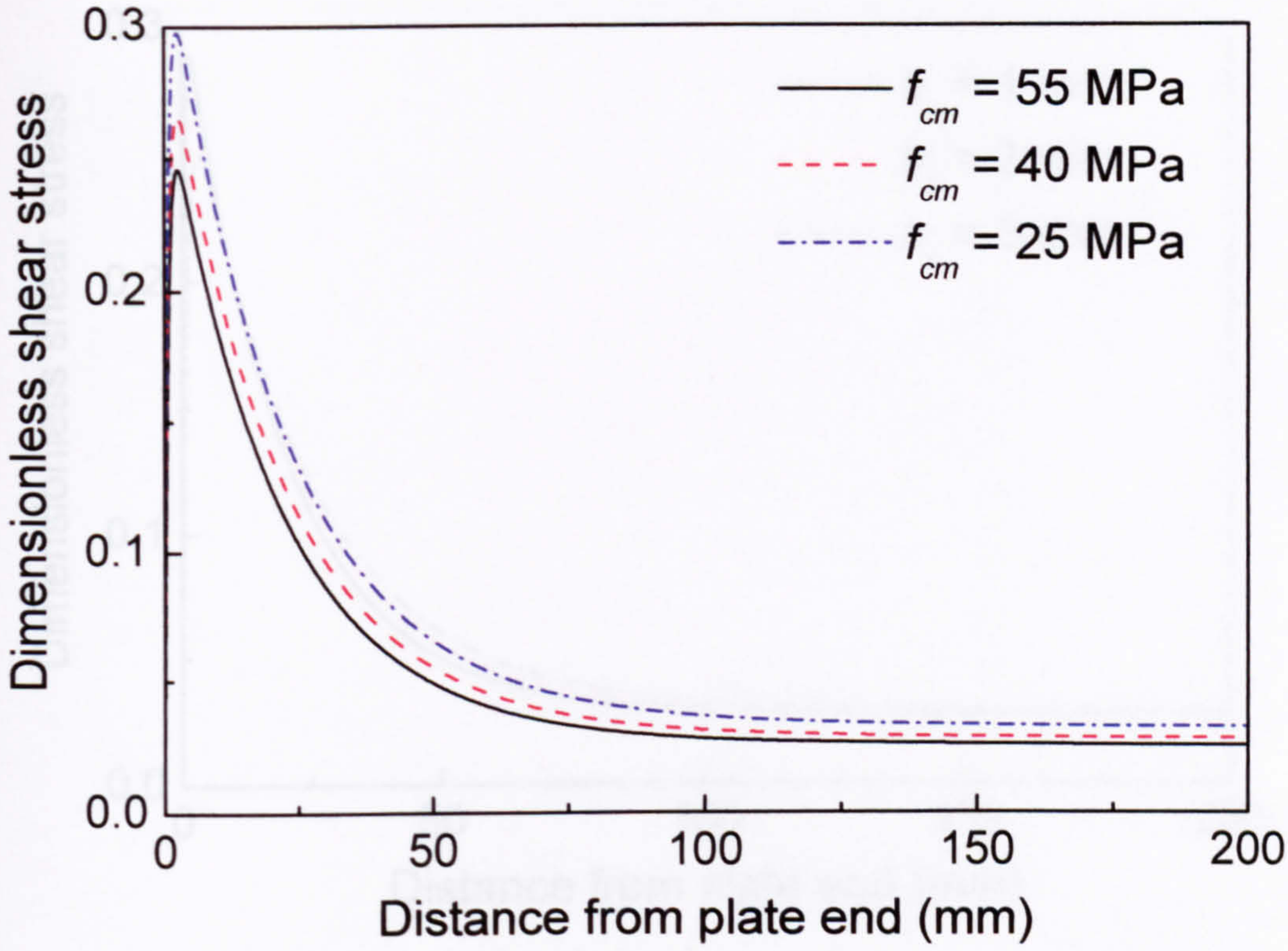

(a) Interfacial shear stress

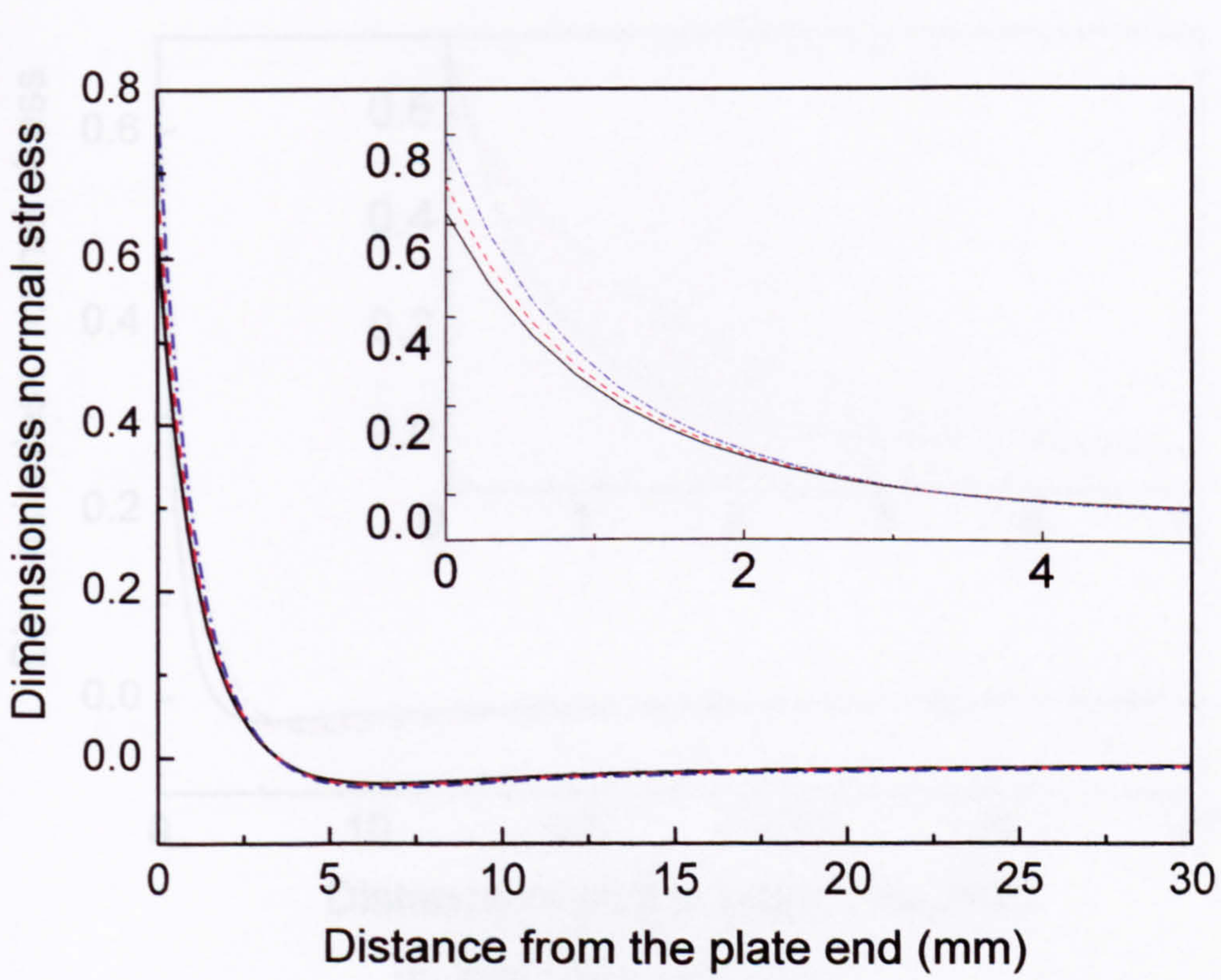

(b) Interfacial normal stress

Fig. 8.7 Effect of the concrete mean cylinder strength on the interfacial stresses

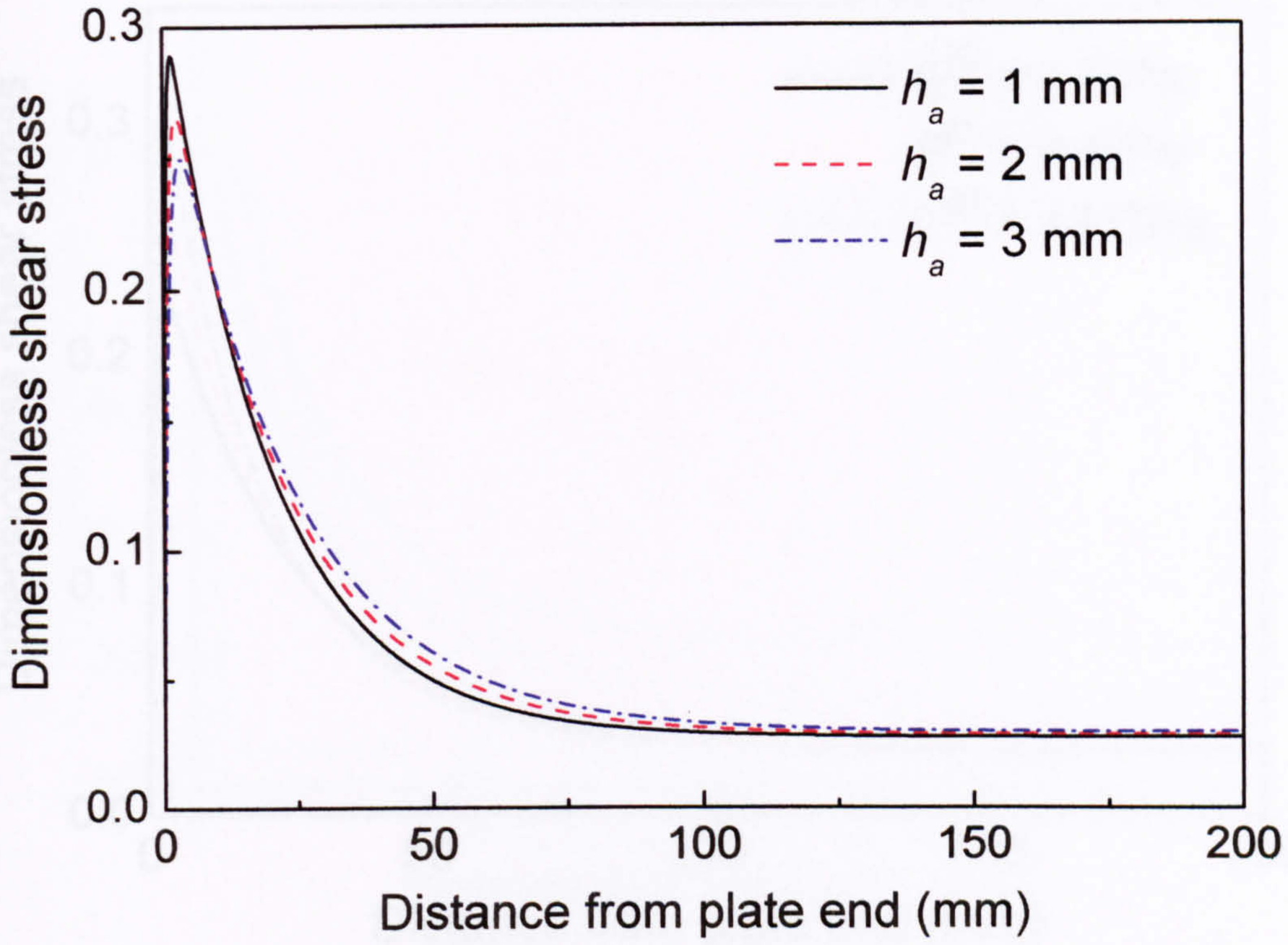

(a) Interfacial shear stress

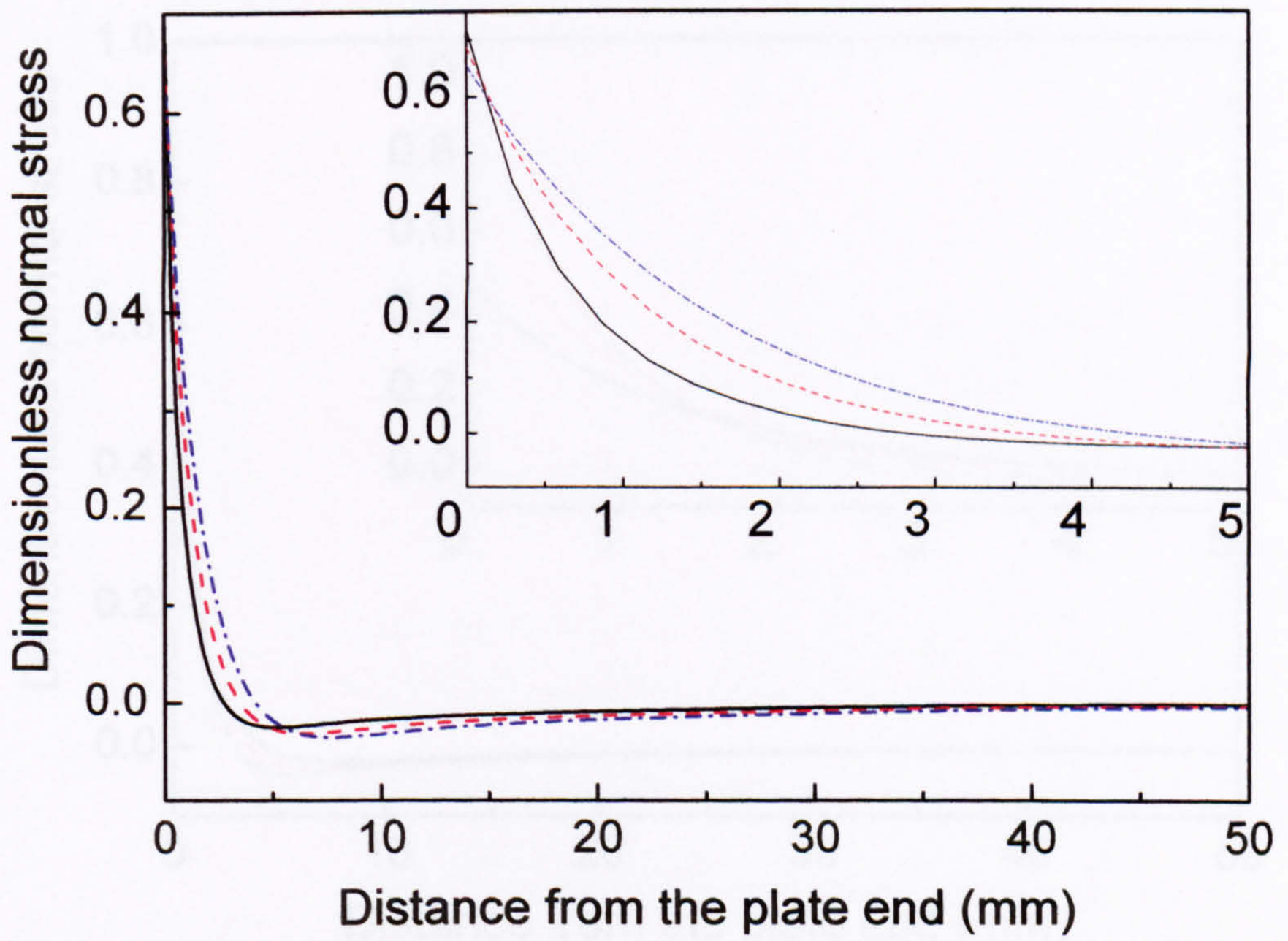

(b) Interfacial normal stress

Fig. 8.8 Effect of the adhesive thickness on the interfacial stresses

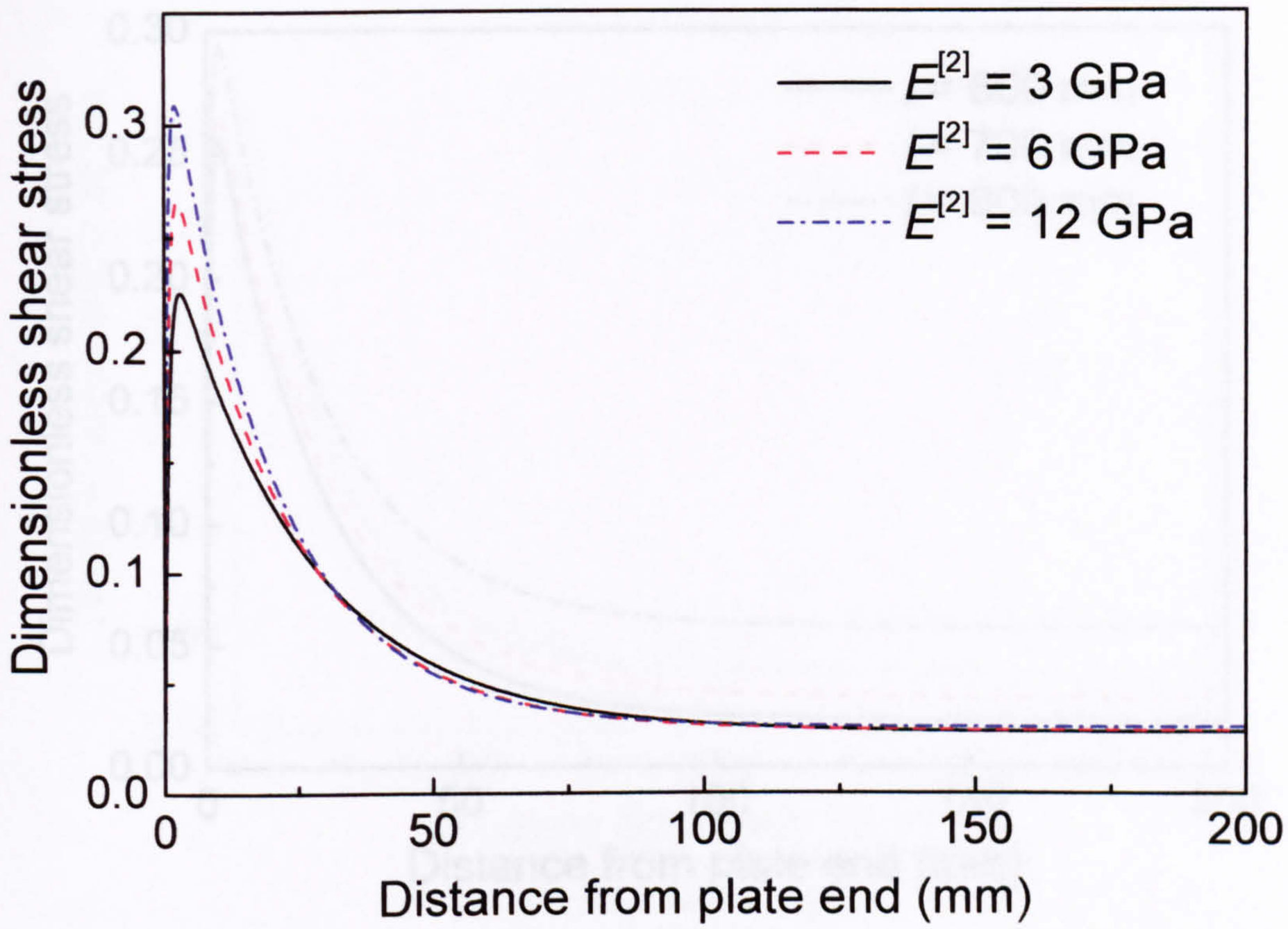

(a) Interfacial shear stress

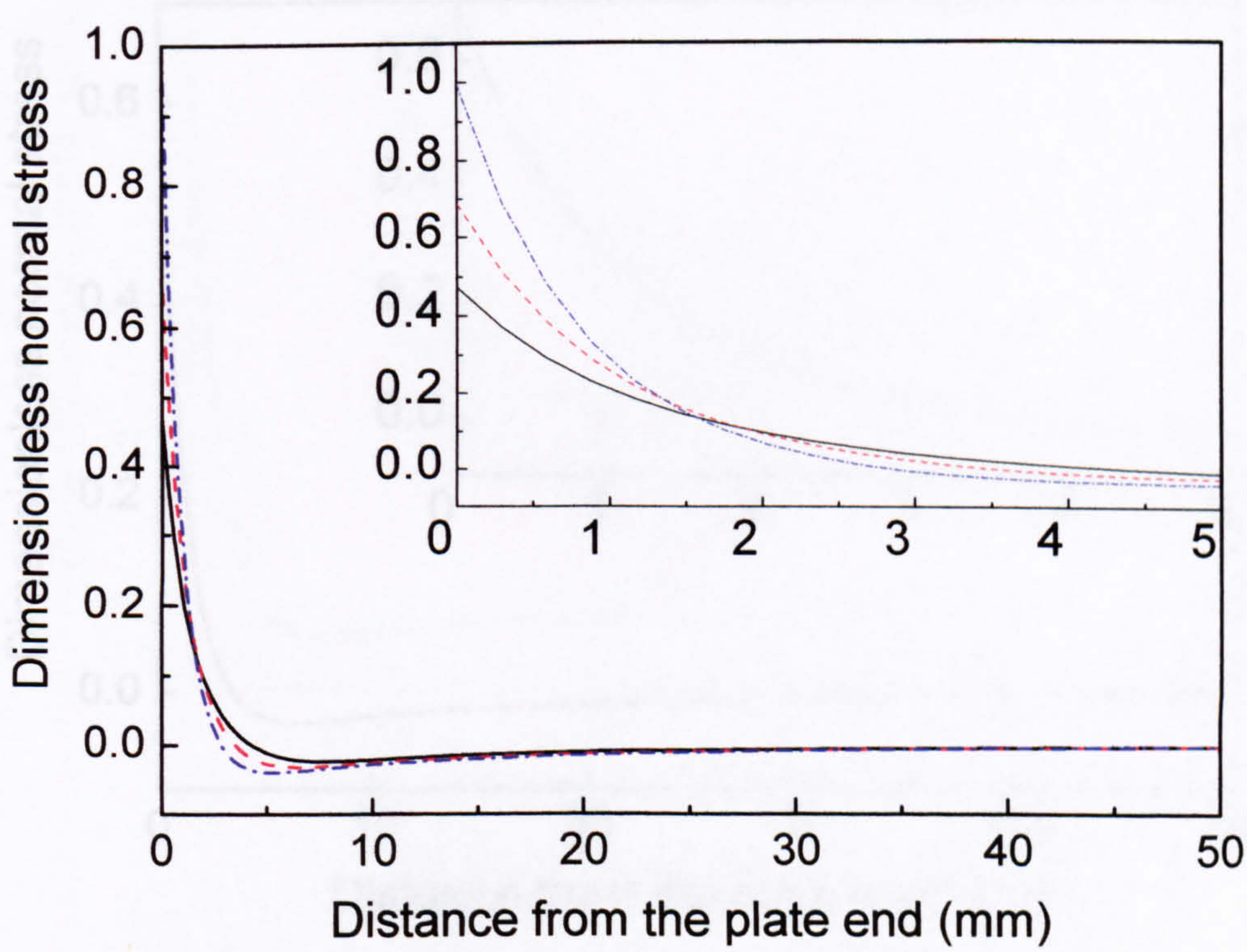

(b) Interfacial normal stress

Fig. 8.9 Effect of the adhesive material property on the interfacial stresses

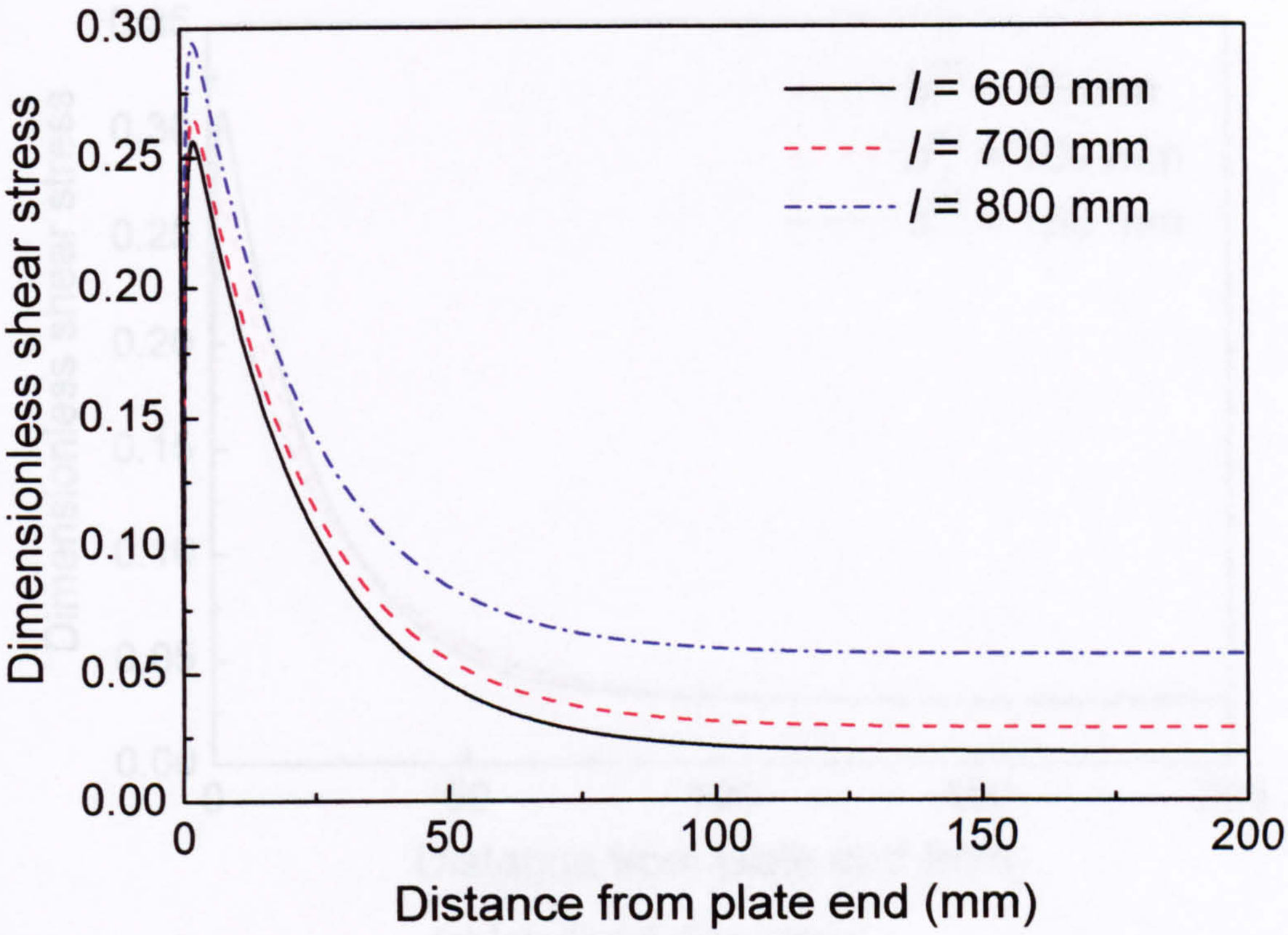

(a) Interfacial shear stress

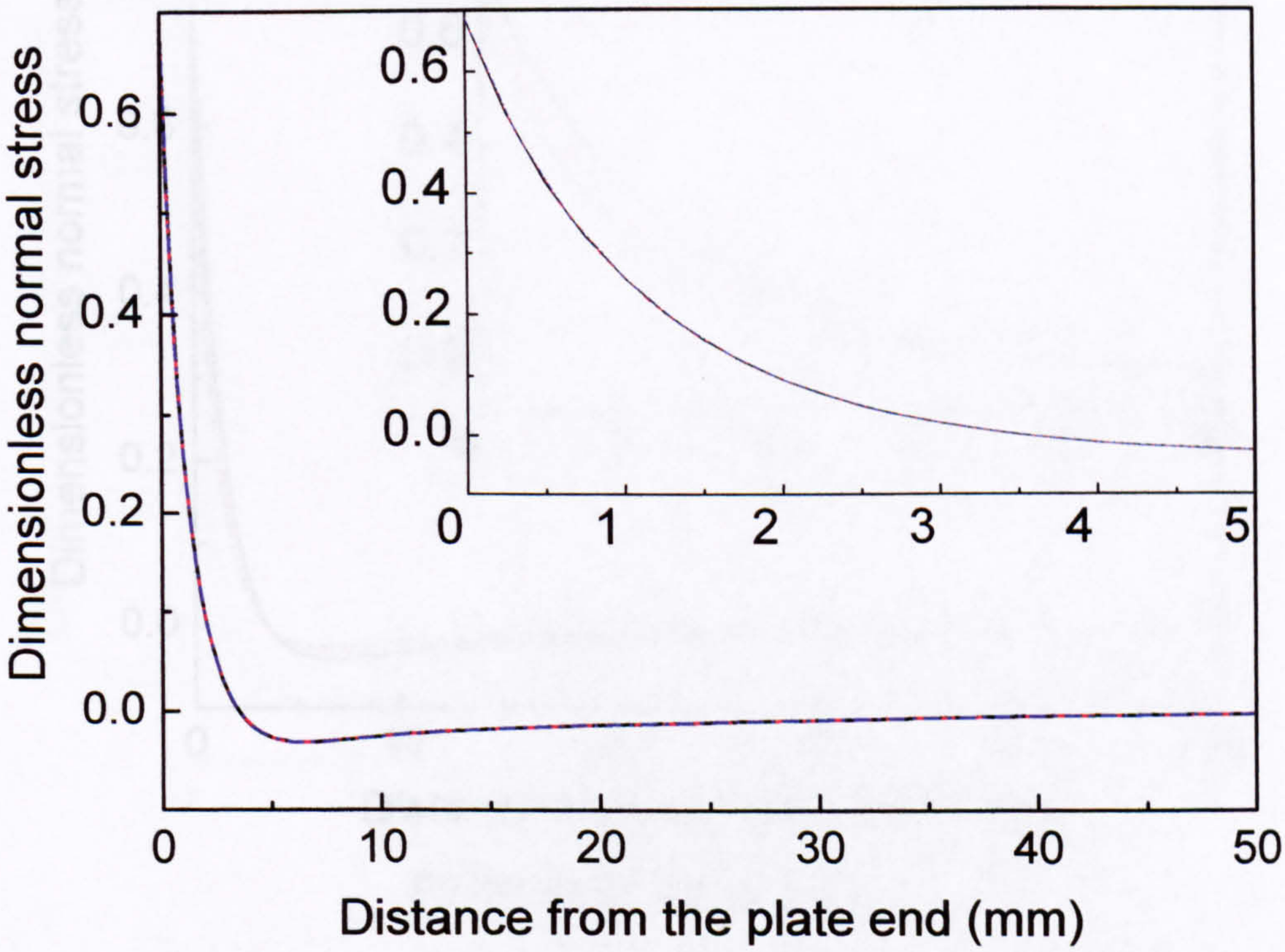

(b) Interfacial normal stress

Fig. 8.10 Effect of the plate length on the interfacial stresses

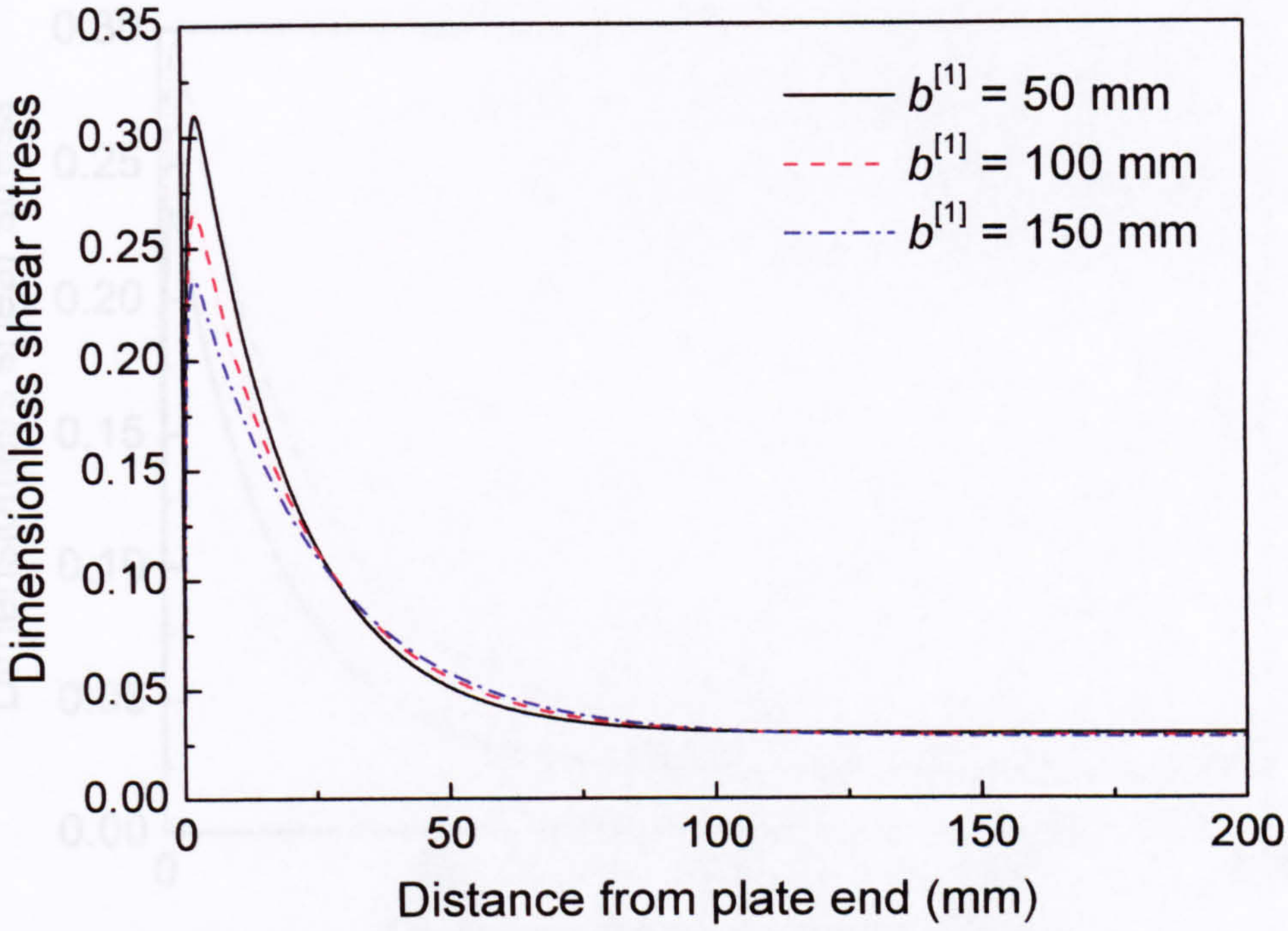

(a) Interfacial shear stress

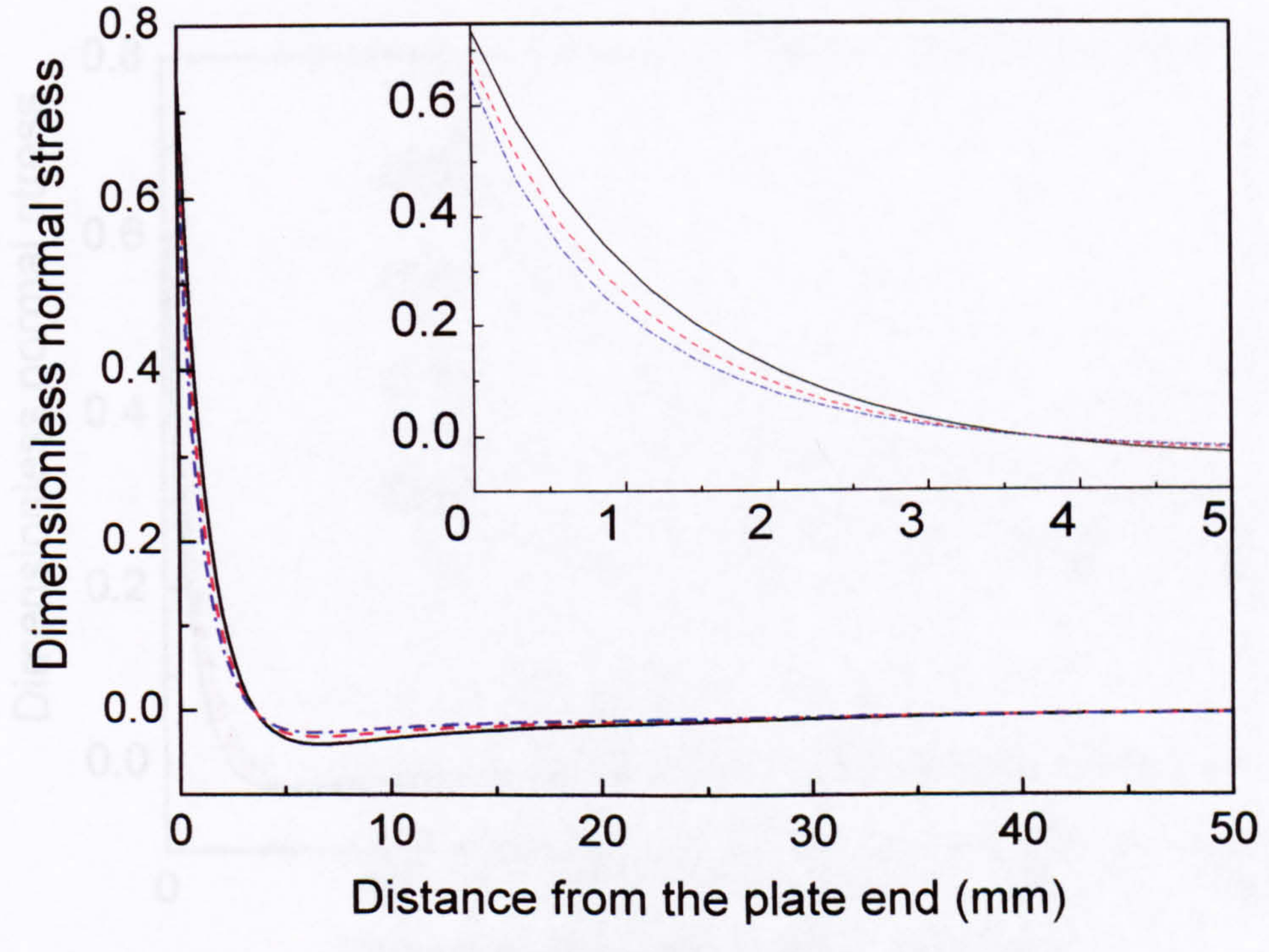

(b) Interfacial normal stress

Fig. 8.11 Effect of the plate width on the interfacial stresses

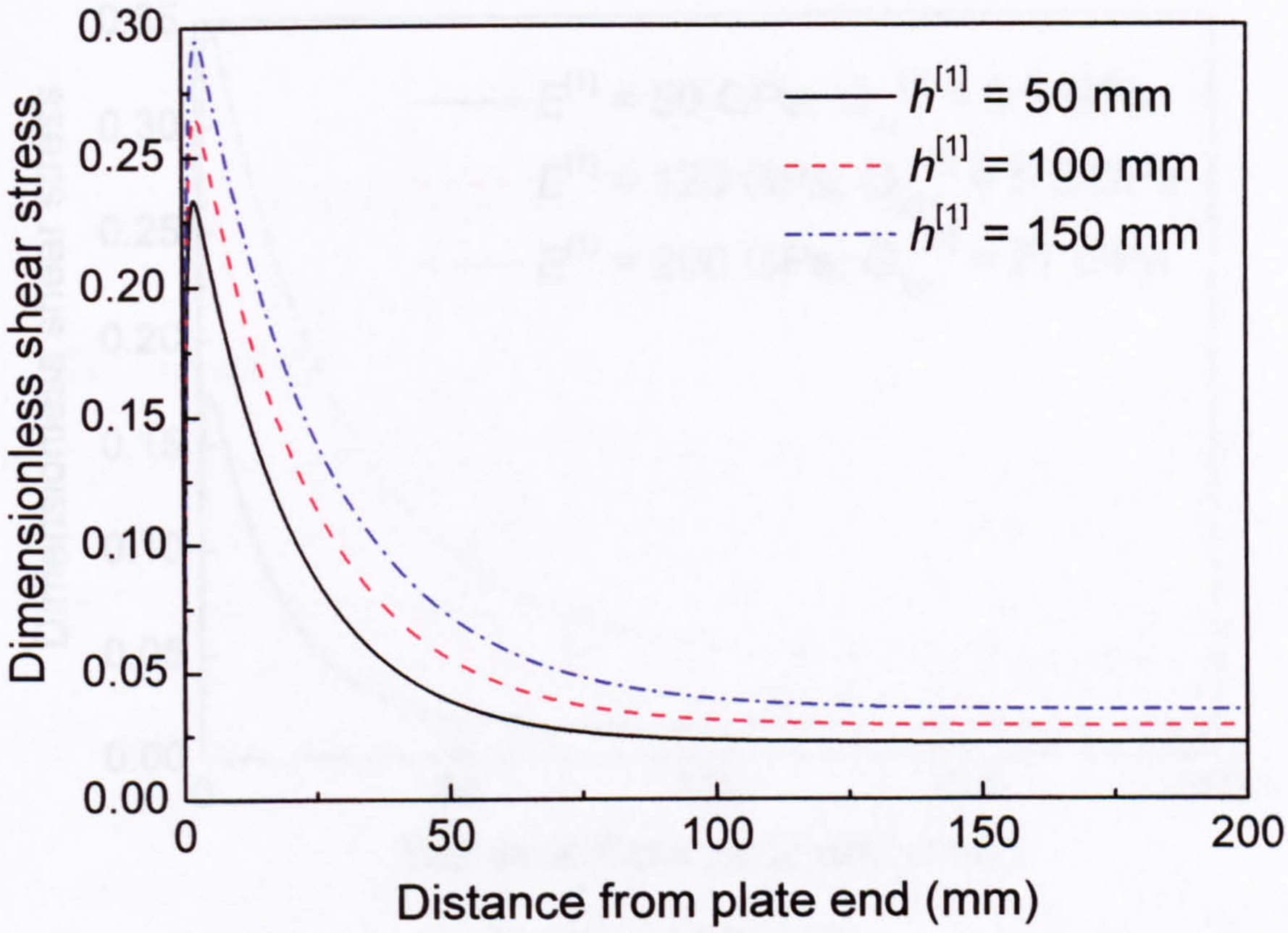

(a) Interfacial shear stress

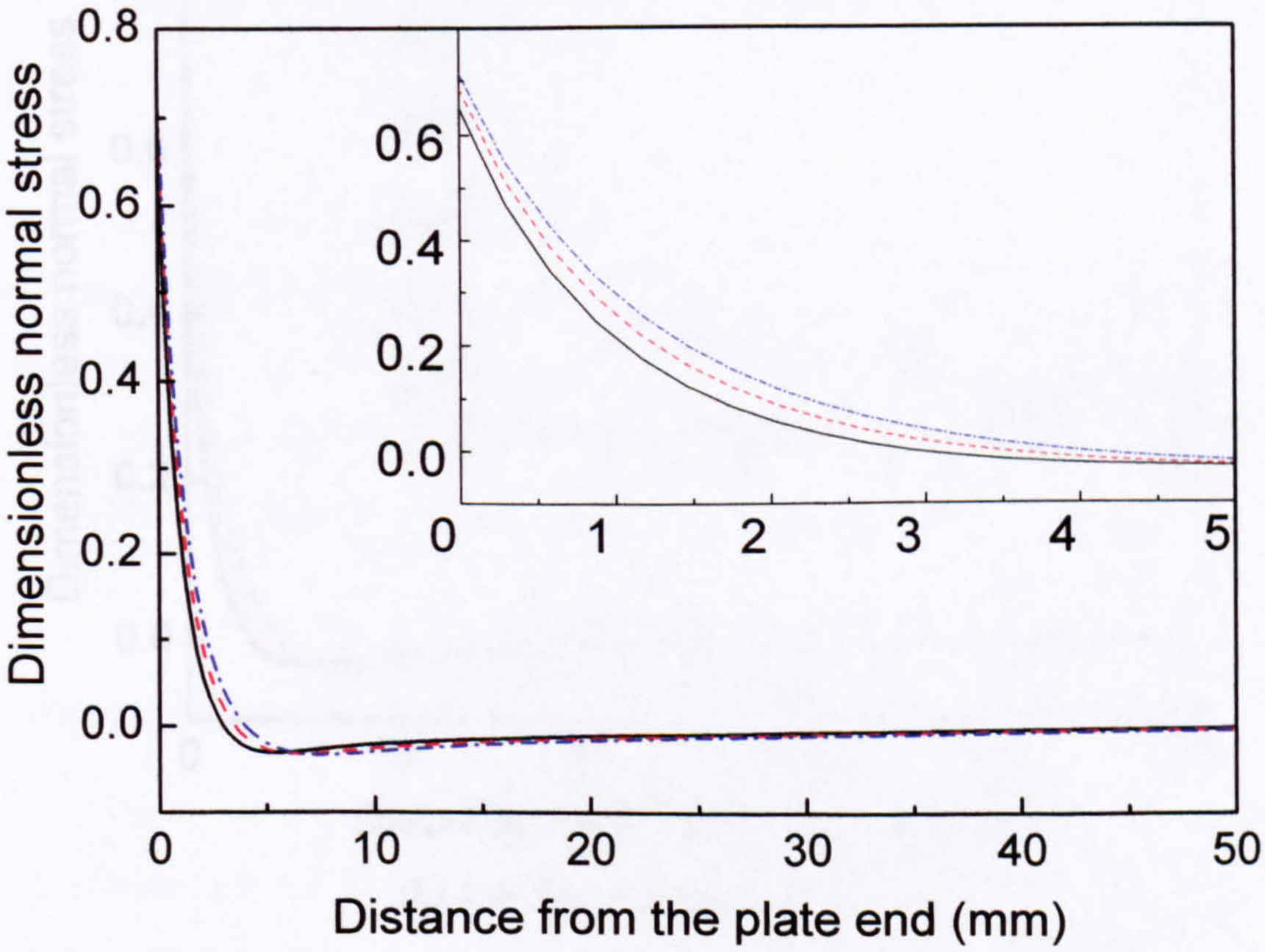

(b) Interfacial normal stress

Fig. 8.12 Effect of the plate height on the interfacial stresses

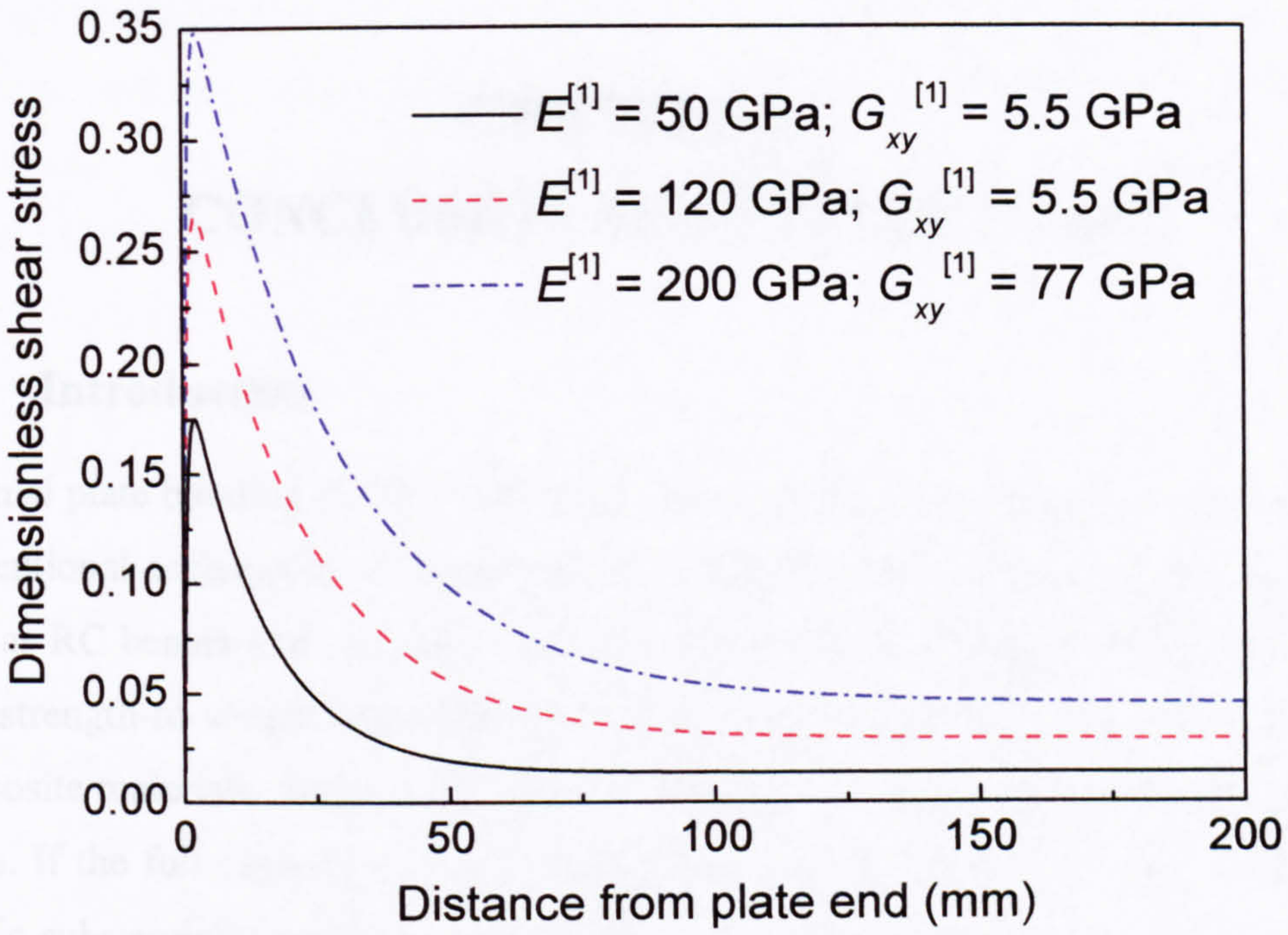

(a) Interfacial shear stress

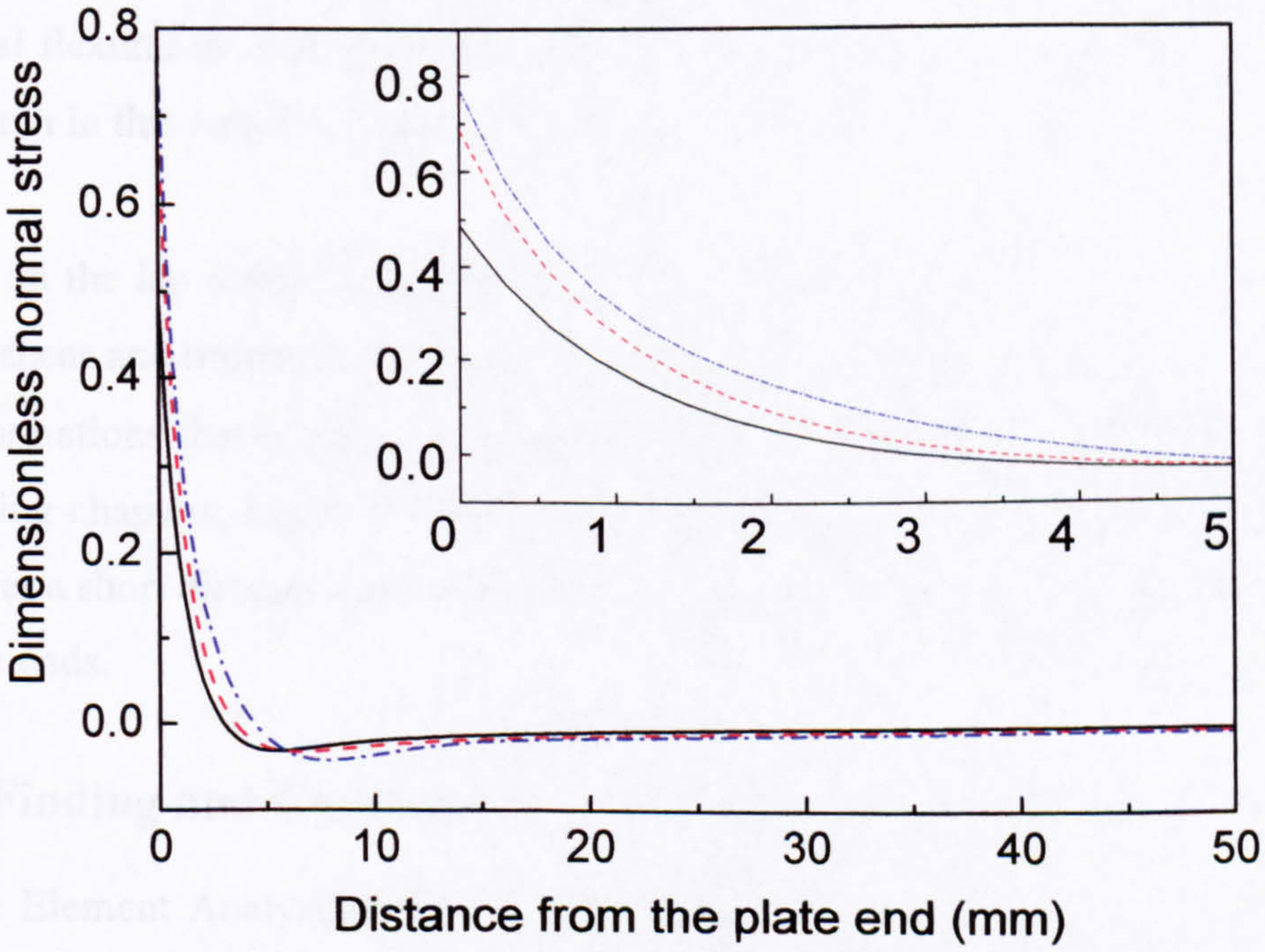

(b) Interfacial normal stress

Fig. 8.13 Effect of the plate material on the interfacial stresses

CHAPTER 9.
CONCLUSION AND FUTURE WORK

9.1 Introduction

External plate bonding (EPB) technology has proved to be a competitive alternative to conventional techniques of improving the strengths and stiffness of RC members, such as RC beams and RC slabs. Due to the features of composite materials, such as high strength-to-weight and stiffness-to-weight ratios, excellent corrosion resistance, composite materials, such as FRP, provide a better substitute to the conventional steel plates. If the full capacity of the concrete-FRP section can be achieved, the ultimate load is substantially increased for a FRP plated beam. However, the full capacity is usually prevented by premature failures, e.g. plate debonding. The theoretical mechanism for this undesirable failure mode has not been developed as maturely as the conventional flexural or shear failure modes. It is this impetus that has drive a great deal of research in this subject, including the work in this thesis.

Studies on the lap joints and externally plated beams have shown that the adherents impose shear and transverse normal stress/strain in the adhesive due to their differential deformations that occur under applied loads. In plated beams, as discussed in the proceeding chapters, highly localised shear and normal stresses exist in the adhesive layer over a short distance near the plate ends. These stresses decay away rapidly from the plate ends.

9.2 Finding and Conclusion

A Finite Element Analysis (FEA) based on elastic fracture mechanics (LEFM) was carried out to provide a detailed study on the stress fields near the plate end for plated RC beams. A severe stress singularity was found near the plate ends. The utilization of the LEFM and global-sub structural modeling technologies in FEA reduced the computation cost and provided a more accurate solution. This analysis also became the benchmark for the analytic solutions presented in the following chapters.

A completed analytical solution was developed by the principle of complementary energy and provided consistent results with the FEA with less computational efforts. The resulting solution not only takes into consideration the non-uniform stress distribution in the adhesive layer and the stress-free boundary condition at the ends of the plate, but also correctly predicts the drastic difference in the interfacial normal stress between the PA and AC interfaces. This solution included all types of loading by using the distribution functions.

A closed-form rigorous solution was proposed such that a spreadsheet package was sufficient to obtain the numerical results. This rigorous solution provided more accurate results than other closed-form solutions available in the publications. It was the basis to further develop a simplified solution of the interfacial stresses that were subsequently used to predict the failure loads.

Numerical examples showed that the stress concentration was dominated by the bending moment experienced by the cross-sections at the plate ends. A simplified solution was developed to calculate the interfacial stresses in the strengthened RC beam subjected to arbitrary loads. It was a portable calculator-based solution showing high accuracy. The development length can also be predicted by this solution.

To consider the nonlinear properties of concrete, a detailed nonlinear FEA simulation was conducted and extensive results were computed at various load levels, from the elastic state to the ultimate state. Some results, which are difficult to measure by test, were also revealed using this analysis. These included the interfacial stresses and the load level at the onset of plate end cracking (serviceability load). In addition, a Nonlinear Fracture Mechanics (NLFM) method was developed taking into account the pre- and post-cracking behaviours and the interactions between the shear and transverse normal stresses. This solution was able to predict serviceability load and the load at the ultimate failure state (ultimate load).

Finally some of the developed solutions were applied to selected beams whose test results are available for comparison. In combination with existing material failure criteria, the elastic simplified solutions were used to predict serviceability loads. Two groups of serviceability loads predicted from the elastic solution and NLFM solution,

respectively, and one group of ultimate load predicted from NLFM solution were all compared with the experimental data. Encouraging correlations were achieved. Other useful results, such as development length, the size of Fracture Process Zone (FPZ) were also calculated.

Extensive parametric analyses suggested some rule of thumb principles in optimizing the strengthening scheme to avoid the plate debonding failure at the absence of additional anchorages. These included that, subjected to other restrictions, that the bonded plate should have a close stiffness to the concrete material, a thin and wide cross section, and be adequately close to the beam supports. The adhesive material should be flexible and thick enough with adequate strength.

9.3 Suggested Future Work

EPB is a new technology used for RC structures. There is a wide range of problems to be solved. Even if the plate end debonding failure had been fully understood, there are still a lot of exiting and new problems about this subject. For example, the problem of ductility, durability, dynamic behaviours and so on are all imperative. In this section, only the subject about the plate end debonding for plate bonded RC beam is focused on.

After a thorough literature review, it is found that only limited test results about interfacial shear stresses for the plated beam are available in the publications. Most of them were calculated by the strains measured at the lower surface of the bonded plate. More accurate results are required for better understanding interfacial behaviours. None of the test research has measured the interfacial normal strain/stress, perhaps due to the lack of appropriate measuring apparatus. However, the interaction between the interfacial transverse normal and shear strain/stress is significant. These test results are useful for defining the correct model concerning the interaction. The white light speckle interferometer may be used to tackle these two problems.

Another issue about the test results is lack of the serviceability load for plate end debonding. Although this load is much lower than the ultimate load, it is useful to understand the complex stress state at the plate ends, the post-cracking structure behav-

iour and the combined failure mechanism. Some techniques to study the flexural cracks occurring in the early loading stages can be used for the plate end cracking.

The fracture mechanics method has been applied to study the plate debonding in many researches including the NLFM solution developed in this thesis. However, the next step would be taking into account the effects of the full properties of concrete material, the interactions of multiple cracks and the behaviours of rebars and shear links. This method can also be used to study other failure modes, such as the intermediate debonding due to flexural cracks, shear cracks or flexural/shear cracks. It is also necessary to propose a standard method to measure the fracture toughness for Mode I and II fracture within the concrete and along the interface between the concrete and another material. The present NLFM solution should be further calibrated with sufficient amount of experimental data to be developed a sound strength models for both serviceability and ultimate loads.

The elastic solutions to the interfacial stresses presented in this thesis can be improved to consider the effect of reinforcement and extended into a 3-D solution to consider the cases of non-identical widths of the beam and plate and non-uniform geometrical dimensions.

Most of the commercial FEA packages can only take into account a few features that the real structures present according to the sophistication of the packages. Even the most sophisticated packages use the smeared theory to simulate the concrete cracks. Although some specific packages can simulate the discrete cracks, they are only based on simple assumptions such as LEFM. To develop a comprehensive software, which combines the NLFEA, NLFE and discrete crack approach and has a user-friendly interface and strong post-processor is of great importance.

Finally, another suggested future work is the optimisation of the strengthening scheme. A comprehensive and sensible optimisation algorithm should be proposed to allow for almost all the affecting parameters.

9.4 Originality and Contribution

The author feels his main contributions to the understanding of the structural behaviours of the plated beam include:

- A highly thorough and systematic investigation of the stress behaviour near the plate ends in the plated RC beams;
- Most of the solutions are first developed and their applicabilities can be extended to other composite material or structures and include other load cases such as thermal loading;
- A comprehensive parametric study provides principle information for the selection and optimisation of the strengthening scheme;
- The predictions of the serviceability and ultimate load show a very favourable correlation with the experimental results.
- A comprehensive literature review of the plated beams and the interfacial stresses in the plated beams.

To summarise, this integrated study has helped elucidate interfacial stress distributions of the reinforced concrete member externally bonded by plates of various materials and have developed a series of innovative solutions. Most of the solutions have great improvement than those available in the literature. Although they offered very encouraging results, some further calibrations to the solutions are required before they can be presented as sound design equations.

APPENDIX A

The sub-matrices in Equation 3.49 are given in Equations A1 to A3.

$$\mathbf{C_{mm}} = \begin{bmatrix} (C_{mm})_{11} & (C_{mm})_{12} & (C_{mm})_{13} & (C_{mm})_{14} \\ & (C_{mm})_{22} & (C_{mm})_{23} & (C_{mm})_{24} \\ & & (C_{mm})_{33} & (C_{mm})_{34} \\ sym. & & & (C_{mm})_{44} \end{bmatrix} \tag{A1}$$

in which

$$(C_{mm})_{11} = b^{(1)} l \left\{ \frac{18l^4}{m^4\pi^4} \left[\frac{1}{E_x^{[1]}\left(h^{[1]}\right)^3} + \frac{1}{E_x^{[2]}\left(h^{[2]}\right)^3} \right] + \frac{3l^2}{5m^2\pi^2} \left[\frac{1}{G_{xy}^{[1]}h^{[1]}} + \frac{1}{G_{xy}^{[2]}h^{[2]}} - \frac{2\nu_{xy}^{[2]}}{E_x^{[2]}h^{[2]}} \right] + \frac{13h^{[2]}}{70E_y^{[2]}} \right\} \tag{A2a}$$

$$(C_{mm})_{12} = b^{(1)} \left\{ \frac{9l^4}{m^3\pi^3} \left[\frac{1}{E_x^{[2]}\left(h^{[2]}\right)^2} - \frac{1}{E_x^{[1]}\left(h^{[1]}\right)^2} \right] + \frac{l^2}{20m\pi} \left[\frac{1}{G_{xy}^{[2]}} - \frac{1}{G_{xy}^{[1]}} - \frac{12\nu_{xy}^{[2]}}{E_x^{[2]}} \right] + \frac{11m\pi\left(h^{[2]}\right)^2}{40E_y^{[2]}} \right\} \tag{A2b}$$

$$(C_{mm})_{13} = b^{(1)} l \left[-\frac{18l^4}{m^4\pi^4} \frac{1}{E_x^{[2]}\left(h^{[2]}\right)^3} - \frac{3l^2}{5m^2\pi^2} \left(\frac{1}{G_{xy}^{[2]}h^{[2]}} - \frac{2\nu_{xy}^{[2]}}{E_x^{[2]}h^{[2]}} \right) + \frac{9h^{[2]}}{140E_y^{[2]}} \right] \tag{A2c}$$

$$(C_{mm})_{14} = b^{(1)} \left[\frac{9l^4}{m^3\pi^3} \frac{1}{E_x^{[2]}\left(h^{[2]}\right)^2} + \frac{l^2}{20m\pi} \left(\frac{1}{G_{xy}^{[2]}} - \frac{2\nu_{xy}^{[2]}}{E_x^{[2]}} \right) - \frac{13m\pi\left(h^{[2]}\right)^2}{840E_y^{[2]}} \right] \tag{A2d}$$

$$(C_{mm})_{22} = b^{(1)} \left[\frac{6l^3}{m^2\pi^2} \left(\frac{1}{E_x^{[1]}h^{[1]}} + \frac{1}{E_x^{[2]}h^{[2]}} \right) + \frac{l}{15} \left(\frac{h^{[1]}}{G_{xy}^{[1]}} + \frac{h^{[2]}}{G_{xy}^{[2]}} - \frac{2\nu_{xy}^{[2]}h^{[2]}}{E_x^{[2]}} \right) + \frac{m^2\pi^2\left(h^{[2]}\right)^3}{210lE_y^{[2]}} \right] \tag{A2e}$$

$$(C_{mm})_{23} = -(C_{mm})_{14} \tag{A2f}$$

$$(C_{mm})_{24} = b^{(1)} \left[\frac{3l^3}{m^2\pi^2} \frac{1}{E_x^{[2]}h^{[2]}} - \frac{h^{[2]}}{60} \left(\frac{1}{G_{xy}^{[2]}} - \frac{2\nu_{xy}^{[2]}}{E_x^{[2]}} \right) - \frac{m^2\pi^2\left(h^{[2]}\right)^3}{280lE_y^{[2]}} \right] \tag{A2g}$$

$$(C_{mm})_{33} = b^{(1)} l \left\{ \frac{18l^4}{m^4\pi^4} \left[\frac{1}{E_x^{[2]}\left(h^{[2]}\right)^3} + \frac{1}{\beta E_x^{[3]}\left(h^{[3]}\right)^3} \right] + \frac{3l^2}{5m^2\pi^2} \left[\frac{1}{G_{xy}^{[2]} h^{[2]}} + \frac{1}{\beta G_{xy}^{[3]} h^{[3]}} - \frac{2\nu_{xy}^{[2]}}{E_x^{[2]} h^{[2]}} \right] + \frac{13h^{[2]}}{70E_y^{[2]}} \right\}$$

(A2h)

$$(C_{mm})_{34} = b^{(1)} \left\{ -\frac{9l^4}{m^3\pi^3} \left[\frac{1}{E_x^{[2]}\left(h^{[2]}\right)^2} - \frac{1}{\beta E_x^{[3]}\left(h^{[3]}\right)^2} \right] - \frac{l^2}{20m\pi} \left[\frac{1}{G_{xy}^{[2]}} - \frac{1}{\beta G_{xy}^{[3]}} - \frac{12\nu_{xy}^{[2]}}{E_x^{[2]}} \right] - \frac{11m\pi\left(h^{[2]}\right)^2}{40E_y^{[2]}} \right\}$$

(A2i)

$$(C_{mm})_{44} = b^{(1)} \left[\frac{6l^3}{m^2\pi^2} \left(\frac{1}{E_x^{[2]} h^{[2]}} + \frac{1}{\beta E_x^{[3]} h^{[3]}} \right) + \frac{l}{15} \left(\frac{h^{[2]}}{G_{xy}^{[2]}} + \frac{h^{[3]}}{\beta G_{xy}^{[3]}} - \frac{2\nu_{xy}^{[2]} h^{[2]}}{E_x^{[2]}} \right) + \frac{m^2\pi^2\left(h^{[2]}\right)^3}{210lE_y^{[2]}} \right]$$

(A2j)

where $\beta = b^{(3)}/b^{(1)}$ is the ratio of the beam to plate width.

$$\mathbf{C_{mn}} = \begin{bmatrix} (C_{mn})_{11} & (C_{mn})_{12} & (C_{mn})_{13} & (C_{mn})_{14} \\ (C_{mn})_{21} & (C_{mn})_{22} & (C_{mn})_{23} & (C_{mn})_{24} \\ (C_{mn})_{31} & (C_{mn})_{32} & (C_{mn})_{33} & (C_{mn})_{34} \\ (C_{mn})_{41} & (C_{mn})_{42} & (C_{mn})_{43} & (C_{mn})_{44} \end{bmatrix} \tag{A3}$$

in which

$$(C_{mn})_{11} = \frac{12b^{(1)}l^5(-1)^{m+n}}{m^2n^2\pi^4} \left[\frac{1}{E_x^{[1]}\left(h^{[1]}\right)^3} + \frac{1}{E_x^{[2]}\left(h^{[2]}\right)^3} \right] \tag{A4a}$$

$$(C_{mn})_{12} = \frac{6b^{(1)}l^4(-1)^{m+n}}{m^2n\pi^3} \left[\frac{1}{E_x^{[2]}\left(h^{[2]}\right)^2} - \frac{1}{E_x^{[1]}\left(h^{[1]}\right)^2} \right] \tag{A4b}$$

$$(C_{mn})_{13} = \frac{12b^{(1)}l^5(-1)^{m+n+1}}{m^2n^2\pi^4} \frac{1}{E_x^{[2]}\left(h^{[2]}\right)^3} \tag{A4c}$$

$$(C_{mn})_{14} = \frac{6b^{(1)}l^4(-1)^{m+n}}{m^2n\pi^3} \frac{1}{E_x^{[2]}\left(h^{[2]}\right)^2} \tag{A4d}$$

$$(C_{mn})_{22} = \frac{4b^{(1)}l^3(-1)^{m+n}}{mn\pi^2} \left(\frac{1}{E_x^{[1]} h^{[1]}} + \frac{1}{E_x^{[2]} h^{[2]}} \right) \tag{A4e}$$

$$(C_{mn})_{23} = \frac{6b^{(1)}l^4(-1)^{m+n}}{mn^2\pi^3} \frac{1}{E_x^{[2]}\left(h^{[2]}\right)^2} \tag{A4f}$$

$$(C_{mn})_{24} = \frac{2b^{(1)}l^3(-1)^{m+n}}{mn\pi^2} \frac{1}{E_x^{[2]} h^{[2]}} \tag{A4g}$$

$$(C_{mn})_{33} = \frac{12b^{(1)}l^5(-1)^{m+n}}{m^2n^2\pi^4} \left[\frac{1}{E_x^{[2]}\left(h^{[2]}\right)^3} + \frac{1}{\beta E_x^{[3]}\left(h^{[3]}\right)^3} \right] \tag{A4h}$$

$$(C_{mn})_{34} = \frac{6b^{(1)}l^4(-1)^{m+n+1}}{m^3\pi^3}\left[\frac{1}{E_x^{[2]}\left(h^{[2]}\right)^2} - \frac{1}{\beta E_x^{[3]}\left(h^{[3]}\right)^2}\right] \tag{A4i}$$

$$(C_{mn})_{44} = \frac{4b^{(1)}l^3(-1)^{m+n}}{mn\pi^2}\left(\frac{1}{E_x^{[2]}h^{[2]}} + \frac{1}{\beta E_x^{[3]}h^{[3]}}\right) \tag{A4j}$$

and $(C_{mn})_{ij}$ $(i=1,\cdots,4; \quad j<i)$ could be easily obtained by swapping m and n in $(C_{mn})_{ji}$.

In Equation 3.19, the sub-vector is

$$\mathbf{P}_m = [(P_m)_1, (P_m)_2, (P_m)_3, (P_m)_4]^T \tag{A5}$$

where

$$(P_m)_1 = 0 \tag{A6a}$$

$$(P_m)_2 = 0 \tag{A6b}$$

$$(P_m)_3 = \frac{12l^2(-1)^m}{m^2\pi^2\beta E_x^{[3]}\left(h^{[3]}\right)^3}\left[l\left(M_0 + M_{ql}\right) + L\int_0^l\int_0^l q(x)dxdx - \int_0^l x^2q(x)dx - \frac{l^2}{2}\int_0^l q(x)dx + \frac{1}{2}\int_0^x x^2q(x)dx\right]$$

$$-\frac{6l^2}{5m^2\pi^2\beta G_{xy}^{[3]}h^{[3]}}\left[(-1)^{m+1}\int_0^l q(x)dx + \int_0^l q(x)\cos\frac{m\pi x}{l}dx\right]$$

$$-\frac{12l^4}{m^4\pi^4\beta E_x^{[3]}h^{[3]}}\left[\int_0^l q(x)\cos\frac{m\pi x}{l}dx - (-1)^m\int_0^x q(x)dx\right] \tag{A6c}$$

$$(P_m)_4 = \frac{12l^2(-1)^m}{m\pi\beta E_x^{[3]}\left(h^{[3]}\right)^2}\left[l\left(N_0h^{[3]} + 6M_0 + 6M_{ql}\right) + 6L\int_0^l\int_0^l q(x)dxdx\right.$$

$$\left. - 6\int_0^l x^2q(x)dx - 3l^2\int_0^l q(x)dx + 3\int_0^x x^2q(x)dx\right]$$

$$-\frac{l}{10m\pi\beta G_{xy}^{[3]}}\left[(-1)^{m+1}\int_0^l q(x)dx + \int_0^l q(x)\cos\frac{m\pi x}{l}dx\right]$$

$$-\frac{l^3}{m^3\pi^3\beta E_x^{[3]}\left(h^{[3]}\right)^2}\left[\int_0^l q(x)\cos\frac{m\pi x}{l}dx - (-1)^m\int_0^x q(x)dx\right] \tag{A6d}$$

in which M_{ql} is the bending moment at the plate end cross section due to the applied transverse loads:

$$M_{ql} = \int_l^L q(x)(L-x)\ dx \tag{A7}$$

APPENDIX B

In Equation 3.56, the sub-matrixes are given as Equation B1 and B3, *i.e.*

$$\mathbf{C}_{ss} = \begin{bmatrix} (C_{ss})_{11} & (C_{ss})_{12} & (C_{ss})_{13} & (C_{ss})_{14} \\ (C_{ss})_{21} & (C_{ss})_{22} & (C_{ss})_{23} & (C_{ss})_{24} \\ (C_{ss})_{31} & (C_{ss})_{32} & (C_{ss})_{33} & (C_{ss})_{34} \\ (C_{ss})_{41} & (C_{ss})_{42} & (C_{ss})_{43} & (C_{ss})_{44} \end{bmatrix} \tag{B1}$$

where the elements are

$$(C_{ss})_{11} = b^{(1)} l \left[-\frac{6l^4}{S^2\pi^4}\left(\frac{1}{E_x^{[1]}\left(h^{[1]}\right)^3}+\frac{1}{E_x^{[2]}\left(h^{[2]}\right)^3}\right) - \frac{3l^2}{5S^4\pi^2}\left(\frac{1}{G_{xy}^{[1]}h^{[1]}}+\frac{1}{G_{xy}^{[2]}h^{[2]}}-\frac{2\nu_{xy}^{[2]}}{E_x^{[2]}h^{[2]}}\right) + \frac{13h^{[2]}}{70E_y^{[2]}}\left(1-\frac{1}{S^2}-\frac{1}{S^4}\right)\right] \tag{B2a}$$

$$(C_{ss})_{12} = b^{(1)} \left[\frac{3l^4}{S^2\pi^3}\left(\frac{1}{E_x^{[1]}\left(h^{[1]}\right)^2}-\frac{1}{E_x^{[2]}\left(h^{[2]}\right)^2}\right) - \frac{l^2}{20S\pi}\left(\frac{1}{G_{xy}^{[2]}}-\frac{1}{G_{xy}^{[1]}}+\frac{12\nu_{xy}^{[2]}}{E_x^{[2]}}\right)\left(1-\frac{1}{S}-\frac{1}{S^2}\right) + \frac{11S\pi\left(h^{[2]}\right)^2}{420E_y^{[2]}}\left(1-\frac{1}{S^3}-\frac{1}{S^4}\right)\right] \tag{B2b}$$

$$(C_{ss})_{13} = b^{(1)} l \left[\frac{6l^4}{S^2\pi^4}\frac{1}{E_x^{[2]}\left(h^{[2]}\right)^3} + \frac{3l^2}{5S^4\pi^2}\left(\frac{1}{G_{xy}^{[2]}h^{[2]}}-\frac{2\nu_{xy}^{[2]}}{E_x^{[2]}h^{[2]}}\right) + \frac{9h^{[2]}}{140E_y^{[2]}}\left(1-\frac{1}{S^2}-\frac{1}{S^4}\right)\right] \tag{B2c}$$

$$(C_{ss})_{14} = b^{(1)} \left[-\frac{3l^4}{S^2\pi^3}\frac{1}{E_x^{[2]}\left(h^{[2]}\right)^2} + \frac{l^2}{20S\pi}\left(\frac{1}{G_{xy}^{[2]}}-\frac{2\nu_{xy}^{[2]}}{E_x^{[2]}}\right)\left(1-\frac{1}{S}-\frac{1}{S^2}\right) - \frac{13S\pi\left(h^{[2]}\right)^2}{840E_y^{[2]}}\left(1-\frac{1}{S^3}-\frac{1}{S^4}\right)\right] \tag{B2d}$$

$$(C_{ss})_{21} = b^{(1)} \left[\frac{l^2}{20S\pi}\left(\frac{1}{G_{xy}^{[2]}}-\frac{1}{G_{xy}^{[1]}}-\frac{12\nu_{xy}^{[2]}}{E_x^{[2]}}\right)\left(1-\frac{1}{S^2}\right) + \frac{11S\pi\left(h^{[2]}\right)^2}{420E_y^{[2]}}\left(1-\frac{1}{S^4}\right)\right] \tag{B2e}$$

$$(C_{ss})_{22} = b^{(1)} \left[\frac{l}{15}\left(\frac{h^{[1]}}{G_{xy}^{[1]}}+\frac{h^{[2]}}{G_{xy}^{[2]}}-\frac{2\nu_{xy}^{[2]}h^{[2]}}{E_x^{[2]}}\right)\left(1-\frac{1}{S^2}\right) + \frac{S^2\pi^2\left(h^{[2]}\right)^3}{210lE_y^{[2]}}\left(1-\frac{1}{S^4}\right)\right] \tag{B2f}$$

$$(C_{ss})_{23} = b^{(1)} \left[-\frac{l^2}{20S\pi}\left(\frac{1}{G_{xy}^{[2]}}-\frac{2\nu_{xy}^{[2]}}{E_x^{[2]}}\right)\left(1-\frac{1}{S^2}\right) + \frac{13S\pi\left(h^{[2]}\right)^2}{840E_y^{[2]}}\left(1-\frac{1}{S^4}\right)\right] \tag{B2g}$$

$$(C_{ss})_{24} = b^{(1)} \left[-\frac{h^{[2]}}{60}\left(1-\frac{1}{S^2}\right)\left(\frac{1}{G_{xy}^{[2]}}-\frac{2\nu_{xy}^{[2]}}{E_x^{[2]}}\right) - \frac{S^2\pi^2\left(h^{[2]}\right)^3}{280lE_y^{[2]}}\left(1-\frac{1}{S^4}\right)\right] \tag{B2h}$$

$$(C_{ss})_{31} = b^{(1)} l \left[-\frac{3l^2}{5S^2\pi^2}\left(\frac{1}{G_{xy}^{[2]}h^{[2]}}-\frac{2\nu_{xy}^{[2]}}{E_x^{[2]}h^{[2]}}\right)\left(1-\frac{1}{S^2}\right) + \frac{9h^{[2]}}{140E_y^{[2]}}\left(1-\frac{1}{S^4}\right)\right] \tag{B2i}$$

$$(C_{ss})_{32} = b^{(1)}\left[-\frac{l^2}{20S\pi}\left(\frac{1}{G_{xy}^{[2]}}-\frac{2\nu_{xy}^{[2]}}{E_x^{[2]}}\right)\left(1-\frac{1}{S^2}\right)+\frac{13S\pi\left(h^{[2]}\right)^2}{840E_y^{[2]}}\left(1-\frac{1}{S^4}\right)\right] \tag{B2j}$$

$$(C_{ss})_{33} = b^{(1)}l\left[\frac{3l^2}{5S^2\pi^2}\left(\frac{1}{G_{xy}^{[2]}h^{[2]}}+\frac{1}{\beta G_{xy}^{[3]}h^{[3]}}-\frac{2\nu_{xy}^{[2]}}{E_x^{[2]}h^{[2]}}\right)\left(1-\frac{1}{S^2}\right)+\frac{13h^{[2]}}{70E_y^{[2]}}\left(1-\frac{1}{S^4}\right)\right] \tag{B2k}$$

$$(C_{ss})_{34} = b^{(1)}\left[-\frac{l^2}{20S\pi}\left(\frac{1}{G_{xy}^{[2]}}-\frac{1}{\beta G_{xy}^{[3]}}-\frac{12\nu_{xy}^{[2]}}{E_x^{[2]}}\right)\left(1-\frac{1}{S^2}\right)-\frac{11S\pi\left(h^{[2]}\right)^2}{40E_y^{[2]}}\left(1-\frac{1}{S^4}\right)\right] \tag{B2l}$$

$$(C_{ss})_{41} = b^{(1)}\left[-\frac{l^2}{10S\pi}\left(\frac{1}{G_{xy}^{[2]}}-\frac{2\nu_{xy}^{[2]}}{E_x^{[2]}}\right)\left(1-\frac{1}{S^2}\right)-\frac{13S\pi\left(h^{[2]}\right)^2}{840E_y^{[2]}}\left(1-\frac{1}{S^4}\right)\right] \tag{B2m}$$

$$(C_{ss})_{42} = b^{(1)}\left[-\frac{h^{[2]}}{60}\left(\frac{1}{G_{xy}^{[2]}}-\frac{2\nu_{xy}^{[2]}}{E_x^{[2]}}\right)\left(1-\frac{1}{S^2}\right)-\frac{S^2\pi^2\left(h^{[2]}\right)^3}{280lE_y^{[2]}}\left(1-\frac{1}{S^4}\right)\right] \tag{B2n}$$

$$(C_{ss})_{43} = b^{(1)}\left[-\frac{l^2}{20S^2\pi}\left(\frac{1}{G_{xy}^{[2]}}-\frac{1}{\beta G_{xy}^{[3]}}-\frac{12\nu_{xy}^{[2]}}{E_x^{[2]}}\right)\left(1-\frac{1}{S^2}\right)-\frac{11S\pi\left(h^{[2]}\right)^2}{40E_y^{[2]}}\left(1-\frac{1}{S^4}\right)\right] \tag{B2o}$$

$$(C_{ss})_{44} = b^{(1)}\left[\frac{l}{15}\left(\frac{h^{[2]}}{G_{xy}^{[2]}}+\frac{h^{[3]}}{\beta G_{xy}^{[3]}}-\frac{2\nu_{xy}^{[2]}h^{[2]}}{E_x^{[2]}}\right)\left(1-\frac{1}{S^2}\right)+\frac{S^2\pi^2\left(h^{[2]}\right)^3}{210lE_y^{[2]}}\left(1-\frac{1}{S^4}\right)\right] \tag{B2p}$$

where the ratio of beam to plate width $\beta = b^{(3)}/b^{(1)}$.

$$\mathbf{C}_{st} = \begin{bmatrix} (C_{st})_{11} & (C_{st})_{12} & (C_{st})_{13} & (C_{st})_{14} \\ (C_{st})_{21} & (C_{st})_{22} & (C_{st})_{23} & (C_{st})_{24} \\ (C_{st})_{31} & (C_{st})_{32} & (C_{st})_{33} & (C_{st})_{34} \\ (C_{st})_{41} & (C_{st})_{42} & (C_{st})_{43} & (C_{st})_{44} \end{bmatrix} \tag{B3}$$

$$(C_{st})_{11} = \frac{b^{(1)}l}{S^2T^2}\left[-\frac{6l^4}{\pi^4}\left(\frac{1}{E_x^{[1]}\left(h^{[1]}\right)^3}+\frac{1}{E_x^{[2]}\left(h^{[2]}\right)^3}\right)-\frac{3l^2}{5\pi^2}\left(\frac{1}{G_{xy}^{[1]}h^{[1]}}+\frac{1}{G_{xy}^{[2]}h^{[2]}}-\frac{2\nu_{xy}^{[2]}}{E_x^{[2]}h^{[2]}}\right)-\frac{13h^{[2]}}{70E_y^{[2]}}\right]$$

(B4a)

$$(C_{st})_{12} = \frac{b^{(1)}\pi}{S^2T}\left[\frac{3l^4}{\pi^4}\left(\frac{1}{E_x^{[1]}\left(h^{[1]}\right)^2}-\frac{1}{E_x^{[2]}\left(h^{[2]}\right)^3}\right)+\frac{l^2}{20\pi^2}\left(\frac{1}{G_{xy}^{[1]}}+\frac{1}{G_{xy}^{[2]}}-\frac{12\nu_{xy}^{[2]}}{E_x^{[2]}}\right)-\frac{11h^{[2]}}{420E_y^{[2]}}\right]$$

(B4b)

$$(C_{st})_{13} = \frac{b^{(1)}l}{S^2T^2}\left[\frac{6l^4}{\pi^4}\frac{1}{E_x^{[2]}\left(h^{[2]}\right)^3}-\frac{3l^2}{5\pi^2}\left(\frac{1}{G_{xy}^{[2]}h^{[2]}}-\frac{2\nu_{xy}^{[2]}}{E_x^{[2]}h^{[2]}}\right)-\frac{9h^{[2]}}{140E_y^{[2]}}\right]$$

(B4c)

$$(C_{st})_{14} = \frac{b^{(1)}\pi}{S^2T}\left[-\frac{3l^4}{\pi^4}\frac{1}{E_x^{[2]}\left(h^{[2]}\right)^2}-\frac{l^2}{20\pi^2}\left(\frac{1}{G_{xy}^{[2]}}-\frac{2\nu_{xy}^{[2]}}{E_x^{[2]}}\right)+\frac{13\left(h^{[2]}\right)^2}{E_y^{[2]}}\right]$$

(B4d)

$$(C_{st})_{22}=\frac{b^{(1)}\pi^2}{STl}\left[-\frac{2l^4}{\pi^4}\left(\frac{1}{E_x^{[1]}h^{[1]}}+\frac{1}{E_x^{[2]}h^{[2]}}\right)-\frac{l^2}{15\pi^2}\left(\frac{1}{G_{xy}^{[1]}h^{[1]}}+\frac{1}{G_{xy}^{[2]}h^{[2]}}-\frac{2\nu_{xy}^{[2]}h^{[2]}}{E_x^{[2]}}\right)-\frac{\left(h^{[2]}\right)^3}{210E_y^{[2]}}\right] \tag{B4e}$$

$$(C_{st})_{23}=\frac{b^{(1)}\pi}{ST^2}\left[\frac{3l^4}{\pi^4}\frac{1}{E_x^{[2]}\left(h^{[2]}\right)^2}+\frac{l^2}{20\pi^2}\left(\frac{1}{G_{xy}^{[2]}}-\frac{2\nu_{xy}^{[2]}}{E_x^{[2]}}\right)-\frac{13\left(h^{[2]}\right)^2}{840E_y^{[2]}}\right] \tag{B4f}$$

$$(C_{st})_{24}=\frac{b^{(1)}\pi^2}{STl}\left[-\frac{l^4}{\pi^4}\frac{1}{E_x^{[2]}h^{[2]}}+\frac{l^2h^{[2]}}{60\pi^2}\left(\frac{1}{G_{xy}^{[2]}}-\frac{2\nu_{xy}^{[2]}}{E_x^{[2]}}\right)-\frac{\left(h^{[2]}\right)^3}{280E_y^{[2]}}\right] \tag{B4g}$$

$$(C_{st})_{33}=\frac{b^{(1)}l}{S^2T^2}\left\{-\frac{6l^4}{\pi^4}\left[\frac{1}{E_x^{[2]}\left(h^{[2]}\right)^3}+\frac{1}{\beta E_x^{[3]}\left(h^{[3]}\right)^3}\right]-\frac{3l^2}{5\pi^2}\left(\frac{1}{G_{xy}^{[2]}h^{[2]}}+\frac{1}{\beta G_{xy}^{[3]}h^{[3]}}-\frac{2\nu_{xy}^{[2]}}{E_x^{[2]}h^{[2]}}\right)-\frac{13h^{[2]}}{70E_y^{[2]}}\right\} \tag{B4h}$$

$$(C_{st})_{34}=\frac{b^{(1)}\pi}{S^2T}\left[\frac{3l^4}{\pi^4}\left[\frac{1}{E_x^{[2]}\left(h^{[2]}\right)^2}-\frac{1}{\beta E_x^{[3]}\left(h^{[3]}\right)^2}\right]+\frac{l^2}{20\pi^2}\left(\frac{1}{G_{xy}^{[2]}}-\frac{1}{\beta G_{xy}^{[3]}}-\frac{12\nu_{xy}^{[2]}}{E_x^{[2]}}\right)-\frac{11\left(h^{[2]}\right)^2}{420E_y^{[2]}}\right] \tag{B4i}$$

$$(C_{st})_{44}=\frac{b^{(1)}\pi^2}{STl}\left[-\frac{2l^4}{\pi^4}\left(\frac{1}{E_x^{[2]}h^{[2]}}+\frac{1}{\beta E_x^{[3]}h^{[3]}}\right)-\frac{l^2}{15\pi^2}\left(\frac{h^{[2]}}{G_{xy}^{[2]}}+\frac{h^{[3]}}{\beta G_{xy}^{[3]}}-\frac{2\nu_{xy}^{[2]}h^{[2]}}{E_x^{[2]}}\right)-\frac{\left(h^{[2]}\right)^3}{210E_y^{[2]}}\right] \tag{B4j}$$

where

$$S=2s+1;\ T=2t+1 \tag{B5a, b}$$

And $(C_{st})_{ij}$ $(i=1,\cdots,4;\quad j<i)$ could be easily obtained by swapping s and t in $(C_{st})_{ji}$.

In Equation 3.19, the sub-vector $\mathbf{c}_s=\left[a_{s+1}^{(1)},b_{s+1}^{(1)},a_{s+1}^{(2)},b_{s+1}^{(2)}\right]^T$ and

$$\mathbf{P}_s=\left[(P_s)_1,(P_s)_2,(P_s)_3,(P_s)_4\right]^T \tag{B6}$$

where

$$(P_s)_1=0 \tag{B7a}$$

$$(P_s)_2=0 \tag{B7b}$$

$$(P_s)_3=\frac{12l^4\left(S^2-1\right)}{S^4\pi^4\beta E_x^{[3]}\left(h^{[3]}\right)^3}\left[-2lQ_l+\int q(x)dx+\int q(x)\cos\frac{S\pi x}{l}dx\right]$$

$$-\frac{6l^2}{5S^2\pi^2\beta G_{xy}^{[3]}h^{[3]}}\left[\int q(x)\cos\frac{S\pi x}{l}dx-\int q(x)\cos\frac{\pi x}{l}dx\right] \tag{B7c}$$

$$(P_s)_4 = \frac{6l^4\left(S^2-1\right)}{S^3\pi^3\beta E_x^{[3]}\left(h^{[3]}\right)^3}\left[-2lQ_l + \int_0^l q(x)dx + \int_0^l q(x)\cos\frac{S\pi x}{l}dx\right]$$

$$-\frac{l}{10S\pi\beta G_{xy}^{[3]}}\left[\int_0^l q(x)\cos\frac{S\pi x}{l}dx - \int_0^l q(x)\cos\frac{\pi x}{l}dx\right] \qquad \text{(B7d)}$$

REFERENCES

ABAQUS manual, 2000, ABAQUS, Inc.

ACI 318-95. *Building Code Requirements for Structural Concrete (318-95) and commentary (318R-95).* American Concrete Institute (ACI), Fifth Printing, Farmington Hills, Michigan, USA, 1999.

ACI Committee 440. Guide for the Design and Construction of Externally Bonded FRP Systems for Strengthening of Concrete Structures, ACI, Farmington Hills, MI, USA, 2001.

Adams, R. D. and Mallick , V. A method for the stress analysis of lap joints. *J. Adhesion* 1992; 38, 199-217.

Adams, R. D. Strength predictions for lap joints, especially with composite adherends. A review. *Journal of Adhesion 1*989; 30(1-4), 219-242.

Adams, R.D. and Peppiatt, N.A. Stress analysis of adhesive-bonded lap Joints. *Journal of Strain Analysis* 1974; 9(3), 185-196.

Adams, V. and Askenazi, A. *Building Better Products with Finite Element Analysis.* OnWord Press, Santa Fe, New Mexico, 1998.

Ahmed, O. Van Gemert, D, Vandewalle, L. Improved model for plate-end shear of CFRP strengthened RC beams. *Cement and Concrete Composites* 2001; 23, 3-19.

Ahmed, O. Van Gemert, D. Shear behavior of RC beams strengthened by longitudinal CFRP laminates. *Proceedings of the Sixth International Conference 'Modern Building Materils, Structures and Techniques'*, May, Vilnius, Lithuania, 1999; 5-11.

Ali, M.S.M. and Oehlers, D.J. and Bradford, M.A. Shear peeling of steel plates adhesively bonded to the sides of reinforced concrete beams. *Proc. Instn. Civ. Engrs. Structs & Bldgs*, 2000; 140, 249-259.

Altus, E. and Rotem, A. A 3-D fracture mechanics approach to the strength of composites materials. *Eng. Fract. Mech.* 1981; 14, 637-644.

An, W, Saadatmanesh, H. and Ehsani, M. R. RC beams strengthened with FRP plates, II: Analysis and parametric study. *Journal of structural engineering* 1991; 117(11), 3434-3455.

Anandarajah, A. and Vardy, A.E. A theoretical investigation of the failure of open sandwich beams due to interfacial shear fracture. *The structural Engineer*, 1985; 63B(4), 85-92.

Aprile, A., Spacone, E. and Limkatanyu, S. Role of bond in RC beams strengthened with steel and FRP plates. *Journal of Structural Engineering, ASCE* 2001. 127(12), 1445-1452.

Arduini, M. and Nanni, A. Parametric study of Beams with externally bonded FRP reinforcement. *ACI Structural Journal* 1997a; 94(5), 493-501.

Arduini, M. and Nanni, A. Behavior of precracked RC beams strengthened with carbon FRP sheets. *Journal of Composites for Construction* 1997b; 1(2), 63-70.

Arduini, M. Di Tommaso, A. and Nanni, A. Brittle Falure in FRP Plated and Sheet Bonded Beams. *ACI Structural Journal* 1997; 94(4), 363-370.

AS3600. *Concrete Structures, AS3600*. Standards Australia, Sydney, Australia; 1988.

Ascione, L. Feo, L. Modeling of composite/concrete interface of RC beams strengthened with composite laminates. *Composites: Part B* 2000; 31, 535-540.

Ashour, A.F. Flexural strength of reinforced concrete beams strengthened with FRP laminates. Concrete Communication Conference 2001, *Proceedings of the Eleventh Annual BCA/Concrete Society Conference on Higher Education and the Concrete Industry*, UMIST, Manchester, 2001; 267-279.

Baluch, M. H. et al. Shear strength of plated RC beams. *Magazine of Concrete Research* 1994; 47(173), 369-374.

Bangash, M.Y.H. *Concrete and concrete structures: Numerical modeling and applications*. Elsevier Science Publishers Ltd. London, England, 1989.

Baniface, L, Smith, P.A. Reazifard, A.H. Bader, M.G. Transverse ply cracking in composite laminates – initiation or propagation controlled? *J. Comp. Mater.* 1997; 31, 1080-1112.

Barrett, N. Plates Steel Leeds Floor. *New Civil Engineer* 1985; 20, 18.

Bazant ZP. Instability, ductility and size effect in strain-softening concrete. *ASCE J Eng. Mech. Div.* 1976; 102(EM2): 331-344.

Bencardino, F. Colotti, V. Spadea, G. Swamy, R.N. Failure analysis of RC beams with bonded FRP laminates. *Proceeding of International Conference in Composites in Constructions*. Porto, Portugal, Oct. 10-12, 2001; 505-510.

Berthelot, J. M. Leblond, P. EI-Mahi, A. and Le Corre, J. F. Transverse cracking of cross-ply laminates: Part 1. Analysis. *Composites Part A 1996*; 27A, 989-1001.

Bogy, D.B. 1968. Edge-bonded dissimilar orthogonal elastic wedges under normal and shear longing. *J. Appl. Mech.* 35, 460-466.

Bonacci, J.F. and Maalej, M. Behavioural trends of RC beams strengthened with externally bonded FRP. *Journal of Composites for Construction ASCE* 2001; 5(2) 102-113.

Bonacci, J.F. and Maalej, M. Externally bonded fiber-reinforced polymer for rehabilitation of corrosion damaged concrete beams. *ACI Structural Journal* 2000 a; 97(5), 703-711.

Bonacci, J.F. and Maalej, M. Externally bonded FRP for service-life extension of RC infrastructure. *Journal of Infrastructure Systems ASCE* 2000 b; 6(1), 41-51.

Boniface, L. Ogin, S. L. and Smith, P. A. Strain energy release rates and the fatigue growth of matrix cracks in model arrays in composite laminates. *Proc. R. Soc. Lond* 1991; A 432, 427-444.

Bresson, J. Realisation Pratique d'un Reinforcement par Collage d'Armatures. *Annales De I'ITBTP, Suppliment 1971*; 278, 50-52.

Bresson, J. Reinforcement par Collage d'Armatures du Passage inferieur du CD 126 sous 1', Autoroute du Sud. *Annales de 1'Institute du Batiment et des Tavaux Publics, Suppliment 297, Concrete and Reinforcement 1972*; Series 122, 3-24.

British Standards Institution (BSI). *Structural use of concrete, Part 1: Code of practice for design and construction.* 1985, *BSI 8110*. London.

Broek, D. 1986. *Elementary Engineering Fracture Meachnics,* 4th rev. ed. Martinus Nijhoff, Dordrecht.

Brosens, K and Van Gemert, D. Plate end shear design for external CFRP laminates. Fracture Mechanics of Concrete Structures, Proceedings FRAMCOS-3, Aedificatio Publishers, D-79104, Germany, 1998, 1793-1804.

Buyukozturk, O. and Hearing, B. Failure behavior of precracked concrete beams retrofitted with FRP. *Journal of Composites for Construction* 1998; 2(3), 138-144.

Caslini, M, Zanotti, C. and O'Brien, T.K. Study of matrix cracking and delamination in glass/epoxy laminates. *J. Composites Tech. Res* 1987; 9, 121-130.

CEB-FIP MC 90. *Design of Concrete Structurs.* Thomas Telford, 1993.

Chaallal, O., Nollet, M. J. and Perraton, D. Strengthening of reinforced concrete beams with externally bonded fiber reinforced plastic plates: design guidelines for shear and flexural. *Can. J. Civ. Eng.* 1998; 25, 692-704.

Chajes, M.J. Finch, W.W. Januszka, T.F. Thomson, T.A. Bond and force transfer of composite material plates bonded to concrete. *ACI Struct J* 1996; 208-217.

Chajes, M.J., Thomson, T.A., Januszka, T.F. and Finch, W.W. Jr., Flexural strengthening of concrete beams using externally bonded composite materials. *Construction and Building Materials* 1994; 8(3), 191-201.

Chaudhuri, R. A. On boundary-discontinuous double Fourier series solution to a system of completely coupled P.D.E.'s. *Int. J. Engng. Sci.* 1989; 27(9) 1005-1022,

Chen, J.F. and Teng, J.G. Anchorage strength models for FRP and steel plates bonded to concrete. *Journal of Structural Engineering, ASCE* 2001; 127(7), 784-791.

Cheng, S. Chen, D. and Shi, Y. Analysis of adhesive-bonded joints with nonidentical adherends, *Journal of Engineering Mechanics* 1991; 117(3), 605-623.

Colotti, V. and Sapdea, G. Shear strength of RC beams strengthened with bonded steel of FRP plates. *Journla of Strucrual Enginerring* 2001; 127(4), 367-373.

Colotti, V. Spadea, G. Swamy, R.N. Shear and flexural behavior of RC beams externally reinforced with bonded FRP laminates: a truss model approach. *Proceeding of International Conference in Composites in Constructions*. Porto, Portugal, Oct. 10-12, 2001; 517-522.

Concrete Society, 2000. *Design guidance for strengthening concrete structures using fibre composite materials*, Technical report 55, The Concrete Society, U.K.

Crisfield, M. A., Snap-Through and Snap-Back Response in Concrete Structures and the Dangers of Under-Integration. *International Journal for Numerical Methods in Engineering*, vol. 22, 751-767, 1986.

CSA. *Design of Concrete Structures*. CSA Standard A23.3-94, Canadian Standards Association, Ontario, Canada; 1994.

Davies, B. L. and Powell, J. Strengthening of Brinsworth Road Bridge, Rotherham, *IABSE, 12th Congress*, Vancouver, BC, September 1984; 401-407.

Delale, F. Erdogan, F. and Aydinoglu, M.N. Stress in adhesively bonded joint: a closed-form solution. *Journal of Composite Materials* 1981; 15, 249-270.

Desayi, P. and Krishnan, S. Equation for the stress-strain curve of concrete. *Journal of the American Concrete Institute*, 61, 345-350, 1964.

Dussek, I. J. Strengthening of bridge beams and similar structures by means of Epoxy-Resin-Bonded external reinforcement. *Transportation Research Record* 785, Transportation Research Board 1980, 21-24.

El-Mihilmy, M.T. and Tedesco, J.W. Analysis of reinforced concrete beams strengthened with FRP laminates. *Journal of Structural Engineering ASCE* 2000; 126(6), 684-691.

Etman, E.E. Beeby, A.W. Experimental program and analytical study of bond stress distributions on a composite plate bonded to a reinforced concrete beam. *Cement and Concrete Composites* 2000; 22, 281-291.

Fanning P. J. and Kelly, O. Ultimate response of RC beams strengthened with CFRP plates. *Journal of Composites for Construction* 2001; 5(2), 122-127.

Fib. Design and use of externally bonded fibre reinforced polymer reinforcement (FRP EBR) for reinforced concrete structures. Technical report of *fib* Task Group

9.3, EBR group, International Federation for Structural Concrete, Lausanne, Switzerland, 2001.

Flaggs, D.L. Prediction of tensile matrix failure in composite laminates. *J. Comp. Mater.* 1985; 19, 29-50.

Forde, M. C. (ed.) *Structural faults and repair – 99: 8th International Conference London.*Ediburgh, Eingeering Technics Press 1999.

Fukunaga, H. Chou, T. W. Peters, P.W.N. and Schulte, K. Probabilistic failure strength analyses of Graphite/Epoxy cross ply laminates. *J. Composite Materials* 1984; 18, 339-356.

Garden, H.N. and Hollaway, L.C. An experimental study of the influence of plate end anchorage of carbon fibre composite plates used to strengthen reinforced concrete beams. *Composite Structures 1*998a; 42, 175-188.

Garden, H.N. and Hollaway, L.C. An experimental study of the failure modes of reinforced concrete beams strengthened with prestressed carbon composite plates. *Composite Part B* 1998b; 29B, 411-424.

Garden, H.N. et al. An experimental study of the anchorage length of carbon fiber composite plates used to strengthen reinforced concrete beams. *Construction and Building Materials* 1998; 12, 203-219.

Garden, H.N. Hollaway, L.C. Thorne, A.M. A preliminary evaluation of carbon fibre reinforced polymer plates for strengthening reinforced concrete members. *Proc. Instn. Civ. Engrs. Structs. & Bldgs* 1997; 123, 127-142.

Garden, H.N. *Strengthening Reinforced Concrete Members Using Externally Bonded Composite Materials.* Ph.D Thesis, University of Surrey, U.K. 1997.

Garrett, K. W. and Bailey, J. E. Multiple transverse fracture in 90° cross-ply laminates of a glass fibre-reinforced polyester. *J. Mater. Sci.* 1977; 12, 157-168.

Gere, J.M. and Timoshenko S. P. *Mechanics of Materials.* (4th Edition), Stanley Thornes Ltd. London, 1999.

Gibbs, J. W. Fourier Series. *Nature* 1899: 59, 200 and 606.

Gibson, R.F. *Principles of Composite Material Mechanics*. McGraw-Hill, Inc. New York, New York, 1994.

Goland, M. Buffalo, N.Y. and Reissner, E. The stresses in cemented joints. *Journal of Applied Mechanics, Transaction of the ASME* 1944; 11, A17-A27.

Goldstein S. The stability of viscous fluid flow under pressure between parallel planes. *Proc. Camb. Phil. Soc.* 32, 40-49, 1936.

Grace, N.F., Soliman, A.K., Sayed, G.A. and Saleh, K.R. Behaviour and ductility of simple and continuous FRP reinforced beams, *Journal of Composites for Construction, ASCE* 1998; 2(4)186-194.

Guild, G. J. Ogin, S. L. and Smith, P. A., Modelling of 90° ply cracking in cross ply laminates, including three-dimensional effects. *J. Compos. Mater.* 1993; 27, 646-667.

Gurvich, M.R., Dibenedetto, A.T. and Pegoretti, A. Evaluation of the statistical parameters of a Weibull distribution. *Journal of Mateiral Science*, 1997; 32, 3711-3716.

Hamelin, P. Recommendations concerning repairing and strengthening of concretes structures by composite materials. *Proceedings of the International Conference on FRP Composites in Civil Engineering* (*CICE 2001*), Hong Kong, China, edited by J.G. Teng, 165-175, 2001.

Hamilton, H.R. and Dolan, C.W. Durability of FRP reinforcements for concrete. *Progress in Structural Engineering and Materials* 2000; 2, 139-145.

Hashin, Z. Analysis of cracked laminates: a variational approach. *Mechanics of Materials 1985*; 4, 121-136.

Hashin, Z. Analysis of orthogonally cracked laminates under tension. *J. Appl. Mech. Transactions of the ASME* 1987. 872-879.

Hashin, Z. Thermal expansion coefficients of cracked laminates. *Composites Sci. and Tech. 1988*; 31, 247-260.

Hau, K.M. *Experiments on Concrete Beams Strengthened by Bonding Fibre Reinforced Plastic Sheets*. Msc Thesis, The Hong Kong Polytechinc University, 1999.

Heffernan, P.J. and Erki, M.A. Equivalent capacity and efficiency of reinforced concrete beams strengthened with carbon fibre reinforced plastic sheets. *Canadian Journal of Civil Engineering* 1996; 23, 21-29.

Hein, V.L. and Erdogan, F. Stress singularities in a two-material wedge. *Int. J. Fracture Mech.* 1971: 7(3): 317-330

Highsmith, A. L. and Reifsnider, K. L. Stiffness reduction mechanisms in composites. *ASTM STP 775* 1982; 103-117.

Hilleborg, A., Modeer, M. and Petersson, P. E. Analysis of Crack Formation and Crack Growth in Concrete by Means of Fracture Mechanics and Finite Elements. *Cement and Concrete Research* 1976; 6, 773-782.

Hobson, E. W. *The theory of Functions of a Real Variable and the Theory of Fourier's Series*, 2nd edn. Vol. 2. Cambridge, 1926.

Hollaway, L.C.and Leeming, M.B. *Strengthening of Reinforced Concrete Structures Using Externally-Bonded FRP Composites in Structural and Civil Engineering.* Woodhead Publishing, Cambridge, U.K. 1999.

Hugenschmidt, H. Epoxy adhesive for concrete and steel. *Proc. First Internat. Congress on Polymers in Concrete*, London, 1975, The Construction Press Ltd. Hornby, 195-209,1976.

Hussain, M. Sharif, A. Basunbul, I. A. Baluch, M. H. and Al-Sulaimani. Flexural Behavior of precracked reinforced concrete beams strengthened externally by steel plates. *ACI Structural Journal* 1995; 92(1), 14-22.

Hutchinson, A. R. and Rahimi, H. Behavior of reinforced concrete beams with externally bonded fiber reinforced plastics. *Proc. 5th Int. Conf. On Structural Faults and Repair*, University of Edinburgh 1993; 3, 221-228.

Li, S. Reid, S. R. and Soden, P. D. A finite strip analysis of cracked laminates. *Mechanics of Materials* 1994; 18, 289-311.

Iino, T. and Otokawa, K. Application of Epoxy resins in strengthening of concrete structures. *Proceedings, Third International Congress on Polymers in Concrete*, Koriyama, Japan, 1981; V.II, 997-1011.

Jansze, W. Anchorage of externally bonded plates under static flexural loading. *Prog. Concr. Res.* 1995; 4.

Jansze, W. *Strengthening of RC members in bending by externally bonded steel plates*. PhD thesis, Delft University of Technology, Delft, 1997.

Japan Building Disaster Prevention Association (JPDPA). *Seismic Retrofitting Design and Construction Guidelines for Existing Reinforced Concrete (RC) and Steel-encased Reinforced Concrete (SRC) Buildings with FRP Materials*, (in Japanese), 1999.

Johnson, R.P. Tait, C.J. The strength in combined bending and tension of convete beams with externally bonded reinforcing plates. *Build Environ* 1981; 16, 287-299.

Jones, R. Swamy, R. N. and Charif, A. Plate separation and anchorage of reinforced concrete beams strengthened by epoxy-bonded steel plates. *The Structural Engineer* 1988; 66(5): 85-94.

Jones, R. Swamy, R. N. and Bloxham, J. Crack control of reinforced concrete beams through epoxy bonded steel plates. *Adhesion between polymers and concrete, Proceedings of an international symposium* 1986; 542-555.

Jones, R. Swamy, R. N. Bloxham J. and Bouderbalah, A. Composite behavior of concrete beams with epoxy bonded external reinforcement. *Int J Cement Comp* 1980; 2, 91-107.

JSCE Concrete Committee. *Recommendations for Upgrading of Concrete Structures with Use of CFRP Sheet*, JSCE, 2001.

Kaiser, H. P. *Strengthening of reinforced concrete with epoxy-bonded carbon-fiber plastics.* PhD thesis. ETH Zurich, Switzerland, 1989. (in Germany).

Kajfasz, S. Concrete beams with external reinforcement bonded by gluing. *RILEM Internat. Symposium, Synthetic Resins in Building Construction*, Part 2, Paris, 1967; 142-151.

Kani, G. N. J. The riddle of shear failure and its solution. *Am. Concr. Ints. Journal* 1964; 61, 441-467.

Karbhari, V. M. and Seible, F. Fiber reinforced composites-advanced materials for the renewal of civil infrastructure. *Applied Composite Materials* 2000; 7, 95-124.

Kim, W. and White, R. N. Initiation of shear cracking in reinforced concrete beams with no web reinforcement. *ACI Stru. J.* 1991; 88(3), 301-308.

Kupfer, H.B and Gerstle, K.H. Behavior of concrete under biaxial stresses. *Journal of the Engineering Mechanics Division, ASCE* 99(EM4) 1973; 853-865.

L'Hermite, R. and Bresson, J. Beton arme d'armatures colleed. *Rilem International Symposium Synthetic Resins in Building Construction*. Paris, 1967; 175-203

L'hermite, R. L. Vresson, J. Beton arme par collage des armature. *RILEM Internat. Symposium, Resins in Building Construction*, Part2, Paris 1967; 175-203.

Ladner, M. Webber, C. *Concrete structures with bonded external reinforcement.* EMPA Report No. 206, Dubendorf, 1981.

Lam, L. and Teng, J. G. Strength of cantilever RC slabs bonded with GFRP strips. *Journal of Composites for Construction, ASCE* 2001; 5(4), 221-227.

Laws, N. and Dvorak, G.J. Progressive transverse cracking in composite laminates. *J. Comp. Mater.* 1988; 22, 900-916.

Leadbeater, A. D. and Russell, C. The practical applications of externally strengthening existing highway bridges using steel. *Symposium on Strengthening and Repair of Bridges*, Leamington Sap, 1988; 6/1-6/9.

Lerchental, H. Bonded sheet metal reinforcement for concrete slabs. *RILEM Internat. Symposium, Resins in Building Construction*, Paris 1967; 165-173

Leung, C.K.Y. Delamination failure in concrete beams retrofitted with a bonded plate. *Journal of Materials in Civil Engineering ASCE* 2001; 13(2), 106-113.

Leung, C.K.Y., Luk, H, C.Y. and Wan, K.T. Plate end shear stress in composite strengthened beams with cracked concrete section. *Proceedings of the International Conference on FRP Composites in Civil Engineering* (*CICE 2001*), Hong Kong, China, 2001, edited by J.G. Teng, 129-136.

Liu, J. and Sawa, T. Stress analysis and strength evaluation of single-lap band adhesive joints subjected to external bending moments. *J. Adhesion Sci. Technol* 1999; 13(6), 729-749.

Liu, Z. and Zhu, B. Analytical solutions for R/C beams strengthened by externally bonded steel plates. *J Tongji Univ* 1994; 22(1) 21-26 (in Chinese).

Maalej, M, Goh, W.H. and Paramasivam, P. Analysis and design of FRP externally-reinforced concrete beams against debonding-type failures. *Materials and Structures* 2001; 34, 418-425.

Maalej, M. and Bian, Y. Interfacial shear stress concentration in FRP-strengthened beams. *Composite Structures* 2001; 54, 417-426.

MaCartney, L. N. A recursive method of calculating stress transfer in multiple-ply cross-ply laminates subject to biaxial loading. *NPL report DMMA(A)* 150, 1995.

MaCartney, L. N. Schoeppner, G. A. and Becker, W. Comparison of models for transverse ply cracks in composite laminates. *Composites Science and Technology* 2000; 60, 2347-2359.

MaCartney, L. N. Theory of stress transfer in a 0-90-0 cross-ply laminate containing a parallel array of transverse cracks. *J. Mech. Phys. Solids* 1992; 40, 27-69.

MaCartney, L.N. Pierse, C. Stress transfer mechanics for multiple ply laminates subject to bending. *NPL report CMMT(A)* 55, 1997a.

MaCartney, L.N. Pierse, C. Stress transfer mechanics for multiple ply laminates for axial loading and bending. *Proceedings of the 11th International Conference on Composite Materials*, Gold Coast, Australia, 14-18, July 1997b.

MacDonald, M. D. 1982. The flexural performance of 3.5 m concrete beams with various bonded external reinforcements. *Transport and Road Research Laboratories (TRRL0), Supplemental Rep. No. 728*, Dept. of the Environment, Crowthorne, U.K.

MacDonald, M. D. and Calder, A. J. J. Bonded steel plating for strengthening concrete structures. *International Journal of Adhesion and Adhesives* 1982; 2(2), 119-127.

Malek, A.M. Saadatmanesh, H. Ehsani, M.R. Prediction of failure load of R/C beams strengthened with FRP plate due to stress concentration at the plate end. *ACI Structural Journal* 1998; 95 (1), 142-152.

Mander, R. F. Bonded external reinforcement, a method of strengthening structures. *Department of the Environment Report on Quinton Interchange for the M5 Motorway*, 1974.

Manders, P.W. Chou, T. W. Jones, F. R. and Rock, J. R. Statistical analysis of multiple fracture in 0°/90°/0° glass fibre/epoxy resin laminates. *J. Materials Science* 1983; 18: 2876-2889.

Mays, G. C. and Turnball, J. D. Strengthening bridges with bonded external reinforcement. *Symp. On Bridges- Extending the Lifespan*, Leamington Spa, 1992; paper 3.

Meier, U, Kaiser, H. Strengthening of structures with CFRP laminates. *Proceedings of the Specialty Conference Advances Composite Materials in Civil Engineering*, Structures, Nevada, 1991; 224-232.

Meier, U. Bridge repair with high performance composite materials. *Material und Technik* 1987; 15, 125-128. (in French and Germany).

Meier, U. Deuring, M. Maier, H. and Schwegier, G. Strengthening of structures with CFRP laminates: research and applications in Switzerland. *Advanced Composite Materials in bridges and Structures, 1st International Conference*, Sherbrooke, Quebec, 1992; 243-251.

Meier, U. Post strengthening by continuous fiber laminates in Europe. Non-metallic FRP reinforcement for concrete structures. *Japan Concrete Institute*, 1997; Vol. 1, 41-56.

Meier, U. Rehabilitation and retrofitting of existing structures through external bonding of thin carbon fiber sheets. *Bridges Assessment, Management and Design*. London: Elsevier Applied Science, 1994; 373-378.

Meier, U. Strengthening of structures using carbon fibre/epoxy composites. *Construction and Building Materials* 1995; 9(6), 341-351.

Mirza, S., Hatzinikolas, M., and MacGregor, J. Statistical descriptions of the strength of concrete. *Journal of Structural Engineering*, ASCE 1979; 105(516), 1021-1037.

Mohr, O. 1911. Die scherfestigkeit des betons (Shear strength of concrete). *Armierter Beton*, IV: 247-250.

Mukhopadhyaya, P. and Swamy, R. N. Critical review of plate anchorage stresses in premature debonding failures of plate bonded reinforced concrete beams. *Proceedings of the 4th international symposium on fiber reinforced polymer reinforcement for reinforced concrete structures*, Baltimore, ACI 1999; 188-33, 359-368.

Mukhopadhyaya, P. and Swamy, R. N. Interface shear stress: A new criterion for plate debonding. *Journal of composites for construction* 2001; 5(1). 35-43.

Mukhopadhyaya, P. and Swamy, R. N. Lynsdale, C. Optimizing structural response of beams strengthened with GFRP plates. *Journal of composite for Construction* 1998; 2(2), 87-95.

Murakami, Y. et al. *Stress Intensity factors handbook.* Pergamon, New York, 1987

Nairn, J. The strain energy release rate of composite microcracking: A variational approach. *J. Composite Materials* 1989; 23, 1106-1129.

Nairn J. A. Some new variational mechanics results on composite microcracking. *Proc. 10th International conference on composite materials* 1995; Vol I, 423-430.

Nanni, A. Focacci, F. and Cobb, C.A. Poroposed prodedure for the design of RC flexural members strengthened with FRP sheets. *Proceedings of the Second International Conference on Composites in Infrastructure (ICCI 1998)*, Tucson, Arizona, USA; 1998. Edited by H. Saadatmanesh and M.R. Ehsani.

Neale, K.W. FRPs for structural rehabilitation: a survey of recent progress. *Progress in Structural Engineering and Materials* 2000; 2, 133-138.

Neubauer, U. and Rostasy, F.S. Bond failure of concrete fiber reinforced polymer plates at inclined cracks-experiment and fracture mechanics model. *Proceedings of the 4th international symposium on fiber reinforced polymer reinforcement for reinforced concrete structures*, Baltimore, ACI, 1999; SP188-34, 369-381.

Ngo, D. and Scordelis, A. C. Finite Element Analysis of Reinforced Concrete Beams. *Journal of the American Concrete Institute* 1967; 64(3), 152-163.

Nguyen, D. M., Chan, T.K. and Cheong, H. K. Brittle failure and bond development length of CFRP-concrete beams. *Journal of Composites for Construction, ASCE* 2001; 5(1), 12-17

Niedermeier, R. *Envelope line of tensile forces while using externally bonded reinforcement*. Ph.D. Thesis, TU Munch; 2000 (in Germany).

Nilson, A. H. Nonlinear Analysis of Reinforced Concrete by the Finite Element Method. *Journal of the American Concrete Institute* 1968; 65(9), 757-766.

Oehlers, D. J. Moran, J. P. Premature failure of externally plated reinforced concrete beams. *Journal of Structural Engineering, ASCE* 1990; 116(4), 978-995.

Oehlers, D. J. Reinforced concrete beams with plates glued to their soffits. *Journal of Structural Engineering, ASCE* 1992; 118(8), 2023-2038.

Oehlers, D.J. and Nguyen, N.T. Retrofitting by adhesive bonding steel plates to the sides of R.C. beams. Part 1: Debonding of plates due to flexure. *Structural Engineering and Mechanics* 2000a; 9(5), 491-504.

Oehlers, D.J. and Nguyen, N.T. Retrofitting by adhesive bonding steel plates to the sides of R.C. beams. Part 2: Debonding of plates due to shear and design rules. *Structural Engineering and Mechanics* 2000b; 9(5), 505-518.

Ogin, S.L. Smith, P.A. and Beaumont, P.W.R. A stress intensity factor approach to the fatigue growth of transverse ply cracks. *Composites Sci. & Tech.* 1985; 24, 47-59.

Ong, K.C.G., Mays, G.C. and Cusens, A.R. Flexural testes of steel-concrete open-sandwiches. *Magazine of Concrete Research* 1982; 34(120), 130-138.

Peters, P.W.M. The strength distribution of 90o plies in 0/90/0 Graphite-Epoxy laminates. *J. Composite Materials* 1984; 18, 545-556.

Popovics, S. *Strength and related properties of concrete*. John Wiley & Sons, Inc. N.Y. 1998.

Poursartip, A. *Aspects of damage growth in fatigue of composites*. Ph.D thesis, Cambridge University Engineering Dept. 1983.

Quantill, R.J and Hollaway, L.C. The flexural rehabilitation of reinforced concrete beams by the use of prestressed advanced composite plates. *Composite Science and Technology*, 1998; 58, 1259-1275.

Quantrill, R. J. Hollaway L.C. Thornem A.M. Experimental and analytical investigation of FRP strengthened beam response: Part I. *Magazine of Concrete Research* 1996a; 48(177), 331-342.

Quantrillm R. J. Hollaway, L.C. Thorne, A.M. Predictions of the maximum plate end stresses of FRP strengthened beams Part II. *Magazine of Concrete Research* 1996b; 48(177), 343-351.

Rabinovich, O. Frostig, Y. Closed-form high-order analysis of RC beams strengthened with FRP strips. *Journal of composites for Construction ASCE* 2000; 4(2), 65-74.

Rabinovich, O. Frostig, Y. On edge stress control in strengthened RV beams with FRP strips: adhesive layer profile effect. *Journal of Engineering Mechanics ASCE* 2001a; 127(4), 317-325.

Rabinovich, O. Frostig, Y. Nonlinear high-order analysis of cracked RC beams strengthened with FRP strips. *Journal of structural Engineering ASCE* 2001b; 127(4), 381-389.

Rabinovich ,O. Frostig, Y. Delamination failure of RC beams strengthened with FRP strips-A closed-form high-order and fracture mechanics approach. *Journal of structural Engineering ASCE* 2001c; 127(8), 852-861.

Rahimi, H. and Hutchinson A. Concrete beams strengthened with externally bonded FRP plates. *Journal of Composites for Construction, ASCE* 2001; 5(1), 44-56.

Raithby, K.D. External strengthening of concrete bridges with bonded steel plates. *Transport and Road Research Laboratory, Supplementary Report* 612, 1980.

Raoof, M and Hassanen, M.A.H. Peeling failure of reinforced concrete beams with fibre-reinforced plastic or steel plates glued to their soffits. *Proc. Instn. Civ. Engrs. Structs. & Bldgs.* 2000; 140, 291-305.

Raoof, M. and Zhang, S. An insight into the structural behaviour of reinforced concrete beams with externally bonded plates. *Proc. Instn. Civ. Engrs. Structs. &Bldgs.* 1997; 122, 477-492.

Raoof, M., El-Rimawi, J. A. and Hassanen, M.A.H. Theoretical and experimental study on externally plated R.C. beams. *Engineering Structures* 2000; 22, 85-101.

Rashid, Y. R. Ultimate Strength Analysis of Prestressed Concrete Pressure Vessels. *Nuclear Engineering and Design* 1968; 7(4). 334-344.

Reineck, K. et al. Shear database for reinforced concrete members without shear reinforcement. *ACI Structural Journal* 2003;100(2): 240-214.

Renton, W. J. and Vinson, J. R. Analysis of adhesively bonded joints between panels of composite materials. *Journal of Applied Mechanics, Transactions of the ASME,* 1977.

Rice, J. R. A path independent integral and the approximate analysis of strain concentration by Notches and cracks. *Journal of Applied Mechanics, ASME,* 1968; 35(6), 79-386.

Rice, J. R. and Sih, G.C. 1965, Plane problems or cracks in dissimilar media. *J. Appl. Mech.* 32, 418-423.

Ritchie, P. A. Thomas, D. A. Lu, L. W. and Connelly, G. M. External reinforcement of concrete beams using glass reinforced plastics. *ACI Structural Journal* 1991; 88(4), 490-500.

Roberts, T. M. Approximate analysis of shear and normal stress concentrations in the adhesive layer of plated RC beams. *The Structural Engineering,* 1989; 67(2), 229-223.

Roberts, T.M. Haji-Kazemi, H. Theoretical study of the behavior of reinforced concrete beams strengthened by externally bonded steel plates. *Proc Instn Civil Engrs Part 2* 1989; 87, 39-55.

Rolfe, S.T., and Barsom, J.M.1977. *Fracture and Fatigue Control in Structures: Applications of Fracture Mechanics.* Prentice-Hall, Englewood Cliffs, NJ.

Ross, C.A, Jerome, D.M., Tedesco, J.W. and Hughes, M.L. Strengthening of reinforced concrete beams with externally bonded composite laminates. *ACI Structural Journal* 1999; 96(2) 212-220.

Rostasy, F.S. Hankers, C. and Ranisch, E.H. Strengthening of RC and PC structures with bonded FRP plates. *1st Int Conf. Adv Comp Mat Bridges Struct,* Sherbrooke, 1992; 253-263.

Ryback, M. Reinforcement of bridges by gluing of reinforcing steel. *RILEM Materials and Structures* 1981; 16(91), 13-17.

Saadatmanesh, H. and Ehsani, M. R. RC beams strengthened with GFRP plates, I: Experimental study. *Journal of Structural Engineering ASCE* 1991; 117(11), 3417-3433.

Saadatmanesh, H. and Malek, A.M. Design guidelines for flexural strengthening of RC beams with FRP plates. *Journal of Composites for Construction ASCE* 1998; 2(4), 158-164.

Schoeppner, G. A. and Pagano, N. J. Stress fields and energy release rates in cross-ply laminates. *Int. J. Solids Structures* 1998; 35(11), 1025-1055.

Seible, F. Designing with FRP composites in the civil structural environment, FRP Composites in Civil Engineering, *Proceedings of the International Conference on FRP Composites in Civil Engineering* (*CICE 2001*), Hong Kong, China, edited by J.G. Teng, 73-84, 2001.

Shah, S.P., Swartz, S.E. and Ouyang, C. 1995. *Fracture mechanics of concrete: applications of fracture mechanics to concrete, rock, and other quasi-brittle material.* John Wiley & Sons, Inc. NY.

Shah, S.P., Swartz, S.E. and Ouyang, C. *Fracture mechanics of concrete*. John Wiley & Sons, Inc., New York, New York, 1995.

Shahawy, M.A., Arockiasamy, M., Beitelman, T. and Sowrirajan, R. Reinforced concrete rectangular beams strengthened with CFRP laminates. *Composites: Part B* 1996; 27B, 225-233.

Shahid, I. and Chang, F.K. An accumulative damage model for tensile and shear failure of laminates composite plates. *J. Composite Materials* 1995, 29: 926-981.

Sharif, A. Al-Sulaimani, G. J. Basunbul, I. A. Baluch, M. H. and Ghaleb, B. N. Strengthening of initially loaded reinforced concrete beams using FRP plates. *ACI Structural Journal* 1994a; 91(2), 160-168.

Sharif, A., Al-Sulaimani, G. J., Basunbul, I. A., Baluch, M. H. and Husain, M. Strengthening of shear-damaged RC beams by external bonding of steel plates. *Magazine of Concrete Research* 1994b; 47(173), 329-334.

Shaw, M. A. and Drewett, J.F. Case studies of carbon fibre bonding worldwide, *Strengthening of Reinforced Concrete Structures Using Externally-Bonded FRP Composites in Structural and Civil Engineering* 1999, edited by L.C.Hollaway and M.B.Leeming, Woodhead Publishing, Cambridge, UK.

Shen, H.S, Teng, J.G, Yang, J. Interfacial stresses in beams and slabs bonded with thin plate. *Journal of Engineering Mechanics ASCE* 2001; 127(4), 399-406.

Smith, P. A. and Ogin, S. L. Characterization and modeling of matrix cracking in a $(0/90)_{2s}$ GFRP laminates loaded in flexure. *Proc. R. Soc. Lond.* 2000; A456, 2755-2770.

Smith, P. A. and Ogin, S. L. On transverse matrix cracking in cross-ply laminates loaded in simples bending. *Composite: Part A* 1999; 30, 1003-1008.

Smith, S.T. and Teng, J.G. FRP Strengthened RC beam-I: review of debonding strength models. *Engineering Structures*, 2002a; 24(4), 385-395.

Smith, S.T. and Teng, J.G. FRP Strengthened RC beam-II: assessment of debonding strength models. *Engineering Structures*, 2002a; 24(4), 397-417.

Smith, S.T. Teng, J.G. Interfacial stresses in plated beams. *Engineering Structures* 2001; 23, 857-871.

Spadea, G. Bencardino, F. and Swamy, R.N. Structural behavior of composite RC beams with externally bonded CFRP. *Journal of composites for construction* 1998; 2(3), 132-137.

Spadea, G. Bencardino, F. and Swamy, R.N. Optimizing the performance characteristics of beams strengthened with bonded CFRP laminates. *Material and Structures* 2000; 33, 119-126.

Suidan, M and Schnobrich, W. C. Finite Element Analysis of Reinforced Concrete. *Journal of the Structural Division, ASCE;* 1973, ST10, 2109-2122,

Swamy, R. M. Jones, R. and Bloxham, J. W. Structural behavior of reinforced concrete beams strengthened by epoxy-bonded steel plates. *The Structural Engineer* 1987; 65A(2), 59-68.

Swamy, R. M. Jones, R. and Charif, A. Effect of external reinforcement on the strengthening of structurally damaged RC beams. *The Structural Engineer* 1989; 67(3/7), 45-56.

Swamy, R. N. and Mukhopadhyaya, *P. Discussion* of 'Flexural behavior of pre-cracked reinforced concrete beams strengthened externally by steel plates. *ACI Struct. J* 1995; 92(6), 781.

Swamy, R. N. and Mukhopadhyaya, P. Lynsdale, C.J. Strengthening for shear of RC beams by external plate bonding. *The Structural Engineer* 1999; 77(12), 19-30.

Swamy, R. N., Jones, R. Charif, A. Shear adhesion properties of epoxy resin adhesives. In: Sasse, HR, editor. *Proceedings of International Symposium on Adhesion between Polymers and Concrete*, Aix-en-Provence, 1986, organized by RILEM. London: Chapman & Hall, 1986. 741-755,

Swamy, R.N. Hobbs, B, and Roberts, M. Structural behavior of externally bonded steel plate reinforced concrete beams after long term natural exposure. *The Structural Engineer* 1995; 73(16), 255-261.

Swamy, R.N. Mukhopadhyaya, P. Debonding of carbon-fiber-reinforced polymer plates from concrete beams. Proc Instn Civ Engrs Structs & Bldgs 1999; 134, 301-317.

Takeda, K., Mitsui, Y., Murakami, K., Sakai, H. and Nakamura, M. Flexural behaviour of reinforced concrete beams strengthened with carbon fibre sheets. *Composites Part A* 1996; 27A, 981-987.

T ä ljsten, B. *Plate Bonding, Strengthening of Existing Concrete Structures with Epoxy Bonded Plates of Steel or Fibre Reinforced Plastics*. Ph.D thesis, Lulea University of Technology, 1994.

T ä ljsten, B. Strengthening of beams by plate bonding. *J Mater Civil Eng ASCE* 1997; 9(4), 206-212.

T ä ljest B, 1996. Strengthening of concrete prisms using the plate-bonding technique. *Internal Journal of Fracture*, 82: 253-266.

T ä ljsten, B. 1999. Strengthening of existing concrete structures with carbon fibre fabrics or laminates – Dimensioning, materials and execution. *An extract from Swedish National Railroad and Road Codes*, Lulea University, Sweden.

Tedesco, J. W., Stallings, J. M. and El-Mihilmy, M. Finite Element Method Analysis of a Concrete Bridge Repaired with Fiber Reinforced Plastic Laminates. *Computers and Structures*, 72, 379-407, 1999.

Teng, J.G., Chen, J.F., Smith, S.T. and Lam, L. *RC structures Strengthened with FRP Composites*. Research Center for Advanced Technology in Structural Engineering, The Hong Kong Polytechnic University, Hong Kong, China, December, 2000.

Teng, J.G., Chen, J.F., Smith, S.T. and Lam, L. *FRP strengthened RC Structures* 2001; Wiley, Chichester, U.K.

Teng, J.G., Smith, S.T., Yao, J. and Chen, J.F. Intermediate crack induced debonding in RC beams and slabs. *Proceedings of the International Conference on FRP Composites in Civil Engineering,* Hong Kong, 2001, 579-587.

Teng, J.G., Zhang, J.W. and Smith, S.T. Interfacial stresses in RC beams bonded with a soffit plate: a finite element study. *Constuction and Building Materials*, 2002; 16(1), 1-14..

Tong, J. Guild, F. J. Ogin, S. L. and Smith, P. A. On matrix crack growth in quasi-isotropic laminates-II. Finite Element Analysis. *Composites Science and Technology* 1997; 57, 1537-1545.

Trantafillou, T.C. Shear strengthening of reinforced concrete beams using epoxy-bonded FRP composites. *ACI Structural Journal* 2000; 95(2), 107-115.

Trantafillou, T. C. and Deskovic, N. and Deuring, M. Strengthening of concrete structures with prestressed fiber reinforced plastic sheets. *ACI structural Journal* 1992; 89(3), 235-244.

Trantafillou, T. C. and Deskovic, N. Innovative prestressing with FRP sheets: Mechanics of short-term behavior. *J Engrg. Mech. ASCE* 1991; 117(7), 1652-1672.

Trantafillou, T. C. Antonopoulos CP. Design of concrete flexural members strengthened with shear with FRP. *Journal of composite for construction* 2000; 4(4), 198-205.

Triantafillou, T. C. and Plevris, N. Post-strengthening of R/C beams with epoxy-bonded fiber composite materials. In: *Proceedings of the special conference on advance composite materials in civil engineering structures*, Nevada, 1991; 245-256.

Triantafillou, T. C. and Plevris, N. Strengthening of RC beams with epoxy-bonded fiber-composite materials. *Mater. Struct.* 1992; 25, 201-211.

Triantafillou, T.C. and Matthys, S. *fib* report on design of concrete members strengthened with externally bonded reinforcement, FRP Composites in Civil Engineering,

Proceedings of the International Conference on FRP Composites in Civil Engineering (*CICE 2001*), Hong Kong, China, edited by J.G. Teng, 129-136, 2001.

Tsai, M. Y. Morton, J. and Matthews, F. L. Experimental and numerical studies of a laminated composite single-lap adhesive joint. *Journal of composite materials* 1995; 29(9), 1254-1275.

Tumialan, G. Serra, P., Nanni, A. and Belarbi, A. Concrete conver delamination in reinforced concrete beams strengthened with carbon fiber reinforced polymer sheets. *Proceedings of the 4th International Symposium on Fiber Reinforced Polymer Reinforcement for Reinforced Concrete Structures* 1999a, Baltimore, Maryland, USA, edited by C.W. Dolan, S.H. Rizkalla and A.Nanni, 725-735, ACI, Farmington Hills, Michigan, USA.

Tumialan, G., Belarbi, A. and Nanni, A. *Reinforced Concrete Beams Strengthened with CFRP Composites: Failure Due to Concrete Cover Delamination*, Department of Civil Engineering, Center for Infrastructure Engineering Studies, Report No. CIES 99/01, University of Missouri-Rolla, USA 1999b.

Van Gemert, D. A. Repairing of Concrete structures by externally bonding steel plates. *Proceedings ICP/RILEM/IBK International Symposium on Plastics in Material, Prague, June 1981*. Elsevier Scientific Publishing Company, 1982; 519-526.

Varastehpour, H. and Hamelin, P. Strengthening of concrete beams using fiber-reinforced plastics. *Materials and Structures* 1997; 30, 160-166.

Vilnay, O. The analysis of reinforced concrete beams strengthened by epoxy bonded steel plates. *The international Journal of Cement Composites and lightweight Concrete* 1988; 10(2), 73-78.

Wang, A.S.D. and Crossman, F.W. Initiation and growth of transverse cracks and edge delamination in composite laminates I. An energy method. *J. Composite Materials 1*980; 14, 71-87.

Wang, C.Y. and Ling, F.S. Prediction model for the debonding failure of cracked RC beams with externally bonded FRP sheets. *Proceedings of the Second International Conference of Composites in Infrastructure (ICCI)*, 1998, Arizona, U.S.A., 548-562.

Weder, C.H. Ladner, M. Application of epoxy adhesives in the field of bonded externally reinforced concrete structures. *IABSE colloquium*, 7th-8th September 1981.

William, K. J. and Warnke, E.P. Constitutive model for the triaxial behavior of concrete, Proceedings. *International associateion for Bridge and Structural Engineering*, 19, ISMES, Bergamo, Italy, 174, 1975.

Williams, M.L. The stress around a fault or crack in dissimilar media. *Bull. Seismol. Soc. Am.* 1959; 49, 199-204.

Wu, Z.S., Yuan, H., Niu, H. Stress transfer and fracture propagation in different kinds of adhesive joints. *J Engng Mech ASCE* 2002;128(5):562– 73.

Wu, Z. J. Romeijn, A. and Wardenier, J. Stress expressions of single-lap adhesive joints of dissimilar adherends. *Composite Structures* 1997; 38(1-4), 273-280.

Wu, Z. Matsuzaki, T. and Tanabe, K. Interface crack propagation in FRP-strengthened concrete structures. *Non-metallic reinforcement for concrete structures.* Vol 1, Japan Concrete Institute 1997; 319-326.

Yang, Z. J., Chen, J. F. and Proverbs D. Finite element modelling of concrete cover separation failure in FRP plated RC beams. *Constructions and Building Material* 2003; 17 3-13.

Yang, C. and Pang, S. Stress-strain analysis of single-lap composite joints under tension. Journal of engineering materials and technology 1996; 118, 247-255.

Yang, J., Teng, J.G. and Chen, J.F. A high order closed-form solution for interfacial stresses in soffit plated RC beams under arbitrary loads, *Proceedings of the Institution of Civil Engineers – Structures and Buildings* 2004; 157(SB1): 77-89.

Yang, J. and Ye, J. Q. Interfacial stresses in plated beams with cracks. Composite Structures 2002; 57(14), 125-134.

Yang, J., Ye, J. Q. A parametric study to interfacial shear stress in FRP-plated RC beams. 2004, Submitted.

Yang, J., Chen, J.F. and Teng, J.G. Interfacial Stresses in Plated RC Beams under Arbitrary Symmetric Loads: a High-Order Closed-Form Solution. In: *Proceedings of Advanced Polymer Composites for Structural Applications in Construction*, Southampton, 2002.

Ye, J.Q. Interfacial shear transfer of RC beams strengthened by bonded composite plates. *Cement and Concrete Composite* 2001; 23, 411-417.

Ye, J, Yang, J and Liew K. M. Stress transfer in cross-ply laminates with transverse matrix cracks. Submitted.

Yuan, H. Teng, J.G. et al. 2004. Full-range behavior of FRP-to-concrete bonded joints. *Engineering Structures* 26: 553-565.

Zhang, J.P. Diagonal cracking and shear strength of reinforced concrete beams. *Magazine of Concrete Research* 1997; 49, 178, 55-65.

Zhang, S., Raoof, M. and Wood, L. A. Prediction of peeling failure of reinforced concrete beams with externally bonded steel plates. *Proc. Instn Civ. Engrs Structs. & Bldgs.* 1995; 110, 257-268.

Zhao, M., Zhao, Y. and Ansari, F. Debonding failure of reinforced concrete beams strengthened with external CFRP fabric. *Proceedings of the International Conference on FRP Composites in Civil Engineering* (*CICE 2001*), Hong Kong, China, 2001, edited by J.G. Teng, 597-605.

Ziraba, Y.N. Baluch, M.H. Computational model for reinforced concrete beams strengthened by epoxy bonded steel plates. *Finite Elements in Analysis and Design* 1995; 20, 253-271.

Ziraba, Y.N. et al. Guidelines toward the design of reinforced concrete beams with external plates. *ACI Structural Journal* 1994; 91(6), 639-646.